Dielectric Resonator Antennas

Edited by

Kwai-Man Luk and
Kwok-Wa Leung

Dielectric Resonator Antennas

**ELECTRONIC & ELECTRICAL ENGINEERING
RESEARCH STUDIES**

Series Editor: **Professor J. R. James**
*The Royal Military College of Science
(Cranfield University), Shrivenham, Wiltshire,UK*

Dielectric Resonator Antennas

Edited By

K. M. Luk
and
K. W. Leung
Both of the City University of Hong Kong

Marketing:

Distribution:

Editorial Foreword

There is now a massive research literature on the Dielectric Resonator Antenna (DRA) giving ample evidence that the topic has reached an age of maturity. This new book is therefore very timely and fills a gap in the literature. In fact the absence of any such reference book to date, that collates research findings and significant achievements, is somewhat surprising in view of the growing interest in DRAs. Like microstrip antennas, DRAs offer many degrees of design freedom and exploit the properties of innovative materials that make possible the manufacture of stable low cost products. Again, like microstrip antennas, DRAs evolved from components in shielded microwave circuits where radiation is an unwanted by-product. Making use of the latter to create the DRA illustrates once again the ingenuity of antenna designers.

The reader will find the book coverage both wide and deep, with copious details of how to analyse and efficiently compute numerous DRA shapes and feeding arrangements. Engineering design data on extending the bandwidth and controlling the radiation pattern characteristics are focussed on throughout and specific chapters address DRA arrays and leaky-wave derivatives. When I visited the City University of Hong Kong in 1999 I was most impressed with Professor Luk's research leadership and the dynamic environment in which he is working. Without doubt the enthusiasm of Kwai Man Luk and Kwok Wa Leung has energised both the writing of this book and their team of distinguished authors, many of whom, if not most, have made foremost contributions to this field of research.

The book will have widespread appeal to postgraduate researchers, antenna design engineers in general and particularly those engaged in the innovative design of mobile and wireless/Bluetooth systems. May I congratulate Professor Luk and Dr Leung and their co-authors on the production of this significant text, which will be a milestone in the advancement of the DRA concept and of great benefit to the international antenna community.

Professor Jim R James
April 2003

Preface

The field of wireless communications has been undergoing a revolutionary growth in the last decade. This is attributed to the invention of portable mobile phones some 15 years ago. The success of the second-generation (2G) cellular communication services motivates the development of wideband third-generation (3G) cellular phones and other wireless products and services, including wireless local area networks, home RF, Bluetooth, wireless local loops, local multi-point distributed networks (LMDS), to name a few. The crucial component of a wireless network or device is the antenna. Very soon, our cities will be flooded with antennas of different kinds and shapes. On the other hand, for safety and portability reasons, low power, multi-functional and multi-band wireless devices are highly preferable. All these stringent requirements demand the development of highly efficient, low-profile and small-size antennas that can be made imbedded into wireless products.

In the last 2 decades, two classes of novel antennas have been investigated and extensively reported on. They are the microstrip patch antenna and the dielectric resonator antenna. Both are highly suitable for the development of modern wireless communications.

The use of a dielectric resonator as a resonant antenna was proposed by Professor S. A. Long in the early nineteen eighties. Since the dielectric resonator antenna has negligible metallic loss, it is highly efficient when operated at millimetre wave frequencies. Conversely, a high-permittivity or partially-metallised dielectric resonator can be used as a small and low-profile antenna operated at lower microwave frequencies. Low loss dielectric materials are now easily available commercially at very low cost. This would attract more system engineers to choose dielectric resonator antennas when designing their wireless products.

Although dielectric resonator antennas are so promising in practical applications, surprisingly, no edited books or reference books summarising the research results on dielectric resonator antennas are available in the literature. Actually, hundreds of articles on the design and analysis of dielectric resonator antennas can be found in reputable international journals or in major international conference proceedings. It is the objective of this edited book to update and to present new information on dielectric resonator antennas. We have been very fortunate to receive contributions from most of the distinguished scholars working in this exciting area. The book is intended to serve as a compendium of essential

principles, design guidelines and references for practicing engineers, research engineers, graduate students and professors specialising in the areas of antennas and RF systems.

The book was organised into a coherent order of proper perspectives, although we have over 10 contributors reviewing mainly their individual contributions. A historical perspective on the development of dielectric resonator antennas is provided in Chapter 1. Chapter 2 to 4 are more on rigorous analysis of dielectric resonator antennas of different geometries; in particular Chapter 2 on rectangular shapes, Chapter 3 on hemispherical shapes and Chapter 4 on cylindrical shapes. Although some wideband dielectric resonator antenna structures are introduced in these chapters, Chapter 5 reviews, in more detail, different bandwidth enhancement techniques, including the reduction of Q-factor by loading effect, the employment of matching networks, and the use of multiple resonators. In this era of wireless communications, low-profile and small-size antennas are highly preferable for mobile devices, such as cellular phones, notebook computers, personal digital assistant (PDA), etc. The design of low-profile dielectric resonator antennas is presented in Chapter 6, while the development of small compact circular sectored dielectric resonator antennas is described in Chapter 7. In these two chapters, techniques for the generation of circular polarisation are also included.

For applications requiring high-gain antennas, dielectric resonator antenna arrays may be a good choice. Chapter 8 introduces a new perpendicular feed structure suitable for antenna arrays with active circuits. Detailed study on linearly-polarised and circularly-polarised dielectric resonator arrays are reviewed in Chapter 9. A section of a non-radiative dielectric (NRD) guide can be considered as a rectangular dielectric resonator sandwiched between two parallel plates. With the introduction of an aperture-coupled microstripline feed, this simple structure, as described in Chapter 10, becomes an efficient antenna element with reasonably high gain. This novel antenna, which is leaky and resonant in nature, is designated as a NRD resonator antenna. Due to its low-loss characteristic, the antenna is highly attractive for wideband mobile communication systems operated at millimetre waves.

Kwai Man Luk and Kwok Wa Leung
April 2003

This page intentionally left blank

Contents

CHAPTER 3   **Analysis of Multi-Layer Hemispherical DR Antennas By Kin-Lu Wong**

CHAPTER 4   **Body of Revolution (BOR) - Analysis of Cylindrical Dielectric Resonator Antennas By Ahmed A. Kishk**

CHAPTER 5   Broadband Dielectric Resonator Antennas
By Aldo Petosa, Apisak Ittipiboon, Yahia Antar

CHAPTER 6   Low-Profile Dielectric Resonator Antennas
By Karu Esselle

CHAPTER 7   **Compact Circular Sector and Annular Sector Dielectric Resonator Antennas For Wireless Communication Handsets By R. D. Murch and T. K. K. Tam**

CHAPTER 8   **Feeding Methods for the Dielectric Resonator Antenna:**
            Conformal Strip and Aperture Coupling with a
            Perpendicular Feed
            By K. W. Leung

CHAPTER 9   **Dielectric Resonator Antenna Arrays**
            By Z. Wu

Abbreviations and Symbols

AF	array factor
AR	axial ratio
BOR	body of revolution
BW	bandwidth
CP	circular polarisation
CPW	co-planar waveguide
Copol	co-polarisation
dB	decibel
D	diffraction coefficient
DBOR	dielectric body of revolution
DOA	direction of arrival
DR	dielectric resonator
DRA	dielectric resonator antenna
E	electric field
f	frequency
F	normalised frequency
FDTD	finite-difference time-domain
FEM	finite-element method
GO	geometric optics
GPS	global positioning system
GSM	group special mobile
GTD	geometric theory of diffraction
H	magnetic field
HE	hybrid electric
HEM	hybrid electromagnetic
HFSS	high frequency structure simulator
$\hat{H}_n^{(2)}(x)$	Schelkunoff-type spherical Hankel function of the second kind of order n
$J_n(x)$	cylindrical Bessel function of order n
$\hat{J}_n(x)$	Schelkunoff-type spherical Bessel function of the first kind of order n
k	wave number
LAN	local area network
LP	linear polarisation
LHCP	left-hand circular polarisation
LNA	low-noise amplifier
LSE	longitudinal section electric

LSM	longitudinal section magnetic
ME	modal expansion
MoM	method of moments
MSDRA	multi-segment dielectric resonator antenna
NRD	non-radiative dielectric
$P_n(x)$	Lengendre polynominal of order n
$P_n^m(x)$	associated Lengendre function of the first kind of order m and degree n
PCS	personal communication system
PD	phase detector
PMWM	perfect magnetic wall model
PWS	piecewise sinusoidal
Q-factor	quality factor
RF	radio frequency
RHCP	right-hand circular polarisation
SDM	spectral domain method
SWR	standing-wave ratio
TE	transverse electric
TEM	transverse electromagnetic
TLM	transmission line method
TM	transverse magnetic
VSWR	voltage standing wave ratio
XDRA	cross dielectric resonator antenna
Xpol	cross-polarisation
Z	impedance

CHAPTER 1

Overview of the Dielectric Resonator Antenna

Kowk Wa Leung* and Stuart A. Long[+]

* Department of Electronic Engineering
  City University of Hong Kong
  Kowloon, Hong Kong SAR

+ Department of Electrical and Computer Engineering
  University of Houston
  TX 77204-4005, USA

1.1   INTRODUCTION

For many years, the dielectric resonator (DR) has primarily been used in microwave circuits, such as oscillators and filters [1], where the DR is normally made of high-permittivity material, with dielectric constant $\varepsilon_r > 20$. The unloaded Q-factor is usually between 50 and 500, but can be as high as 10,000. Because of these traditional applications, the DR was usually treated as an energy storage device rather than as a radiator. Although open DRs were found to radiate many years ago [2-4], the idea of using the DR as an antenna had not been widely accepted until the original paper on the cylindrical dielectric resonator antenna (DRA) [5] was published in 1983. At that time, it was observed that the frequency range of interest for many systems had gradually progressed upward to the millimeter and near-millimeter range (100-300 GHz). At these frequencies, the conductor loss of metallic antennas becomes severe and the efficiency of the antennas is reduced significantly. Conversely, the only loss for a DRA is that due to the imperfect dielectric material, which can be very small in practice. After the cylindrical DRA had been studied [5], Long and his colleagues subsequently investigated the rectangular [6] and hemispherical [7] DRAs. The work created the foundation for future investigations of the DRA. Other shapes were also studied, including the triangular [8], spherical-cap [9], and cylindrical-ring [10-11] DRAs. Fig. 1.1 shows a photo of various DRAs. It was found that DRAs operating at their fundamental modes radiate like a magnetic dipole, independent of their shapes. A few DR suppliers are listed in Table 1.1, where the materials and dielectric constants of the DRs are also shown.
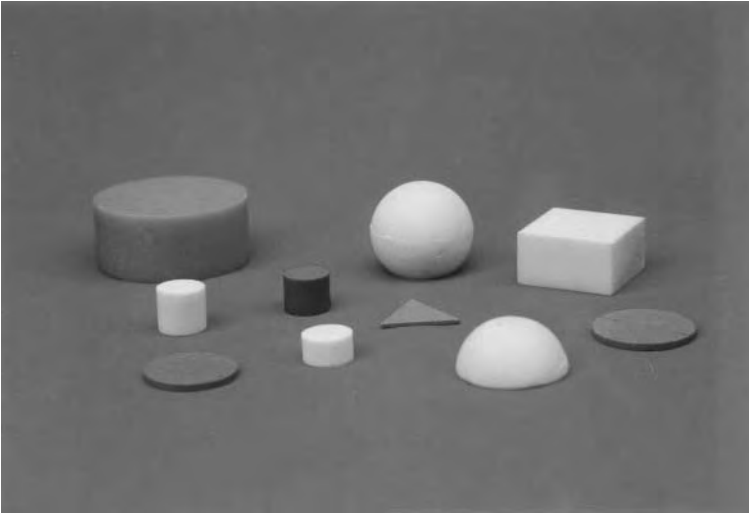
Fig. 1.1   DRAs of various shapes. The photo shows cylindrical, rectangular, hemispherical, low-profile circular-disk, low-profile triangular, and spherical-cap DRAs.

As compared to the microstrip antenna, the DRA has a much wider impedance bandwidth (~ 10 % for dielectric constant ε_r ~ 10). This is because the microstrip antenna radiates only through two narrow radiation slots, whereas the DRA radiates through the whole DRA surface except the grounded part. Avoidance of surface waves is another attractive advantage of the DRA over the microstrip antenna. Nevertheless, many characteristics of the DRA and microstrip antenna are common because both of them behave like resonant cavities. For example, since the dielectric wavelength is smaller than the free-space wavelength by a factor of $1/\sqrt{\varepsilon_r}$, both of them can be made smaller in size by increasing ε_r. Moreover, virtually all excitation methods applicable to the microstrip antenna can be used for the DRA. The basic principle and mode nomenclatures of the DRA were discussed in a previous review paper [12] and will not be repeated here. Instead, this Chapter will present the development of the DRA, including sections on approximate analyses, linearly polarised (LP) DRAs, circularly polarised (CP) DRAs, broadband DRAs, and arrays of these elements. In the next section, we will review approximate analyses for the cylindrical and hemispherical DRAs.

Company	Material	Dielectric Constant
Countis Laboratories	CD-Series (solid state solutions of magnesium, calcium, silicon, and titanium oxides)	6.3 − 140.0
Emerson & Cuming (Materials not specified)	Eccostock	3 − 30
Hiltek Microwave Ltd.	Magnesium Manganese Aluminum Iron Ferrite	9.2 (+/- 0.46)
	Magnesium Titanate	16.0 (± 0.8)
	Lithium Ferrite	20.0 (± 1)
	Zirconium Tin Titanate	37.0 (± 1)
	Titania Ceramic	80 − 100
Morgan Electro Ceramics	Zr, Sn titanate	37
	Mg, Ca titanate	20
	Ba, Nd titanate	88
	Ba, Zn titanate	30
	Steatile	6
Murata (Materials not specified)	U series	36.6 − 38.9 (± 0.5)
	M series	37.7 − 39.2 (± 1)
	V series	33.5 − 35.1 (± 0.5)
	R series	29.7 − 31.5 (± 0.8)
	B series	27.9 ± 0.5
	E series	24.2 − 24.9 (± 0.4)
	F series	23.8 − 24.2 (± 0.5)
	Dielectric substrate	38 − 92 (± 1)
Pacific Ceramics, Inc. (Materials not specified)	PD-Series	6.5 − 270
Temex Components & Temex Telecom	$(Zr, Sn, Ti) O_4$	37.3 − 37.7
	Ba, Zn, Ta, O	29.5 − 32
	Ba, Sm, Ti	78 ± 0.5
Trans-Tech	Zirconium titanate based	44.7 − 46.2
	Ba, Zn, Ta-oxide	29.0 − 30.7
	Barium titanate	35.0 − 36.5
	Ba, Zn, Ta-oxide (perovskite)	29.5 − 31.0

Table 1.1   Some DR suppliers, along with the materials and dielectric constants of their DRs.

This book has ten chapters on various topics concerning the DRA. For quick reference, Table 1.2 lists some sections of those chapters that address bandwidth, efficiency, and radiation patterns in a more detailed fashion.

	Section
Bandwidth	2.3.3, 3.2.3, 3.3.2, 5.2-5.5, 6.2.1, 7.3.4, 10.2.2.1, 10.3.1.1, 10.3.2.1
Efficiency	2.7, 9.3, 9.4
Radiation Pattern	2.4, 2.5, 3.2.3, 4.5, 5.3 – 5.5, 6.2.1, 6.3-6.7, 7.4.4, 7.4.5, 9.2.2, 9.3-9.5, 10.2.1.2, 10.3.2.1

Table 1.2   Quick references for bandwidth, efficiency, and radiation pattern.

1.2   EXCITATION METHODS APPLIED TO THE DRA

A number of excitation methods have been developed. Examples are the coaxial probe [5-7, 13-15], aperture-coupling with a microstrip feedline [8, 9, 15-23], aperture-coupling with a coaxial feedline [24, 25], direct microstrip feedline [26, 27], co-planar feed [28], soldered-through probe [11], slotline [29], stripline [30], conformal strip [31-33], and dielectric image guide [34]. A photo of the coaxial probe excitation scheme is shown in Fig. 1.2, and that of the aperture-coupling excitation scheme is given in Fig. 1.3. Some of the feeding methods are addressed in Chapter 2, whereas the rigorous analyses of the aperture coupling with a perpendicular feed [22] and conformal strip feed [31] are presented in Chapter 8.

1.3   ANALYSES OF THE DRA

1.3.1   Cylindrical DRA

A simple analysis for the cylindrical DRA was carried out in [5] using the magnetic wall model. Fig. 1.4 shows the DRA configuration, along with standard cylindrical coordinates.

1.3.1.1   Resonant frequencies

In the analysis, the DRA surfaces are assumed to be perfect magnetic conductors, with the feed probe temporarily ignored. For such a cavity, wave functions which are transverse electric (TE) to z and transverse magnetic (TM) to z can be written as

$$\psi_{\mathrm{TE}_{npm}} = J_n\left(\frac{X_{np}}{a}\rho\right)\begin{Bmatrix}\sin n\phi \\ \cos n\phi\end{Bmatrix}\sin\left[\frac{(2m+1)\pi z}{2d}\right] \tag{1.1}$$

$$\psi_{\mathrm{TM}_{npm}} = J_n\left(\frac{X'_{np}}{a}\rho\right)\begin{Bmatrix}\sin n\phi \\ \cos n\phi\end{Bmatrix}\cos\left[\frac{(2m+1)\pi z}{2d}\right] \tag{1.2}$$
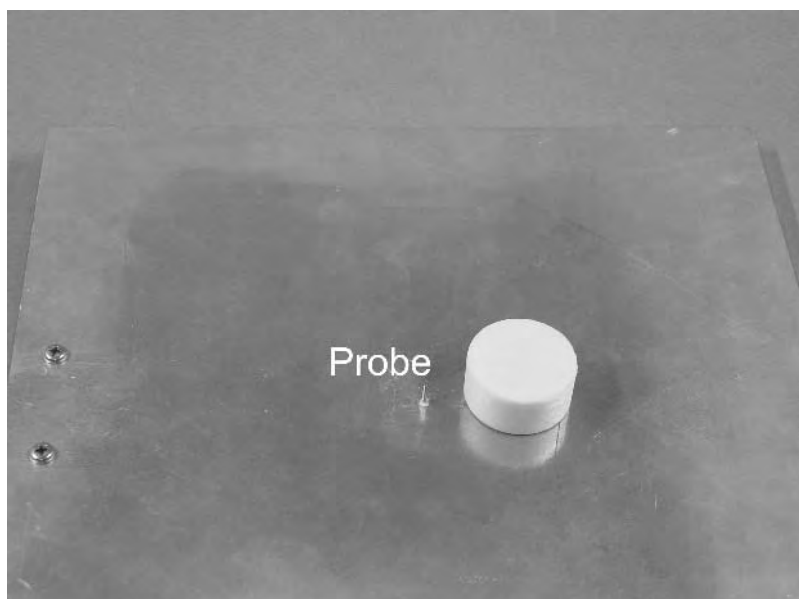
(a)
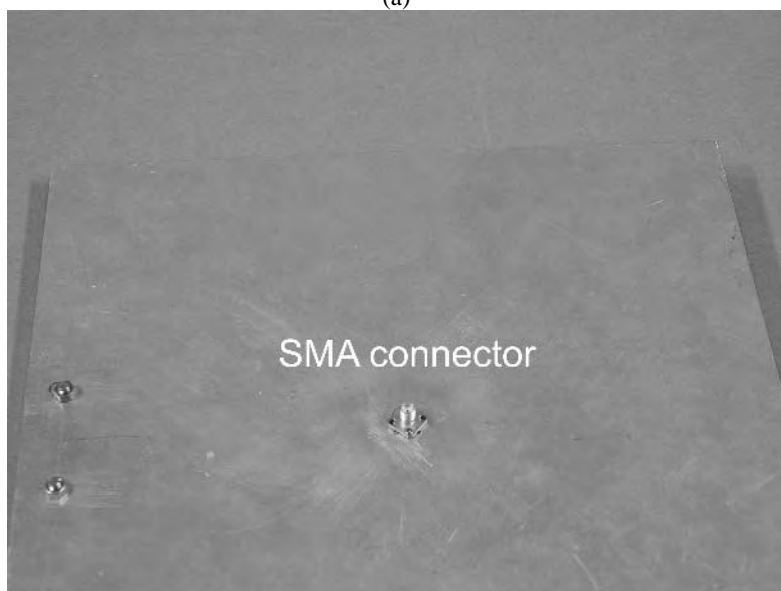
(b)

Fig. 1.2   Photos of a probe-fed DRA. (a) Above the ground plane are the coaxial probe and DRA. (b) Below the ground plane is the SMA connector for the coaxial probe. Normally the probe is inside the DRA.
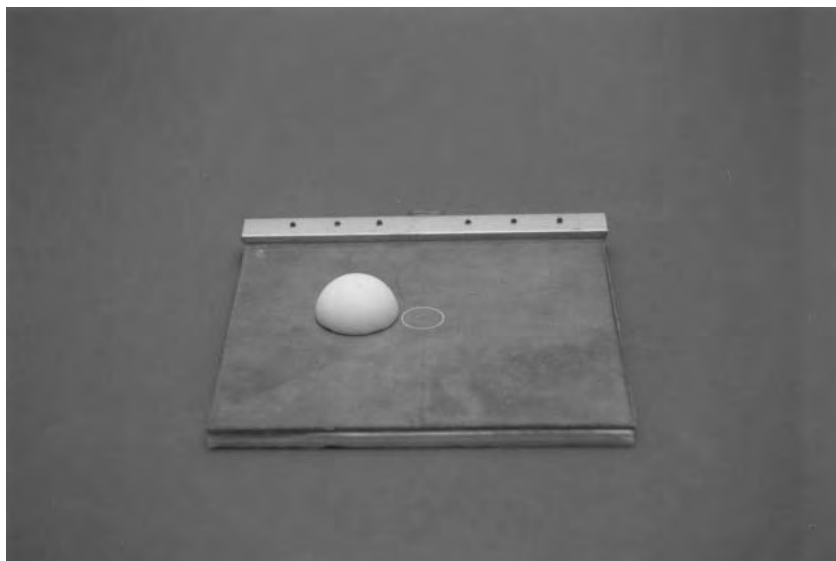
(a)
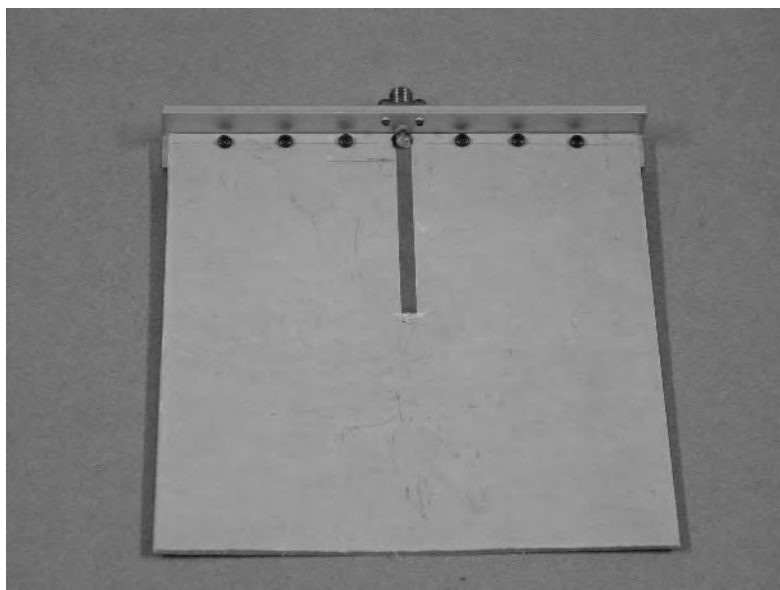
(b)

Fig. 1.3 Photos of an aperture-coupled DRA. (a) Above the ground plane are the circular aperture and DRA. (b) Below the ground plane is the microstrip feedline. Normally the DRA covers the aperture.

where J_n is the Bessel function of the first kind, with $J_n(X_{np}) = 0, J'_n(X'_{np}) = 0, n = 1,$ 2, 3, $\cdots$, $p = 1, 2, 3, \cdots$, $m = 0, 1, 2, 3, \cdots$

From the separation equation $k_\rho^2 + k_z^2 = k^2 = \omega^2 \mu \varepsilon$, the resonant frequency of the npm mode can be found as follows:

$$f_{npm} = \frac{1}{2\pi a \sqrt{\mu \varepsilon}} \sqrt{\left\{ \begin{matrix} X_{np}^2 \\ X'_{np}^2 \end{matrix} \right\} + \left[\frac{\pi a}{2d} (2m+1) \right]^2} \qquad (1.3)$$

In practical applications, we are interested in the fundamental (dominant) mode, which has the lowest resonant frequency. It is found that the fundamental mode is the TM_{110} mode, with the resonant frequency given by

$$f_{TM_{110}} = \frac{1}{2\pi a \sqrt{\mu \varepsilon}} \sqrt{X_{11}'^2 + \left(\frac{\pi a}{2d} \right)^2} \qquad (1.4)$$

where $X'_{11} = 1.841$.
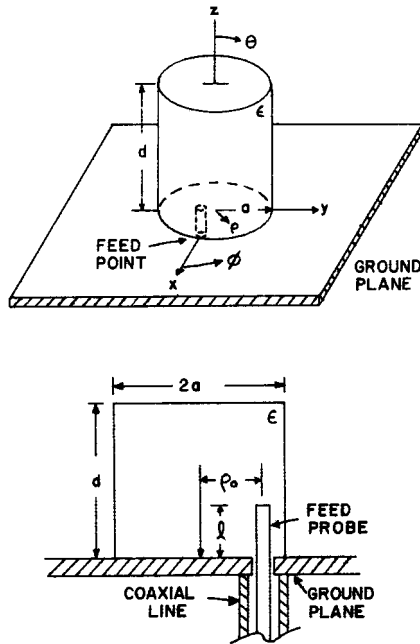
Fig. 1.4 The geometry of cylindrical DRA. (From [5], © 1983 IEEE)

1.3.1.2   Equivalent magnetic surface currents

The TM_{110}-mode fields inside the cylindrical DRA are used for the derivation of the far-field expressions. To begin, the wave function of the fundamental TM_{110} mode is found:

$$\psi_{TM_{110}} = \psi = J_1\left(\frac{X'_{11}\rho}{a}\right)\cos\phi\cos\frac{z\pi}{2d} \tag{1.5}$$

The $\cos\phi$ term is selected because the feed position is at $\phi = 0$. Conversely, the $\sin\phi$ term should be used if the probe is located at $\phi = \pi/2$. From the wave function, the various E-fields can be easily found:

$$E_\phi = \frac{1}{j\omega\varepsilon\rho}\frac{\partial^2\psi}{\partial\phi\partial z},\ E_z = \frac{1}{j\omega\varepsilon}\left(\frac{\partial^2}{\partial z^2}+k^2\right)\psi,\ E_\rho = \frac{1}{j\omega\varepsilon}\frac{\partial^2\psi}{\partial\rho\partial z} \tag{1.6}$$

Use is made of the equivalence principle to find the equivalent magnetic currents on the DRA surfaces. The equivalent currents will be treated as the radiating sources for the radiation fields. In the following expressions, the primed and unprimed coordinates are used to indicate the source and field, respectively. From $\vec{M} = \vec{E}\times\hat{n}$, where $\hat{n}$ is a unit normal pointing out of the DRA surface, the following equivalent currents are obtained:

(i)   for the side wall

$$M_{z'} = \frac{\pi}{2j\omega\varepsilon ad}J_1(X'_{11})\sin\phi'\sin\frac{\pi z'}{2d} \tag{1.7}$$

$$M_{\phi'} = \frac{1}{j\omega\varepsilon}\left(\frac{X'_{11}}{a}\right)^2 J_1(X'_{11})\cos\phi'\cos\frac{\pi z'}{2d} \tag{1.8}$$

(ii) for the top and bottom

$$M_{\phi'} = \frac{\pi X'_{11}}{2j\omega\varepsilon ad}J'_1\left(\frac{X'_{11}\rho'}{a}\right)\cos\phi' \tag{1.9}$$

$$M_{\rho'} = \frac{\pi}{2j\omega\varepsilon d\rho'}J_1\left(\frac{X'_{11}\rho'}{a}\right)\sin\phi' \tag{1.10}$$

1.3.1.3   Far-field patterns

Usually, radiation fields are expressed in spherical coordinates $(r,\ \theta,\ \phi)$. Therefore the source currents are transformed:

$$M_\theta = M_{\rho'}\cos\theta\cos(\phi-\phi')+M_{\phi'}\cos\theta\sin(\phi-\phi')-M_{z'}\sin\theta \tag{1.11}$$

$$M_\phi = -M_{\rho'}\sin(\phi-\phi')+M_{\phi'}\cos(\phi-\phi') \tag{1.12}$$

The transformed currents are used in calculations of the electric vector potentials:

$$F_\theta = \frac{e^{-jk_0 r}}{4\pi r} \iiint M_\theta e^{jk_0[\rho'\sin\theta\cos(\phi-\phi')+z'\cos\theta]} \rho' d\rho' d\phi' dz \tag{1.13}$$

$$F_\phi = \frac{e^{-jk_0 r}}{4\pi r} \iiint M_\phi e^{jk_0[\rho'\sin\theta\cos(\phi-\phi')+z'\cos\theta]} \rho' d\rho' d\phi' dz \tag{1.14}$$

where $k_0 = \omega\sqrt{\mu_0 \varepsilon_0}$ is the free space wavenumber. It can be shown that the electric potentials are given by

$$F_\theta = C_1 \{I_2 - I_1 - 0.5k_\rho (I_3 + I_4 - I_5 - I_6) + 1.16k_0 \sin\theta J_1(k_0 a \sin\theta)D_1 - 0.581k_\rho^2 a$$
$$\cdot [J_0(k_0 a \sin\theta) + J_2(k_0 a \sin\theta)]D_1\} \tag{1.15}$$

$$F_\phi = C_2 \{-I_1 - I_2 - 0.5k_\rho (I_3 - I_4 - I_5 + I_6) - 0.581k_\rho^2 a [J_0(k_0 a \sin\theta) - J_2(k_0 a \sin\theta)] D_1\} \tag{1.16}$$

where

$$C_1 = \frac{\pi^2}{j\omega\varepsilon d} \frac{1}{4\pi r} \sin\phi \cos(k_0 d \cos\theta)\cos\theta \tag{1.17}$$

$$C_2 = \frac{\pi^2}{j\omega\varepsilon d} \frac{1}{4\pi r} \cos\phi \cos(k_0 d \cos\theta) \tag{1.18}$$

$$D_1 = \left[\frac{\pi^2}{4d^2} - k_0^2 \cos^2\theta\right]^{-1} \tag{1.19}$$

$$k_\rho = \frac{X'_{11}}{a} = \frac{1.841}{a} \tag{1.20}$$

$$I_1 = \int_0^a J_1(k_\rho \rho') J_0(k_0 \rho' \sin\theta)d\rho' \tag{1.21}$$

$$I_2 = \int_0^a J_1(k_\rho \rho') J_2(k_0 \rho' \sin\theta)d\rho' \tag{1.22}$$

$$I_3 = \int_0^a J_0(k_\rho \rho') J_0(k_0 \rho' \sin\theta)\rho' d\rho' \tag{1.23}$$

$$I_4 = \int_0^a J_0(k_\rho \rho') J_2(k_0 \rho' \sin\theta)\rho' d\rho' \tag{1.24}$$

$$I_5 = \int_0^a J_2(k_\rho \rho') J_0(k_0 \rho' \sin\theta)\rho' d\rho' \tag{1.25}$$

$$I_6 = \int_0^a J_2(k_\rho \rho') J_2(k_0 \rho' \sin\theta)\rho' d\rho'. \tag{1.26}$$

In the far-field region, the electric fields E_θ, E_ϕ are proportional to the vector potentials F_ϕ, F_θ, respectively, i.e., $E_\theta \propto F_\phi$ and $E_\phi \propto F_\theta$.

1.3.1.4 Results

1.3.1.4.1 Input impedance and resonant frequency

Since the input impedance cannot be calculated using the magnetic wall model, the input impedance studied in [5] was solely experimental. Four cylindrical DRAs of dielectric constant $\varepsilon_r = 8.9$ were fabricated with radius-to-height ratios $a/d = 0.3$, 0.5, 1.67, and 0.15. Each DRA was fed near its edge by a coaxial probe that extended $l = 0.38$ cm into the DRA. The results are reproduced in Fig. 1.5. Note that for $a/d = 0.15$ (Fig. 1.5 d) the first two modes, TM_{110} and TM_{111} modes, are very close to each other in frequency, corresponding to the predicted values of 9.90 and 10.52 GHz, respectively.
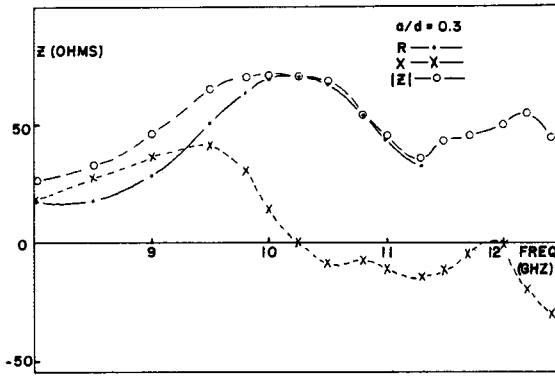
(a)
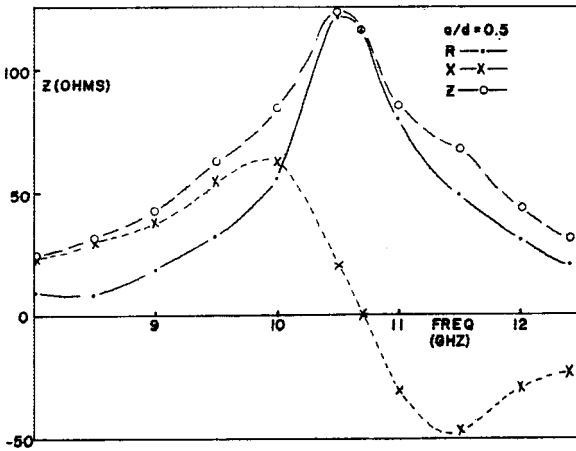
(b)
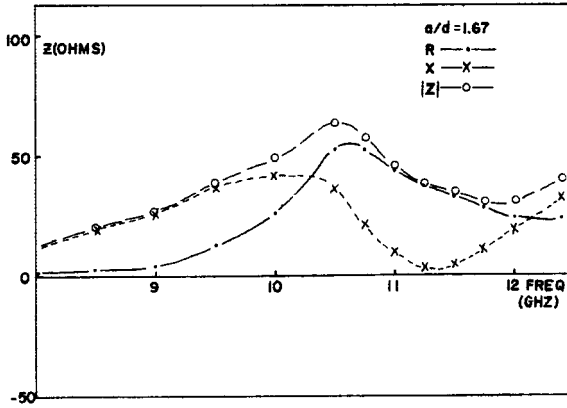
(c)
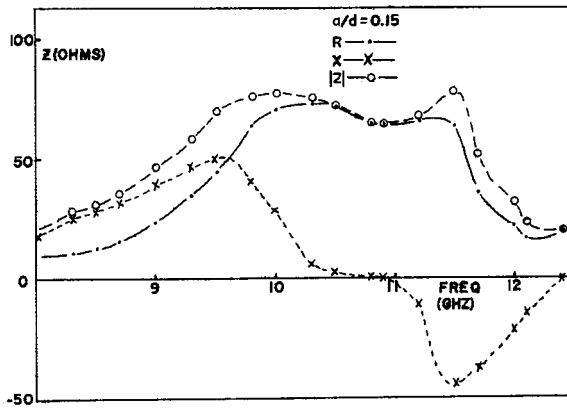
(d)

Fig. 1.5   Measured impedance versus frequency for various a/d ratios: $\varepsilon_r = 8.9$. (a) $a/d = 0.3$ (b) $a/d = 0.5$ (c) $a/d = 1.67$ (d) $a/d = 0.15$. (From [5], © 1983 IEEE)

Table 1.3 compares the calculated and measured TM_{110}-mode resonant frequencies for the four DRAs. As can be observed from the previous figure, the input reactance has an upward shift due to the inductive loading of the probe. Consequently, the frequency at which the input resistance is a maximum does not coincide with the zero-reactance frequency. In the table, each measured frequency

was taken at the point where the resistance is a maximum, and good agreement between theory and experiment is obtained.

Sample no.	a (cm)	d (cm)	a/d	Calculated f_r ,GHz	Measured f_r ,GHz
1	0.3	1.0	0.3	10.13	~10.1
2	0.3	0.6	0.5	10.67	~10.5
3	0.5	0.3	1.67	10.24	~10.5
4	0.3	2.0	0.15	9.90	~9.9

Table 1.3 Comparison between calculated and measured resonant frequencies.

1.3.1.4.2 Radiation patterns

Fig. 1.6 shows the calculated and measured field patterns for the four cylindrical DRAs. Reasonable agreement is observed for the first three DRAs, with the only differences being some scalloping and a roll-off near $\theta = 90^o$ for the measured values of E_θ due to the finite ground plane. For the last case of $a/d = 0.15$, a dip near $\theta = 0^o$ is observed in both the measured and calculated results.
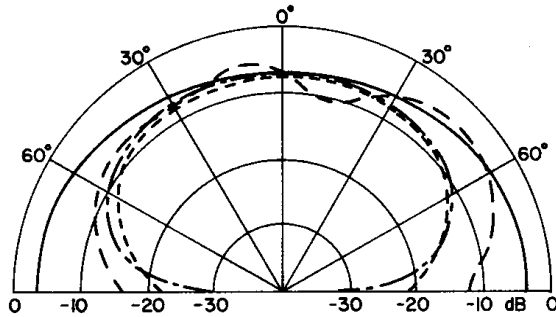
(a)
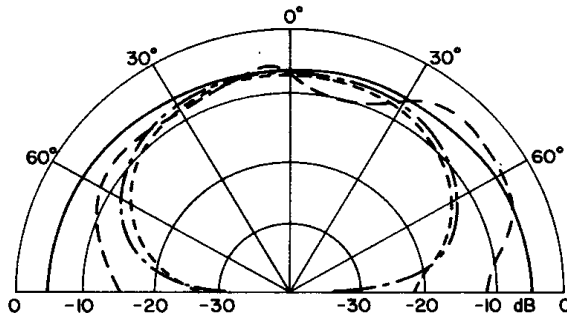
(b)
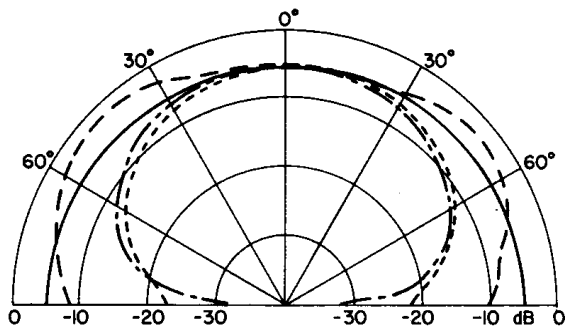
(c)
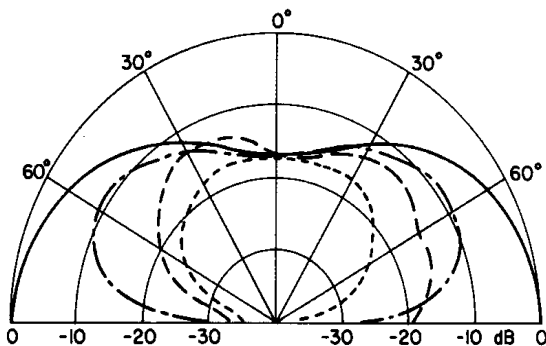
(d)

Fig. 1.6   Measured and calculated fields of various *a/d* ratios: (a) *a/d* = 0.3 (b) *a/d* = 0.5 (c) *a/d* = 1.67 (d) *a/d* = 0.15.   (From [5], © 1983 IEEE)

E_θ: ———————— Theory E_θ: – – – – – – – – – Experiment

E_ϕ: ·············· Theory E_ϕ: ······························ Experiment

A rigorous analysis of the cylindrical DRA was carried out by Junker *et al.* [13] using the body of revolution (BOR) method. Details of the analysis can be found in Chapter 4. Alternatively, Shum and Luk used the finite-difference time-domain (FDTD) method [14, 15] to analyze the cylindrical DRA.

1.3.2   Hemispherical DRA

As mentioned previously, the magnetic wall model cannot be used to calculate the input impedance of the DRA. Leung *et al.* [35] carried out the first theoretical analysis of the input impedance for the hemispherical DRA. Fig. 1.7 shows the configuration. The hemisphere offers an advantage over the rectangular and

cylindrical shapes in that the interface between the dielectric and air is simpler; and thus, a closed form expression can be obtained for the Green's function.
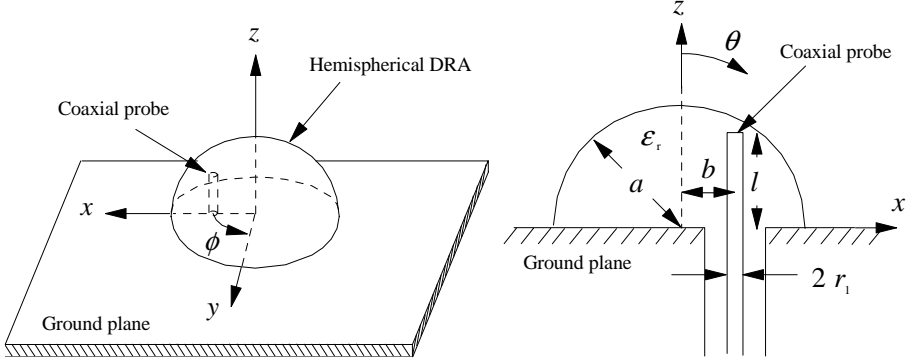
Fig. 1.7   Configuration of a probe-fed hemispherical DRA. (From [36], © 1993 IEEE)

The theory is summarised here. The field and source points are denoted by $\vec{r}(r,\theta,\phi)$ and $\vec{r}'(r',\theta',\phi')$, respectively. To begin, the image theory is employed. The z-directed current is resolved into the θ- and r-directed components. Since a θ-directed current will excite both TE and TM to r modes, the magnetic potential, F_r, as well as the electric potential, A_r, are required to represent all possible fields. Conversely, an r-directed current can excite only TM to r modes, and therefore only the electric potential is required in this case. Each potential function is represented by an infinite series of modal functions. The modal coefficients are then obtained by matching the boundary conditions at the source point and on the DRA surface. The detailed analysis can be found in [36].

1.3.2.1   Single TE$_{111}$-mode approximation
At frequencies around the TE$_{111}$-mode resonance, we may take the single-mode approximation [35, 37]. As a result, the z-component of the E-field Green's function inside the DRA is given by ($r < a$):

$$G_{\text{TE}_{111}} = \frac{-3k}{8\pi\omega\varepsilon rr'}\sin\theta\sin\theta'\cos(\phi-\phi')\Big[\Phi(kr')\Psi(kr)+\alpha_{TE}\hat{J}_1(kr')\hat{J}_1(kr)\Big] \quad (1.27)$$

where

$$\Phi(kr) = \begin{cases} \hat{J}_1(kr'), & r > r' \\ \hat{H}_1^{(2)}(kr'), & r < r' \end{cases} \quad (1.28)$$

$$\Psi(kr) = \begin{cases} \hat{H}_1^{(2)}(kr), & r > r' \\ \hat{J}_1(kr), & r < r' \end{cases} \quad (1.29)$$

$$\alpha_{TE} = \frac{-1}{\Delta_{TE}} \left[\hat{H}_1^{(2)}(ka)\hat{H}_1^{(2)\prime}(k_0 a) - \sqrt{\varepsilon_r}\,\hat{H}_1^{(2)\prime}(ka)\hat{H}_1^{(2)}(k_0 a) \right] \qquad (1.30)$$

$$\Delta_{TE} = \hat{J}_1(ka)\hat{H}_1^{(2)\prime}(k_0 a) - \sqrt{\varepsilon_r}\,\hat{J}_1{}'(ka)\hat{H}_1^{(2)}(k_0 a) \qquad (1.31)$$

with $k_0 = \omega\sqrt{\mu_0 \varepsilon_0}$ and $k = \sqrt{\varepsilon_r}\,k_0$. In the above expressions, $\hat{j}_1(x)$ and $\hat{H}_1^{(2)}(x)$ are the first-order spherical Bessel function of the first kind and spherical Hankel function of the second kind, respectively. A prime denotes a derivative with respect to the whole argument, except that r' denotes the source point. From the Green's function $G_{\mathrm{TE}_{111}}$, the z-directed electric field E_z due to the probe current J_z can be evaluated as follows:

$$E_z(\vec{r}) = \iint_{S_0} G_{\mathrm{TE}_{111}}(\vec{r},\vec{r}')J_z(z')dS' \qquad (1.32)$$

where

$$J_z(z') = J_0 \sin k(l - |z'|), \qquad -l \le z \le l \qquad (1.33)$$

is the assumed surface current flowing on the imaged probe surface S_0. The input impedance is then determined using the variational formula:

$$Z_{\mathrm{in}} = \frac{-1}{I_z^2(0)} \iint_{S_0} E_z(\vec{r})J_z(z)dS \qquad (1.34)$$

or

$$Z_{\mathrm{in}} = \frac{-1}{I_z^2(0)} \iiint_{S_0} \iint_{S_0} J_z(z)G_{\mathrm{TE}_{111}}(\vec{r},\vec{r}')J_z(z')dS'dS \qquad (1.35)$$

where $I_z(z) = 2\pi r_1 J_z(z)$ is a valid assumption for a thin probe ($r_1 \ll l$ and $k r_1 \ll 1$). The input impedance obtained by (1.35) is correct to second order for an assumed current distribution J_z which is correct to first order [38]. The input impedance given by (1.35) is the input impedance of the imaged configuration. To obtain the input impedance of the original configuration, the impedance, Z_{in}, should be divided by two.

The calculated TE_{111}-mode input impedance, using the above theory, is conveniently compared with the previous measurement made by McAllister and Long [7]. The DRA used in [7] had a radius of 2.54 cm, with $\varepsilon_r = 8.9$, and a probe of length $l = 1.52$ cm penetrated inside the DRA with offset $b = 1.74$ cm. The comparison [37] is shown in Fig. 1.8. From the theory, the resonant frequency is 1.88 GHz, which is very close to the theoretical value of 1.89 GHz as obtained by solving the characteristic equation $\Delta_{TE} = 0$ (Eq. 1.31). Moreover, it agrees with the

measured value of 1.90 GHz. Measured and predicted bandwidths also match reasonably well at 10.3 and 13.1 %, respectively.

Fig. 1.9 shows the variation of the input impedance with frequency for different probe lengths [37]. It is observed that while the input impedance increases significantly with probe length, the resonant frequency shifts only slightly. It is in contrast to the bare monopole case, in which the resonant frequency will vary considerably with probe length.
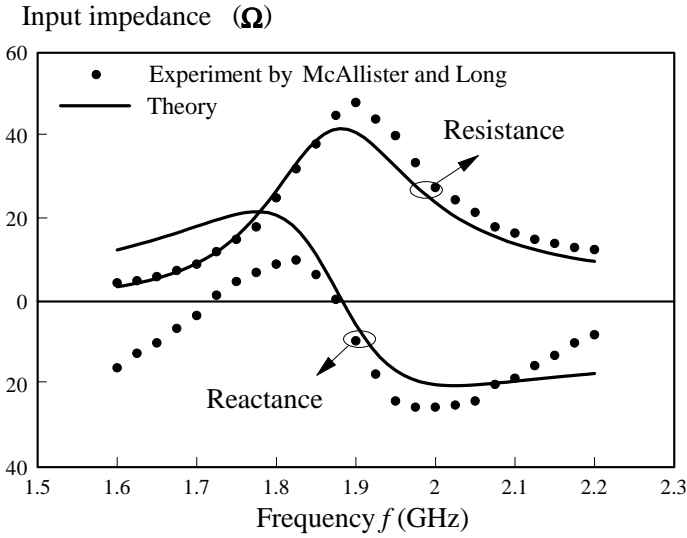
Input impedance (Ω)

Fig. 1.8 Input impedance of the TE_{111} mode: $a = 2.54$ mm, $b = 1.74$ mm, $l = 1.52$ mm, $\varepsilon_r = 8.9$, $r_1 = 0.075$ mm.
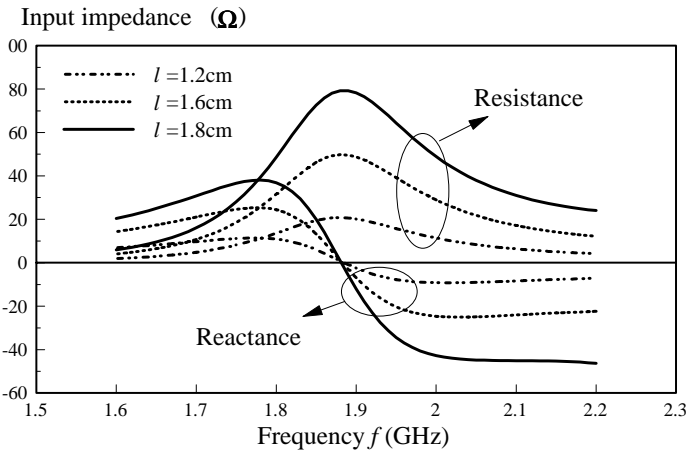
Input impedance (Ω)

Fig. 1.9 Input impedance of the TE_{111} mode for different probe lengths: $a = 2.54$ mm, $b = 1.74$ mm, $\varepsilon_r = 8.9$, $r_1 = 0.075$ mm.

The variation of input resistance at resonance with feed position for different probe lengths is shown in Fig. 1.10. The input resistance increases as the probe is displaced away from the DRA center, until a maximum point is reached. It then decreases slightly as the displacement increases further. Note that the input resistance is small when b is small. This is caused by the fact that the TE_{111} mode cannot be excited properly when the feed position is near the center, since in this case the probe current is dominated by the r-directed component, which excites TM modes only. From the figure, it is seen that the longer the probe length is, the higher the input resistance.
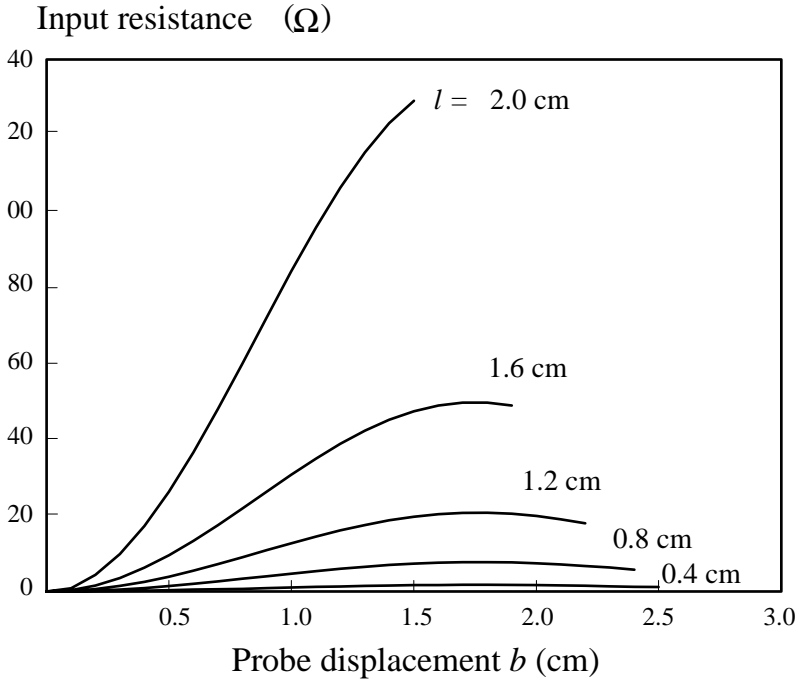
Input resistance   (Ω)

Fig. 1.10   Input resistance calculated at TE_{111}-mode resonance versus probe displacement b: $a = 2.54$ mm, $f = 1.88$ GHz, $\varepsilon_r = 8.9$, $r_1 = 0.075$ mm. (From [35], reprinted with permission from IEE)

Fig. 1.11 shows the resonant input resistance of the TE_{111} mode as a function of ε_r [37]. As can be observed, the input resistance increases with ε_r. Again, the longer the probe length is, the higher the input resistance.
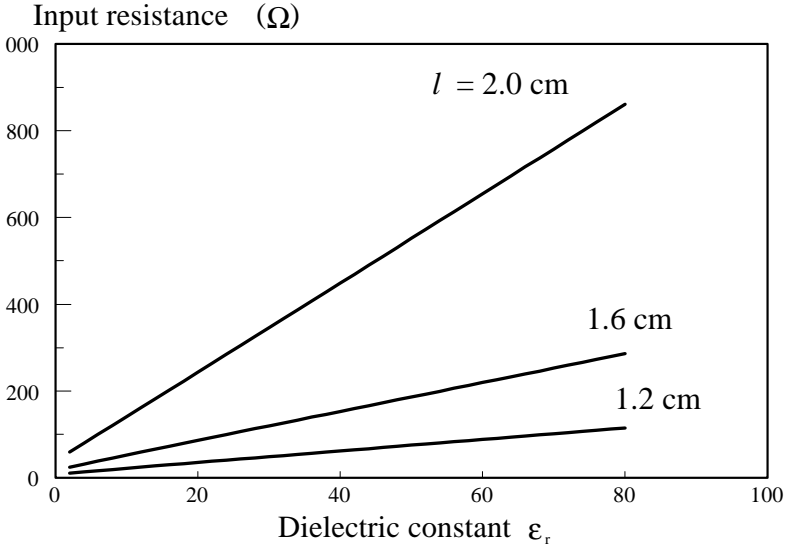
Fig. 1.11 Input resistance of the TE_{111} mode at resonance versus dielectric constant ε_r: $a = 2.54$ mm, $b = 1.74$ GHz, $f = f_{TE_{111}}$, $r_1 = 0.075$ mm.

1.3.2.2   Single Tm$_{101}$-mode approximation

A similar study was carried out for the TM_{101} mode of the hemispherical DRA [37, 39]. The TM_{101}-mode Green's function is given by

$$
\begin{aligned}
G_{\mathrm{TM}_{101}} =& \frac{-3\omega\mu_0}{2\pi k^3 r^2 r'^2}\cos^2\theta\cos^2\theta'\Big[\Phi(kr')\Psi(kr)+\alpha_{TM}\hat{J}_1(kr')\hat{J}_1(kr)\Big] \\
&-\frac{3\omega\mu_0}{4\pi k^2 r^2 r'}\cos^2\theta\sin^2\theta'\Big[\Phi'(kr')\Psi(kr)+\alpha_{TM}\hat{J}_1'(kr')\hat{J}_1(kr)\Big] \\
&-\frac{3\omega\mu_0}{4\pi k^2 rr'^2}\sin^2\theta\cos^2\theta'\Big[\Phi(kr')\Psi'(kr)+\alpha_{TM}\hat{J}_1(kr')\hat{J}_1'(kr)\Big] \\
&-\frac{3\omega\mu_0}{8\pi krr'}\sin^2\theta\sin^2\theta'\Big[\Phi'(kr')\Psi'(kr)+\alpha_{TM}\hat{J}_1'(kr')\hat{J}_1'(kr)\Big]
\end{aligned}
\tag{1.36}
$$

where

$$
\alpha_{TM} = \frac{-1}{\Delta_{\mathrm{TM}}}\Big[\hat{H}_1^{(2)}{}'(ka)\hat{H}_1^{(2)}(k_0a)-\sqrt{\varepsilon_r}\,\hat{H}_1^{(2)}(ka)\hat{H}_1^{(2)}{}'(k_0a)\Big]
\tag{1.37}
$$

$$
\Delta_{\mathrm{TM}} = \hat{J}_1{}'(ka)\hat{H}_1^{(2)}(k_0a)-\sqrt{\varepsilon_r}\,\hat{J}_1(ka)\hat{H}_1^{(2)}{}'(k_0a)
\tag{1.38}
$$

and $\Phi(kr')$ and $\Psi(kr)$ have been defined in (1.28) and (1.29), respectively. To find

the input impedance, (1.35) is applied again here, except only that the Green's function $G_{TM_{101}}$ is in place of $G_{TE_{111}}$. Moreover, the same current density given by (1.33) is assumed along the imaged probe.

An experiment was carried out in [39] to verify the theory. In the experiment, a hemispherical DR with $\varepsilon_r = 9.8$ and radius 11.5 mm was used. The DR was mounted on a 60×60 cm copper ground plane and fed by a coaxial launcher with a probe diameter of 1.25 mm, penetrating 4.5 mm into the dielectric. The input impedance as a function of frequency is shown in Fig. 1.12 [37]. From the theory, the resonant frequency is 5.85 GHz, which is very close to the measured value of 5.95 GHz. In view of the predicted resonant frequency of 5.70 GHz obtained by solving the characteristic equation $\Delta_{TM} = 0$ (Eq. 1.38), the results are quite consistent. Reasonably good agreement is observed for the bandwidth (20.4 % measured versus 23.5 % calculated). The TM_{101}-mode input impedance was studied for different probe lengths. The results are similar to those of the TE_{111} mode and are therefore omitted here.
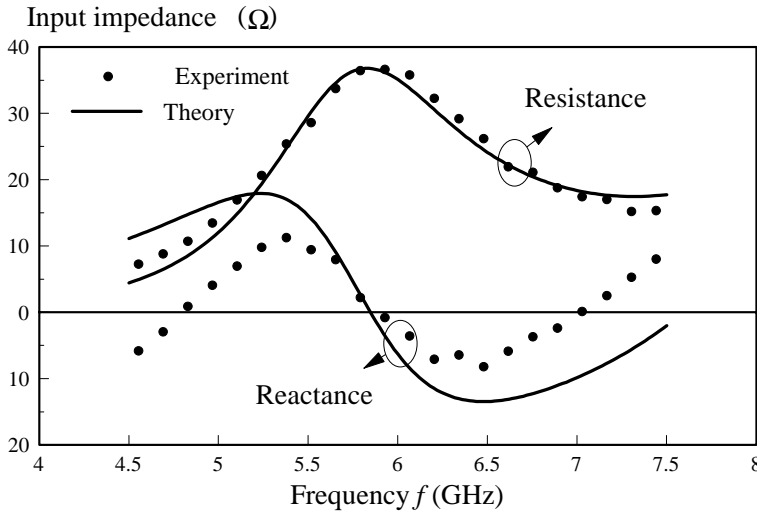
Fig. 1.12   Input impedance of the TM_{101} mode versus frequency: $a = 11.5$ mm, $b = 0.0$ mm, $l = 4.5$ mm, $\varepsilon_r = 9.8$, $r_1 = 0.075$ mm.

The effect of ε_r on the TM_{101}-mode input impedance is shown in Fig. 1.13. While it has been found that the TE_{111}-mode input resistance increases linearly with ε_r, the TM_{101}-mode input resistance is seen to increase exponentially with ε_r. It is because H_ϕ, which is tangential to the DRA surface, is the only magnetic field for the TM_{101} mode. Thus, the fields of the TM_{101} mode are of a confined mode [40], i.e., the DRA surface can be treated as a real magnetic wall as $\varepsilon_r \to \infty$. Since the resonance is of a parallel type, the magnetic wall effect causes the input resistance to increase, and the radiation decreases, rapidly with ε_r.
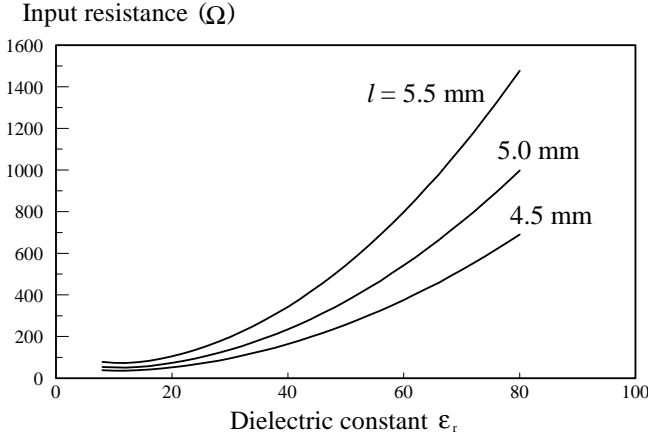
Input resistance (Ω)

Fig. 1.13 Input resistance of the TM_{101} mode at resonance versus dielectric constant ε_r for different probe lengths: $a = 11.5$ mm, $b = 0.0$ GHz, $l = 4.5$ mm, $f = f_{TM_{101}}$, $r_1 = 0.63$ mm. (From [39], © 1993 John Wiley & Sons, Inc.)

1.3.2.3 Rigorous solution for axial probe feed

When the DRA is fed axially, only TM modes can be excited. In this special case, a rigorous and yet simple general solution can be obtained [41]. Using the result of [36], the Green's function for a thin dipole (or imaged monopole) embedded inside a spherical DR (or grounded hemispherical DR) can be given by

$$G(z,z') = G_P(z,z') + G_H(z,z') \tag{1.39}$$

where

$$G_P(z,z') = \frac{-j}{\omega\varepsilon}\left(\frac{\partial^2}{\partial z^2} + k^2\right)\frac{e^{-jkR}}{4\pi R} \tag{1.40a}$$

$$G_H(z,z') = -\frac{1}{4\pi\omega\varepsilon k} \cdot \frac{1}{z^2 z'^2} \sum_{n=1}^{\infty} n(n+1)(2n+1)\alpha_n^{TM}\hat{J}_n(kz')\hat{J}_n(kz) \tag{1.40b}$$

in which

$$\alpha_n^{TM} = \frac{-[\hat{H}_n^{(2)}{}'(ka)\hat{H}_n^{(2)}(k_0a) - \sqrt{\varepsilon_r}\hat{H}_n^{(2)}(ka)\hat{H}_n^{(2)}{}'(k_0a)]}{\hat{J}_n{}'(ka)\hat{H}_n^{(2)}(k_0a) - \sqrt{\varepsilon_r}\hat{J}_n(ka)\hat{H}_n^{(2)}{}'(k_0a)} \tag{1.40c}$$

is the TM-mode reflection coefficient at the DRA boundary and $R = \sqrt{r_1^2 + (z-z')^2}$. It is worth mentioning that α_{TM} in (1.37) is the special case

of α_n^{TM} for $n = 1$. The method of moments (MoM) with Galerkin's procedure is used to solve for the probe current. To begin, the current is expanded as

$$I(z) = \sum_{q=1}^{N} I_q f_q(z),$$ (1.41)

where $f_q(z)$ is a piecewise sinusoidal (PWS) function given by

$$f_q(z) = \begin{cases} \dfrac{\sin k(d - |z - z_q|)}{\sin kd}, & |z - z_q| < d \\ 0, & \text{otherwise} \end{cases}$$ (1.42)

with $z_q = -l + qd$ and $d = 2l/(N+1)$ being the center point of the qth expansion mode and the PWS mode half-length, respectively. The unknown expansion coefficients I_q's are solved via the matrix equation

$$[Z_{pq}^{P} + Z_{pq}^{H}][I_q] = [f_p(0)],$$ (1.43)

where

$$Z_{pq}^{P,H} = \int_{-l}^{l} \int_{-l}^{l} f_p(z) G_{P,H}(z, z') f_q(z) dz' dz$$ (1.44)

The result for efficient calculations of the impedance integral Z_{pq}^{P} can be found in [42]. Here we concentrate on obtaining a computationally efficient expression for the integral Z_{pq}^{H}. To begin, we write Z_{pq}^{H} as

$$Z_{pq}^{H} = \frac{1}{4\pi\omega\varepsilon k} \sum_{n=1}^{\infty} n(n+1)(2n+1)\alpha_n^{TM} \Lambda_n(p)\Lambda_n(q)$$ (1.45)

where, for $i = p, q$,

$$\Lambda_n(i) = \int_{z_{i-1}}^{z_{i+1}} \frac{\hat{J}_n(kz)}{z^2} \cdot \frac{\sin k(d - |z - z_i|)}{\sin kd} dz$$ (1.46)

It was found that (1.46) is analytically integrable. After tedious manipulation, the result of $\Lambda_n(i)$ is found to be surprisingly simple:

$$\Lambda_n(i) = \frac{-k}{n(n+1)\sin kd} \sum_{j=1}^{1} A(j)\hat{J}_n(ku_{ij})$$ (1.47)

where $u_{ij} = -l + (i + j)d$, $A(\pm 1) = 1$, and $A(0) = -2 \cos kd$. Note that Z_{pq}^{H} does not involve any integration, and, thus, the calculation is extremely fast. Moreover,

implementation of (1.45) is very easy. The only care that has to be exercised is that u_{ij} may be zero for some i,j, for which $\hat{J}_n(ku_{ij}) = 0$. Therefore, u_{ij} should be checked in the program, as the (backward) recurrence formula for $\hat{J}_n(x)$ cannot be used when $x = 0$. After the I_q's are found, the input impedance can be obtained by simply using $Z_{in} = \beta / \sum_{n=1}^{N} I_n f_n(0)$, where $\beta = 1$ for the equivalent dipole configuration and $\beta = 1/2$ for the original (monopole) configuration.

When only the first term ($n = 1$) is taken, an even simpler result can be obtained [43]

$$Z_{mn}^{H} = \frac{3k\alpha_1^{TM}}{4\pi\omega\,\varepsilon\sin^2 kd} \cdot L(m)L(n) \tag{1.48}$$

where, for $i = m, n$,

$$L(i) = \sum_{j=-1}^{1} A(j)\text{sinc}\,(ku_{ij}) \tag{1.49}$$

in which sinc $(x) = (\sin x)/x$.

Fig. 1.14 compares the input impedances calculated from the theory for $n = 1$ with that of the rigorous solution [36] for different probe lengths. The comparison for different dielectric constants is given in Fig. 1.15. Three expansion modes ($N = 3$) were used for the current. With reference to the figures, the present theory agrees almost exactly with the rigorous one. The case for different DRA radii was also studied; and, again, excellent agreement between the simplified and rigorous theories was observed.
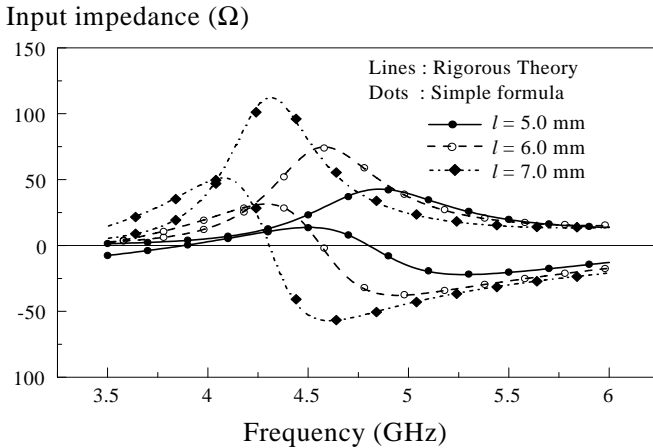
Fig. 1.14 Input impedance versus frequency for different probe lengths: $a = 12.5$ mm, $\varepsilon_r = 9.5$, $r_1 = 0.63$ mm. (From [43], reprinted with permission from IEE)
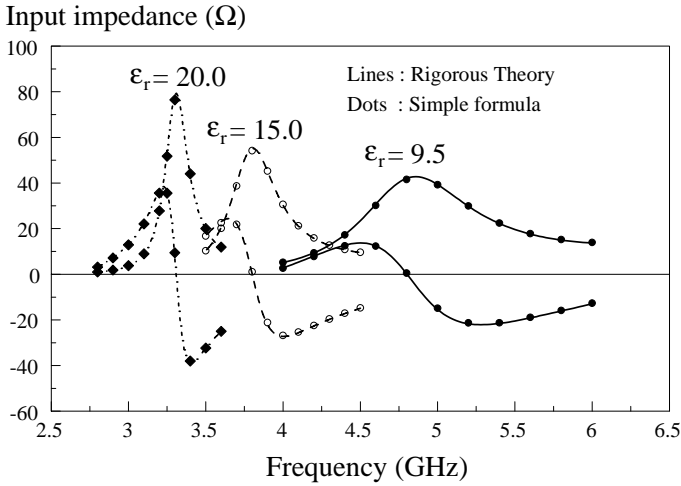
Input impedance (Ω)

Fig. 1.15   Input impedance versus frequency for different dielectric constants: a = 12.5 mm, l = 5.0 mm, r_1 = 0.63 mm. (From [43], reprinted with permission from IEE)

1.3.3   Rectangular DRA

The rectangular DRA is even more difficult to analyze than the cylindrical one because of the increase in edge-shaped boundaries. Usually the dielectric waveguide model is used to analyze the problem [44-47]. In this approach, the top surface and two sidewalls of the DRA are assumed to be perfect magnetic walls; whereas the two other sidewalls are imperfect magnetic walls. Since normally the DRA resides on a conducting ground plane, an electric wall is assumed for the bottom surface. With these assumptions, the fields of the DR are expanded in TE and TM modes using the modal expansion (ME) method. The fields inside and outside the DRA are expressed in terms of sinusoidal and exponentially decaying functions, respectively. The wave propagation numbers and attenuation constants are then found by matching the boundary conditions. Details can be found in Chapter 2.

A more accurate, but time-consuming, approach is to use the FDTD method, which was adopted by Shum and Luk [48] in analyzing the aperture-coupled rectangular DRA.

1.4   CROSS-POLARISATION OF PROBE-FED DRA

For radiation patterns of the DRA residing on an infinite ground plane, theoretical studies were focused only on the co-polarised (copol) fields [49]. However, the cross polarisation is also an important consideration in antenna design [50]. Furthermore, for probe-fed excitation, the impedance matching is usually achieved by varying the probe length and/or probe displacement. Apart from these

parameters, the dielectric constant ε_r can also be used in the DRA design. For example, it can be used to change the resonant (operation) frequency, since as the dielectric constant increases, the resulting resonant frequency is reduced. The effects of these design parameters on the cross-polarisation level are of interest. Leung *et al.* [51] studied the cross-polarisation characteristics of a probe-fed hemispherical DRA, which is excited in the fundamental TE_{111} mode. It should be mentioned that as DRAs of different shapes show very similar behavior, knowledge of the hemispherical DRA can be used to anticipate the characteristics of other shapes, such as the rectangular and cylindrical DRAs.

Refering to Fig. 1.7 for the geometry, the electric fields E_θ and E_ϕ were obtained using a rigorous modal solution. The third definition of Ludwig [52] is used to define the co-polarised field as

$$E_{copol} = E_\theta \cos \phi - E_\phi \sin \phi \tag{1.50}$$

and the cross-polarised (xpol) field

$$E_{xpol} = E_\theta \sin \phi + E_\phi \cos \phi. \tag{1.51}$$

Note that for $\phi = 0$, $E_{copol} = E_\theta$, and for $\phi = 90^\circ$, $E_{copol} = -E_\phi$. Further, at $\theta = 0$ (along the positive z-axis) E_{copol} and E_{xpol} are in the x- and y-directions, respectively.

Fig. 1.16 shows the normalised co- and cross-polarised fields for the probe-fed hemispherical DRA. Observe that the H-plane cross-polarised field is very weak in the broadside direction ($\theta = 0$). The E-plane cross-polarised field is theoretically zero.
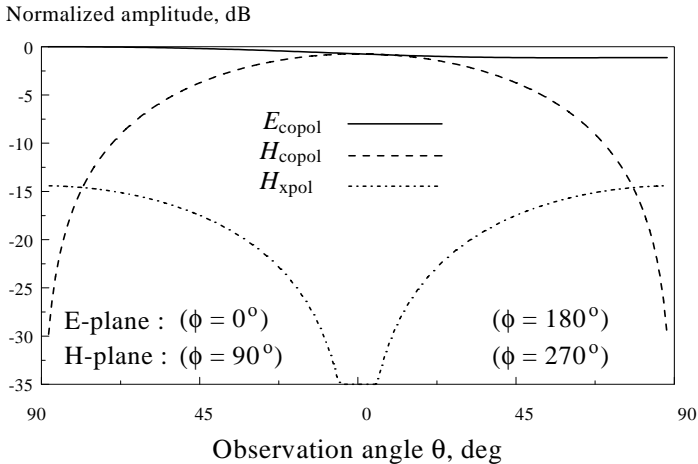
Fig. 1.16 The co- and cross-polarised fields of the probe-fed hemispherical DRA: *a* = 12.5 mm, *b* = 6.5 mm, *l* = 6.5 mm, r_1 = 0.5 mm, r_2 = 1 mm, ε_r = 9.5 and *f* = 3.68 GHz. (From [51], © 1999 IEEE)

Fig. 1.17 shows the ratio E_{copol}/E_{xpol} as a function of ϕ for different dielectric constants. For each ε_r, the resonant frequency was determined by solving the characteristic equation $\Delta_{TE} = 0$ (Eq. 1.31). With reference to the figure, the higher the dielectric constant is, the better the ratio E_{copol}/E_{xpol} is obtained. When ε_r is above a certain value, say $\varepsilon_r \geq 9.5$, the highest cross-polarisation level (the smallest E_{copol}/E_{xpol} ratio) occurs at $\phi \approx 50^0$, which is near the diagonal-plane. It should be noted that very strong cross-polarised fields are produced for $\varepsilon_r \leq 2$. This is important information, since one may use materials with very small ε_r to increase the operating frequency, without realising that the cross-polarisation level is being deteriorated.

Fig. 1.18 shows the ratio E_{copol}/E_{xpol} as a function of ϕ for different probe displacements. It is seen that the cross-polarisation level increases with decreasing b. This is because, when b is small, stronger TM but weaker TE modes are excited, reducing the E_{copol}/E_{xpol} ratio. Therefore, if polarisation purity is of primary concern, the probe should be placed as near the edge of the DRA as possible, although in this case a pure resistance for proper impedance matching cannot be obtained [36].

It was found that the ratio E_{copol}/E_{xpol} remains almost unchanged when the probe length l is varied, so the probe length can be used to vary the input impedance without the need to worry about increases in the cross-polarisation level.
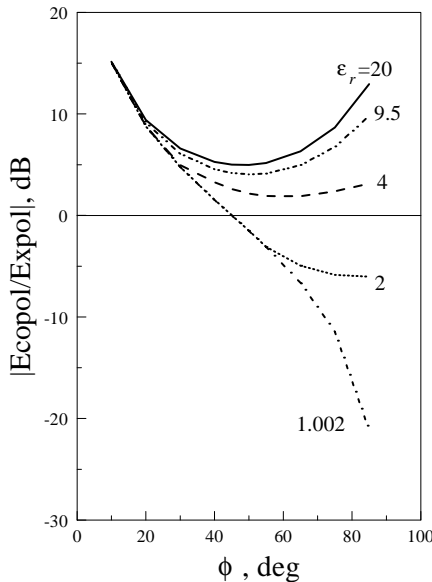
Fig. 1.17   The ratio E_{copol}/E_{xpol} versus ϕ for different dielectric constants: $a = 12.5$ mm, $l = 6.5$ mm, $b = 6.5$ mm, $r_1 = 0.5$ mm, $r_2 = 1$ mm. (From [51], © 1999 IEEE)
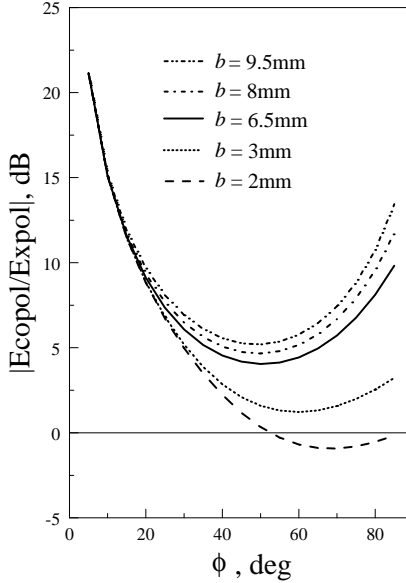
Fig. 1.18 The ratio $E_{\text{copol}}/E_{\text{xpol}}$ versus ϕ for different probe displacements: $a = 12.5$ mm, $l = 6.5$ mm, $r_1 = 0.5$ mm, $r_2 = 1$ mm, $\varepsilon_r = 9.5$ and $f = 3.68$ GHz. (From [51], © 1999 IEEE)

1.5 APERTURE-COUPLED DRA WITH A THICK GROUND PLANE

Thus far, the aperture-coupling excitation method with a microstrip feedline has been commonly used for the DRA. First, it allows a direct integration with active circuitry [53] and, second, it separates the DRA and feed network from one another. Most of the studies have concentrated on the case where the ground plane is infinitesimally thin. Sometimes, however, a thick ground plane is required to serve as a heat sink for active components. In other cases, the thick ground plane may be used as a mechanical support for thin substrates. Leung *et al.* [54] investigated the aperture-coupled hemispherical DRA with a thick ground plane. The DRA, as usual, is excited in the fundamental broadside TE$_{111}$ mode.

The DRA configuration is shown in Fig. 1.19, where for ease of formulation, the DRA is shown beneath the thick ground plane. The slot of length L and width W is located at the center of the DRA to obtain the strongest coupling [55].

Let M_{y1} and M_{y2} be the equivalent magnetic currents at the upper and lower interfaces of the slot, respectively. Then by enforcing the boundary condition that the tangential magnetic field is continuous across each of the apertures, we have

(i) across the upper aperture ($z = t$):

$$H_y^f + H_y^s(M_{y1}) = H_y^c(-M_{y1}) + H_y^{cb}(M_{y2}) \tag{1.52a}$$
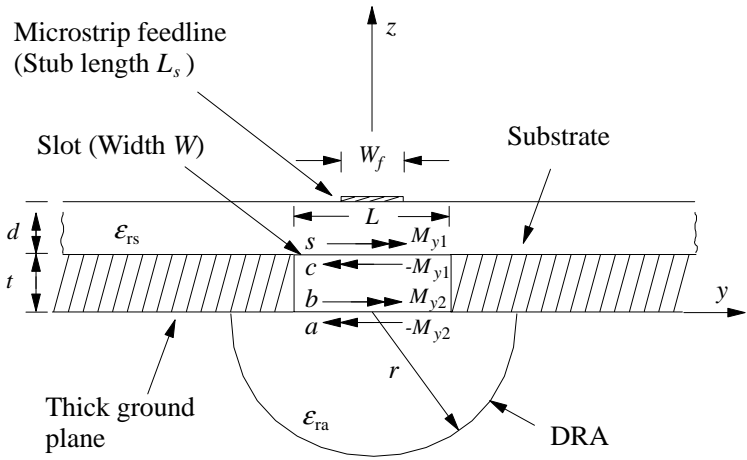
Fig. 1.19 Geometry of the DRA with a thick ground plane. (From [54], © 1998 IEEE)

(ii) across the lower aperture ($z = 0$):

$$H_y^b(M_{y2}) + H_y^{bc}(-M_{y1}) = H_y^a(-M_{y2}) \qquad (1.52b)$$

where H_y^f is the magnetic field caused by the feedline current. The superscripts a, b, c, and s denote the fields at their corresponding interfaces in Fig. 1.19, and bc (cb) denotes the field at surface b (c) due to the magnetic current at surface c (b). Using the MoM, the magnetic currents are expanded for $i = 1, 2$, as

$$M_{yi}(x, y) = \sum_{n=1}^{N_i} V_{ni} f_u(x) f_{ni}(y) \qquad (1.53)$$

where

$$f_u(x) = \begin{cases} \dfrac{1}{W} & |x| < W/2 \\ 0 & |x| > W/2 \end{cases} \qquad (1.54)$$

$$f_{ni}(y) = \begin{cases} \dfrac{\sin k_{ei}(h - |y - y_n|)}{\sin k_{ei}h}, & |y - y_n| < h \\ 0, & |y - y_n| \geq h \end{cases} \quad (1.55)$$

in which $h = L/(N+1)$, $y_n = (-L/2) + nh$, $k_{e1} = \sqrt{(\varepsilon_{rs}+1)/2}\, k_0$, and $k_{e2} = \sqrt{(\varepsilon_{ra}+1)/2}\, k_0$. Galerkin's procedure is used to obtain the following set of matrix equations:

$$\begin{cases} \left\{ \left[Y_{mn}^c - Y_{mn}^s \right] + \dfrac{1}{2}[\Delta v_m][\Delta v_n]^t \right\}[V_{n1}] + \left[Y_{mn}^{cb} \right][V_{n2}] = [\Delta v_m] \\ \left[Y_{mn}^{bc} \right][V_{n1}] + \left[Y_{mn}^b - Y_{mn}^a \right][V_{n2}] = 0 \end{cases} \quad (1.56)$$

where t denotes the transpose of a matrix, Δv_m is associated with the feedline field, and Y_{mn}^a and Y_{mn}^s are the DRA and substrate admittances, respectively. All of these quantities are given in [55]. Other admittances Y_{mn}^α ($\alpha = b$, c, bc, or cb) are related to H_y^α (1.52) and given by:

$$Y_{mn}^\alpha(z, z') = \pm \int_{-L/2}^{L/2} \int_{-L/2}^{L/2} f_{mi}(y)\, G_y^c(y, z; y', z')\, f_{nj}(y')\, dy\, dy' \quad (1.57)$$

where

$$G_y^c = \frac{j2}{k_0\eta_0 WL} \sum_{l=1}^{\infty} \frac{\beta_c}{\sin \beta_c t} \sin \beta_y\left(y + \frac{L}{2}\right)\sin \beta_y\left(y' + \frac{L}{2}\right) \cdot \begin{cases} \cos \beta_c(z - t)\cos \beta_c z', & z > z' \\ \cos \beta_c(z' - t)\cos \beta_c z, & z < z' \end{cases} \quad (1.58)$$

and z, $z' = 0$ or t, subscripts i, $j = 1$ or 2, $\beta_c^2 = k_0^2 - \beta_y^2$, and $\beta_y = (l\pi)/L$. The wavenumber and wave impedance in vacuum are denoted by k_0 and η_0, respectively. The sign in (1.57) is determined by that of the magnetic current in (1.52). Note that the Green's function G_y^c has only one summation and is independent of x. This implies that G_y^c contains only TE$_{0l}$ modes, which is a valid approximation for a narrow slot (or waveguide). After the magnetic currents are obtained, the input impedance and the radiation fields can be found easily.

A comparison between theory and experiment for $t = 0.0187$, 0.4 and 0.8 mm is displayed in Fig. 1.20, where reasonable agreement between theory and experiment is obtained. As can be observed from the figure, increasing t moves the impedance circle to the low impedance part of the Smith chart. It shows that the coupling between the DRA and the slot decreases with increasing t, since the thick

slot now acts as a waveguide below cutoff. Thus, the energy transferred to the DRA is solely through evanescent waves, which attenuate quickly as t increases.
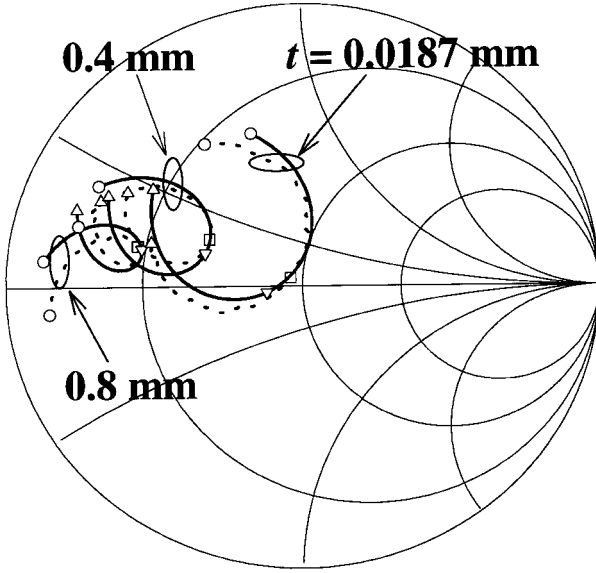
Fig. 1.20 Input impedance of the DRA for $t = 0.0187$, 0.4, and 0.8 mm: $r = 12.5$ mm, $\varepsilon_{ra} = 9.5$, $L = 11.8$ mm, $W = 1.0$ mm, $d = 1.58$ mm, $\varepsilon_{rs} = 2.33$, $W_f = 4.68$ mm, and $L_s = 11.5$ mm. (From [54], © 1998 IEEE)
Theory, ●●●●●●●●●●● Experiment;
$\bigcirc$: 3.30GHz, ∇ : 3.55GHz (Theory), $\square$: 3.55GHz (Exp.), Δ : 3.90 GHz.

Fig. 1.21 shows the measured and calculated peak resistances as a function of the ratio t/λ_0, where λ_0 (= 86.7 mm) is the resonant wavelength in vacuum for $t = 0.0187$ mm. It is seen that excellent agreement between theory and experiment is obtained. The coupling decays quickly when t is small, and it approaches the one-way attenuation rate of the TE_{01} waveguide (slot) mode as t increases. A similar phenomena has been discovered and explained in the study of the microstrip antenna version [56]. Also shown in the figure are the measured and calculated resonant frequencies (peak-resistance point) as a function of t/λ_0. Good agreement between theory and experiment is observed, with errors less than 1.2 %. It is observed that the larger the thickness t, the higher the resultant resonant frequency, since the effective dielectric constants k_{e1} and k_{e2} decrease as t increases.
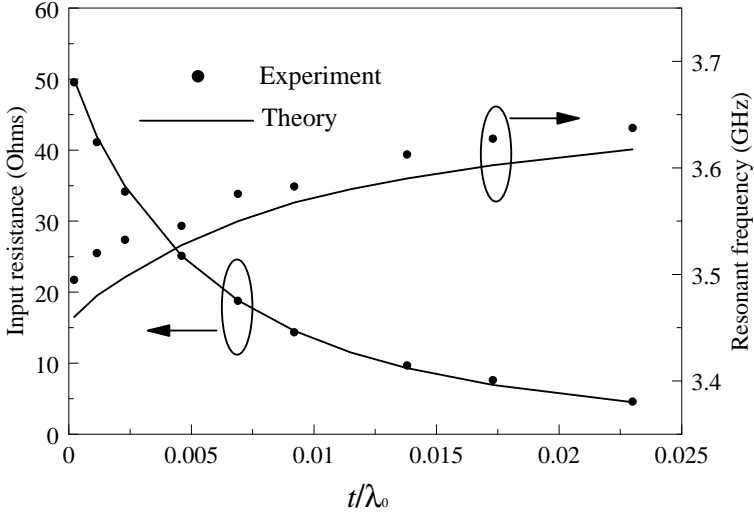
Fig. 1.21 Input resistance and resonant frequency of the DRA versus the normalised thickness t/λ_0. The parameters are the same as Fig. 1.20. (From [54], © 1998 IEEE)

1.6   SIMPLE   RESULTS   FOR   THE   SLOT-COUPLED HEMISPHERICAL DRA

As mentioned previously, slot coupling is often used for the DRA. Using the Green's function technique together with the MoM, a quadruple integral naturally results for the DRA part. Although the quadruple integral can be reduced to a double integral by taking the narrow-slot approximation ($kW \ll 1$, $W \ll L$), numerical calculations of the double integral still require substantial computation time and programming effort. Based on the single-mode theory [35], a computationally efficient formula for the integral can be obtained when the slot is at the center of the hemispherical DRA [57].

Fig. 1.22 shows the geometry of a slot-coupled DRA. Only the region that contains the DRA is considered here, and the actual excitation of the slot is not considered. Taking the single-mode approximation from the rigorous Green's function of H_y [55], we have

$$G(y, y') = G_P(y, y') + G_H(y, y') \tag{1.59}$$

where

$$G_P(y, y') = \frac{-j}{\omega \mu_0} \left(\frac{\partial^2}{\partial y^2} + k^2 \right) \frac{e^{-jkR}}{4\pi R} \tag{1.60}$$

$$G_H(y, y') = \frac{-3\alpha_{TE}}{2\pi\omega\mu_0 k} \cdot \frac{\hat{J}_1(ky')\hat{J}_1(ky)}{r^2 r'^2} \tag{1.61}$$

in which α_{TE} is given in (1.30), $R = \sqrt{(W/4)^2 + (y - y')^2}$, and S_0 is the slot surface. Using the MoM, the equivalent magnetic current is expanded as

$$M_y(z) = \sum_{n=1}^{N} V_n f_n(z), \tag{1.62}$$

where $f_n(z)$ is the piecewise sinusoidal (PWS) basis function given by (1.55) with $i = 2$. For convenience, the subscript i of (1.55) is dropped hereafter.
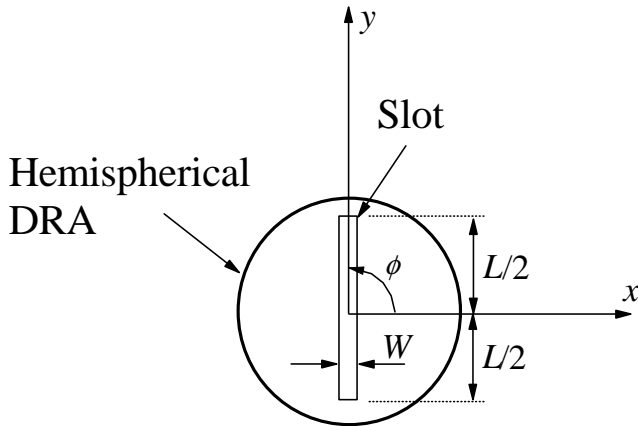
Fig. 1.22   The geometry of a slot coupled DRA.

The unknown voltage coefficients V_n's are solved via the following matrix equation

$$[Y_{mn}^P + Y_{mn}^H][V_m] = [I_m], \tag{1.63}$$

where

$$Y_{pq}^{P,H} = -2\int_{-l}^{l}\int_{-l}^{l} f_m(y) G_{P,H}(y, y') f_n(y) dy' dy \tag{1.64}$$

and I_m is associated with the actual excitation of the configuration. In (1.64), the factor of "−2" has been added to the integrals. The factor of two accounts for the ground plane effect, whereas the minus sign ensures that the tangential E-field is continuous across the slot. For the general case Y_{mn}^H must be calculated using

numerical integration, but it is found that for a narrow slot, Y_{mn}^H can be given by the following expression:

$$Y_{mn}^H = \frac{3\alpha_{TE}}{\pi\omega\mu_0 k} \cdot \left(\frac{1}{2k\sin k_e h}\right)^2 \Lambda(m)\Lambda(n) \tag{1.65}$$

where, for $i = m$ or n,

$$\Lambda(i) = \sum_{j=-1}^{1}\left[A(j)\cdot\frac{k_e\sin ku_{ij}}{u} + \frac{k_e^2 - k^2}{2}\sum_{q=-1,2}^{1}q\left[(\sin k_e u_{ij})\mathrm{Si}(vu_{ij}) + (\cos k_e u_{ij})\mathrm{Ci}(|vu_{ij}|)\right]\right] \tag{1.66}$$

with $A(\pm1) = 1$, $A(0) = -2\cos k_e h$, $u_{ij} = -L/2 + (i+j)h$, and $v = k_e - qk$. In (1.66), $\mathrm{Si}(x)$ and $\mathrm{Ci}(x)$ are Sine and Cosine integrals given by

$$\mathrm{Ci}(x) = -\int_x^\infty \frac{\cos t}{t}\,dt \tag{1.67}$$

$$\mathrm{Si}(x) = \int_0^x \frac{\sin t}{t}\,dt \tag{1.68}$$

and their simple formulas are given in the Appendix. When $u = 0$, $\Lambda(i)$ can be simplified to

$$\Lambda(i) = \sum_{j=-1}^{1}A(j)\left[k_e k + \frac{(k_e^2 - k^2)}{2}\ln\left|\frac{(k_e - k)}{(k_e + k)}\right|\right]. \tag{1.69}$$

Note that Y_{mn}^H can now be calculated easily and quickly without the need for any numerical integration. For Y_{mn}^P, no simple results are available and numerical integration must be used.

To verify the theory, the previously calculated and measured results of the aperture-coupled DRA using a microstrip feedline [55] are used. This comparison is shown in Fig. 1.23, where excellent agreement between the present and previous theories is obtained.

It should be mentioned that although the result starts with the single-mode theory, it can be used for a rather wide frequency range - from extremely low frequencies (virtually dc) to frequencies below the resonance of the TE$_{3m1}$ mode. Note that as the TE$_{2m1}$ mode cannot be excited for this particular slot position, the theory is valid even at the resonance of the mode.
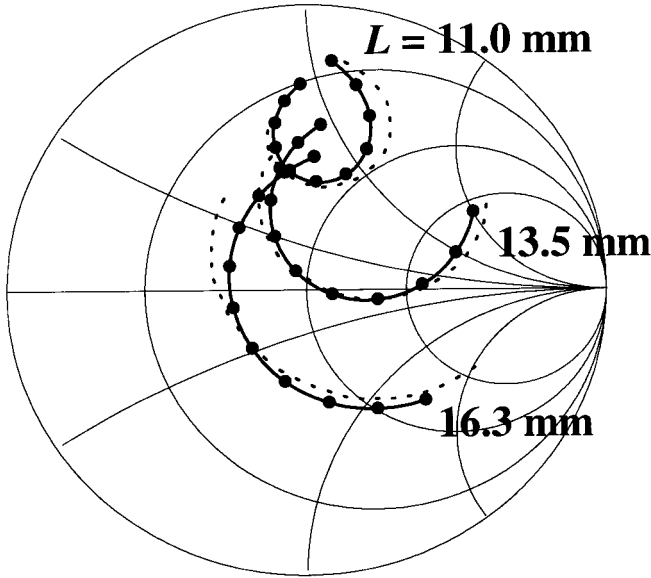
Fig. 1.23 Input impedance of the slot-coupled hemispherical dielectric resonator antenna (microstrip-feedline). The DRA has radius a = 12.5 mm and dielectric constant ε_{ra} = 9.5. The microstrip feedline has width W_f = 1.45 mm, printed on a substrate of dielectric constant ε_{rs} = 2.96 and thickness d = 0.635 mm. It has an open-circuited stub length of L_s = 13.6 mm from the center of the slot. The slot is placed at the center of the DRA. Solid line: rigorous theory, dots: simplified theory, dashed line: experiment.

1.7   LOW-PROFILE AND SMALL DRAs

Usually, the DRA is made of a dielectric material with a low permittivity (ε_r < 40) to enhance the radiation. In 1994, Mongia *et al.* demonstrated the radiation properties of a low-profile rectangular DRA with a very high permittivity (ε_r = 100) [58]. An excellent impedance match was obtained with ~3 % impedance bandwidth. Latter, low-profile, high-permittivity circular [59] and triangular [60] DRAs were investigated and similar results were obtained. Esselle studied the low-profile DRA of low-permittivity (ε_r = 10.8) [61], and its feasibility was also confirmed. A comprehensive study of the low-profile DRA is given in Chapter 6.

Apart from using high-permittivity material, Mongia [62] inserted a shorted metallic cylinder at the center of a cylindrical DRA to reduce the antenna size. Alternatively, the DRA size can be reduced by utilising a metal plate perpendicular to the conducting ground plane [63, 64]. A half-cylindrical DRA was placed against the vertical metal plate. By virtue of the image effect, the size of the DRA

was reduced roughly by one half. Tam and Murch [65] extended the method for the annular sector DRA, details of which can be found in Chapter 7.

1.8   BROADBAND DRAs

Bandwidth enhancement techniques for the DRA have been a popular topic. It was first done in 1989 by Kishk *et al*. [66], who stacked two different DRAs on top of one another. Since the DRAs had different resonant frequencies, the configuration had a dual-resonance operation, broadening the antenna bandwidth. Sangiovanni *et al*. [67] employed the stacking method with three DRAs to further increase the antenna bandwidth. Leung *et al*. [68] introduced an air gap between the stacking and active DRA elements. They used a high-permittivity, low-profile DR as the stacking element, and good results were obtained. Junker *et al*. [69] analyzed the stacking configuration that employs a conducting or high-ε_r loading disk. Simon and Lee [70] used another method in which two parasitic DRs were placed beside the DRA to increase the impedance bandwidth. Alternatively, Leung *et al*. [71] used the dual-disk method to enhance the bandwidth of the low-profile DRA of very high permittivity.

The above methods require extra DR elements. Some bandwidth-enhancement techniques are based on single-DRA configurations. For example, Wong *et al*. [72] introduced an air gap inside a hemispherical DRA to widen the impedance bandwidth. Ittipiboon *et al*. [73] performed a similar work with the rectangular DRA. Shum and Luk [74] placed an air gap between the DRA and ground plane to broaden the impedance bandwidth. Leung [75] investigated the case where the air gap inside the DRA is replaced by a conductor. Chen *et al*. [76] added a dielectric coating to the DRA to increase the impedance bandwidth. Similar work was also carried out by Shum and Luk [77]. Lately, a parasitic conducting patch has been used to increase the impedance bandwidth of the DRA [78, 79]. The new method does not require any extra DR elements nor special DRAs and, hence, should facilitate designs of broadband DRAs.

The expanded work for the broadband hemispherical DRA can be found in Chapter 3, whereas that for the broadband rectangular- and cylindrical-DRAs is given in Chapter 5.

1.9   CIRCULARLY POLARISED DRAs

For a long time, studies DRAs have concentrated on those producing linearly polarisation (LP). Sometimes, however, systems using circular polarisation (CP) are preferred because they are insensitive to the transmitter and receiver orientations. In some applications, such as satellite communications, it also offers less sensitivity to propagation effects. In contrast, an LP signal cannot be received properly when the transmitter is orthogonal to the received field. Consequently, more effort has been devoted to the CP DRA in recent years.

The first CP DRA was presented in 1985 by Haneishi & Takazawa [80]. They truncated two opposite corners of a rectangular DRA to produce CP fields. About ten years later, Mongia *et al*. [81] studied a CP DRA that employed a quadrature feed. Later some other CP DRAs with quadrature feeds were demonstrated [82-

84]. The quadrature feeding method gives a wide axial ratio (AR) bandwidth, but it substantially increases the size and complexity of the feed network.

A single feed point can be used if a few percent of AR bandwidth is sufficient for the application. The basic principle of this approach is to excite two nearly degenerate orthogonal modes with space-time quadrature. For example, Petosa *et al*. [85] employed a cross-shaped slot-coupled DRA to excite CP fields. Alternatively, Oliver *et al*. [86] and Esselle [87] used a conventional rectangular DRA, with the coupling slot inclined at 45^0 with respect to the DRA to obtain a CP DRA. The method, however, cannot be applied to a DRA with a circular circumference (e.g., cylindrical or hemispherical). These geometries can, however, be attacked by using a cross-slot, as demonstrated by Huang *et al*. [88]. A CP excitation method that utilised a pair of parasitic conducting strips was proposed by Lee *et al*. [89]. Leung and Ng [90, 91] and Long *et al*. [79] found that a single parasitic patch can also be used to excite CP fields. Recently, Leung and Mok [92] used a perturbed annular slot to excite a CP DRA. In this section, the work of Leung and Mok is shown as an example for the CP DRA.

Fig. 1.24 shows the antenna configuration of the annular-slot excited CP cylindrical DRA. The annular slot is perturbed by two opposing stubs located at 45° and 225° from the *x*-axis. Each stub has width *t* and depth *d*. A hemispherical backing cavity of radius *b* is placed below the slot to eliminate undesirable backside radiation.
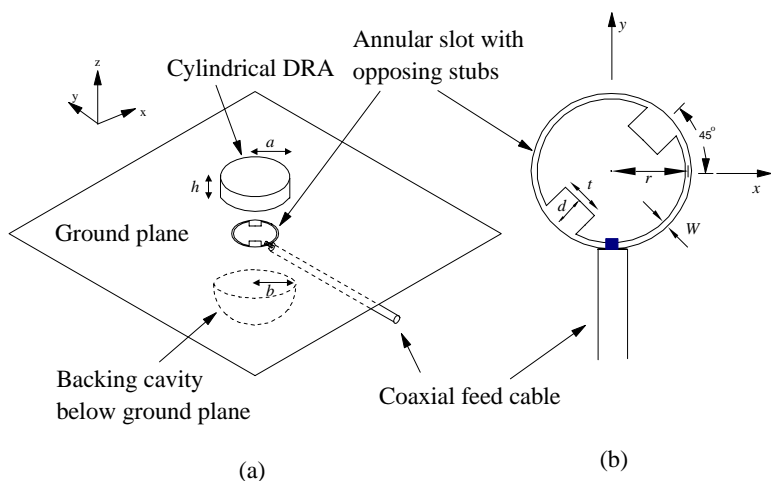
Fig. 1.24   The CP cylindrical DRA excited by the perturbed annular slot with a backing cavity. (a) Perspective view. (b) Perturbed annular slot with opposing stubs. (From [92], reprinted with permission from IEE)

A cylindrical DRA of $a = 2$ cm, $h = 2$ cm, and $\varepsilon_r = 9.5$ and a backing cavity of $b = 2.5$ mm were used in [92]. Fig. 1.25(a) shows the measured return loss for different slot radii of $r = 8, 10,$ and 12 mm, with $W = 1$ mm, $t = 7$, and $d = 5$ mm fixed. It is observed in the figure that an excellent impedance match is obtained at

the resonant frequency (min. $\left|S_{11}\right|$) $f = 1.96$ GHz, which agrees reasonably well with the predicted value of 2.07 GHz (5% error) using the following design formula [93]:

$$f_r = \frac{c}{2\pi a \sqrt{\varepsilon_r}}\left[1.71 + 2\left(\frac{a}{2h}\right) + 0.1578\left(\frac{a}{2h}\right)^2\right] \tag{1.70}$$

where c is the speed of light in vacuum. In (1.70) the height h is multiplied by two to account for the image effect of the ground plane. The corresponding ARs are shown in Fig. 1.25(b). It is found that an AR of 0.2 dB is obtained at $f = 1.92$ GHz, which is very close to the resonant frequency (1.96 GHz), as desired. The 3-dB axial ratio bandwidth is 3.4 %, which is typical for a singly fed CP DRA. Although it is seen in Fig. 1.25(a) that the input impedance can be changed by varying the slot radius, care has to be exercised, since the axial ratio will also change accordingly as is observed in Fig. 1.25(b).

(a)   (b)
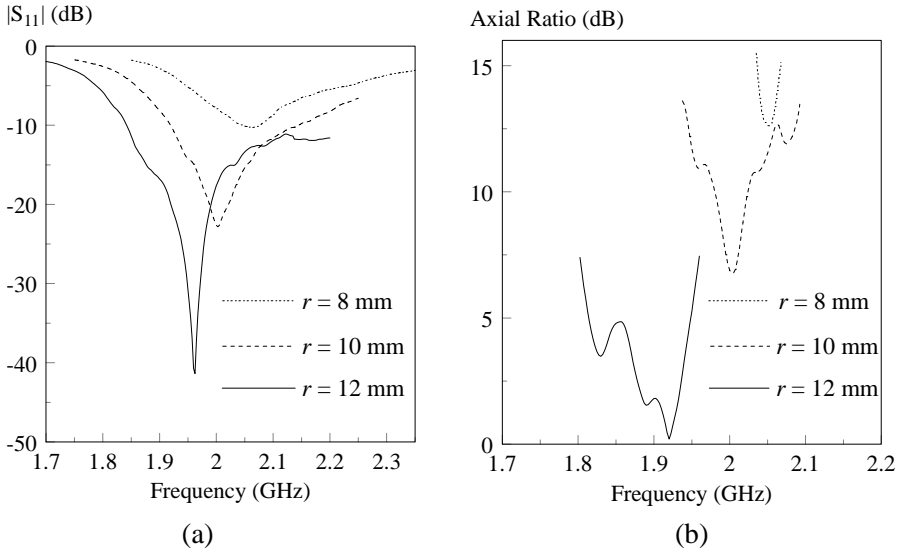
Fig. 1.25 Measured return loss and axial ratio against frequency for different slot radii: (a) Return loss; (b) Axial ratio. (From [92], reprinted with permission from IEE)

Fig. 1.26 shows the measured return loss and axial ratio for different stub depths of $d = 3$, 5, and 7 mm, with $r = 12$ mm and the other parameters unchanged. Again, the return loss and axial ratio are affected simultaneously, but the changes are much smaller in extent than in the previous case. Therefore, the stub depth can be used for fine-tuning in the final design. For the stub width t, it was found that its effect is even smaller than that of varying the stub depth.

Fig. 1.27 shows the measured y-z and x-z plane radiation patterns at resonance (f = 1.96 GHz) with r = 12 mm and d = 5 mm. Very good left-hand CP (LHCP) fields are obtained. The isolation between the right-hand CP (RHCP) and LHCP fields is at least 20 dB in the broadside direction (θ = 0°). Note that the radiation below the ground plane is due to the finite ground plane diffraction only, since the backside radiation of the slot is already blocked by the backing cavity. The measured antenna gain of the configuration with r = 12 mm and d = 5 mm is about 4.5 dBi around resonance, as shown in Fig. 1.28.
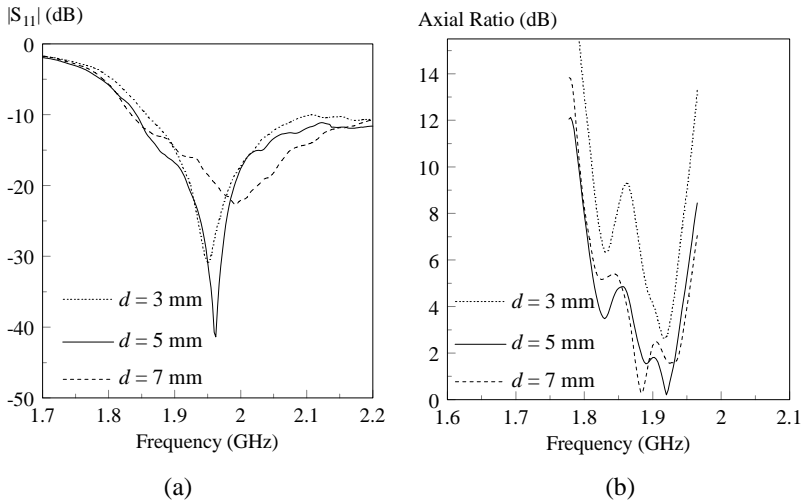
Fig. 1.26 Measured return loss and axial ratio against frequency for different stub depths. (a) Return loss; (b) Axial ratio. (From [92], reprinted with permission from IEE)

1.10 DRA ARRAYS

Since the antenna gain of a DRA is limited to ~5 dBi, different types of DRA arrays [94-99] have been studied for increasing the antenna gain. In this section, the array performance of the cylindrical DRA is demonstrated using 2×2 and 4×4 square arrays of aperture-coupled cylindrical DRAs. The designs start with the single-element DRA, whose configuration is shown in Fig. 1.29. The DRA has radius a = 5.96 mm, height h = 9.82 mm, and dielectric constant ε_{ra} = 16. A rectangular slot of length L = 8 mm and width W = 0.8 mm is located at the center of the DRA. The grounded dielectric slab has dielectric constant ε_{rs} = 2.33 and thickness d = 1.57 mm, whereas the 50-Ω microstrip feedline has width W_f = 4.7 mm. An open stub of length L_s = 12 mm extends from the center of the slot.

y-z plane

x-z plane

LHCP ——————

RHCP - - - - - - - -

(a)　　　　　　　　　　　　　　(b)
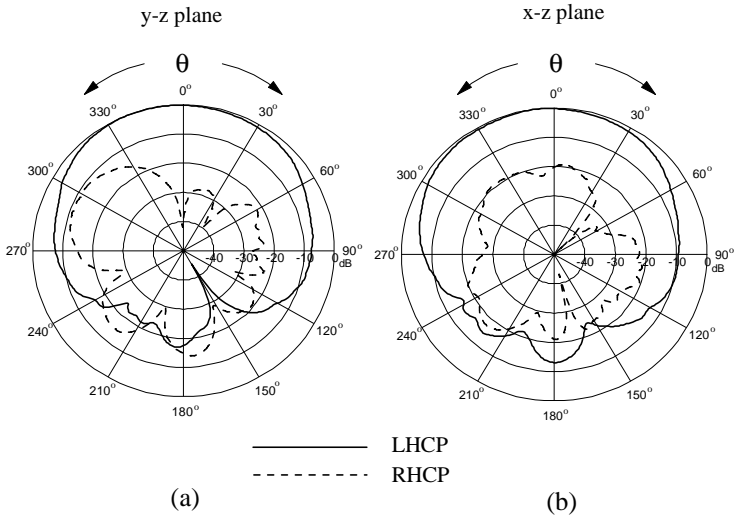
Fig. 1.27　Measured radiation patterns at f = 1.96 GHz. The parameters are the same as in Fig. 1.25 with r = 12 mm. (a) y-z plane; (b) x-z plane. (From [92], reprinted with permission from IEE)

Antenna Gain (dBi)

Frequency (GHz)
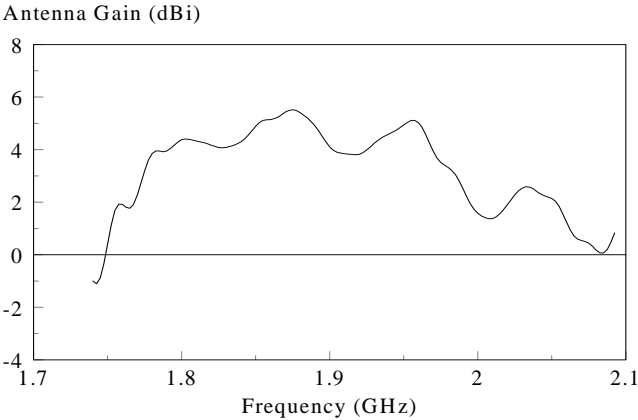
Fig. 1.28　Measured antenna gain of the configuration. The parameters are the same as in Fig.1.25 with r = 12 mm. (From [92], reprinted with permission from IEE)
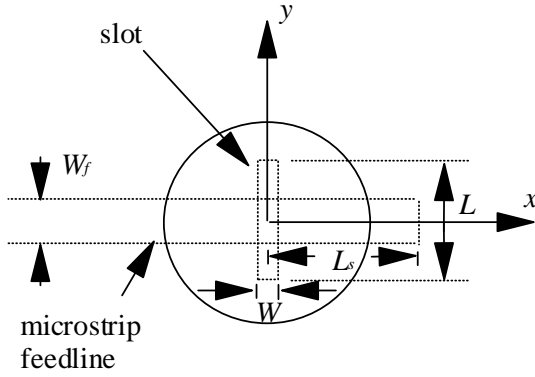
Fig.1.29 Geometry of the single element aperture-coupled cylindrical DRA.

Top views of the 2×2 and 4×4 DRA arrays are shown in Fig. 1.30. The spacing between adjacent array elements is D = 33.5 mm, which is one-half of the free-space wavelength at f = 4.46 GHz. Fig. 1.31 shows the photos of the 4×4 DRA array.
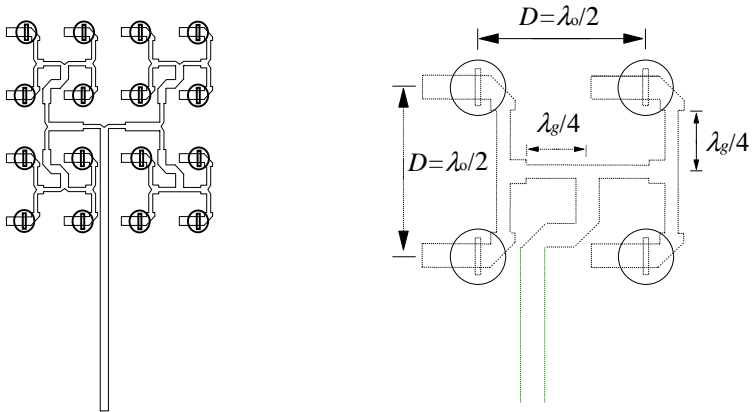
Fig. 1.30 4×4 and 2×2 DRA arrays.
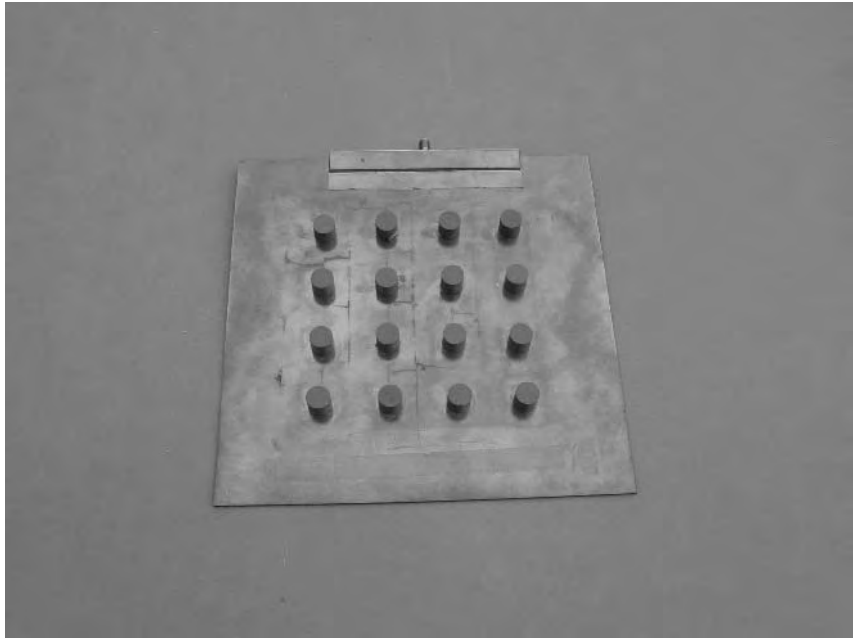
(a)
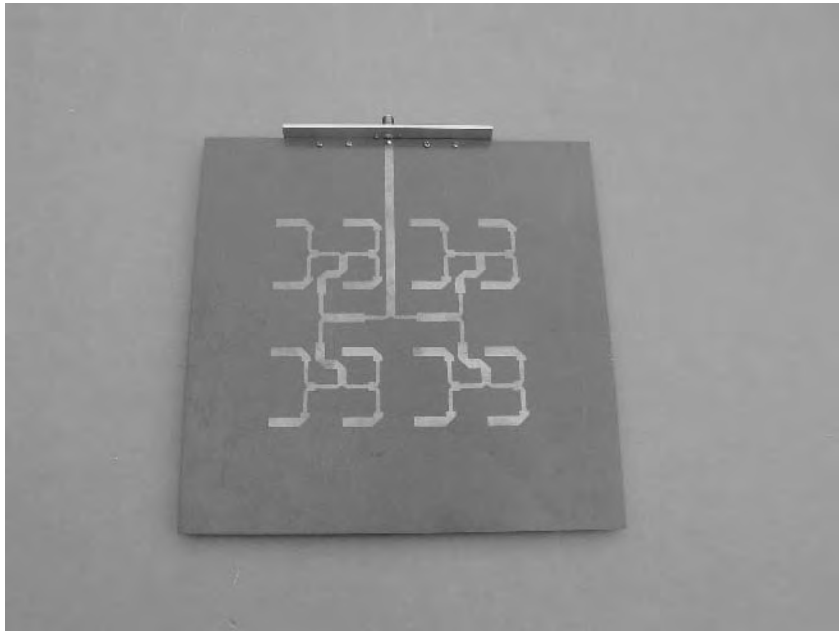
(b)

Fig. 1.31   Photos of the 4×4 DRA array. (a) The array elements above the ground plane. (b) The corporate microstrip feedline below the ground plane.

Fig. 1.32 displays the measured return loss of the single-element, 2×2 subarray and 4×4 array. Because of the mutual coupling between array elements and fabrication tolerances, the resonant frequencies and bandwidths of the arrays deviate a bit from that of the single element. The results are summarised in Table 1.4, where the resonant frequency is defined as the minimum point of the return loss.
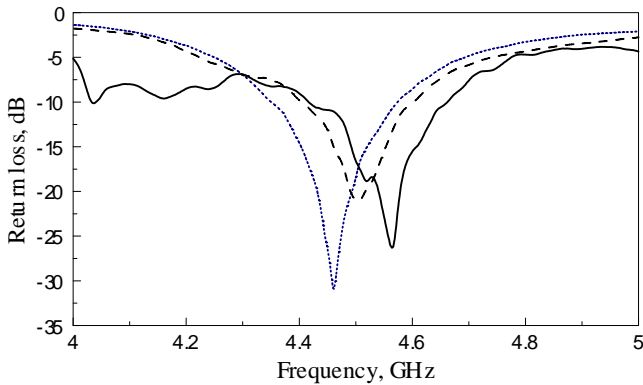
Fig. 1.32 Comparison of the measured return losses. ·················· Single element, -------- 2×2 subarray, ———— 4×4 array.

	Resonant Frequency GHz	Min. Return Loss dB	Bandwidth, % ($\left|S_{11}\right| < -10$ dB)
Single-element DRA	4.46	−30.0	4.93
2x2 DRA subarray	4.51	−20.0	4.43
4x4 DRA array	4.56	−26.3	5.48

Table 1.4 Summary of the return loss measurements.

Figs. 1.33-1.35 display the radiation patterns for the three cases. Obviously, the beamwidth decreases with increasing the number of array elements, as expected. The results of the radiation patterns are summarised in Table 1.5.
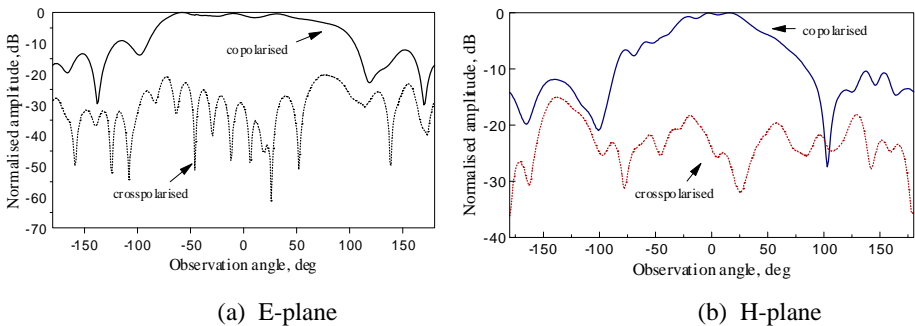
(a) E-plane

(b) H-plane

Fig. 1.33 Measured radiation patterns of the single element.

(a) E-plane   (b) H-plane
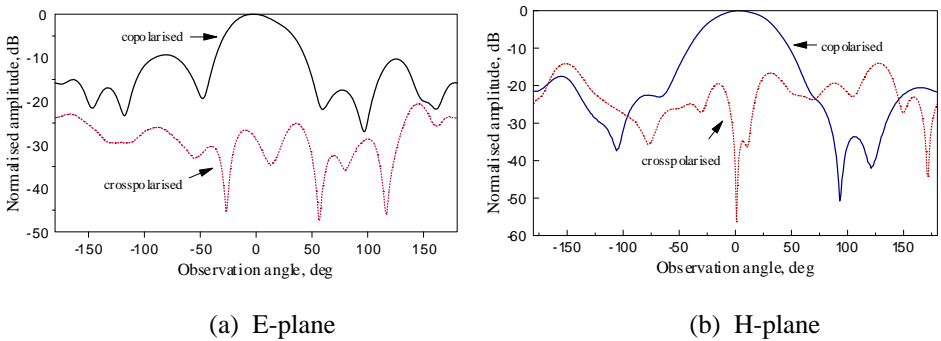
Fig. 1.34   Measured radiation patterns of the 2×2 subarray.

(a) E-plane   (b) H-plane
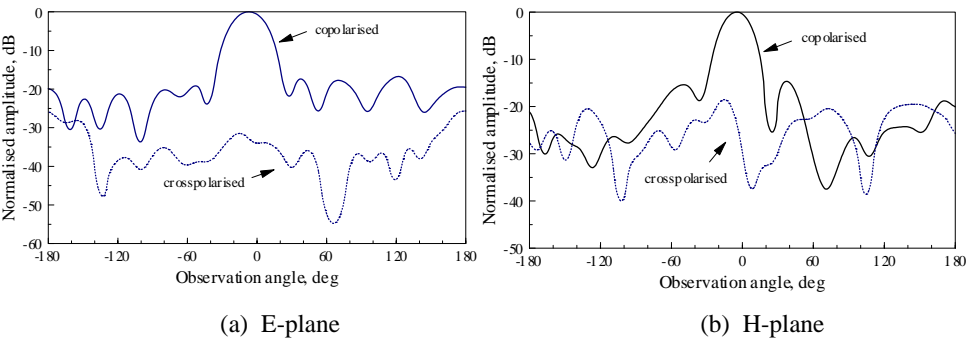
Fig. 1.35   Measured radiation patterns of the 4×4 array.

	E-plane Field Pattern		H-plane Field Pattern	
	3-dB Beamwidth, degree	Front-to-back Ratio, dB	3dB Beamwidth, degree	Front-to-back ratio, dB
Single-element DRA	148	11	75	14
2x2 DRA subarray	49	11	54	22
4x4 DRA array	26.7	22	24	22

Table 1.5   Summary of the radiation pattern characteristics.

Fig. 1.36 displays the overall comparison of the antenna gains for the single element, 2×2 subarray, and 4×4 array. The gain of the 4×4 array at its resonant frequency (4.56 GHz) is about 16 dBi, which is 5.2 dBi and 11.2 dBi higher than those of the 2×2 subarray and single element, respectively. Note that the gains are near their maximum values around the resonances, which is to be expected.
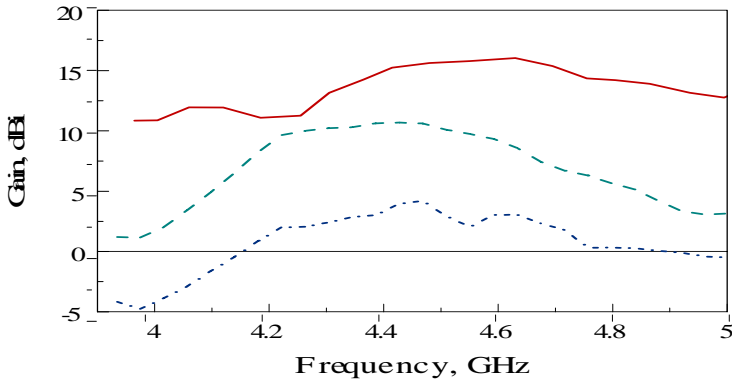
Fig. 1.36 Measured antenna gains. ‒·‒·‒·‒·‒·‒·‒· single element,
‒ ‒ ‒ ‒ ‒ ‒ ‒ ‒ 2×2 subarray, ————— 4×4 subarray.

Early radar installations were not very efficient due to the slow rotational speeds of their massive antennas. Even though smaller antenna sizes and lighter materials have been employed, rotational speed limitations still restrict the scanning rate of the antenna. The problem can be solved by using a phased array antenna, where each element is fed with a differently phased signal, such that the angle of the main lobe changes in response to the phase of the current. Thus, the antenna can be motionless while the direction of maximum radiation is changed. Leung *et al*. [96] have investigated the input impedance of the cylindrical DRA element when it is operated in an infinite phased array environment, as illustrated in Fig. 1.37(a). For measurements, the infinite phased array environment can be simulated using a waveguide simulator technique [100], as shown in Fig. 1.37(b). In [96], the equivalent array element spacing D_x and D_y were 28.8 and 29 mm, respectively. The waveguide simulator effectively scans in the H-plane to an angle θ, where $\sin\theta = \lambda_o/(4D_y)$. The waveguide simulator, covering the DR element, was put on a grounded dielectric slab. Through mirror images formed inside the waveguide simulator, there are infinite numbers of DRA elements in different directions, forming an infinite DRA phased array environment. For measurements, the waveguide simulator supports the TE_{10} waveguide mode only.

The measured return loss of the simulator is displayed in Fig. 1.38. The scan angle of the waveguide simulation is also shown in the same figure, where it is seen that as frequency increases from 4 to 5GHz, the scan angle of the waveguide simulator decreases from 40.3^o to 31.1^o. It also shows that the resonant frequency of the phased array is 4.57GHz, corresponding to a scan angle of 34.5^o. Because of the mutual coupling between the array elements, the resonant frequency of the infinite array has shifted 2.5% from that of the single element (4.46GHz).
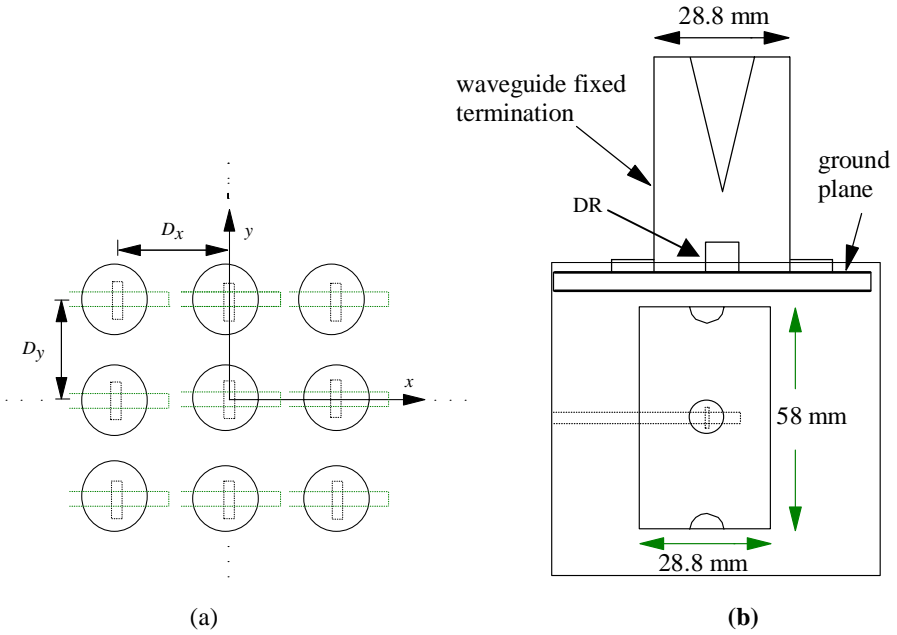
Fig. 1.37 Infinite DRA phased array. (a) Top view; (b) measurement apparatus. (From [96], reprinted with permission from IEE)
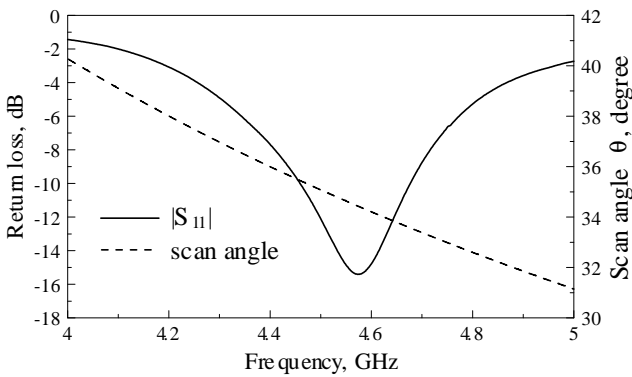
Fig. 1.38 Return loss and scan angle of waveguide simulator. (From [96], reprinted with permission from IEE)

The above arrays generate LP fields. Some CP DRA arrays were also investigated [80, 85, 101]. It is worth mentioning that by using sequential rotation,

CP fields can be obtained by using LP elements [101]. An exhaustive survey on the LP and CP DRA arrays can be found in Chapter 9.

Mutual coupling is an important consideration in array designs and some work has been done on this topic. Interested readers may refer to [94, 102-107] and Chapter 9.

Apart from building a DRA array, some researchers have increased the antenna gain by using a double-layered DRA [108], or by using the DR as a non-radiative dielectric (NRD) guide antenna. More information on the latter can be obtained from Chapter 10.

1.11   AIR GAP EFFECT ON THE DRA

In applying the probe feed method to the DRA, a hole has to be drilled inside the DRA for the probe penetration. Since normally the probe does not perfectly fit the hole, an air gap usually exists between the probe and DRA. Junker *et al.* [109, 110] have studied the air gap effect for the broadside $HEM_{11\delta}$ (or TM_{110}) mode of the cylindrical DRA. It was noted that the air gap increases the operation frequency and, in addition, lowers the resonance impedance. The 3-dB bandwidth, however, is not significantly affected by the air gap.

An air gap may also exist between the bottom of the DRA and ground plane. The problem was investigated, again, by Junker *et al.* [110, 111], but the resonant mode of the study was the endfire TM_{01} mode. It was found that, in general, the resonant frequency increases, the resonance resistance decreases, and the 3-dB impedance bandwidth is significantly broadened, as the size of the air gap becomes larger. Drossos *et al.* [112] studied the effect of an air gap between the DRA and microstrip substrate for a microstrip-fed DRA. Approximate correction factors were given that help antenna engineers incorporate the air gap effect into their designs. It was pointed out that the air gap can be used to tune the operating frequency and to obtain a wider bandwidth. It is worth mentioning that the frequency tuning can also be achieved by using a top-loaded conducting plate [113].

1.12   CONCLUSION

The DRA has received increasing attention in the last two decades, and its development is more rapid than ever before. Different aspects of the DRA have already been addressed, including the basic operating principle, excitation method, design of LP, CP, and array configurations, compact design, and air-gap problems. Various theories have been developed and confirmed by measurements. Engineering results are also available for the design engineer. There is no doubt that the DRA is ready for commercial applications.

1.13 APPENDIX

The Sine and Cosine integrals can be approximated as follows [114].

(1) For $x < 1$,

$$Si(x) = x - \frac{x^3}{18} + \frac{x^5}{600} - \frac{x^7}{35,280} + \frac{x^9}{3,265,920} - \frac{x^{11}}{439,084,800} \tag{1.71}$$

$$Ci(x) = \gamma + \ln x - \frac{x^2}{4} + \frac{x^4}{96} - \frac{x^6}{4,320} + \frac{x^8}{322,560} - \frac{x^{10}}{36,288,000} \tag{1.72}$$

where $\gamma = 0.5772156649\cdots$ is the Euler's constant.

(2) For $x \geq 1$,

$$Si(x) = \frac{\pi}{2} - f(x)\cos x - g(x)\sin x \tag{1.73}$$

$$Ci(x) = f(x)\sin x - g(x)\cos x \tag{1.74}$$

where

$$f(x) = \frac{1}{x}\left(\frac{x^8 + a_1 x^6 + a_2 x^4 + a_3 x^2 + a_4}{x^8 + b_1 x^6 + b_2 x^4 + b_3 x^2 + b_4} \right) + \varepsilon(x), \ |\varepsilon(x)| < 5\times10^{-7} \tag{1.75}$$

$$
\begin{aligned}
a_1 &= 38.027264 & b_1 &= 40.021433 \\
a_2 &= 256.187033 & b_2 &= 322.624911 \\
a_3 &= 335.677320 & b_3 &= 570.236280 \\
a_4 &= 38.102495 & b_4 &= 157.105423
\end{aligned}
$$

$$g(x) = \frac{1}{x^2}\left(\frac{x^8 + a_1 x^6 + a_2 x^4 + a_3 x^2 + a_4}{x^8 + b_1 x^6 + b_2 x^4 + b_3 x^2 + b_4} \right) + \varepsilon(x), \ |\varepsilon(x)| < 3\times10^{-7} \tag{1.76}$$

$$
\begin{aligned}
a_1 &= 42.242855 & b_1 &= 48.196927 \\
a_2 &= 302.757865 & b_2 &= 482.485984 \\
a_3 &= 352.018498 & b_3 &= 1114.978885 \\
a_4 &= 21.821899 & b_4 &= 449.690326
\end{aligned}
$$

REFERENCES

[1] D. Kajfez and P. Guillon, Eds., *Dielectric Resonators*. Norwood, MA: Artech House, 1986

[2] R. D. Richtmyer, "Dielectric Resonators," *J. Appl. Phys*., vol. 10, pp. 391-398, June 1939

[3] M. Gastine, L. Courtois and J. L. Dormann, "Electromagnetic resonances of free dielectric spheres," *IEEE Trans. Microwave Theory Tech.*, vol. 15, pp. 694-700, Dec. 1967

[4] O. Sager and F. Tisi, "On eigenmodes and forced resonance-modes of dielectric spheres," *Proc. IEEE*, pp. 1593-1594, Sept. 1968

[5] S. A. Long, M. W. McAllister and L. C. Shen, "The resonant cylindrical dielectric cavity antenna", *IEEE Trans. Antennas Propagat.*, vol. 31, pp. 406-412, May 1983

[6] M. W. McAllister, S. A. Long and G. L. Conway, "Rectangular dielectric resonator antenna", *Electron. Lett*., vol. 19, pp. 218-219, Mar. 1983

[7] M. W. McAllister and S. A. Long, "Resonant hemispherical dielectric antenna", *Electron. Lett*., vol. 20, pp. 657-659, Aug. 1984

[8] A. Ittipiboon, R. K. Mongia, Y. M. M. Antar, P. Bhartia and M. Cuhaci, "Aperture-fed rectangular and triangular dielectric resonators for use as magnetic dipole antennas," *Electron. Lett*., vol. 29, pp. 2001-2002, Nov. 1993

[9] K. W. Leung, K. M. Luk and E. K. N Yung, "Spherical cap dielectric resonator antenna using aperture coupling," *Electron. Lett.*, vol. 30, No. 17, pp. 1366-1367, Aug. 1994

[10] R. K. Mongia, A. Ittipiboon, P. Bhartia and M. Cuhaci, "Electric-monopole antenna using a dielectric ring resonator," *Electron. Lett*., vol. 29, pp. 1530-1531, Aug. 1993

[11] K. W. Leung, K. Y. Chow, K. M. Luk and E. K. N. Yung, "Excitation of dielectric resonator antenna using a soldered-through probe," *Electron. Lett.*, vol. 33, pp. 349 - 350, Feb. 1997

[12] R. K. Mongia and P. Bhartia, "Dielectric resonator antennas – A review and general design relations for resonant frequency and bandwidth," *International J. of Microwave and Millimeter-Wave Computer-Aided Engg*., vol. 4, pp. 230-247, 1994

[13] G. P. Junker, A. A. Kishk and A. W. Glisson, "Input impedance of dielectric resonator antennas excited by a coaxial probe," *IEEE Trans. Antennas Propagat*., vol. 42, pp. 960-966, July 1994

[14] S. M. Shum and K. M. Luk, "FDTD analysis of probe-fed cylindrical dielectric resonator antenna," *IEEE Trans. Antennas Propagat*., vol. 46, pp. 325-333, Mar. 1998

[15] K. M. Luk, K. W. Leung and S.M. Shum, "Numerical study of dielectric resonator antenna", *Advances in Microstrip and Printed Antennas* (Editors: K.F. Lee and W. Chen). Chapter 11, pp. 553-592, John Wiley, 1997

[16] J. T. H. St. Martin, Y. M. M. Antar, A. A. Kishk and A. Ittipiboon, "Dielectric resonator antenna using aperture coupling," *Electron. Lett.*, vol. 26, pp. 2015-2016, Nov. 1990

[17] G. P. Junker, A. A. Kishk and A. W. Glisson, "Input impedance of aperture-coupled dielectric resonator antennas", *IEEE Trans. Antennas and Propagat.*, vol. 44, pp. 600-607, May 1996

[18] K. W. Leung, W. C. Wong, K. M. Luk, and E. K. N. Yung, "Annular-slot-coupled dielectric resonator antenna," *Electron. Lett.*, vol. 34, No. 13, pp. 1275-1277, June 1998

[19] K. W. Leung and K. M. Luk, "Radiation characteristics of aperture-coupled hemispherical dielectric resonator antenna," *Microw. and Opt. Techn. Lett.*, vol. 7, No. 14, pp. 677-679, Oct. 1994

[20] K. W. Leung and M. W. To, "Aperture-coupled dielectric resonator antenna with a perpendicular feed," *Electron. Lett.*, vol. 33, No. 12, pp. 1000-1001, June 1997

[21] K. W. Leung and M. W. To, "Slot-coupled dielectric resonator antenna using a proximity feed on a perpendicular substrate," *Electron. Lett.*, vol. 33, No. 20, pp. 1665-1666, Sept. 1997

[22] K. W. Leung, "Analysis of aperture-coupled hemispherical dielectric resonator antenna with a perpendicular feed," *IEEE Trans. Antennas Propagat.*, vol. 48, No. 6, pp. 1005-1007, June 2000

[23] G. P. Junker, A. A. Kishk, D. Kajfez, A. W. Glisson and J. Guo, "Input impedance of microstrip-slot-coupled dielectric resonator antennas mounted on thin dielectric layers," *International J. Microwave and Millimeter-Wave Computer-Aided Engineering*, vol. 6, pp. 174-182, 1996

[24] K. Y. Chow and K. W. Leung, "Theory and experiment of the cavity-backed slot-excited dielectric resonator antenna," *IEEE Trans. Electromagnetic Compatibility*, vol. 42, No. 3, pp. 290-297, Aug. 2000

[25] K. Y. Chow, K. W. Leung, K. M. Luk and E. K. N. Yung, "Input impedance of the slot-fed dielectric resonator antenna with/without a backing cavity," *IEEE Trans. Antennas Propagat.*, vol. 49, No. 2, pp. 307-309, Feb. 2001

[26] R. A. Kranenburg and S. A. Long, "Microstrip transmission line excitation of dielectric resonator antennas", *Electron. Lett.*, vol. 24, pp. 1156-1157, Sept. 1988

[27] K. W. Leung, K. Y. Chow, K. M. Luk and E. K. N. Yung, "Low-profile circular disk DR antenna of very high permittivity excited by a microstripline," *Electron. Lett.*, vol. 33, No. 12, pp. 1004-1005, June 1997

[28] R. A. Kranenburg, S. A. Long and J. T. Williams, "Coplanar waveguide excitation of dielectric resonator antennas", *IEEE Trans. Antennas Propagat.* vol. 39, pp. 119-122, 1991

[29] H. Y. Lo, K. W. Leung and K. M. Luk, "Slotline excited equilateral-triangular dielectric resonator antenna of very high permittivity," *Microw. and Opt. Techn. Lett.*, vol. 29, No. 4, pp. 230-231, Apr. 2001

[30]   K. W. Leung, M. L. Poon, W. C. Wong, K. M. Luk and E. K. N. Yung, "Aperture-coupled dielectric resonator antenna using a stripline feed," *Microw. and Opt. Techn. Lett.*, vol. 24, No. 2, pp. 120-121, Jan. 2000

[31]   K. W. Leung, "Conformal strip excitation of dielectric resonator antenna," *IEEE Trans. Antennas Propagat.*, vol. 48, No. 6, pp. 961-967, June 2000

[32]   K. W. Leung, "Simple result for a conformal-strip excited hemispherical dielectric resonator antenna," *Electron. Lett.*, vol. 36, No. 11, pp. 933-935, May 2000

[33]   H. Y. Lo and K. W. Leung, "Excitation of low-profile equilateral-triangular dielectric resonator antenna using a conducting conformal strip," *Microw. and Opt. Techn. Lett.*, vol. 29, No. 5, pp. 317-319, June 2001

[34]   M. T. Birand and R. V. Gelsthorpe, "Experimental millimetric array using dielectric radiators fed by means of dielectric waveguide," *Electron. Lett.*, vol. 17, pp. 633-635, Sept. 1981

[35]   K. W. Leung, K. M. Luk, K. Y. A. Lai and D. Lin, "Input impedance of hemispherical dielectric resonator antenna," *Electron. Lett.*, vol. 27, pp. 2259-2260, Nov. 1991

[36]   K. W. Leung, K. M. Luk, K. Y. A. Lai and D. Lin, "Theory and experiment of a coaxial probe fed dielectric resonator antenna," *IEEE Trans. Antennas Propagat.*, vol. 41, pp. 1390-1398, Oct. 1993

[37]   K. W. Leung, *Rigorous analysis of dielectric resonator antenna*. PhD Dissertation, The Chinese University of Hong Kong, Hong Kong, May 1993

[38]   R. E. Collin, *Field Theory of Guided Waves*. New York: McGraw Hill, pp. 260-261, 1960

[39]   K. W. Leung, K. M. Luk, K. Y. A. Lai and D. Lin, "On the TM_{101} mode of dielectric resonator antenna," *Microw. and Opt. Techn. Lett.*, vol. 6 No. 11, pp. 626-629, Sept. 1993

[40]   J. Van Bladel, "On the resonances of a dielectric resonator of very high permittivity," *IEEE Trans. Microwave Theory and Techn.*, vol. MTT-23, pp. 199-208, Feb. 1975

[41]   K. W. Leung, "General solution of a monopole loaded by a dielectric hemisphere for efficient computation," *IEEE Trans. Antennas Propagat.*, vol. 48, pp. 1267-1268, Aug. 2000

[42]   D. M. Pozar, *Antenna Design Using Personal Computer*. Dedham, MA : Artech House, pp. 35-43, 1985

[43]   K. W. Leung, K. W. Ng, K. M. Luk and E. K. N. Yung, "Simple formula for analyzing the center-fed hemispherical dielectric resonator antenna," *Electron. Lett.*, vol. 33, pp. 440-441, Mar. 1997

[44]   R. K. Mongia, "Theoretical and experimental resonant frequencies of rectangular dielectric resonators," *IEE Proc.-H*, vol. 139, pp. 98-104, Feb. 1992

[45]   R. K. Mongia and A. Ittipiboon, "Theoretical and experimental investigations on rectangular dielectric resonator antennas," *IEEE Trans. Antennas Propagat.*, vol. 45, pp. 1348-1356, Sept. 1997

[46]   Y. M. M. Antar and Z. Fan, "Theoretical investigation of aperture-coupled rectangular dielectric resonator antenna," *IEE Proc.-Microw. Antennas Propaga.*, vol. 143, pp. 113-118, Apr. 1996

[47]   A. Petosa, N. R. S. Simons, R. Siushansian, A. Ittipiboon and M. Cuhaci, "Design and analysis of multi-segment dielectric resonator antennas," *IEEE Trans. Antennas Propagat.*, vol. 48, pp. 738-742, May 2000

[48]   S. M. Shum and K. M. Luk, "Analysis of aperture-coupled rectangular dielectric resonator," *Electron. Lett.*, vol. 30, pp. 1726-1727, Oct. 1994

[49]   A. A. Kishk, H. A. Auda and B. C. Ahn, "Radiation characteristics of cylindrical dielectric resonator antennas with new applications," *IEEE Antennas Propagat. Soc. Newslett.*, vol. 31, pp. 7-16, 1989

[50]   K. F. Lee, K. M. Luk and P. Y. Tam, "Crosspolarisation characteristics of circular patch antennas," *Electron. Lett.*, vol. 28, pp. 587-589, 1992

[51]   K. W. Leung, K. K. Tse, K. M. Luk and E. K. N. Yung, "Cross-polarisation characteristics of a probe-fed hemispherical dielectric resonator antenna," *IEEE Trans. Antennas Propagat.*, vol. 47, No.7, pp. 1228-1230, July 1999

[52]   A. C. Ludwig, "The definition of cross polarisation," *IEEE Trans. Antennas Propagat.*, vol. 21, pp. 116-119, 1973

[53]   M. G. Keller, D. J. Roscoe, M. B. Oliver, R. K. Mongia, Y. M. M. Antar and A. Ittipiboon, "Active aperture-coupled rectangular dielectric resonator antenna," *IEEE Micro. and Guided Wave Lett.*, vol. 5, pp. 376-378, Nov. 1995

[54]   K. W. Leung, Z. N. Chen, K. M. Luk and E. K. N. Yung, "Aperture-coupled dielectric resonator antenna with a thick ground plane," *IEEE Trans. Antennas Propagat.*, vol. 46, No. 8, pp. 1242-1243, Aug. 1998

[55]   K. W. Leung, K. M. Luk, K. Y. A. Lai and D. Lin, "Theory and experiment of an aperture-coupled hemispherical dielectric resonator antenna," *IEEE Trans. Antennas Propagat.*, vol. 43, pp. 1192-1198, Nov. 1995

[56]   P. R. Haddad and D. M. Pozar, "Characterisation of aperture coupled microstrip patch antenna with thick ground plane", *Electron. Lett.*, vol. 30, pp. 1106-1107, July 1994

[57]   K. W. Leung and K. W. Ng, "Efficient computation for structures consisting of a slot and a metallic/dielectric hemisphere cavity," *IEEE Trans. Antennas Propagat.* vol. 46, No. 3, pp. 457-458, Mar. 1998

[58]   R. K. Mongia, A. Ittipiboon and M. Cuhaci, "Low-profile dielectric resonator antennas using a very high permittivity material," *Electron. Lett.*, vol. 30, pp. 1362-1363, Aug. 1994

[59]   K. W. Leung, K. M. Luk, E. K. N. Yung and S. Lai, "Characteristics of a low-profile circular disk DR antenna with very high permittivity", *Electron. Lett.*, vol. 31, No. 6, pp. 417-418, Mar. 1995

[60]   H. Y. Lo, K. W. Leung, K. M. Luk and E. K. N. Yung, "Low profile equilateral-triangular dielectric resonator antenna of very high permittivity," *Electron. Lett.*, vol. 35, No. 25, pp. 2164-2166, Dec. 1999

[61]   K. P. Esselle, "A low-profile rectangular dielectric-resonator antenna," *IEEE Trans. Antennas Propagat.*, vol. 44, pp. 1296-1297, Sept. 1996

[62]   R. K. Mongia, "Small electric monopole mode dielectric resonator antenna," *Electron. Lett.*, vol. 32, pp. 947-949, May 1996

[63]   M. T. K. Tam and R. D. Murch, "Half volume dielectric resonator antenna," *Electron. Lett.*, vol. 33, pp. 1914-1916, Nov. 1997

[64]   A. Petosa, A. Ittipiboon, Y. M. M. Antar, D. Roscoe and M. Cuhaci, "Recent advances in dielectric-resonator antenna technology," *IEEE Antennas Propagat. Magazine*, vol. 40, pp. 35-48, June 1998

[65]   M. T. K. Tam and R. D. Murch, "Compact circular sector and annular sector dielectric resonator antennas," *IEEE Trans. Antennas Propagat.*, vol. 47, pp. 837-842, May 1999

[66]   A. A. Kishk, B. Ahn and D. Kajfez, "Broadband stacked dielectric resonator antennas," *Electron. Lett.*, vol. 25, pp. 1232-1233, Aug. 1989

[67]   A. Sangiovanni, J. Y. Dauvignac and Ch. Pichot, "Stacked dielectric resonator antenna for multifrequency operation", *Microw. and Opt. Techn. Lett.*, vol. 18, pp. 303-306, July 1998

[68]   K. W. Leung, K. M. Luk, K. Y. Chow and E. K. N. Yung, "Bandwidth enhancement of dielectric resonator antenna by loading a low-profile dielectric disk of very high permittivity," *Electron. Lett.*, vol. 33, pp. 725-726, Apr. 1997

[69]   G. P. Junker, A. W. Glisson and A. A. Kishk, "Input impedance of dielectric resonator antennas top loaded with high permittivity and conducting disks," *Microw. and Opt. Techn. Lett.*, vol. 9, pp. 204-207, July 1995

[70]   R. N. Simons and R. Q. Lee, "Effect of parasitic dielectric resonators on CPW/aperture-coupled dielectric resonator antennas," *IEE Proc.-H*, vol. 140, pp. 336-338, Oct. 1993

[71]   K. W. Leung, K. Y. Chow, K. M. Luk and E. K. N. Yung, "Offset dual-disk dielectric resonator antenna of very high permittivity," *Electron. Lett.*, vol. 32, pp. 2038-2039, Oct. 1996

[72]   K.-L. Wong, N.-C. Chen and H.-T. Chen, "Analysis of a hemispherical dielectric resonator antenna with an airgap," *IEEE Microwave and Guided Wave Lett.*, vol. 3, pp. 355-357, Oct. 1993

[73]   A. Ittipiboon, A. Petosa, D. Roscoe and M. Cuhaci, "An investigation of a novel broadband dielectric resonator antenna," *IEEE Antennas and Propagation Society International Symposium Digest*, Baltimore, USA, pp. 2038-2041, July 1996

[74]   S. M. Shum and K. M. Luk, "Characteristics of dielectric ring resonator antenna with an air gap," *Electron. Lett.*, vol. 30, pp. 277-278, Feb. 1994

[75]   K. W. Leung, "Complex resonance and radiation of hemispherical dielectric resonator antenna with a concentric conductor," *IEEE Trans. Microwave Theory and Techn.*, vol. 49, No. 3, pp. 524-531, Mar. 2001

[76]   N. C. Chen, H. C. Su, K. L. Wong and K. W. Leung, "Analysis of a broadband slot-coupled dielectric-coated hemispherical dielectric resonator antenna," *Microw. and Opt. Techn. Lett.*, vol. 8, pp. 13-16, Jan. 1995

[77]   S. M. Shum and K. M. Luk, "Numerical study of a cylindrical dielectric-resonator antenna coated with a dielectric layer," *IEE Proc.-Microw. Antennas Propag.*, vol. 142, pp. 189-191, Apr. 1995

[78]   H. K. Ng and K. W. Leung, "Conformal-strip-excited dielectric resonator antenna with a parasitic strip," *IEEE Antennas and Propagation Society International Symposium Digest*, vol. 4, pp. 2080-2083, Salt Lake City, USA, July 2000

[79]   R. T. Long, R. J. Dorris, S. A. Long, M. A. Khayat and J. T. Williams, "Use of parasitic strip to produce circular polarisation and increased bandwidth for cylindrical dielectric resonator antenna," *Electron. Lett.*, vol. 37, pp. 406-408, Mar. 2001

[80]   M. Haneishi and H. Takazawa, "Broadband circularly polarized planar array composed of a pair of dielectric resonator antennas," *Electron. Lett.*, vol. 21, pp. 437-438, May 1985

[81]   R. K. Mongia, A. Ittipiboon, M. Cuhaci and D. Roscoe, "Circularly polarized dielectric resonator antenna," *Electron. Lett.*, vol. 30, pp. 1361-1362, Aug. 1994

[82]   G. Drossos, Z. Wu and L. E. Davis, "Circular polarized cylindrical dielectric resonator antenna," *Electron. Lett.*, vol. 32, pp. 281-283, Feb. 1996

[83]   G. Drossos, Z. Wu and L. E. Davis, "Switchable cylindrical dielectric resonator antenna," *Electron. Lett.*, vol. 32, pp. 862-864, May 1996

[84]   K. W. Leung, W. C. Wong, K. M. Luk and E. K. N. Yung, "Circular-polarised dielectric resonator antenna excited by dual conformal strips," *Electron. Lett.*, vol. 36, No. 6, pp. 484-486, Mar. 2000

[85]   A. Petosa, A. Ittipiboon and M. Cuhaci, "Array of circular-polarized cross dielectric resonator antenna," *Electron. Lett.*, vol. 32, pp. 1742-1743, Sept. 1996

[86]   M. B. Oliver, Y. M. M. Antar R. K. Mongia, and A. Ittipiboon, "Circularly polarized rectangular dielectric resonator antenna," *Electron. Lett.*, vol. 31, pp. 418-419, Mar. 1995

[87]   K. P. Esselle, "Circularly polarised higher-order rectangular dielectric-resonator antenna," *Electron. Lett.*, vol. 32, pp. 150-151, Feb. 1996

[88]   C. Y. Huang, J. Y. Wu and K. L. Wong, "Cross-slot-coupled microstrip antenna and dielectric resonator antenna for circular polarisation", *IEEE Trans. Antennas Propagat.*, vol. 47, pp. 605-609, 1999

[89]   M. T. Lee, K. M. Luk, E. K. N. Yung and K. W. Leung, "Microstrip-line feed circularly polarized cylindrical dielectric resonator antenna," *Microw. and Opt. Techn. Lett.*, vol. 24, pp. 206-207, Mar. 2000

[90]   K. W. Leung and H. K. Ng, "Theory and experiment of circularly polarized dielectric resonator antenna with a parasitic patch," *IEEE Trans. Antennas Propagat.*, vol. 51, Feb. 2003 (in press)

[91]   H. K. Ng and K. W. Leung, "Excitation of CP aperture-coupled dielectric resonator antenna with a parasitic patch," IEEE Antennas and Propagation Society International Symposium Digest, vol. 4, pp. 202-205, Boston, Massachusetts, USA, July 2001

[92]   K. W. Leung and S. K. Mok, "Circularly polarized dielectric resonator antenna excited by a perturbed annular slot with a backing cavity," *Electron. Lett.*, vol. 37, No. 15, pp. 934-936, July 2001

[93]   A. A. Kishk, A. Ittipiboon, Y. M. M. Antar and M. Cuhaci, "Slot excitation of the dielectric disk radiator," *IEEE Trans. Antennas Propagat.*, vol. 43, pp. 198-201, Feb. 1995

[94]   G. D. Loos and Y. M. M. Antar, "A new aperture-coupled rectangular dielectric resonator antenna array," *Microw. and Opt. Techn. Lett.*, vol. 7, pp. 642-644, Oct. 1994

[95]   K. Y. Chow, K. W. Leung, K. M. Luk and E. K. N. Yung, "Cylindrical dielectric resonator antenna array," *Electron. Lett.*, vol. 31, pp. 1536-1537, Aug. 1995

[96]   K. W. Leung, H. Y. Lo, K. M. Luk and E. K. N. Yung, "Two-dimensional cylindrical dielectric resonator antenna array," *Electron. Lett.*, vol. 34, No. 13, pp. 1283-1285, June 1998

[97]   G. Drossos, Z. Wu and L. E. Davis, "Aperture-coupled cylindrical dielectric resonator antennas forming four-element linear arrays," *Microw. and Opt. Techn. Lett.*, vol. 20, pp. 151-153, Jan. 1999

[98]   A. Petosa, R. K. Mongia, A. Ittipiboon and J. S. Wight, "Design of microstrip-fed series array of dielectric resonator antennas," *Electron. Lett.*, vol. 31, pp. 1306-1307, Aug. 1995

[99]   A. Petosa, A. Ittipiboon, M. Cuhaci and R. Larose, "Bandwidth improvement for a microstrip-fed series array of dielectric resonator antennas," *Electron. Lett.*, vol. 32, pp. 608-609, Mar. 1996

[100]   D. M. Pozar, "Analysis of an infinite phased array of aperture coupled microstrip patches", *IEEE Trans. Antennas Propagat.*, vol. 37, pp. 418-425, Apr. 1989

[101]   K. K. Pang, H. Y. Lo, K. W. Leung, K. M. Luk and E. K. N. Yung, "Circularly-polarized dielectric resonator antenna subarrays," *Microw. and Opt. Techn. Lett.*, vol. 27, No. 6, pp. 377-379, Dec. 2000

[102]   K. M. Luk, W. K. Leung and K. W. Leung, "Mutual impedance of hemispherical dielectric resonator antenna," *IEEE Trans. Antennas Propagat.*, vol. 42, No. 12, pp. 1652-1654, Dec. 1994

[103]   B. Henry, A. Petosa, Y. M. M. Antar and G. A. Morin, "Mutual coupling between rectangular multisegment dielectric resonator antennas," *Microw. and Opt. Techn. Lett.*, vol. 21, pp. 46-48, Apr. 1999

[104]   Y. X. Guo, K. M. Luk and K. W. Leung, "Mutual coupling between rectangular dielectric resonator antennas by FDTD," *IEE Proc.-Microw. Antennas Propag.*, pt.H, vol. 146, No. 4, pp. 292-294, Aug. 1999

[105]   Y. X. Guo, K. M. Luk and K. W. Leung, "Mutual coupling between millimeter wave dielectric resonator antennas," *IEEE Trans. Microwave Theory and Techn.*, vol. 47, No. 11, pp. 2164-2166, Nov. 1999

[106]   G. P. Junker, A. A. Kishk and A. W. Glisson, "Multiport network description and radiation characteristics of coupled dielectric resonator antennas," *IEEE Trans. Antennas Propagat.*, vol. 42, No. 12, pp. 1652-1654, Dec. 1994

[107]   R. J. Dorris, R. T. Long, S. A. Long, M. A. Khayat and J. T. Williams, "Mutual coupling between cylindrical, probe-fed, dielectric resonator antennas", *IEEE Antennas and Wireless Propagat. Lett.*, vol. 1, No. 1, pp. 8-9, Jan. 2002

[108]   Y. Hwang, Y. P. Zhang, K. M. Luk and E. K. N. Yung, "Gain-enhanced miniaturized rectangular dielectric resonator antenna," *Electron. Lett.*, vol. 33, pp. 350-352, Feb. 1997

[109]   G. P. Junker, A. A. Kishk, A. W. Glisson and D. Kajfez, "Effect of an air gap around the coaxial probe exciting a cylindrical dielectric resonator antenna," *Electron. Lett.*, vol. 30, pp. 177-178, Feb. 1994

[110]   G. P. Junker, A. A. Kishk, A. W. Glisson and D. Kajfez, "Effect of fabrication imperfections from ground-plane-backed dielectric resonator antennas," *IEEE Antennas Propagat. magazine*, vol. 37, pp. 40-47, 1995

[111]   G. P. Junker, A. A. Kishk, A. W. Glisson and D. Kajfez, "Effect of an air gap on cylindrical dielectric resonator antenna operating in TM_{01} mode," *Electron. Lett.*, vol. 30, pp. 97-98, Jan. 1994

[112]   G. Drossos, Z. Wu and L. E. Davis, "The air gap effect on a microstrip-coupled cylindrical dielectric resonator antenna," *Microw. and Opt. Techn. Lett.*, vol. 20, pp. 36-40, Jan. 1999

[113]   Z. Li, C. Wu and J. Litva, "Adjustable frequency dielectric resonator antenna," *Electron. Lett.*, vol. 32, pp. 606-607, Mar. 1996

[114]   M. Abramowitz and I. A. Stegun, *Handbook of Mathematical Functions*. National Bureau of Standards, AMS No. 55, pp.231-233, 1964

CHAPTER 2

Rectangular Dielectric Resonator Antennas

Aldo Petosa, Apisak Ittipiboon and Yahia Antar*

Communications Research Centre Canada,
Ottawa,
Canada

*Royal Military College of Canada,
Kingston,
Canada

2.1   INTRODUCTION

One of the attractive features of a dielectric resonator antenna (DRA) is that it can assume any one of a number of simple shapes, the most common being ones with circular or rectangular cross-sections, as shown in Figure 2.1. The DRA with rectangular cross-section (henceforth referred to as simply a rectangular DRA), is the most versatile since it has two degrees of freedom. For any given resonant frequency and fixed dielectric constant, two of the three dimensions of the rectangular DRA can be chosen independently. (The cylindrical DRA has one degree of freedom while the hemispherical DRA has none.) This chapter examines various aspects of the rectangular DRA. In the first section, the dielectric waveguide model, first presented by Marcatili [1], is used to predict the resonant frequency and radiation Q-factor of an isolated rectangular DRA. A simple model for the radiation of an isolated DRA is also presented, along with the effects caused by a finite ground plane. The next section looks at the various feeding mechanisms which can be used to excite rectangular DRAs. It is intended to give the reader an understanding of the coupling mechanisms, and how the various feeds couple to the DRA. The radiation efficiency of DRAs is then examined, using a method for small antennas known as the Wheeler's cap method. The final section reviews a few numerical techniques which have been used to simulate the input impedance and radiation patterns of DRAs.

2.2 DIELECTRIC WAVEGUIDE MODEL FOR RECTANGULAR DIELECTRIC GUIDES

As is the case with many antennas, the deceivingly simple geometry of the DRA poses a significantly complex electromagnetic fields problem. An analytical closed-form solution for all but the hemispherical DRA does not exist. Various numerical techniques such as the Method of Moments (MoM) or the Finite Difference Time Domain (FDTD) method can be used to solve for these fields, but these techniques are time consuming, memory intensive, and are not amenable to design or optimisation. In order to aid with the design of DRAs, several relatively simple models have been developed to estimate the resonant frequency, Q-factor, and radiation patterns. Simple models have not yet been developed to estimate the input impedance of DRAs, and numerical techniques or experimental data must still be relied upon to determine this parameter. This section examines the dielectric waveguide model, used to estimate the resonant frequency and Q-factor for the rectangular DRA.
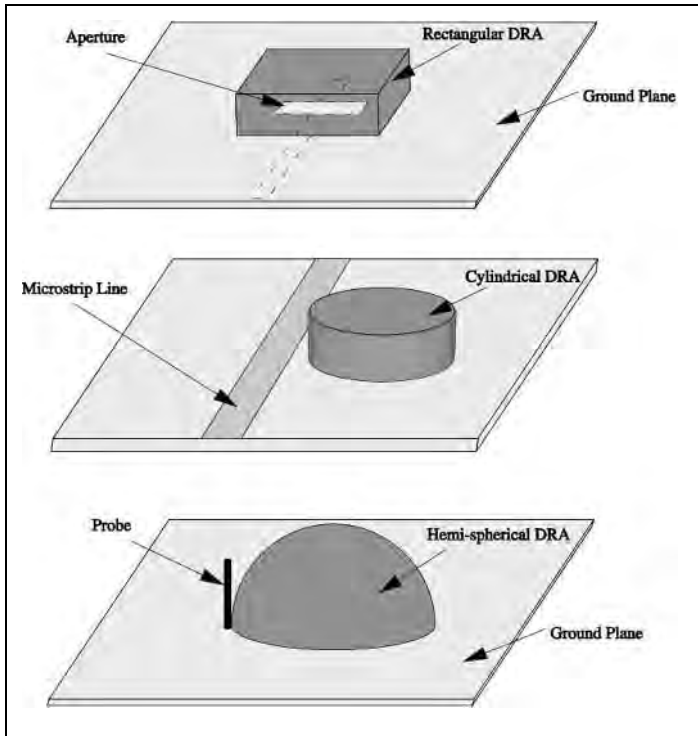
Figure 2.1 Typical dielectric resonator antennas and feeding mechanisms.

The dielectric waveguide model was first proposed by Marcatili [1] to determine the guided wavelength in dielectric guides with rectangular cross-section. The dielectric guide is shown in Figure 2.2a, having a rectangular cross-section of width a in the x-direction, height b in the y-direction and the waves propagating in the z-direction. The field modes in the guide can be divided into TE^y_{mn} and TM^y_{mn}, (where m and n denotes the number of field extrema in the x- and y-direction, respectively inside the guide). The fields within the guide are assumed to vary sinusoidally, while the fields outside the guide are assumed to decay exponentially. In order to simplify the analysis, the fields in the shaded regions of Figure 2.2b are assumed to be zero.
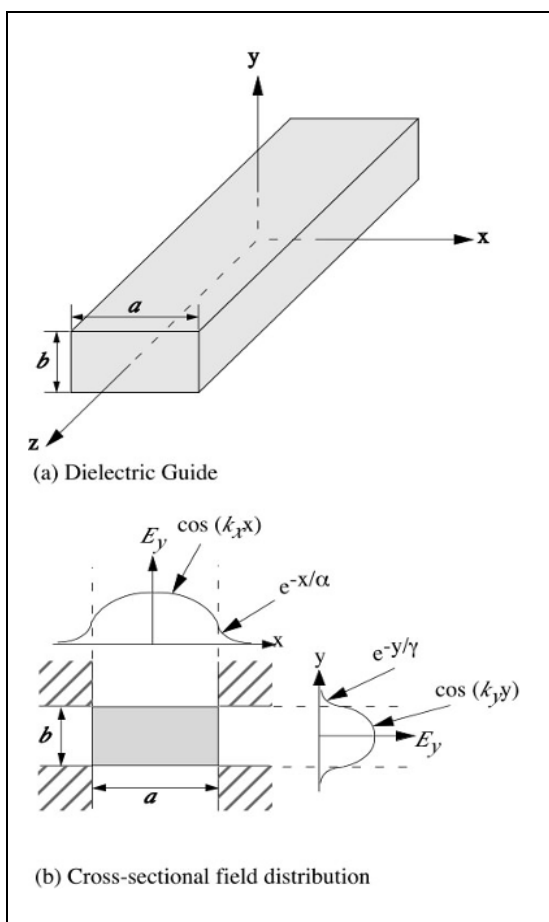
Figure 2.2 Dielectric waveguide. Adapted from [1] © 1969.

By matching the fields at the boundary conditions, the wave propagation numbers in the x-, y-, and z-directions (k_x, k_y, and k_z) (for $|x| \leq a/2$ and $|y| \leq b/2$) and the attenuation constants in the x- and y-directions (α, γ) (for $|x| \geq a/2$ and $|y| \geq b/2$) can be determined, using:

$$k_z = \sqrt{\varepsilon_r k_o^2 - k_x^2 - k_y^2} \tag{2.1}$$

$$k_x = \frac{m\pi}{a}\left(1 + \frac{2}{ak_o\sqrt{\varepsilon_r - 1}}\right)^{-1} \tag{2.2}$$

$$k_y = \frac{n\pi}{b}\left(1 + \frac{2}{bk_o\sqrt{\varepsilon_r - 1}}\right)^{-1} \tag{2.3}$$

$$\alpha = \frac{1}{\sqrt{(\varepsilon_r - 1)k_o^2 - k_x^2}} \tag{2.4}$$

$$\gamma = \frac{1}{\sqrt{(\varepsilon_r - 1)k_o^2 - k_y^2}} \tag{2.5}$$

where k_o is the free-space wave number given by:

$$k_o = \frac{2\pi}{\lambda_o} = \frac{2\pi f_o}{c} \tag{2.6}$$

where c is the speed of light in free space, f_o is the operating frequency, and λ_o is free space wavelength. For well-guided modes, the fields are confined within the guide and a further approximation can be made:

$$k_x = \frac{m\pi}{a} \tag{2.7}$$

$$k_y = \frac{n\pi}{b} \tag{2.8}$$

This approximation is equivalent to assuming that magnetic walls exist at $x = \pm a/2$ and $y = \pm b/2$.

2.3   DIELECTRIC WAVEGUIDE MODEL FOR RECTANGULAR DRAs

To model the dielectric resonator antenna, the waveguide is truncated along the z-direction at $\pm d/2$, as shown in Figure 2.3b, with magnetic walls. This model can be used for an isolated DRA in free space (with dimensions a, b, and d), or as is used in practice, for a DRA (with dimensions a, $h=b/2$, and d) mounted on a ground plane, as shown in Figure 2.3c. In this latter case, image theory was used to remove the ground plane and double the height of the DRA.

(a) Infinite Dielectric Waveguide   (b) Truncated Dielectric Waveguide

(c) DRA on Ground Plane
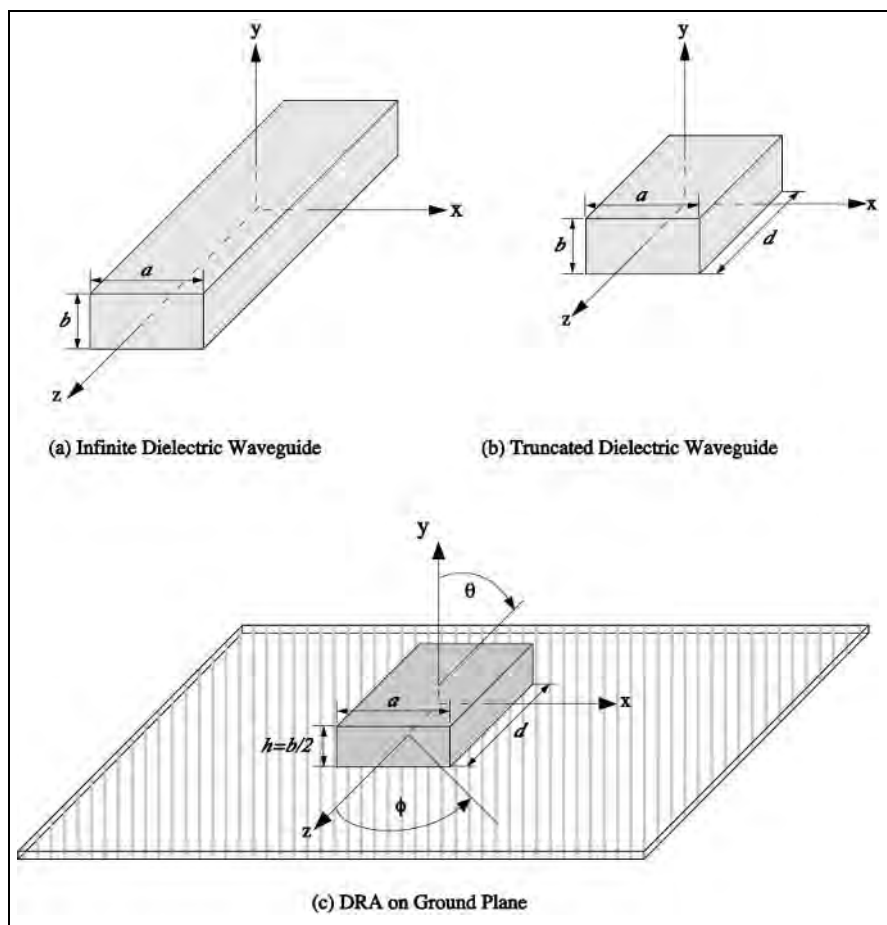
Figure 2.3 Geometry for the dielectric resonator antenna model.

2.3.1 Field Configuration

For a rectangular DRA with dimensions a, $b > d$, the lowest order mode will be $TE^z_{11\delta}$. Using the dielectric waveguide model, this leads to the following fields within the DRA [2]:

$$H_x = \frac{(k_x k_z)}{j\omega\mu_o} \sin(k_x x)\cos(k_y y)\sin(k_z z) \qquad (2.9)$$

$$H_y = \frac{(k_y k_z)}{j\omega\mu_o} \cos(k_x x)\sin(k_y y)\sin(k_z z) \qquad (2.10)$$

$$H_z = \frac{(k_x^2 + k_y^2)}{j\omega\mu_o} \cos(k_x x)\cos(k_y y)\cos(k_z z) \qquad (2.11)$$

$$E_x = k_y \cos(k_x x)\sin(k_y y)\cos(k_z z) \qquad (2.12)$$

$$E_y = -k_x \sin(k_x x)\cos(k_y y)\cos(k_z z) \qquad (2.13)$$

$$E_z = 0 \qquad (2.14)$$

where:

$$k_x^2 + k_y^2 + k_z^2 = \varepsilon_r k_o^2 \qquad (2.15)$$

$$k_z \tan(k_z d / 2) = \sqrt{(\varepsilon_r - 1)k_o^2 - k_z^2} \qquad (2.16)$$

and where (2.7) and (2.8) are used for k_x and k_y, respectively. The $e^{j\omega t}$ time dependence is assumed in the above equations. The value δ can be defined as the fraction of a half cycle of the field variation in the z-direction and is given by:

$$\delta = \frac{k_z}{\pi / d} \qquad (2.17)$$

The fields for the $\mathrm{TE}^z_{11\delta}$ mode of an isolated DRA in free space with $a = b = 4d$ are sketched in Figure 2.4. These fields are similar to those produced by a short magnetic dipole.

2.3.2   Resonant Frequency

To solve for the resonant frequency of the DRA, (2.7), (2.8) and (2.15) are first substituted into (2.16), and this transcendental equation is solved for k_z. The resonant frequency can then be obtained by solving for k_o in (2.15).

The above equations have been used to plot the curves in Figure 2.5. These curves plot the normalised frequency (F) versus the ratio of DRA dimensions d/b for various ratios of a/b. The normalised frequency is defined as:

$$F = \frac{2\pi a f_o \sqrt{\varepsilon_r}}{c} \qquad (2.18)$$

These curves are quite general and can be used to quickly determine the resonant frequency of the DRA without having to solve the transcendental equation. For example, to solve for the resonant frequency of a DRA with $\varepsilon_r = 10$ and dimensions $a = b = d = 10$ mm then, from the $a = b$ curve in Figure 2.5, at $d/b = 1$, the value of $F = 5$. Then using (2.18), $f_o = 7.55$ GHz.
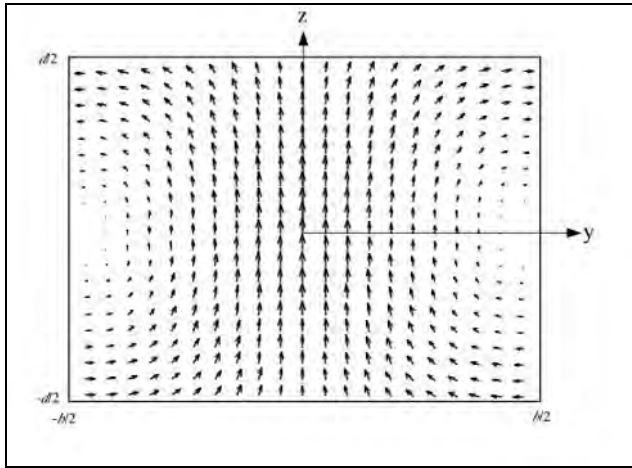
Figure 2.4 (a) DRA fields H_y and H_z at x = 0.
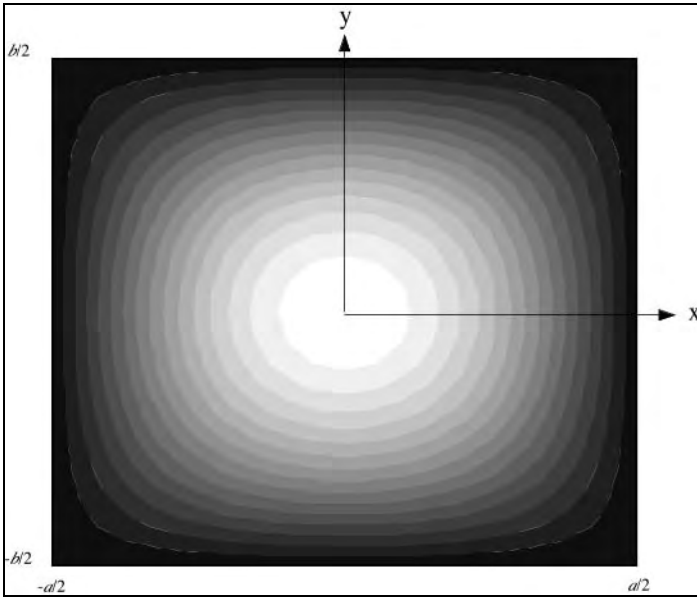
Figure 2.4 (b) DRA fields H_z at z = d/2.
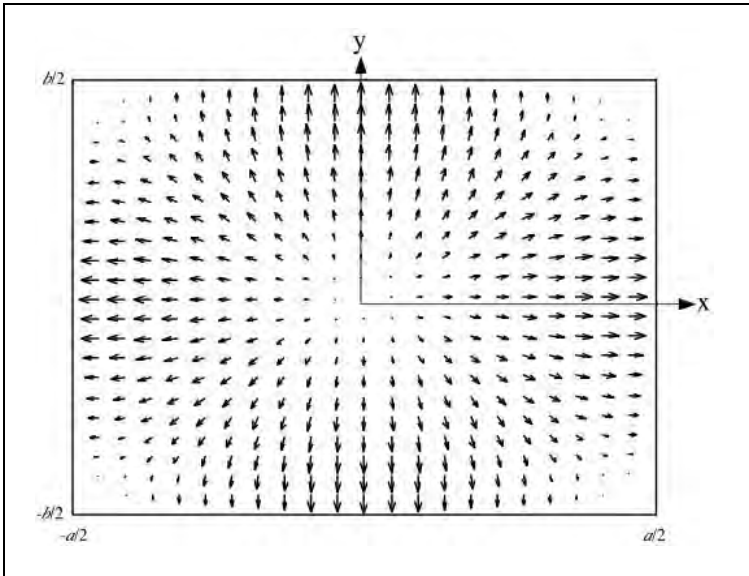
Figure 2.4 (c) DRA fields H_x and H_y at z = d/2.
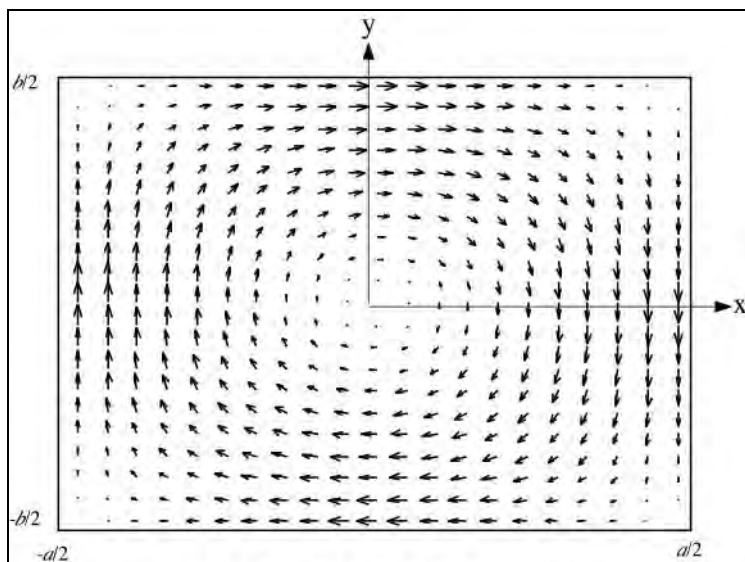
Figure 2.4 (d) DRA fields E_x and E_y at z = $d/2$.
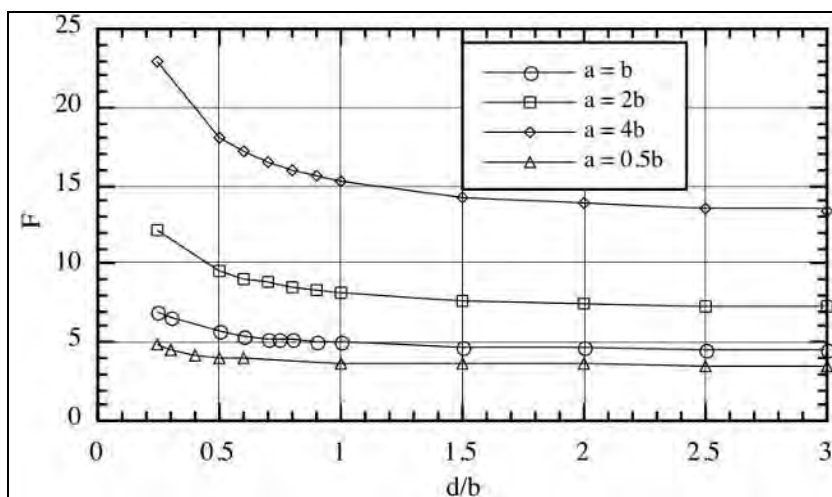
Figure 2.5 Normalised frequency of a rectangular DRA.

2.3.3 Q-Factor

The radiation Q-factor of the DRA is determined using [2]:

$$Q = \frac{2\omega W_e}{P_{rad}} \qquad (2.19)$$

where W_e and P_{rad} are the stored energy and radiated power, respectively. These quantities are given by:

$$W_e = \frac{\varepsilon_o \varepsilon_r abd}{32}\left(1 + \frac{\sin(k_z d)}{k_z d}\right)\left(k_x^2 + k_y^2\right) \qquad (2.20)$$

$$P_{rad} = 10k_o^4 |\boldsymbol{p_m}|^2 \qquad (2.21)$$

where $\boldsymbol{p_m}$ is the magnetic dipole moment of the DRA:

$$\boldsymbol{p_m} = \frac{-j\omega 8\varepsilon_o(\varepsilon_r - 1)}{k_x k_y k_z}\sin(k_z d/2)\hat{\boldsymbol{z}} \qquad (2.22)$$

The impedance bandwidth (BW) of the DRA can be estimated from the radiation Q-factor using:

$$BW = \frac{S - 1}{Q\sqrt{S}} \qquad (2.23)$$

where S is the maximum acceptable voltage standing-wave ratio (VSWR). The above equations were used to generate the graphs in Figure 2.6. These graphs plot the normalised Q-factor (Q_e) as a function of the DRA dimensions d/b for various values of dielectric constant and various values of a/b. The normalised Q-factor is defined as:

$$Q_e = \frac{Q}{\varepsilon_r^{3/2}} \qquad (2.24)$$

These curves can be used to estimate the Q-factor of a DRA without having to rely on the preceding equations.
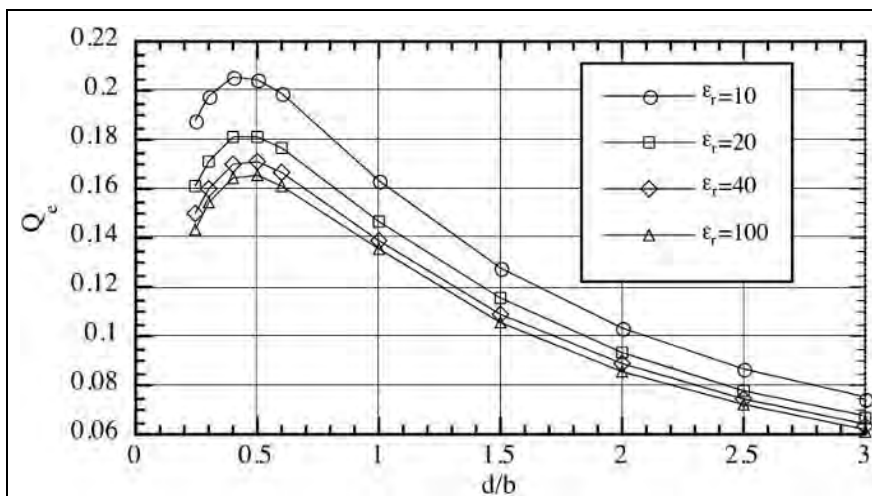
Figure 2.6 (a) Normalised Q-factor of a rectangular DRA with $2a = b$.
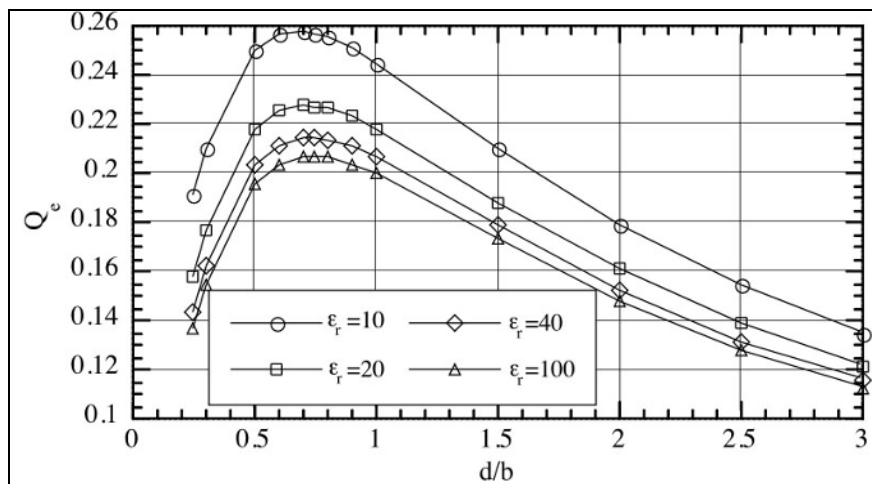
Figure 2.6 (b) Normalised Q-factor of a rectangular DRA with $a = b$.
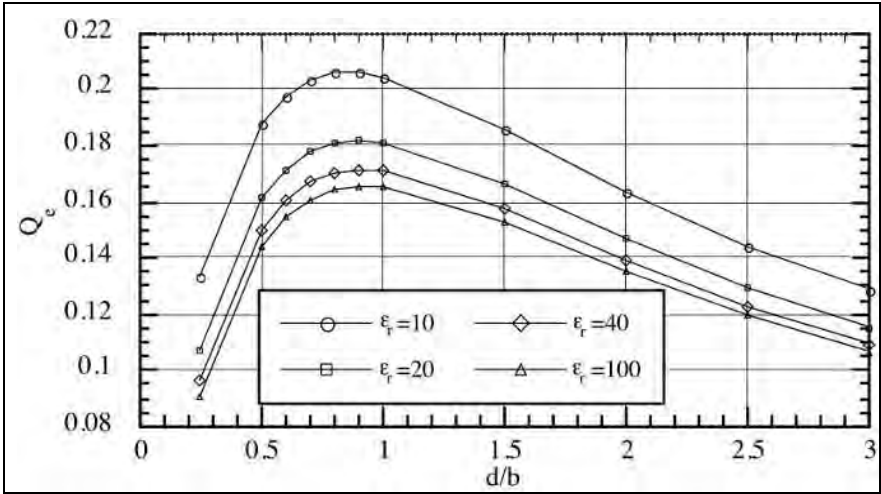
Figure 2.6 (c) Normalised Q-factor of a rectangular DRA with $a = 2b$.
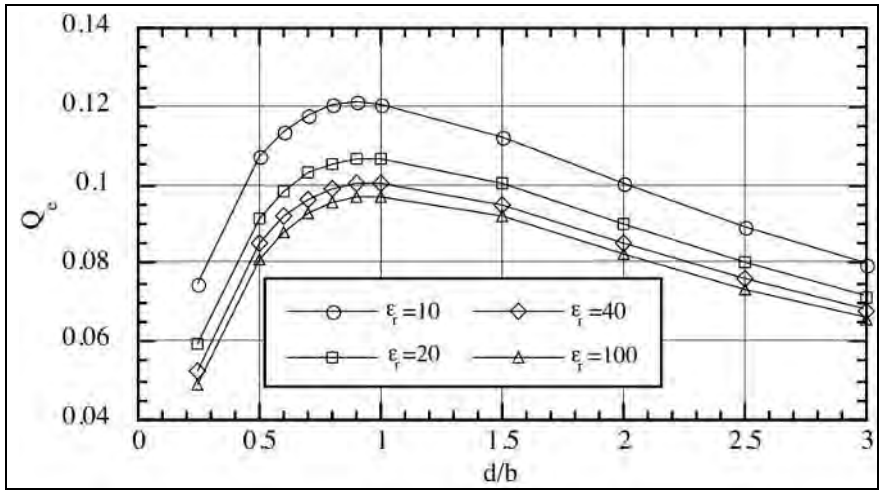
Figure 2.6 (d) Normalised Q-factor of a rectangular DRA with $a = 4b$.

2.4   RADIATION MODEL

The field distribution of the lowest order mode of the rectangular DRA, determined by the dielectric waveguide model equations, is similar to that of a short magnetic dipole. The radiation patterns generated by the DRA can therefore be approximated using the short magnetic dipole. Figure 2.7 depicts the equivalent model for a rectangular DRA mounted on an infinite ground plane and excited in the $TE^z_{11\delta}$ mode. This corresponds to a horizontal magnetic dipole aligned along the z-axis (Figure 2.7b). The resulting radiation patterns (Figure 2.7c) assume that the DRA is mounted on an infinite ground plane. For practical applications, DRAs are mounted on finite ground planes, which will have an effect on the radiation patterns due to diffraction from the edges. These effects will be considered in the next section.

2.5   FINITE GROUND PLANE EFFECTS

The dielectric waveguide model equations used in the previous sections were all based on the assumption that the DRAs were mounted on infinite ground planes. In most practical applications, however, DRAs are mounted on finite ground planes. This will have an impact on the radiation patterns since there will be scattering from the edges of the ground plane. These effects are not predicted by the simple short magnetic dipole model. There are techniques such as numerical methods (method of moments, finite element method, transmission line matrix method) or the Geometric Theory of Diffraction (GTD) available for predicting these effects. Numerical methods are only practical when the size of the geometry is small (with ground planes ~ 1 λ) due to computer memory requirements. For larger ground planes, GTD can be used. GTD produces reasonable agreement and is not computer intensive. GTD is a ray tracing technique first introduced to predict the behaviour of optical rays near finite edges or grazing surfaces [3]. The technique has been adapted for electromagnetic wave problems [4]. This section provides a brief review of the GTD and presents an example of its application to a probe-fed rectangular DRA mounted on a finite ground plane.

The Geometric Theory of Diffraction (GTD) is an extension of Geometric Optics (GO). GO is a ray tracing technique in which direct and reflected rays are superimposed to obtain the overall field. GTD extends the principles of GO by the addition of a diffracted field. Figure 2.8 shows the direct and diffracted fields of a DRA placed on a finite ground plane and located a distance d_1 from edge 1 and d_2 from edge 2. The total radiated field (E_t) can then be expressed as a vector sum of the GO fields (E_{go}) and the diffracted fields (E_d):

$$E = E_{go} + E_{d1} + E_{d2} \qquad (2.25)$$
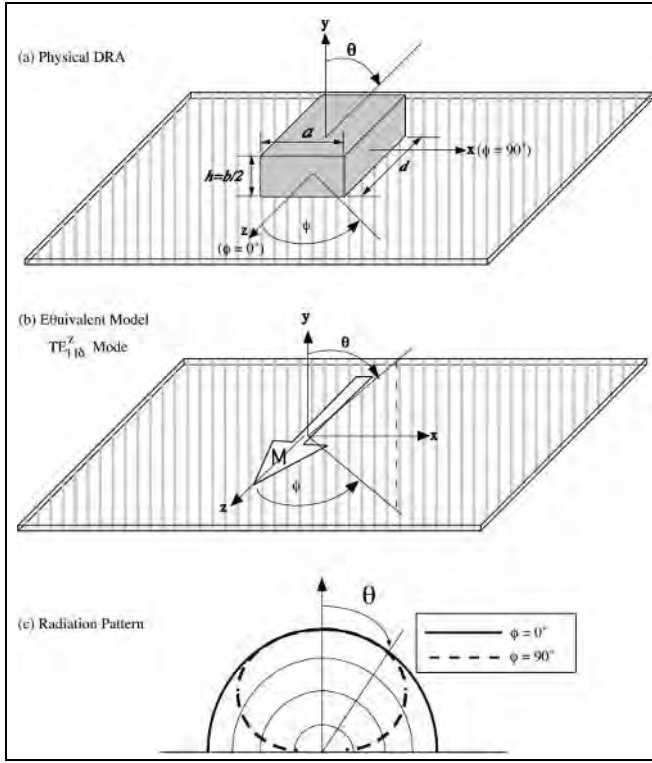
Figure 2.7 Radiation model of the rectangular DRA.

The strength of the diffracted field can be determined by calculating the diffraction coefficient (*D*) [5]. The diffracted fields from each edge are then found using:

$$\boldsymbol{E}_{d_i} = 0.5 \cdot \boldsymbol{E}_{go}(\theta = \pm 90°) \cdot D(d_i, \psi_i, n) \cdot \frac{e^{-jkd_i(1\pm\sin\theta)}}{\sqrt{d_i}} \cdot e^{-jkr} \tag{2.26}$$

where:
  $i = 1,2$, corresponding to the two edges;
  $D(d_i, \psi_i, n)$ is the diffraction coefficient, found in [5];
  θ, r, d_i and ψ_i are shown in Figure 2.8;
  n is the wedge angle number ($n=2$ for a plane wedge);
  and the $\pm$ refers to $i=1$ and $i=2$, respectively.
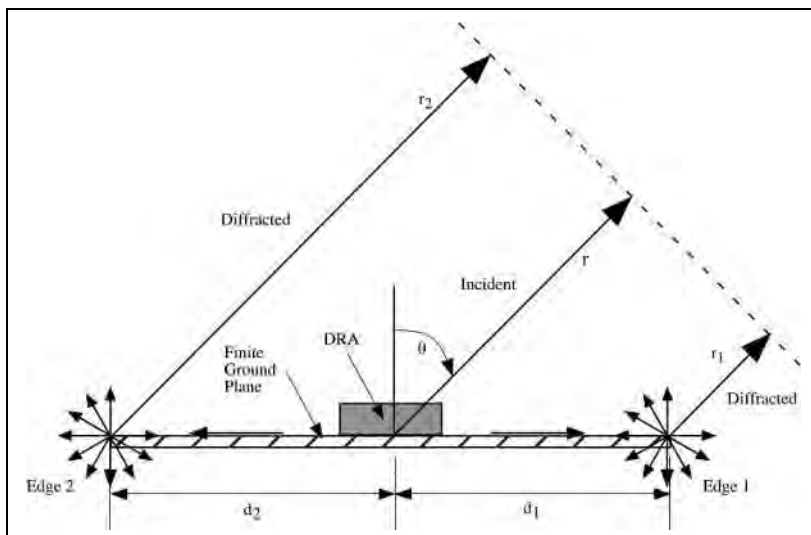
Figure 2.8. Diffraction from a finite ground plane. Adapted from [5] © 1982, Harper and Row.

As an example, GTD has been used to predict the finite ground plane effect on the radiation pattern of a probe-fed rectangular DRA mounted on a 30 cm circular ground plane. The measured and predicted radiation patterns at 3.7 GHz are compared in Figure 2.9. The finite ground plane introduces ripples in the pattern and backlobe radiation, which are not predicted by the short magnetic dipole model. GTD is seen to predict these effects with reasonable accuracy [6]. GTD has proven to be a useful tool in predicting the effects of finite ground planes on the radiation patterns of DRAs. It is not a computer intensive method, and results can be obtained in a matter of seconds compared to the hours of computation time required for some numerical techniques.

2.6   COUPLING METHODS TO DRAs

Up to this point, the DRAs analyzed were treated as being isolated in free space or mounted on an infinite ground plane. The equations that have been presented for the fields within the DRAs, their resonant frequency and Q-factors do not take into consideration the method of coupling energy to the DRA. These coupling mechanisms can have a significant impact on the resonant frequency and Q-factor, which the above equations will fail to predict. This section begins with a brief review of coupling theory, then the various methods of coupling to DRAs will be described and performance of several configurations will be highlighted.
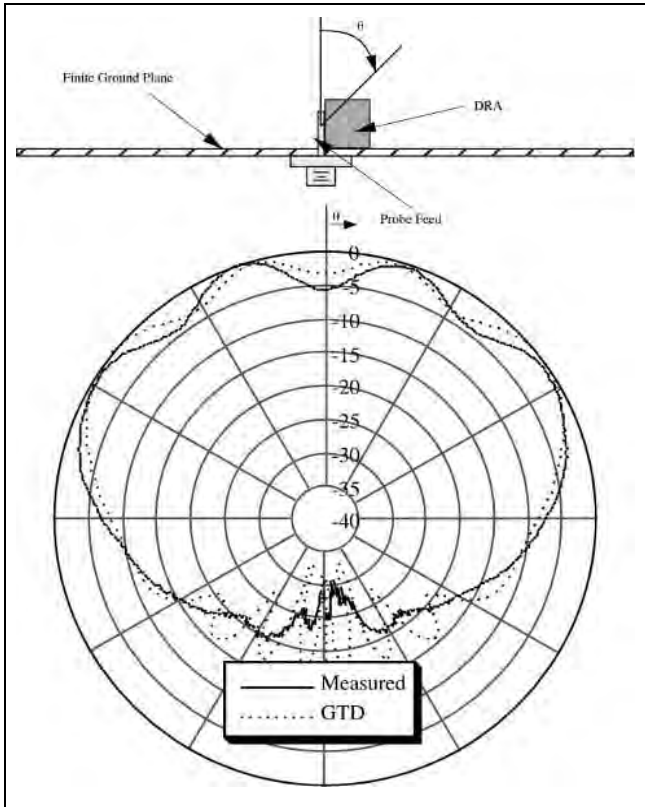
Figure 2.9 E-plane pattern of a DRA on a 30 cm ground plane at 3.7 GHz.

2.6.1 Review of Coupling Theory

For most practical applications, in order for the DRA to be of any use, energy must be coupled into or out of the element through one or more ports. (One notable exception to this is when the DRA is used in a reflectarray configuration [7].) The type of port used, and the location of the port with respect to the DRA will determine which mode will be excited and how much energy will be coupled between the port and the antenna. The mode or modes generated, the amount of coupling, and the frequency response of the impedance are all important in determining the performance of the DRA. Although these quantities are difficult to determine without using numerical methods, a great deal of insight can be obtained by knowing the approximate field distributions of the modes of the isolated DRA, making use of the Lorentz Reciprocity Theorem and some coupling theory borrowed from resonator circuits [8].

Given two electric current sources, J_1 and J_2 in a volume V enclosed by a surface S, which give rise to electric fields E_1 and E_2, respectively, and two magnetic currents M_1 and M_2 giving rise to magnetic fields H_1 and H_2, then the Lorentz Reciprocity Theorem can be expressed as [9]:

$$\oint_S (E_1 \times H_2 - E_2 \times H_1) \cdot dS = \int_V (E_2 \cdot J_1 - E_1 \cdot J_2 - H_2 \cdot M_1 - H_1 \cdot M_2) dV \quad (2.27)$$

which reduces to:

$$\int_V (E_1 \cdot J_2 - H_1 \cdot M_2) dV = \int_V (E_2 \cdot J_1 - H_2 \cdot M_1) dV \quad (2.28)$$

The theorem states that the component of the electric field E_1 along source J_2, is the same as the component of the field E_2, along source J_1. The same holds true for two magnetic sources and magnetic fields. When coupling to a DRA, there is typically only one source (either electric or magnetic) and the amount of coupling, k, between the source and the fields within the DRA can be determined by applying (2.28) with the appropriate boundary conditions. For an electric source J_1,

$$k \propto \int_V (E_2 \cdot J_1) dV \quad (2.29)$$

and for a magnetic source M_1,

$$k \propto \int_V (H_2 \cdot M_1) dV \quad (2.30)$$

Equation (2.29) states that in order to achieve strong coupling using an electric current source (like a probe), then that source should be located in an area of strong electric fields within the DRA. On the other hand, to achieve strong coupling using a magnetic current source (like a loop) then from equation (2.30) the source should be located in an area of strong magnetic fields. It is thus necessary to have a good understanding of the field structures of the isolated DRA, to determine where the feed should be placed to excite the appropriate mode in the DRA.

The coupling mechanism to the DRA, in addition to transferring energy, has a loading effect which will influence the Q-factor of the DRA. An external Q-factor (Q_{ext}) can be defined in terms of the coupling factor:

$$Q_{ext} = \frac{Q}{k} \tag{2.31}$$

and the loaded Q-factor (Q_L) of the DRA can then be expressed as:

$$Q_L = \left(\frac{1}{Q} + \frac{1}{Q_{ext}}\right)^{-1} = \frac{Q}{1+k} \tag{2.32}$$

Maximum power is transferred between the coupling port and the DRA when the coupling factor is unity. This condition is called critical coupling. When $k < 1$, the DRA is said to be under coupled, while when $k > 1$, the DRA is over coupled. The following sections will review some of the more common coupling methods to DRAs.

2.6.2 Slot Aperture

Figure 2.10 depicts a DRA fed by an aperture. Although a rectangular DRA is shown, aperture coupling is applicable to DRAs of any shape. The aperture behaves like a magnetic current running parallel to the length of the slot, which excites the magnetic fields in the DRA. The aperture consists of a slot cut in a ground plane and fed by a microstrip line beneath the ground plane. This coupling mechanism has the advantage of having the feed network located below the ground plane, thus avoiding spurious radiation. The microstrip stub can be designed to cancel out the reactive component of the slot, thus allowing for an impedance match to the DRA. Moreover, slot coupling is an attractive method for integrating DRAs with printed feed structures [10-12]. The coupling level can be adjusted by moving the DRA with respect to the slot. An example of this is shown in Figure 2.11 for a rectangular DRA designed at 5.5 GHz. A significant amount of impedance tuning can be obtained by moving the location of the DRA with respect to the slot. Figure 2.12 shows return loss plots for the DRA centred over the slot, and for the DRA at an offset position. A tuning range of almost 1.5 GHz can be achieved by offsetting the DRA away from the centre of the slot, allowing for a large degree of design flexibility. Coupling using slot apertures is practical at frequencies above L-Band. At and below L-Band, the slot size becomes excessively large.

2.6.3. Coaxial Probe

Another common method for coupling to DRAs is using a probe, as shown in Figure 2.13. The probe can either be located adjacent to the DRA or can be embedded within it. The amount of coupling can be optimised by adjusting the probe height and the DRA location. Also, depending on the location of the probe,

various modes can be excited. For the probe located adjacent to the DRA, as in Figure 2.13, the magnetic fields of the $TE_{11\delta}$ mode of the rectangular DRA are excited (which radiate like a horizontal magnetic dipole). For a probe located in the centre of a cylindrical DRA, the TE_{011} mode is excited (radiating like a vertical dipole). Another advantage of using probe coupling is that one can couple directly into a 50Ω system, without the need for a matching network. Probes are useful at lower frequencies where aperture coupling may not be practical due to the large size of the slot required [13-16].
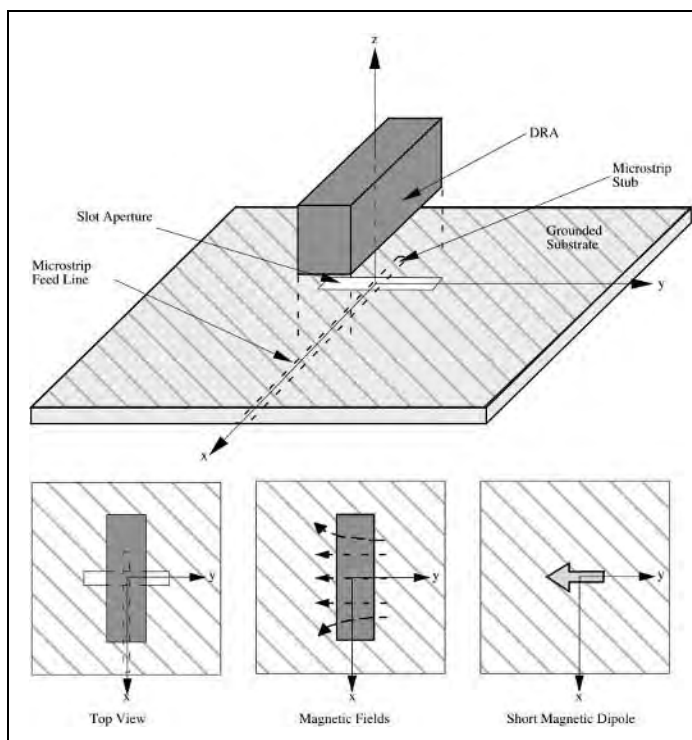
Figure 2.10 Aperture-fed DRA.

2.6.4 Microstrip Line

A common method for coupling to dielectric resonators in microwave circuits is by proximity coupling to microstrip lines. This approach is equally applicable to DRAs, as shown in Figure 2.14. Microstrip coupling will excite the magnetic

fields in the DRA to produce the short horizontal magnetic dipole mode. The level of coupling can be adjusted by the lateral position of the DRA with respect to the microstrip line and on the relative permittivity of the DRA. For lower permittivity values (necessary for DRAs requiring wide bandwidth), the amount of coupling is generally quite small. Thus, in order to have an acceptable radiation efficiency, an array of DRAs is required. Microstrip lines can be used as a series feed for a linear array of DRAs, provided that a sufficient number of elements are used. One disadvantage of this method is that the polarisation of the array is dictated by the orientation of the microstrip line (as shown in Figure 2.14, the direction of the magnetic fields in the DRA will be parallel to the microstrip line) [17].

2.6.5 Co-Planar Feeds

Coupling to DRAs can also be achieved using co-planar feeds. Figure 2.15 shows a cylindrical DRA coupled to a co-planar loop. The coupling level can be adjusted by positioning the DRA over the loop. The coupling behaviour of the co-planar loop is similar to that of the coaxial probe, but the loop offers the advantage of being non-obtrusive. By moving the loop from the edge of the DRA to the centre, one can couple into either the $HE_{11\delta}$ mode or the TE_{011} mode of the cylindrical DRA [18]. A co-planar slot can also be used to feed the DRA as shown in Figure 2.16 [19- 21].
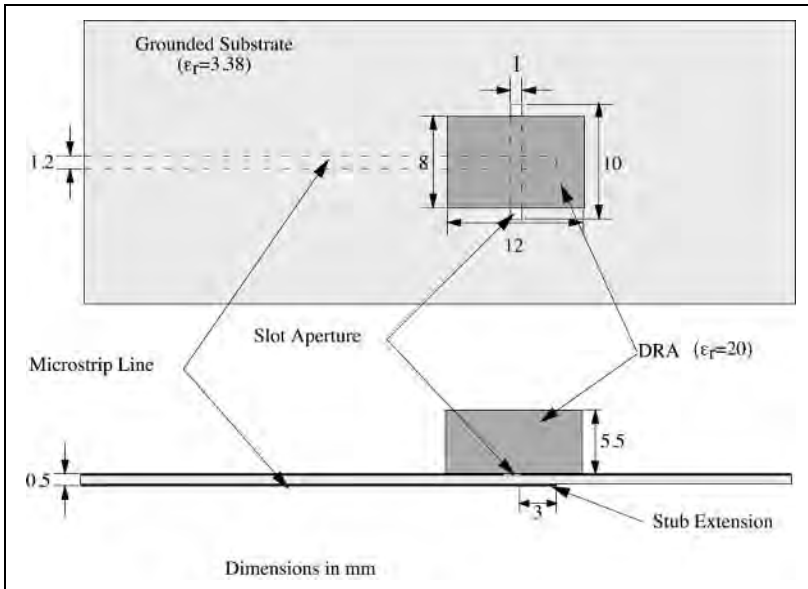
Figure 2.11 Aperture-fed DRA at 5.5 GHz.
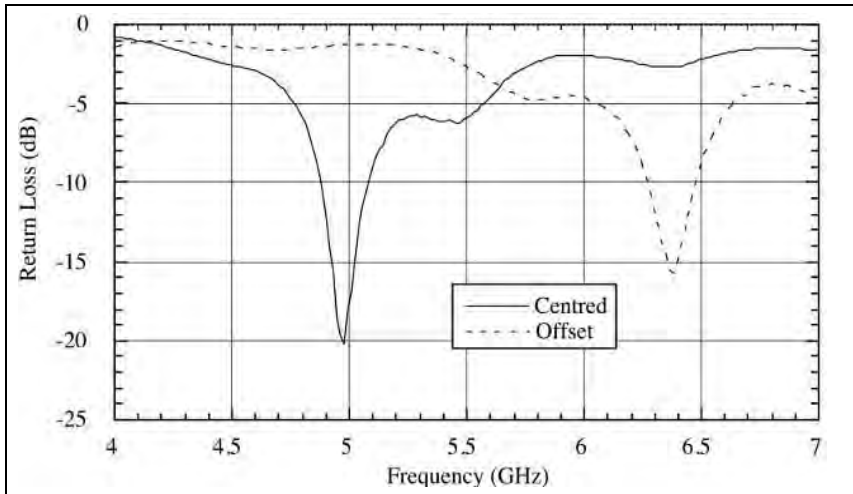
Figure 2.12 Measured return loss of aperture-fed DRA.
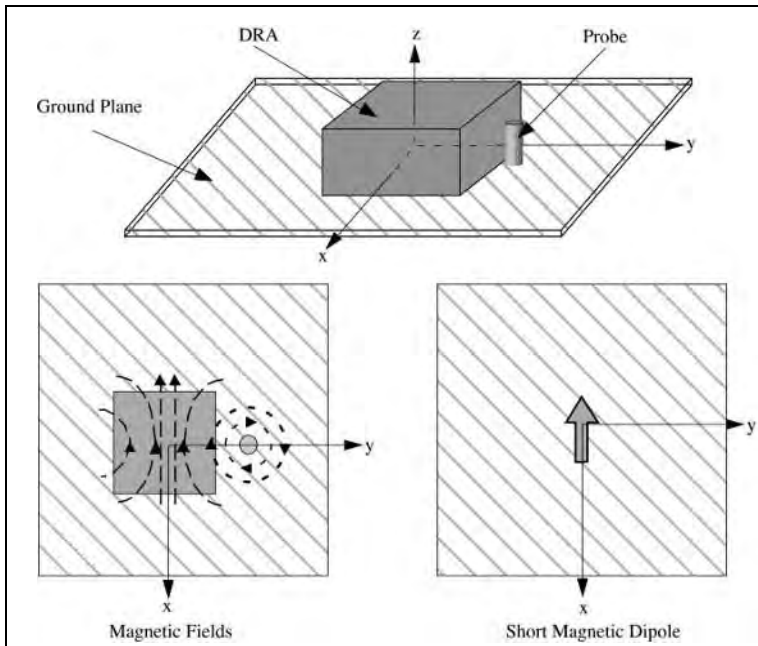
Figure 2.13 Probe-fed DRA.
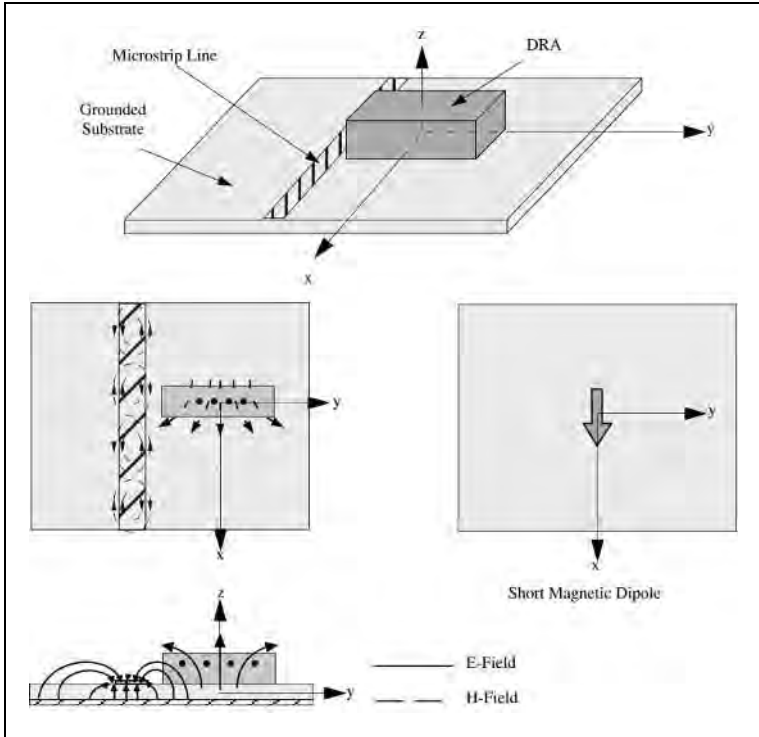
Figure 2.14 Microstrip-fed DRA.

2.6.6 Dielectric Image Guide

DRAs can also be coupled to dielectric image guides, as shown in Figure 2.17. Dielectric image guides offer advantages over microstrip at millimeter-wave frequencies since they do not suffer as severely from conductor losses. As with microstrip lines, the amount of coupling to the DRA is generally quite small, especially for DRAs with lower permittivity values, although it may be possible to increase the coupling by operating the guide closer to the cut-off frequency. The dielectric image guide is thus best utilised as a series feed to a linear array of DRAs [22-23].
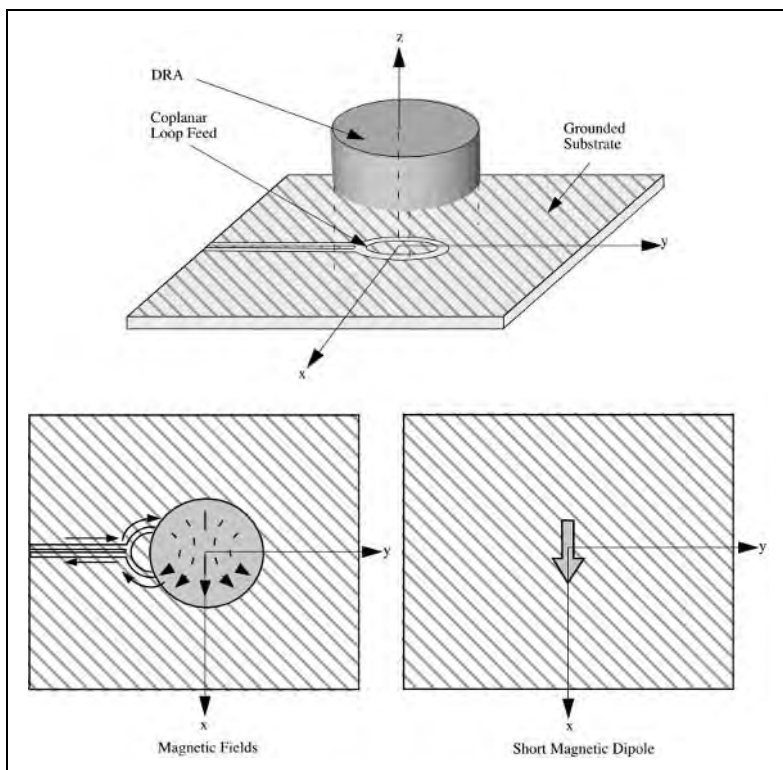
Figure 2.15 Co-planar loop-fed DRA. Adapted from [18] © 1991 IEEE.
Reprinted with permission.

2.7   RADIATION EFFICIENCY OF A RECTANGULAR DRA

There are several methods for estimating the radiation efficiency of antennas. For physically small antennas a useful technique is the Wheeler cap method [24]. This method is based on the Q-factor of an antenna (2.19). The total power lost (P) can be divided into two components: radiated power (P_{rad}) and power dissipated as heat (P_{dis}):

$$P = P_{rad} + P_{dis} \tag{2.33}$$
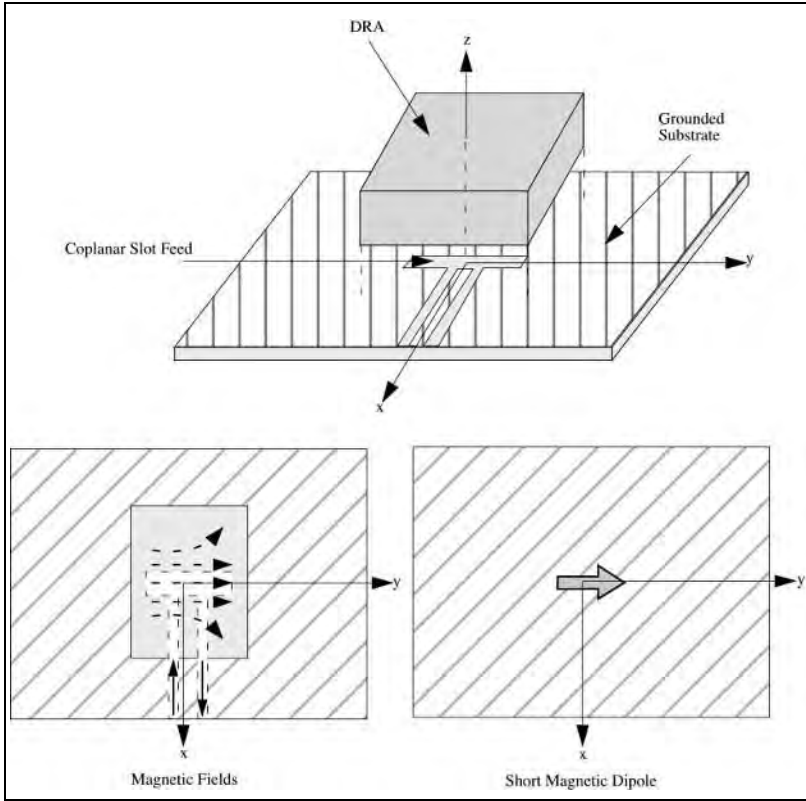
Figure 2.16 Co-planar slot-fed DRA.

The Q-factor of the antenna can thus be decomposed into a radiation Q-factor (Q_{rad}) and a dissipation Q-factor (Q_{dis}):

$$\frac{1}{Q_o} = \frac{P_{rad} + P_{dis}}{\omega W} = \frac{1}{Q_{rad}} + \frac{1}{Q_{dis}} \tag{2.34}$$

The radiation efficiency (η) of the antenna is the ratio of the radiated power (P_{rad}) to the total power which can also be expressed in terms of Q-factors as:

$$\eta = \frac{P_{rad}}{P_{rad} + P_{dis}} = 1 - \frac{Q_o}{Q_{dis}} \tag{2.35}$$
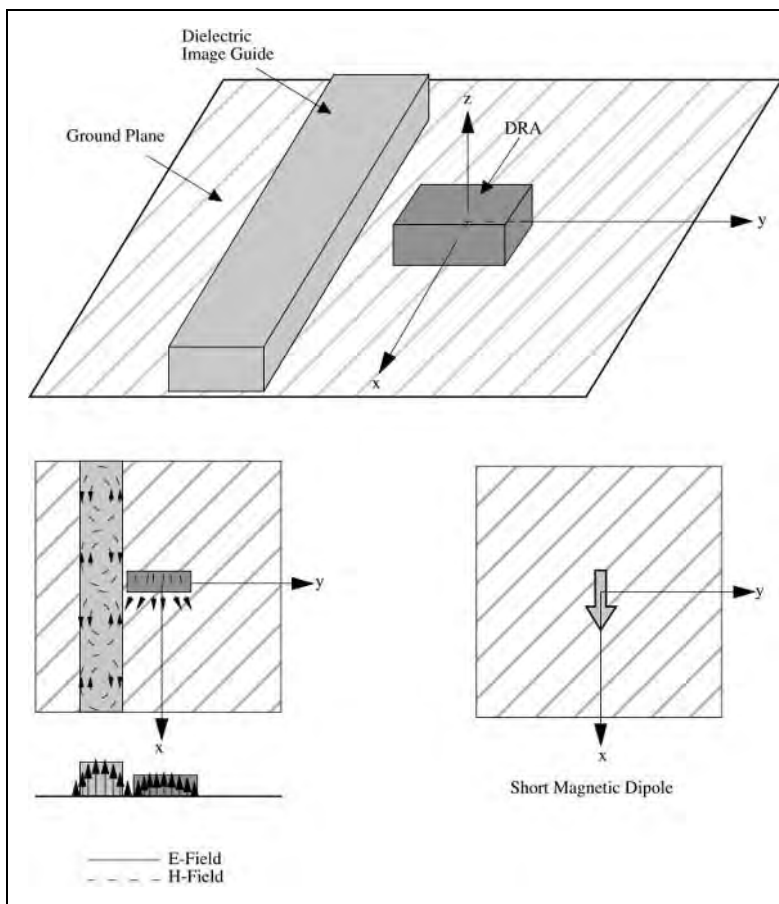
Figure 2.17 Dielectric image guide-fed DRA.

The values of Q_o and Q_{dis} can be determined experimentally by measuring the return loss of the antenna with and without a radiation shield. Figure 2.18 shows a DRA covered by a metallic radiation shield (also known as a Wheeler's cap). Without the shield, the measured bandwidth represents Q_o. When the shield is placed over the antenna, the radiation of the DRA is suppressed and the measured bandwidth represents Q_{dis}. As an example, an estimation of the radiation efficiency of a rectangular DRA operating at 10.5 GHz was carried out and the results of the measured return loss with and without the Wheeler's cap are shown in Figure 2.19.
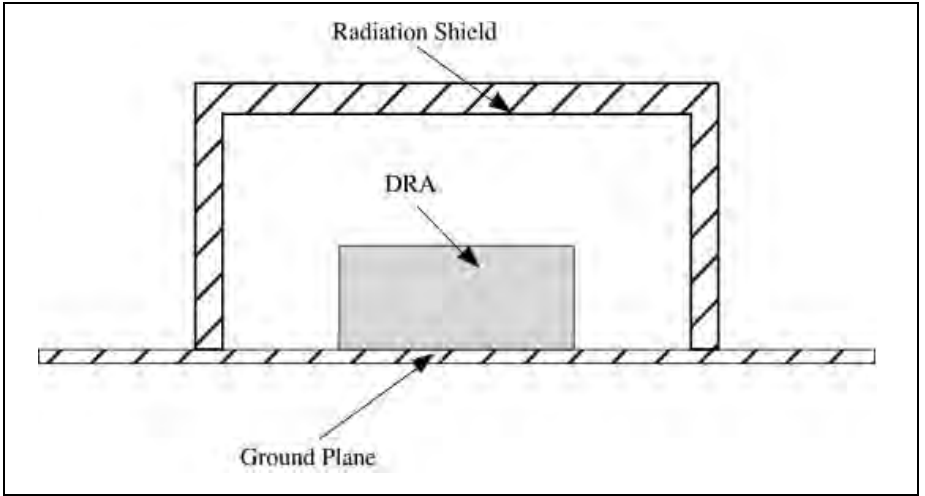
Figure 2.18 Wheeler cap method for determining radiation efficiency.

The 10 dB return loss bandwidth (BW_o) without Wheeler's cap was measured to be:

$$BW_o = (10.90 - 10.14)/10.52 = 0.0722$$

The 10 dB return loss bandwidth (BW_{dis}) with Wheeler's cap was measured to be:

$$BW_{dis} = (10.58 - 10.57)/10.57 = 0.000945$$

Thus the Q-factors were determined to be:

$$Q_o = \frac{\sqrt{S-1}}{S \cdot BW_o} = \frac{\sqrt{1.925-1}}{1.925 \cdot 0.0722} = 6.92$$

$$Q_{dis} = \frac{\sqrt{S-1}}{S \cdot BW_{dis}} = \frac{\sqrt{1.925-1}}{1.925 \cdot 0.000945} = 660.0$$
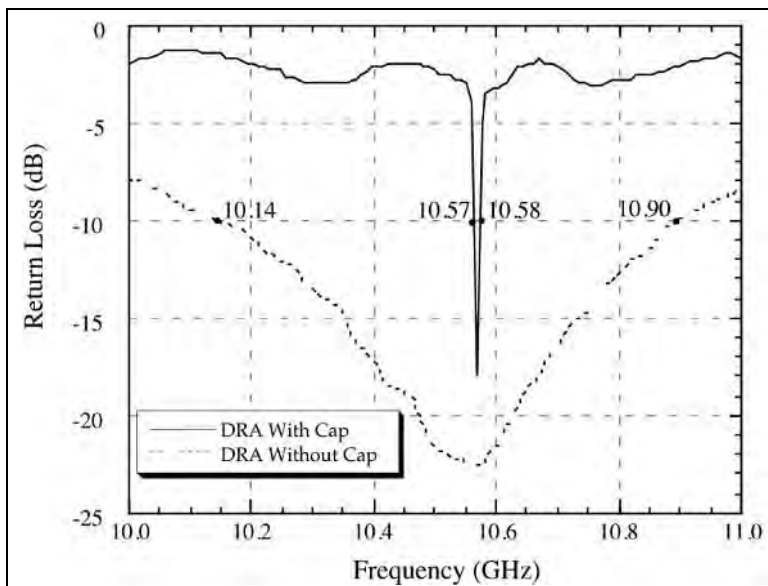
Figure 2.19 Return loss of a DRA with and without a Wheeler cap

The radiation efficiency for this antenna was thus:

$$\eta = 1 - \frac{Q_o}{Q_{dis}} = 1 - \frac{6.92}{660.0} = 0.990 = 99.0\%$$

Similar performance of the radiation efficiency of DRAs has been reported [25].

2.8 NUMERICAL METHODS FOR ANALYZING DRAs

The equations presented thus far were based on various cavity models, waveguide models, or curve fitting to empirically derived data. These equations are useful for estimating the resonant frequency and bandwidth of DRAs in free space or mounted on ground planes. Accuracy can be within a few percent and calculations are straight forward. These equations, however, have certain limitations: they can only handle simple DRA geometries (cylindrical, rectangular, hemispherical); they do not account for the coupling mechanism used to excite the DRA; and they cannot predict input impedance or exact radiation patterns. To solve these problems, more rigorous analysis techniques are required. These methods are

memory and CPU intensive, but can generate accurate solutions. They can also be used to predict mutual coupling between elements in an array, or the effects of air gaps on DRA performance.

Numerical methods for analyzing DRAs can be categorised into two groups: frequency domain techniques and time domain techniques. Each category offers advantages for particular antenna geometries. Frequency domain techniques, such as the spectral domain method (SDM), modal expansion (ME) and method of moments (MoM), have been used to analyze simpler geometries or configurations involving bodies of revolution. These methods are typically not as time or computer intensive as time domain methods. Time domain methods such as the finite-difference time domain (FDTD) and transmission line matrix (TLM) methods have been used to analyze more complex antenna geometries, however, they are time and computer intensive. A few examples of the various geometries successfully analyzed using numerical are presented below:

- MoM used to investigate the effect of air gaps of cylindrical DRAs [26].
- MoM used to calculate internal field patterns of various modes of a cylindrical DRA [27].
- ME used to calculate mutual impedance between probe-fed hemispherical DRAs [28] and split-cylinders DRAs [29].
- FDTD used to calculate cp patterns of cross-shaped DRAs [30].
- FDTD used to calculate input impedance of slot-fed rectangular DRA [31].
- TLM used to calculate input impedance of microstrip-fed multi-segment DRAs [32].

The following example illustrates the performance of numerical models in analyzing a complex DRA geometry. Figure 2.20 shows a multi-segment DRA (MSDRA) fed by a microstrip line [33]. (The MSDRA will be described in detail in Chapter 5.) The return loss of the MSDRA is a strong function of the insert thickness (t), insert permittivity, and the position of the MSDRA with respect to the microstrip line. It is desirable to be able to predict the return loss of the MSDRA in order to be able to optimise the insert parameters. Since the dielectric waveguide model equations presented earlier cannot be used to predict return loss, numerical modelling is required. Figure 2.21 compares the measured return loss of the MSDRA with results obtained by both TLM and FDTD models. Predicted results are in fairly close agreement with the measurements. Both FDTD and TLM are well-suited to analyze inhomogeneous structures with good agreement between measurements and simulations.

As a final example, an aperture-coupled rectangular DRA is analyzed using a hybrid approach using a combination of the modal expansion (ME) method to analyze the DRA, and the spectral domain method (SDM) to analyze the feed structure and the two formulations are coupled through the continuity conditions across the slot-aperture [34]. The integral equations obtained are solved by the Galerkin's method.
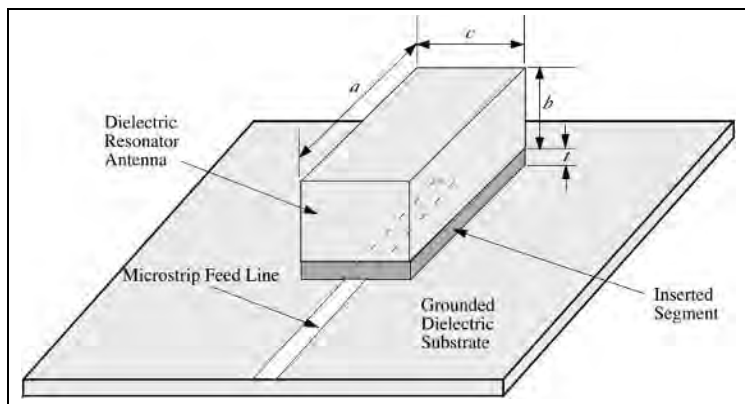
Figure 2.20 Microstrip line fed multi-segment DRA.
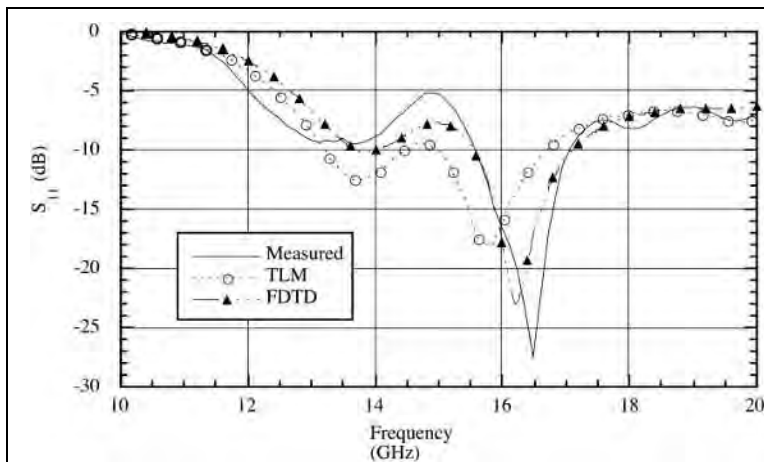
Figure 2.21 Comparison of measured versus simulated return loss of the MSDRA. From [33] © 2000 IEEE. Reprinted with permission.

The slot-coupled microstrip-fed rectangular DRA is shown in Figure 2.22. The equivalent magnetic current density in the slot for the fundamental mode is $\vec{M}^s$ on the resonator side while it is $-\vec{M}^s$ on the feed side. The current density $\vec{M}^s$ is defined as:

$$\vec{M}^s(x,y) = E_x^s(x,y)\hat{\mathbf{x}} \times \hat{\mathbf{z}} = -E_x^s(x,y)\,\hat{\mathbf{y}} \tag{2.36}$$

where the electric field is assumed to be in the x-direction since the width of the slot is very small compared to the wavelength. The problem can be formulated separately on the feed side and on the DRA side, and the two formulations are then combined using the continuity of the tangential magnetic field across the slot. The magnetic field of the rectangular DRA is represented by a modal expansion [35] with the y-component of the magnetic field expressed as:

$$H_y^d(\vec{M}^s) = \sum_{nlm} C_{nlm} H_{y,nlm}^d(x,y,z) \tag{2.37}$$

where

$$C_{nlm} = C_{nlm}^{yy} \int_S E_x^s H_{y,nlm}^d \, dS, \quad C_{nlm}^{yy} = -\frac{j\omega}{2W_T\left\{\omega^2 - \dfrac{\omega_{nlm}^2}{1-j\dfrac{1}{Q_{nlm}}}\right\}} \tag{2.38}$$

and S is the slot area. For the microstrip feed side, the reflection coefficient R and the transmission coefficient T may be written as [36]:

$$R = 1 - T = \frac{1}{2}\int_S E_x^s(x,y)\, h_y(\vec{J}^f)\, dS \tag{2.39}$$

where h_y is the y-component of the normalised magnetic field due to the electric current $\vec{J}^f$ on the microstrip transmission line of the fundamental mode. The y-component of the total magnetic field near the slot can be written as:

$$H_y(x,y,0^-) = H_y(-\vec{M}^s) + (1-R)\,h_y(\vec{J}^f) \tag{2.40}$$

where $H_y(-\vec{M}^s)$ is generated by the magnetic current in the slot. The y-component of the total magnetic field should be continuous across the slot:

$$H_y(\vec{M}^s) = H_y(-\vec{M}^s) + (1-R)\,h_y(\vec{J}^f) \tag{2.41}$$

To solve this equation, the Galerkin's method is applied where the electric field in the slot is expanded in terms of entire domain basis functions. The electric field is expanded as follows:

$$E_x^s(x,y) = \sum_{m=1}^{M} C_m \, E_m^s(x,y) = \sum_{m}^{M} \frac{C_m}{w_s} \sin\!\left(\frac{m\pi}{l_s}(y + \frac{l_s}{2})\right) \tag{2.42}$$

where l_s and w_s are the slot length and width, respectively. Similarly, the x- and y-components of the electric current J^f in equation (2.41) are expanded in terms of the Tchebyshev polynomials weighted by a suitable singular function.

$$J_x^f(y) = \sum_{m=0}^{N_x} C_{xm} \, J_{xm}^f(y) \tag{2.43}$$

$$J_y^f(y) = \sum_{m=0}^{N_y} C_{ym} \, J_{ym}^f(y) \tag{2.44}$$
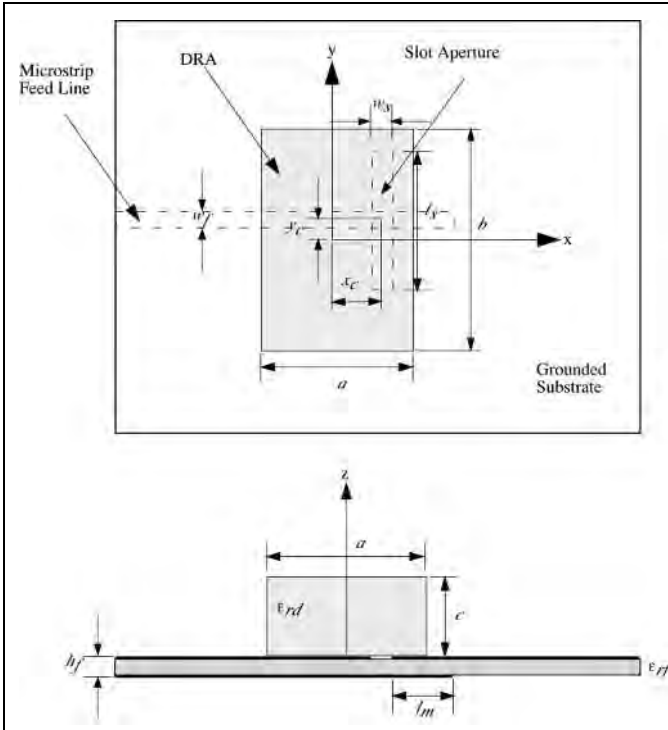
Figure 2.22 Aperture-coupled DRA analyzed using model expansion.
DRA: ε_{rd}= 10, a= b= 20.3mm, c=5.1mm,
Slot: l_s= 7.5mm, w_s= 0.7mm, x_c= 4.8mm, y_c= 0,
Microstrip Feed: ε_{rf}= 10.2, w_f= 0.6mm, h_f= 0.635mm, l_m= 1.804mm.

The basis functions for the fundamental mode are:

$$J_{xm}^f(y) = \frac{\partial J_{ym}^f(y)}{\partial y} = W(y) T_{2m}(\frac{2y}{w_f}) \qquad for \quad |y| < \frac{w_f}{2} \tag{2.45}$$

where

$$W(y) = \left[1 - \left(\frac{2y}{w_f} \right)^2 \right]^{-1/2} \tag{2.46}$$

where T_m is the Tchebyshev polynomial. Substituting (2.42-2.44) into (2.41) and testing the resulting equation by the above described basis functions, a matrix system of algebraic equations is obtained, which can be solved by any standard technique.

From transmission line theory, the slot impedance Z_s is given by:

$$Z_s = Z_0 \frac{2R}{1-R} \tag{2.47}$$

where Z_0 is the characteristic impedance of the microstrip feed line for the fundamental mode. The input impedance at the center of the slot is the summation of the slot impedance and the stub impedance:

$$Z_{in} = Z_s - j Z_0 \frac{1}{\tan(\beta l_m)} \tag{2.48}$$

where β is the propagation constant along the feed line.

This ME-SD hybrid method can be used to quickly predict the effects of the aperture-slot dimensions (w_s, l_s) and microstrip feed extension (l_m) on the input impedance, as shown in the Smith charts of Figure 2.23. By judicious choice of the slot parameters and microstrip extension, the DRA can be matched to the characteristic impedance of the feed line. In Figure 2.24, the return loss predicted by the ME-SD method is compared to the measured data.

The agreement between the two is quite good: the measured resonance frequency was 5.475 GHz compared to the computed resonance frequency of 5.625 GHz, which is a relative difference in only 2.7%. The measured 10 dB return loss bandwidth was 16.4% compared to the computed value of 16.8%.
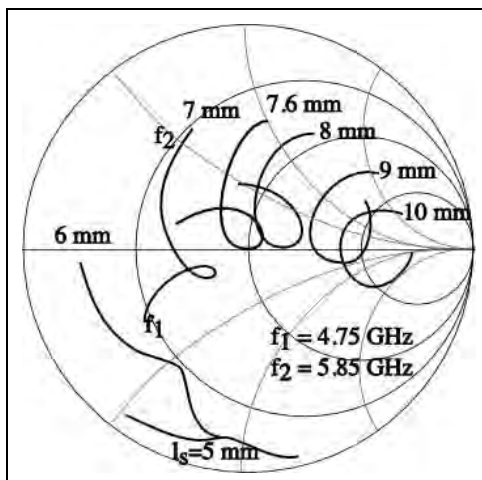
Figure 2.23 (a) Normalised input impedance of slot-coupled DRA for different values of slot length (l_m= 1.674 mm).
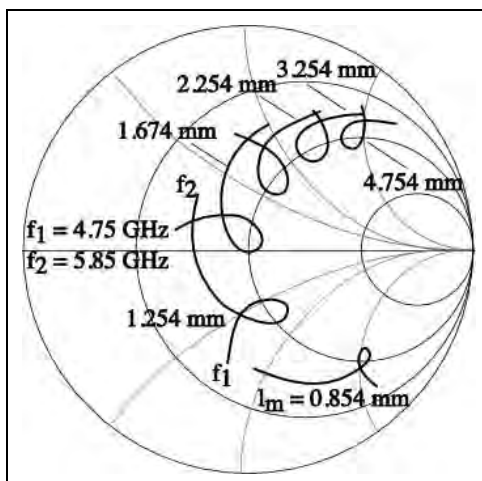
Figure 2.23 (b) Normalised input impedance of slot-coupled DRA for different stub lengths (l_s= 7.6 mm)
DRA: ε_{rd}= 10, a= b= 21.1 mm, c= 5.3 mm, x_c= 6.1 mm, y_c= 0,
Microstrip Feed: w_f= 0.6, ε_{r2}= 10.2, h_2= 0.635, h_1= h_3= 0,
Slot: w_s= 0.7 mm.

2.9   SUMMARY

The rectangular-shaped dielectric resonator antenna has been found to offer the antenna engineer with a significant amount of design flexibility. This flexibility arises from the two degrees of freedom of the rectangular DRA which allow for a wide range of aspect ratios for a given design frequency. Thus the rectangular DRA can be made very compact with a small footprint area, or very low profile, or its bandwidth can be adjusted for a given material permittivity. This flexibility is further enhanced by the fact that a wide variety of feed mechanisms can be used to excite the rectangular DRA, making it amenable integration with current technology. By applying the fairly simple dielectric waveguide model, the resonant frequency and bandwidth of the rectangular DRA can be predicted fairly accurately without having to resort to time-consuming numerical methods.
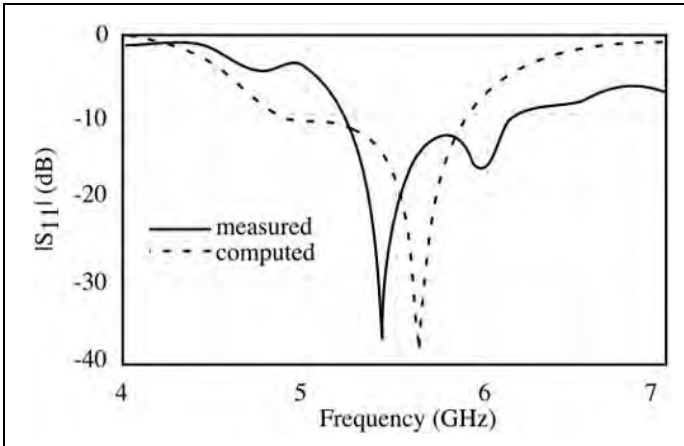
Figure 2.24 Computed and measured return losses of the DRA of Figure 2.22.

This model offers the engineer a good starting point for the design of rectangular DRAs. For more accurate predictions, and for the estimation of the input impedance of the DRA, numerical techniques are required. With the advent of various commercial electromagnetic simulation software tools and with the ever-increasing speed of computer processors, numerical analysis is becoming more accessible to antenna designers, and can be used to reduce the number of iterations in the design cycle of the DRA.

REFERENCES

[1]   E.A.C. Marcatili, "Dielectric Rectangular Waveguide and Directional Coupler for Integrated Optics," *Bell Systems Technical Journal*, Mar. 1969, pp. 2071-2103.

[2]   R.K. Mongia, A. Ittipiboon, "Theoretical and Experimental Investigations on Rectangular Dielectric Resonator Antennas," *IEEE Transactions on Antennas and Propagation*, Vol. 45, No. 9, Sept. 1997, pp. 1348 - 1356.

[3]   J.B. Keller, "Geometric Theory of Diffraction," *J. Opt. Soc. of America*, Vol. 52, No. 2, Feb. 1962, pp. 116-130.

[4]   R.G. Kouyoumjian, P.H. Pathak, "A Uniform Geometric Theory of Diffraction for an Edge in a Perfectly Conducting Surface," *Proc. IEEE*, Vol. 62, Nov. 1974, pp. 1448-1461.

[5]   C.A. Balanis, *Antenna Theory: Analysis and Design*, Harper and Row, 1982

[6]   A. Petosa, "Ferrite and Dielectric Antennas for Personal Communications," Ph.D. Dissertation, Carleton University, 1995.

[7]   M.G. Keller, M. Cuhaci, J. Shaker, A. Petosa, A. Ittipiboon, Y.M.M. Antar, "A Ka-Band Dielectric Resonator Antenna Reflectarray", *European Microwave Conference* EMC 2000, Paris, France, Oct. 2000, pp. 272-275.

[8]   R.E. Collin, *Foundation for Microwave Engineering*, McGraw-Hill, 1966.

[9]   R.E. Collin, F. Zucker, *Antenna Theory: Part 1,* McGraw Hill, 1969, pp. 24-25.

[10]   A. Ittipiboon, R.K. Mongia, Y.M.M. Antar, P. Bhartia, M. Cuhaci, "Aperture Fed Rectangular and Triangular Dielectric Resonators for Use as Magnetic Dipole Antennas," *IEE Electronics Letters*, Vol. 29, No. 3, 1993, pp. 2001-2002.

[11]   A.A. Kishk, A. Ittipiboon, Y.M.M. Antar, M. Cuhaci, "Dielectric Resonator Antenna Fed by a Slot in the Ground Plane of a Microstrip Line," *Proc. Eight Int. Conf. on Antennas and Propagation, ICAP'93*, Apr. 1993, Part 1, pp. 540-543.

[12]   K.W. Leung, K.Y.A. Lai, K.M. Luk, D. Lin, "Input Impedance of Aperture Coupled Hemispherical Dielectric Resonator Antenna," *IEE Electronics Letters,* Vol. 29, 1993, pp. 1165-1167.

[13]   G. Zhou, A.A. Kishk, A.W. Glisson, "Input Impedance of a Hemispherical Dielectric Resonator Antenna Excited by a Coaxial Probe," *IEEE Antennas and Propagation Symposium*, Ann Arbour Michigan, June 1993, pp. 1038-1041.

[14]   G.P. Junker, A.A. Kishk, A.W. Glisson, D. Kajfez, "Effect of an Air Gap Around the Coaxial Probe Exciting a Cylindrical Dielectric Resonator Antenna," *IEE Electronics Letters*, Vol. 30, No. 3, Feb. 1994, pp. 177-178.

[15]   G.P. Junker, A.A. Kishk, and A.W. Glisson, "Input Impedance of Dielectric Resonator Antennas Excited by a Coaxial Probe," *IEEE Trans. Antennas and Propagation*, Vol. 42, No. 7, July 1994, pp. 960-966.

[16]   M. Cooper, A. Petosa, A. Ittipiboon, J.S. Wight, "Investigation of Dielectric Resonator Antennas for L-Band Communications," *Antenna Technology and Applied Electromagnetics Symp ANTEM '96*, Ottawa, Canada, Aug. 1996, pp. 167-170.

[17]   R.A. Kranenburg, S.A. Long, "Microstrip Transmission Line Excitation of Dielectric Resonator Antennas," *IEE Electronics Letters,* Vol. 24, Sept. 1988, pp. 1156-1157.

[18]   R. Kranenberg, S.A. Long, J.T. Williams, "Coplanar Waveguide Excitation of Dielectric-Resonator Antennas," *IEEE Transactions on Antennas and Propagation*, Vol. 39, Jan. 1991, pp. 119-122.

[19] C. Curry, "Novel Size-Reduced Circularly Polarized Antennas," Master's Thesis, Royal Military College, Kingston, Canada, July 2000.

[20] M.S. Al Salameh, Y.M.M. Antar, G. Seguin, A. Petosa, "Analysis and Measurement of Compact-Size DRA with CPW Feed," *USNC/URSI National Radio Science Meeting*, Boston, MA, July 2001, pp. 221.

[21] J.P.S. McKenzie, "Dielectric Resonator Antennas Fed by Coplanar Waveguide at Extremely High Frequency," Master's Thesis, Royal Military College, Kingston, Canada, July 2001.

[22] M.T. Birand, R.V. Gelsthorpe, "Experimental Millimetric Array Using Dielectric Radiators Fed by Means of Dielectric Waveguide," *IEE Electronics Letters,* Vol. 17. No. 18, Sept. 1981, pp. 633-635.

[23] A. Petosa, R.K. Mongia, A. Ittipiboon, J.S. Wight, "Investigation of Various Feed Structures for Linear Arrays of Dielectric Resonator Antennas," *IEEE Antennas and Propagation Symposium*, Newport Beach, California, June 1995, pp. 1982-1985.

[24] H. A. Wheeler, "The Rradiansphere Around a Small Antenna," *Proc. IRE*, Vol. 47, Aug. 1959, pp. 1325-1331.

[25] R.K. Mongia, A. Ittipiboon, M. Cuhaci, "Measurements of Radiation Efficiency of Dielectric Resonator Antennas," *Microwave and Guided Wave Letters*, Vol. 4, No. 3, Mar. 1994, pp. 80-82.

[26] D. Kajfez, and P. Guillon, P., Eds., *Dielectric Resonators*, Artech House, Dedham, MA, 1986.

[27] G.P. Junker, A.A. Kishk, A.W. Glisson, D. Kajfez, "Effects of Fabrication Imperfections for Ground-plane-backed Dielectric Resonator Antennas with Coaxial Excitation," *IEEE Antennas and Propagation Magazine*, Vol. 37, 1995, pp. 40-47.

[28] A.A. Kishk, A. Ittipiboon, Y. Antar, M. Cuhaci, "Slot-Excitation of the Dielectric Disk Radiator," *IEEE Trans. on Antennas and Propagation*, Vol. 43, No. 2, Feb. 1995, pp. 198-201.

[29] G.P. Junker, A.A. Kishk, A.W. Glisson, "Two-port Analysis of Dielectric Resonator Antennas Excited in TE_{10} mode," *IEE Electronics Letters,* Vol. 32, No. 7, Mar. 1996, pp. 617-618.

[30] S.M. Shum, K.M. Luk, "Analysis of Aperture Coupled Rectangular Dielectric Resonator Antenna," *IEE Electronics Letters*, Vol. 30, No. 21, Oct. 1994, pp. 1727-1728.

[31] K.P. Esselle, "Circular Polarized Dielectric Resonator Antennas: Analysis of Near and Far Fields using the FDTD Method," *URSI Radio Science Meeting*, June 1995, Newport Beach, CA, pp. 28.

[32] N.R.S. Simons, A. Petosa, M. Cuhaci, A. Ittipiboon, R. Siushansian, J. Lovetri, S. Gutschling, "Validation of Transmission Line Matrix, Finite-Integration Technique, and Finite-Difference Time-Domain Simulations of a Multi-Segment Dielectric Resonator Antenna," *Applied Computational Electromagnetic Symposium (ACES-97)*, Mar. 1997, Monterey, CA.

[33] A. Petosa, N.R.S. Simons, R. Siushansian, A. Ittipiboon, M. Cuhaci, "Design and Analysis of Multi-Segment Dielectric Resonator Antennas," *IEEE Trans. Antennas and Propagation*, May 2000, pp. 738 - 742.

[34] Y.M.M. Antar, Z. Fan, "Theoretical Investigation of Aperture-coupled Rectangular Dielectric Resonator Antenna," *IEE Proceedings Microwave Antennas and Propagation,* Vol. 143, No. 2, Apr. 1996, pp. 113-118.

[35] R. F. Harrington, *Time-Harmonic Electromagnetic Fields*, McGraw-Hill, New York, 1961.

[36] D. M. Pozar, "A Reciprocity Method of Analysis for Printed Slot and Slot-coupled Microstrip Antennas," *IEEE Transactions on Antennas and Propagation.,* Vol. 34, 1986, pp. 1439-1446.

This page intentionally left blank

CHAPTER 3

Analysis of Multi-Layer Hemispherical DR Antennas

Kin–Lu Wong

Department of Electrical Engineering
National Sun Yat–Sen University
Kaohsiung, Taiwan

3.1 INTRODUCTION

It has been known that dielectric resonators (DRs) of different shapes can be designed to be efficient radiators, and a hemispherical DR resting on a ground plane has been shown to be a good radiator when operated at the TE_{111} mode [1–9]. It has also been reported that, by placing an air gap of hemispherical shape between the DR and the ground plane [6] or by coating the DR with a dielectric material having a relative permittivity about half that of the DR [7, 8], the impedance bandwidth of these multi–layer hemispherical DR antennas can be significantly improved. For the former case, the bandwidth enhancement is largely owing to the lowering of the quality factor of the DR antenna. A similar idea has been successfully applied in a spherical–circular microstrip structure [10], where a significant increase of the half–power bandwidth of the structure is obtained. As for the latter case, the added dielectric coating can serve as a transition region between the DR antenna and the air. This behavior can decrease the reflected wave energy at the DR–air interface due to the large permittivity discontinuity and lead to an improvement of the antenna's impedance bandwidth.

In this chapter, a rigorous full–wave analysis for the reported multi–layer hemispherical DR antennas [6–8] is presented. The case of a probe–fed hemispherical DR antenna with an air gap is first studied by using a Green's function formulation. The electric field Green's function of the antenna fed by a coax is first derived, and the input impedance of the efficiently radiating mode of TE_{111} is then formulated by using the reaction formula. Numerical results of the input impedance are presented as a function of the radius of the hemispherical air gap, and the antenna bandwidth are then analyzed. To verify the correctness of the analysis, the results for the case of no air gap presence are also compared with the experimental and theoretical data obtained from other work. Effects of different probe lengths and feed positions on input resistance are also shown.

The analysis of a probe–fed hemisherical DR antenna with a dielectric coating is also presented. The input impedance for the antenna operated in the TE_{111} mode is formulated, and numerical results of the input impedance are calculated to

analyze the effects of different thicknesses and permittivities of the dielectric coating on the impedance bandwidth. An optimal choice of the dielectric coating is also discussed. Finally, dielectric–coated hemispherical DR antennas fed by a microstrip line through a coupling slot are analysed. The broadside TE_{111} mode is also studied, and the reciprocity theorem [11] is applied in this analysis. In this case, the dielectric–coated DR antenna can be viewed as a series load at the slot position as seen by the microstrip line, and the equivalent impedance of this series load can be calculated from the magnetic field Green's function inside the DR antenna due to an equivalent magnetic current source in the slot. Once this series impedance is obtained, the input impedance of the slot–coupled hemispherical DR antenna can then be obtained by using transmission line theory. Numerical results for the input impedance are calculated and presented, and the antenna bandwidth is then analysed.

3.2   A PROBE–FED DR ANTENNA WITH AN AIR GAP

In this section, the rigorous analysis of the probe–fed hemispherical DR antenna with an air gap shown in Figure 3.1 is presented. Input impedance of the TE_{111} mode is calculated, and the antenna bandwidth is analysed. As shown in Figure 3.1, the air gap is with a radius of d, and the region of $d < r < a$ is the DR with a relative permittivity of ε_r. A probe of length ℓ and radius r_0 is located at $x = b$. The region of $r > a$ is free space with permittivity ε_0 and permeability μ_0. To solve the problem, we first derive the z component of the electric–field Green's function $G_{zz}(\vec{r},\vec{r}')$ for a $\hat{z}$–directed unit source current $\delta(\vec{r}-\vec{r}')\hat{z}'$, where $\vec{r}$ and $\vec{r}'$ represent the field and source coordinates, respectively. By considering the geometry of Figure 3.1 and using the image theorem, the equivalent problem is obtained, as shown in Figure 3.2, and the electric–field Green's function is derived in the following section.

3.2.1 Green's–function Formulation

Since the TE mode is of interest, the Green's function G_{zz} can be expressed in terms of the magnetic Hertz potential $\pi_m\hat{r}$ only [12]. To begin with, by considering the TE to $\hat{r}$ wave, the unbounded Green's function of a current source $\vec{J}$ needs to be derived. First, from the following Maxwell's and continuity equations:

$$\nabla\times\vec{E} = -j\omega\mu\vec{H} \tag{3.1}$$

$$\nabla\times\vec{H} = j\omega\varepsilon\vec{E} + \vec{J}, \tag{3.2}$$

$$\nabla\cdot\vec{E} = \rho_v/\varepsilon, \tag{3.3}$$

$$\nabla\cdot\vec{J} = -j\omega\rho_v, \tag{3.4}$$
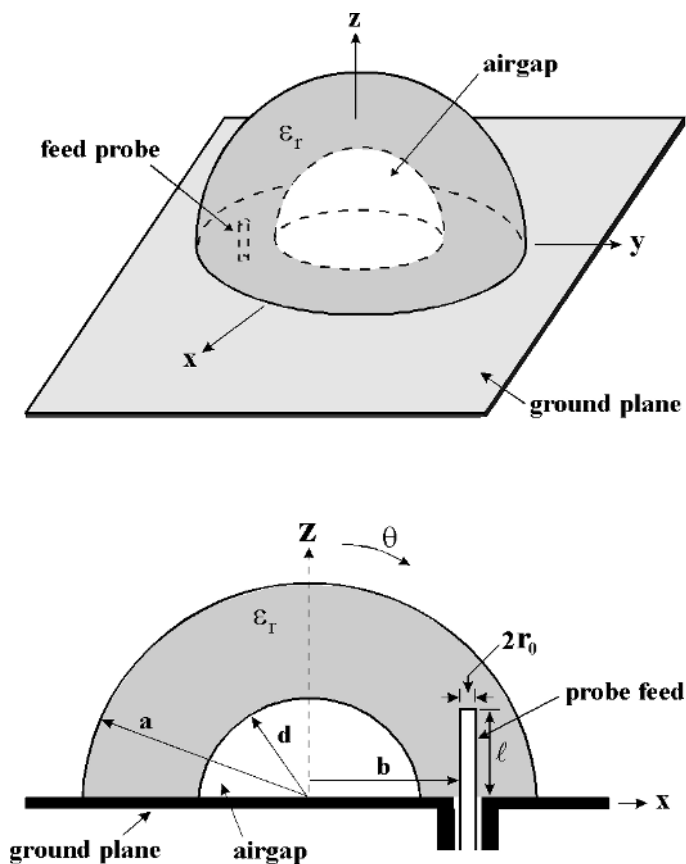
Fig. 3.1 Geometry of a hemispherical DR antenna with an air gap. (From Ref. 6, © 1993 IEEE, reprinted with permission)

we can get

$$(\nabla^2 + k^2)\vec{E} = j\omega\mu\left[\vec{J} + \frac{\nabla(\nabla \cdot \vec{J})}{k^2}\right]. \qquad (3.5)$$

Then, from solving Eq. (3.5), we have
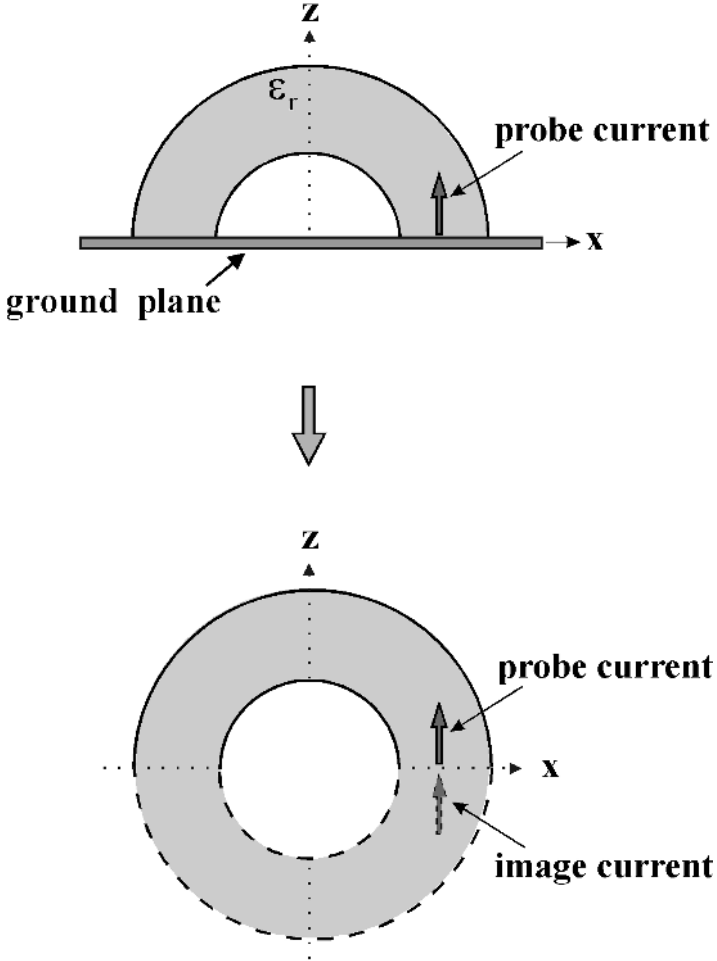
Fig. 3.2 The equivalent problem by using the image theorem for the DR antenna shown in Figure 3.1.

$$\vec{E} = -j\omega\mu\left[\vec{J} + \frac{\nabla(\nabla \cdot \vec{J})}{k^2}\right]g(\vec{r} - \vec{r}'),$$ (3.6)

$$\vec{H} = \nabla \times \vec{J}g(\vec{r} - \vec{r}'),$$ (3.7)

where $g(\vec{r} - \vec{r}')$ is the unbounded Green's function of a unit source for arbitrary direction satisfying the following equation in spherical coordinates:

$$(\nabla^2 + k^2)g(r,\theta,\phi) = -\delta(\vec{r} - \vec{r}') = -\frac{\delta(r - r')\delta(\theta - \theta')\delta(\phi - \phi')}{r^2 \sin\theta}.$$
(3.8)

By following the regular derivation procedure of Green's function, we have

$$g(r,\theta,\phi) = -jk\sum_{n=0}^{\infty}\frac{1}{kr_{<}r_{>}}\hat{J}_n(kr_{<})\hat{H}_n^{(2)}(kr_{>})\sum_{m=0}^{n}A_{mn}(\theta,\phi,\theta',\phi'), \quad (3.9)$$

where

$$A_{mn}(\theta,\phi,\theta',\phi') = \xi_m\frac{(n-m)!}{(n+m)!}P_n^m(\cos\theta)P_n^m(\cos\theta')\cos m(\phi - \phi'),$$
(3.10)

with

$$\xi_m = \begin{cases}1, & m = 0,\\ 2, & m \geq 1,\end{cases} \qquad k = k_0\sqrt{\varepsilon_r} = \omega\sqrt{\mu_0\varepsilon_0\varepsilon_r}. \qquad (3.11)$$

In the above expressions, $r_{>}$ is the larger of r and r', and $r_{<}$ is the smaller of r and r'. $\hat{J}_n(x)$ and $\hat{H}_n^{(2)}(x)$ are, respectively, a spherical Bessel equation of the first kind and a spherical Hankel function of the second kind (Shelkunoff type).

In addition, the r component of Eq. (3.7) can be extracted, that is,

$$rH_r = \vec{r}\cdot\nabla\times\hat{\alpha}'Jg(\vec{r} - \vec{r}'),$$
(3.12)

where $\hat{\alpha}'$ is the unit vector of the current source. By using reciprocity theorem, Eq. (3.12) can be written as

$$rH_r = \hat{\alpha}'\cdot\nabla\times\vec{r}Jg(\vec{r} - \vec{r}').$$
(3.13)

Then, by knowing that [13]

$$\nabla'\times(\vec{r} - \vec{r}')g(\vec{r} - \vec{r}') = 0,$$
(3.14)

Eq. (3.13) can be derived to be

$$rH_r = \hat{\alpha}'\cdot\nabla\times\vec{r}'Jg(\vec{r} - \vec{r}').$$
(3.15)

It should also be noted that, in order to obtain the vector wave equation in a homogeneous, isotropic medium, it is convenient to introduce the scalar potential π_m, which is a solution to the scalar Helmholtz equation,

$$(\nabla^2 + k^2)\pi_m = 0. \tag{3.16}$$

In this case, for TE waves, the field can be shown as [12]

$$\vec{E} = -\nabla \times (\vec{r}\pi_m), \tag{3.17}$$

$$\vec{H} = \frac{1}{j\omega\mu}\nabla \times \nabla \times (\vec{r}\pi_m), \tag{3.18}$$

Subsequently, we can extract the r component of $\vec{H}$ in the above equations to yield

$$H_r = \frac{1}{j\omega\mu}\left[\frac{\partial^2 (r\pi_m)}{\partial r^2} + k^2 r\pi_m\right]. \tag{3.19}$$

Then, from the scalar wave equation in spherical coordinates, we have

$$\frac{\partial^2 (r\pi_m)}{\partial r^2} = -\left[k^2 - \frac{n(n+1)}{r^2}\right](r\pi_m). \tag{3.20}$$

By substituting Eq. (3.20) into Eq. (3.19), we have H_r for the n–th harmonic to be given by

$$H_r = \frac{1}{j\omega\mu}\frac{n(n+1)}{r}\pi_m. \tag{3.21}$$

By applying Eq. (3.21) to Eq. (3.15), we have

$$\pi_m = j\omega\mu\hat{\alpha}' \cdot \nabla' \times \vec{r}'Jg(\vec{r} - \vec{r}')\frac{1}{n(n+1)}. \tag{3.22}$$

By considering the additional reflected wave, we can then obtain π_m for the region of $d < r < a$ in spherical form:

$$\pi_m = \frac{\omega\mu_0}{4\pi} J_z\hat{z}' \cdot \nabla' \times \vec{r}' \cdot \sum_{n=1}^{\infty}\sum_{m=0}^{n}\{\frac{2n+1}{n(n+1)}[\frac{1}{kr_<r_>}\hat{J}_n(kr_<)\hat{H}_n^{(2)}(kr_>)$$

$$+\frac{b_n}{r}\hat{H}_n^{(2)}(kr)+\frac{c_n}{r}\hat{J}_n(kr)][A_{mn}(\theta,\phi,\theta',\phi')+A_{mn}(\theta,\phi,\pi-\theta',\phi')]\} \ .$$

(3.23)

Expanding Eq. (3.23), we have

$$\pi_m=\frac{-\omega\mu_0}{4\pi}J_z\sum_{n=1}^{\infty}\sum_{m=0}^{n}\{\frac{m(2n+1)}{n(n+1)}[\frac{1}{kr_<r_>}\hat{J}_n(kr_<)\hat{H}_n^{(2)}(kr_>)$$

$$+\frac{b_n}{r}\hat{H}_n^{(2)}(kr)+\frac{c_n}{r}\hat{J}_n(kr)][B_{mn}(\theta,\phi,\theta',\phi')+B_{mn}(\theta,\phi,\pi-\theta',\phi')]\} \ ,$$

(3.24)

where

$$B_{mn}(\theta,\phi,\theta',\phi')=\xi_m\frac{(n-m)!}{(n+m)!}P_n^m(\cos\theta)P_n^m(\cos\theta')\sin m(\phi-\phi') \ . \ \ (3.25)$$

Similarly, we can obtain π_m for the region of $r>a$,

$$\pi_m=\frac{-\omega\mu_0}{4\pi}J_z\sum_{n=1}^{\infty}\sum_{m=0}^{n}\{\frac{m(2n+1)}{n(n+1)}\frac{a_n}{r}\hat{H}_n^{(2)}(k_0r)$$

$$\times[B_{mn}(\theta,\phi,\theta',\phi')+B_{mn}(\theta,\phi,\pi-\theta',\phi')]\} \ ,$$

(3.26)

and, for the region of $r<d$,

$$\pi_m=\frac{-\omega\mu_0}{4\pi}J_z\sum_{n=1}^{\infty}\sum_{m=0}^{n}\{\frac{m(2n+1)}{n(n+1)}\frac{d_n}{r}\hat{J}_n(k_0r)$$

$$\times[B_{mn}(\theta,\phi,\theta',\phi')+B_{mn}(\theta,\phi,\pi-\theta',\phi')]\} \ .$$

(3.27)

Next, by matching the boundary conditions at each interface, the coefficients of interest, b_n and c_n, can be derived as

$$b_n=\frac{\alpha_4\beta_1-\alpha_2\beta_2}{\alpha_1\alpha_4-\alpha_2\alpha_3} \ ,$$

(3.28)

$$c_n=\frac{\alpha_1\beta_2-\alpha_3\beta_1}{\alpha_1\alpha_4-\alpha_2\alpha_3} \ ,$$

(3.29)

with

$$\alpha_1=k_0\hat{H}_n^{(2)'}(k_0a)\hat{H}_n^{(2)}(ka)-k\hat{H}_n^{(2)}(k_0a)\hat{H}_n^{(2)'}(ka) \ ,$$

(3.30)

$$\alpha_2 = k_0 \hat{J}_n(ka)\hat{H}_n^{(2)'}(k_0 a) - k\hat{J}_n'(ka)\hat{H}_n^{(2)}(k_0 a), \qquad (3.31)$$

$$\alpha_3 = k_0 \hat{J}_n'(kd)\hat{H}_n^{(2)}(kd) - k\hat{J}_n(k_0 d)\hat{H}_n^{(2)'}(kd), \qquad (3.32)$$

$$\alpha_4 = k_0 \hat{J}_n'(k_0 d)\hat{J}_n(kd) - k\hat{J}_n(k_0 d)\hat{J}_n'(kd), \qquad (3.33)$$

$$\beta_1 = -\left(\frac{\alpha_1}{kr'}\right)\hat{J}_n'(kr'), \qquad (3.34)$$

$$\beta_2 = -\left(\frac{\alpha_4}{kr'}\right)\hat{H}_n^{(2)'}(kr'). \qquad (3.35)$$

By knowing that $\vec{E} = -\nabla \times (r\pi_m \hat{r})$ and $E_z = -E_\theta \sin\theta$ due to the TE to $\hat{r}$ mode of interest, the Green's function inside the dielectric region ($d < r < a$) can be expressed as

$$G_{zz}(\vec{r},\vec{r}') = \frac{-\omega\mu_0}{4\pi}\sum_{n=1}^{\infty}\sum_{m=0}^{n}\{\frac{m(2n+1)}{n(n+1)}[\frac{\hat{J}_n(kr_<)}{kr_< r_>}\hat{H}_n^{(2)}(kr_>) + \frac{b_n}{r}\hat{H}_n^{(2)}(kr)$$

$$+ \frac{c_n}{r}\hat{J}_n(kr)][A_{mn}(\theta,\phi,\theta',\phi') + A_{mn}(\theta,\phi,\pi-\theta',\phi')]\}. \quad (3.36)$$

3.2.2 Single–mode Approximation

To simplify the analysis, the single-mode approximation is applied in the theoretical study. In this case, the electric field Green's function inside the dielectric region can be expressed as

$$G_{zz}(\vec{r},\vec{r}') = \frac{-3\omega\mu_0}{4\pi}\sin\theta'\sin\theta\cos(\phi-\phi')$$

$$\times \begin{cases} \frac{1}{krr'}\hat{J}_1(kr')\hat{H}_1^{(2)}(kr) + \frac{b_1}{r}\hat{H}_1^{(2)}(kr) + \frac{c_1}{r}\hat{J}_1(kr), & r > r', \\ \frac{1}{krr'}\hat{J}_1(kr)\hat{H}_1^{(2)}(kr') + \frac{b_1}{r}\hat{H}_1^{(2)}(kr) + \frac{c_1}{r}\hat{J}_1(kr), & r < r', \end{cases} \quad (3.37)$$

where b_1 and c_1 are given, respectively, in Eqs. (3.28) and (3.29) by assuming $n = 1$. Using Eq. (3.37), the electric field E_z due to a probe surface current J_z can be expressed as

$$\vec{E}_z(\vec{r}) = \iint\limits_{S_0} G_{zz}(\vec{r},\vec{r}')\vec{J}_z(z')\,dS' \,, \tag{3.38}$$

where S_0 is the source surface. The input impedance is then determined by

$$Z_{in} = -\frac{1}{I_z^2(0)}\iint\limits_{S_0} E_z(\vec{r})J_z(z)\,dS$$

$$= -\frac{1}{I_z^2(0)}\iint\limits_{S_0}\iint\limits_{S_0} J_z(z)G_{zz}(\vec{r},\vec{r}')J_z(z')\,dS'dS \,. \tag{3.39}$$

The above equation can be evaluated by assuming the probe surface current as [14]

$$J_z(z) = J_0 \sin k(\ell - z) \,, \tag{3.40}$$

and $I_z(z) = 2\pi r_0 J_z(z)$ is a valid assumption for small probe radius r_0.

3.2.3   Numerical Results and Discussion

In this section, typical numerical results of the input impedance in the TE_{111} mode are presented. The effects of introducing an air gap into the hemispherical DR antenna are first observed in Figure 3.3, where the input impedance for the antenna with different radii of the hemispherical air gap is shown. To confirm the correctness of the numerical results presented here, the data obtained in [1, 2] for the case of no air gap presence (i.e., $d = 0$) are also shown in the figure, for comparison. It is clearly seen that the calculated input resistance results of $d = 0$ in Figure 3.3(a) agree well with the data obtained in [1, 2]. As for the input reactance curve shown in Figure 3.3(b), the calculated results obtained here are also in good agreement with the theoretical data in [2] and the measured data around resonance [1]. This can ascertain the correctness of the numerical calculation here. From the results, it is found that, for d less than $0.3a$, the effects of the air gap on the input impedance is negligible. For $d > 0.3a$, the resonant frequency shifts to higher frequencies, and the resonant input resistance is gradually decreased until reaching a minimum value of about 35 Ω at $d = 0.6a$. Figure 3.4 shows the variation of the bandwidth, obtained from the half–power impedance bandwidth [15], with the air gap radius d. The half–power impedance bandwidth is defined as $(f_U - f_L)/f_R \times 100\%$, where f_U and f_L denote, respectively, the upper and lower frequencies having the half resonant resistance, and f_R is the resonant frequency of the DR antenna.)   It is seen that, with the presence of the air gap, the antenna bandwidth increases and reaches a maximum value of about 24% at $d = 0.6a$, which is nearly two times of that for no air gap presence.
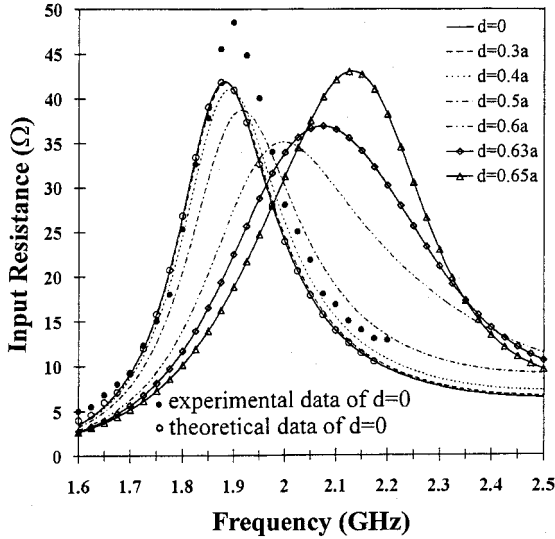
(a)
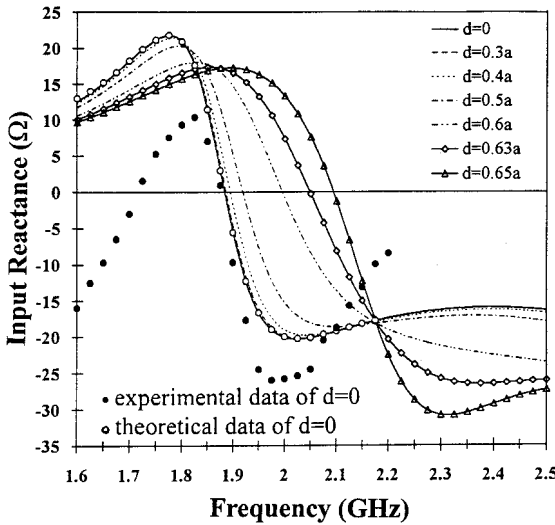
(b)

Fig. 3.3 (a) Input resistance and (b) input reactance of a hemispherical DR antenna shown in Figure 3.1 with $a = 25.4$ mm, $b = 17.4$ mm, $\ell = 15.2$ mm, $r_0 = 0.75$ mm, $\varepsilon_r = 8.9$. The solid and open circles denote, respectively, the experimental data in [1] and the theoretical data in [2] for the case of no air gap presence. (From Ref. 6, © 1993 IEEE, reprinted with permission)
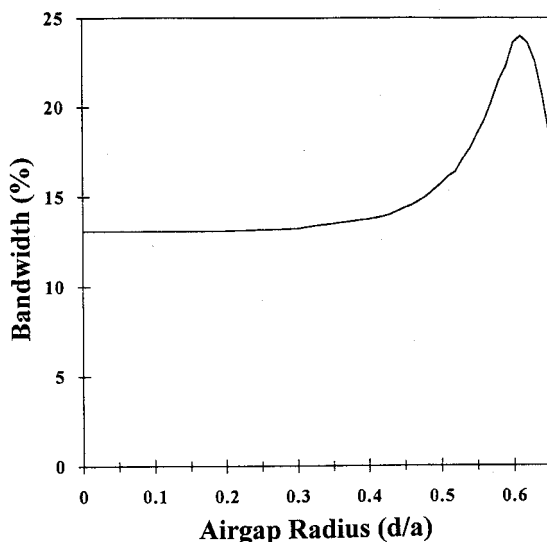
Fig. 3.4 Bandwidth versus normalised air gap radius *d/a* for the antenna shown in Figure 3.1. Antenna parameters are the same as in Figure 3.3. (From Ref. 6, © 1993 IEEE, reprinted with permission)
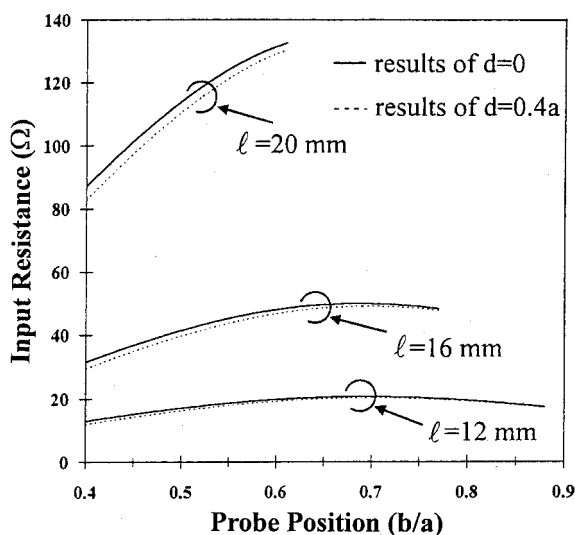
Fig. 3.5 Resonant input resistance for different probe lengths for the antenna shown in Figure 3.1. Antenna parameters are the same as in Figure 3.3. (From Ref. 6, © 1993 IEEE, reprinted with permission)
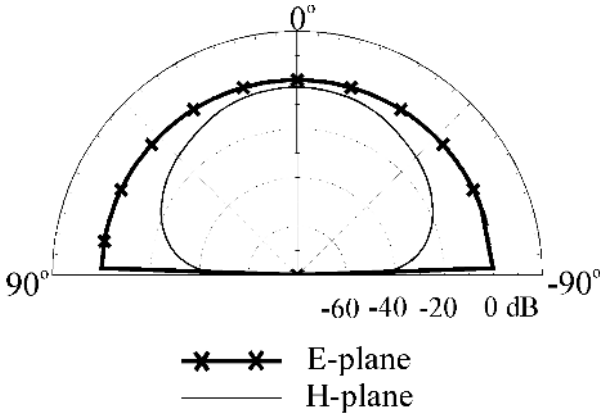
Fig. 3.6 Typical calculated radiation patterns of the TE_{111} mode for the antenna shown in Figure 3.1.

Variations of input resistance at resonance with feed position for different probe lengths are also studied. The results are shown in Figure 3.5, where two cases of $d = 0$ (no air gap) and $d = 0.4a$ (with an air gap) are presented. The open circles in the figure are the data obtained in [2] for $d = 0$. Again, good agreement with the results calculated here is observed. From the results shown in Figure 3.5, it is clear that, for both cases, the input resistance increases until reaching a maximum value, as the probe moves away from the center. This behavior is useful for impedance matching. Furthermore, numerical results for the normalised radiation pattern are also calculated and shown in Figure 3.6. Comparing the calculated radiation pattern with that of the no air gap case [4], it is concluded that the air gap does not alter the radiation pattern of the DR antenna in the TE_{111} mode.

3.3   A PROBE–FED DR ANTENNA WITH A DIELECTRIC COATING

With a comparison to DR antennas of various shapes, the hemispherical DR antenna has a simple structure with a smooth interface between the dielectric and air. At the dielectric–air interface, parts of the wave energy from the feed are reflected due to the large permittivity discontinuity at the interface, which reduces the radiation loss of the structure and limits the impedance bandwidth of the DR antenna. In this section, the method of impedance bandwidth improvement by coating the hemispherical DR antenna with a dielectric material having a relative permittivity smaller than that of the DR antenna is presented and analysed. This dielectric coating can serve as a transition region between the DR antenna and air. The wave energy reflected at the interface due to the large permittivity discontinuity can thus be reduced and the radiation loss of the DR antenna can be increased. This can lead to an improvement of the antenna impedance bandwidth, and a broadband DR antenna can be achieved. To verify this prediction, a rigorous theoretical investigation by deriving the electric field Green's function of the

dielectric–coated hemispherical DR antenna, shown in Figure 3.7, is conducted. The input impedance is formulated by using the reaction formula, and numerical results of the input impedance are then calculated to analyse the effects of different thicknesses and permittivities of the dielectric coating on the impedance bandwidth.
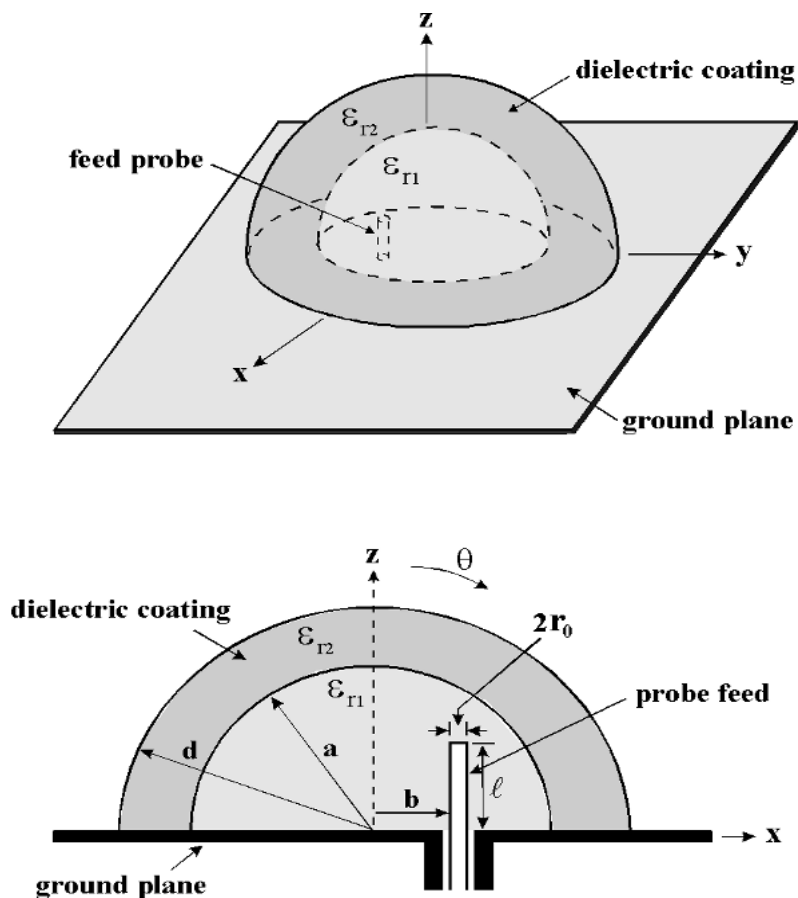
Fig. 3.7 Geometry of a dielectric–coated hemispherical DR antenna. (From Ref. 7, © 1994 John Wiley & Sons, Inc.)

3.3.1 Green's function Formulation

Figure 3.7 shows the geometry under consideration. The dielectric coating has a thickness of d–a and a relative permittivity of ε_{r2}. The region of $r < a$ is the DR with a relative permittivity of ε_{r1}. A probe of length ℓ and radius r_0 is located at $x = b$. The region of $r > d$ is again free space with permittivity ε_0 and permeability μ_0. For this geometry, similar to that in Section 3.2, the z component of the electric field Green's function $G_{zz}(\vec{r},\vec{r}')$ for a $\hat{z}$–directed unit current source $\delta(\vec{r}-\vec{r}')\hat{z}'$ is first derived. By applying the image theorem to the geometry of Figure 3.7 and following the procedure similar to that in Section 3.2, we can derive π_m in spherical coordinates expressed to be

$$\pi_m = \frac{-\omega\mu_0}{4\pi} \sum_{n=1}^{\infty} \sum_{m=0}^{n} \{\frac{m(2n+1)}{n(n+1)}[B_{mn}(\theta,\phi,\theta',\phi') + B_{mn}(\theta,\phi,\pi-\theta',\phi')]$$

$$\times \begin{cases} \dfrac{1}{k_1 r_< r_>} \hat{J}_n(k_1 r_<)\hat{H}_n^{(2)}(k_1 r_>) + \dfrac{a_n}{r}\hat{J}_n(k_1 r), & r > a, \\[2ex] \dfrac{b_n}{r}\hat{H}_n^{(2)}(k_2 r) + \dfrac{c_n}{r}\hat{J}_n(k_2 r), & a < r < d, \\[2ex] \dfrac{d_n}{r}\hat{H}_n^{(2)}(k_0 r), & r > d, \end{cases} \qquad (3.41)$$

where $B_{mn}(\theta,\phi,\theta',\phi')$ is given in Eq. (3.25), and

$$a_n = \frac{\alpha_5\alpha_8\beta_1 + \alpha_3\alpha_7\beta_2 - \alpha_6\alpha_7\beta_1 - \alpha_2\alpha_8\beta_2}{\Delta}, \qquad (3.42)$$

$$b_n = \frac{\alpha_1\alpha_8\beta_2 - \alpha_4\alpha_8\beta_1}{\Delta}, \qquad (3.43)$$

$$c_n = \frac{\alpha_4\alpha_7\beta_1 - \alpha_1\alpha_7\beta_2}{\Delta}, \qquad (3.44)$$

$$d_n = \frac{b_n\hat{H}_n^{(2)}(k_2 d) + c_n\hat{J}_n(k_2 d)}{\hat{H}_n^{(2)}(k_0 d)}, \qquad (3.45)$$

with

$$k_i = k_0\sqrt{\varepsilon_{ri}} = \sqrt{\mu_0\varepsilon_0\varepsilon_{ri}}, \qquad i = 1, 2,$$

$$\Delta = \alpha_1\alpha_5\alpha_8 + \alpha_3\alpha_4\alpha_7 - \alpha_1\alpha_6\alpha_7 - \alpha_2\alpha_4\alpha_8,$$

$$\alpha_1 = \hat{J}_n(k_1 a),$$

$$\alpha_2 = -\hat{H}_n^{(2)}(k_2 a),$$

$$\alpha_3 = -\hat{J}_n(k_2 a),$$

$$\alpha_4 = k_1 \hat{J}_n^{'}(k_1 a),$$

$$\alpha_5 = -k_2 \hat{H}_n^{(2)'}(k_2 a),$$

$$\alpha_6 = -k_2 \hat{J}_n^{'}(k_2 a),$$

$$\alpha_7 = k_0 \hat{H}_n^{(2)'}(k_0 d)\hat{H}_n^{(2)}(k_2 d) - k_2 \hat{H}_n^{(2)}(k_0 d)\hat{H}_n^{(2)'}(k_2 d),$$

$$\alpha_8 = k_0 \hat{H}_n^{(2)'}(k_0 d)\hat{J}_n(k_2 d) - k_2 \hat{H}_n^{(2)}(k_0 d)\hat{J}_n^{'}(k_2 d),$$

$$\beta_1 = -\frac{1}{k_1 r'}\hat{J}_n(k_1 r')\hat{H}_n^{(2)}(k_1 a),$$

$$\beta_2 = -\frac{1}{r'}\hat{J}_n(k_1 r')\hat{H}_n^{(2)'}(k_1 a).$$

Next, by substituting Eq. (3.41) into Eq. (3.17), we can have the Green's function inside the DR region ($r < a$) written as

$$G_{zz}(\vec{r},\vec{r}') = \frac{-\omega\mu_0}{4\pi}\sum_{n=1}^{\infty}\sum_{m=0}^{n}\{\frac{m^2(2n+1)}{n(n+1)}[\frac{\hat{J}_n(kr_<)}{k_1 r_< r_>}\hat{H}_n^{(2)}(k_1 r_>) + \frac{a_n}{r}\hat{J}_n(k_1 r)]$$
$$\times[A_{mn}(\theta,\phi,\theta',\phi') + A_{mn}(\theta,\phi,\pi-\theta',\phi')]\} \qquad (3.46)$$

where $A_{mn}(\theta,\phi,\theta',\phi')$ is given in Eq. (3.10).

Then, by taking the single–mode approximation for the frequencies around the resonance of the TE_{111} mode, we have

$$G_{zz}(\vec{r},\vec{r}') = \frac{-3\omega\mu_0}{4\pi}\sin\theta'\sin\theta\cos(\phi-\phi')$$

$$\times \begin{cases} \dfrac{1}{krr'}\hat{J}_1(k_1r')\hat{H}_1^{(2)}(k_1r)+\dfrac{a_1}{r}\hat{J}_1(k_1r), & r>r', \\[2mm] \dfrac{1}{krr'}\hat{J}_1(k_1r)\hat{H}_1^{(2)}(k_1r')+\dfrac{a_1}{r}\hat{J}_1(k_1r) & r<r', \end{cases} \tag{3.47}$$

where a_1 is given in Eq. (3.42) by assuming $n = 1$. The input impedance is then determined by using Eq. (3.39).

3.3.2 Numerical Results and Discussion

In this section, the effects of dielectric coating on the input impedance of the hemispherical DR antenna are studied. A typical result for the case of $d = 1.5a$ (i.e., the dielectric coating has a thickness of $0.5a$) with $\varepsilon_{r1} = 8.9$, $a = 2.54$ cm, $b = 1.74$ cm, $\ell = 1.52$ cm, and $r_0 = 0.075$ cm is shown in Figure 3.8. The results for different dielectric permittivities of $\varepsilon_{r2} = 1$ (no coating), 2, 4, 8.9, 13, and 20 are presented. The solid circles in the figure denote the data obtained in [2] for the case of no dielectric coating, which agree well with the calculated results here. This ascertains the correctness of our numerical calculation. From the results, it is clearly seen that the dielectric coating decreases the resonant frequency of the DR antenna, and the input resistance at resonance also decreases due to the dielectric coating. On the other hand, it is found that the half–power impedance bandwidth [15] for $\varepsilon_{r2} = 2$ and 4 is increased as compared with that of the case of $\varepsilon_{r2} = 1$.

To show it more clearly, the variation of the impedance bandwidth with ε_{r2} for different coating thicknesses is shown in Figure 3.9. It is interesting to see that, for $\varepsilon_{r2} < \varepsilon_{r1}$ (= 8.9), the impedance bandwidth increases and reaches an optimal value around $\varepsilon_{r2} = 4$, which is about half the value of ε_{r1}. For the coating thickness $d = 1.6a$, the optimal bandwidth reaches about 22%, which is about 70% higher than that of the case of no dielectric coating (13%). These results indicate that, by coating the DR antenna with a dielectric material having a relative permittivity about half of that of the DR antenna, a significant improvement of the antenna impedance bandwidth can be achieved. A second case of $\varepsilon_{r1} = 14.3$ is also calculated and shown in Figure 3.10. Again, it can be seen that, around the value of ε_{r2} to be about half the value of ε_{r1}, an optimal impedance bandwidth occurs. Moreover, it can also be seen that, in Figures 3.9 and 3.10, the impedance bandwidth decreases when ε_{r2} is greater than ε_{r1}. These results can justify the bandwidth improvement method studied here by coating the DR antenna with a dielectric material having a relative permittivity about half of that of the DR antenna. The dielectric coating, in this case, serves as a transition region for the waves inside the DR antenna and the free–space wave. The large permittivity discontinuity at the dielectric–air interface is now decreased due to this dielectric coating. This increases the radiation loss of the DR structure, which leads to a greater impedance bandwidth. A broadband DR antenna can thus be obtained, and the bandwidth improvement also increases with increasing coating thickness.
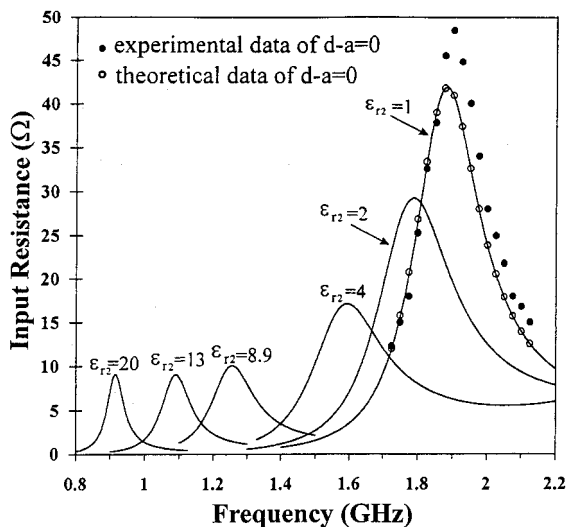
(a)
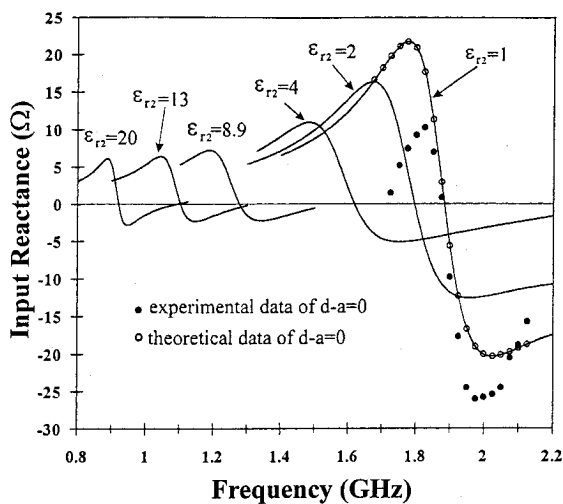
(b)

Fig. 3.8 (a) Input resistance and (b) input reactance of a dielectric–coated hemispherical DR antenna, shown in Figure 3.7, excited in the TE_{111} mode; $a = 25.4$ mm, $b = 17.4$ mm, $\ell = 15.2$ mm, $r_0 = 0.75$ mm, $\varepsilon_{r1} = 8.9$, $d = 1.5a$. The open and solid circles denote, respectively, the theoretical data in [2] and the measured results in [1], both for the case with $\varepsilon_{r2} = 1.0$. (From Ref. 7, © 1994 John Wiley & Sons, Inc.)
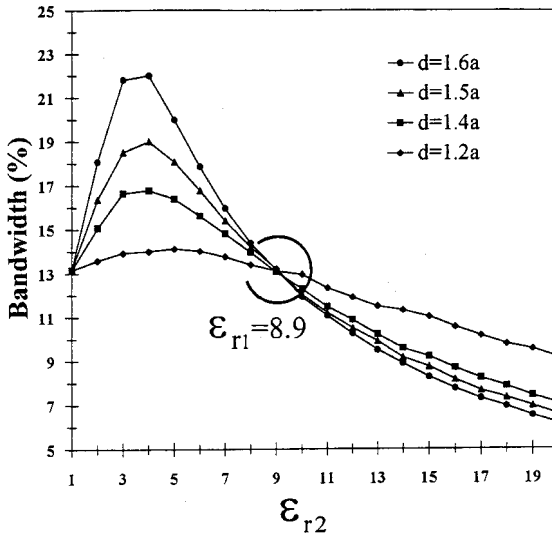
Fig. 3.9 Bandwidth versus ε_{r2} for the DR antenna shown in Figure 3.7 with $\varepsilon_{r1} =$ 8.9. Other antenna parameters are given in Figure 3.8. (From Ref. 7, © 1994 John Wiley & Sons, Inc.)
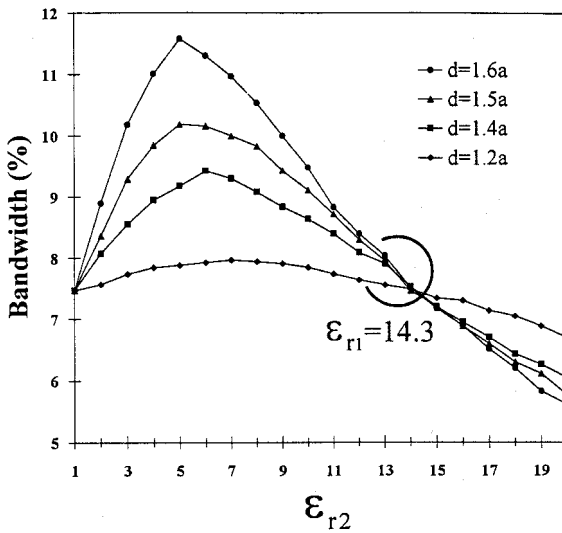
Fig. 3.10 Bandwidth versus ε_{r2} for the DR antenna shown in Figure 3.7 with $\varepsilon_{r1} =$ 14.3. Other antenna parameters are given in Figure 3.8. (From Ref. 7, © 1994 John Wiley & Sons, Inc.)
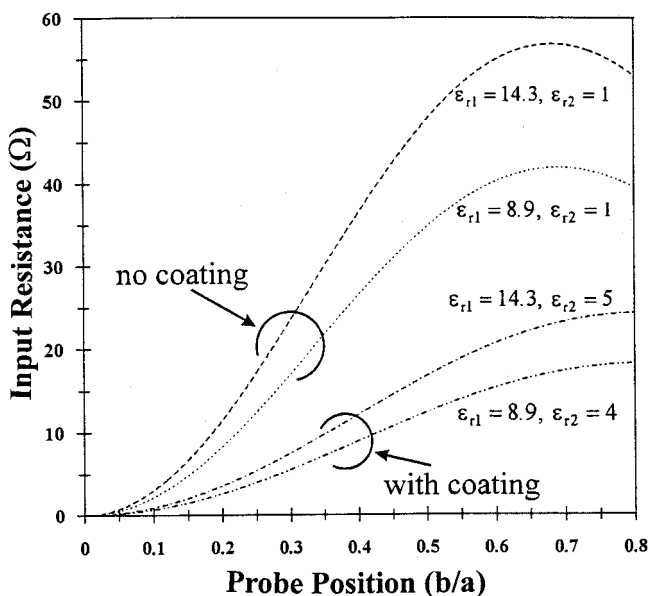
Fig. 3.11 Resonant input resistance versus feed position for $\varepsilon_{r1} = 8.9$, $\varepsilon_{r2} = 1.0$ (no coating), 4.0 (with coating) and $\varepsilon_{r1} = 14.3$, $\varepsilon_{r2} = 1.0$ (no coating), 5.0 (with coating). Other antenna parameters are given in Figure 3.8. (From Ref. 7, © 1994 John Wiley & Sons, Inc.)

The effects of dielectric coating on the input resistance at resonance for various feed positions are also calculated and shown in Figure 3.11. It should be noted that this graph must terminate at $b/a = 0.8$, due to the fact that larger b/a values will result in the probe extending beyond the dielectric boundary. The results for both the cases of no coating ($\varepsilon_{r2} = 1$) and coating the DR antenna with an optimal ε_{r2} are presented. The input resistance is seen to be decreased by about a factor of 2 due to the adding of the dielectric coating. However, the input resistances for both cases show a similar trend. Thus, impedance matching by moving the probe from the center to the edge [2] is also applicable to this kind of dielectric–coated DR antennas. Furthermore, since the input resistance can be improved by increasing the probe length ℓ [2], the input resistance decrease due to the dielectric coating can be lessened by suitably increasing the probe length. We also analyze the dielectric coating effect on the radiation pattern of the DR antenna. The far–zone radiated fields of the DR antenna with dielectric coating are also calculated. Numerical results indicate that the dielectric coating does not alter the radiation pattern of the hemispherical DR antenna.

3.4   A SLOT–COUPLED DR ANTENNA WITH A DIELECTRIC COATING

In this section, dielectric–coated hemispherical DR antennas fed by a microstrip line through a coupling slot in the ground plane are analysed. This kind of DR antennas, using slot coupling, has the advantage of mechanical simplicity, as compared to the DR antenna fed by a coaxial probe, and has potential applications at millimeter wave frequencies. Various DR antennas using slot coupling is thus worthy of investigations. In the present analysis for a slot–coupled dielectric–coated hemispherical DR antenna, the broadside TE_{111} mode is studied, and the reciprocity theorem is applied in the analysis. Details of the theoretical formulation and the calculated results are presented in the following.

3.4.1   Theoretical Formulation

The geometry of a slot–coupled dielectric–coated hemispherical DR antenna is shown in Figure 3.12. The feeding microstrip line has a width of W_f and is printed on a substrate of relative permittivity ε_{rs} and thickness t. The region $a < r < d$ is the dielectric coating with a relative permittivity ε_{r2}, and the region $r < a$ is the DR antenna with a relative permittivity ε_{r1}. The outside medium ($r > d$) is free space with permittivity ε_0 and permeability μ_0. The coupling slot of length L and width W ($L \gg W$) is centered below the DR antenna. In this case, the excitation of the broadside TE_{111} mode is the strongest [3]. By first applying the reciprocity analysis [11], the microstrip line is assumed to be infinitely long and propagates in a quasi–TEM mode. The transverse modal fields are given by

$$\vec{e}(y,z) = e_y \hat{y} + e_z \hat{z} , \tag{3.48}$$

$$\vec{h}(y,z) = h_y \hat{y} + h_z \hat{z} . \tag{3.49}$$

These fields are normalised as follows:

$$\int_{y=-\infty}^{\infty} \int_{z=0}^{-\infty} (\vec{e} \times \vec{h}) \cdot \hat{x} dy dz = 1 . \tag{3.50}$$

By adopting the $\exp(j\omega t)$ time dependence, the propagating microstrip–line fields are given as

$$\vec{E}^{\pm} = \vec{e} e^{\mp j\beta x} , \tag{3.51}$$

$$\vec{H}^{\pm} = \pm \vec{h} e^{\mp j\beta x} , \tag{3.52}$$

where β is the propagating constant of the microstrip line. The discontinuity is centred at $x = 0$ due to the presence of the slot in the ground plane. The total microstrip–line fields can then be written as
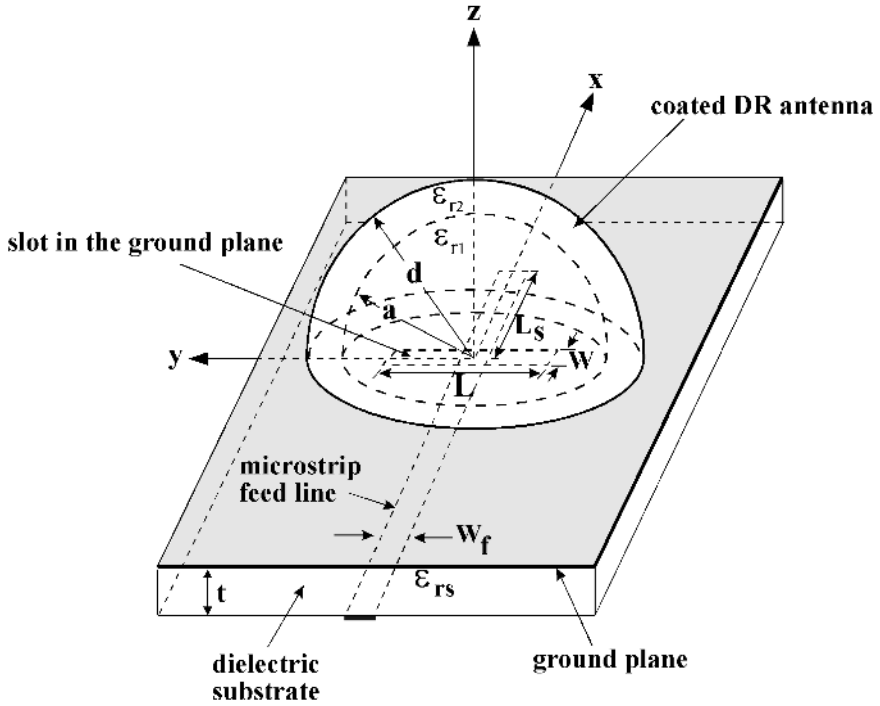
Fig. 3.12 Geometry of a slot–coupled hemispherical DR antenna a dielectric coating. (From Ref. 8, © 1995 John Wiley & Sons, Inc.)

$$\vec{E} = \begin{cases} \vec{E}^+ + R\vec{E}^-, & x < 0, \\ T\vec{E}^+, & x > 0, \end{cases} \tag{3.53}$$

$$\vec{H} = \begin{cases} \vec{H}^+ + R\vec{H}^-, & x < 0, \\ T\vec{H}^+, & x > 0, \end{cases} \tag{3.54}$$

where R and T are the voltage reflection and the transmission coefficients on the microstrip line, respectively. Then, by applying the reciprocity theorem to the total fields and the positive travelling fields, we can obtain

$$\iint_S \vec{E} \times \vec{H}^+ \cdot dS = \iint_S \vec{E}^+ \times \vec{H} \cdot dS , \tag{3.55}$$

where S is a closed surface consisting of three surfaces (see Figure 3.13, $S = S_0 + S_a + S_w$). The above equation can then be evaluated to give
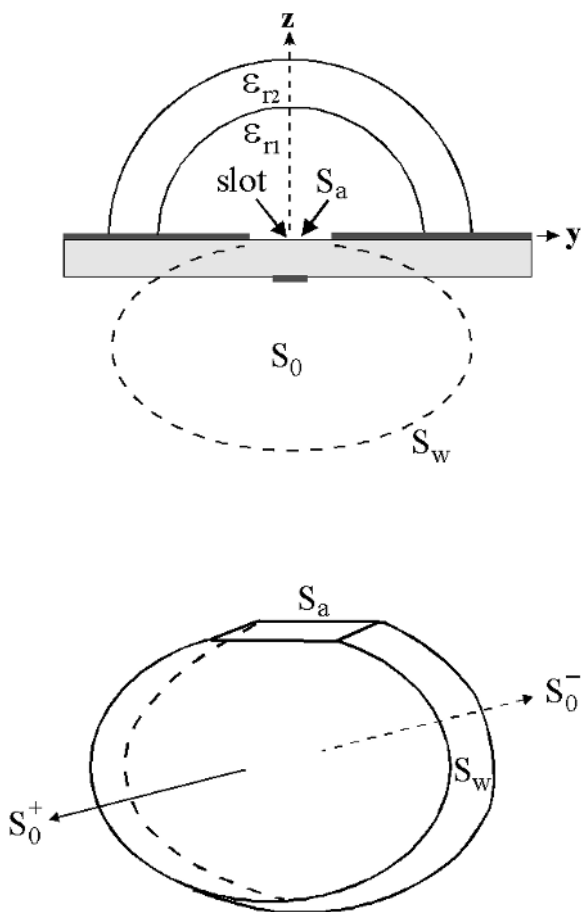
Fig. 3.13 The closed surface $S = S_0 + S_a + S_w$ used in the reciprocity analysis for the antenna shown in Figure 3.12.

$$R = \frac{1}{2} \iint_{S_a} M_y(x,y) h_y(x,y) dS ,$$ (3.56)

where M_y is the equivalent magnetic current in the coupling slot. Another application of the reciprocity theorem to the total field and the negative travelling fields gives

$$\iint_S \vec{E} \times \vec{H}^- \cdot dS = \iint_S \vec{E}^- \times \vec{H} \cdot dS ,$$ (3.57)

which can be evaluated to give the following expression:

$$T = 1 - \frac{1}{2} \iint_{S_a} M_y(x,y) h_y(x,y) dS = 1 - R . \tag{3.58}$$

The above results suggest that the dielectric–coated DR antenna can be viewed as a series load at the slot position. Also, the two applications of the reciprocity theorem lead to two equations for the three unknowns R, T, and M_y. The required third equation comes from enforcing the continuity of magnetic field H_y across the coupling slot. By invoking the equivalence principle, the coupling slot can be closed off and replaced by magnetic surface current M_y just above and below the ground plane. Continuity of the tangential electric field through the coupling slot is ensured by making the magnetic current above the ground plane equal to the negative of that below the ground plane (see Figure 3.14). Then, we define two Green's functions, $G_{yy}^{HM(a)}$ and $G_{yy}^{HM(f)}$. The former represents the $\hat{y}$–directed magnetic field H_y at $(x, y, 0)$ inside an isolated spherical DR antenna due to a unit $\hat{y}$–directed magnetic current M_y at $(x', y', 0)$, and the latter is the $\hat{y}$–directed magnetic field H_y at $(x, y, 0)$ inside the grounded dielectric slab due to a unit $\hat{y}$–directed magnetic current M_y at $(x', y', 0)$. By further applying the image theorem, we can obtain the equivalent problem (see Figure 3.15), and we have

$$\iint_{S_a} G_{yy}^{HM(a)}(x,y,x',y')[-2M_y(x',y')]dS'$$

$$- \iint_{S_a} G_{yy}^{HM(f)}(x,y,x',y')M_y(x',y')dS' = (1-R)h_y(x,y) . \tag{3.59}$$

In order to employ the moment method, the unknown magnetic current is expanded using piecewise–sinusoidal (PWS) basis functions and written as

$$M_y(x,y) = \sum_{n=1}^{N} V_n f_n(x,y) , \tag{3.60}$$

with

$$f_n(x,y) = f_u(x) f_p(y - y_n) ,$$

$$f_u(x) = 1/W , \qquad |x| < W/2 ,$$

Equivalent theorem
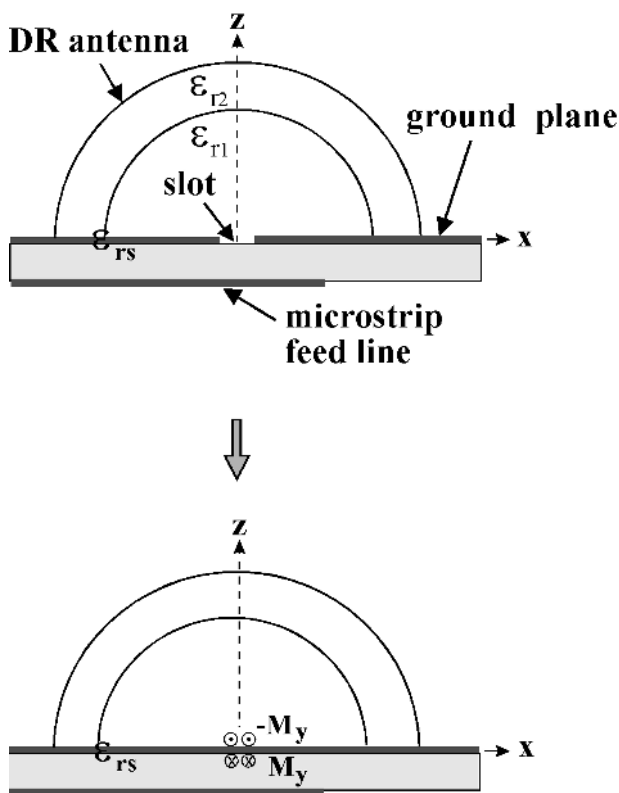
Fig. 3.14 The equivalent theorem for the antenna shown in Figure 3.12.

$$f_p(y) = \begin{cases} \dfrac{\sin k_e(y - |h|)}{\sin k_e h}, & |y| < h, \\ 0, & |y| > h, \end{cases}$$

$$k_e = k_0 \sqrt{(\varepsilon_{rs} + \varepsilon_{r1})/2}, \qquad k_0 = \omega\sqrt{\mu_0\varepsilon_0}, \qquad h = L/(N+1), \qquad y_n = nh - L/2.$$

Substitution of Eq. (3.60) into Eq. (3.59) and using the Galerkin's procedure, the following equation in matrix form is obtained:

Image theorem
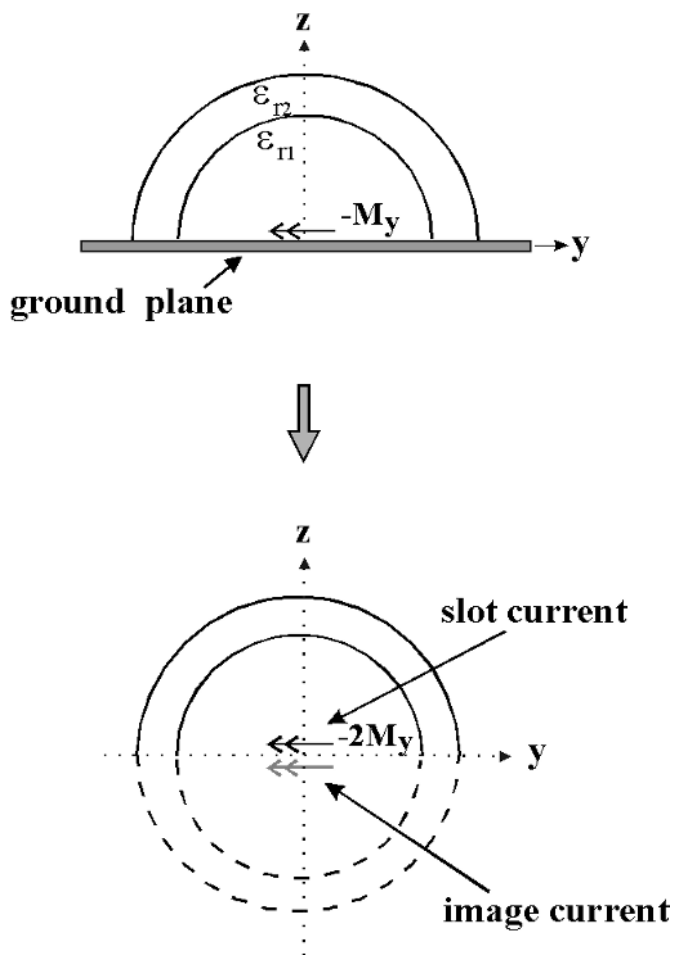
Fig. 3.15 The image theorem for the antenna shown in Figure 3.12.

$$[Y_{mn}^{f} + Y_{mn}^{a}][V_n] = (1 - R)[\Delta v_m] \, , \tag{3.61}$$

where

$$Y_{mn}^{f} = -\iint\limits_{S_a} \iint\limits_{S_a} f_m(x, y) G_{yy}^{HM(f)}(x, y, x', y') f_n(x', y') dS dS' \, , \tag{3.62}$$

$$Y_{mn}^a = -2 \iint\limits_{S_a} \iint\limits_{S_a} f_m(x,y) G_{yy}^{HM(a)}(x,y,x',y') f_n(x',y') dS dS', \qquad (3.63)$$

$$\Delta v_m = \iint\limits_{S_a} f_m(x,y) h_y(x,y) dS. \qquad (3.64)$$

Note that Y_{mn}^f in Eq. (3.62) is the admittance at the slot discontinuity due to the microstrip–line contribution and is derived as

$$Y_{mn}^f = \frac{-1}{2\pi} \int\limits_{-\infty}^{\infty} \int\limits_{-\infty}^{\infty} [\sin c(\frac{k_x W}{2}) \frac{k_e(\cos k_y h - \cos k_e h)}{(k_e^2 - k_y^2)\sin k_e h}]^2$$
$$\times \tilde{G}_{yy}^{HM(f)}(k_x,k_y) \cos(y_m - y_n) dk_x dk_y, \qquad (3.65)$$

where $\tilde{G}_{yy}^{HM(f)}(k_x,k_y)$ is the Green's function in the spectral domain for $G_{yy}^{HM(f)}(x,y,x',y')$, and can be written as

$$\tilde{G}_{yy}^{HM(f)}(k_x,k_y) = \frac{-j}{377 k_0}[(\varepsilon_{rs} k_0^2 - k_y^2)$$
$$\times \frac{q_1 \cosh(q_1 t) + \varepsilon_{rs} q_2 \sinh(q_1 t)}{q_1 T_m} + \frac{k_y^2 q_1(1 - \varepsilon_{rs})}{T_e T_m}] \qquad (3.66)$$

with

$$T_e = q_1 \cosh(q_1 t) + q_2 \sinh(q_1 t),$$

$$T_m = q_1 \sinh(q_1 t) + \varepsilon_{rs} q_2 \cosh(q_1 t),$$

$$q_1 = \sqrt{k_x^2 + k_y^2 - \varepsilon_{rs} k_0^2}, \qquad q_2 = \sqrt{k_x^2 + k_y^2 - k_0^2}.$$

As for Y_{mn}^a in Eq. (3.63), it is the admittance contributed due to the DR antenna, and the Green's function $G_{yy}^{HM(a)}$ in the space domain is derived as

$$G_{yy}^{HM(a)}(x,y) = \frac{-je^{-jk\rho}}{4\pi\omega\rho\mu_0}\left(\frac{\partial^2}{\partial y^2} + k_1^2\right)$$

$$-12AC_1 \frac{\sin\phi\sin\phi'\cos(\phi-\phi')}{r^2 r'^2} \hat{J}_1(k_1 r')\hat{J}_1(k_1 r)$$

$$-6AC_1 k_1 \frac{\sin\phi\cos\phi'\sin(\phi-\phi')}{r^2 r'} \hat{J}_1{}'(k_1 r')\hat{J}_1(k_1 r)$$

$$+6AC_1 k_1 \frac{\sin\phi'\cos\phi\sin(\phi-\phi')}{rr'^2} \hat{J}_1(k_1 r')\hat{J}_1{}'(k_1 r)$$

$$-3AC_1 k_1^2 \frac{\cos\phi'\cos\phi\cos(\phi-\phi')}{rr'} \hat{J}_1{}'(k_1 r')\hat{J}_1{}'(k_1 r) \,. \quad (3.67)$$

with

$$A = \frac{1}{8\pi\omega\mu_0 k_1} \,,$$

$$\rho = \sqrt{(x-x')^2 + (y-y')^2} \,,$$

$$C_1 = \frac{1}{\Delta_{TE}} [k_1 X_1 \hat{H}_1^{(2)}{}'(k_1 a) - X_2 \hat{H}_1^{(2)}(k_1 a)] \,,$$

$$\Delta_{TE} = X_2 \hat{J}_1(k_1 a) - k_1 X_1 \hat{J}_1{}'(k_1 a) \,,$$

$$\begin{aligned}
X_1 &= k_0 \hat{J}_1(k_2 a)\hat{H}_1^{(2)}(k_2 d)\hat{H}_1^{(2)}{}'(k_0 d) \\
&\quad + k_2 \hat{J}_1{}'(k_2 d)\hat{H}_1^{(2)}(k_0 d)\hat{H}_1^{(2)}(k_2 a) \\
&\quad + k_2 \hat{J}_1(k_2 a)\hat{H}_1^{(2)}(k_0 d)\hat{H}_1^{(2)}{}'(k_2 d) \\
&\quad + k_0 \hat{J}_1{}'(k_2 d)\hat{H}_1^{(2)}{}'(k_0 d)\hat{H}_1^{(2)}(k_2 a)
\end{aligned}$$

$$\begin{aligned}
X_2 &= k_0 k_2 \hat{J}_1{}'(k_2 a)\hat{H}_1^{(2)}(k_2 d)\hat{H}_1^{(2)}{}'(k_0 d) \\
&\quad + k_2^2 \hat{J}_1{}'(k_2 d)\hat{H}_1^{(2)}(k_0 d)\hat{H}_1^{(2)}{}'(k_2 a) \\
&\quad + k_2^2 \hat{J}_1{}'(k_2 a)\hat{H}_1^{(2)}(k_0 d)\hat{H}_1^{(2)}{}'(k_2 d) \\
&\quad + k_0 k_2 \hat{J}_1(k_2 d)\hat{H}_1^{(2)}(k_0 d)\hat{H}_1^{(2)}{}'(k_2 a)
\end{aligned}$$

$$k_i = k_0 \sqrt{\varepsilon_i} \,, \quad i = 1, 2.$$

With Y_{mn}^f, Y_{mn}^a, and Δv_m in Eqs. (3.62)–(3.64) evaluated, the reflection coefficient R in Eq. (3.61) can be obtained. Then, the input impedance of the

dielectric–coated hemispherical DR antenna can be obtained from the equivalent circuit, as shown in Figure 3.16, where the DR element is treated as a series load as seen by the microstrip line. Therefore, we can calculate the input impedance from

$$Z_{in} = Z_c \frac{2R}{1-R} - jZ_c \cot \beta L_s \, , \tag{3.68}$$

where Z_c is the characteristic impedance of the microstrip line and L_s is the length of the open–circuited tuning stub. By choosing Z_c to be 50 Ω, various input impedances calculated from Eq. (3.68), showing the effects of the dielectric coating, are presented in the next section. The antenna bandwidth of a slot–coupled dielectric–coated DR antenna is then studied.
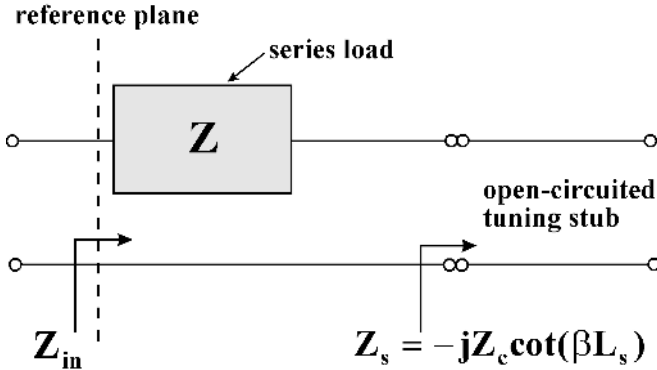
Fig. 3.16   The equivalent circuit for the antenna shown in Figure 3.12.

3.4.2   Numerical Results and Discussion

Figure 3.17 shows the numerical results of the normalised input impedance of a slot–coupled DR antenna by using different numbers of the PWS basis functions for the expansion of the slot magnetic current. The cases of $N = 1$, 3, and 4 are shown. For more basis functions used ($N > 4$), the obtained results show very small differences as compared to the case of $N = 4$, and the antenna bandwidth, determined from VSWR $\leq$ 2.0, is about 7.8% [(3.72–3.44)/3.56 × 100%]. It is also seen that the result of $N = 4$ agrees with the measured data [9]. In the following analysis, the number of the basis functions is thus chosen to be four.

Figure 3.18 shows the dielectric coating effects on the input impedance of a slot–coupled DR antenna. The relative permittivity of the coating is chosen to be 5.0, which is about half that of the DR antenna ($\varepsilon_{r1} = 9.8$). Due to the dielectric coating, the resonant frequency is decreased, and the resonant input resistance is also decreased. This behaviour resembles the observations for a probe–fed

dielectric–coated DR antenna shown in Section 3.3. In the figure, two cases of L = 13.5 mm, L_s = 8.5 mm (case 1) and L = 14.5 mm, L_s = 8.0 mm (case 2) are shown. In case 2, the slot length L is increased from 13.5 mm (case 1) to 14.5 mm such that the resonant input resistance is 50 Ω, while the open–circuited stub L_s is adjusted such that the input reactance is zero at the frequency where the resonant input resistance occurs. From the half–power impedance bandwidth, the same definition as studied in Section 3.2, the impedance bandwidths for cases 1 and 2 are seen to be greater than that of the no coating case. To show it more clearly, we plot the result of case 2 on a Smith chart, as shown in Figure 3.19. The antenna bandwidth is increased to be about 14.7% [(3.14–2.72)/2.85 × 100%], which is nearly two times that of the DR antenna without coating (7.8%). Another case of ε_{r2} = 4.0, which is also about half of ε_{r1}, is also plotted in Figure 3.20. The antenna bandwidth in this case is found to be about 15.3%. The increase in antenna bandwidth due to the dielectric coating is thus significant.
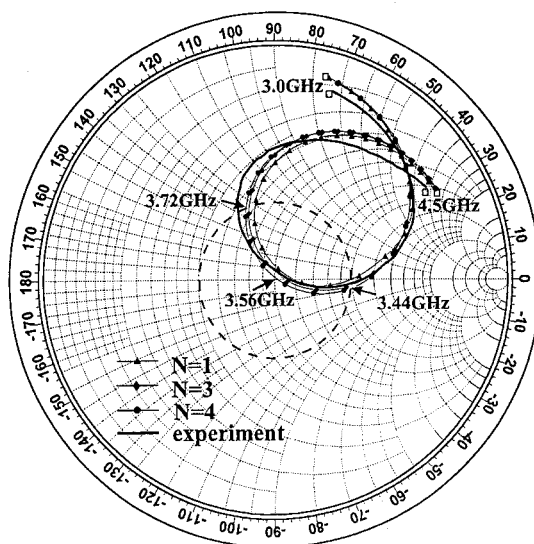
Fig. 3.17 Calculated input impedance on a Smith chart for the antenna shown in Figure 3.12 with $a = d$ = 12.5 mm, ε_{r1} = 9.5, L = 13.5 mm, W = 0.87 mm, W_f = 1.45 mm, t = 0.635 mm, ε_{rs} = 2.96, L_s = 13.6 mm. Results are obtained using different numbers of the PWS basis functions for the expansion of the slot magnetic current. The solid line denotes the measured results [9]. (From Ref. 8, © 1995 John Wiley & Sons, Inc.)
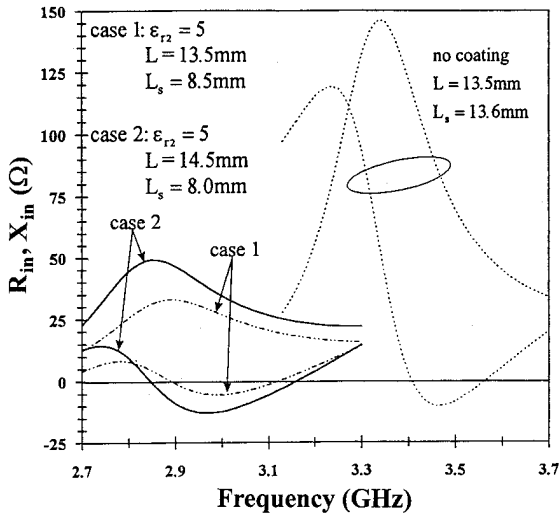
Fig. 3.18 Calculated input impedance, $R_{in} + jX_{in}$, of the antenna shown in Figure 3.12 with $d = 1.5a$, $a = 12.5$ mm, $\varepsilon_{r1} = 9.5$, $L = 13.5$ mm, $W = 0.87$ mm, $W_f = 1.45$ mm, $t = 0.635$ mm, $\varepsilon_{rs} = 2.96$, $L_s = 13.6$ mm. (From Ref. 8, © 1995 John Wiley & Sons, Inc.)
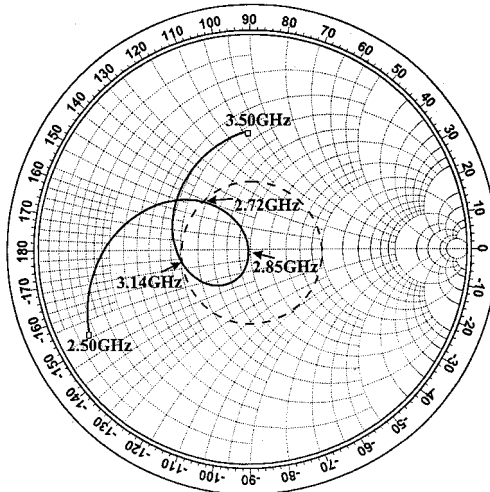
Fig. 3.19 Calculated input impedance on the Smith chart for the antenna shown in Figure 3.12 with $d = 1.5a$, $L = 14.5$ mm, $L_s = 8.0$ mm, $\varepsilon_{r2} = 5.0$. Other antenna parameters are given in Figure 3.18. (From Ref. 8, © 1995 John Wiley & Sons, Inc.)
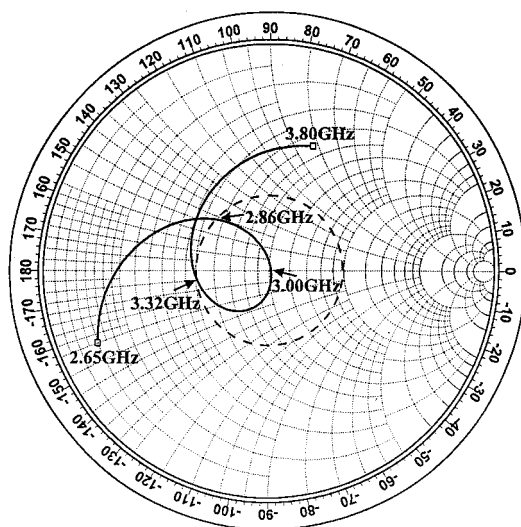
Fig. 3.20 Calculated input impedance on the Smith chart for the antenna shown in Figure 3.12 with $d = 1.5a$, $L = 13.8$ mm, $L_s = 7.5$ mm, $\varepsilon_{r2} = 4.0$. Other antenna parameters are given in Figure 3.18. (From Ref. 8, © 1995 John Wiley & Sons, Inc.)
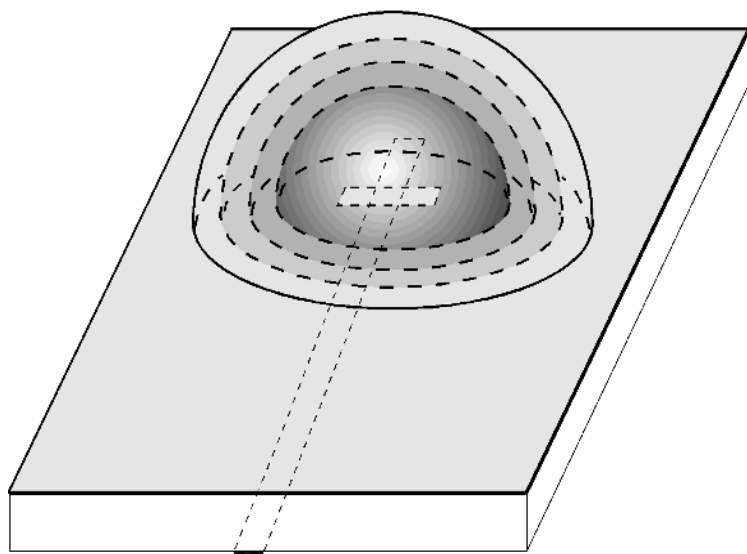
Fig. 3.21 Geometry of a slot–coupled multi–layer dielectric–coated hemispherical DR antenna.

Various coating thicknesses and permittivities other than the cases of $\varepsilon_{r2} = 4.0$ and 5.0 have also been calculated. It is found that the antenna bandwidth improvement increases with increasing coating thickness, and the optimal bandwidth improvement is observed when the coating permittivity is about half that of the DR antenna. This behaviour is similar to the results obtained in Section 3.3. Furthermore, numerical results of the far–zone radiated fields are also calculated, and results indicate that the dielectric coating does not alter the radiation pattern of the DR antenna excited in the broadside TE_{111} mode. Finally, it can be expected that, when there are more than one coating layer (see the structure in Figure 3.21) and the coating permittivity is decreased by about one half for each coated layer, better antenna bandwidth enhancement than that obtained here can still be possible.

REFERENCES

1. M. W. McAllister and S. A. Long, "Resonant hemispherical dielectric antenna," *Electron. Lett.*, vol. 20, pp. 657–659, 1984.
2. K. W. Leung, K. M. Luk, K. Y. A. Lai and D. Lin, "Input impedance of hemispherical dielectric resonator antenna," *Electron. Lett.*, vol. 27, pp. 2259–2260, 1991.
3. K. W. Leung, K. Y. A. Lai, K. M. Luk and D. Lin, "Input impedance of aperture coupled hemispherical dielectric resonator antenna," *Electron. Lett.*, vol. 29, pp. 1165–1167, 1993.
4. K. W. Leung, K. Y. A. Lai, K. M. Luk and D. Lin, "Theory and experiment of a coaxial probe fed hemispherical dielectric resonator antenna," *IEEE Trans. Antennas Propagat.*, vol. 41, pp. 1390–1398, 1993.
5. K. W. Leung, K. M. Luk, K. Y. A. Lai and D. Lin, "Theory and experiment of an aperture–coupled hemispherical dielectric resonator antenna," *IEEE Trans. Antennas Propagat.*, vol. 43, pp. 1192–1198, 1995.
6. K. L. Wong, N. C. Chen and H. T. Chen, "Analysis of a hemispherical dielectric resonator antenna with an air gap," *IEEE Microwave Guided Wave Lett.*, vol. 3, pp. 355–357, 1993.
7. K. L. Wong and N. C. Chen, "Analysis of a broadband hemispherical dielectric resonator antenna with a dielectric coating," *Microwave Opt. Technol. Lett.*, vol. 7, pp. 73–76, 1994.
8. N. C. Chen, H. C. Su, K. L. Wong and K. W. Leung, "Analysis of a broadband slot–coupled dielectric–coated hemispherical dielectric resonator antenna," *Microwave Opt. Technol. Lett.*, vol. 8, pp. 13–16, 1995.
9. K. W. Leung, *Rigorous Analysis of Dielectric Resonator Antennas Using the Method of Moments*, Ph.D. dissertation, Dept. of Electrical Eng., The Chinese University of Hong Kong, 1993.
10. K. L. Wong and H. T. Chen, "Resonance in a spherical–circular microstrip structure with an air gap," *IEEE Trans. Microwave Theory Tech.*, vol. 41, pp. 1466–1468, 1993.

11. D. M. Pozar, "Reciprocity method of analysis for printed slot and slot–coupled microstrip antennas," *IEEE Trans. Antennas Propagat.*, vol. 34, pp. 1439–1446, 1986.
12. R. F. Harrington, *Time–Harmonic Electromagnetic Fields*, McGraw–Hill, New York, 1961, pp. 267–269.
13. W. C. Chew, *Waves and Fields in Inhomogeneous Media*, Van Nostrand Reinhold, New York, 1990, p. 194.
14. R. E. Collin, *Field Theory of Guided Waves*, McGraw–Hill, New York, 1960, p. 264.
15. T. M. Au and K. M. Luk, "Effects of parasitic element on the characteristics of microstrip antenna," *IEEE Trans. Antennas Propagat.*, vol. 39, pp. 1247–1251, 1991.

This page intentionally left blank

CHAPTER 4

Body of Revolution (BOR) - Analysis of Cylindrical Dielectric Resonator Antennas

Ahmed A. Kishk

Department of Electrical Engineering
University of Mississippi
University,
MS 38677,
USA

4.1   INTRODUCTION

Dielectric resonators made of high dielectric constant material are well known as a high Q-factor circuit element. Therefore, they have been used as resonators in microwave filters and oscillators [1]. These circuits are normally shielded in conductor cavities. Recently, dielectric resonators have been used as an antenna element. It was proven experimentally that these elements are efficient radiators [2]-[5].   To achieve a good efficiency, the proper modes have to be excited. Therefore, the proper excitation mechanism must be used. That requires knowledge of the field distribution of the desired mode to know how one can couple to it through the proper excitation mechanism.   Here, we choose to analyze the isolated dielectric disc [6]-[8]. The analysis will provide data suitable for the design of this antenna above an infinite electric ground plane.

In this chapter, the analysis of the body of revolution dielectric resonator antenna will be considered. Many possible geometries of body of revolution can be analyzed as a DRA. Here, we concentrate on the analysis of circular discs because it is the most popular type. The investigation and analysis will concentrate on the first four modes that have low radiation Q-factor, because they are the most

efficient radiating modes. Mode charts will be provided for natural resonant frequencies of the circular dielectric disc as well as the near field distributions [9]-[11]. The DRA is excited by a coaxial probe or by a narrow slot [12-13]. The surface integral equations are used to formulate the problem [14]. Then the method of moments is used to reduce the integral equations to a system of matrix equation. The natural resonant frequencies are defined as the frequencies that make the determinant of the matrix vanish. Since the dielectric disc is rotationally symmetric, Fourier expansions are used to increase the surface equivalent unknown currents, which allow us to search for the zeros of a particular azimuthal mode. Such procedure is lengthy and requires significant, elaborate computations and careful study to identify the modes. The modes that can be obtained are of two types. These modes are: the modes that are corresponding to half of the dielectric disc above a perfect electric ground plane; and the modes that are corresponding to half of the dielectric disc above a perfect magnetic plane or a perfect conducting plane across its axis of symmetry.

After obtaining the resonant frequencies, the radiation Q-factor is computed and used as a measure of the radiation efficiency of the dielectric disc and also as a measure of the radiation bandwidth of the disc.

4.2   FORMULATION OF THE PROBLEM

In this section we present the formulation of the problem in a general sense, as a body of revolution. Normally, the dielectric resonator is located above an infinite ground plane. Using the image theory, the ground plane is removed to end up with the dielectric object double its size when it is located above the ground plane. This concept will be used when we compute the resonant frequencies and the input impedance. The finite size ground plane will have a significant effect on the far field radiation patterns. Therefore, the effect of the finite ground plane will be considered only in such cases. We will consider the problem as a body of revolution dielectric object, as shown in Fig. 4.1. The object is characterised by the permittivety and permeability (ε_d, μ_d) and bounded by the surface S_d. The object is in the free space with (ε_0, μ_0). The total electric and magnetic fields inside the object and out side are denoted by ($\mathbf{E}^d$, $\mathbf{H}^d$) and ($\mathbf{E}^0$, $\mathbf{H}^0$), respectively.

The problem will be analyzed in two situations. First, when no source is considered (source free) to compute the natural resonant frequencies in the complex frequency plane - in this case the azimuthal modes are decoupled and we can consider one mode at a time. Second, when a real source is present and causes all the azimuthal modes to couple with each other. In this case a special treatment of the problem will be considered.

4.2.1   Wire Probe Excitation

For the general case, the problem will be formulated with the presence of the real source, in this case a thin wire. Using the surface equivalent principle, the surface integral equations are obtained based on the E-PMCHW formulation [14]. Thin wire means that the wire radius, as a function of the operating frequency, is small

enough in terms of wavelengths in the medium in which it resides so that the only component of current induced on the wire is the axially directed component and circumferentially invariant [15]. The geometries in Figs. 4.2 and 4.3 are two possible structures consisting of thin wires and a dielectric body of revolution (DBOR).
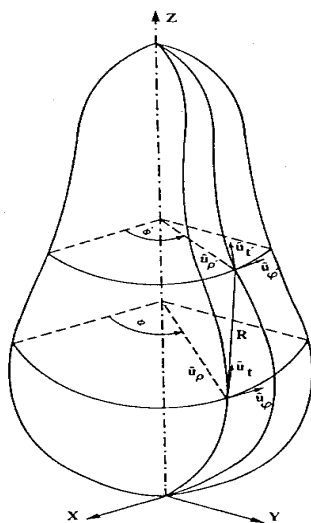
Fig. 4.1 Coordinates of the body of revolution

The DBOR is bounded by the surface of revolution, S_d. The surface S_d has been created by the rotation of the generating curve, in xz-plane, about the z-axis in a cylindrical coordinate system. S_{wd} and S_{w0} present the wires, where the subscripts "wd" and "w0" refer to wire elements interior and exterior to the DBOR, respectively. In the ensuing derivation of the integral equations, the superscript "i" refers to the known field, that is, the source field, which excites the wire radiator. The equivalent electric and magnetic surface currents, which arise from application of the surface equivalence principle, are represented by the symbols **J** and **M,** respectively.

Using image theory, the ground plane in Fig. 4.2 can be removed to end up with the geometries in Fig. 4.3. In accordance with the field equivalence principle [16], the original problem of Fig. 4.3 can be divided into two problems: one for the interior region, and the other for the exterior region. By enforcing the boundary

conditions that the tangential component of the electric field must vanish at the conductor surface, and that the tangential components of both the electric and magnetic fields must be continuous across the dielectric surface, a system of integral equations is obtained from which the unknowns $\mathbf{J}_{wd}$, $\mathbf{J}_{w0}$, $\mathbf{M}_d$, and $\mathbf{J}_d$ can be determined. This system of equations can be written in operator form as follows:

$$
\begin{aligned}
\mathbf{E}_{\tan}^0(\mathbf{J}_d) &+ \mathbf{E}_{\tan}^0(\mathbf{J}_{we}) + \mathbf{E}_{\tan}^0(\mathbf{M}_d) \\
&+ \mathbf{E}_{\tan}^d(\mathbf{J}_d) + \mathbf{E}_{\tan}^d(\mathbf{J}_{wd}) + \mathbf{E}_{\tan}^d(\mathbf{M}_d) = \mathbf{E}_{\tan}^{id} - \mathbf{E}_{\tan}^{i0} \qquad \text{on} \quad S_d
\end{aligned}
\tag{4.1}
$$

$$
\begin{aligned}
\mathbf{H}_{\tan}^0(\mathbf{J}_d) &+ \mathbf{H}_{\tan}^0(\mathbf{J}_{we}) + \mathbf{H}_{\tan}^0(\mathbf{M}_d) \\
&+ \mathbf{H}_{\tan}^d(\mathbf{J}_d) + \mathbf{H}_{\tan}^d(\mathbf{J}_{wd}) + \mathbf{H}_{\tan}^d(\mathbf{M}_d) = \mathbf{H}_{\tan}^{id} - \mathbf{H}_{\tan}^{i0} \quad \text{on} \quad S_d
\end{aligned}
\tag{4.2}
$$

$$
\mathbf{E}_{\tan}^d(\mathbf{J}_d) + \mathbf{E}_{\tan}^d(\mathbf{J}_{wd}) + \mathbf{E}_{\tan}^d(\mathbf{M}_d) = \mathbf{E}_{\tan}^{id} \qquad \text{on} \quad S_{wd}
\tag{4.3}
$$

$$
\mathbf{E}_{\tan}^0(\mathbf{J}_d) + \mathbf{E}_{\tan}^0(\mathbf{J}_{we}) + \mathbf{E}_{\tan}^0(\mathbf{M}_d) = -\mathbf{E}_{\tan}^{i0} \qquad \text{on} \quad S_{w0}
\tag{4.4}
$$

Equations (4.1) to (4.4) are referred to as E-PMCHW formulation [14]. In these equations $\mathbf{E}()$ and $\mathbf{H}()$ represent operators on the unknown electric and magnetic currents $\mathbf{J}$ and $\mathbf{M}$. These operators are defined as

$$
\mathbf{E}^q(\mathbf{J}) = \text{-j}\omega\mu_q \iint_s \mathbf{J}(\mathbf{r}')\, G^q(\mathbf{r}, \mathbf{r}')\, ds' - \frac{1}{\varepsilon_q} \nabla \iint_s \rho(\mathbf{r}')\, G^q(\mathbf{r}, \mathbf{r}')\, ds'
\tag{4.5}
$$

$$
\mathbf{H}^q(\mathbf{J}) = \nabla \times \iint_s \mathbf{J}(\mathbf{r}')\, G^q(\mathbf{r}, \mathbf{r}')\, ds'
\tag{4.6}
$$

q stands for d or 0 and ρ is the electric charge density. $\mathbf{r}$ and $\mathbf{r}'$ are the field and source position vectors, respectively. The function G^q is the scalar free space Green's function, which is given as

$$
G^q(\mathbf{r}, \mathbf{r}') = \frac{1}{4\pi} e^{-\text{j}k_q|\mathbf{r}-\mathbf{r}'|} \qquad \text{and} \qquad k_q = \omega\sqrt{\mu_q \varepsilon_q}
\tag{4.7}
$$

$\mathbf{E}^q(\mathbf{M})$ and $\mathbf{H}^q(\mathbf{M})$ can be obtained from (4.5) and (4.6) using duality [16]. The surface charge density is related to the electric surface current using the continuity equation [16] as

$$
\nabla' \bullet \mathbf{J}(\mathbf{r}') = -\text{j}\omega\rho(\mathbf{r}')
\tag{4.8}
$$
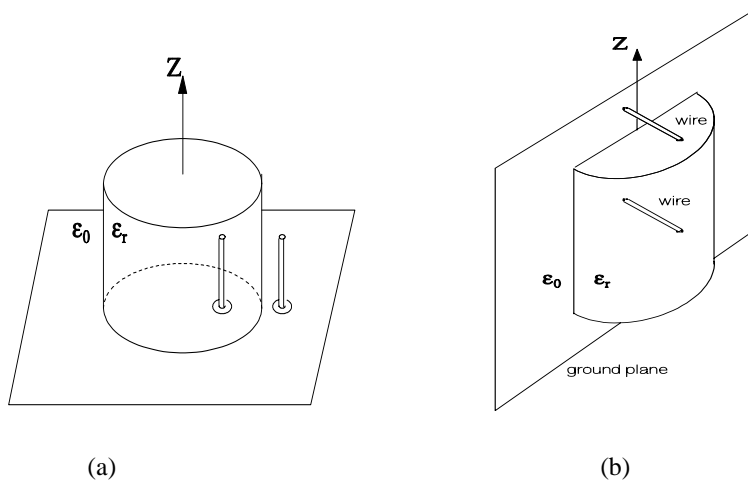
Fig. 4.2 Geometry of the DRA above a ground plane with the monopole wire
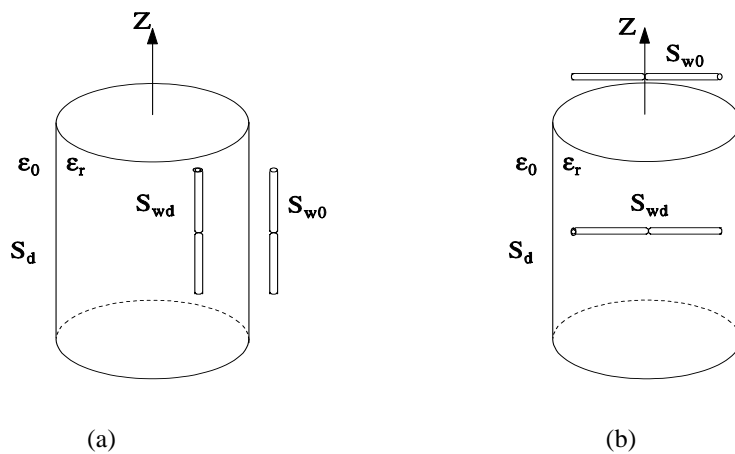
Fig. 4.3 Geometry of the DRA after using image theory

4.2.2   Method of Moments

Using the method of moments the surface integral equations (4.1) to (4.4) are reduced to a system of matrix equations [16].

The unknown equivalent electric and magnetic currents on the BOR are modeled as harmonic ($e^{jm\varphi}$) entire domain expansion functions for the circumferential

variation, where m is the mth Fourier mode, and as piecewise linear sub-domain functions for the dependence on axial curvature [14, 17] as

$$\mathbf{J}(\mathbf{r'}) = \sum_{m=-M}^{M} \sum_{j=1}^{N} [\, I_{mj}^{t} J_{mj}^{t}(t', \varphi') \, \hat{u}'_{t} + I_{mj}^{\varphi} J_{mj}^{\varphi}(t', \varphi') \, \hat{u}'_{\varphi} \,] \qquad (4.9)$$

$$\mathbf{M}(\mathbf{r'}) = \eta_0 \sum_{m=-M}^{M} \sum_{j=N+1}^{N+N_d} [\, K_{mj}^{t} M_{mj}^{t}(t', \varphi') \, \hat{u}'_{t} + K_{mj}^{\varphi} M_{mj}^{\varphi}(t', \varphi') \, \hat{u}'_{\varphi} \,] \qquad (4.10)$$

where the range –M to M are the total azimuthal modes. I_{mj}^{t}, I_{mj}^{ϕ}, k_{mj}^{t}, and k_{mj}^{ϕ} are the unknown current coefficients on the BOR surface. J_{mj}^{t}, J_{mj}^{ϕ}, M_{mj}^{t}, and M_{mj}^{ϕ} are the expansion functions (basis functions) defined as

$$J_{mj}^{\gamma} = M_{mj}^{\gamma} = T_j(t') / (\rho(t') \, e^{im\varphi'}, \qquad \gamma = t \text{ or } \varphi \qquad (4.11)$$

The function $T_j(t)$ is the triangle function, $\rho(t)$ is the radial distance from the axis of the BOR. The superscript/subscript γ denotes a tangential component of either t or φ on the body of revolution. The wire currents are expanded into a series form as

$$\mathbf{J}_w = \sum_{k} I_k \, T_k^{w}(w') \, \hat{u}_w \qquad \text{on } S_{wq} \qquad (4.12)$$

T_k^{w} is the triangle basis function used on the wire [17] and $\hat{u}_w$ is the unit vector along the wire axis. Substituting equations (4.9), (4.10) and (4.12) into the integral equations (4.1) to (4.4) and testing the integral equations (4.3) and (4.4) by the testing functions J_{ℓ}^{w} and equations (4.1) and (4.2) by the testing functions $W_{\ell i}^{t}$ and $W_{\ell i}^{\phi}$ to form the matrix equation, where the testing functions on the BOR are defined as:

$$W_{\ell i}^{\gamma} = \hat{u}_{\gamma} f_i(t) \, e^{-j\ell\phi}, \qquad \gamma = t \text{ or } \varphi \qquad (4.13)$$

After application of the Galerkin's procedure [17], the integral equations (4.1)-(4.4) are expressed in a matrix form as follows:

$$
\begin{bmatrix}
[BB]_{-m} & \cdot & \cdots & \cdot & \cdots & \cdot & \cdot & [BW]_{-m} \\
\cdot & [BB]_{-m+1} & \cdots & \cdot & \cdots & \cdot & 0 & [BW]_{-m+1} \\
\cdot & \cdot & \cdots & \cdots & \cdots & \cdots & & \cdots \\
\cdot & \cdot & \cdots & [BB]_0 & \cdots & \cdot & \cdot & [BW]_0 \\
\cdot & 0 & \cdots & \cdot & \cdots & \cdots & \cdot & \cdots \\
\cdot & \cdot & \cdots & \cdot & \cdots & [BB]_{m-1} & \cdot & [BW]_{m-1} \\
\cdot & \cdot & \cdots & \cdot & \cdots & \cdot & [BB]_m & [BW]_m \\
[WB]_{-m} & [WB]_{-m+1} & \cdots & [WB]_0 & \cdots & [WB]_{m-1} & [WB]_m & [WW]
\end{bmatrix}
\times
$$

$$
\begin{bmatrix}
[JM]_{-m} \\
[JM]_{-m+1} \\
\cdots \\
[JM]_0 \\
\cdots \\
[JM]_{m-1} \\
[JM]_m \\
[J_w]
\end{bmatrix}
=
\begin{bmatrix}
0 \\
0 \\
\cdots \\
0 \\
\cdots \\
0 \\
0 \\
[V_w]
\end{bmatrix}
\qquad (4.14)
$$

where $[JM]_m$ represents the electric and magnetic current coefficients for the mth Fourier mode of the basis functions that reside on S_d.

The vector $[J_w]$ represents the current expansion coefficients on the surface S_{wq}. Since a delta gap source, a common dipole excitation, is used to model the impressed (incident) electric field, the right hand sides of equation (4.1) and (4.2) may be set equal to zero. Thus the right hand side column matrix, which represents the generalised voltage vector, is zero except for the known wire excitation voltage $[V_w]$. The sub-matrices in the method of moment matrix, i.e., the above square matrix, represent the electromagnetic interactions between specific surface components on the DRA. The large square sub-matrix involving the partitions [BB] represent the inner products in the Galerkin's procedure for the case when the testing and basis functions are on the surface S_d. The banded nature of this part of the matrix is due to the orthognality of the exponential function $e^{jm\varphi}$. The partitioned row matrix comprises the sub-matrices [BW], and the partitioned column matrix comprising the sub-matrices [WB] represent inner products resulting from the Galerkin's procedure when the testing functions are on S_d and the basis functions are on S_{wq} (q=d or e) for [BW] and vice versa for [WB]. The square matrix [WW] represents the results of the Galerkin's procedure when both the testing and basis functions are on S_{wq}.

The matrix $[BB]_m$ is further partitioned as

$$
\begin{bmatrix}
([Z_{d,d}^0]+\eta_r[Z_{d,d}^d]) & ([Y_{d,d}^0]+\ [Y_{d,d}^d]) \\
([Y_{d,d}^0]+\ [Y_{d,d}^d]) & (-[Z_{d,d}^0]-\dfrac{1}{\eta_r}[Z_{d,d}^d])
\end{bmatrix}_m
\tag{4.15}
$$

where $\eta_r^2=\mu_q/\varepsilon_q$, and a typical $[Z]$ or $[Y]$ matrix [18] and each sub-matrix consists of four sub-matrices in the form

$$
\begin{bmatrix}
[B_{tt}] & [B_{t\varphi}] \\
[B_{\varphi t}] & [B_{\varphi\varphi}]
\end{bmatrix}_m
=
\begin{bmatrix}
[B_{tt}] & -[B_{t\varphi}] \\
-[B_{\varphi t}] & [B_{\varphi\varphi}]
\end{bmatrix}_{-m}
\tag{4.16}
$$

where $[B] = [Z]$ or $[Y]$, a square matrix of order N_t for each Fourier mode m. The integral expressions for the matrices $[BB]_m$ are the same as those in [18]. The matrix $[BW]_m$ is given by

$$
\begin{bmatrix} BW \end{bmatrix}_m =
\begin{bmatrix}
\eta_r[Z_{t,w}^d] & [Z_{t,w}^0] \\
\eta_r[Z_{\varphi,w}^d] & [Z_{\varphi,w}^0] \\
[Y_{t,w}^d] & [Y_{t,w}^0] \\
[Y_{\varphi,w}^d] & [Y_{\varphi,w}^0]
\end{bmatrix}_m
\tag{4.17}
$$

and the matrices $[WB]_m$ is given by

$$
\begin{bmatrix} WB \end{bmatrix}_m =
\begin{bmatrix}
\eta_r[Z_{w,t}^d] & \eta_r[Z_{w,\varphi}^d] & [Y_{w,t}^d] & [Y_{w,\varphi}^d] \\
[Z_{w,t}^0] & [Z_{w,\varphi}^0] & [Y_{w,t}^0] & [Y_{w,\varphi}^0]
\end{bmatrix}_m
\tag{4.18}
$$

The matrix $[BW]_m$ is of order $(4N_t \times p_w)$, where N_t and p_w are the number of expansion functions on the BOR and wire, respectively, and $[WB]_m$ is of order $(p_w \times 4N_t)$. An increase in computational efficiency can be obtained by using the relationship, $[WB]_m=[BW]_{-m}^T$, where T for the sub-matrix transpose and the + or - signs are used for $[Z]$ and $[Y]$ matrices, respectively. The integral expressions for the matrix elements $[BW]_m$ are given as [17]

$$Z_{t,w}^{q} = \frac{jk_q\eta_q}{4\pi} \int_{N_t} dt \int_0^{2\pi} d\phi \int_{P_w} dw' \{T(t)T(w')\hat{u}_t \bullet \hat{u}_w - \frac{1}{k_q^2}T'(t)T'(w')\}\frac{e^{-j(k_qR+m\phi)}}{R}$$

(4.19)

$$Z_{\phi,w}^{q} = \frac{jk_q\eta_q}{4\pi} \int_{N_t} dt \int_0^{2\pi} d\phi \int_{P_w} dw' \{T(t)T(w')\hat{u}_\phi \bullet \hat{u}_{w'} + \frac{jn}{k_q^2\rho}T(t)T'(w')\}\frac{e^{-j(k_qR+m\phi)}}{R}$$

(4.20)

$$Y_{t,w}^{q} = \frac{1}{4\pi} \int_{N_t} dt \int_0^{2\pi} d\phi \int_{P_w} dw' T(t)T(w')\hat{u}_t \bullet (\hat{u}_w x \mathbf{R})\frac{(1+jk_qR)}{R^3}e^{-j(k_qR+m\phi)}$$

(4.21)

$$Y_{\phi,w}^{q} = \frac{1}{4\pi} \int_{N_t} dt \int_0^{2\pi} d\phi \int_{P_w} dw' T(t)T(w')\hat{u}_\phi \bullet (\hat{u}_{w'} x \mathbf{R})\frac{(1+jk_qR)}{R^3}e^{-j(k_qR+m\phi)}$$

(4.22)

where k_N is the k_N^{th} testing function on S_d and p_w is the pth basis function on S_{wq}. $\mathbf{R} = \mathbf{r} \cdot \mathbf{r}'$ and R=$|\mathbf{R}|$. T(t) and T(w) are the triangle functions on the BOR and wire, respectively. Finally, the matrix [WW] is given by

$$\begin{bmatrix} [Z_{wd,wd}^d] & [0] \\ [0] & [Z_{w0,w0}^0] \end{bmatrix}$$

(4.23)

Equation (4.23) illustrates that there is no direct interaction between the wires in the interior and exterior regions.

Since the final goal is the computation of input impedance, the following steps, which are in essence a "mode by mode" elimination procedure, can be performed to obtain the solution for the current coefficients, $\mathbf{J}_{wq}$, from which the input impedance can be calculated:

$$[JM]_m = -[BB]_m^{-1}[BW]_{-m}[J_w], \qquad m = -N,...,N$$

(4.24)

These results can be substituted into the last equation system (last row) of (4.14) to obtain

$$[[WB]_{-m}[BB]_{-m}^{-1}[BW]_{-m}+\bullet\bullet\bullet$$
$$+[WB]_0[BB]_0^{-1}[BW]_0+\bullet\bullet\bullet+[WB]_m[BB]_m^{-1}[BW]_m-[WW]][J_w]=[V_w]$$

(4.25)

The wire current is easily obtained by inverting the bracketed matrix and multiplying the result by the vector $[V_w]$ as:

$$[J_w]=[[WB]_{-m}[BB]_{-m}^{-1}[BW]_{-m}+\bullet\bullet\bullet$$
$$+[WB]_0[BB]_0^{-1}[BW]_0+\bullet\bullet\bullet+[WB]_m[BB]_m^{-1}[BW]_m-[WW]]^{-1}[V_w]$$

(4.26)

If quantities other than the impedance of the antenna are desired this can be an efficient approach. If storage is at a premium, the sub-matrices can be recomputed as necessary to determine other quantities, such as the currents on S_d. Alternatively, the matrix products indicated in the right side of (4.26) can be stored. Storage of these products will generally require less space than even the non-zero sub-matrices shown in (4.14). For the radiation far field, this process is not necessary and a simpler method can be used. If the electric wire is replaced by the known electric current distribution, such as few infinitesimal electric dipoles (no physical presence of the wire), only the body of revolution part of the object will be considered and the method of moment matrix can be solved for each mode separately. Then, the contribution of each mode is added in a superposition form to get the total far field radiation patterns [7].

4.2.3   Narrow Slot Excitation

The other type of excitation is the narrow slot of width w_s on the ground plane and coupled to a microstrip line, as shown in Fig. 4.4. The slot surface is denoted by S_s. For generality, we choose the coordinate system above the ground plane to be different from the coordinate system below the ground plane. The narrow slot is short circuited and replaced by an equivalent magnetic current on both sides. These currents are equal in magnitude and opposite in phase to assure the continuity of the tangential electric fields across the slot. This situation gives rise to two problems. The upper part of the ground plane is denoted by "U" and the lower part of the ground plane is denoted by "L". Again, the image theory is used to remove the ground plane, as shown in Fig. 4.5, for the upper half of the problem. The image of the magnetic current doubles its value. The lower part is considered as a printed microstrip line, which is excited and coupled to the equivalent magnetic current. The integral equation on the slot surface can be written as

$$\mathbf{H}_{tan}^d(\mathbf{J}_d)+\mathbf{H}_{tan}^d(\mathbf{M}_d)-2\mathbf{H}_{tan}^d(\mathbf{M}_s)=\mathbf{H}_{tan}^L(\mathbf{M}_s)+\mathbf{H}_{tan}^{inc} \qquad \text{on} \quad S_s \qquad (4.27)$$
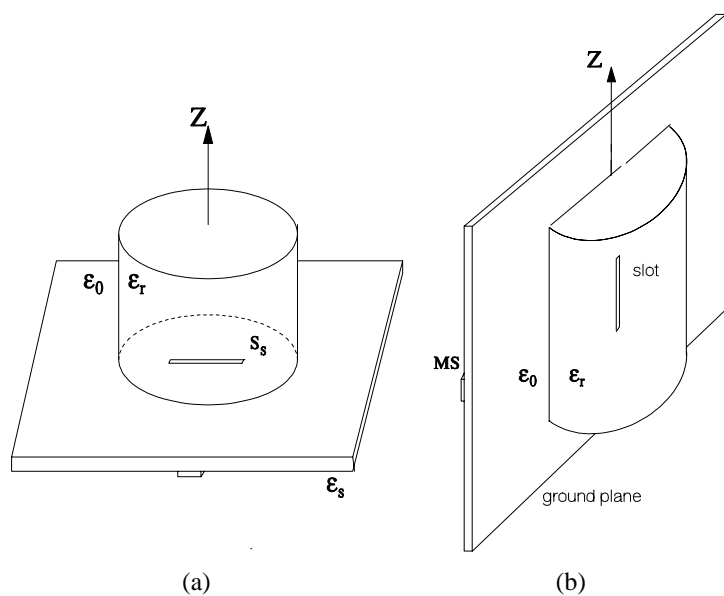
Fig. 4.4 Geometry of slot-microstrip excitation of the dielectric resonator disc
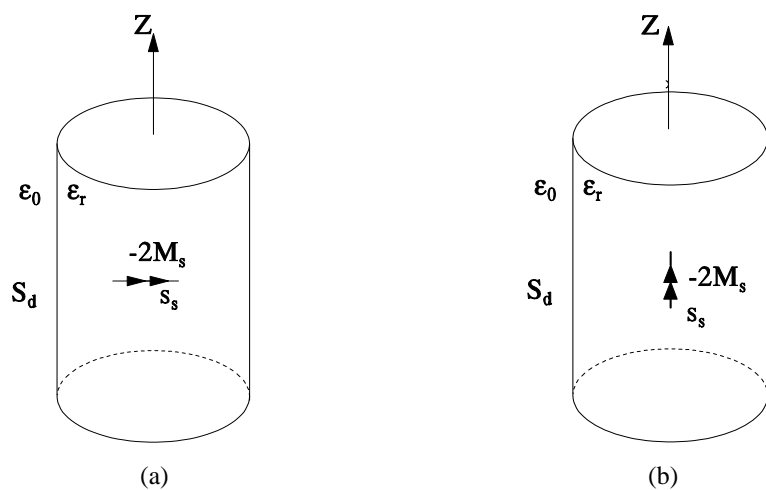
Fig. 4.5 The equivalent problem of the dielectric resonator side after image

Now, the integral equations that formulate the problem consists of equation (4.26) and (4.1) and (4.2) after replacing the electric currents on the wire with the negative of double the equivalent magnetic current of the slot. This formulation is referred to as H-PMCHW [14]. The operator $\mathbf{H}^L$ is the magnetic field due to the equivalent magnetic current in the dielectric substrate environment. The operator $\mathbf{H}^L$ is left in the right hand side intentionally for a reason that will be presented later. $\mathbf{H}^{inc}$ represents the impressed magnetic field due to the sources in the lower part of the ground plane. The H-PMCHW integral equations are reduced to a matrix form by using the method of moments. Since the slot is assumed to be narrow, we assume that there is no variation of the magnetic current across the slot width and the magnetic current is only varying along the slot. The equivalent magnetic currents on the slots are expanded in the form

$$\mathbf{M}_s = \sum_k \frac{M_k}{w_s}\ T_k^s(s')\ \hat{u}_s \qquad\qquad \text{on } S_s \qquad\qquad (4.28)$$

T_k^s is the triangle basis function used on the slot [19] and $\hat{u}_s$ is the unit vector along the slot. The vector [M_s] (unknown current coefficients on the slot) replaces the vector [J_w] in (4.14) and the vector [I_s] replaces the vector [V_w]. The sub-matrix [SS] replaces the sub-matrix [WW], where the sub-matrix [SS] is due to slot-to-slot interaction of the upper part problem. The characteristics of the method of moment matrix due to the left hand side of the integral equations are exactly the same as those described for the wire case.

4.2.4   The Slot-Coupled Microstrip Line Feed

The lower half space, "L", is described in the rectangular coordinate system (α, ν, ξ) and consists of a thin dielectric substrate and an infinitesimally thin conducting transmission line at $\xi = -d$. The microstrip line, as illustrated in Fig. 4.6, is assumed to be both α-directed and infinitely long, and propagating a quasi-transverse electromagnetic (TEM) mode. The ν-directed surface equivalent magnetic current $\mathbf{M}_s$, as illustrated in Fig. 4.6, replaces the narrow slot aperture. The transmission line is analyzed using the same method as that documented in [13,19]. This method is a combination of reciprocity and moment method analyses, using the exact Green's functions for the planar structure. This method treats the slot aperture as a transmission line discontinuity. It is an efficient method for computing the input impedance of a thin slot aperture in the conducting ground plane of a planar structure whose substrate thickness is such that only the TM_0 mode surface wave propagates. Only the application of the transmission line model to this problem shall be discussed since the details can be found in [19].
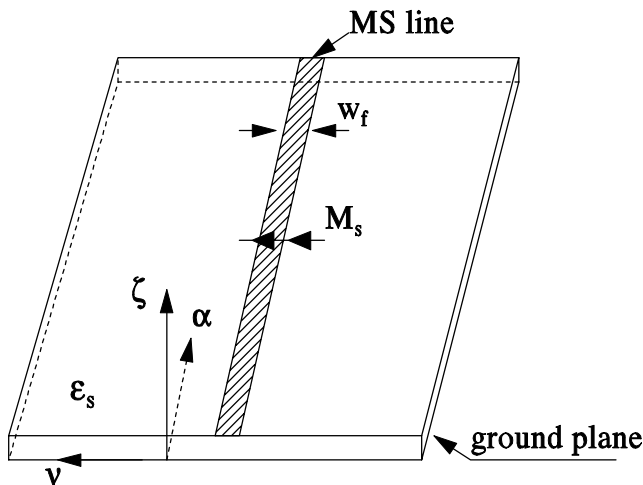
Fig. 4.6 The lower problem of the microstrip line with the equivalent magnetic current of the slot

Similar to equation (4.24) we can obtain a system of equations in the form

$$[[SB]_{-m} [BB]_{-m}^{-1} [BS]_{-m} + \bullet \bullet \bullet + [SB]_0 [BB]_0^{-1} [BS]_0 + \bullet \bullet \bullet$$
$$+ [SB]_m [BB]_m^{-1} [BS]_m - [SS]][M_s] = [[Y^{\mu s}] + \frac{1}{2}[\Delta V][\Delta V]^T][M_s] + [I_s] \qquad (4.29)$$

where T denotes transpose of the vector or matrix. Equation (4.29) can be further simplified in the form

$$[[Y^{BS}] + [Y^{\mu s}] + \frac{1}{2}[\Delta V][\Delta V]^T][M_s] = [I_s] \qquad (4.30)$$

where $[Y^{BS}]$ is given by

$$[Y^{BS}] = [[SB]_{-m} [BB]_{-m}^{-1} [BS]_{-m} + \bullet \bullet \bullet + [SB]_0 [BB]_0^{-1} [BS]_0$$
$$+ \bullet \bullet \bullet + [SB]_m [BB]_m^{-1} [BS]_m - [SS]] \qquad (4.31)$$

The slot current is easily obtained by inverting the bracketed matrix and multiplying the result by vector $[I_s]$ as:

$$[M_s] = [[Y^{BS}] + [Y^{\mu s}] + \frac{1}{2}[\Delta V][\Delta V]^T]^{-1}[\Delta V] \qquad (4.32)$$

The elements of $[Y^{\mu s}]$, admittance matrix, are defined in terms of the Green's function of a magnetic dipole impressed on a ground plane coated with a dielectric substrate in the spectral domain as [19]

$$Y_{\ell n}^{\mu s} = \frac{1}{4\pi^2} \int\int_{-\infty}^{\infty} F_u^2(k_\alpha) \, \tilde{G}_{vv}^{HM}(k_\alpha, k_v) F_p^2(k_v) \cos(v_\ell - v_n) dk_\alpha dk_v \quad . \qquad (4.33)$$

where $F_{u,p}$ are one dimensional Fourier transforms of the α and v variations, respectively, of the basis and testing functions and $\tilde{G}$ is the appropriate Green's function for the layered medium. The voltage discontinuity vector $[\Delta V]$, as defined in [19], may be written in spectral form as

$$\Delta V_\ell = \frac{1}{2\pi\sqrt{Z_c}} \int\int_{-\infty}^{\infty} F_u(k_v) \tilde{G}_{v\alpha}^{HJ}(k_\alpha = \beta_f, k_v) F_p(k_v) \cos(k_v(v_\ell - v_s)) \, dk_v \qquad (4.34)$$

where β_f is the effective propagation constant of the line and v_s is a displacement of the microstrip line from the slot center. The effective propagation constant is computed by considering an infinite, α-directed microstrip line of width w_f supporting a traveling wave current of the form $\exp(-j\beta_f v)$. Using the results listed in [19], the expression for the α-component of the electric field is then evaluated as [19] .

$$E_{\alpha\alpha} = -2\pi \int\int_{-\infty}^{\infty} \delta(k_\alpha + \beta_f) F_v(k_v) \tilde{G}_{\alpha\alpha}^{EJ}(k_\alpha, k_v) e^{jk_\alpha \alpha} e^{jk_v v} dk_\alpha dk_v \qquad (4.35)$$

where F_v is the Fourier transform of the v-variation of the α-directed electric current distribution (assumed to be uniform since the strip is very thin), and is given by $F_v(k_v) = 2\sin(k_v w_f/2)/k_v$. Enforcement of the electric field boundary condition at the surface of the conducting transmission line (after performing the k_α

integration) yields the following equation for β_f, which can be solved quickly by using Muller's method [20]

$$\int_{-\infty}^{\infty} \tilde{G}_{\alpha\alpha}^{EJ}(\beta_f, k_v) F_v^2(k_v) dk_v = 0 \qquad (4.36)$$

The voltage reflection coefficient, R, may be computed from the magnetic current (voltage) and the voltage discontinuity vector as

$$R = 0.50 \, [M_s]^T \, [\Delta V] \qquad (4.37)$$

The slot impedance may be computed from the expression.

$$Z_s = Z_c \frac{2R}{1-R}. \qquad (4.38)$$

where Z_c is the characteristic impedance of the transmission line. In many applications, the transmission line is an open circuit terminated by a stub of length L_t (from the slot center). To compute the impedance of the slot under this condition, one simply computes the input impedance under the infinite line assumption and adds to this result a series reactance, $X = -jZ_c \cot(\beta_f L_t)$. Then, the total impedance is $Z_s + X$.

4.3   RESONANT FREQUENCY AND RADIATION Q-FACTOR

To determine the resonant frequency and radiation Q-factor of the dielectric resonator for a particular azimuthal mode, the actual excitation is removed. Therefore, all the wires are removed and we end up with the matrix related to the body of revolution from which we can see that the azimuthal modes are decoupled and we can treat each azimuthal mode separately. Now, each (jω) is replaced by S in the matrix equation to transfer from the real frequency to the complex frequency plane [10], where ω is the real angular frequency. The natural frequencies are the frequencies for which the system can have a response with no excitation. Therefore, the system poles occur at values of S where the determinant of $[BB]_m$ vanishes as

$$\det [BB]_m = 0 \qquad (4.39)$$

the roots of (4.29) in the complex frequency plane are designated by

$$S_{m,\upsilon} = \sigma_{m,\upsilon} + j\omega_{m,\upsilon} \tag{4.40}$$

where $\omega_{m,\upsilon}$ is the resonant frequency of the mode (m,υ) and $\sigma_{m,\upsilon}$ is the decay time constant of the mode (a negative number). The subscript υ is an integer used to denote unique complex frequency values for which (4.39) is satisfied. For each value of "m" in (4.40), there will be solutions for $\upsilon = 1,2,3, \ldots$ Each of these solutions corresponds to a different resonant mode, in agreement with the proposed two-subscript notation mentioned in the introduction. Alternatively, once the electromagnetic field distribution is determined for a particular solution, it is sometimes possible to replace υ by other two subscripts (m,p), which denote the radial and axial behaviors of the field [21]. The dielectric materials are lossless. Therefore, the quantity $\sigma_{m,\upsilon}$ in (4.40) is inversely proportional to the radiation Q factor of a particular mode, as follows:

$$Q_{m,\upsilon} = -\frac{\omega_{m,\upsilon}}{2\sigma_{m,\upsilon}} \tag{4.41}$$

The roots of (4.39) are found by searching in the complex frequency plane using Muller's method [20]. The resonant frequency and the radiation Q-factor are computed through the roots search, as described above and plotted in Fig. 4.7 and Fig. 4.8, respectively, for the azimuthal modes, TM_{01}, TE_{01}, HEM_{11}, and HEM_{12} with $\varepsilon_r = 38$.

Empirical expressions are obtained for the resonant frequency and the radiation Q-factor for the four modes [21]. For the TM_{01} mode, the expressions are given as

$$k_0a = 0.8945(1 + 3.017x^{0.881} + e^{0.962-1.6252x})/\varepsilon_r^{0.45} \tag{4.42}$$

$$Q = 10.9x(1 + 217.96x^{3.4796}e^{-3.67x}) \tag{4.43}$$

where $x = a/2h$. The resonant frequency can be obtained from $f(GHz) = 30k_0a/(2\pi a(cm))$. For the TE_{01} mode, the expressions are given as

$$k_0a = (2.1439 + 0.6604x + 0.2733x^2 - 0.1919x^3)/\varepsilon_r^{0.475} \tag{4.44}$$

$$Q = 5.72x(1 + 18.387x^{-0.3795}e^{-1.64x}) \tag{4.45}$$

For the HEM_{11} mode, the expressions are given a

$$k_0a = \{1.6 + 0.513x + 1.392x^2 - 0.575x^3 + 0.088x^4\}/\varepsilon_r^{0.42} \qquad (4.46)$$

$$Q = x\varepsilon_r^{1.2}\{0.01893 + 2.925e^{-2.08x(1-0.08x)}\} \qquad (4.47)$$

For the HEM_{12} mode, the expressions are given as

$$k_0a = \{3.72 + 0.4464x + 0.2232x^2 + 0.0521x^3 - 2.65e^{-1.25x(1+4.7x)}\}/\sqrt{\varepsilon_r} \qquad (4.48)$$

$$Q = \varepsilon_r^2\{0.068 - 0.0388x + 0.0064x^2 + 0.0007e^{x(37.59-63.8x)}\} \qquad (4.49)$$

In equations (4.48) and (4.49), the resonant frequency can be obtained accurately for wide range of materials, but the accuracy of the Q-factor deteriorates as the dielectric constant decreases.
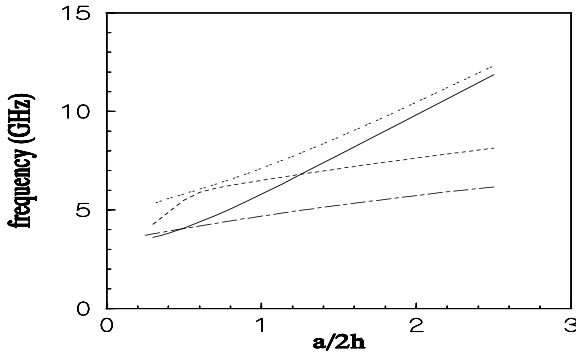
Fig. 4.7 The resonant frequency of a dielectric disc with radius a, and height 2h and dielectric constant ε_r= 38. (**- - - -** TM_{01}, -- - -- TE_{01}, ___ HEM_{11}, - - - HEM_{12})

4.4 NEAR FIELDS

Once the resonant frequency is determined for a particular azimuthal mode of a source-free system, the equivalent surface currents can be computed in the complex frequency plane and consequently both the near field and far field can be computed for this particular mode. The near field distribution can help us to determine the proper method to couple to a particular mode.
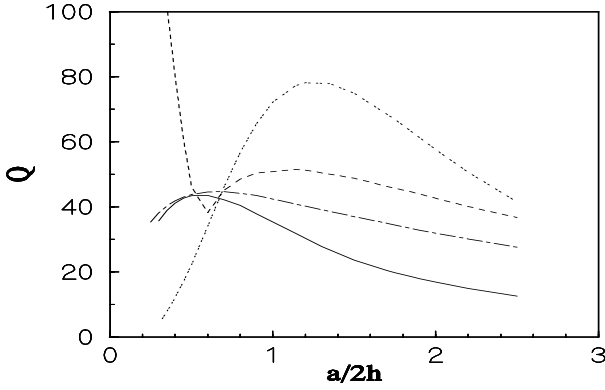
Fig. 4.8 The radiation Q-factor of a dielectric disc with radius a, and height 2h and dielectric constant $\varepsilon_r = 38$. (**- · - ·** TM_{01}, -- - -- TE_{01}, ____ HEM_{11}, - - - HEM_{12})

Usually, an electric current probe can be used to couple to the electric field lines when it is oriented along the electric field line or a narrow slot along the magnetic field lines. Figs. 4.9 to 4.12 show sketches of the electric and magnetic field lines in two perpendicular planes, respectively, for the TM_{01}, HEM_{11}, TE_{01} and HEM_{12} modes. Notice that these sketches are for the cases without ground plane. For more details about the near field distribution, the reader may find more information in [1].
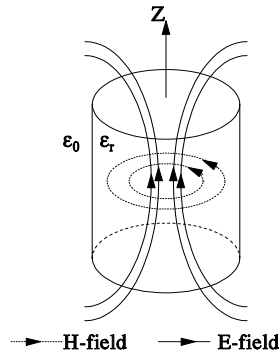
Fig. 4.9 Sketch for the field distributions of the $TM_{01\delta}$ mode
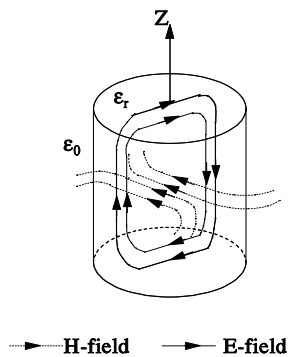
H-field   E-field

Fig. 4.10 Sketch for the field distributions of the HEM_{11} mode
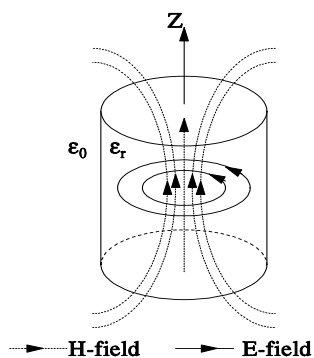
H-field   E-field

Fig. 4.11 Sketch for the field distributions of the TE_{01} mode

H-field   E-field
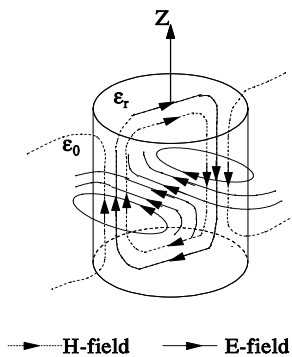
Fig. 4.12 Sketch for the field distributions of the HE_{12} mode

4.5.1   FAR FIELDS

4.5.1   Ideal Far Field Patterns

It can be seen from the sketches of the field distributions of the modes that the TM_{01} and HEM_{11} modes can be supported if a perfectly conducting plane divides the DR from the middle of its height, as shown in Fig. 4.13, the field distribution will not be disturbed and the resonant frequency will be of the same value as the full size disc. The radiation patterns for these modes are shown in Fig. 4.14 and Fig. 4.15 for the TM_{01} and HEM_{11} modes, respectively. The radiation pattern of the TM_{01} mode looks like a quarter wavelength monopole above ground plane. The radiation pattern of the HEM_{11} looks like the radiation pattern of a half wavelength narrow slot on a ground plane or a half wavelength electric dipole parallel to the ground plane along the electric field lines and of a quarter wavelength above the ground plane.
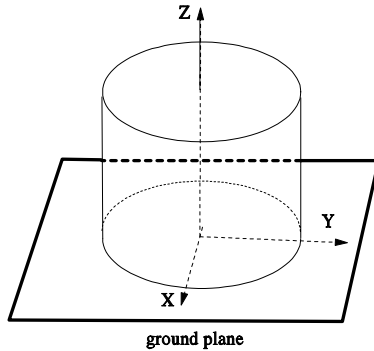
Fig. 4.13 Geometry of a dielectric disk above a ground plane
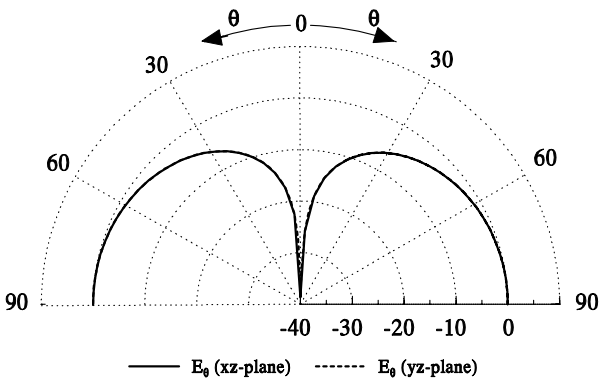
Fig. 4.14 Ideal far field radiation patterns for the TM_{01} mode above an infinite ground plane
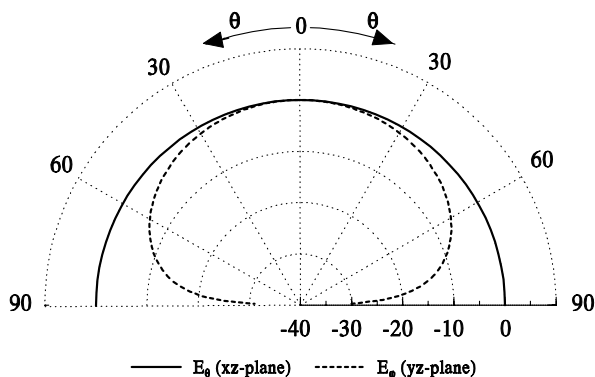
Fig. 4.15 Ideal far field radiation pattern of the HEM$_{11}$ mode above an infinite ground plane

The TE$_{01}$ and HEM$_{12}$ modes can be supported if the dielectric resonator resides on a magnetic conductor ground plane, but since this is not physically possible, we found that if the electric conductor ground plane splits the dielectric disc through its axis, as shown in Fig. 4.16, the field distribution will not be disturbed and the radiation patterns are as shown in Figs. 4.17 and 4.18, respectively. The radiation pattern of the TE$_{01}$ mode looks like the radiation pattern of half wavelength narrow slot on a ground plane and directed along the dielectric resonator axis or a half wavelength electric dipole parallel to the ground plane and of a quarter wavelength above the ground plane and directed normal to the dielectric resonator axis. The radiation pattern of the HEM$_{12}$ mode looks like the radiation pattern of a quarter wavelength monopole above a ground plane. These patterns will be considered the ideal radiation patterns that can be used as a measure of the purity of the radiation patterns obtained by actual excitation of the dielectric resonators.

4.5.2 Far Field Radiation Patterns due to Dipole Excitation

In principle, the excitation source can excite many modes. The field strength for each mode depends on the source location and orientation as well as on the operating frequency. Choosing the proper location and orientation of the excitation source stimulates specific azimuthal modes. Therefore, the system of equations (4.14) can be solved to obtain the induced electric and magnetic current distributions on all the surfaces, for each mode. The far field components E$_\theta$ and E$_\varphi$ can be determined from the current distribution on the outer surfaces of the antenna due to all azimuthal modes as in [7]. Here, an infinitesimal dipole is used as a driving source. The electric dipole is placed at the position where the practical coaxial probe is located in the actual experiment.
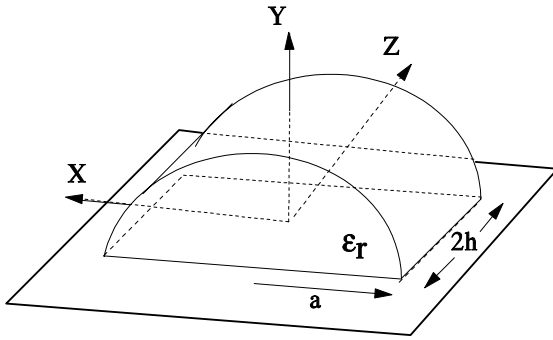
Fig. 4.16 Geometry of a split disc above a ground plane

E_φ (xy-plane) E_φ (yz-plane)
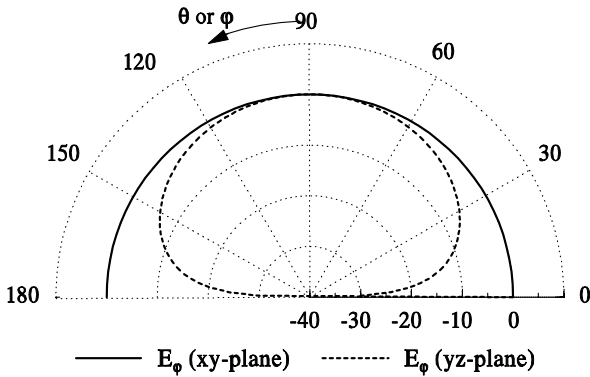
Fig. 4.17 Ideal far field radiation patterns for the TE_{01} mode of a split disc above an infinite ground plane

To compute the radiation patterns due to the infinitesimal electric dipole excitation, we solve the moment matrix $[BB]_m$ for the equivalent surface currents on the body of revolutions mode by mode, and accumulate the response due to all possible azimuthal modes. It is believed that the radiation patterns computed by this excitation model will not be different from those radiation patterns that can be computed by using a more rigorous current source, or another excitation mechanism (as long as same modes with the same strength are excited).
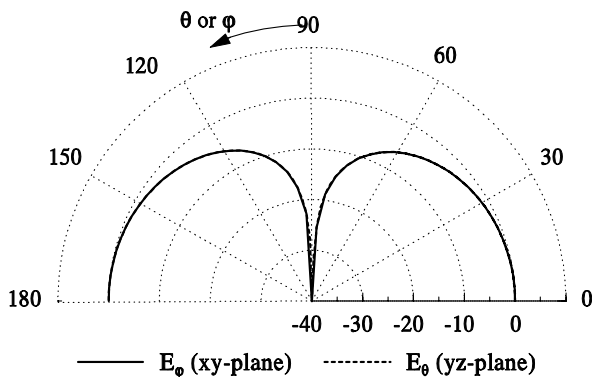
Fig. 4.18 Ideal far field radiation patterns for the HEM$_{12}$ mode of a split disc above an infinite ground plane

The model used here is adequate for the computation of far fields, but it cannot be used to solve for input impedances. To show the proper position of the excitation and the contributions of the excited modes on the total far field radiation patterns, Fig. 4.19 illustrates the normalised field strength of different modes as a function of the probe radial position for a dielectric resonator disc with a=1.283cm, h=1.283cm and ε_r = 12 at f=2.15GHz with a z-directed probe.
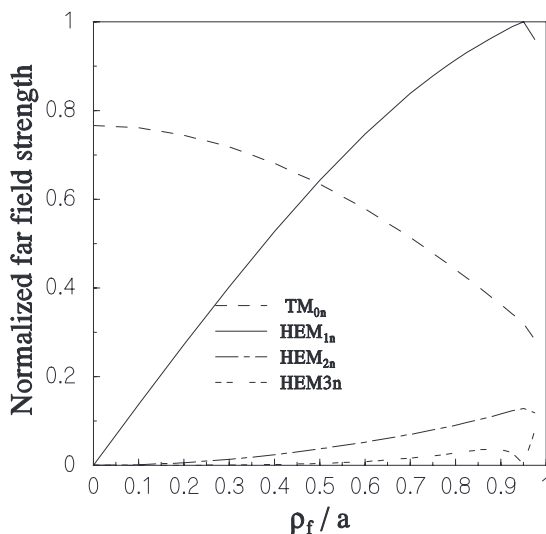
Fig. 4.19 The normalised field strength for the first four modes due to a z-directed infinitesimal probe as a function of the probe radial position

The frequency of operation is for the HEM_{11} mode. It can be seen that if the probe is close to the dielectric disc center, this mode is not excited efficiently and the TM_{01} mode is the dominating mode, although we are not operating at its resonant frequency. The HEM_{11} mode strengthens as the probe gets closer to the dielectric disc radius and at the same time the TM_{01} mode becomes weaker, but very slowly. The other higher order mode has no significant contributions. Now, the total radiation patterns due to all these modes are shown in Figs. 4.20 to 4.22 for three different feed positions. When the feed is located at the center of the disc, only the TM_{01} mode is excited and the other modes are suppressed, as shown in Fig. 4.19. Because, the body of revolution solution can only have a control on the azimuthal mode suffix m, we refer to the modes in the figure with only two indices, where the second index is not clearly determined. When the probe is located at a position where the TM_{01} and HEM_{11} modes are excited by almost the same strength, we can see that the contribution of the TM_{01} mode (E_θ, yz-plane) is mainly shown in the form of a high cross-polarisation level and the symmetry of the E-plane patterns (E_θ, xz-plane) is not perfect, as shown in Fig. 4.20. When the probe is moved close to the DR surface, the TM_{01} mode effect is reduced in the cross-polarisation level and results in an improving of the radiation pattern symmetry around the antenna axis.
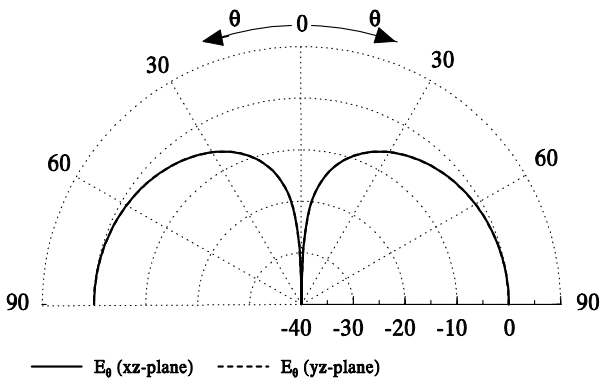
Fig. 4.20 The far field radiation patterns of the DRA excited by an infinitesimal probe oriented in the z-direction and located at the disc center

4.5.3 Far Field Radiation Patterns due to Narrow Slot Excitation

Another possible excitation of the DRA is the slot excitation. A narrow slot excitation is modeled by an equivalent magnetic current on the ground plane oriented in the direction of the slot. Here, and infinitesimal magnetic current is used and oriented in the y-direction. The far field strengths due to the first four azimuthal modes are computed and plotted versus the radial position of the slot center, as shown in Fig. 4.23. It can be seen that the HEM_{11} mode is the only excited mode when the slot is located at the DRA center and the other modes are not excited. As the slot radial position moves away from the center, the other modes start to be excited. The TM_{01} mode is rapidly growing as ρ_f/a increases and the HEM_{11} mode is decreasing. The total far field radiation patterns are also computed due to the contributions of all modes for three magnetic dipole radial positions.

When the dipole is at the center, the radiation pattern is shown in Fig. 4.24. One can notice that the symmetry of the radiation patterns is perfect and compare very well with the radiation pattern of the HEM_{11} mode in Fig. 4.15. Also, one can notice that there is no cross-polarisation. As ρ_f/a increases, the radiation patterns symmetry is destroyed because of the strong influence of the TM_{01} mode, as shown in Figs. 4.25 and 4.26. These results strongly recommend the use of the narrow slot excitation for the HEM_{11} mode that provides a broadside radiation pattern. The reader should be aware that the slot excitation also causes radiation in the back of the ground plane, but by a small amount if the slot is smaller than its resonance length.

Fig. 4.21 The far field radiation patterns of the DRA excited by an infinitesimal probe oriented in the z-direction and located at $\rho_f/a=0.5$
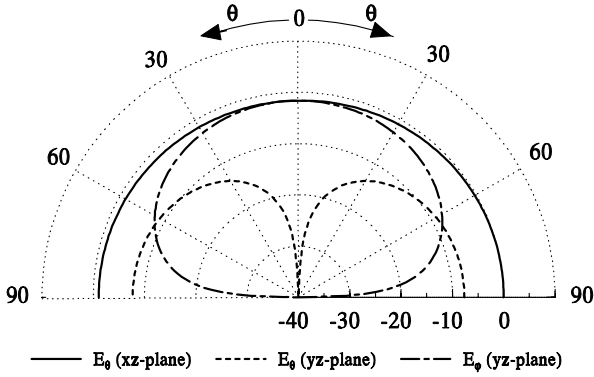
Fig. 4.22 The far field radiation pattern of the DRA excited by an infinitesimal probe oriented in the z-direction and located at $\rho_f/a=0.95$
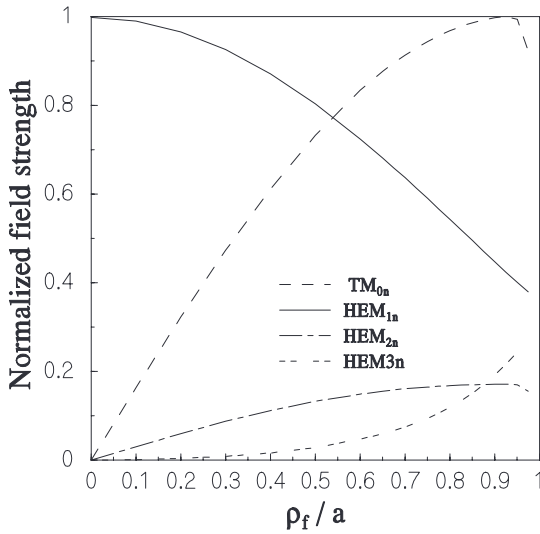
Fig. 4.23 The normalised field strength for the first four modes due to a y-directed infinitesimal magnetic dipole as a function of the probe radial position
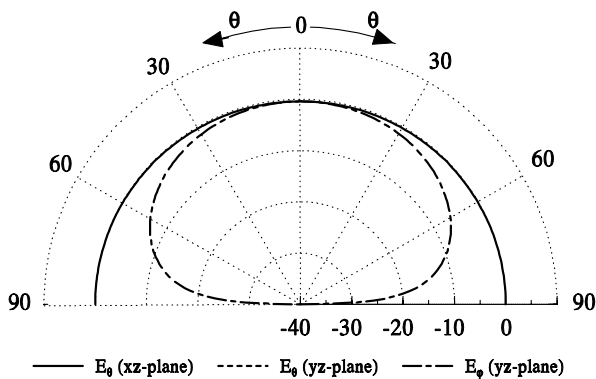
Fig. 4.24 The far field radiation pattern of the DRA excited by an infinitesimal magnetic dipole oriented in the y-direction and located at $\rho_f/a=0.0$

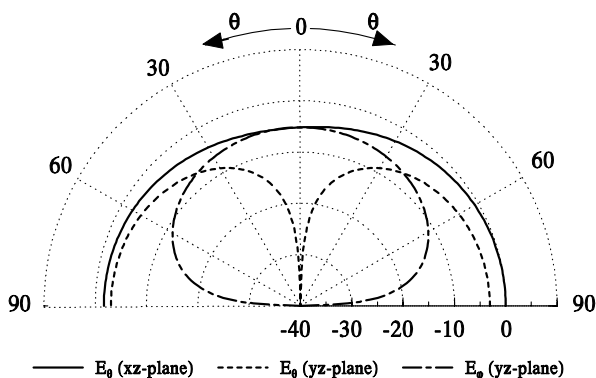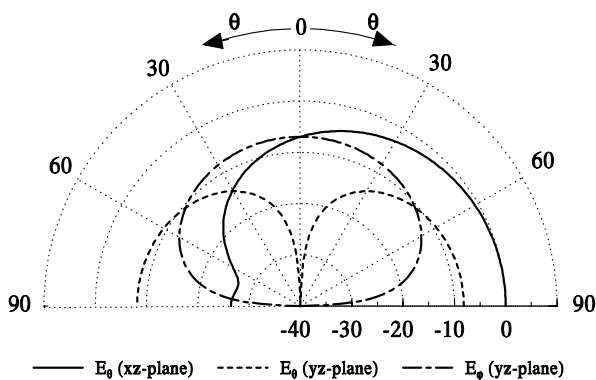**Fig. 4.25** The far field radiation pattern of the DRA excited by an infinitesimal magnetic dipole oriented in the y-direction and located at $\rho_f/a=0.5$
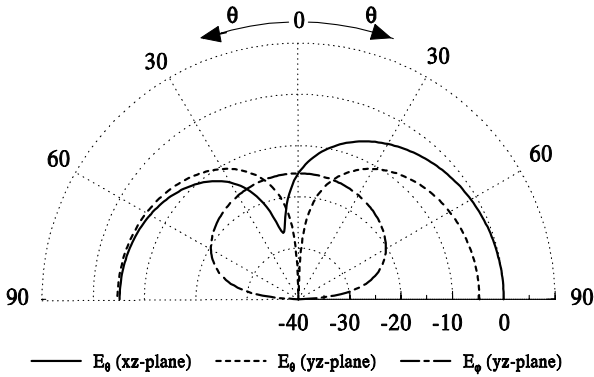
Fig. 4.26 The far field radiation pattern of the DRA excited by an infinitesimal magnetic dipole oriented in the y-direction and located at $\rho_f /a=0.95$

4.5.4   Verifications of the Radiation Patterns

To verify the far field radiation patterns we must use a finite size ground plane, as shown in Fig. 4.27. The far field radiation patterns of a DRA with a=0.1706λ, a/h=1.67, ρ_f/a=0.95 ε_r=8.9, and a circular ground plane of radius 1.297λ are computed, as shown in Fig. 4.28, and compared with the measured results in [2]. Excellent agreement between computed and measured results is obtained.

Remember that the computed radiation patterns are obtained when the infinitesimal probe normal to the ground plane is used in the position of the actual wire, as explained before. This is a broadside radiation patterns due to the excitation of the HEM$_{11}$ mode. The effect of the finite size ground plane is clear from the presence of back radiation. Because the ground plane size is relatively small, high back radiation level exists. To reduce the back radiation, a larger ground plane of radius 4λ is used and the far field radiation patterns are computed, as shown in Fig. 4.29. Three observations can be pointed out here. First, the back radiation level has not been reduced significantly as opposed to what was expected. Second, the radiation on the forward direction shows an increase in the field oscillations. Both effects are due to the high diffraction effect from the ground plane edges. Third, the H-plane pattern becomes broader than when the ground plane size is smaller and approaches the E-plane level. This might trigger the possibility of achieving far field radiation patterns with axial symmetry.
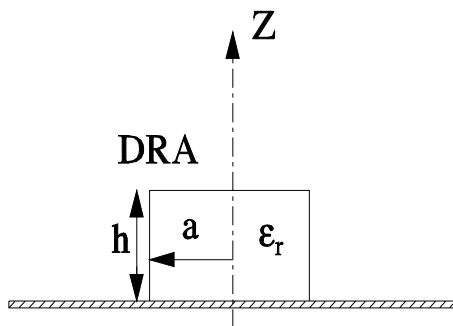
Fig. 4.27 Cross section of the DRA above finite size ground plane

4.5.5 DRA Feed for Parabolic Reflector

We know that some applications require the symmetry of the radiation patterns, such as the antenna feeds for the parabolic reflector antenna. Therefore, the dielectric resonator is placed inside an open circular cavity, as shown in Fig. 4. 30. This configuration can be looked at as the dielectric resonator acting as a feeding probe for the waveguide to excite the dominant TE_{11} mode of the circular waveguide. Because the DRA is exciting the HEM_{11} mode, which has a cross sectional field distribution at its top similar to the cross-sectional field distribution of the TE_{11} mode of the circular waveguide, the waveguide high order modes are rapidly decaying allowing a shorter waveguide. Fig. 3.31 shows the computed far field radiation patterns of the antenna in Fig. 4.30 with a=0.1706λ, a/h=1.67, ρ_f/a=0.95, ε_r=8.9, inner waveguide radius of 0.45λ, inner waveguide length of 0.45λ and conducting wall thickness of 0.05λ.

The cross-polarisation is computed based on the Ludwige's third definition [22]. Comparing the radiation patterns in Fig. 4.28 with those in Fig. 4.31, we can see that the radiation pattern is much smother, has a lower back radiation level and has also a better symmetry between E-plane and H-plane patterns. The performance of this antenna is improved by adding a quarter wavelength choke around the circular waveguide opening, as shown in Fig. 4.32. The radiation patterns are computed and given in Fig. 4.33. Adding the choke further improves the symmetry of the radiation patterns, expands the back radiation level and reduces the cross-polarisation level. This antenna has excellent characteristics as a feed for the reflector antenna. This antenna can also be used as an array element for a feed cluster with small distance between the waveguides because the feeding is coming from the waveguide back and will not requires any more space between the elements of the array.
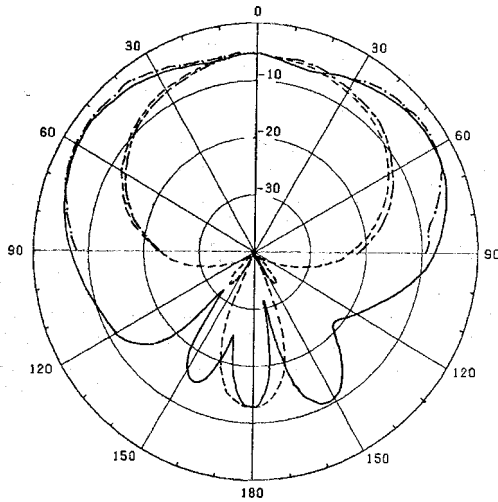
Fig. 4.28 Computed and measured far field radiation patterns of a dielectric resonator with a=0.1706λ, a/h=1.67, ρ_f/a=0.95, ε_r=8.9, and a circular ground plane of radius 1.297λ. (solid line) computed E-plane, (short dashes) computed H-plane, (dash dot) measured E-plane), and (long dashes) measured H-plane. (from [7] © 1989 IEEE Antenna and Propagation Magazine)
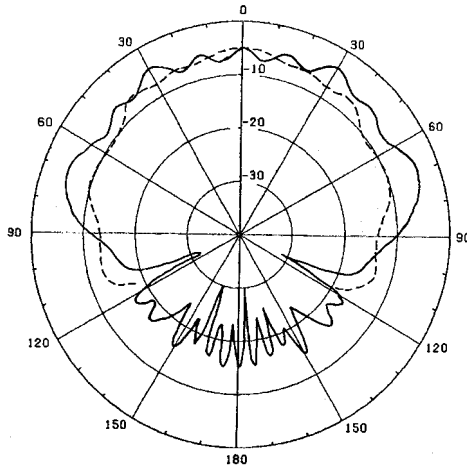
Fig. 4.29 Computed far field radiation patterns of a dielectric resonator with a=0.1706λ, a/h=1.67, ρ_f/a=0.95, ε_r=8.9, and a circular ground plane of radius 4λ (solid line) E-plane, (dashes) H-plane. (from [7] © 1989 IEEE Antenna and Propagation Magazine)
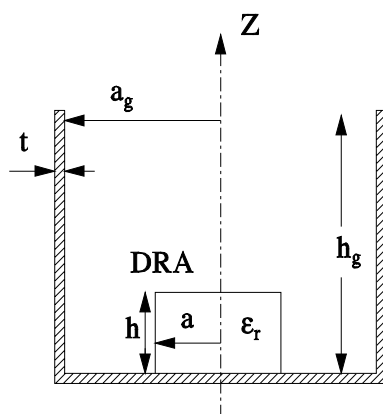
Fig. 4.30 Cross section of the DRA inside a circular waveguide
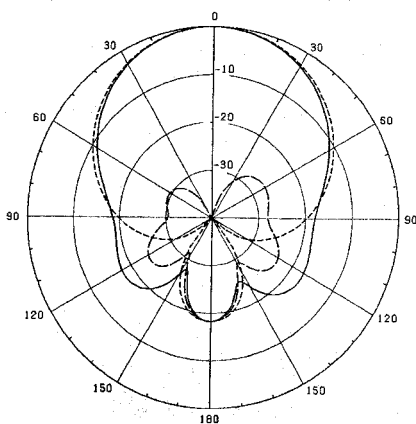
Fig. 4.31 Computed far field radiation patterns of a dielectric resonator with a=0.1706λ, a/h=1.67, ρ_F/a=0.95, ε_r=8.9, and a circular waveguide with radius 0.45λ, and length of 0.45λ. (solid line) E-plane, (dashes) H-plane, and (long dashes) Cross-polarisation. (from [7] © 1989 IEEE Antenna and Propagation Magazine)
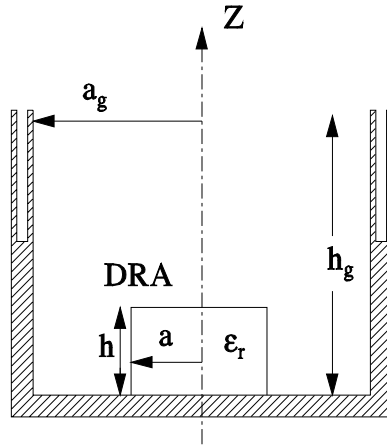
Fig. 4.32 Cross section of the DRA inside a circular waveguide surrounded by a quarter wavelength choke
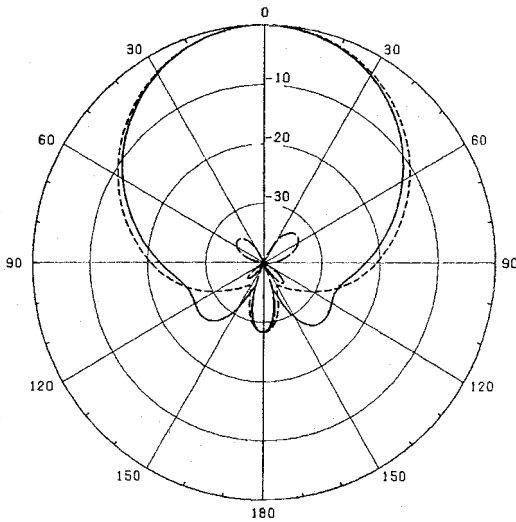
Fig. 4.33 Computed far field radiation patterns of a dielectric resonator with a=0.1706λ, a/h=1.67, ρ_F/a=0.95, ε_r=8.9, and a circular waveguide with radius 0.45λ, and length of 0.45λ. (solid line) E-plane, (dashes) H-plane, and (long dashes) Cross-polarisation. (from [7] © 1989 IEEE Antenna and Propagation Magazine)

4.5.6   INPUT IMPEDANCE

4.6.1   Wire Probe Excitation

To verify the numerical solution a dielectric resonator disc of radius 2.75cm and height 2.6cm with a dielectric constant of $\varepsilon_r = 12$ is made of dielectric powder surrounded by a PVC container of low dielectric constant, which has a negligible effect because its dielectric constant is much smaller than the high dielectric constant of the powder. It was found that this is an ideal model to be used for verifications of the numerical method because it eliminates any possibility of air gap between the dielectric disc and the ground plane or around the probe excitation [23-24]. Fig. 4.34 shows the input impedance of the above disc excited by a coaxial probe with length l_w=2.0cm, radial position ρ_f=1.4cm and wire radius, a_w=0.381mm. This radial probe position is set up to excite the HEM_{11} mode, which has a resonant frequency f=1.377GHz. Excellent agreement between computed and measured input impedance is achieved. However, the source free resonant frequency is found to be different from that obtained with the presence of the probe as a source. This is due to the effect of the probe coupling effect and also due to the physical presence of the probe inside the dielectric disc.
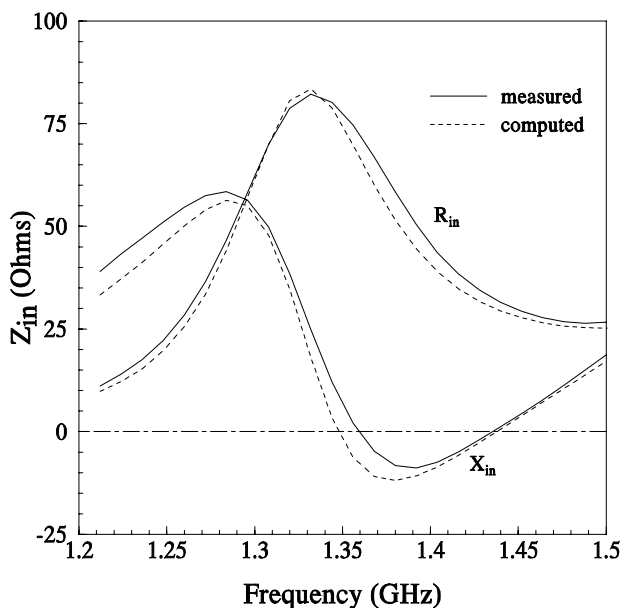
Fig. 4.34   Impedance vs. frequency for the dielectric disc resonator with ε_r=12, a=2.75cm, h=2.6cm, ρ_f=1.4cm, and l_w=2.0cm. (from [12] © 1994 IEEE Transactions on Antennas and Propagation)

Here, we concentrate on the excitation of the HEM_{11} mode because it has broadside radiation patterns and we study the effect of different parameters on the input impedance of the dielectric disc. The dielectric disc with radius, a=1.283 cm, h = 2.566 cm, and ε_r=8.9. The resonant frequency is computed to be 2.72GHz. The coaxial probe has radius a_w = 0.0118 cm. Therefore, the parametric study was conducted over the frequency range of 2.0 to 3.2 GHz. In order for the numerical solution to converge, when the HEM_{11} mode is the desired mode, seven azimuthal modes are considered because the other modes are also excited, as explained before. Fig. 4.35 shows the computed input impedance as a function of frequency for various feed positions ρ_f. Fig. 4.36 shows the peak value of input resistance, R_{in}, as a function of feed position and the frequency at which the input resistance occurs.

From the study of Figs. 4.35 and 4.36, the HEM_{11} mode is observed to be dominant for feed positions of $0.4 < \rho_f < 1.2$ cm as evident from the steep resonant curves of R_{in} versus frequency of Fig. 4.35 and the operating frequency indicated in Fig. 4.36. This also indicates that the zero order mode has a strong effect when $\rho_f < 0.4$ cm.
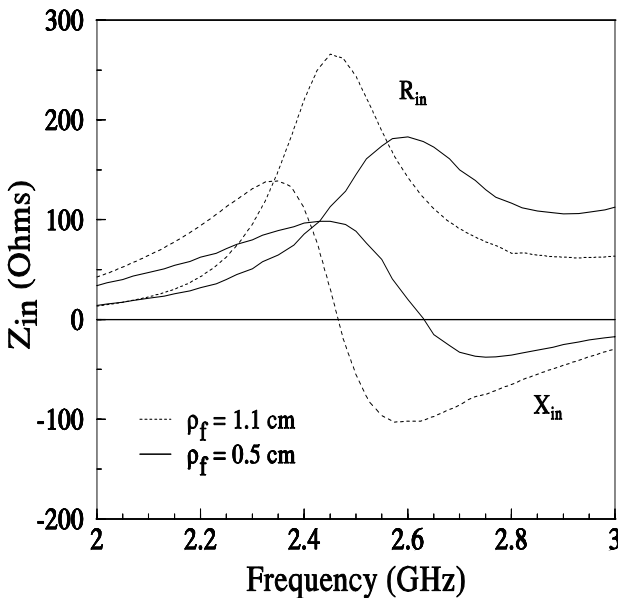
Fig. 4.35 Effect of coaxial probe feed position on the antenna input impedance with ε_r=8.9, h=2.566cm, a=1.283cm, a_w=0.0118cm, and l_w=1.5cm. (from [12] © 1994 IEEE Transactions on Antennas and Propagation)

The effect of the probe length is examined with ε_r=8.9, h=2.566cm, a=1.283cm, a_w=0.0118cm, and ρ_f=0.962cm, and varying the length of the feed l_w. The computed input impedance versus frequency and different probe length is given in Fig. 4.37. Also, the computed and the peak value of R_{in} versus l_w together with the frequency at which this peak value occurs are shown in Fig. 4.38. It can be observed that the probe length has two effects on the input impedance and the resonant frequency.
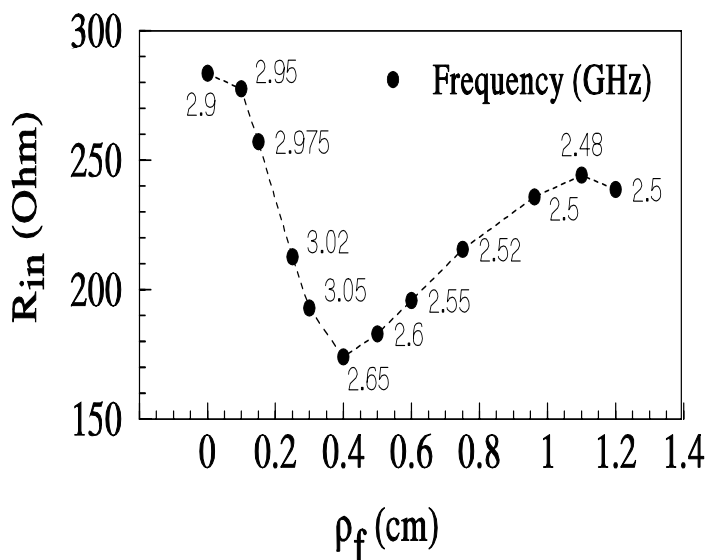
Fig. 4.36   Effect of coaxial feed probe position on the peak value of the antenna input resistance with ε_r=8.9, h=2.566cm, a=1.283cm, a_w=0.0118cm, and l_w=1.5cm. (from [12] © 1994 IEEE Transactions on Antennas and Propagations)

As the probe length increases the input resistance increases and strong tuning for the resonant frequency is clear. In this case, we operate around the resonant frequency of the HEM_{11} mode, which is strongly coupled with 1.25<l_w<1.75 cm. This is clear from the steep slope of R_{in} and X_{in} as a function of frequency and the high peak values of R_{in}. It can also be seen that the resonant frequency, i.e., that frequency at which R_{in} achieves a maximum, is tuned to a lower frequency by increasing the probe length.

When the probe length is short we have a smaller coupling and small tuning to the resonant frequency with $l_w < 1.1$ cm, while the peak value of R_{in} occurs at frequencies from 2.7 to 2.77 GHz. This range of frequencies is close to the resonant frequency of the pure HEM_{11} mode.
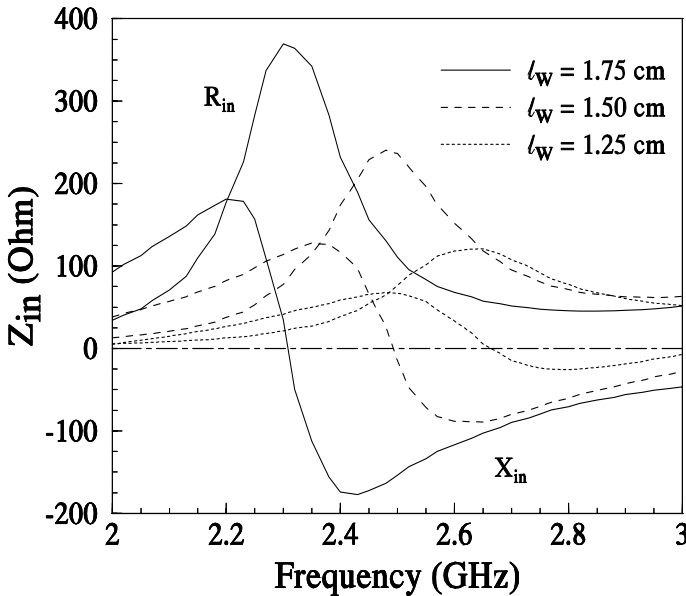
Fig. 4.37 Effect of coaxial probe length on the antenna input impedance with $\varepsilon_r=8.9$, h=2.566cm, a=1.283cm, a_w=0.0118cm, and ρ_f=0.962cm. (from [12] © 1994 IEEE Transactions on Antennas and Propagation)

To study the effect of the dielectric constant on the input impedance and the resonant frequency, a DRA with h=2.566cm, a=1.283cm, a_w=0.0118cm, ρ_f=0.962cm, l_w=1.5cm is considered with different dielectric constant materials varying from 7 to 12. Fig. 4.39 shows the effect of varying the dielectric constant of the DRA on the input impedance. With the chosen antenna parameters, the input impedances of these antennas are computed. It is clear that as the dielectric constant increases, the resonant frequency and the bandwidth decreases. This is clear from the rapid change of the real and imaginary part of the input impedance around the resonant frequency. This behavior is expected since increasing the permittivity for a fixed dimension resonator

results in a higher Q-factor. However, the resonant frequency cannot be scaled linearly with the square root of the dielectric constant as has been clarified earlier in the case of free source resonance.
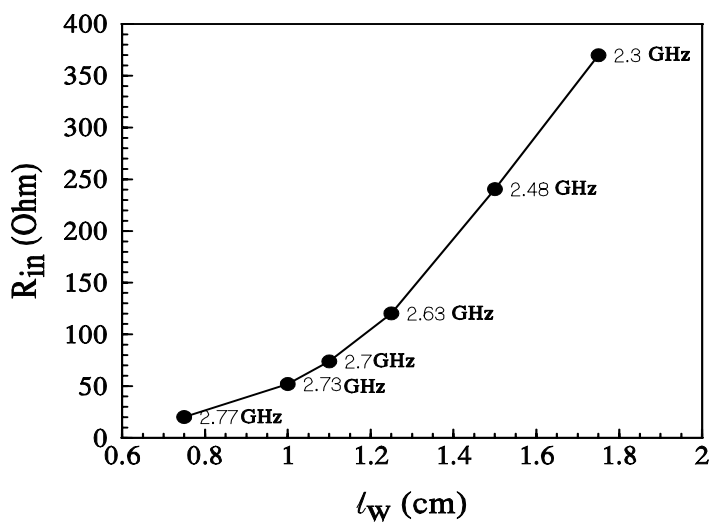
Fig. 4.38 Effect of coaxial feed probe length on the peak value of the antenna input resistance with ε_r=8.9, h=2.566cm, a=1.283cm, a_w=0.0118cm, and ρ_f=0.962cm. (from [12] © 1994 IEEE Transactions on Antennas and Propagation)

The studied parameters are the dimensional ratio between the disc radius and height. Fig. 4.40 shows the effect of the DR a/h ratio on the input impedance with a) a/2h=0.25: h=1.588cm, a=1.283cm, l_w=1.25cm, ρ_f=0.962cm, a_w=0.0118cm ε_r=8.9,; and b) a/2h=0.5: h=1.6cm, a=1.6cm, l_w=1.25cm, ρ_f=1.2cm, a_w=0.0118cm, ε_r=8.9. Notice that in both cases the wire radius and the ratio of the probe position to the disc radius (ρ_f/a=0.75) are the same. It can be seen that as the height increases, the resonance frequency decreases based on the volume effect, but the peak of the input resistance decreases. This is opposite to the conducting wire antenna near the first resonance. These results indicate that the DRA volume parameters can also be used as design parameters to achieve matching for DRA.

4.6.2   Slot Excitation

The second type of excitation that we will discuss here is the narrow slot excitation. The narrow slot excitation has some advantages over the wire probe excitation in that it does not require any penetration of the excitation to the DRA. However, it has direct back radiation from the slot. The present method is verified with the solution of the hemispherical DRA, which is based on the use of the Green's function of the spherical objects [13]. Here, few examples will be presented with the slot parameters shown in Fig. 4.41.   Fig. 4.42 shows the computed input impedances for the DRA excited by a slot/microstrip transmission line with a=2.75 cm, h=2.6cm, ε_r=12, W_s=0.6mm, ε_s=2., d=0.16cm, w_f =0.5cm, and different slot lengths.
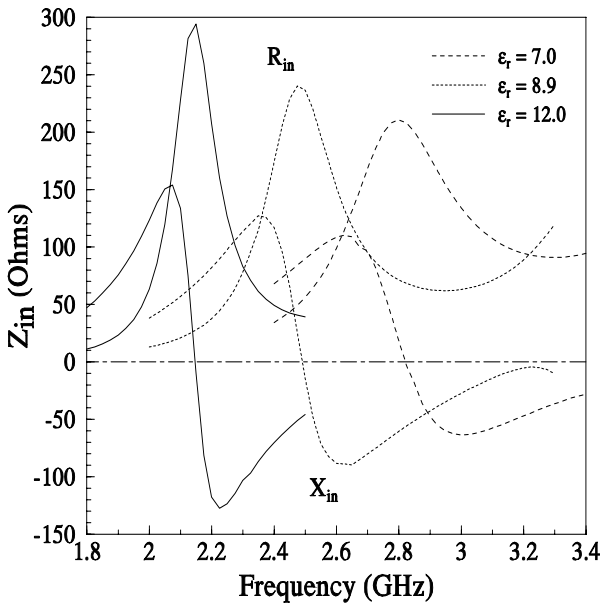
Fig. 4.39 Effect of the dielectric constant on antenna input impedance with h=2.566cm, a=1.283cm, a_w=0.0118cm, ρ_f=0.962cm, l_w=1.5cm. (from [12] © 1994 IEEE Transactions on Antennas and Propagation)

The slot is centered with the DRA axis to excite the HEM_{11} mode. The transmission line is also centered with the slot. It can be observed that as the slot length increases, the resonant frequency decreases and the input resistance increases.

When the microstrip line is displaced from the slot center by a distance y_s, the input impedances are computed for different displacement values as shown in Fig. 4.43 for the same resonator in Fig. 4.41 with L_s=4.0cm. It can be seen that the microstrip line position from the slot center did not affect the resonant frequency of the antenna, but changes the input impedance levels. The input resistance decreases as the microstrip line moves away from the slot center. This indicates that the slot length and the microstrip position can be used as parameters for matching the antenna and tuning the resonant frequency. The other parameter that can be used is the microstrip stub length.
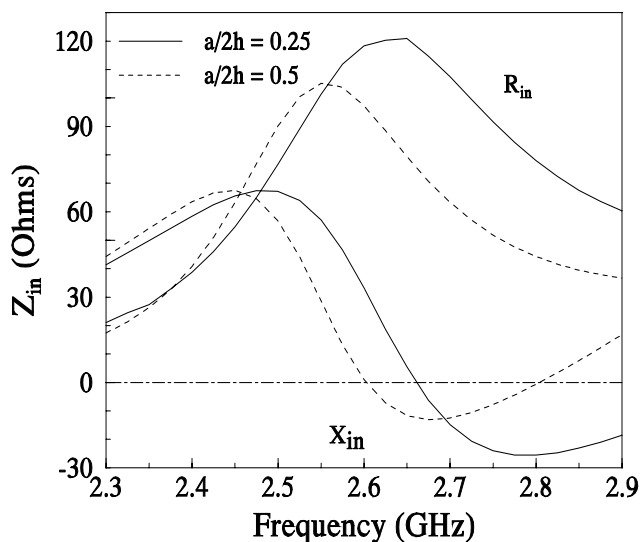
Fig. 4.40 Effect of various a/h ratios on antenna resonant impedance with ε_r=8.9; a) a/2h=0.25: h=1.588cm, a=1.283cm, l_w=1.25cm, ρ_f=0.962cm, a_w=0.0118cm; b) a/2h=0.5: h=1.6cm, a=1.6cm, l_w=1.25cm, ρ_f=1.2cm, a_w=0.0118cm. (from [12] © 1994 IEEE Transactions on Antennas and Propagation)

Adding the stub will change only the imaginary part of the input impedance because we assume lossless transmission line. The parameter will not be presented here. The reader may test this parameter by shifting the imaginary part up or down, based on the corresponding value of the stub reactance.
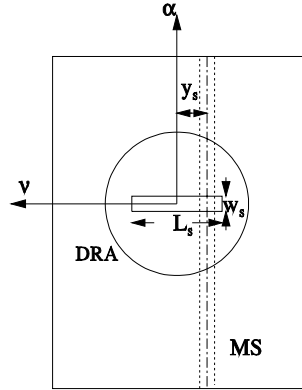
Fig. 4.41 Top view for the DRA with the slot and the microstrip transmission line
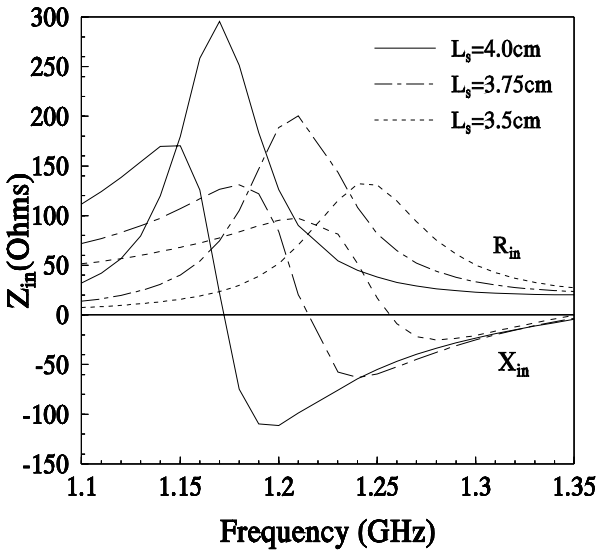
Fig. 4.42 Computed input impedances for the DRA excited by a slot/microstrip transmission line with a=2.75 cm, h=2.6cm, ε_r=12, W_s=0.6mm, ε_s=2, d=0.16cm, w_f =0.5cm, and different slot lengths. (from [13] © 1996 IEEE Transactions on Antennas and Propagation)
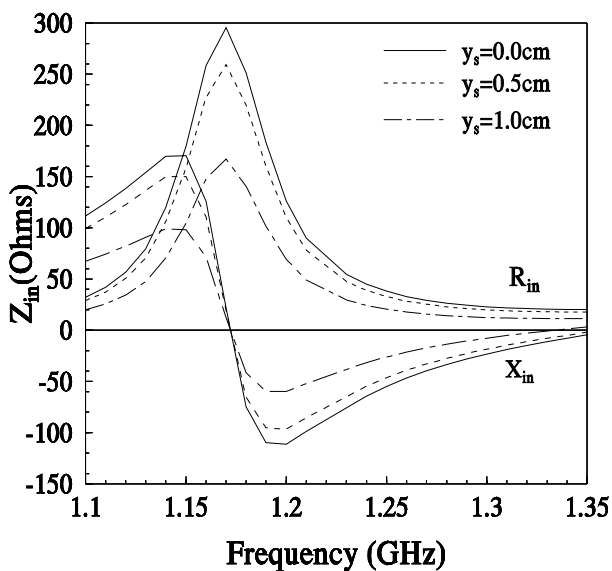
Fig. 4.43 Computed input impedances for the DRA excited by a slot/microstrip transmission line with a=2.75 cm, h=2.6cm, ε_r=12, L_s = 4.0cm, W_s=0.6mm, ε_s=2, d=0.16cm, w_f =0.5cm, and different microstrip line positions

ACKNOWLEDGEMENT

REFERENCES

[1]D. Kajfez and P. Guillon, *Dielectric resonators*, Vector Fields, Oxford, Mississippi, 1990.

[2]S. A. Long, M. W. McAllister and L. C. Shen, "The resonant cylindrical dielectric cavity antenna", *IEEE Trans. on Antennas and Propagation*, Vol. AP-31, pp. 406-412, 1983.

[3]M. W. McAllister, S. A. Long and G. L. Conway, "Rectangular dielectric resonator antenna," *Electron. Letters,* Vol. 19, pp. 218-219, 1983.

[4]M. W. McAllister and S. A. Long, "Resonant hemispherical dielectric antenna," *Electron. Letters*, Vol. 20, pp. 657-659, 1984.

[5]R.K. Mongia, A. Ittipiboon and M. Cuhaci, "Measurement of radiation efficiency of dielectric resonator antennas," *IEEE Microwave and Guided Letters*, Vol. 4, No. 3, pp. 80-82, 1994.

[6]A. A. Kishk, H. A. Auda and B. C. Ahn, "Accurate prediction of radiation patterns of dielectric resonator antennas," *Electronics Letters*, Vol. 23, No. 25, pp. 1374-1375, 1987.

[7]A. A. Kishk, H. A. Auda and B. C. Ahn," Radiation characteristics of cylindrical dielectric resonator antennas with new applications," *IEEE Antennas and Propag. Society Newsletter*, Vol. 31, pp. 7-16, Feb. 1989.

[8]G. P. Junker, A. A. Kishk and A. W. Glisson, "MOM Solution of Wire Radiators Coupled to Dielectric Bodies of Revolution," *IEEE Antennas and Propagation Society International Symposium Digest*, Vol. 1, pp. 40-43, 1993.

[9]A.W. Glisson, D. Kajfez and J. James, "Evaluation of modes in dielectric resonators using a surface integral equation formulation," *IEEE Trans. Microwave Theory Tech*., Vol. MTT-31, pp. 1023-1029, 1983.

[10]D. Kajfez, A. W. Glisson and J. James, "Computed modal field distributions for isolated dielectric resonators," *IEEE Trans. Microwave Theory Tech*., Vol. MTT-32, pp. 1609-1616, 1984.

[11]A.A. Kishk, A.W. Glisson and D. Kajfez, "Computed resonant frequency and far fields of isolated dielectric discs," *IEEE Antennas and Propagation Society International Symposium Digest*, Vol. 1, pp. 408-411, 1993.

[12]G.P. Junker, A. A. Kishk and A.W. Glisson, "Input Impedance of dielectric resonator antennas excited by a coaxial probe," *IEEE Trans. on Antennas and Propagation*, Vol. 42, pp. 960-966, July 1994.

[13]G.P. Junker, A. A. Kishk A. W. Glisson, "Input impedance of aperture coupled dielectric resonator antenna," *IEEE Trans. on Antennas and Propagation*, Vol. 44, No. 5, pp. 600-607, May 1996.

[14]A.A. Kishk and L. Shafai, "Different formulations for numerical solution of single and multibodies of revolution with mixed boundary conditions," *IEEE Trans. Antennas Propagat.*, Vol. AP-34, pp. 666-673, 1986.

[15] R.W.P. King, *Tables of Antenna Characteristics*, New York, IFI/Plenum Data Corporation, 1971.

[16]R.F. Harrington, *Field Computation by Moment Methods*, Malabar, Fla., Robert E. Kreiger Publishing, 1968.

[17]G.P. Junker," Analysis of Dielectric Resonator Antennas Excited by a coaxial Probe or Narrow Slot Aperture," PhD Dissertation, University of Mississippi, August 1994.

[18]A.A. Kishk, *Different Integral Equations for Numerical Solution of problems Involving Conducting or Dielectric Objects and their Combination,* PhD Thesis, University of Manitoba, Manitoba, Canada, 1986.

[19] D.M. Pozar, "A Reciprocity Method of Analysis for Printed Slot and Slot-Coupled Microstrip Antennas," *IEEE Trans. Antennas and Propagat.,* Vol. AP-34, No. 12, pp. 1439-1446, 1986.

[20]W. H. Press, B. P. Flannery, S. A. Teukolsky and W. T. Vetterling, *Numerical Recipes*, Cambridge University Press, Chapter 9, 1986.

[21]Mongia, R. K. and Prakash Bhartia, "Dielectric resonator antennas-A review and general design relations for resonant frequency and bandwidth," *International Journal of Microwave and Millimeter-wave Computer Aided Engineering*, Vol. 4, No. 3, pp. 230-247, 1994.

[22]A. C. Ludwig," The definition of cross-polarisation," *IEEE Transactions on Antennas and Propagation*, Vol. AP-21, No. 1, pp. 116-119, 1973.

[23]G. P. Junker, A. A. Kishk, A. W. Glisson and D. Kajfez," Effect of an air gap on a cylindrical dielectric resonator antennas operating in the TM_{01} mode," *Electronics Letters*, Vol. 30, No. 2, pp. 97-98, 1994.

[24]G. P. Junker, A. A. Kishk, A. W. Glisson, and D. Kajfez, "Effect of an air gap around the coaxial probe exciting a cylindrical dielectric resonator antenna," *Electronics Letters*, Vol. 30, No. 3, pp. 177-178, 1994.

[25]A. A. Kishk, G. Zhou and A.W. Glisson, "Analysis of dielectric resonator antennas with emphasis on hemispherical structures," *IEEE Antennas and Propagation Magazine*, Vol. 36, No. 2, pp. 20-31, April 1994.

Miscellaneous References

A.A. Kishk, B. Ahn and D. Kajfez, "Broadband stacked dielectric resonator antennas," *Electronics Letters*, Vol. 25, No. 18, pp. 1232-1233, 1989.

R.A. Kranenburg and S.A. Long, "Microstrip transmission line excitation of dielectric resonator antennas," *Electronics Letters*, Vol. 24, No. 18, pp. 1156-1157, 1988.

J.T. St. Martin, Y.M.M. Antar, A.A. Kishk, A. Ittipiboon and M. Cuhaci, " Dielectric resonator antenna using aperture coupling," *Electronics Letters*, Vol. 26, No. 24, pp. 2015-2016, 1990.

A.A. Kishk, A. Ittipiboon, Y.M.M. Antar and M. Cuhaci, "Dielectric resonator antenna fed by a slot in the ground plane of a microstrip line," *IEE publication No. 370, Antennas and Propagation*, Part I, pp. 540-543, 1993.

R. Kranenburg, S.A. Long and J.T. Williams, "Coplanar waveguide excitation of dielectric resonator antennas," IEEE Transactions on Antennas and Propagat., Vol. 39, No. 1, pp. 119-122, 1991.

R.K. Mongia, A. Ittippiboon, Y.M.M. Antar, P. Bhartia and M. Cuhaci," A half-split cylindrical dielectric resonator antenna using slot-coupling," *IEEE Microw. & Guided Wave Lett.*, Vol. 3, pp. 38-39, 1993.

G.P. Junker, A. A. Kishk and A. W. Glisson, "Numerical analysis of dielectric resonator antennas excited in quasi-TE modes," *Electronics Letters*, Vol. 29, No. 21, pp. 1810-1811, 1993.

A.A. Kishk and A.Z. Elsherbeni, "Radiation characteristics of dielectric resonator antennas loaded with a beam-forming ring," *Archiv für Elektronik und Übertragungstechnik*., Band 43, Helf 3, pp. 158-165, 1989.

D. Kajfez and P. Guillon, (Eds.), *Dielectric Resonators*. Artech House, Inc. Norwood, MA, 1986.

A.A. Kishk, M.R.Zunoubi and D. Kajfez, "A numerical study of a dielectric disc antenna above grounded dielectric substrate," *IEEE Transactions on Antennas and Propagation*, Vol. 41, No. 6, pp. 813-821, 1993.

W. Huang, A.A. Kishk and A.W. Glisson, "Numerical analysis of fat monopole antenna loaded with dielectric material," *Archiv für Elektronik und Übertragungstechnik*., Vol. 48, pp. 177-183, June 1994.

K.W. Leung, K.M. Luk and K.Y.A., Lai, "Input impedance of hemispherical dielectric resonator antenna," *Electronics Letters*, Vol. 27, pp. 2259-2260, 1991.

G. Zhou, A.A. Kishk and A.W. Glisson, "Input Impedance of a hemispherical dielectric resonator antenna excited by a coaxial probe," *IEEE Antennas and Propagation Society International Symposium Digest*, Vol. 1, pp. 1038-1041, 1993.

K.W. Leung, K.Y.A. Lai, K.M. Luk and D. Lin," Input impedance of aperture coupled hemispherical dielectric resonator antenna," *Electron. Lett.*, Vol. 29, No. 13, pp. 1165-1167, 1993.

G. Zhou, "Analysis of a hemispherical dielectric resonator antenna (DRA) excited by a coaxial probe or a narrow slot," *Master's Thesis*, Department of Electrical Engineering, University of Mississippi, December 1993.

M. Gastine, L. Courtois and J. L. Dormann, "Electromagnetic resonances of free dielectric spheres," *IEEE Trans., Microwave Theory and Techniques*, Vol. MTT-15, No. 12, pp. 694-670, 1967.

D. Kajfez and J. A. Gerald, "Plotting vector fields with a personal computer," *IEEE Trans. Microwave Theory Tech.*, Vol. MTT-35, pp. 1069-1072, 1987.

G.P. Junker, A.A. Kishk and A.W. Glisson, "Numerical analysis of dielectric resonator antennas excited in quasi TE modes," *Electronics Letters*, Vol. 29, No. 21, pp. 1810-1811, October 1993

G.P. Junker, A.A. Kishk, A.W. Glisson and D. Kajfez," Effect of an air gap on a cylindrical dielectric resonator antennas operating in the TM_{01} mode," *Electronics Letters*, Vol. 30, No. 2, pp. 97-98, 1994.

G.P. Junker, A.A. Kishk, A.W. Glisson and D. Kajfez," Effect of an air gap around the coaxial probe exciting a cylindrical dielectric resonator antenna," *Electronics Letters*, Vol. 30, No. 3, pp. 177-178, 1994.

G.P. Junker, A.A. Kishk and A.W. Glisson, "Input impedance of an aperture coupled dielectric resonator antenna," *1994 AP-S International Symposium*, Seattle, Vol. 2, pp. 748-751, June 1994.

G.P. Junker, A.A. Kishk, A.W. Glisson and D. Kajfez," The effect of fabrication imperfections for ground-plane-backed coaxial probe fed dielectric resonator antennas," *ANTEM'94 Symposium Antenna Technology and Applied Electromagnetics,* pp. 445-448, August 1994.

G.P. Junker, A.A. Kishk and A.W. Glisson," A novel delta gap source model for center fed cylindrical dipoles," *IEEE Transactions Antennas Propagation*, Vol. 43, No. 5, May 1995.

G.P. Junker, A.A. Kishk, A.W. Glisson and D. Kajfez," The effect of fabrication imperfections for ground-plane-backed coaxial probe fed dielectric resonator antennas," *IEEE Antennas and Propagation Magazine*, Vol. 37, No.1, pp. 40-47, February, 1995.

A.A Kishk, A. Ittipiboon, Y.M.M. Antar and M. Cuhaci," Slot excitation of the dielectric disk radiator," *IEEE Trans. on Antennas and Propagation*, Vol. 43, No. 2, pp. 198-200, February 1995.

G.P. Junker, A.W. Glisson and A. A. Kishk, "Mutual coupling effects and radiation characteristics of a linear array of dielectric resonator elements fed by coaxial probes," *IEEE Antennas and Propagation International Symposium*, Pasadena CA, Vol. 4, pp. 1998-2001, June 1995.

G.P. Junker, A.W. Glisson and A.A. Kishk," Input impedance of dielectric resonator antennas loaded with high permittivity and conducting disks," *Microwave and Optical Technology Letters*, Vol. 9, No. 4, pp. 204-207, July 1995.

G.P. Junker, D. Kajfez, A.A. Kishk and A.W. Glisson," Effect of aperture filling on slot-coupled dielectric resonator antennas operating in HEM_{11} mode," *Electronics Letters*, Vol. 31, No. 10, pp. 774-775, 1995.

G.P. Junker, A.A. Kishk, D. Kajfez, A.W. Glisson and J. Guo, "Microstrip-slot coupled dielectric resonator antennas mounted on thin dielectric layers," *International Journal of Microwave and Millimeter-wave Computer Aided Engine ering*, Vol. 6, No. 3, pp. 174-182, 1996.

M.W. McAllister," Resonant hemispherical dielectric antenna," *Electronic Letters*, Vol. 20, pp. 657-658, 1984.

J.F. Shaeffer and L.N. Medgyesi-Mitschang," Radiation form wire antennas attaches to bodies of revolution: the junction problem," *IEEE Trans. Antennas Propagat.*, Vol. AP-29, pp. 479-487, May 1981.

J.F. Shaeffer," EM scattering from bodies of revolution with attached wires," *IEEE Trans. Antennas Propagat.,* Vol. AP-30, pp. 426-431, May 1982.

R. Pérez-Leal and M.F. Cátedra," Input Impedance of wire antennas attached on-axis to conducting bodies of revolution," *IEEE Trans. Antennas Propagat.,* Vol. AP-36, pp. 1236-1243, Sept. 1988.

T.E. Durham and C.G. Christodoulou," Electromagnetic radiation from structures consisting of combined body of revolution and arbitrary surfaces," *IEEE Trans Antennas Propagat.,* vol. AP-40, pp. 1061-1067, Sept.1992.

R.F. Harrington, *Time Harmonic Electromagnetic Fields*, New York, McGraw Hill, 1961.

W. Zheng and S. Ström," The null-field approach to electromagnetic resonance of composite objects," *Computer Physics Communications*, vol. 68, pp. 157-174, 1991.

G.P. Junker, A.A. Kishk and A.W. Glisson," Multiport network description and radiation characteristics of coupled dielectric resonator antennas," *IEEE Trans. on Antennas and Propagation*, Vol. 46, No. 3, pp. 425-433, March 1998.

A.A. Kishk, A.W. Glisson and Yan Yin, "Conical Dielectric Resonator Antenna Excited by a coaxial probe," To appear in *Microwave and Optical Technology Letters*".

A.A. Kishk, A.W. Glisson and G.P. Junker, " Bandwidth enhancement for split cylindrical dielectric resonator antennas." To appear in the Journal of Progress in Electromagnetics Research, Vol. 33, pp. 97-118, 2001.

A. A. Kishk, Yan Yin and A.W. Glisson, "Conical Dielectric Resonator Antennas For Wideband Applications." To appear in the IEEE Transactions on Antennas and Propagation, January 2002.

This page intentionally left blank

CHAPTER 5

Broadband Dielectric Resonator Antennas

Aldo Petosa, Apisak Ittipiboon and Yahia Antar*

Communications Research Centre Canada
Ottawa
Canada

*Royal Military College of Canada
Kingston
Canada

5.1   INTRODUCTION

In general, all resonant antennas will have a limited bandwidth of operation, due to their resonant nature. This bandwidth limitation is usually defined by the input impedance of the antenna, since it is ordinarily the quantity which changes most rapidly with frequency. However, the radiation pattern can also be used to define the bandwidth, in terms of gain, beamwidth, cross-polarisation levels, or sidelobe levels. The bandwidth enhancement techniques which will be described in this chapter deal with the improvement of the impedance response. Several techniques can be used to increase the operational bandwidth of resonant antennas and many of these have been successfully employed on microstrip patch antennas, which have inherently narrow bandwidth. These various approaches can be classified into three broad categories: lowering the inherent Q-factor of the resonator; using external matching networks; and combining multiple resonators.

Several methods for reducing the inherent Q-factor of the resonant antenna are available. For microstrip patches for instance, one of the simplest techniques is to lower the dielectric constant of the substrate. Since the Q-factor is related to the dielectric constant, a decrease in the dielectric constant will cause a decrease in the Q-factor and thus an increase in the bandwidth. Although this is a simple solution, there are certain drawbacks. As the dielectric constant is reduced, the size of the resonant antenna will increase, for a given frequency. This may not be desirable for many applications where a compact or low-profile antenna is required. Also, the coupling to the antenna may become more difficult. For example, aperture-coupling to an air-filled patch requires a relatively large slot, which results in higher backlobe radiation. Alternatively, if probe-coupling is used, the height of the probe can be significant and cause spurious radiation, leading to higher cross-polarisation levels or distortions in the co-polarised patterns. Other methods for lowering the Q-factor involve loading the antenna. For example, in patch antennas, posts or slots can be added to affect the resonant frequency and Q-factor of the antenna. The advantage of this approach is that there is generally no significant increase in the antenna dimensions. However, there is usually only a modest improvement in bandwidth, and there may be degradations to the radiation pattern, in terms of increased cross-polarisation levels or distortions in the symmetry.

Matching networks, such as quarter-wave transformers, matching stubs, and Tchebyshev impedance networks, can be used to increase the bandwidth of a resonant antenna by transforming its input impedance to better match that of the coupling circuit. These matching networks are usually external to the antenna, occurring after the coupling mechanism to the antenna, but sometimes these networks can be incorporated within the antenna itself. An example of the latter would be a microstrip-fed aperture-coupled patch or DRA, where a microstrip stub extends past the slot to cancel out the reactance of the aperture. External matching networks are less desirable since they require additional real-estate and will increase the insertion loss to the system which will degrade the radiation efficiency of the antenna.

The final approach to increasing the bandwidth of resonant antennas involves the use of multiple resonator configurations. By using two or more resonators, each designed at a somewhat different frequency, the resonators can be combined to give wideband or multi-band operation. The advantage of this approach is that each resonator can be tuned more-or-less independently, allowing for a great deal of design flexibility. The disadvantage lies in the added real-estate required which may preclude some of these configurations from being used in an array environment.

This chapter reviews the various methods of bandwidth enhancement techniques as applied to DRAs. The first section investigates the bandwidth of simple DRA shapes (rectangular and cylindrical) to achieve a sense of the attainable bandwidth without having to resort to enhancement techniques. The second section looks at the bandwidth performance of DRAs whose Q-factors have been reduced using loading techniques. The third section will look at matching networks to improve the bandwidth of DRAs. Finally, the fourth section covers the bandwidth performance of DRAs using multiple resonators in both stacked and co-planar configurations.

5.2   BANDWIDTH OF RECTANGULAR AND CYLINDRICAL DRAS

Before looking at the various bandwidth enhancement techniques, it is instructive to observe the amount of bandwidth attainable by DRAs of simple rectangular and cylindrical shapes. Figure 5.1 shows a rectangular and cylindrical DRA mounted on a finite ground plane, which is the typical configuration for most practical implementations. The $TE_{11\delta}$ mode for the rectangular DRA and the lower order modes of the cylindrical DRA will be considered for this investigation. The dielectric waveguide model described in Chapter 2 is used to determine the resonant frequency and radiation Q-factor of the rectangular DRA. For cylindrical DRAs, the equations have been derived by a combination of the dielectric waveguide model and curve fitting to various rigorous numerical and experimental results [1]. The resonant frequency and Q-factor for the first few modes of the cylindrical resonator are given by the following equations (given to 3 significant digits):

$TE_{01\delta}$ Mode:

$$f_o = \frac{2.921 c \varepsilon_r^{-0.465}}{2\pi A}\left[0.691 + 0.319\left(\frac{A}{2H}\right) - 0.035\left(\frac{A}{2H}\right)^2\right] \tag{5.1}$$

$$Q = 0.012\varepsilon_r^{1.2076}\left[5.270\left(\frac{A}{2H}\right) + 1106.188\left(\frac{A}{2H}\right)^{0.625} e^{-1.0272\left(\frac{A}{2H}\right)}\right] \tag{5.2}$$

$HE_{11\delta}$ Mode

$$f_o = \frac{2.735 c \varepsilon_r^{-0.436}}{2\pi A}\left[0.543 + 0.589\left(\frac{A}{2H}\right) - 0.050\left(\frac{A}{2H}\right)^2\right] \tag{5.3}$$

$$Q = 0.013\varepsilon_r^{1.202}\left[2.135\left(\frac{A}{2H}\right) + 228.043\left(\frac{A}{2H}\right)^{-2.046\left(\frac{A}{2H}\right)+0.111\left(\frac{A}{2H}\right)^2} e\right] \tag{5.4}$$

TM$_{01\delta}$ Mode:

$$f_o = \frac{2.933c\varepsilon_r^{-0.468}}{2\pi A}\left\{1-\left[0.075-0.05\left(\frac{A}{2H}\right)\right]\left[\frac{\varepsilon_r-10}{28}\right]\right\}\cdot$$
$$\left\{1.048+0.377\left(\frac{A}{2H}\right)-0.071\left(\frac{A}{2H}\right)^2\right\}$$

(5.5)

$$Q = 0.009\varepsilon_r^{0.888}e^{0.040\varepsilon_r}\left\{1-\left[0.3-0.2\left(\frac{A}{2H}\right)\right]\left[\frac{38-\varepsilon_r}{28}\right]\right\}\cdot$$
$$\left\{9.498\left(\frac{A}{2H}\right)+2058.33\left(\frac{A}{2H}\right)^{4.322}e^{-3.501\left(\frac{A}{2H}\right)}\right\}$$

(5.6)

where A is the radius and H is the height of the DRA when mounted on a ground plane. The bandwidth (BW) of the DRA is related to the Q-factor by:

$$BW = \frac{s-1}{Q\sqrt{s}}\cdot 100\%$$

(5.7)

where s is the desired VSWR at the input port of the DRA.

From the preceding equations for the Q-factor, it is evident that a lower Q-factor (and thus larger bandwidth) occurs for smaller values of the dielectric constant. In theory, a DRA with a dielectric constant of one would have the lowest Q-factor and therefore the widest bandwidth. In practice, however, there is a lower limit on the value of the dielectric constant required to contain the fields within the DRA in order to resonate. It is instructive to look at the typical bandwidth achievable by DRAs of rectangular and cylindrical shapes of low permittivity. Using a permittivity of 10 (which is close to the practical lower bound for DRAs), the dielectric waveguide model was used to determine the Q-factor of these resonators, for a fixed frequency (arbitrarily chosen at 5 GHz). Figures 5.2 and 5.3 plot the bandwidth and volume of rectangular DRAs of various aspect ratios and of cylindrical DRAs operating in the lower order modes.

The results show that a considerable degree of control over bandwidth is possible by adjusting the aspect ratio of the DRAs. In general, a wider range is achievable for the rectangular DRAs than for the cylindrical DRAs. Also, low-profile rectangular DRAs ($a=8h$) appear to offer the widest bandwidth for a given volume. It is interesting to note that the bandwidth does not increase monotonically with the DRA volume. As the DRA volume increases, the bandwidth initially decreases until it reaches a minimum value, and then increases with volume.
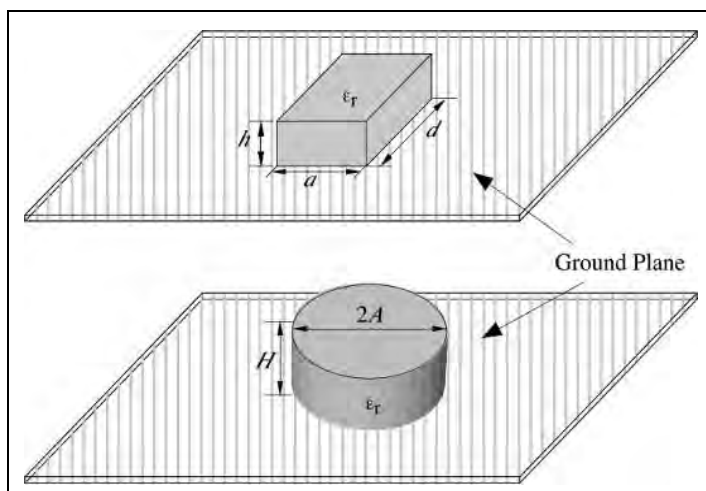
Figure 5.1 Rectangular and cylindrical DRAs mounted on a ground plane

 The curves in Figure 5.2 also show that bandwidths of greater than 20% are possible for certain aspect ratios. It should be kept in mind that the bandwidth curves shown in Figure 5.2 were determined for isolated DRAs and do not account for the coupling mechanisms, which may significantly reduce the achievable bandwidth. Also, as the aspect ratios become quite small ($d/2h \ll 1$, or $A/H \ll 1$), the assumptions made for the dielectric waveguide models begin to break down, so that the curves below values of $d/2h$ (A/H) $= 0.5$ may be less accurate. A study carried out in [2] has compared the measured resonant frequency and Q-factor to those predicted by the dielectric waveguide model for numerous rectangular DRAs of various aspect ratios and dielectric constant. Errors ranged from 1% to 12% depending on the aspect ratio and dielectric constant. The following sections will look at various methods for enhancing the bandwidth of DRAs.

5.3   BANDWIDTH ENHANCEMENT WITH SINGLE DRAS

This section looks at techniques which can be used to improve the impedance bandwidth of a single DRA. These methods all involve the introduction of some form of air gap within the DRA itself or between the DRA and the ground plane. The resultant is a lowering of the Q-factor and thus an increase in the bandwidth. This is usually accompanied by a shift in the resonant frequency and/or an in-

crease in volume. Three examples will be considered: a probe-fed rectangular DRA; an annular DRA; and an aperture-fed notched rectangular DRA.
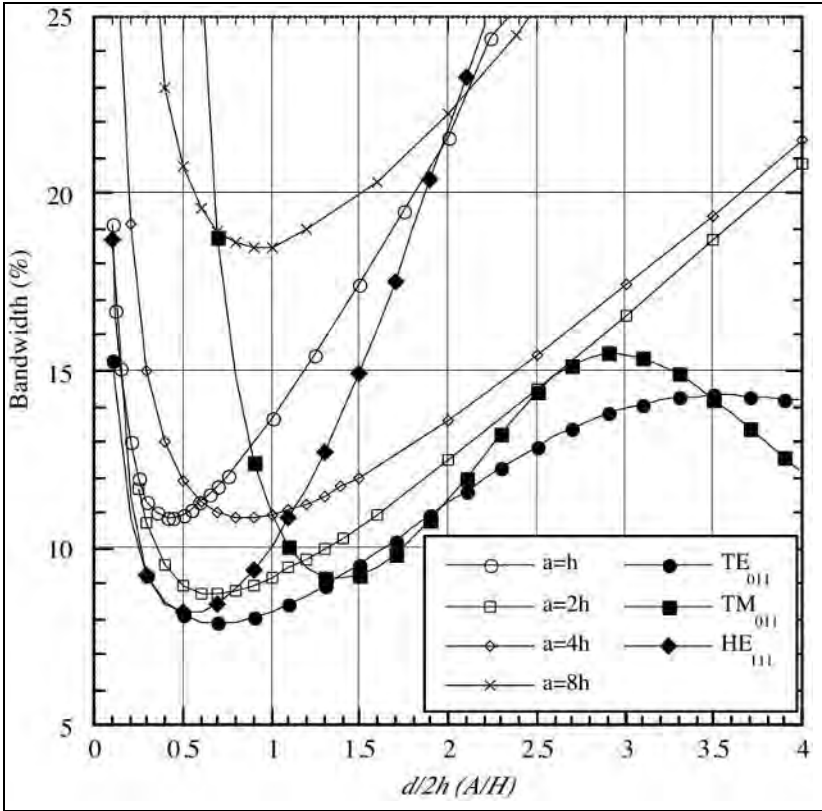
Figure 5.2 Bandwidth of simple rectangular and cylindrical DRAs with $\varepsilon_r = 10$ at 5 GHz

5.3.1 Probe-fed Rectangular DRA with Air Gap

The bandwidth of a rectangular DRA can be improved by introducing a small air gap between the DRA and the ground plane as shown in Figure 5.4 for the case of a probe-fed rectangular DRA. The introduction of this air gap results in a lowering of the effective dielectric constant of the DRA, which in turn lowers the Q-factor, but also increases the resonant frequency. The impact of air gaps can be seen in an

example involving probe-fed rectangular DRAs designed at L-band [3]. The effect of an increasing air gap is an increase in the bandwidth and the resonant frequency. By introducing air gaps of up to 1.5 mm, there was an increase in the measured impedance bandwidth of up to 84%. This was accompanied by a corresponding increase in the resonant frequency of up to 17%.
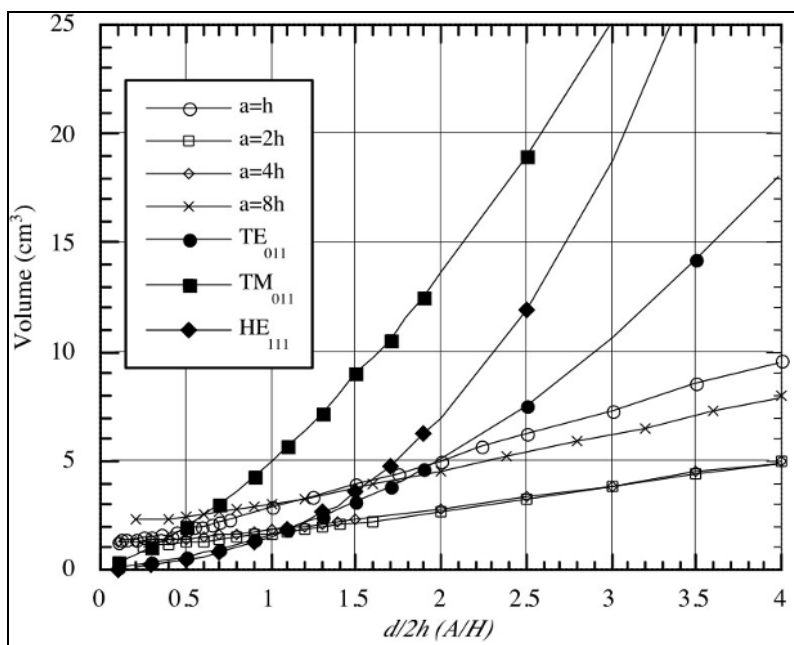
Figure 5.3 Volume of simple rectangular and cylindrical DRAs with $\varepsilon_r=10$, at 5 GHz

The addition of an air gap is seen to be a simple and viable technique for enhancing the bandwidth of the DRA. It does not require parasitic elements nor a complex matching network, and the technique takes up no additional real-estate. Similar work with numerical verification was carried out using cylindrical DRAs [4]. In practice, the air gap spacing is realised by inserting a thin piece of low density foam between the DRA and the ground plane, whose dielectric constant is nearly that of air.

5.3.2   Annular DRAs

One method for increasing the bandwidth of a cylindrical DRA is to remove a section of the central portion of the DRA to form a ring or annulus. The geometry of a probe-fed annular DRA is shown in Figure 5.5. Removing the central portion results in a lowering of the effective dielectric constant of the DRA which lowers the radiation Q-factor, thus increasing the bandwidth. The annular DRA offers a compact configuration which does not require the use of parasitic elements to broaden the bandwidth. A probe located in the centre of the DRA, as shown in Figure 5.5, will excite the $TM_{01\delta}$ mode (which radiates like a short vertical electric monopole), while feeding the DRA near the outer diameter will excite the HE_{11} mode (which radiates like a short horizontal magnetic dipole).
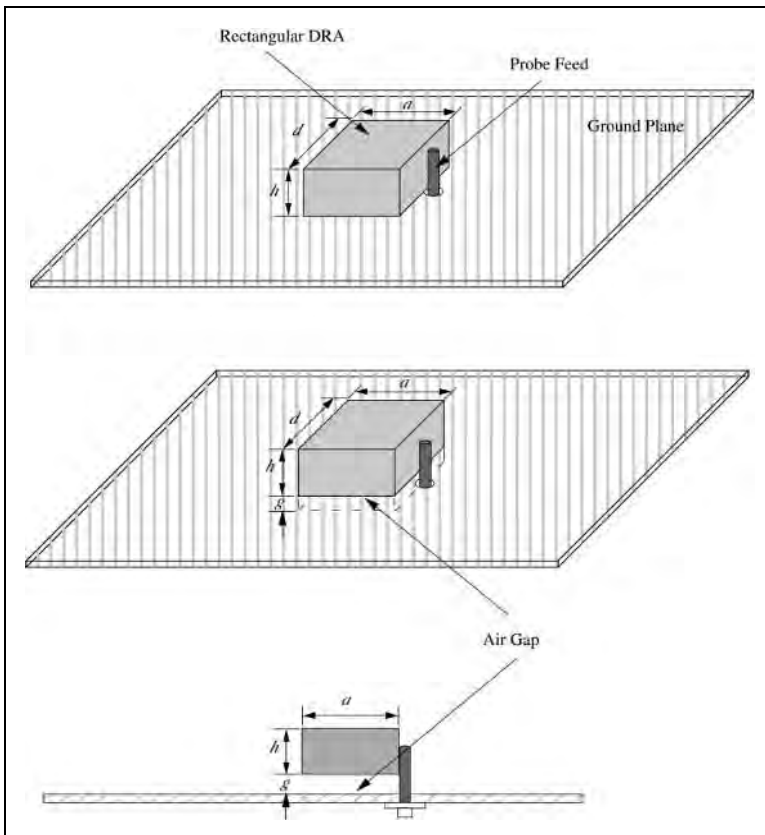
Figure 5.4 Probe-fed DRA with air gap

The resonant frequency of the annular DRA operating in the $TM_{01\delta}$ mode can be estimated using [5, 6]:

$$f = \frac{c}{2\pi\sqrt{\varepsilon_r}} \sqrt{\left(\frac{\pi}{2H}\right)^2 + \left(\frac{x_o}{A}\right)^2} \tag{5.8}$$
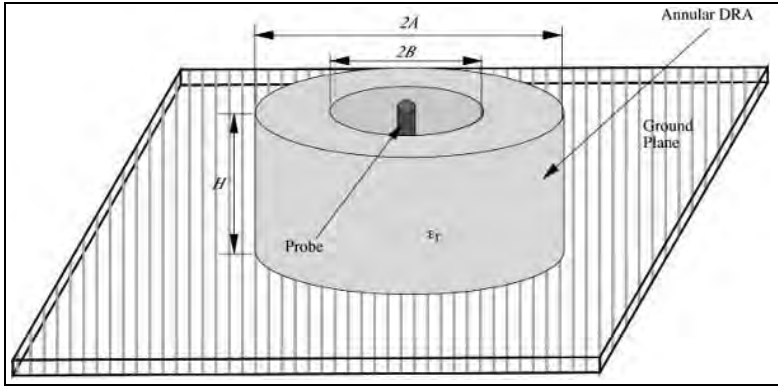
Figure 5.5 Probe-fed annular DRA

where: $c = 3.0 \times 10^8$ m/s, and x_o is the solution to:

$$\frac{J_1(x_o)}{Y_1(x_o)} = \frac{J_1(\frac{B}{A} x_o)}{Y_1(\frac{B}{A} x_o)} \tag{5.9}$$

Values of x_o for various ratios of b/a are shown in Table 5.1 and are plotted in Figure 5.6. The values for the radiation Q-factor were calculated using a rigourous analytical approach and the normalised Q-factors can be found in a graph in [5]. As an example, the effects of various b/a ratios on the bandwidth and resonant frequency of a cylindrical ring DRA with a permittivity of $\varepsilon_r = 36.2$, an outer radius of $A = 0.5975$ cm, height of $H = 0.54$ cm are shown in Table 5.2. As the ratio as b/a increases, the bandwidth increases, but so does the resonant frequency [5, 6].

b/a	x_o	B/A	x_o
0	3.8317	0.5	6.3932
0.1	3.9409	0.6	7.9301
0.2	4.2358	0.7	10.5220
0.3	4.7058	0.8	15.7376
0.4	5.3912	0.9	31.4292

Table 5.1 Values of x_o for various ratios of B/A
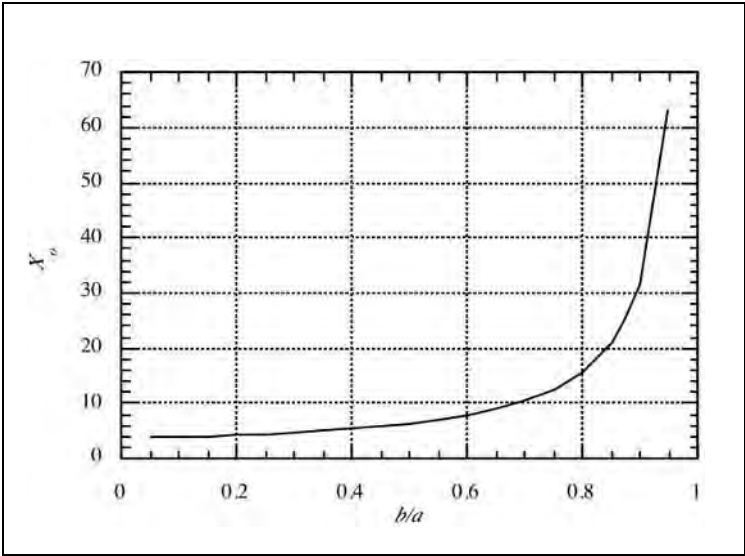
Figure 5.6 Solution of x_o for values of b/a

b/a	f (GHz)	Q	Bandwidth (%)
0.00	5.56	710	0.1
0.50	6.31	39	1.8
0.50	8.75	14.0	5.0
0.75	16.8	1.6	44

Table 5.2 Effect of b/a on the frequency and bandwidth of a cylindrical ring DRA

The use of an air gap has also been incorporated with the annular DRA to further enhance the bandwidth [7]. For an annular DRA designed at 5.6 GHz, with $A = 6.9$ mm, $B = 1.05$ mm, $H = 6.2$ mm, and a dielectric constant of $\varepsilon_r = 36$, the bandwidth was increased from 6.5% to 11.5% when the air gap was increased from 2 mm to 4 mm.

5.3.3   Notched Rectangular DRAs

An analogous configuration to the annular DRA is the notched rectangular DRA, shown in Figure 5.7. It consists of a slot-fed rectangular DRA with a rectangular central portion (notch) removed. The goal of using this configuration is to increase the operational bandwidth or allow for dual band operation using a single point feed. The design concept is to lower the Q-factor by removing the centre portion of the DRA, similar to the annular DRA described in the previous section. The design approach is based on dielectric ring resonators of very high permittivity. As shown in Figure 5.8, by removing the ground plane and replacing it with an image of the notched DRA, the DRA appears like a rectangular ring, similar to the annular DRA. The advantage of the notched rectangular DRA over the annular DRA is that it can be designed either for wide impedance bandwidth or dual-band operation.

The performance of a notched rectangular DRA is demonstrated using an X-band design [8]. A solid rectangular DRA of dimensions $a = 10$ mm, $d = h = 3$ mm, and permittivity of $\varepsilon_r = 10$ was used to compare the performance of the various notched DRAs. The solid DRA achieved a 10 dB return loss bandwidth of 10%. The return loss for three notched DRAs with values of $l = 3$, 5, and 7 mm are plotted in Figure 5.9. The results show the characteristic of a double-tuned resonant circuit. The ratio a/l can be used to adjust the location of the upper and lower resonating frequencies. When the two frequencies are located closer to each other, the antenna has a broad operating bandwidth. When the two frequencies are farther apart, the antenna can be utilised in a dual band mode of operation. For the wideband mode (with $a/l = 10/5$) the notched DRA achieved a 10 dB return loss bandwidth of 28%. The radiation patterns for the wideband notched DRA (with $a/l = 10/5$) are shown in Figure 5.10. The short magnetic dipole mode radiation pattern is maintained over a broad frequency range, with the boresight cross-polarisation levels remaining 20 dB below the peak co-polarised levels.

5.4   BANDWIDTH   ENHANCEMENTS   USING   IMPEDANCE   MATCHING

This section looks at techniques for improving the impedance bandwidth using matching networks. The configurations which will be examined do not resemble the traditional implementations of impedance matching (such as microstrip networks or waveguide steps) but functionally perform in a similar fashion.
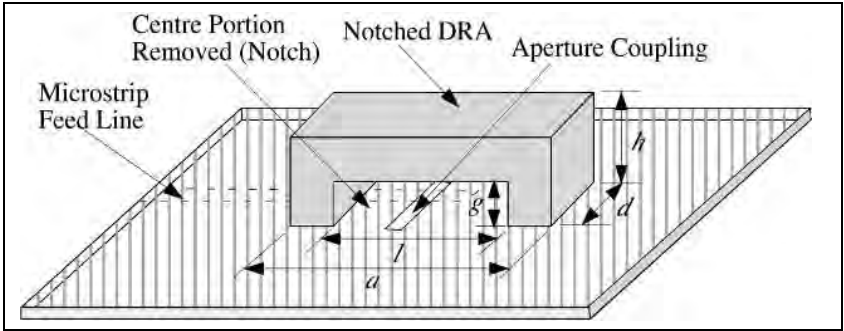
Figure 5.7 Geometry of the notched rectangular DRA. From [8] © 1998 IEEE. Reprinted with permission.
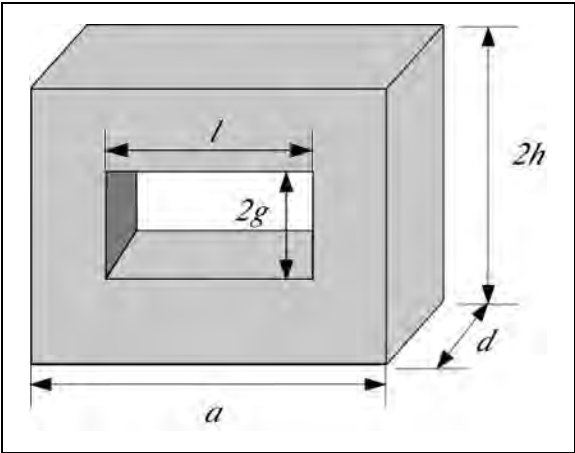
Figure 5.8 Rectangular ring DRA formed by the notched DRA and its image
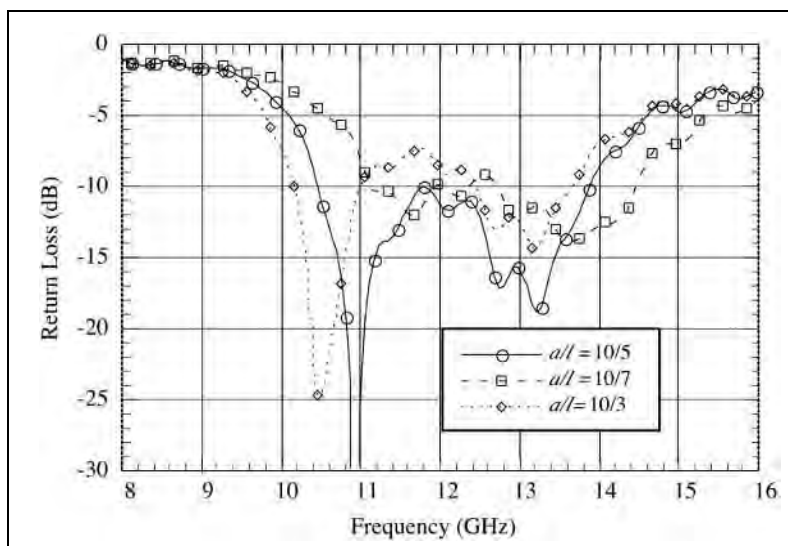
Figure 5.9 Return loss of the notched DRA for various ratios of *a/l*. From [8] © 1998 IEEE. Reprinted with permission.

5.4.1 Flat Matching Strips

Probe feeds are common for exciting DRAs, especially at lower frequencies where aperture-coupling may not be feasible due to the large aperture size required. Probes offer a simple method of exciting DRAs and they can be connected directly to a 50Ω coaxial line, with matching achieved by adjusting the height of the probe. There are some drawbacks in using a probe. Sometimes, in order to provide a good match, the probe must be located within the DRA, which requires drilling a hole in the DRA material. Oftentimes, to avoid drilling holes, the probe is located at the outer edge of the DRA. Although this simplifies fabrication, the optimum match may not be achieved. Also, when a high permittivity DRA is used, the matching becomes very sensitive to the probe location. Small, uncontrolled air gaps between the probe and the DRA may lead to results that are not repeatable.

To improve these problems, a flat metal strip can be printed onto the side of the DRA, as shown in Figure 5.11, for the case of a rectangular DRA [9]. The probe can then be soldered to the strip, eliminating any potential air gaps. The width and height of the strip can be adjusted to improve the match, offering a greater amount of control than if only the height of the probe were adjusted. A similar configuration can also be used for a microstrip-fed DRA [10, 11].

5.4.2 Loaded Notched DRAs

In section 5.3.3, the aperture-fed notched DRA was shown to be a versatile antenna capable of offering either wideband or dual band operation. In the wideband mode, the example selected showed about a tripling of the bandwidth compared to the corresponding solid rectangular DRA. One difficulty with the aperture-fed notched DRA is that it is often difficult to obtain a good impedance match between the aperture and the DRA, due to the air gap. Oftentimes, a large aperture is required to obtain an adequate match, which leads to significantly high levels of backlobe radiation. This difficulty can be overcome by adding a high-permittivity insert, placed over the aperture, as shown in Figure 5.12. The addition of this insert results in a significant improvement in the impedance matching between the aperture and the DRA. Figure 5.13 shows the return loss of a notched DRA fabricated from a material with a dielectric constant of $\varepsilon_r = 10$, loaded with an insert with a dielectric constant of $\varepsilon_r = 40$. Without the insert, there is no appreciable coupling between the slot and the DRA. With the insert, the coupling is significantly enhanced, and the DRA has a 10 dB return loss of 26% [12].

5.4.3 Multi-Segment DRAs

As discussed in Chapter 2, one method of exciting a DRA is by coupling it directly to a microstrip line. This is an attractive configuration, especially for arrays, since it allows for making use of all the advantages offered by printed technology for implementing the feed distribution network. The problem with feeding DRAs directly by a microstrip line is that to achieve strong coupling, a DRA of high permittivity is usually required. Since the DRA Q-factor is proportional to the permittivity, the bandwidth of these DRAs is typically narrow. For wider band DRAs (with lower permittivity), there is only a small amount of coupling achievable between the microstrip line and the DRA which results in poor radiation efficiency. This problem can be overcome by loading the microstrip line with an array of DRAs, each radiating a small amount of power. Several linear arrays have been designed using this approach [13-17]. This solution, however, is not suitable for all applications, due to the fact that a relatively large number of DRAs is required. This configuration also results in beam scanning with frequency which is common to all traveling wave arrays. For practical integration with microstrip technology, strong coupling is required between the microstrip line and the DRA. The multi-segment DRA (MSDRA) was developed to address this issue.

The MSDRA configuration is shown in Figure 5.14. It consists of a rectangular DRA of low permittivity under which one or more thin segments of different permittivity substrates are inserted. These inserts serve to transform the impedance of the DRA to that of the microstrip line by concentrating the fields underneath the DRA; this significantly improves the coupling performance [18, 19]. In general, more than one insert can be added to obtain the required impedance match, but to reduce the complexity of the fabrication process and ultimately the cost, it is desirable to use only a single insert, as shown in Figure 5.15. The radiation patterns of the MSDRAs have been successfully used in linear and planar arrays at C, X, and Ku-bands [20-22].

(a) E-Plane

(b) H-Plane
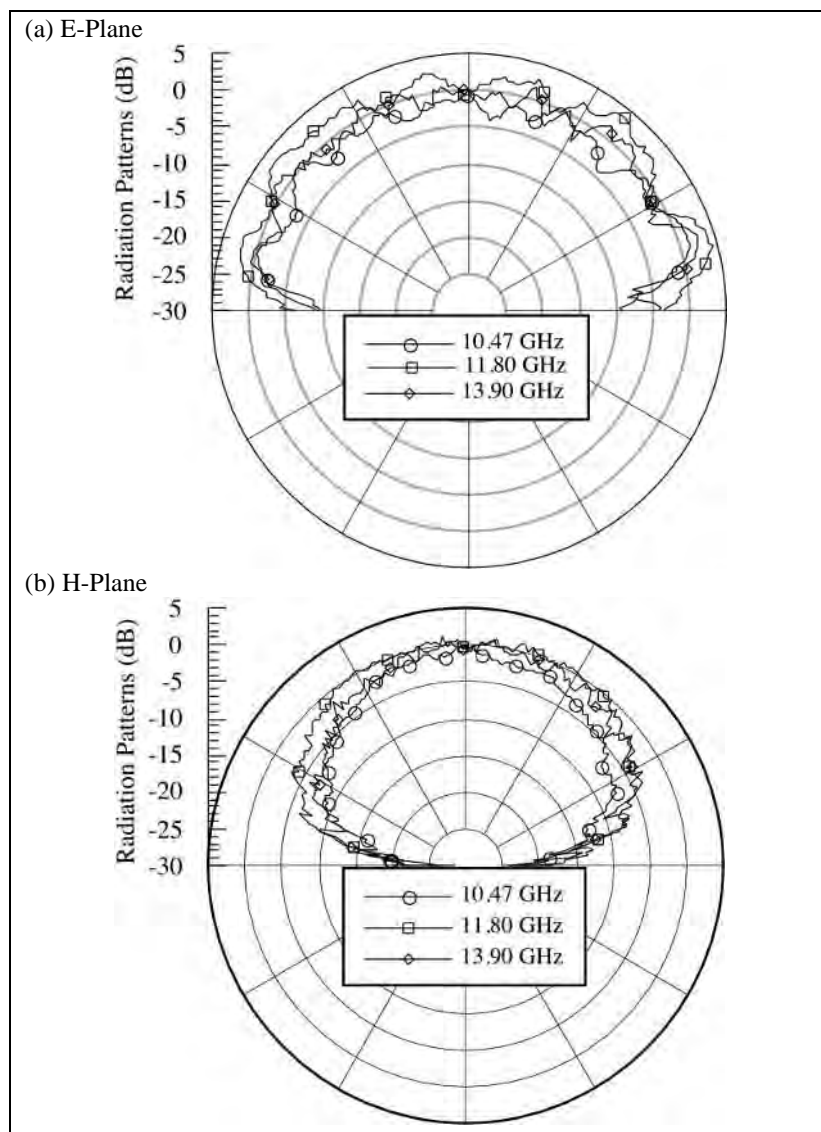
Figure 5.10 Normalised radiation patterns of the notched DRA with *a/l* = 10/5
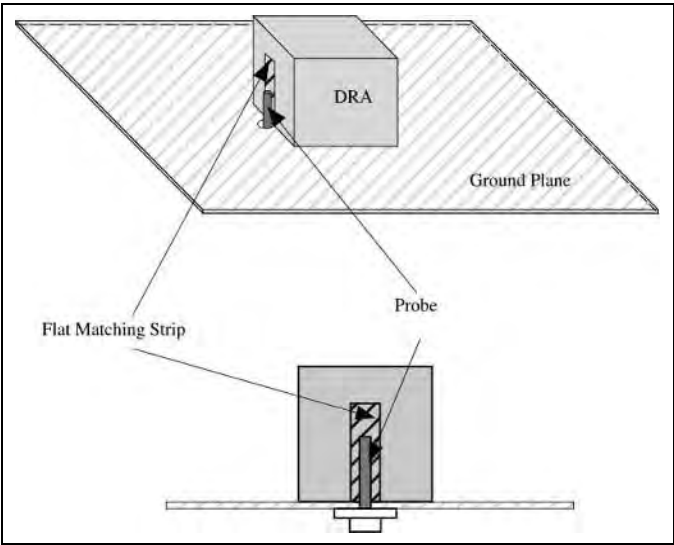
Figure 5.11 Impedance matching using a flat metal strip for a probe-fed DRA
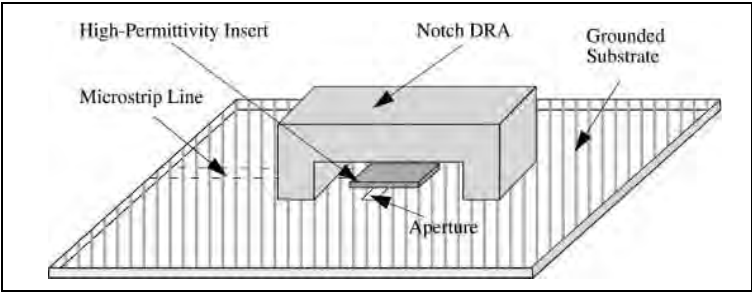
Figure 5.12 Aperture-fed notch DRA with high permittivity matching insert
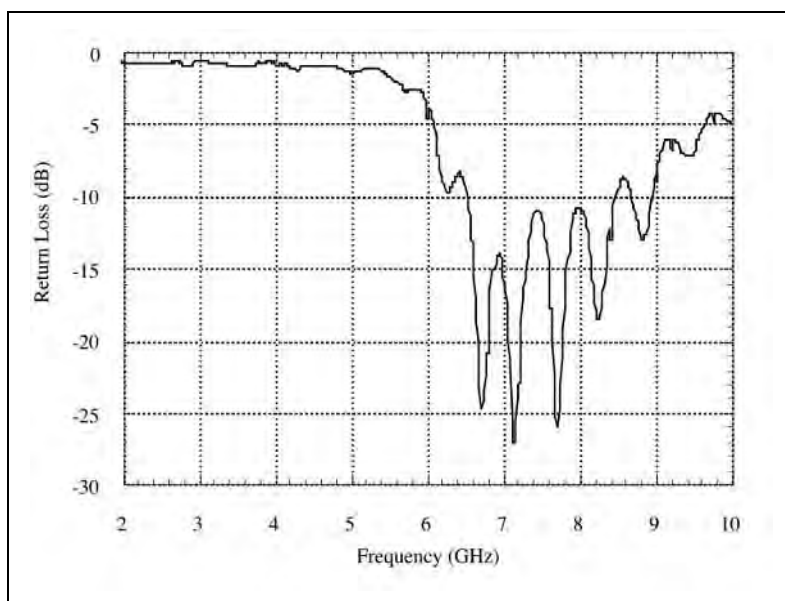
Figure 5.13 Return loss of dielectric-loaded notch DRA

Figure 5.16 demonstrates the impact of using a high permittivity insert, showing the return loss of a DRA made of $\varepsilon_r = 10$ material and corresponding MSDRA which has an insert with $\varepsilon_r = 40$ material. Both antennas are fed with a microstrip line. Without the insert, there is very little coupling between the microstrip line and the DRA. Once the insert is added, very good coupling is achieved. The radiation pattern of the MSDRA is similar to that of a simple rectangular DRA, which radiates like a short horizontal magnetic dipole, as shown in Figure 5.17.

Initial designs of the MSDRA involved a combination of the dielectric waveguide model for determining the DRA parameters, and experimental optimisation to determine the insert parameters. The dimensions of the radiating portion of the MSDRA were determined using the equations developed for the dielectric waveguide model for a rectangular resonator in free space, as given in Chapter 2.
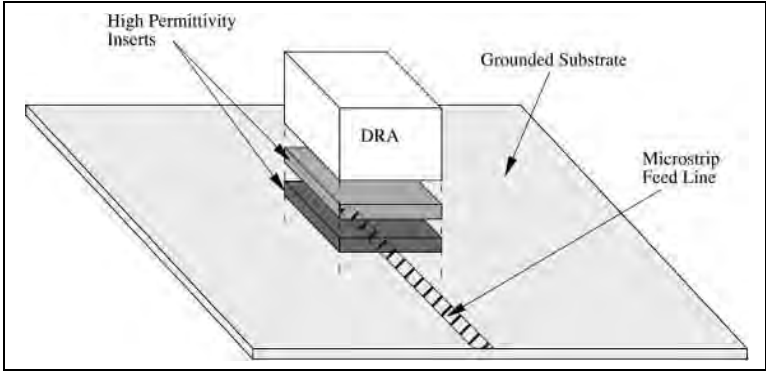
Figure 5.14 Exploded view of the multi-segment DRA
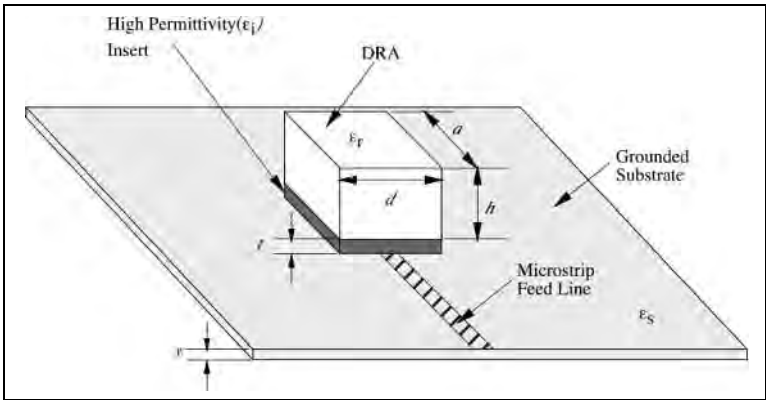
Figure 5.15 MSDRA with a single insert
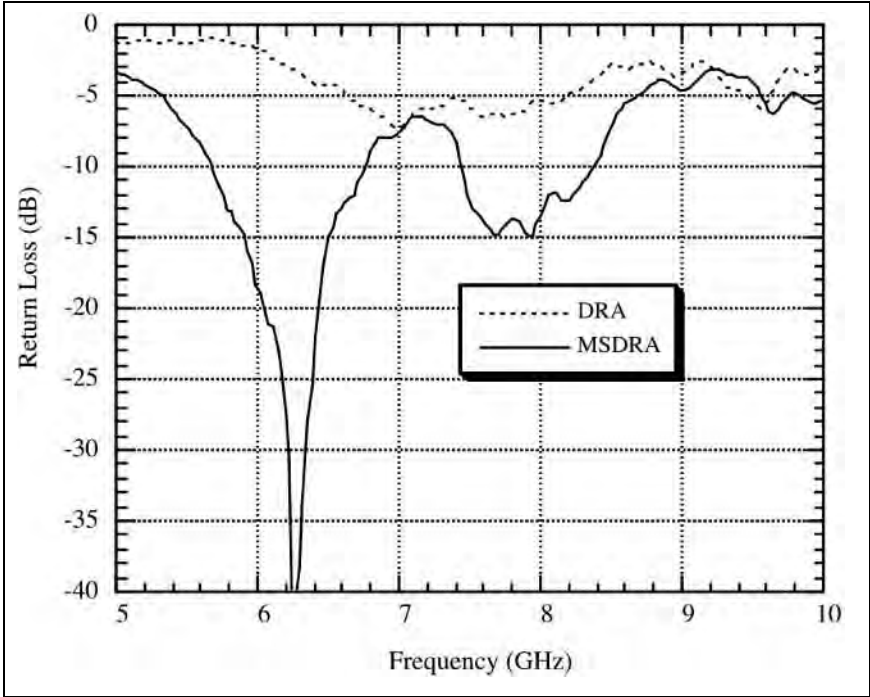
Figure 5.16 Return loss of a microstrip-fed DRA and MSDRA

For the MSDRA, the permittivity and thickness of the insert will affect the resonant frequency, impedance bandwidth, and the coupling level. To account for the effect of the insert and substrate on the resonant frequency of the MSDRA, the dielectric waveguide model equations are modified by including an effective permittivity (ε_{eff}) and effective height (H_{eff}). Adopting a simple static capacitance model, the effective permittivity of the MSDRA was calculated using:

$$\varepsilon_{eff} = \frac{H_{eff}}{h/\varepsilon_r + t/\varepsilon_i + s/\varepsilon_s} \tag{5.10}$$

where ε_r, ε_i, and ε_s are the permittivities of the DRA, insert, and substrate, respectively. The effective height (H_{eff}) is simply the sum of the DRA height (h), insert thickness (t), and substrate thickness (s):

$$H_{eff} = h + t + s \tag{5.11}$$

Equations (5.10) and (5.11) were substituted into the dielectric waveguide model equations in Chapter 2, with ε_{eff} replacing ε_r and $2H_{eff}$ replacing b.

To determine the impact of insert thickness and permittivity on the input impedance of the MSDRA, a systematic study involving nine inserts for a Ku-band MSDRA ($a = 7.875$ mm, $h = 3.175$ mm, $d = 2$ mm, and $\varepsilon_r = 10$), using both experimental and numerical modeling, was performed [23]. The MSDRA was fed with a 50 Ω line printed on a substrate with thickness $s = 0.762$ mm and relative permittivity $\varepsilon_s = 3.0$. The predicted resonant frequencies (f_{oe}) using (5.10) and (5.11) in the dielectric waveguide model are compared to the measured frequencies (f_{om}) for the different inserts, in Table 5.3. Except for one case, the agreement between the predicted and measured resonant frequencies are within 5% or better.

The effects of varying the insert permittivity and thickness on the input impedance of the MSDRA can be seen in the Smith charts of Figures 5.18 and 5.19, which were generated using FDTD simulations. In Figure 5.18, the reflection coefficient of the MSDRA is plotted for various values of insert thickness, for a fixed permittivity of $\varepsilon_r = 20$. Without any insert, the DRA is poorly matched, with the loop of the impedance locus occurring in the lower right quadrant of the Smith chart. As the insert thickness is increased, a progressively better match is obtained, as the loop of the impedance locus moves towards the middle of the Smith chart. A similar trend occurs in Figure 5.19 where, in this case, the insert thickness is held constant at $t = 0.635$ mm and the permittivity is increased from 20 to 100. Thus, using an appropriate combination of insert permittivity and thickness, the impedance of the MSDRA can be matched to that of the microstrip feed line. The optimum coupling can thus be thought of as a function of an "effective insert thickness" (t_{eff}) where $t_{eff} = t \sqrt{\varepsilon_i}$. This gives the designer a degree of flexibility in choosing the physical insert thickness and permittivity for optimal coupling.

There are two considerations to keep in mind when choosing values for insert thickness and permittivity. The first is to ensure that the insert itself does not radiate. The dielectric waveguide model equations can be used with the insert parameters to ensure that the resonant frequency of the insert is well above the desired frequency of operation. The second is the impedance bandwidth obtained by the various inserts. In general, the higher the insert permittivity, the narrower the impedance bandwidth, for a given insert thickness. MSDRAs with higher permittivity inserts also show a greater sensitivity to their position with respect to the open end of the microstrip line. Since one of the objectives of using the MSDRA is to obtain a wide impedance bandwidth, the insert permittivity should be chosen accordingly. This places an upper bound on permittivity.

Based on the investigations carried out in [23], a set of guidelines was proposed for designing the MSDRA:

(1) Determine the dimensions (a, h, d) of the DRA using the dielectric waveguide model equations for the desired resonant frequency, radiation Q-factor (for estimating the expected bandwidth), and the location of higher-order modes (to ensure they are far enough away not to add to the cross-polarisation levels inherent in the desired mode). The permittivity of the DRA should be chosen to be less than or equal to 12, for wideband operation.
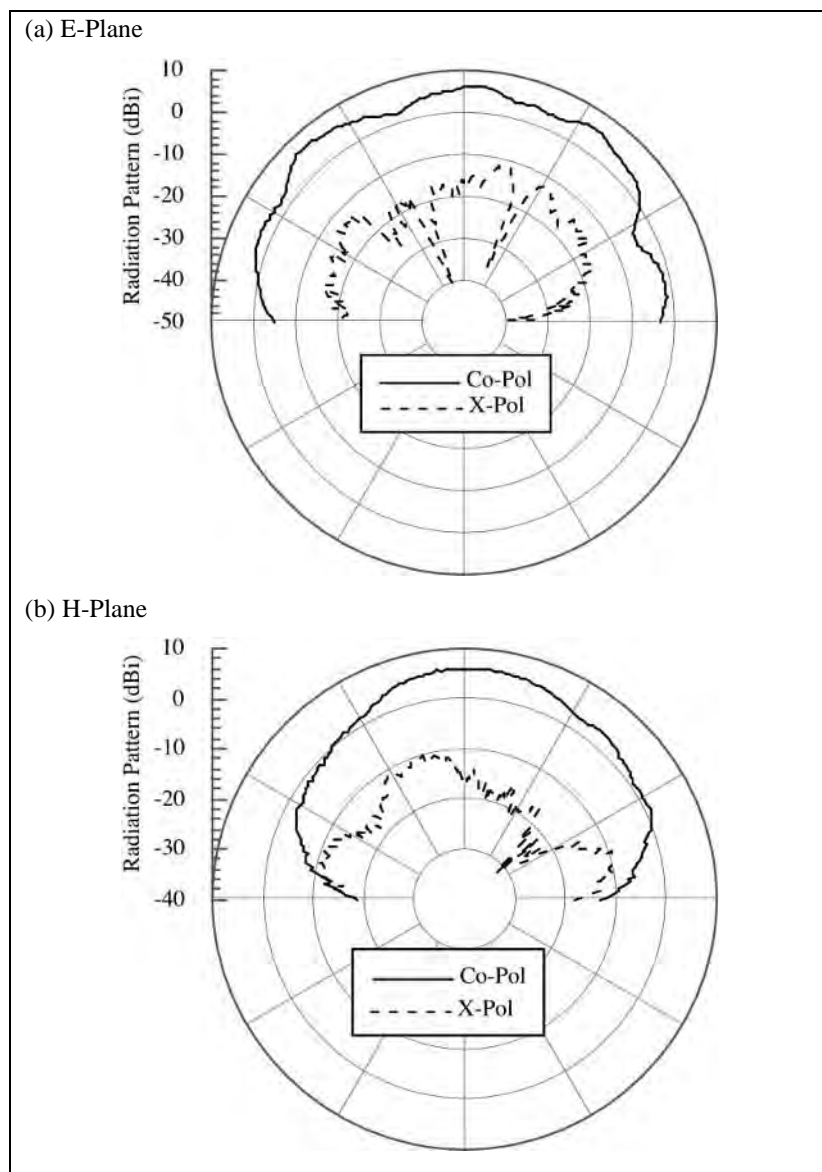
Figure 5.17 Radiation patterns of a MSDRA

t (mm)	ε_i	H_{eff} (mm)	ε_{eff}	f_{oe} (GHz)	f_{om} (GHz)	% Error $(f_{om}-f_{oe})/f_{om}$
0	-	3.935	6.9	14.8	15.2	2.3%
0.25	20	4.185	7.2	14.5	14.7	1.4%
0.635	20	4.750	7.6	14.0	14.5	3.4%
1.0	20	4.935	7.9	13.5	13.9	2.9%
0.25	40	4.185	7.3	14.5	14.7	1.4%
0.635	40	4.750	7.8	13.9	13.7	-1.5%
1.0	40	4.935	8.3	13.2	12.9	-2.3%
0.25	100	4.185	7.3	14.5	14.7	1.4%
0.635	100	4.750	7.9	13.8	13.1	-5.3%
1.0	100	4.935	8.5	13.0	10.8	-21%

Table 5.3 Effects of various inserts on MSDRA parameters
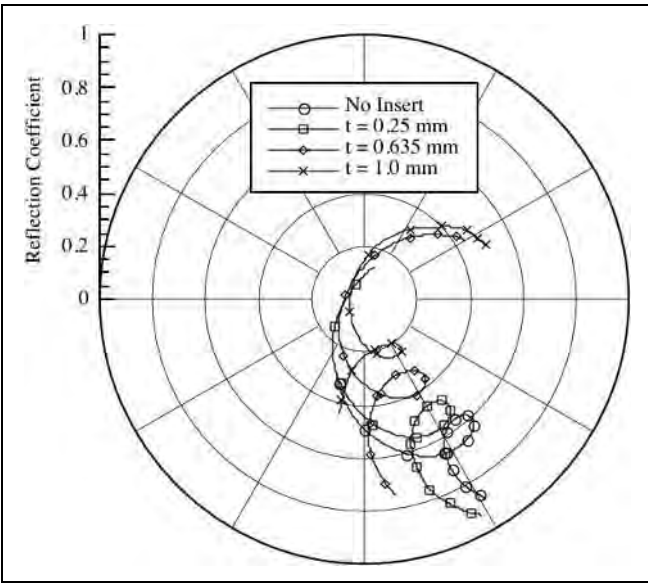
Figure 5.18 Effect of varying insert thickness for a constant permittivity ($\varepsilon_r = 20$)
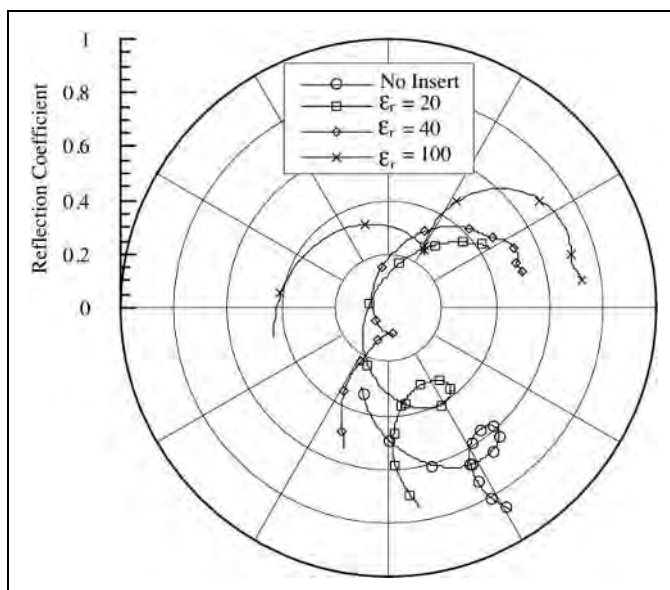
Figure 5.19 Effect of insert permittivity for a constant thickness ($t = 0.635$ mm)

(2) Choose an insert permittivity between 20 to 40 and an insert thickness (t) such that $0.1 < T < 0.3$ (where $T = t/(t+h)$). Ensure that the resonant frequency of the isolated insert is well above the desired frequency of operation by substituting the insert parameters into the dielectric waveguide model equations.

(3) Estimate the resonant frequency of this MSDRA structure by using the dielectric waveguide model equations with the effective permittivity (ε_{eff}) and effective height (H_{eff}) based on the insert parameters chosen in (2). The insert parameters or the DRA dimensions might require some adjustment if there is a significant shift in the desired resonant frequency.

(4) Once fabricated, some experimental optimisation may be required to maximise the coupling. The simplest form of optimisation is done by adjusting the position of the MSDRA with respect to the open end of the microstrip line. If this is not sufficient, a second iteration of the MSDRA parameters may be required.

The MSDRA has also been used with a probe feed, as shown in Figure 5.20. This configuration is closely related to the air gap configuration for the probe-fed DRA described in Section 5.3.1. In this case, the permittivity (ε_i) of the insert is less than the permittivity (ε_r) of the DRA. A bandwidth increase of up to 40% has been achieved for L-Band MSDRAs, with only a modest increase in the resonant frequency [9].
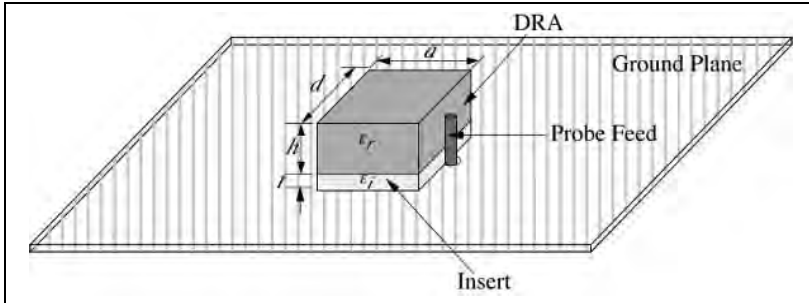
Figure 5.20 Probe-fed MSDRA

5.4.4   Stub Matching

A final method of impedance matching which is considered in this chapter is the use of a microstrip stub. Figure 5.21 shows a microstrip-fed MSDRA and an aperture-fed DRA. In each case, the microstrip line can be extended to form a stub, whose length (s) can be adjusted to improve the impedance match. This technique is commonly used in aperture-fed microstrip patches and it is a convenient method since it makes use of the existing microstrip line, requiring no additional matching circuit. Figure 5.22 shows an example of a microstrip-fed Ku-Band MSDRA whose impedance match is tuned by adjusting the length of the microstrip stub. The negative values of s in Figure 5.22 indicate that the MSDRA overhangs off the end of the microstrip line. In this case, a stub with a length of $s = 0$ results in the best match. This corresponds to the case where the edge of the MSDRA is flush with the end of the microstrip line.

5.5   BANDWIDTH ENHANCEMENT USING MULTIPLE DRAS

An alternative method to achieving wideband or dual-band operation is by using multiple DRAs, with each DRA resonating at a different frequency. This approach is illustrated, using a two lumped-element RLC circuit model, in Figure 5.23, to predict the return loss behaviour of the multiple DRAs. On their own, each resonator will have a resonant frequency of f_l and f_u, and Q-factors Q_l and Q_u. If these

two frequencies are close to each other, then when the two resonators are cascaded together, a wideband response will result (as shown in Figure 5.24b).
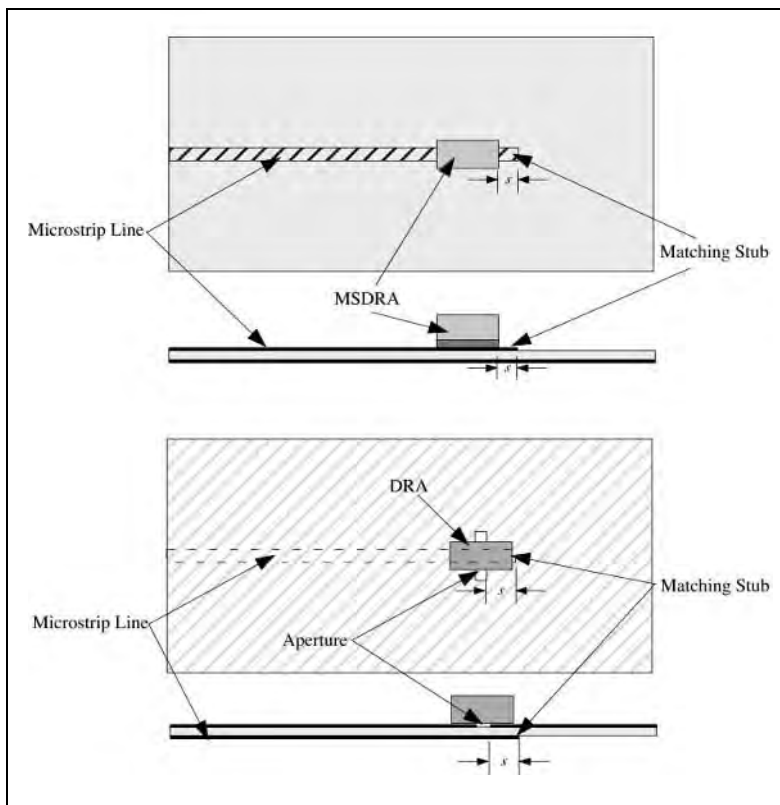
Figure 5.21 Stub matching for a microstrip-fed MSDRA and aperture-fed DRA

If the resonant frequencies are spaced further apart, then a dual-band operation will result (as shown in Figure 5.24c). The boundary between a dual-band and a wide-band response is somewhat arbitrary and depends on the minimum return loss required by the application. One convenient definition, depicted in Figure 5.24a, is given by:

$$\left(\Delta f_u + \Delta f_l\right) = 2\left(f_u - f_l\right) \tag{5.12}$$
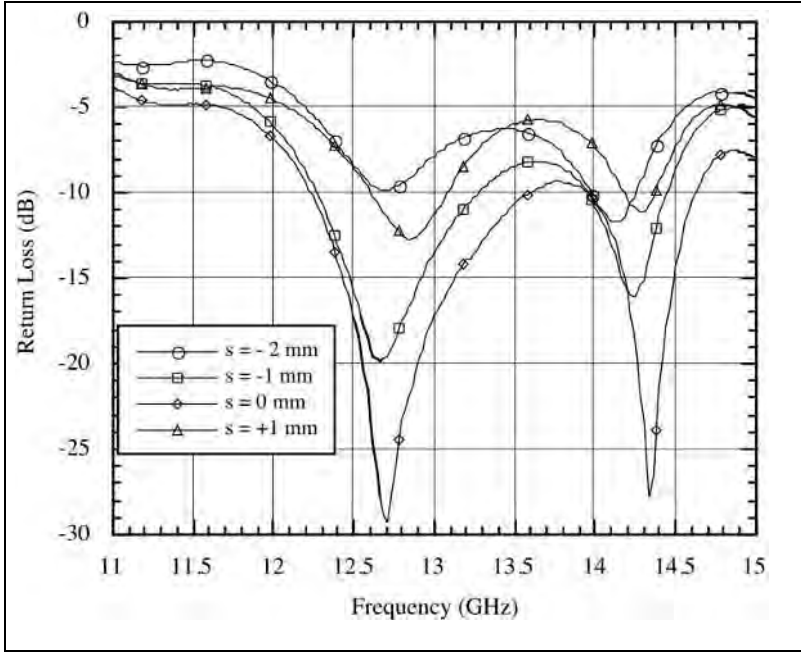
Figure 5.22 Effect of stub length on the return loss of a MSDRA

where Δf is the bandwidth of the 3 dB response of each resonator. Equation (5.12) can be re-written in terms of the Q-factor:

$$\left(\frac{f_u}{Q_u} + \frac{f_l}{Q_l}\right) = 2(f_u - f_l) \tag{5.13}$$

Given the resonant frequencies and Q-factors of the two resonators, equation (5.13) can be used to predict whether a wideband or dual-band performance is expected. If the left term is less than the right term, then a wideband response is obtained. If the left term is greater than the right, then the response is a dual-band one.

In practice, the multiple DRAs can be arranged in a co-planar or stacked configuration. Examples of each are presented in the following sections.
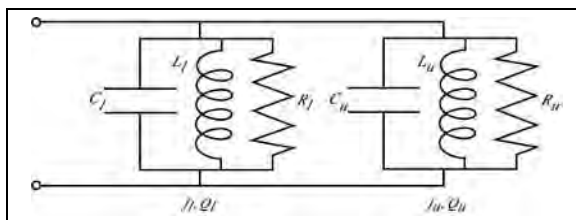
Figure 5.23 Lumped element impedance model for a 2-DRA configuration

5.5.1 Co-planar Parasitic DRAs

The configuration used to investigate the performance of a DRA loaded with co-planar parasitic elements is shown in Figure 5.25 [24]. The centre DRA in this configuration is fed by aperture coupling from a microstrip line, while the outer DRAs are electromagnetically coupled to the centre DRA. This approach is similar to that of co-planar parasitic microstrip patches. The potential advantage of this technique is that each resonator can be individually tuned for either a wide impedance bandwidth or a multi-frequency band overall response. For this study, three rectangular DRAs fabricated from material with $\varepsilon_r = 20$ were used. Each DRA was designed to resonate at a slightly different frequency (5.12 GHz, 5.77 GHz, and 5.40 GHz) and with individual bandwidths of approximately 2.5%, based on the dielectric waveguide model for isolated DRAs. The measured resonant frequencies of the individual DRAs were somewhat higher than the predicted frequencies, and the individual bandwidths were between 3.4% and 5.8%. When the DRAs are combined, as shown in Figure 5.25, with the centre DRA fed by the slot and the outer DRAs electromagnetically coupled, the combined structure has a bandwidth of 17%. The return loss is shown in Figure 5.26, while the H-plane radiation pattern is shown in Figure 5.27. The combined DRAs still radiate like a short horizontal magnetic dipole.

By tuning the individual DRAs, the locations of the resonances can be altered for either a dual or triple frequency operation, which is desirable for certain applications. This configuration allows for flexible design while still maintaining a fairly compact structure [24, 25]. The disadvantage is that it may not be suitable for array applications, since a fairly wide separation would be required between array elements, which would result in grating lobes. This approach is not limited to rectangular DRAs. A similar configuration, using three identical cylindrical DRAs was investigated in [26].

A second configuration involving co-planar DRAs is shown in Figure 5.28. It consists of a cylindrical DRA embedded within an annular DRA, both of which are in contact with the feed probe [27]. This configuration makes use of the two-DRA model, with the resonant frequency and Q-factor of each resonator adjustable to elicit a wideband or dual-band response. An air gap between the DRAs and the ground plane is also used to further enhance the bandwidth. In the example described in [27], bandwidths of over 30% were achieved. This relatively high permittivity results in a fairly compact DRA, whose overall diameter $(2A_l)$ is approximately $\lambda/2$, which makes it a suitable candidate as an array element.
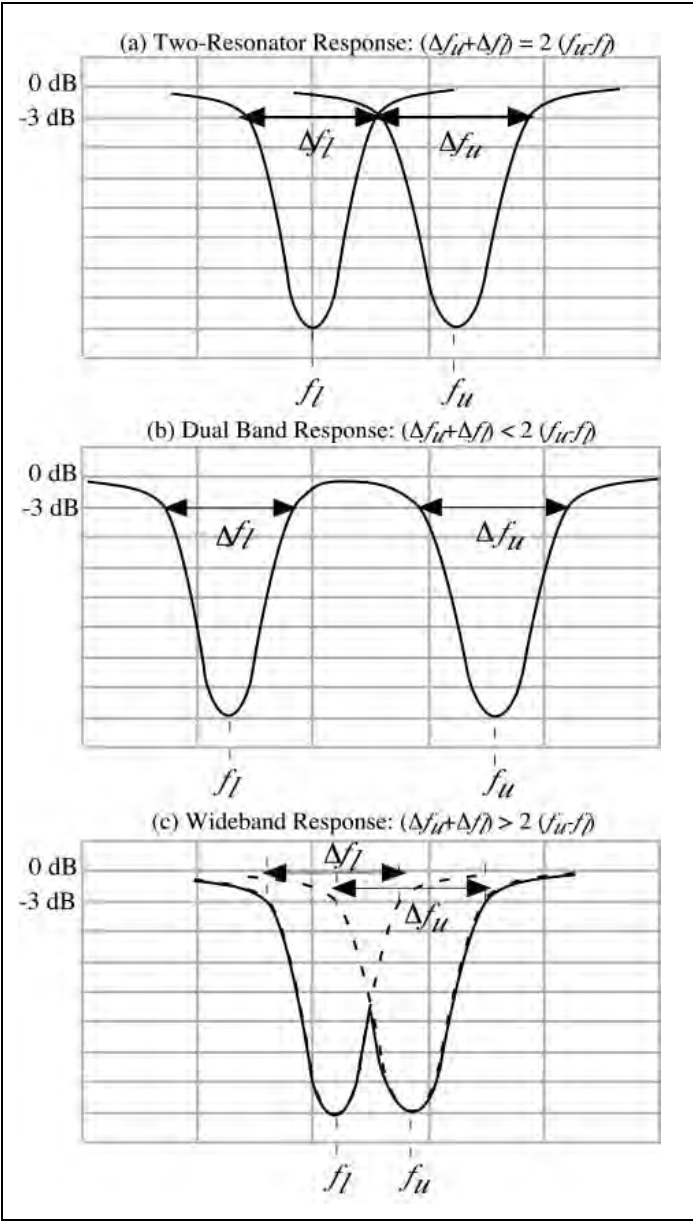
Figure 5.24 Dual band and wideband response for a two-DRA configuration
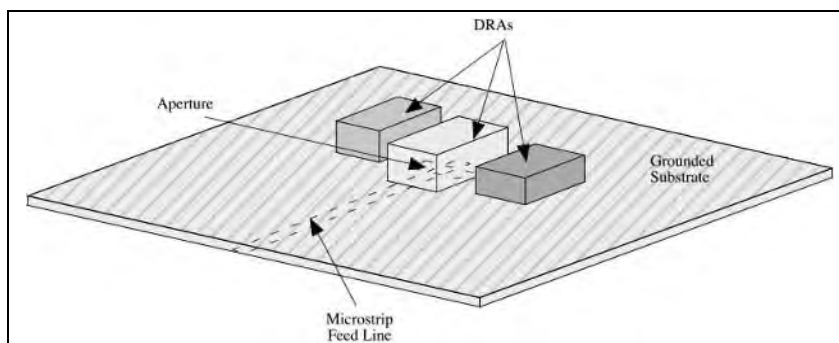
Figure 5.25 Wideband configuration using three DRAs
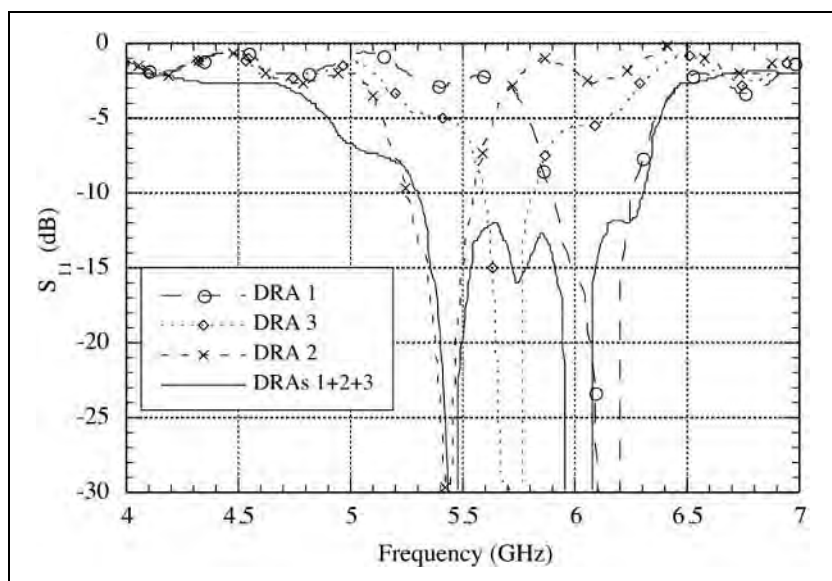
Figure 5.26 Return loss of the three-DRA configuration. From [24] © 1997 IEEE. Reprinted with permission.
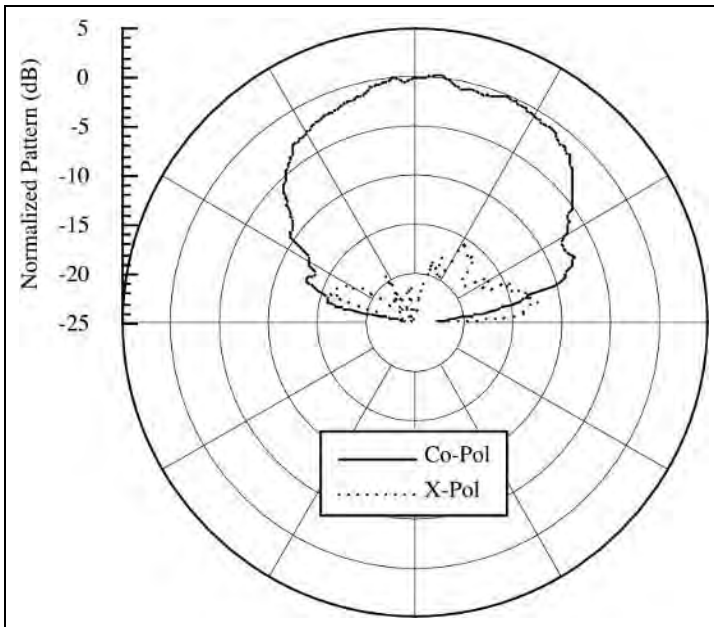
Figure 5.27 Measured H-plane pattern of the 3-DRA configuration. From [24] © 1997 IEEE. Reprinted with permission.

5.5.2 Stacked DRAs

A second approach using multiple DRAs for enhancing bandwidth involves stacking DRAs atop one another. The concept is similar to that of the stacked microstrip patch. A typical configuration is shown in Figure 5.29 involving cylindrical DRAs. The lower DRA is excited by a probe feed, while the upper DRA is electromagnetically coupled. Again, this technique offers the advantage that each DRA can be individually tuned for either wideband or dual-band operation. An example of the performance of stacked DRAs is taken from [28]. The 10 dB return loss bandwidth of the probe-fed DRA 1 was measured to be 10%. In the stacked configuration, with DRA 1 designed to resonate at about 12 GHz and DRA 2 designed to resonate at about 10 GHz, the impedance bandwidth was measured to be 25%. This principle is also valid for other feeding arrangements, such as slot-fed or microstrip-fed DRAs, as demonstrated in [26], while in [29], two annular DRAs are stacked, with the probe feeding the $TM_{01\delta}$ mode. The main disadvantage of this configuration is that the geometry is not very low profile; however, they may still be suitable candidates for array applications.
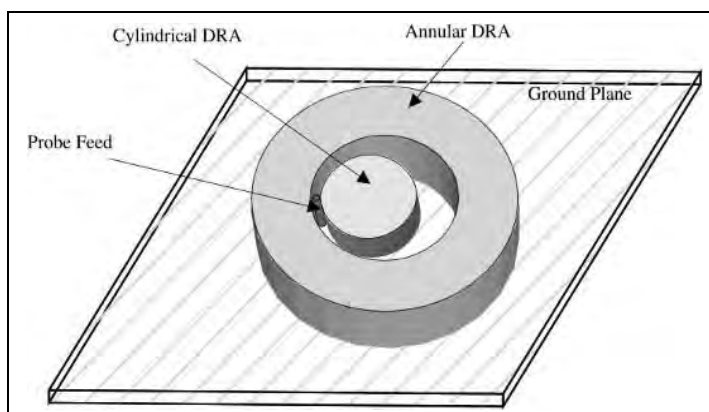
Figure 5.28 Annular DRA with embedded cylindrical DRA. Adapted from [27] © 1997 IEE. Reprinted with permission.
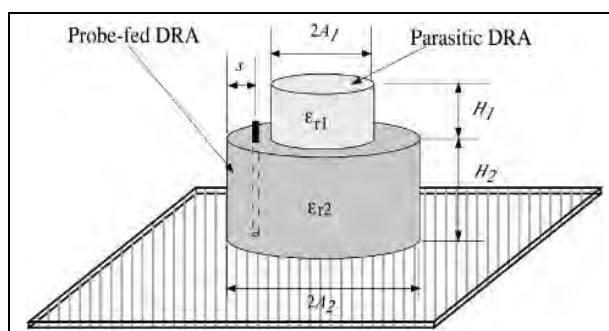
Figure 5.29 Stacked cylindrical DRAs. Adapted from [28] © 1989 IEE. Reprinted with permission.

5.6   SUMMARY

It was observed at the beginning of this chapter that by simply altering the aspect ratio of rectangular or cylindrical DRAs, a wide range of bandwidth is achievable, for a given frequency and dielectric constant. To further extend the bandwidth range, various enhancement techniques were presented. These techniques fell into three categories: lowering the inherent Q-factor of the resonator, using impedance matching techniques, and using multiple DRAs. Each of these approaches has its advantages and drawbacks. Bandwidths of up to 40% have been reported, making DRAs attractive candidates for many communication applications. These bandwidth enhancement techniques offer the antenna designer a wide choice of implementation, allowing for a great degree of flexibility.

REFERENCES

[1] A.A. Kishk, A.W. Glisson and J.P. Junker, "Study of Broadband Dielectric Resonators," *Proceedings of the 1999 Antenna Applications Symposium*, Allerton Park, Monticello, Illinois, Sept. 1999, pp. 45-68.

[2] R.K. Mongia and A. Ittipiboon, "Theoretical and Experimental Investigations on Rectangular Dielectric Resonator Antennas," *IEEE Transactions on Antennas and Propagation*, Vol. 45, No. 9, Sept. 1997, pp. 1348 - 1356.

[3] M. Cooper, A. Petosa, A. Ittipiboon and J.S. Wight, "Investigation of Dielectric Resonator Antennas for L-Band Communications," *Antenna Technology and Applied Electromagnetics Symposium, ANTEM '96*, Ottawa, Canada, Aug. 1996, pp. 167-170.

[4] G.P. Junker, A.A. Kishk, A.W. Glisson and D. Kajfez, "Effects of Fabrication Imperfections for Ground-Plane-Backed Dielectric Resonator Antennas with Coaxial Excitation," *IEEE Antennas and Propagation Magazine*, Vol. 37, No. 1, Feb. 1995, pp. 40-47.

[5] M. Verplanken and J. Van Bladel, "The Electric Dipole Resonances of Ring Resonators of Very High Permittivity," *IEEE Trans. Microwave Theory and Techniques,* Vol. 24, Feb. 1976, pp. 108-112.

[6] R. K. Mongia, A. Ittipiboon, P. Bhartia and M. Cuhaci, "Electric Monopole Antenna using a Dielectric Ring Resonator," *IEE Electronics Letters*, Vol. 29, No. 17, 1993, pp. 1530-1531.

[7] S.M. Shum and K.M. Luk, "Characteristics of Dielectric Ring Resonator Antenna with Air Gap," *IEE Electronics Letters*, Vol. 30, No. 4, Feb. 1994, pp. 277-278.

[8] A. Petosa, A. Ittipiboon, Y.M.M. Antar, D. Roscoe and M. Cuhaci, "Recent Advances in Dielectric Resonator Antennas," *IEEE Antennas and Propagation Magazine*, Vol. 40, No. 3, June 1998, pp. 35-48.

[9] M. Cooper, "Investigation of Current and Novel rectangular Dielectric Resonator Antennas for Broadband Applications at L-Band," Masters Thesis, Carleton University, 1997.

[10] K.M. Luk, M.T. Lee, K.W. Leung and E.K.N. Yung, "Technique for Improving Coupling Between Microstripline and Dielectric Resonator Antenna," *IEE Electronics Letters,* Vol. 35, No. 5, Mar. 1999, pp. 357-358.

[11] K.W. Leung, W.C. Wong, K.M. Luk and E.K.N. Yung, "Circular Polarized Dielectric Resonator Antenna Excited by Dual Conformal Strips*," IEE Electronics Letters*, Vol. 36, No. 6, Mar. 2000, pp. 454-455.

[12] A. Ittipiboon, M. Cuhaci, A. Petosa, D. Roscoe, R. Larose and R.K. Mongia, "Broadband Nonhomogenous Multi-Segment Dielectric Resonator Antennas", United States Patent No. 5,952,972, Sept. 14, 1999.

[13] M.T. Birand and R.V. Gelsthorpe, "Experimental Millimetric Array Using Dielectric Radiators Fed by Means of Dielectric Waveguide," *IEE Electronics Letters,* Vol. 17. No. 18, Sept. 1981, pp. 633-635.

[14] A. Petosa, R.K. Mongia, A. Ittipiboon and J.S. Wight, "Investigation on a Microstrip-Fed Series Array of Dielectric Resonator Antennas," *IEE Electronics Letters*, Vol. 31, No.16, Aug. 1995, pp. 1306-1307.

[15] A. Petosa, R.K. Mongia, A. Ittipiboon and J.S. Wight, "Investigations of Various Feed Structures for Linear Arrays of Dielectric Resonator Antennas," *IEEE AP-S Conference*, Newport Beach, June 1995, pp. 1982-1985.

[16] A. Petosa, A. Ittipiboon, M. Cuhacia and R. Larose, "Bandwidth Improvement for a Microstrip-Fed Series Array of Dielectric Resonator Antennas," *IEE Electronics Letters*, Mar. 1996, Vol. 32 No. 7, pp. 608-609.

[17] M.G. Keller, M. Fleury, E. Philippouci, A. Petosa and M.B. Oliver, "Circularly Polarized Dielectric Resonator Antenna Array," *URSI-Digest*, Baltimore, MD, July 1996, pp. 7.

[18] A. Petosa, M. Cuhaci, A. Ittipiboon, N.R.S. Simons and R. Larose, "Microstrip-Fed Stacked Dielectric Resonator Antenna," *Antenna Technology and Applied Electromagnetics Symp ANTEM '96*, Ottawa, Canada, Aug. 1996, pp. 705-708.

[19] N.R.S. Simons, A. Petosa, M. Cuhaci, A. Ittipiboon, R. Siushansian, J. Lovetri and S. Gutschling, "Validation of Transmission Line Matrix, Finite-Integration Technique, and Finite-Diefference Time-Domain Simulations of a Multi-Segment Dielectric Resonator Antenna," *Applied Computational Electromagnetic Symposium (ACES-97)*, Monterey, CA, Mar. 1997, pp. 1425-1430.

[20] A. Petosa, A. Ittipiboon, M. Cuhaci and R. Larose, "Low Profile Phased Array of Dielectric Resonator Antennas," *IEEE International Symposium Phased Array Systems and Technology*, Oct. 1996, pp. 182-185.

[21] A. Petosa, R. Larose, A. Ittipiboon and M. Cuhaci, "Active Phased Array of Dielectric Resonator Antennas," *IEEE Antennas and Propagation Symposium*, Montreal, Canada, July 1997, pp. 690-693.

[22] A. Petosa, R. Larose, A. Ittipiboon and M. Cuhaci, "Microstrip-fed array of multi-segment dielectric resonator antennas," *IEE Proceedings - Microwaves Antennas and Propagation*, Vol. 144, No. 6, Dec. 1997, pp. 472-476.

[23] A. Petosa, N.R.S. Simons, R. Siushansian, A. Ittipiboon and M. Cuhaci, "Design and Analysis of Multi-Segment Dielectric Resonator Antennas," *IEEE Trans. Antennas and Propagation*, May 2000, pp. 738-742.

[24] Z. Fan and Y.M.M. Antar, "Slot-Coupled DR Antenna for Dual-Frequency Operation," *IEEE Trans. Antennas and Propagation*, Vol. 45, No. 2, Feb. 97, pp. 306-308.

[25] Z. Fan, Y.M.M. Antar, A. Ittipiboon and A. Petosa, "Parasitic Coplanar Three-Element Dielectric Resonator Antenna Subarray," *IEE Electronics Letters,* Vol. 32, No. 9, Apr. 1996, pp. 789-790.

[26] R.N. Simons and R.Q. Lee, "Effect of Parasitic Dielectric Resonators on CPW/Aperture-Coupled Dielectric Resonator Antennas," *IEE Proceedings-H* Vol. 140, No. 5, Oct. 1993, pp. 336-338.

[27] A. Sangiovanni, J.Y. Dauvignac and C. Pichot, "Embedded Dielectric Resonator Antenna for Bandwidth Enhancement," *IEE Electronics Letters*, Vol. 33, No. 25, Dec. 1997, pp. 2090-2091.

[28] A.A. Kishk, B. Ahn and D. Kajfez, "Broadband Stacked Dielectric-Resonator Antennas," *IEE Electronics Letters*, Vol. 25, No. 18, Aug. 1989, pp. 1232-1233.

210

[29] S.M. Shum and K.M. Luk, "Stacked Annular Ring Dielectric Resonator Antenna Excited by Axi-Symmetric Coaxial Probe," *IEEE Transactions on Antennas and Propagation*, Vol. 43, No. 8, Aug. 1995, pp. 889-892.

This page intentionally left blank

CHAPTER 6

Low-Profile Dielectric Resonator Antennas

Karu Esselle

Macquarie University
Sydney
Australia

6.1   INTRODUCTION

Low-profile antennas are required for many modern communication applications. One example is an antenna in a notebook computer connected to a wireless computer network. The antenna may itself be attached to a wireless networking card in PC (formerly PCMCIA) format. For applications like this, it is necessary to design antennas with low profiles. In this chapter, we consider an antenna in which the height is significantly less than the other dimensions as a low-profile antenna.

Designing low-profile dielectric-resonator antennas is a challenge. When the height of a practical dielectric-resonator antenna is significantly reduced, the field distribution in the DR becomes more dependent on secondary items such as coupling apertures and feeds. Then, the field distributions predicted by simplified analytical methods become questionable. The resonance frequencies calculated using approximate methods tend to loose accuracy. This is especially the case when the dielectric constant of the DR is not very high. Furthermore, it becomes harder to achieve a reasonable radiation resistance and good input matching with a 50Ω feed. Therefore, more accurate numerical methods are preferred for the analysis and design of low-profile dielectric-resonator antennas made out of low or medium permittivity material. Such methods include the following differential equation-based methods: the finite-different time-domain (FDTD) method, the transmission line method (TLM) and the finite-element method (FEM), as well as the integral equation-based method of moments (MoM).

In this chapter, we discuss several low-profile DR antennas and the methods available to analyse and design them.

6.2   LINEARLY POLARISED RECTANGULAR DR ANTENNAS

Among the low-profile DR antennas, the rectangular DR antennas are perhaps the easiest to fabricate. Their operation is similar in principle to standard (high-profile) rectangular DR antennas. Although they can be designed to operate in a higher order mode, dominant mode operation is more common as this requires the

smallest dielectric resonators available. The most common coupling methods used for low-profile, rectangular DR antennas are the aperture (slot) coupling and co-planar waveguide (CPW) coupling methods.

6.2.1 Aperture-Coupled Rectangular DR Antennas

A low-profile, aperture-coupled, rectangular DRA is shown in Fig. 6.1 [1]. This antenna was developed to prove the point that medium permittivity rectangular DR antennas can be designed to have a low profile. This DRA has a length-to-height ratio of about 6, whereas the original rectangular DR antennas have a ratio of 2.
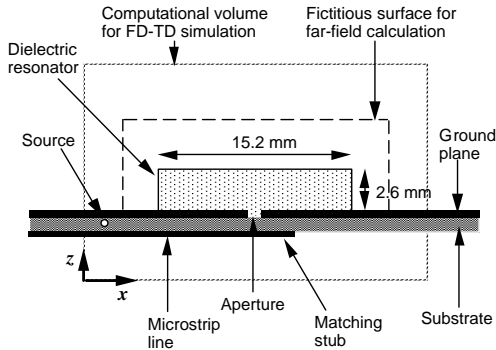
Fig. 6.1 A low-profile, aperture-coupled, rectangular LP DRA (from [1] © 1996 IEEE Transactions on Antennas and Propagation)

The rectangular DR has dimensions of 15.2 (L) × 7.0 (W) × 2.6 (H) mm, and a dielectric constant of 10.8. Like in a standard aperture-coupled rectangular DRA, the low-profile DR is placed on the ground-plane side of a substrate. It is fed by a 50Ω microstrip line through a rectangular 1.2 × 3.4 mm aperture etched in the ground plane. The aperture is perpendicular to both the microstrip line and the DR longer dimension (*i.e.* the 1.2 mm side is in the *x* direction.) This arrangement couples the electromagnetic field in the microstrip feed to the dominant mode of the DR through the aperture. One may consider that the aperture behaves as a magnetic monopole parallel to the y axis. The substrate used in this sample antenna has a thickness of about 0.64 mm, and a dielectric constant of 10.5. The length of the matching stub is 0.8 mm from the centre of the aperture.

At the frequency of 11.6 GHz, this DRA is almost perfectly matched to the 50Ω input, giving a return loss of 38 dB. Its radiation pattern at that frequency is similar to that of a magnetic monopole, as expected from the dominant mode operation. The DRA is also well matched, with a return loss of 25 dB, at 13.0 GHz frequency but the pattern is more directional. This increased directivity appears to be due to the influence of a higher-order mode but that aspect has not been investigated further.

For radiation pattern measurements, the ground plane of the antenna has been extended to form a circle of about 1.2 m in diameter. Microwave absorbers have been placed around the edge of this ground plane in order to minimise edge effects. The measurements have been done in a 12 m antenna range inside an anechoic chamber.

FDTD Analysis

The theoretical radiation patterns of the DRA have been obtained using the FDTD method [2]. The FDTD computational volume used for the simulation fully encloses the dielectric resonator, the aperture and the matching stub. In the simulation, the substrate, the ground plane and the microstrip line are assumed infinitely large and are partly enclosed by the computational volume, as shown in Fig. 6.1. The size of the volume is 50 (L) x 23 (W) x 14 (H) mm, and it contains about 2 million FDTD cells.

The electromagnetic source is defined inside the microstrip line, sufficiently far from the aperture, to prevent higher-order evanescent modes (generated by the source) from reaching the aperture. The source waveform is a Gaussian-modulated sinusoid at 10 GHz. The infinite extent of the substrate, ground plane, microstrip line and the free space are represented by imposing a combination of Mur's first- and second-order absorbing boundary conditions at the boundary of the computational volume [3].

The far field of the antenna has been obtained by applying the field equivalence principle, directly in the time domain, over a fictitious surface enclosing the dielectric resonator (see Fig. 6.1). The image of this fictitious surface on the ground plane has been taken into account, assuming that the ground plane is infinitely large and perfectly conducting. Frequency-domain near and far fields are obtained using standard fast Fourier transform techniques. All calculations have been done using a Cray Y/MP four-processor supercomputer in double precision.

MoM Analysis

This aperture-coupled rectangular DRA can also be accurately analysed using the Method of Moments [4]. The volume-integral-equation formulation for this analysis is outlined here, although a surface-integral-equation approach is also possible. The formulation is based on the equivalent principle. The microstrip feed, denoted by S_C, is replaced by an equivalent surface electric current J_C. The coupling aperture, denoted by S_S, is replaced by an equivalent magnetic current M_S. The dielectric substrate volume is denoted by V_{d1} and the DR by V_{d2}. They are replaced by their equivalent volume electric polarisation currents J_{d1} and J_{d2} respectively, which exist in free space[1].

---

[1] The use of equivalent volume polarisation currents to replace the substrate volume is not an efficient approach but it is described here for simplicity. These volumetric currents can be avoided by using substrate Green's functions for the microstrip line instead of the free-space Green's function [5].

In this analysis both dielectric volumes are assumed to be homogeneous and lossless and the ground plane is assumed to be infinite. The ground plane divides the problem into two separate sub-problems, one for the volume above the ground plane and the other for the region below it. For each sub-problem, the ground plane is removed by using the image theory. The equivalent magnetic current distribution above the aperture, M_s^+, is given by

$$\vec{M}_S^+ = \vec{E}_S \times \hat{z} \tag{6.1}$$

where $\vec{E}_S$ is the electric field in the aperture and $\hat{z}$ is the unit vector perpendicular to the ground plane. Below the aperture there is an equivalent magnetic current of M_s^- which, to ensure the continuity of the tangential electric field across the aperture, is set equal to $-M_s^+$. An integral equation can be derived by considering the continuity of the tangential magnetic field across the aperture:

$$\vec{H}_{\tan}[\vec{J}_{d2}(\vec{r})] + \vec{H}_{\tan}[2\vec{M}_S(\vec{r})] - \vec{H}_{\tan}[\vec{J}_{d1}(\vec{r})] - \vec{H}_{\tan}[\vec{J}_C(\vec{r})] = 0,$$
$$\text{for } \vec{r} \in S_S \text{ (Aperture)} \tag{6.2}$$

Considering that the total tangential electric field on the microstrip line is zero, we have:

$$-\vec{E}_{\tan}[\vec{J}_c(\vec{r})] - \vec{E}_{\tan}[\vec{J}_{d1}(\vec{r})] + \vec{E}_{\tan}[\vec{M}_S(\vec{r})] = \vec{E}_{\tan}^i(\vec{r}),$$
$$\text{for } \vec{r} \in S_c \text{ (Feedline)} \tag{6.3}$$

where E^i is the excitation field. Two more integral equations can be obtained by considering the volume polarisation currents in each dielectric:

$$\frac{\vec{J}_{d2}(\vec{r})}{j\omega\varepsilon_0(\varepsilon_{r2}-1)} - \vec{E}[\vec{J}_{d2}(\vec{r})] - \vec{E}[\vec{M}_S(\vec{r})] = \vec{E}^i(\vec{r}), \quad \text{for } \vec{r} \in V_{d2} \text{ (DR)} \tag{6.4}$$

$$\frac{\vec{J}_{d1}(\vec{r})}{j\omega\varepsilon_0(\varepsilon_{r1}-1)} - \vec{E}[\vec{J}_c(\vec{r})] - \vec{E}[\vec{J}_{d1}(\vec{r})] + \vec{E}[\vec{M}_S(\vec{r})] = \vec{E}^i(\vec{r}),$$
$$\text{for } \vec{r} \in V_{d1} \text{ (Substrate)} \tag{6.5}$$

where ω is the angular frequency, ε_0 is the permittivity of free space, and ε_{r1} and ε_{r2} are the relative permittivity of the substrate and the DR, respectively. By applying the conventional Method of Moments, these coupled integral equations can be converted into a matrix problem using suitable basis and testing functions (e.g. piecewise rectangular pulse basis functions and point matching at the centre of each basis). Then the matrix problem is solved to obtain equivalent electric, magnetic and polarisation currents. The radiation pattern of the antenna can be computed from these currents.

Numerical Results

Fig. 6.2 shows the theoretical (FDTD) and measured far-field patterns of the low-profile DRA in the H-plane at 11.6 GHz. The pattern was measured using a spinning linear-polarised horn antenna in order to simultaneously estimate the cross-polarisation level. Not only does the measured pattern compare extremely well with the theoretical one, but also it reveals that the cross-polarisation is at least 15 dB below the co-polarisation within the 3 dB beamwidth. The MoM theoretical results are almost identical to the FDTD theoretical results [6].
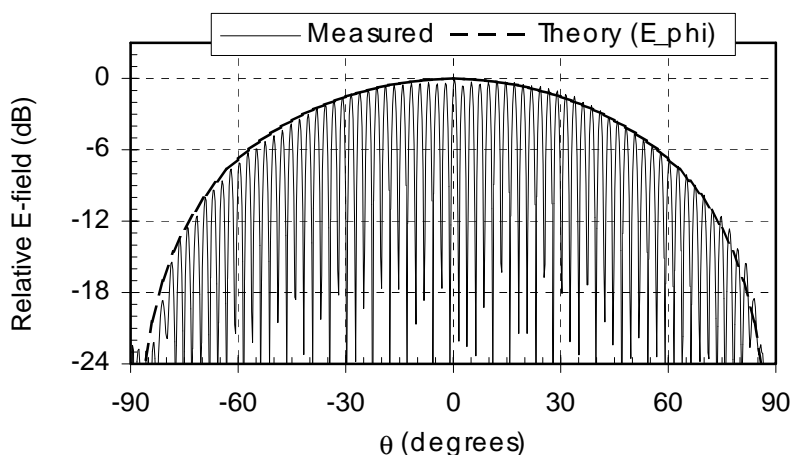
Fig. 6.2 The theoretical and measured radiation patterns of the DRA in the H-plane (*i.e. y-z* plane in Fig. 6.1) at 11.6 GHz (from [1] © 1996 IEEE Transactions on Antennas and Propagation)

The H-plane pattern in Fig. 6.2 approximately follows the $\cos\theta$ shape of the H-plane pattern of an elemental magnetic dipole. For example, at 30° the magnetic dipole pattern drops to -1.2 dB and the DRA theoretical pattern drops to -1.5 dB. At 60°, they are down to -6.0 dB and -6.8 dB respectively. Therefore, even in the ideal case with an infinite ground plane (assumed in the calculations), the DRA seems to have slightly higher directivity than an elemental magnetic monopole. On the other hand, the theoretical H-plane pattern of a high-profile rectangular DRA follows the $\cos\theta$ variation almost exactly [2]. This difference between the low-profile and high-profile rectangular DRA H-plane patterns may increase as the aspect ratio of the dielectric resonator is further increased, but it is not expected to be practically significant.

Fig. 6.3 compares the theoretical and measured patterns of the DRA in the E-plane at 11.6 GHz. The theoretical results, which are based on an infinite ground

plane assumption, predict an almost omni-directional E-plane pattern, but the measured pattern shows some ripples superimposed on a gradual decrease as |θ| increases. However, the agreement between the theoretical and measured patterns is very good (within 1.5 dB) for directions within ±30° from boresight, and the cross-polarisation is more than 15 dB below the co-polarisation for the same directions.
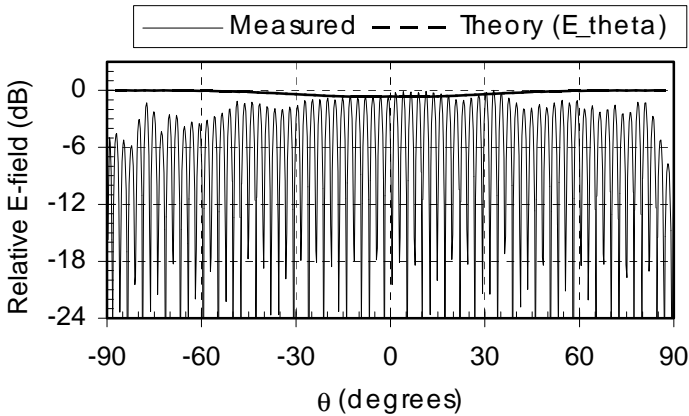

Fig. 6.3 The theoretical and measured radiation patterns of the DRA in the E-plane (*i.e. x-z* plane) at 11.6 GHz (from [1] © 1996 IEEE Transactions on Antennas and Propagation)

The difference between the measured and theoretical E-plane patterns in Fig. 6.3 is probably due to the truncated ground plane used for measurements (while an infinite ground plane is assumed in the theoretical analysis). Similar discrepancies have been found in the past between theoretical [2] and measured [7] patterns of a standard (high-profile) rectangular DRA when an infinite ground plane is assumed in the calculations. Microwave absorbers attached to the ground plane edge almost certainly caused the rapid decrease in the measured pattern at about θ = ±80°.

Fig. 6.4 compares the theoretical and measured H-plane patterns at 13.0 GHz. These results again exhibit an excellent agreement between theory and measurements, and good cross-polarisation performance within the 3 dB beamwidth. The pattern is practically identical to that at 11.6 GHz, shown in Fig. 6.2.

The E-plane theoretical and measured patterns at 13.0 GHz are shown in Fig. 6.5. The theoretical pattern is not omni-directional and the measured pattern is even more directional, and significantly different from the theoretical pattern for certain angles. However, the agreement between theory and measurement is still very good (within 1 dB) for directions within ±20° from boresight, and the directions of the pattern minima are predicted correctly.
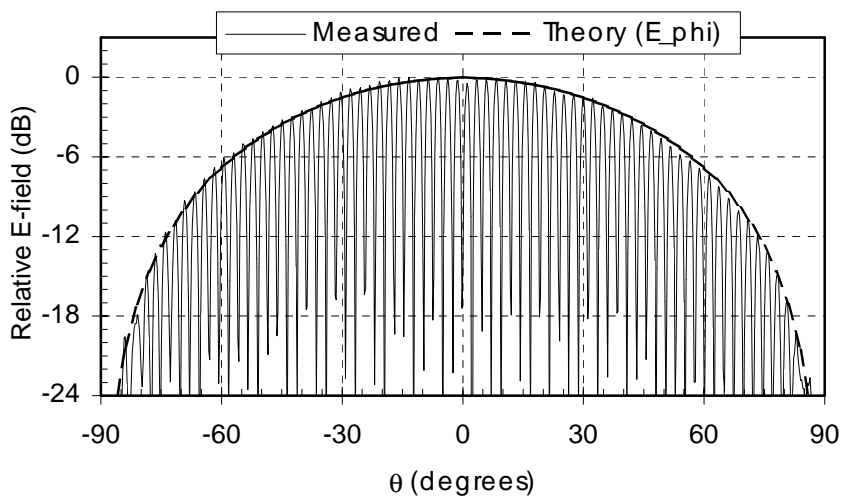
Fig. 6.4 The theoretical and measured radiation patterns of the DRA in the H-plane at 13.0 GHz
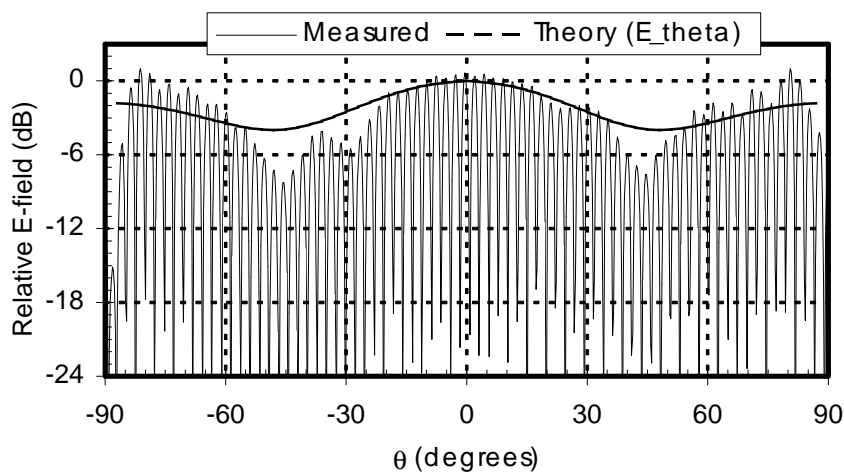
Fig. 6.5 The theoretical and measured radiation patterns of the DRA in the E-plane at 13.0 GHz

The E-plane pattern at 13.0 GHz is different from that at 11.6 GHz in Fig. 6.3. This may be due to the influence of the quadruple mode that radiates best in the $\theta = 0°$ and $\pm 90°$ directions with the minima at $\pm 45°$. It appears that, at 13.0 GHz, the higher-order mode content in the DRA is stronger than predicted, possibly due to manufacturing tolerances, hence the minima in the measured pattern are deeper than in the theoretical pattern.

From these theoretical and experimental results, one may conclude that low-profile rectangular DR antennas radiate in almost the same way as standard rectangular DR antennas when they operate in the dominant mode. Furthermore, the measured cross-polarisation is at least 15 dB below the co-polarisation within the 3 dB beamwidth of the antenna.

High-Permittivity DR Antennas

The size of a DRA is in general proportional to $(\varepsilon_r)^{-1/2}$, where ε_r is the dielectric constant of the resonator. Therefore, for a given operating frequency, the size of the required DR can be reduced by selecting high-permittivity material. Although this space reduction comes at an inevitable cost of bandwidth, even the high-permittivity DR antennas have bandwidths large enough for many practical applications.

A low-profile, aperture-coupled, rectangular DRA made out of high-permittivity material is shown in Fig. 6.6 [8]. Note that, unlike in the rectangular DRA discussed previously, there is an offset from the slot centre to the DR centre. This offset is required to achieve optimum coupling between the microstrip feed and the high-permittivity DR.

One example design has a DR with a dielectric constant of 100, a length (a) of 12.7 mm, a width (d) of 12.7 mm and a height (b) of 1 mm. The length of the slot (L) is 6.1 mm and its width (w) is 1.2 mm. The stub length (s) is 1.5 mm and the distance between the DR edge and the slot end (h) is 1 mm. The substrate thickness is 0.64 mm and the substrate dielectric constant is 10.2. The width of the 50Ω microstrip feed is 0.6 mm. The measured return loss of this antenna is shown in Fig 6.7. Its resonance frequency, loosely defined as the frequency at which the input matching is best, is 7.72 GHz. The 10 dB return-loss bandwidth is 3.24%.

The measured resonance frequencies and bandwidths of several rectangular DR antennas made out of the same material are shown in Table 6.1.

Although all antennas in the table above are made out of the same material, their bandwidths are significantly different. Note that the sample C, which has the largest length-to-height ratio, gives the largest bandwidth. The sample A has the smallest length-to-height ratio and the smallest bandwidth. In general, it is safe to say that as the length-to-height ratio of a DRA is increased, the bandwidth increases. The larger bandwidth is another advantage of low-profile DR antennas over their conventional counterparts. The reason for this improved bandwidth is that, as the aspect ratio of a DR is increased, its radiation Q-factor drops [9].
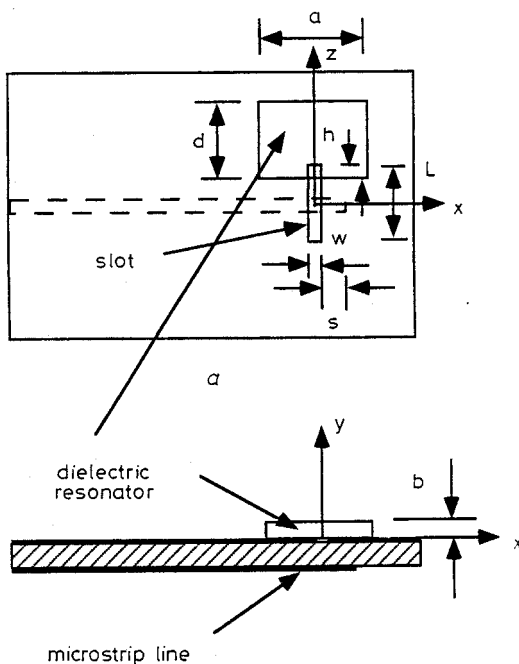
Fig. 6.6 An aperture-coupled, rectangular DRA made out of high permittivity material (from [8], reprinted with permission from IEE)
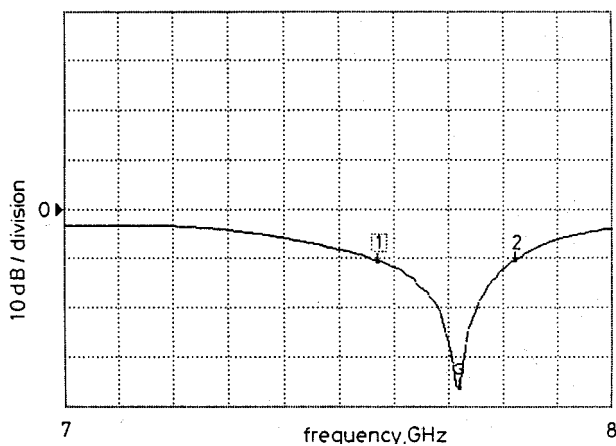
Fig. 6.7 Measured return loss of the rectangular DRA made out of high permittivity material (from [8], reprinted with permission from IEE)

Table 6.1: Measured resonance frequencies and bandwidths of several rectangular DR antennas made out of high-permittivity material ($\varepsilon_r = 100$) [8]

Sample	Length (a) mm	Width (d) mm	Height (b) mm	Resonance frequency (GHz)	Return-loss bandwidth (%)
A	10	10	2	4.57	1.17
B	10	10	1	7.97	2.78
C	12.7	12.7	1	7.72	3.24
D	5	10	1	8.85	2.03
E	10	5	1	8.50	2.00

The resonance frequency of this antenna can be estimated using the approximate analytical expression for the resonance frequency of the TE_{111} mode in a rectangular resonator given by:

$$f_{111} = \frac{c}{2\pi\sqrt{\varepsilon_r}}\sqrt{\left(\frac{\pi}{a}\right)^2 + \left(\frac{\pi}{2b}\right)^2 + \left(\frac{\pi}{d}\right)^2} \tag{6.6}$$

where c is the velocity of light in free space. For a low-profile DR, a,d >> b, and this equation further simplifies to:

$$f_{111} \approx \frac{c}{4b\sqrt{\varepsilon_r}} \tag{6.7}$$

which indicates that the resonance frequency is almost independent of the DR lateral dimensions. The DR height is approximately equal to quater of a wavelength in the dielectric medium at the resonance frequency. These approximate expressions usually give accurate estimates for high-permittivity resonators, such as those considered here. The resonance frequency estimated for the sample C antenna using (6.6) is 7.5 GHz, which is very close to the measured value of 7.72 GHz.

6.2.2 Co-planar Waveguide-Fed Rectangular DR Antennas

Co-planar waveguide (CPW) feeds are preferred when the antennas are required to be integrated with active devices. A low-profile rectangular DR with a very high dielectric constant, operating in the dominant TE_{111} mode, can be coupled to a CPW feed, as shown in Fig. 6.8 [10]. Note that the end of the CPW is open circuited by etching a rectangular slot that connects the two slots of the CPW. In this arrangement, it is possible to vary the amount of coupling between the DR and the CPW feed by moving the DR in the direction of the CPW feed. As the DR is

moved with respect to the feed, both the resistance and reactance of the antenna changes.
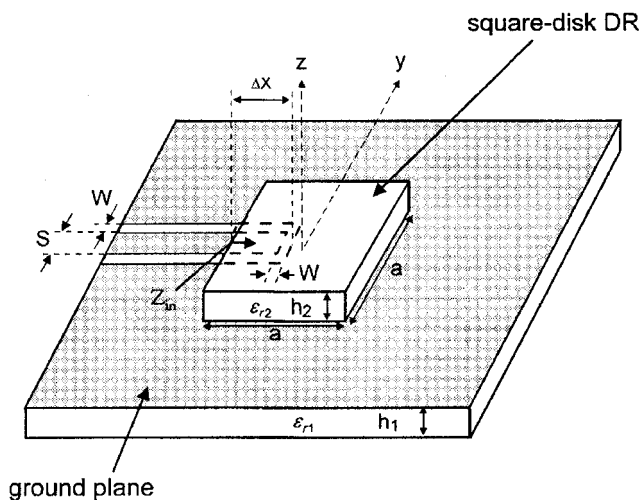
Fig. 6.8 A low-profile rectangular DRA with a co-planar waveguide feed (from [10], © 1999 John Wiley & Sons, Inc.)

One example CPW-fed DRA design [10] has a DR with a square cross section of 28.2 mm × 28.2 mm and a height of 4.9 mm. The DR in this antenna is made out of low-loss ceramic and its dielectric constant is 79. The substrate is FR4 with a dielectric constant of 4.4, and its thickness is 1.6 mm. The CPW feed is composed of two 0.5mm slots on each side of a centre strip, and is 6.37 mm wide, giving a characteristic impedance of 50 Ω. The DRA is placed symmetrically above the CPW feed end and the distance from the DRA edge to the CPW end (Δx in Fig. 6.8) has been adjusted to match the DR to the feed.

Fig. 6.9 shows the measured return loss of the CPW-fed DRA versus frequency, for three values of Δx. It can be seen that the antenna is well matched to the 50 Ω feed at 2090 MHz when Δx is 9.9 mm. The 10 dB return-loss bandwidth of this DRA configuration is about 50 MHz or 2.4%, which is reasonable considering the high permittivity of the DR. As seen from Fig. 6.9, when the DR is moved along the CPW feed a few millimetres, the antenna return loss changes significantly.

The measured radiation pattern of this DRA on the H-plane (y-z plane) is similar in shape to the $\cos\theta$ type pattern of an aperture-fed rectangular DRA on the H-plane, previously shown in Fig. 6.2. Its 3 dB beamwidth is 61°. The E-plane pattern is wider, as expected, with a 3 dB beamwidth of 107°. The cross-polarisation radiation is about 20 dB less than co-polarisation radiation on both

planes. The measured gain in the boresite direction at 2090 MHz frequency is 5.4 dBi.
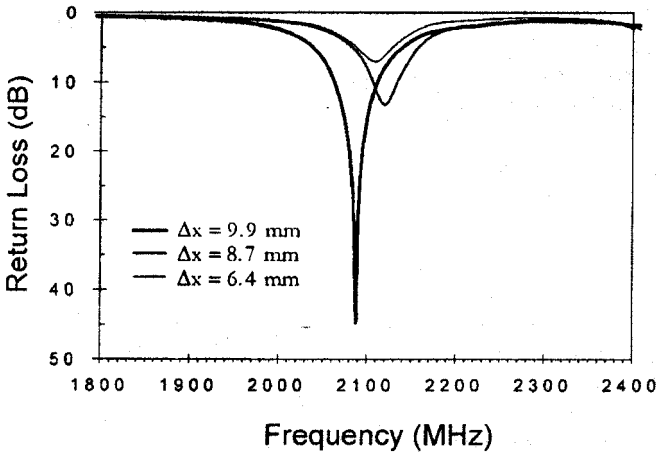
Fig. 6.9 The return loss of the low-profile rectangular DRA with a co-planar waveguide feed, for three values of Δx (from [10], © 1999 John Wiley & Sons, Inc.)

6.3 CIRCULARLY POLARISED RECTANGULAR DR ANTENNAS

In general, circular polarisation can be obtained from DR antennas using single feeds or multiple feeds. Among them, the single-feed configurations usually have simple configurations and they require less space on the feed substrate. The feed losses in the single-feed configurations are likely to be less than those in multiple-feed configurations. However the axial-ratio bandwidth (which is usually smaller than the return loss bandwidth and hence is the limiting bandwidth of a circularly polarised antenna) of a single-feed CP antenna is usually smaller than that of a multiple-feed CP antenna.

One single-feed circularly-polarised (CP) DRA configuration consists of a low-profile rectangular DR fed by a microstrip feed through a coupling aperture. However, unlike in the case of the linearly polarised rectangular DRA discussed in Section 2, the DR is inclined with respect to the coupling aperture by about 45°, as shown in Fig. 6.10. This DR configuration is analogous to the single-feed CP rectangular microstrip patch antenna, where two spatially orthogonal modes are excited in a microstrip resonator using an inclined aperture. It should be noted that a circularly polarised wave consists of two linearly polarised waves that are equal in magnitude but differ in phase and space by 90° (i.e. time and space quadrature). The rectangular geometry naturally supports two spatially orthogonal modes. The phase quadrature between the two modes is obtained by perturbing the dimensions

of the rectangular patch resonator. The same principle applies to rectangular dielectric resonators. The two orthogonal modes do not have to be of the same order; for example, one could be the dominant mode and the other could be a higher-order mode.

This concept has been exploited first to design a high-profile CP DR antenna using relatively high permittivity ($\varepsilon_r=40$) material [11]. This original rectangular CP DR antenna had a height-to-length ratio of 1. This design was based on approximate analytical expressions for the dominant mode in a rectangular DR. Soon afterwards, this concept was extended to design the first low-profile rectangular CP DR antenna using relatively low permittivity materials [12]. In this case, a more accurate numerical analysis method, FDTD, was used for the design.

The low-profile CP DR antenna, shown in Fig. 6.10, consists of a rectangular DR placed on the ground plane side of a dielectric substrate and fed by a 50Ω microstrip line through an aperture in the ground plane. The DR length (a) is 14 mm, width is 3.7 mm and height is 2.6 mm. Note that the length-to-height ratio of this DR is 5.4. The dielectric constants of the DR and the substrate are 10.8 and 10.5, respectively. The aperture width is 1.2 mm (in the *x* direction) and the length is 2.8 mm; the substrate thickness is approximately 0.64 mm; the matching stub length is 0.4 mm from the centre of the aperture. The resonator is rotated by 45° with respect to the aperture.

For pattern measurements, the ground plane of this antenna has been extended to form a circle of about 1.2 m in diameter. Microwave absorbers have been placed around the edge of this ground plane in order to minimise edge effects. The measurements have been done in a 12 m antenna range inside an anechoic chamber.
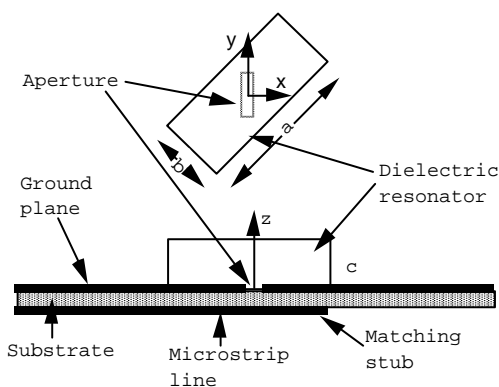
Fig. 6.10 A low-profile rectangular CP DR antenna (from [12], reprinted with permission from IEE)

Numerical Analysis
The antenna has been analysed and designed using the FDTD method combined with Mur's absorbing boundary conditions [2,3]. The far-field waveforms have been obtained by applying the field equivalence principle, directly in the time domain. An infinitely large ground plane has been assumed and image theory has been employed in the near-to-far field transformation. All calculations have been done using a Cray Y/MP four-processor supercomputer, in 64-bit words.

Numerical Results
The magnitude of the measured input reflection coefficient ($|s_{11}|$) of the antenna, shown in Fig. 6.11, indicates an excellent input match at and around 14.75 GHz.

The theoretical and measured patterns at 14.75 GHz, on the elevation plane along the aperture (*i.e.* the *y-z* plane in Fig. 6.10) are shown in Fig. 6.12. The measured pattern has been obtained by spinning a linearly-polarised horn antenna while the test antenna is stationary. The axial ratio can be estimated from this pattern as the difference between an adjacent maximum and minimum. The two theoretical curves (E_{min} and E_{max}) are the relative lengths of the major and minor axes of the polarisation ellipse computed using the FDTD method; the gap between the two gives the theoretical axial ratio. The theoretical and measured results compare well for directions within ±30° from the boresight. Discrepancies between them at higher $|\theta|$ values are attributed to the truncated ground plane in the test antenna and to fabrication tolerances. In general, the axial ratio remains close to 3 dB over a wide range of elevation angles (about 110°) in this plane.
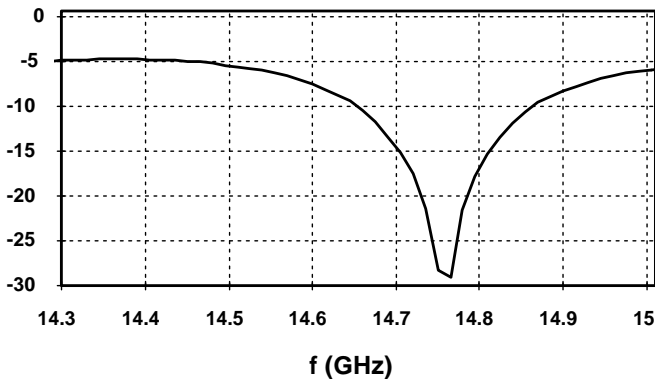
Fig. 6.11 The measured input reflection coefficient of the rectangular CP DRA
(from [12], reprinted with permission from IEE)
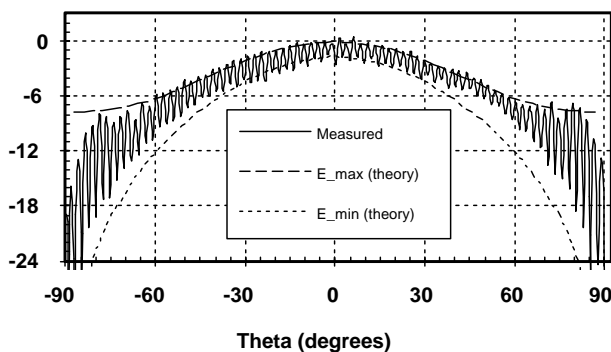
Fig. 6.12 Theoretical and measured patterns in the *y-z* elevation plane (from [12], reprinted with permission from IEE)
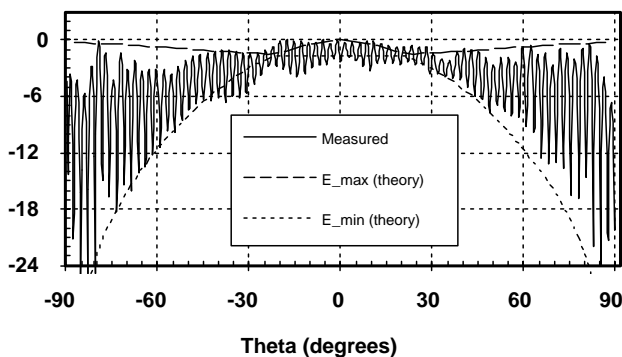
Fig. 6.13 Theoretical and measured patterns in the *x-z* elevation plane (from [12], reprinted with permission from IEE)

The theoretical and measured patterns in the elevation plane perpendicular to the aperture (*i.e.* the *x-z* plane in Fig. 6.10) are shown in Fig. 6.13. The theoretical axial ratio decreases as $|\theta|$ increases from 0° to about 20° and then it increases with $|\theta|$. The measured pattern also follows this trend but the measured results for certain angles are significantly different from the theoretical results. In general, both results indicate that the variation of E_{max} with $|\theta|$ is weak but E_{min} decreases rapidly.

The radiation patterns of this antenna has also been calculated using the Method of Moments, by employing the procedure discussed in Section 2. The theoretical results from the MoM are almost identical to the FDTD results shown here [13].

The measured 3 dB axial-ratio bandwidth of this antenna in the boresight direction is 14.35-14.80 GHz (3%). These results prove that with proper design, good quality circular polarisation can be obtained over a wide range of directions and frequencies using a simple low-profile rectangular DR antenna with a single feed.

6.4   LINEARLY POLARISED CIRCULAR DISK DR ANTENNAS

The circular disk DRA is a special case of the cylindrical DRA where the cylindrical resonator has a low profile and therefore appears like a disk. The DR may be fed by a microstrip line, directly or through an aperture, or by other types of transmission lines such as co-planar waveguides. The dominant mode of the circular disk antenna is the TM_{110} mode [14].

Figure 6.14 shows an aperture-coupled circular disk DRA made out of very high permittivity material [15]. Note that, like the rectangular high-permittivity LP antenna we discussed in the Section 2, this DR is not symmetrically placed above the microstrip line. The coupling between the DR and the microstrip feed can be adjusted by varying the offset distance (y_d) between the centre of the DR and the centre line of the microstrip.
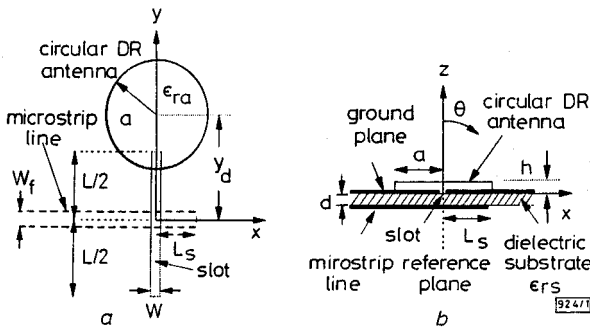
Fig. 6.14 An aperture-coupled circular disk DRA (from [15], reprinted with permission from IEE)

One example configuration has a DR disk with a dielectric constant (ε_{ra}) of 82, diameter ($2a$) of 25 mm and a height (h) of 2 mm. The aperture length (L) is 13.5 mm and its width (W) is 1.3 mm. The substrate dielectric constant (ε_{rs}) is 2.96 and its thickness (d) is 0.635 mm. The 50Ω microstrip line width (W_f) is 1.5 mm and the length of the matching stub (L_s) is 13.6 mm.

Analysis
The very high permittivity of the DR permits the calculation of the resonance frequency of the DRA to a high precision using approximate analytical expressions. The resonance frequency for the TM_{110} mode of a cylindrical DR is given by [14]:

$$f_{110} = \frac{c}{2\pi a\sqrt{\varepsilon_{ra}}}\sqrt{1.841^2 + \left(\frac{\pi a}{2h}\right)^2} \tag{6.8}$$

where c is the velocity of light in free space. For a low-profile disk antenna, $a/h \gg 1.841$ and therefore this expression can be further simplified as

$$f_{110} \approx \frac{c}{4h\sqrt{\varepsilon_{ra}}} \tag{6.9}$$

which is identical to the corresponding simplified expression for low-profile rectangular resonators, given in (6.7).

Numerical Results

Fig. 6.15 shows the return loss characteristics of the circular disk DRA for four values of the offset (y_d). It can be seen that the matching is best with an offset of 15 mm, which gives a return loss of about 58 dB at 4.25 GHz. It is interesting to compare this frequency with the resonance frequencies predicted by the two approximate expressions (6.8) and (6.9). For the DR dimensions considered, expression (6.8) predicts a resonance frequency of 4.21 GHz, which is within 1% of the measured frequency. The value from expression (6.9) is 4.14 GHz and the difference is 2.6%. The measured 10 dB return-loss bandwidth of the antenna is 3.8%. Another observation one can make from the results in Fig. 6.15 is that the DR should be precisely located during the antenna fabrication because a small error in the order of half a millimetre could affect the return loss significantly.
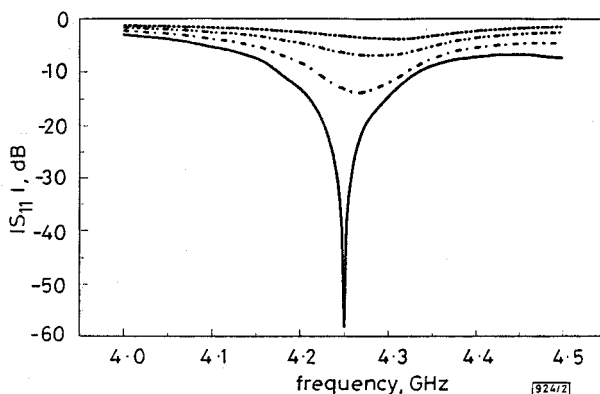
Fig. 6.15 The input reflection coefficient of the aperture-coupled circular disk DRA (from [15], reprinted with permission from IEE)

The measured radiation patterns of the antenna on the E and H elevation planes are shown in Fig. 6.16. It shows both co-polarised and cross-polarised fields

230

on these planes. The cross-polarisation level is about 20 dB below the co-polarisation level for most angles. Despite the asymmetrical feed system, the radiation patterns are reasonably symmetrical and the open part of the aperture does not appear to have contributed much to the radiation. The front-to-back ratio of the radiation pattern is about 10 dB, which is a few dBs less than that for typical DR antennas. The measured gain of the antenna at 4.25 GHz is 4.5 dB. At this frequency, the half-power beamwidth of the H-plane radiation pattern is 65° and the 3 dB bandwidth of the antenna gain is about 12%.

6.5   CIRCULARLY-POLARISED DIELECTRIC DISK ANTENNAS

In Section 3, we have discussed one method of obtaining circular polarisation from a rectangular DRA using a single feed where a rectangular aperture is employed. The aperture in that case is at an angle to the rectangular resonator but for best coupling, the microstrip feed is perpendicular to the aperture (see Fig. 6.10). One possible modification to this configuration is to replace the rectangular aperture by a cross-shaped aperture (cross slot) with *equal* arms. In this case, each arm of the cross would be inclined to the microstrip feed, possibly by 45°, and parallel to one side of the rectangular resonator. They excite two spatially orthogonal modes in the resonator. For circular polarisation these two modes should be in phase quadrature, which may be achieved by selecting suitable *unequal* dimensions for the resonator length and the width.
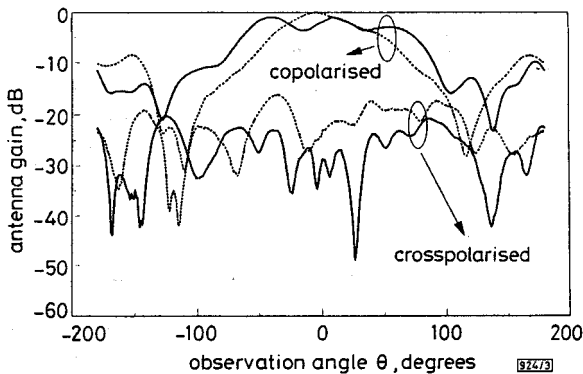
Fig. 6.16 The radiation patterns of the aperture-coupled circular disk DRA (from [15], reprinted with permission from IEE)

Alternatively, a cross slot of *unequal* arms can be used to generate circular polarisation [16]. In this arrangement, the phase quadrature between the two spatially orthogonal modes may be obtained by the proper selection of slot arm lengths. Therefore, a square or circular dielectric resonator can be used instead of a rectangular resonator of unequal length and width. This arrangement is especially useful for circular or disk resonators because the other single-feed arrangements

are not suitable for them unless the shape of the resonator is changed. This concept is applicable to both microstrip patch and dielectric resonators.

A circularly-polarised, low-profile, circular disk DRA fed by a cross slot with unequal arms is shown in Figure 6.17. Note that each arm of the cross is at an angle to the microstrip feed. The angle is 45° in this example but it can be different. Each arm in the slot excites a mode in the DR with a polarisation perpendicular to the arm. This antenna is based on a previous observation that the resonance frequency of a given mode of a resonator depends on the length of the coupling slot. As the two arms of the slot have different lengths, the two excited modes have slightly different resonance frequencies and they are only nearly degenerate. Hence, by proper design, a phase quadrature between the modes can be achieved at the operating frequency.
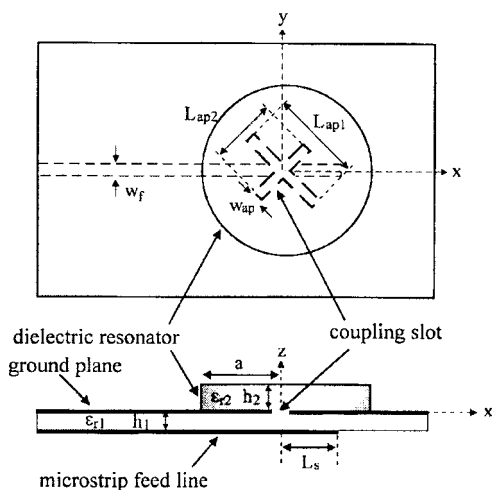
Fig. 6.17 A circularly-polarised circular disk DRA fed by a cross slot with unequal arms (from [16], ©1999 IEEE Transactions on Antennas and Propagation)

One example design has a dielectric disk with a dielectric constant of 79, a radius of 14.72 mm and a height of 5.1 mm. Note that the diameter-to-height ratio of this DRA is about 5.8. The length of the longer arm of the slot is 13 mm, and the other arm is only slightly shorter at 12 mm. The slot width (W_{ap}) is 1 mm. The substrate dielectric constant is 4.4 and the thickness is 0.8 mm. The microstrip line width is 1.5 mm and the matching stub length (L_s) is 10 mm.

Despite the small difference between the two arms of the cross slot, an excellent axial ratio has been achieved in the boresite direction around 2040 MHz. Fig. 6.18 shows the measured axial ratio versus frequency. The 3 dB axial ratio bandwidth is 80 MHz or 3.9%. Fig. 6.19 shows the radiation patterns of the

antenna at 2044 MHz. It can be seen that the antenna radiates high quality right-hand circular polarisation in most directions. The gain of the antenna at this frequency is 6.4 dBi and the front-to-back ratio is 14.7 dB. The gain variation within the 3 dB axial-ratio bandwidth is about 1 dB.

Fig. 6.18 The measured axial ratio of the circular disk DRA fed by a cross slot with unequal arms (from [16], © 1999 IEEE Transactions on Antennas and Propagation)
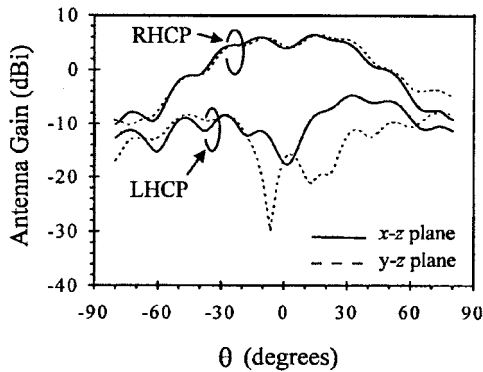
Fig. 6.19 The measured radiation patterns of the circular disk DRA at 2044 MHz (from [16], © 1999 IEEE Transactions on Antennas and Propagation)

The measured return loss of the antenna is shown in Fig. 6.20. The antenna has a good 2:1 VSWR bandwidth of 10%. It is also interesting to compare this circular disk DRA with a similar CP square patch antenna fed by a cross slot with unequal arms [16]. The key parameters and performance figures of the two antennas are shown in the Table 6.2.

Table 6.2: Comparison of two circularly polarised antennas fed by cross slots

CP Antenna	Rectangular Patch	Circular Disc DR
Lateral dimensions	30×30 mm	29.44 mm diameter
Height	1.6 mm	5.1 mm
Dielectric constant	4.4	79
Operating frequency	2302 MHz	2044 MHz
3dB axial-ratio bandwidth	1.4%	3.9%
2:1 VSWR bandwidth	5.9%	10.1%

From this comparison one may reach a general conclusion that the DR antennas with high dielectric constants have lateral dimensions that are comparable to patch antennas with low dielectric constants. However, even the low-profile DR antennas are usually taller than the patch counterparts. The most important observation is that, despite the high dielectric constant, the DR antennas have wider bandwidths, both for the axial ratio and the VSWR.
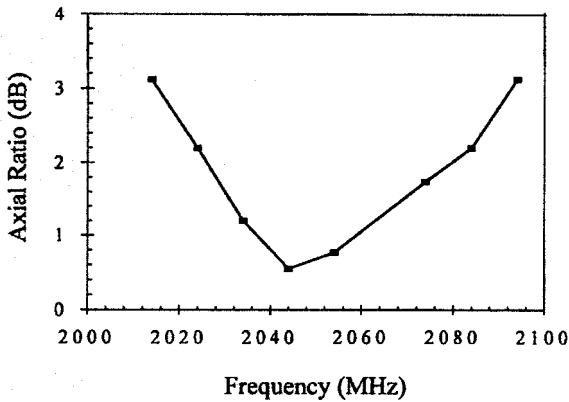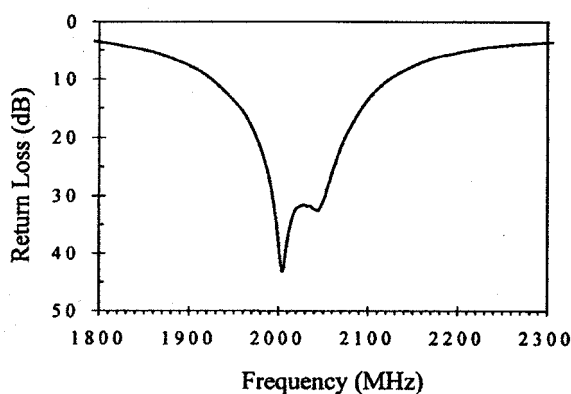

Fig. 6.20 The return loss of the circular disk DRA fed by a cross slot with unequal arms (from [16], © 1999 IEEE Transactions on Antennas and Propagation)

6.6 LINEARLY-POLARISED TRIANGULAR DR ANTENNAS

The motivation to develop triangular DR antennas for linearly polarised applications is due to the fact that, for a given operating frequency and a dielectric constant, the triangular LP DR antennas are considerably smaller than the corresponding rectangular and circular DR antennas [17]. Although this saving in space usually comes at the cost of bandwidth, it may be an advantage in some applications such as antenna arrays.

An example of a low-profile, aperture-coupled, equilateral-triangular LP DR antenna is shown in Fig. 6.21. The DR has a dielectric constant of 82 and a height of 1.1 mm. Each side of the triangular resonator is 20 mm long. The aperture length is 4 mm and its width is 0.4 mm. The dielectric substrate has a dielectric constant of 2.33 and a thickness of 1.57 mm. The microstrip line width is 4.7 mm and the length of the stub, measured from the centre of the resonator (L_s), is 8 mm.
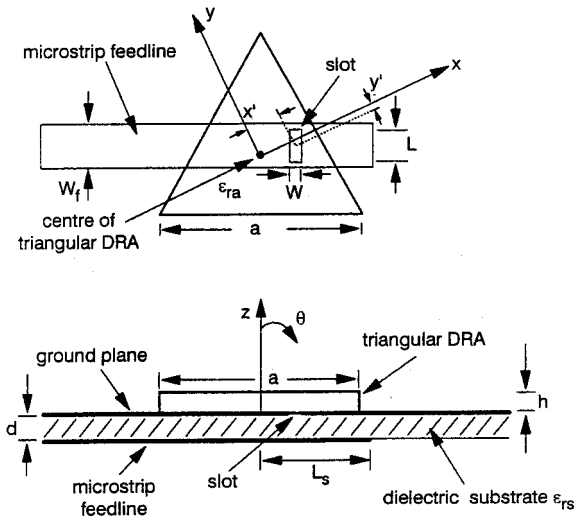
Fig. 6.21 An aperture-coupled, equilateral-triangular DRA (from [17], reprinted with permission from IEE)

Analysis

The resonance frequency of the TM_{mnl} mode in an equilateral-triangular DR on a ground plane is approximately given by [18]

$$f_{mnl} = \frac{1}{2\sqrt{\varepsilon\mu}} \left[\left(\frac{4}{3a}\right)^2 (m^2 + mn + n^2) + \left(\frac{1}{2h}\right)^2 \right] \tag{6.10}$$

where *a* is the length of each side of the triangle and *h* is the height of the resonator. The indices m, n and l should satisfy the condition $l+m+n = 0$ but they all cannot be zero simultaneously. For low-profile resonators where $a \gg h$, this expression can be further simplified as

$$f_{lmn} \approx \frac{1}{4h\sqrt{\varepsilon\mu}} \tag{6.11}$$

which is identical to the corresponding simplified expressions for rectangular circular disk antennas for this limiting case. The dominant mode of an equilateral-triangular DR is the TM_{10-1} mode.

Numerical Results

The return loss of the equilateral-triangular DR antenna is shown in Fig. 6.22, where the offset between the aperture centre and the triangle centre (denoted by x' and y' in Fig. 6.21) is a parameter. It can be seen that the matching is best for x'=0.99 mm and y'=-0.28 mm, giving a return loss of about 28 dB at 7.59 GHz. The authors claim that the antenna impedance changes significantly when the DR is moved slightly away from this optimum position. This appears to be a common disadvantage of all aperture-coupled DR antennas made out of very high permittivity material. The 10 dB return loss bandwidth for the optimum DRA is about 3%, which is smaller than the 3.8% bandwidth of the aperture-coupled circular disk DRA discussed in Section 4. Note that both of these DR antennas are made out of same material but they have different heights and resonance frequencies.
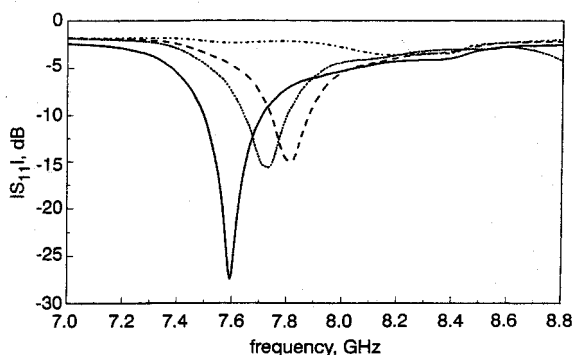
Fig. 6.22 Measured input reflection coefficient of the aperture-coupled triangular
DR antenna for several offsets between the aperture and the resonator:
_____ x'=0.99mm, y'=-0.28mm; .... x'=-2.29mm, y'=-1.03mm
_ _ _ _ _ x'=3.22mm, y'=-0.42mm; _._._._._. x'=5.6mm, y'=-0.98mm
(from [17], reprinted with permission from IEE)

The resonance frequency of this DRA can be predicted to a very good accuracy using expressions (6.10) and (6.11). Expression (6.10) gives a value of 7.61 GHz with an error of 0.26% and the expression (6.11) gives a value of 7.53 GHz with an error of 0.8%.

The radiation patterns of the optimum triangular DRA is shown in Fig. 6.23. The cross-polarised field is about 20 dB below the co-polarised field in the boresite direction and the front-to-back ratios for the E- and H-plane patterns are 17 dB and 13 dB respectively. The gain at the resonance frequency is 5.2 dBi, which is 0.8 dBi higher than the aperture-coupled circular disk DRA in Section 4.
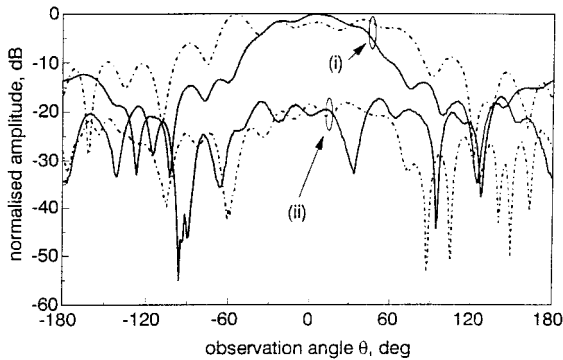
Fig. 6.23 Measured radiation patterns of the optimum triangular DRA at 7.59 GHz: (i) co-polarised; (ii) cross-polarised; _._._._ E-plane; _____ H-plane (from [17], reprinted with permission from IEE)

A low-profile triangular DR may also be fed by a conformal strip connected to a coaxial feed line, as shown in Fig. 6.24 [19]. The conformal strip avoids the need of a hole common that is in conventional probe feed systems. This new feed arrangement has given a larger return-loss bandwidth of 5.5%. Another advantage is that the radiation pattern does not have the back lobes found in the patterns of the aperture-coupled version (see Fig. 6.23), as there is no aperture that could radiate in the backward direction. This leads to a better front-to-back ratio of more than 20 dB. The measured gain at the resonance frequency of 8.8 GHz is 5 dBi.

6.7   CIRCULARLY POLARISED CROSS DRA

We have briefly discussed a circularly polarised DRA based on a square resonator and a cross slot in Section 5. Alternatively, a cross-shaped DR can be used with a

simple rectangular slot, as shown in Fig. 6.25, to generate circular polarisation [20]. A first cross DRA was designed using approximate analytical expressions based on the waveguide model [20]. Later, an antenna with improved performance was designed using a more accurate method based on FDTD [21]. The second antenna has been further investigated theoretically using a conformal FDTD method [22].
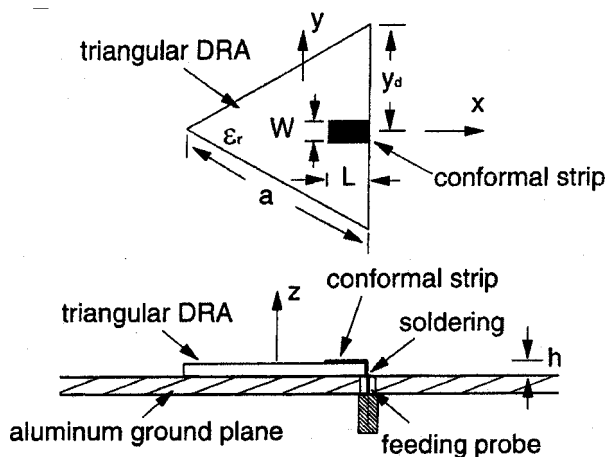
Fig 6.24 A low-profile triangular DR fed by a conformal strip connected to a coaxial feed line (from [19], © 2001 John Wiley & Sons, Inc.)
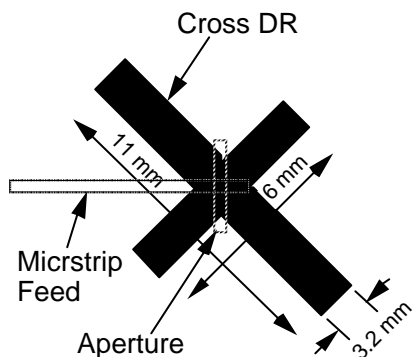
Fig. 6.25 An aperture-coupled, circularly-polarised cross DRA

The cross DR may be considered as two rectangular resonators kept orthogonal to each other. Both rectangular resonators are fed by the same microstrip feed through a single rectangular aperture that is at 45° with respect to each resonator. Each rectangular resonator is expected to radiate a linearly polarised wave in the boresite direction. Nevertheless, as the two rectangular DRs differ in length, they have different resonance frequencies. In other words, at the operating frequency, the waves from the two resonators differ in phase. Therefore, by properly selecting the lengths of the two resonators, a phase quadrature between the two linearly polarised waves can be obtained. This together with the 90° spatial separation lead to circular or elliptic polarisation in the boresite direction.

The two arms of the cross DR has the lengths of 11 mm and 6 mm (see Fig. 6.25). Each arm has a width of 3.2 mm and a height of 3.15 mm. The dielectric constant of the cross is 10.8. The rectangular aperture has the dimensions of 4.6 mm × 0.67 mm. The substrate thickness is 0.64 mm and the dielectric constant is 10.2. The microstrip feed has a characteristic impedance of 50 Ω.

The measured magnitude of the antenna input reflection coefficient is shown in Fig. 6.26, where a good match can be observed over a wide range of frequencies. Figure 6.27 shows the measured axial ratio of the antenna in the boresite direction, obtained by averaging four separate measurements. It can be seen that the axial ratio is very good around 11.5 GHz, and the 3 dB axial ratio bandwidth is about 6%, which is an excellent figure for such a simple structure.
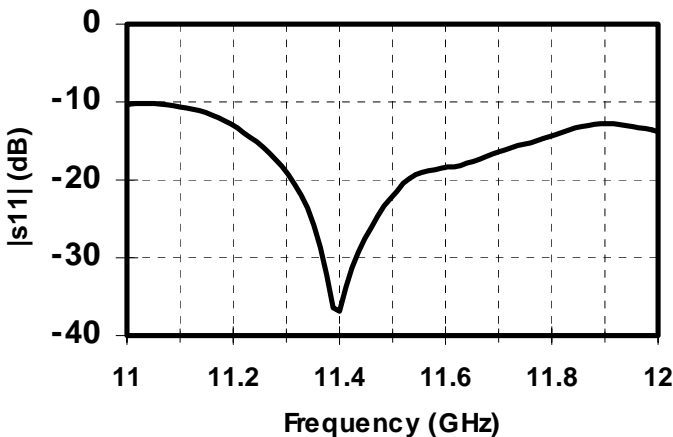
Fig. 6.26 The measured magnitude of the input reflection coefficient of the cross DRA
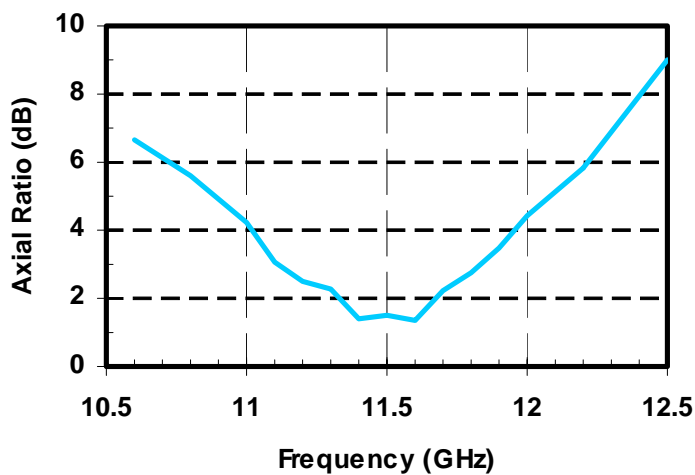
Fig. 6.27 The axial ratio of the cross DRA in the boreside direction versus frequency
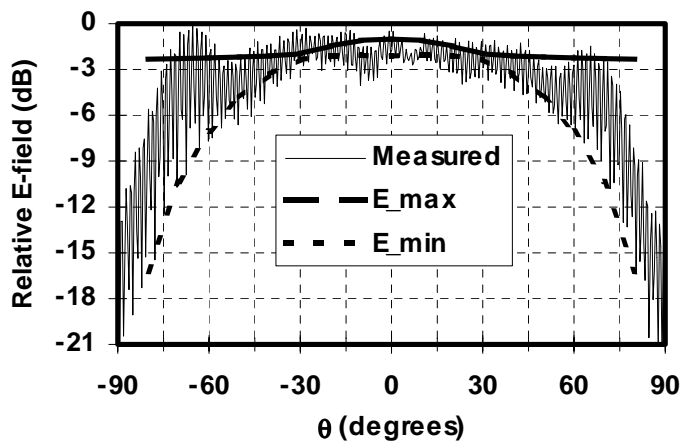
Fig. 6.28 The measured and theoretical radiation patterns of the cross DRA

The radiation pattern of the cross DRA on one elevation plane (along the shorter arm) is shown in Fig. 6.28. The measured pattern was obtained by spinning a linear-polarised horn antenna while the test antenna was stationary. The axial ratio can be estimated from this pattern as the difference between an adjacent maximum and minimum. The two theoretical curves (E_{max} and E_{min}) are the relative lengths of the major and minor axes of the polarisation ellipse calculated using the FDTD method; the gap between the two gives the theoretical axial ratio.

6.8   CONCLUSIONS

In addition to the advantages common to all DR antennas described elsewhere in this book, the low-profile DR antennas have an additional advantage of small height, which is desirable for many emerging wireless and mobile communication systems. The radiator footprint (area), which is an important factor in space-conscious applications, of a DR antenna can be reduced using high-permittivity material. It has been shown that both the axial-ratio and return-loss bandwidths of a low-profile DR antenna are significantly larger than those of a comparable microstrip patch antenna, even when the DR footprint is made smaller than the patch area using high-permittivity material. Although low-profile DR antennas are usually taller than conventional single-patch microstrip antennas[2], they offer a much better bandwidth to footprint ratio and an acceptable height.

---

[2] The bandwidth to footprint ratio of a microstrip antenna can be improved by stacking several patches but that leads to extra complexity in the fabrication.

REFERENCES

[1]   Esselle K.P., "A low-profile rectangular dielectric-resonator antenna," *IEEE Transactions on Antennas and Propagation*, Vol. 44, No. 9, pp. 1296-97, September 1996.

[2]   Esselle K.P.**,** "The finite-difference time-domain analysis of a rectangular dielectric resonator antenna*," Journal of Electrical and Electronics Engineers, Australia*, Vol. 15, No. 1, pp. 63-70, March 1995.

[3]   Mur G., "Absorbing boundary conditions for the finite-difference time-domain approximation of the time-domain electromagnetic-field equations," *IEEE Transactions on Electromagnetic Compatibility*, pp. 377-382, November 1981.

[4]   Ge Y. and Esselle K.P., "The analysis of a rectangular dielectric resonator antenna using the method of moments," *IEEE Antennas and Propagation Society (AP-S) International Symposium*, Salt Lake City, Utah, USA, pp. 1454-57, July 16-21, 2000.

[5]   Ge Y. and Esselle K.P., "New closed-form Green's functions for microstrip structures: theory and results," *IEEE Transactions on Microwave Theory and Techniques*. Accepted.

[6]   Ge Y. and Esselle K.P., "Computations of the radiation patterns of a rectangular dielectric-resonator antenna using the method of moments," *Microwave and Optical Technology Letters*, Vol. 27, No. 6, pp. 382-384, December 20, 2000.

[7]   Ittipiboon A., Mongia R.K., Antar Y.M.M., Bhartia P. and Cuhaci M., "An integrated rectangular dielectric resonator antenna," *IEEE Antennas and Propagation Society (AP-S) International Symposium*, Ann Arbor, MI, USA, pp. 604-607, July 1993.

[8]   Mongia R.K., Ittipiboon A. and Cuhaci M., "Low-profile dielectric resonator antennas using a very high permittivity material," *Electronics Letters*, Vol. 30, No. 17, pp. 1362-63, August 18, 1994.

[9]   Zheng W., "Computation of complex resonnace frequencies of isolated complex objects," *IEEE Transactions on Microwave Theory and Techniques*, Vol. MTT-37, pp. 953-961, 1989.

[10] Wu J.-Y., Huang C.-Y. and Wong K.-L., "Low-profile, very-high permittivity dielectric resonator antenna excited by a co-planar waveguide," *Microwave and Optical Technology Letters*, Vol. 22, No. 2, pp. 96-97, July 20, 1999.

[11] Oliver M.B., Antar Y.M.M., Mongia R.K. and Ittipiboon A., "Circularly polarised rectangular dielectric resonator antenna," *Electronics Letters*, Vol. 31, No. 6, pp. 418-419, March 16, 1995.

[12] Esselle K.P., "Circularly polarised higher-order rectangular dielectric-resonator antenna," *Electronics Letters,* Vol. 32, No. 3, pp. 150-151, February 1, 1996.

[13] Ge Y. and Esselle K.P., "The analysis of circularly polarised rectangular dielectric-resonator antennas using the method of moments," *Seventh Australian Symposium on Antennas*, Sydney, Australia, pp. 22, 14-15, February 2001.

[14] Long S.A., McAllister M.W. and Shen L.C., "The resonant cylindrical dielectric cavity antenna," *IEEE Transactions on Antennas and Propagation*, Vol. AP-31, pp. 406-412, 1983.

[15] Leung K.W., Luk K.M., Yung E.K.N. and LaiS., "Characteristics of a low-profile circular disk DR antenna with very high permittivity," *Electronics Letters,* Vol. 31, No. 6, pp. 417-418, March 16, 1995.

[16] Huang C.-Y., Wu J.-Y. and Wong K.-L., "Cross-slot coupled microstrip antenna and dielectric resonator antenna for circular polarisation," *IEEE Transactions on Antennas and Propagation*, Vol. AP-47, No. 4, pp. 605-609, April 1999.

[17] Lo H.Y., Leung K.W., Luk K.M. and Yung E.K.N., "Low-profile equilateral-triangular dielectric resonator antenna of very high permittivity," *Electronics Letters,* Vol. 35, No. 25, pp. 2164-65, December 9, 1999.

[18] Yoshihiko A., "Operation modes of a waveguide Y circulator," *IEEE Transactions on Microwave Theory and Techniques*, Vol. MTT-23, pp. 954-960, 1974.

[19] Lo H.Y. and Leung K.W., "Excitation of low-profile equilateral-triangular dielectric resonator antenna using a conducting conformal strip," *Microwave and Optical Technology Letters*, Vol. 29, No. 5, pp. 317-319, June 5, 2001.

[20] Ittipiboon A., Roscoe D., Mongia R. and Cuhaci M., "A circularly polarised dielectric guide antenna with a single slot feed', ANTEM'94 Digest, Ottawa, Canada, 1994, pp. 427-430.

[21] Esselle K.P. and Ittipiboon A., "Circularly polarised dielectric cross antenna: theory and experiment," *Progress in Electromagnetics Research Symposium* (*PIERS'96*), Innsbruck, Austria, July 8-12, 1996.

[22] Farahat N., Yu W., Mittra R. and Koleck T., "Cross-shaped dielectric resonator antenna analysis using conformal finite difference time domain method," *Electronics Letters*, Vol. 37, No. 18, pp. 1105-06, August 30, 2001.

This page intentionally left blank

CHAPTER 7

Compact Circular Sector and Annular Sector Dielectric Resonator Antennas for Wireless Communication Handsets

R.D. Murch and T.K.K. Tam

Department of Electrical and Electronic Engineering
Hong Kong University of Science and Technology
Clear Water Bay
Kowloon, Hong Kong SAR

7.1   INTRODUCTION

This chapter introduces a range of compact circular sectored dielectric resonator antenna (DRA) designs that are potentially useful for wireless communication applications. Our approach concentrates on integrated antennas for wireless handsets as these offer several advantages compared to conventional external antennas such as monopoles or helix. They are less easily broken off, more fashionable to today's consumers and generally reduce power absorption by the head. Together with the need to provide multiple antennas at the handset for diversity, there is considerable interest in designing integrated antennas that are compact. A potential candidate for an integrated antenna is the DRA [1-4]. However the DRA is still considered too large for applications at 900MHz and therefore one of our goals of this chapter is to provide designs for DRAs that are sufficiently compact for use in mobile handsets. The material presented brings together results from several previous publications [5-9] and we hope it can provide a comprehensive account of these investigations.

In addition to cellular based wireless systems we also wish to consider satellite communication systems, such as global positioning systems (GPS) and satellite-mobile communication systems, which employ circular polarisation. The number of DRA designs for circular polarisation is very limited and the techniques involved usually incorporate additional hardware, such as quadrature couplers or phase shifters. This increases the size and the complexity of the antenna, thus preventing it from being used for compact applications. Therefore, research on integrated circularly polarisat DRAs is also important.

7.1.1 Challenges

At a given resonant frequency the dimensions of a DRA are closely related to the material dielectric constant ε_r. With a high ε_r material, the dimensions can be reduced to the order of $\lambda_0 / \sqrt{\varepsilon_r}$, where λ_0 is the free space wavelength. The drawbacks, however, are a great increase in the Q-factor and a consequent reduction in bandwidth, with the resonance becoming very sensitive to temperature changes. In order to be suitable for GSM and PCS antenna applications, ε_r needs to be <30, so that necessary bandwidth can be achieved. However, the dimensions of DRAs with ε_r <30 at frequencies below 3GHz are generally too large to be used for handsets. For example, at 900MHz the dimensions of a circular cylindrical DRA will be 74mm in diameter and 74mm in height for ε_r =12. A rectangular DRA is $80 \times 80 \times 60 \text{mm}^3$ for the same frequency and material. At 1800MHz the dimensions of circular and rectangular DRAs are linearly reduced by half, and the volume is reduced by eight.

A simple technique to further reduce the volume is to put DRAs on large ground planes so that they act as image planes. This halves the linear dimension that is normal to the ground plane, thus further reducing the volume by a factor of two. This technique can only be applied when the introduction of the ground plane does not violate the boundary conditions of certain resonant modes. At 1800MHz the dimensions of a circular cylindrical DRA become 37mm in diameter and 18.5mm in height; this is, however, still too large to be used in handsets. Therefore, the need to devise and improve more compact DRAs remains.

Another issue that is beginning to have more significance is the controversial health issue of absorption of RF power from handset antennas by the heads of users. Future handset antenna designs therefore need to take this into account by reducing the near fields in the head area. This would not only reduce any potential health risk but it would also make the antenna more efficient.

Apart from terrestrial communications systems, antenna designs for satellite communications face more constraints owing to their circularly polarised requirements. One of the main reasons for using circularly polarised antennas for satellite communications is that the radio link is mainly a direct line-of-sight path. With regard to a linearly polarised transmitter and receiver antenna pair, it is necessary to maintain matched polarisation while the land user travels, otherwise increased polarisation loss or link interruption may happen from time to time. To overcome this shortfall, circularly polarised antennas are adopted because they avoid the need for polarisation tracking with transceivers in space.

DRAs are not new candidates for circular polarisation. The use of ring and circular cylindrical DRAs, proposed by [10],[11], incorporated additional hardware consisting of 3dB quadrature couplers or $90°$ transmission line phase shifters, and with double coaxial feeds. Circularly polarised rectangular DRAs developed by [12], with a simpler single-feed construction, and without any

external quadrature devices, is a better approach. However, simple structure single-feed circular cylindrical DRAs for circular polarisation have not been investigated to date.

7.1.2   Approaches

To tackle the problems addressed in the previous section, we introduce circular sector DRAs. These DRA geometries are obtained by removing a sector of dielectric material from the conventional circular cylinders. The extra tunable parameter for sector DRAs is the sector angle. Unfortunately removing a sector out of the conventional cylinder would increase the resonant frequency. However, the boundary conditions on the sector faces can be managed by putting metallic plates or leaving the faces open. Therefore incorporating the sector angle in conjunction with the combinations of boundary conditions, volume reduction can be achieved. In section 7.3, various circular sector DRAs are investigated.

Because shielded helix and monopole antennas are isotropic in the azimuthal direction, power is radiated to the head of the user. Low profile antennas supported with ground planes, such as patch, PIFA and DRA, concentrate the power to a hemisphere. By properly orientating these antennas, a reduction of nearfield power to the head of the user could be achieved.

For integrated circular polarisation DRA designs, the removal of external quadrature phase hardware could be achieved by using two spatially orthogonal modes resonating at two slightly separated frequencies. This is straightforward for a rectangular DRA because there are more dimensional parameters to tune. The situation for circular cylindrical DRA is, however, not trivial. The geometry may only resort to an oval shape which is mechanically complicated. In this section, the additional dimensional parameter (sector angle) of circular sector DRAs is chosen such that the difficulties of conventional cylindrical DRAs could be solved. Detailed investigations on circular sector DRAs for circular polarisation will be discussed in section 7.4.

7.1.3   Section Summary

Section 7.2 introduces the basic concepts of DRAs in order to allow an understanding of the terms used in subsequent sections. In section 7.3, circular sector and annular sector DRAs are presented and investigated. FDTD simulations are used to design and test sector DRAs are discussed. In particular, a sector DRA which has 75% less volume than a conventional cylindrical DRA yet maintains the same resonant frequency and bandwidth is demonstrated. Using our volume minimisation technique and low profile considerations to optimise the antenna dimensions, a $180°$ compact circular sector DRA, is proposed and tested for use in a personal communication systems (PCS). In section 7.4, a novel compact DRA approach to produce circular polarisation which may be useful for satellite communications is discussed. Simulations used to evaluate the designs and prototypes are fabricated to verify the findings. Dual band designs are provided in section 7.5 and finally overall conclusions are presented in section 7.6.

7.2 DIELECTRIC RESONATOR ANTENNAS

Having addressed the problems and highlighted the approaches to this chapter, the basic understandings and formulations of dielectric resonator antennas (DRAs) are briefly introduced before the key investigations are described. In this section, the salient features that make DRAs an attractive and popular topic are stated.

7.2.1 Features

The potential of DRAs for practical use is supported by the following key features [1], [13], [14]:

- DRAs come in simple geometries: hemisphere, circular cylinder and rectangular. These are readily available and can be easily fabricated.

- They are very compact in size when operating at a high frequency and with a large ε_r, 30-100. The dimensions are in the order of $\lambda_0 / \sqrt{\varepsilon_r}$.

- There is no inherent conductor loss for a DRA. High radiation efficiency is therefore a major merit. Especially attractive for high frequency millimeter wave applications, the loss from metallic antennas can be high.

- The feeding mechanism is simple, flexible and easily controlled. Different kinds of transmission line feeds are suitable for DRA coupling. Conducting probes, microstrips, microstrip-slots are frequently used.

- Impedance bandwidth varies over a wide range with resonator parameters. It can be as small as a few percent with high ε_r material, or over 20% with small ε_r in conjunction with certain geometries and resonant modes.

- Different far field radiation patterns are supported. For a given DRA geometry, the radiation patterns can be made to change by exciting different resonant modes.

7.2.2 Geometries

Simple shapes are adopted basically because of their mechanical simplicity. Along with the spherical, cylindrical and Cartesian coordinate systems, hemisphere [15], circular cylinder [2] and rectangular DRAs [16] are simple in mathematical formulations and mechanical fabrications.

To compare the geometries of spherical, circular cylindrical and rectangular DRAs, the dimensional degrees of freedom are considered. Tunable dimensions for hemispherical, circular cylindrical and rectangular shapes are one, two and three respectively. For example, with a certain material, once the resonant frequency of a hemispherical DRA is determined by the radius, everything else is fixed, including the bandwidth. One-dimensional freedom makes hemispherical

DRAs easy to design but difficult to optimise for particular requirements. At a result, hemispherical DRAs are, in practice, less frequently used.

A circular cylinder on the other hand resonates at a certain frequency with a number of radius-height pairs. Different pairs may give different values of bandwidth, directivity and volume occupations.

Hemispheres and circular cylinders always support degenerate resonant modes because of the existence of certain symmetry. These modes may increase the cross polarisation ratio that is unwanted for linear polarisations but may be necessary for dual or circular polarisations designs. Rectangular DRAs offer an advantage over hemispherical and cylindrical DRAs in that the mode degeneracy can be controlled by choosing the appropriate dimensions of the resonator.

In addition, raw dielectric materials are usually manufactured and shipped in long rods. The circular cylindrical shape may ease the fabrication process while maintaining certain degrees of freedom for characteristic optimisations. As a result, the circular cylindrical family is popular and we will mainly focus on circular cylindrical and rectangular DRAs.

7.2.3   Resonant Modes

The design of a DRA in any geometry must satisfy various specifications including: the resonant frequency, the field distribution inside the resonator, the radiated field and also the bandwidth. Resonator modes are usually classified into two main categories, *Transverse Electric* (TE) and *Transverse Magnetic* (TM). TE and TM must refer to a coordinate axis. In general, **TE** to an axis implies the *E*lectric field component in that axis vanishes, or equivalently two electric components *T*ransverse (perpendicular) to that axis exist. Similarly for **TM,** *M*agnetic is replaced with *E*lectric in the above statement.

7.2.4   Circular Cylindrical DRAs

Figure 7.1 shows a circular cylindrical DRA with radius a and height d on a large ground plane at z=0. It supports three distinct modes, TE (to z), TM (to z) and hybrid. TE ($E_z = 0$) and TM ($H_z = 0$) are axisymmetric and have no ϕ variation. The hybrid mode, ϕ dependent, is further classified into two groups, HE and EH [17]. In HE mode, E_z mainly contributes to the resonance and the comparatively small H_z is neglected. The other field components are derived from knowledge of E_z only. For EH mode the reverse is true.

To provide an approximate analysis of the fields inside the resonator and also predict its resonant frequency, the cavity resonator model is invoked. In this model, the outer surfaces of the cavity are approximated by perfect magnetic walls so that well known eigenfunction expansions for the fields can be utilised [1], [2]. This model provides reasonable accuracy for prediction of resonant frequency but does not predict more intricate field behavior, such as hybrid modes. Thus, in the subsequent parts of this chapter, TM and HE will be simply grouped as TM and, similarly, TE and EH grouped as TE.
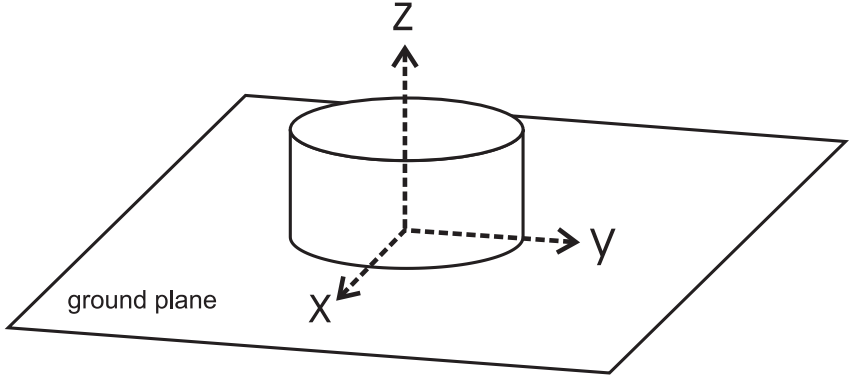
Figure 7.1: A circular cylindrical DRA on a large ground plane at z=0

To identify the field variations along ϕ, r and z directions respectively, the three indices n, p and m are added as subscripts after the mode classification. In general, all modes may be written in the form of $TE_{npm+\delta}$ and $TM_{npm+\delta}$. This nomenclature is historically based on the mode nomenclature of cylindrical dielectric waveguides.

With a circular cylindrical DRA of radius a and height d, the normalised field distribution can be described as [1], [2], [18]

$$TE: \qquad H_z^{npm} = J_n\left(\frac{X_{np}^{TE}}{a}r\right)\begin{bmatrix} \sin(n\phi) \\ \cos(n\phi) \end{bmatrix} \sin\left[\frac{(2m+1)\pi}{2d}z\right] \qquad (7.1)$$

$$TM: \qquad E_z^{npm} = J_n\left(\frac{X_{np}^{TM}}{a}r\right)\begin{bmatrix} \sin(n\phi) \\ \cos(n\phi) \end{bmatrix} \cos\left[\frac{(2m+1)\pi}{2d}z\right] \qquad (7.2)$$

$$n = 1,2,3,... \qquad p = 1,2,3,... \qquad m = 0,1,2,...$$

where $J_n(\cdot)$ is the nth order Bessel function of the first kind, the selection of $\sin(n\phi)$ or $\cos(n\phi)$ depends on the feed position and X_{np}^{TE}, X_{np}^{TM} are the roots satisfying the corresponding characteristics equations given by

$$TE: \qquad J_n(X_{np}^{TE}) = 0 \qquad (7.3)$$

$$TM: \qquad J_n'(X_{np}^{TE}) = 0 \qquad\qquad (7.4)$$

where $J_n'(.)$ is the derivative of the nth order Bessel function of the first kind with respect to r. Figures 7.2 to 7.5 show the fields inside the resonator for $TE_{011+\delta}$, $TM_{01\delta}$, $TM_{11\delta}$, $TM_{21\delta}$ respectively, in top and side views [19].

  The resonant frequencies are determined by the mode subscripts npm. Different npm combinations indicate different degenerate modes. The resonant frequency of a particular mode can be solved from the separation equation

$$k_r^2 + k_z^2 = \varepsilon_r \left(\frac{2\pi f}{c} \right)^2 \qquad\qquad (7.5)$$

where f is frequency and c is the velocity of light in free space. k_r and k_z are the wavenumbers inside the resonator in r and z directions respectively. By assuming magnetic walls for the outer surfaces, the wavenumbers are found as

$$k_r = \frac{1}{a} \begin{Bmatrix} X_{np}^{TE} \\ X_{np}^{TM} \end{Bmatrix} \qquad\qquad (7.6)$$

$$k_z = \frac{(2m+1)\pi}{2d} \qquad\qquad (7.7)$$

After rearrangement, the resonant frequency for the mode governed by npm is given by

$$f_{npm} = \frac{c}{2\pi a \sqrt{\varepsilon_r}} \sqrt{ \begin{Bmatrix} X_{np}^{TE^2} \\ X_{np}^{TM^2} \end{Bmatrix} + \left[\frac{\pi a}{2d}(2m+1) \right]^2 } \qquad\qquad (7.8)$$

7.2.5   Excitation Schemes

Widely adopted schemes include conducting probes, microstrips and micro-strip-slots, as shown in Figure 7.6. Nothing could be simpler than coupling to a DRA through a conducting probe. To tune the impedance the probe can be put at different positions and the length can be changed. However, care should be taken in regard to the imperfect fabrication effect of air gaps between the probe and the DRA [20]. Good coupling can be achieved by aligning the probe along the electric

field components, usually E_z, when the DRA is on a ground plane. For example, the probe should be placed along the axis of a circular cylinder to excite $TM_{11\delta}$ or near the circumference to excite $TM_{11\delta}$ as shown in Figures 7.3a(ii) and 7.4a(ii).

a(i) z=d, t=0

b(i) z=0, t=T/4

a(ii) ϕ=0, t=0

b(ii) ϕ=0, t=T/4
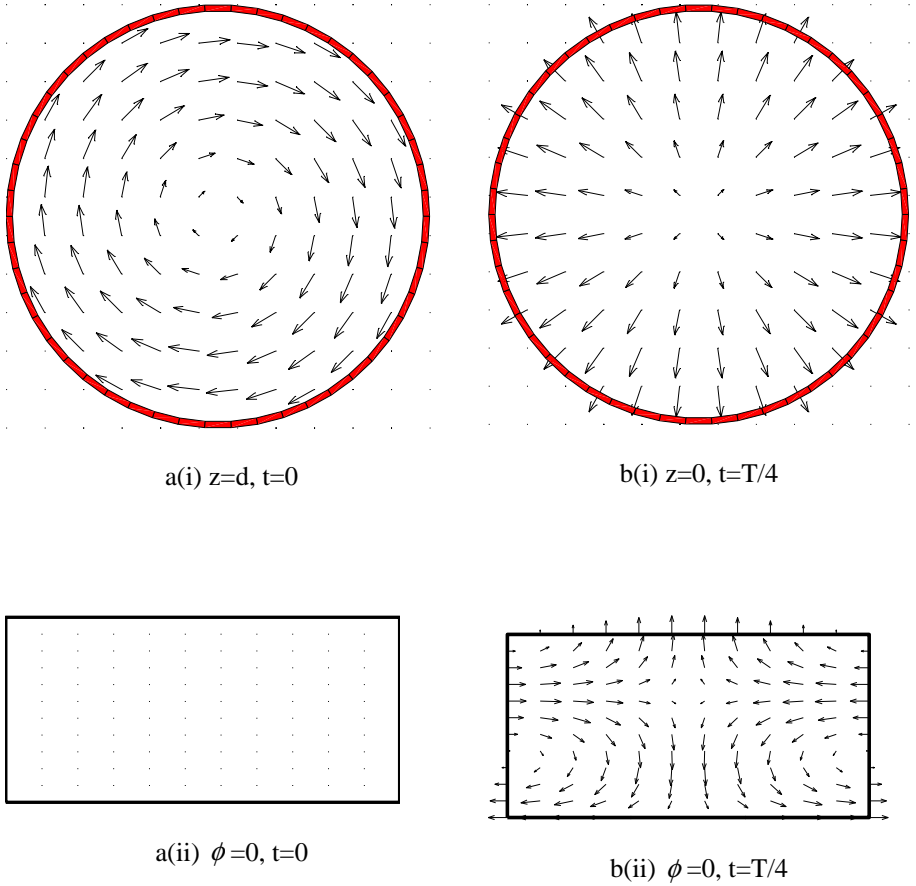
Figure 7.2: Fields inside the cylindrical DRA for the mode $TE_{011+\delta}$, with a(i),(ii) showing E-field in top, side views respectively, and b(i),(ii) showing H-field in top, side views, respectively (T being the time period of one resonant cycle)

a(i) z=d, t=0

b(i) ϕ =0, t=T/4

a(ii) ϕ =0, t=0

b(ii) ϕ =0, t=T/4
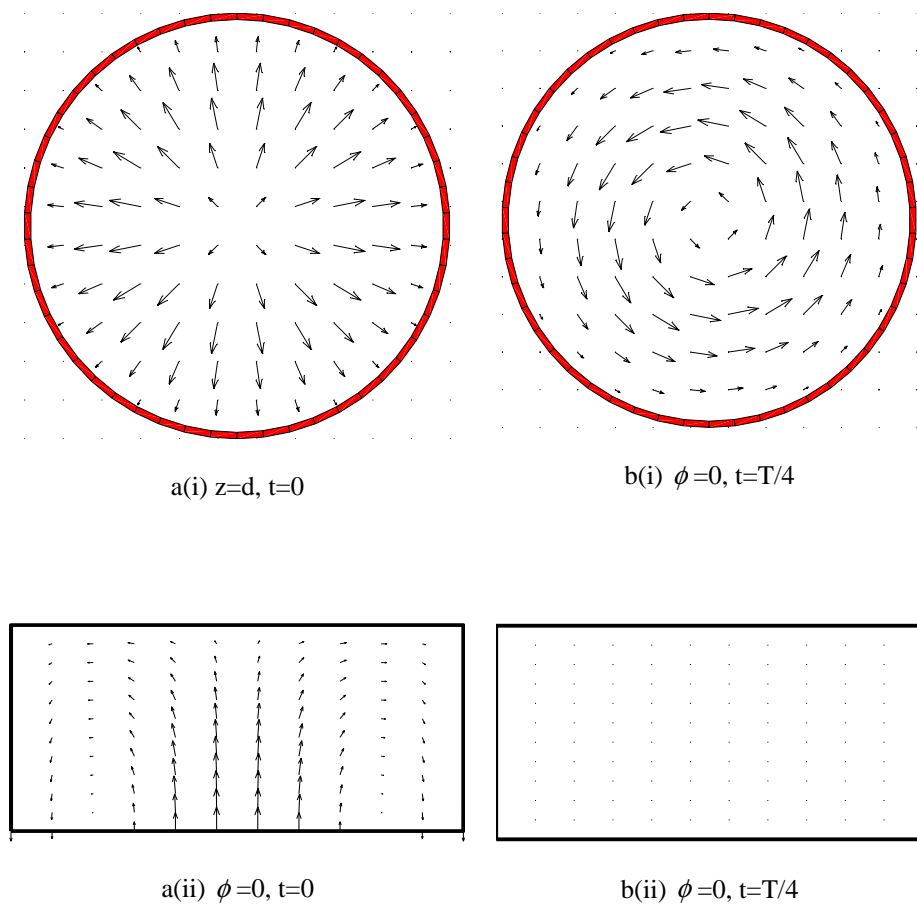
Figure 7.3: Fields inside the cylindrical DRA for the mode $TM_{01\delta}$, with a(i),(ii) showing E-field in top, side views respectively, and b(i),(ii) showing H-field in top side views, respectively (T being the time period of one resonant cycle)

a(i) z=d, t=0

b(i) z=0, t=T/4

a(ii) $\phi = 0$, t=0

b(ii) $\phi = \pi/2$, t=T/4
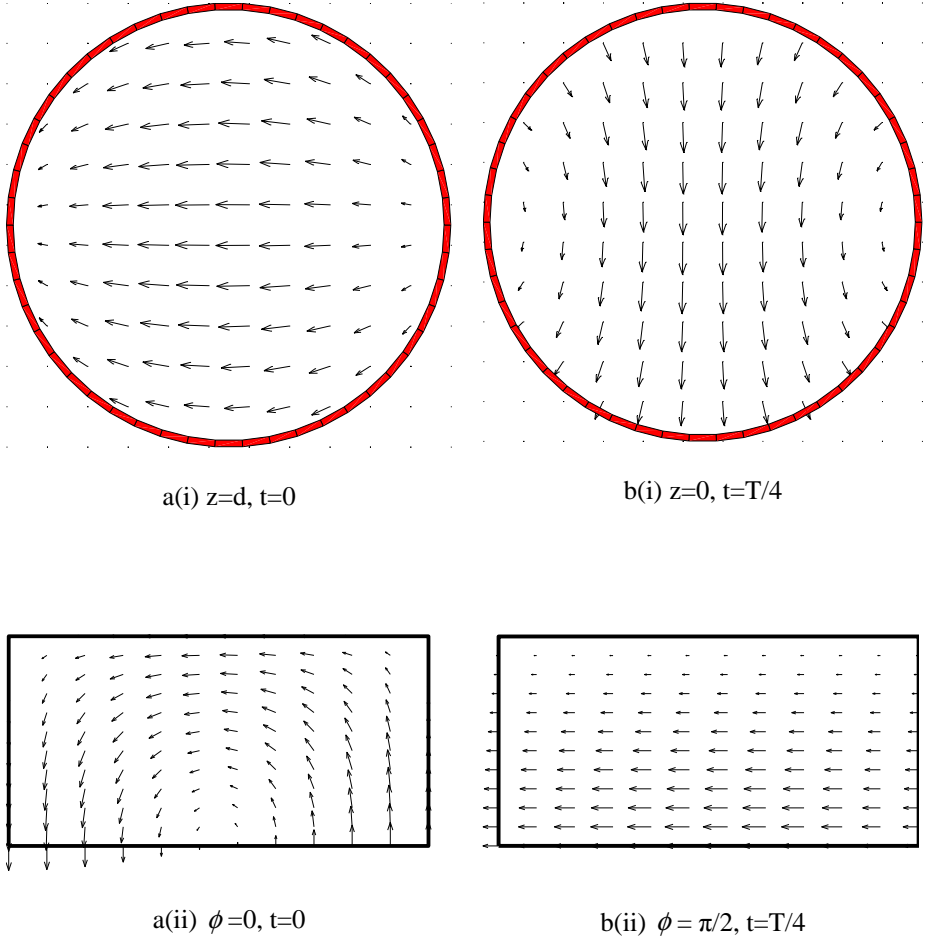
Figure 7.4: Fields inside the cylindrical DRA for the mode $TM_{11\delta}$, with a(i),(ii) showing E-field in top, side views respectively, and b(i),(ii) showing H-field in top side views, respectively (T being the time period of one resonant cycle)

a(i) z=d, t=0

b(i) z=0, t=T/4

a(ii) ϕ =0, t=0

b(ii) ϕ =π/4, t=T/4

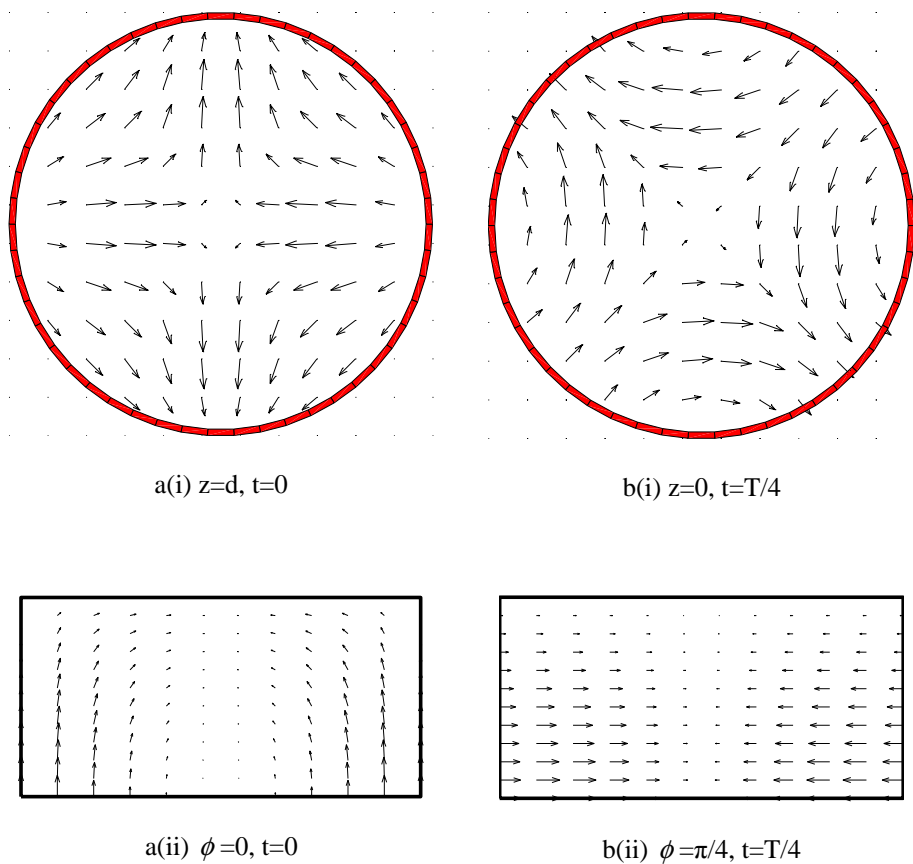**Figure 7.5**: Fields inside the cylindrical DRA for the mode $TM_{21\delta}$, with a(i),(ii) showing E-field in top, side views respectively, and b(i),(ii) showing H-field in top side views, respectively (T being the time period of one resonant cycle)
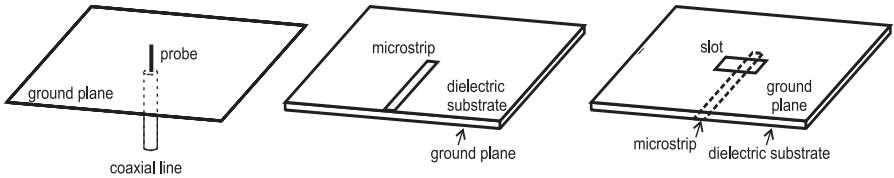
The microstrips and microstrip-slots potentially help the integration of DRAs with microwave ICs. The excitation fields 'leak' through the slot and the microstrip. Half-split cylindrical, hemispherical DRAs use microstrip-slots to excite their TE modes. More degrees of freedom can be tuned in these two schemes. In regard to microstrips, one point which should be noted is that a 'leak' in other areas, apart from the coupling area, would affect the radiation patterns of the DRAs.

Figure 7.6: The three common excitation mechanisms from left to right: probes, microstrips and microstrip-slots

7.2.6 Dielectric Resonator Antenna Modelling

To facilitate accurate and efficient antenna analysis, the Finite Difference Time Domain (FDTD) method is employed [21],[22]. FDTD discretises Maxwell's equations and steps them through discrete time. The complete electric and magnetic fields inside and outside the antenna, or even at the finite ground plane, are calculated at every time step. With this information the components of *E* and *H* fields, impedance, and the power radiated, everywhere and at any frequency, are determined in a single analysis. Secondary quantities, such as input impedance, reflection coefficient, voltage standing wave ratio (VSWR) and far field radiation pattern are obtained by post processing [23].

7.3 COMPACT CIRCULAR SECTOR AND ANNULAR SECTOR DRAS

Circular sector and annular sector DRA geometries are formed by removing a sector (or equivalently a wedge) of dielectric material from a circular or annular cylinder. In this section, we demonstrate that significant reductions in the volume of the DRAs can be obtained by utilising circular sector and annular sector DRAs. DRA volume minimisation for compact antenna design is also discussed and a design is proposed and tested for a mobile telephone handset suitable for the DCS1800 system. To our knowledge, these have not been reported elsewhere [5].

7.3.1 General Geometry

The general DRA to be considered is shown in Figure 7.7. It consists of a circular DRA of radius a and height d, on a metallic ground plane, with a sector and circular core of dielectric material removed. The sector angle is denoted as β, while b is taken as the inner radius so that the ratio defined by $\alpha = b/a$ is between zero and unity. The sector faces (I), (II) and the inner circular surface (III) can be metallised or left open. Depending on the setting of β and α, circular ($\beta = 2\pi, \alpha = 0$), sectored ($\beta < 2\pi, \alpha = 0$), annular ($\beta = 2\pi, \alpha > 0$) and sectored-annular ($\beta < 2\pi, \alpha > 0$) DRAs can be formed.
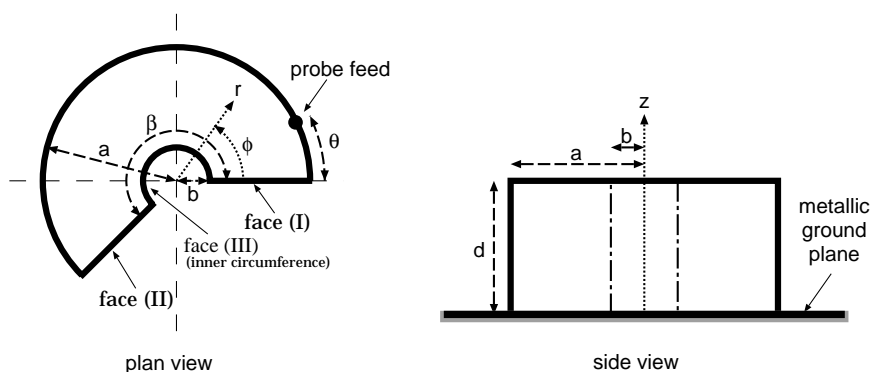
Figure 7.7: General geometry of a circular or annular sector DRA. Sector faces (I) or (II) and inner circumference (III) can be metallic plates or left open (from [5], © 1999 IEEE)

7.3.2 An Approximate Cavity Model

Based on (7.2) for $TM_{vpm+\delta}$, the normalised z-component electric field inside the resonator, shown in Figure 7.7, is described as

$$E_z = \left[AJ_V(k_r r) + BY_V(k_r r)\right] \begin{Bmatrix} \sin(v\phi) \\ \cos(v\phi) \end{Bmatrix} \cos(k_z z) \tag{7.9}$$

$$k_r = \frac{X_{vp}}{a} \tag{7.10}$$

$$k_z = \frac{(2m+1)\pi}{2d} \qquad (7.11)$$

$$b \leq r \leq a, \qquad 0 \leq \phi \leq \beta, \qquad 0 \leq z \leq d, \qquad p = 1,2,3,... \qquad m = 0,1,2,... \qquad (7.12)$$

where ν is a positive real number that depends on the boundary conditions on the sector faces as well as the sector angle. $J_\nu(.)$ and $Y_\nu(.)$ denote the ν th order Bessel functions of the first and second kind respectively. The term $Y_\nu(.)$ appears when the inner surface (III) is present, or equivalently b>0. A and B are arbitrary constants to be determined. $X_{\nu p}$ is the root satisfying the characteristic equation (see later sections) governed by the resonator geometry and boundary types. The selection of $\sin(\nu\phi)$ or $\cos(\nu\phi)$ depends on the geometry and feed position.

The resonant frequency of the $TM_{\nu pm+\delta}$ mode can be derived from the separation equation and has the same form as (7.8). With n replaced with ν, it is written as

$$f = \frac{c}{2\pi a \sqrt{\varepsilon_r}} \sqrt{X_{\nu p}^2 + \left[\frac{\pi a}{2d} (2m+1) \right]^2} \qquad (7.13)$$

7.3.2.1 Conventional circular DRA

A conventional circular DRA, formed when $\beta = 2\pi, \alpha = 0$ (the surfaces (I), (II) and (III)) are not present, has been well investigated in the literature [1],[2]. For this geometry $\nu = n$ where n is an integer and B=0 so that the normalised z-component of the electric field inside the cavity can be written as

$$E_z^{\nu pm} = A J_\nu(k_r r) \begin{Bmatrix} \sin(\nu\phi) \\ \cos(\nu\phi) \end{Bmatrix} \cos(k_z z) \qquad (7.14)$$

where the root $X_{\nu p}$ can be solved from the characteristic equation given by

$$J_n'(X_{\nu p}) = 0 \qquad (7.15)$$

Table 7.1 lists some values of $X_{\nu p}$ in which integer values of ν and $\alpha = 0$ are designated for this geometry.

7.3.2.2 Circular sector DRA

Circular sector DRAs are formed by setting $\beta < 2\pi, \alpha = 0$ and the resonant frequency and the fields inside the DRA then depend on whether the faces (I) and

(II) are metallic or open. The three possible combinations for these faces include both metallic, both open, or one metallic and one open face.

Metallic Sector Faces
In this geometry metallic walls are placed on the faces (I) and (II). Since any electric field tangential to the metallic walls will vanish, the corresponding boundary conditions can be written as

$$E_z \mid_{\phi=0} = 0 \quad \text{and} \quad E_z \mid_{\phi=\beta} = 0 \tag{7.16}$$

To satisfy the boundary condition at $\phi = 0$ on face (I) the term $\cos(\nu\phi)$ will vanish. To satisfy the remaining boundary condition at $\phi = \beta$ on face (II),

$$\sin(\nu\beta) = 0 \tag{7.17}$$

$$\nu\beta = n\pi \quad \text{where} \quad n = 1,2,... \tag{7.18}$$

It is noted that though n=0 is a numerical solution to the above equation, it is not a physical resonance. The solutions for ν becomes

$$\nu = \frac{n\pi}{\beta} \quad \text{where} \quad 0 < \beta \le 2\pi \tag{7.19}$$

where n is a non-zero positive integer [24]. The z-component of the electric field and characteristic equation are then also given by (7.14) and (7.15) respectively. Table 7.1 lists some values of $X_{\nu p}$ for different non-zero real values of ν in which $\alpha = 0$ is for this cavity.

		$\nu = 0$	$\nu = 1/4$	$\nu = 1/3$	$\nu = 1/2$	$\nu = 2/3$	$\nu = 1$	$\nu = 2$
$\alpha = 0$	p=1	3.832	0.769	0.910	1.166	1.401	1.841	3.054
	p=2	7.016	4.225	4.353	4.604	4.851	5.331	6.706
$\alpha = 0.1$	p=1	3.932	0.770	0.911	1.166	1.402	1.841	3.054
	p=2	7.307	4.279	4.396	4.632	4.868	5.338	6.707
$\alpha = 0.2$	p=1	4.204	0.776	0.917	1.171	1.406	1.844	3.055
	p=2	7.797	4.490	4.588	4.789	4.995	5.419	6.723
$\alpha = 0.5$	p=1	6.120	0.847	0.993	1.253	1.488	1.921	3.104
	p=2	16.14	6.336	6.406	6.543	6.679	6.954	7.826

Table 7.1: Values of $X_{\nu p}$ for circular sector and annular sector (open inner surface) DRAs. From the characteristic equation $J'_\nu (X_\nu p) = 0$ for $\alpha = 0$, and equation (7.26) for $\alpha > 0$, $\varepsilon_r = 12$, as described in the text (from [5], © 1999 IEEE).

The resonant frequency for a given DRA with radius a and height d depends only on X_{vp} through the variable v. From Table 7.1 it can be seen that the smaller v is the lower X_{vp} and therefore provides a lower resonant frequency. To make v as small as possible, β must be large and hence for the lowest resonant frequency $\beta = 2\pi$. Therefore, a thin metallic plate between faces (I) and (II), with a length equal to the radius of the resonator placed from the center provides the lowest resonant frequency. Using this geometry, the Bessel root is then $X_{\frac{1}{2}-1} = 1.166$, and

the corresponding mode as $TM_{\frac{1}{2}-1\delta}$.

Open Sector Faces
When the sector faces are left open, a magnetic wall approximation is invoked to give a field expansion inside the cavity. Correspondingly the boundary conditions on faces (I) and (II) are written as

$$\frac{\partial E_z}{\partial \phi}\Big|_{\phi=0}= 0 \quad \text{and} \quad \frac{\partial E_z}{\partial \phi}\Big|_{\phi=\beta}= 0 \tag{7.20}$$

To satisfy the boundary condition at face (I), the term $\sin(v\phi)$ will vanish. To satisfy the condition at face (II), (7.19) must be imposed. The situation is then similar to that of both metallic faces, and the characteristic equation and resonant frequency are also given by (7.15) and (7.13) respectively.

Metallic and Open Sector Faces
Sector faces can also be made with one metallic and leave the other open. With the corresponding boundary conditions introduced previously for metallic and open faces, the new conditions become

$$E_z\big|_{\phi=0}= 0 \quad \text{and} \quad \frac{\partial E_z}{\partial \phi}\Big|_{\phi=\beta}= 0 \tag{7.21}$$

To satisfy the boundary condition at $\phi = 0$, $\cos(v\phi)$ will vanish. The boundary condition at $\phi = \beta$ requires

$$\cos(v\beta) = 0$$
$$v\beta = (2n-1)\frac{\pi}{2} \quad \text{where} \quad n = 1,2,... \tag{7.22}$$
$$\beta = (2n-1)\frac{\pi}{2\beta} \quad \text{where} \quad 0 < \beta < 2\pi$$

and n is a non-zero positive integer. Should the sector angle β approach 2π, the root of Bessel derivative becomes $X_{\frac{-1}{4}1}$ This provides further reductions in volume and resonant frequency. In practice, however, it is impossible to have both open and metallic walls at $\phi = 0$, so this mode can only be approached for β close to 2π.

7.3.2.3 Annular DRA

When α is greater than zero and $\beta = 2\pi$ (faces (I) and (II) not present), annular DRAs are formed, also known as ring DRAs. For this geometry the z-component electric field inside the cavity can be written as (7.9) for $v = n$, where n is an integer. The wavenumber k_r, however, now depends on the boundary condition on the inner surface (III), which can be either metallic or left open.

Metallic Inner Surface
When the inner surface (III) is metallic, it is a cylindrical ring DRA with a metal cylinder at $r=b$. This geometry has been previously considered by [25]. Inside the cavity ($b \leq r \leq a$) the field (7.9) must satisfy the following boundary conditions

$$E_r \mid_{r=b}=0 \quad \text{and} \quad \frac{\partial E_z}{\partial r}\mid_{r=a}=0 \tag{7.23}$$

giving

$$AJ_V\left(\frac{X_{vp}}{a}b\right)+ BY_V\left(\frac{X_{vp}}{a}b\right)=0 \tag{7.24}$$

$$AJ'_V\left(X_{vp}\right)+ BY'_V\left(X_{vp}\right)=0 \tag{7.25}$$

so that the characteristic equation is

$$J'_V\left(X_{vp}\right)Y_V(\alpha X_{vp}) + J_V(\alpha X_{vp})Y'_V\left(X_{vp}\right)=0 \tag{7.26}$$

where $\alpha = b/a$ is the inner to outer radius ratio. Typical values for the solution X_{vp} are listed in Table 7.2 in which integer values of v are valid. It is noted that as α gets larger X_{vp} increases, and therefore the resonant frequency increases. For small values of α, say α =0.05, (in practice when α is smaller than 0.05 the

DRA will be difficult to construct and achieve a $50 \, \Omega$ match) the Bessel root will obtain a value of $X_{vp} = 0.930$ for mode $TM_{01\delta}$.

Open Inner Surface

When the inner circular surface (III) is left open, it becomes a ring DRA. To find the field in the DRA, the inner free-space circular region ($0 \leq r \leq b$) is modeled using an eigenfunction expansion as

$$E_z = CI_v(k_{0r}r) \begin{Bmatrix} \sin(v\phi) \\ \cos(v\phi) \end{Bmatrix} \cos(k_z z) \quad (7.27)$$

where C is an arbitrary constant, I_v is the v th order modified Bessel function of the first kind. In this inner region, the dielectric constant of air is much lower than ε_r and the mode is evanescent [18]. As a result the pure imaginary wavenumber is denoted as jk_{0r}. The separation equation becomes

$$k_z^2 - k_{or}^2 = \left(\frac{2\pi f}{c}\right)^2 \quad (7.28)$$

Referred to (7.5) and [26], k_{0r} is given as

$$k_{or}^2 = k_z^2 - \frac{k_z^2 + k_r^2}{\varepsilon_r} \quad (7.29)$$

Matching (7.27) with the expansion (7.9) across the boundary $r=b$ to give

$$CI_v(k_{0r}b) = AJ_v(k_r b) + BY_v(k_r b) = 0 \quad (7.30)$$

$$C\frac{k_{0r}}{k_r} I'_v(k_{0r}b) = AJ'_v(k_r b) + BY'_v(k_r b) \quad (7.31)$$

By assuming a perfect magnetic wall around the outer circular surface at $r=a$. (7.27) becomes

$$AJ'_v(k_r b) + BY'_v(k_r a) = 0 \quad (7.32)$$

and solving the equations (7.30), (7.31), (7.32) simultaneously, the characteristic equation will be

$$k_{0r}aI'_\nu(\alpha k_{0r}a)\left[J_\nu(\alpha X_{\nu p})Y'_\nu\left(X_{\nu p}\right)-J'_\nu\left(X_{\nu p}\right)Y_\nu(\alpha X_{\nu p})\right]$$
$$-X_{\nu p}I_\nu(\alpha k_{0r}a)\left[J'_\nu(\alpha X_{\nu p})Y'_\nu\left(X_{\nu p}\right)-J'_\nu\left(X_{\nu p}\right)Y'_\nu(\alpha X_{\nu p})\right]=0 \tag{7.33}$$

Table 7.1 lists some typical values of $X_{\nu p}$ for $\nu = n$, $\varepsilon_r = 12$, optimised a/d ratio and $m=0$ in which integer values of ν and $\alpha > 0$ are for this cavity. Again it is noted that as α increases, $X_{\nu p}$ increases, and therefore the resonant frequency increases.

7.3.2.4 Annular sector DRA

Combining the results in Sections 7.3.2.2 and 7.3.2.3, annular sector DRAs in which $\beta < 2\pi$ and $\alpha > 0$ are considered. The fields inside the annular sector DRA take the most general form as written in (7.9). The feasible modes are determined by the value of β, and the boundary conditions are imposed on faces (I) and (II) in the same way as described in Section 7.3.2.2. Using this analysis the exact value of the mode parameter ν can be calculated using (7.19) or (7.22). The resonant frequency (7.13), however, depends on the particular mode and hence the value of the root $X_{\nu p}$. It is determined by α and the boundary conditions imposed on the inner surface (III). For a particular α, the characteristic equation is either (7.26) or (7.33) (replacing n with ν) for metallic or open inner circular surfaces (III) respectively. Particular values of $X_{\nu p}$ can be found in Table 7.1 or 7.2 for different α and modes.

For example, consider an annular sector with $\alpha = 0.1$, $\beta = \pi$ with surfaces (I), (II) and (III) being metallic. From (7.19), $\nu = n$ and select characteristic equation (7.26) whose solutions are given in Table 7.2 for $\alpha = 0.1$ and non-zero integer values of ν. The lowest resonant frequency possible is due to mode $TM_{11\delta}$ (n must be non-zero) as that with the root X_{11} from which the resonant frequency can be calculated by (7.13).

		$\nu = 0$	$\nu = 1/4$	$\nu = 1/3$	$\nu = 1/2$	$\nu = 2/3$	$\nu = 1$	$\nu = 2$
$\alpha = 0$	p=1	0.930*	0.769	0.910	1.166	1.401	1.841	3.054
	p=2	4.635*	4.225	4.353	4.604	4.851	5.331	6.706
$\alpha = 0.1$	p=1	1.103	1.171	1.221	1.352	1.512	1.879	3.056
	p=2	4.979	5.017	5.046	5.128	5.239	5.532	6.724
$\alpha = 0.2$	p=1	1.412	1.456	1.489	1.581	1.699	1.993	3.073
	p=2	5.696	5.718	5.735	5.783	5.849	6.033	6.910
$\alpha = 0.5$	p=1	2.722	2.738	2.751	2.786	2.836	2.973	3.619
	p=2	9.292	9.298	9.303	9.318	9.338	9.394	9.696

Table 7.2: Values of $X_{\nu p}$ for annular sector DRAs with metallic inner surface. From the characteristic equation $J'_\nu\left(X_{\nu p}\right)Y_\nu(\alpha X_{\nu p})+J_\nu(\alpha X_{\nu p})Y'_\nu\left(X_{\nu p}\right)=0$

* The ratio α =b/a is limited to α =0.05 (from [5] © 1999 IEEE).

7.3.3   Simulation Results

The predictions of the approximate theory presented in Section 7.3.2 are confirmed by using simulation results from FDTD with the same setup as [27],[28],[8]. For the simulations, circular sector DRAs are selected with radius a=18mm, height d=18mm, $\varepsilon_r = 12$ and a finite ground plane of $150 \times 150 \text{mm}^2$.

Table 7.3 provides results from 15 simulations for various sector angles β for $\alpha = 0$ or $\alpha > 0$ with surface (III) left open. Each row of the table lists the inner to outer radius ratio α, sector angle β, type of boundary conditions on surfaces (I) and (II), the predicted resonant frequency, modes from (7.13) and the corresponding resonant frequency and bandwidth from FDTD simulations. A figure of merit γ is the FDTD resonant frequency multiplied with the circular sector DRA volume [GHz cm^3]. The smaller γ is, the smaller the DRA size for a given resonant frequency.

The first two entries 1 and 2 with $\beta = 2\pi$ are equivalent to the fundamental and the higher order modes of a conventional cylindrical DRA. Theory and FDTD simulations both predict resonant frequencies close to 1.96 and 2.88GHz. Entry 3 is an annular DRA with a small inner to outer radius ratio. Cavity theory predicts a reasonable frequency compared to entry 1, and this is confirmed by simulation.

From table entries 4-7, in which both faces (I) and (II) are metallic, it can be seen that a close agreement between the theory and simulations and the percentage error is not larger than 5%. Reductions in both volume and resonant frequency are achieved as evidenced by a smaller γ.

For entries 8-11, larger variations between theory and simulations occur. This indicates the assumption of a perfect magnetic wall of the faces is not accurate. Entry 8 does not have any simulation results since in practice it is not possible to construct this geometry.

The final four entries are formed when one face is metallic and the other is open. Again simulation results for entry 12 are not included since this geometry is impossible to construct.

One of the more significant circular sector DRAs designs is in entry 15. This design maintains the same mode, frequency and bandwidth as that in entry 1, but takes up 25% of the volume. For the resonance of DCS1800 mobile telephone band, a DRA of approximately $2 \times 2 \times 2 \text{cm}^3$ would be achievable, making this design a possible candidate for usage.

7.3.4   Experimental Results

Experimental results are obtained for most of the geometries listed in Table 7.3 by constructing the circular sector DRAs by machining `ECCOSTOCK HiK' dielectric rod with $\varepsilon_r = 12$ manufactured by Emerson and Cuming Inc. The measurements were obtained using an HP8753D network analyser.

For the entries 4-7, both of their sector faces being metallic plates, close agreements of frequency and bandwidth among the theory, simulations and measurements are obtained. For entries 9-11 and 13-15, the measurements agree well with the corresponding simulations for frequency and bandwidth. A plot of the VSWR measurement for entry 15 is provided in Figure 7.8. In general, FDTD simulations predict smaller resonant frequencies than actual measurements, but differences are generally less than 5%. In addition, simulation and experimental results in entry 6 agree with the findings in [8].

7.3.5   Compact DRA Designs

An important part of our investigation is to determine DRA designs that are the most compact in some sense for a given mode or resonant frequency f. Here I define compact as having minimum volume or minimum profile.

|			Faces		Theory		FDTD		γ	Experiment	
	α	β	I	II	f GHz	Mode	f GHz	B.W.	GHz cm^3	f GHz	B.W.
1	0	360	n.a.		1.85	$TM_{11\delta}$	1.96	7.5%	35.9	2.04	6.6%
2	0	360	n.a		2.63	$TM_{21\delta}$	2.88+	3.1%	52.8	Not meas.	
3	0.2	360	n.a.		1.85	$TM_{11\delta}$	2.02	8.3%	35.5	2.08	7.7%
4	0	360	M	M	1.50	$TM_{\frac{1}{2}1\delta}$	1.44	4.0%	26.4	1.46	2.1%
5	0	270	M	M	1.61	$TM_{\frac{2}{3}1\delta}$	1.59	5.4%	21.8	1.60	3.8%
6	0	180	M	M	1.85	$TM_{11\delta}$	1.86	6.1%	17.0	1.88	6.4%
7	0	90	M	M	2.63	$TM_{21\delta}$	2.70	13.6%	12.4	2.78	10.3%
8	0	360	O	O	1.50	$TM_{11\delta}$	n.a.	n.a.		n.a.	
9	0	270	O	O	1.61	$TM_{11\delta}$	2.09	7.7%	28.7	2.15	9.8%
10	0	180	O	O	1.85	$TM_{11\delta}$	2.28	9.5%	20.9	2.39	9.4%
11	0	90	O	O	2.63	$TM_{11\delta}$	2.99	9.9%	13.7	3.05	8.0%
12	0	360	M	O	1.34	$TM_{11\delta}$	n.a.	n.a.		n.a.	
13	0	270	M	O	1.39	$TM_{11\delta}$	1.59	3.9%	21.8	1.58	2.9%
14	0	180	M	O	1.50	$TM_{11\delta}$	1.69	4.2%	15.5	1.70	5.3%
15	0	90	M	O	1.85	$TM_{11\delta}$	2.01	7.7%	9.2	1.99	6.5%

Table 7.3: Performance of various circular sector and annular sector DRAs as described in the text. a=d=18mm on a 150×150mm^2 ground plane, FDTD cell is $1 \times 1 \times 1$mm^3. * face (I) defined at $\phi = 0$; face (II) at $\phi = \beta$, letter 'M' for Metallic face; `O' for Open face + matched to $75\,\Omega$ instead of $50\,\Omega$ (from [5] © 1999 IEEE).

7.3.5.1   Minimum volume DRAs

The volume of the DRA designs considered can be written as

$$V = \pi a^2 d (1 - \alpha^2) \frac{\beta}{2\pi} \tag{7.34}$$

subject to the conditions imposed by (7.13). A necessary condition for a minimisation of the volume is when the derivatives of V with respect to the independent variables a, d, α and β are zero.
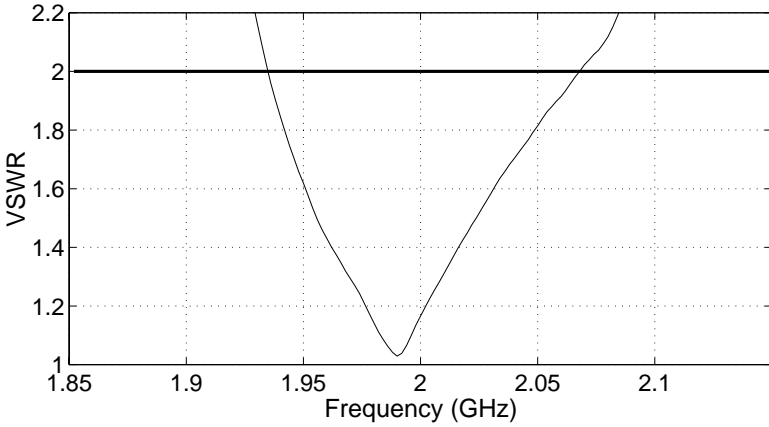
Figure 7.8: 50 Ω VSWR measurement of the 90 degrees circular sector DRA listed as entry 15 in Table 7.3 (from [5], © 1999 IEEE)

For a given mode X_{vp}, α and β are intricately related by (7.15), (7.26) or (7.33) and therefore the minimisation is restricted to when α and β are fixed leaving the free variables a and d. d is eliminated using the constraint (7.13) as

$$d = \frac{(2m+1)\pi}{2\sqrt{\left(\dfrac{f}{\xi}\right)^2 - \left(\dfrac{X_{vp}}{a}\right)^2}} \quad \text{where} \quad \xi = \frac{c}{2\pi\sqrt{\varepsilon_r}} \tag{7.35}$$

so that the condition for a minimum then becomes $\partial V / \partial a = 0$. Therefore the value of a for a minimum volume is

$$a_{opt} = \sqrt{\frac{3}{2}} \frac{\xi X_{vp}}{f} = \sqrt{\frac{3}{8\varepsilon_r}} \frac{cX_{vp}}{\pi f} \qquad (7.36)$$

and the corresponding value of d can be determined from (7.35) as

$$d_{opt} = \sqrt{\frac{3}{\varepsilon_r}} \frac{(2m+1)c}{4f} \qquad (7.37)$$

Equations (7.36) and (7.37) provide the minimum volume for a particular α, β and mode $TM_{vpm+\delta}$. From Tables 7.1 and 7.2, and equations (7.19) and (7.22), the minimum resonant frequency (minimum X_{vp}) for $TM_{vpm+\delta}$ mode occurs when $\alpha = 0$ and when face (I) is open and face (II) is metallic. Combining this geometry with the optimised a and d from (7.36) and (7.37) provides us with the global minimum. These are listed in Table 7.4 for various modes at f=1.80GHz and $\varepsilon_r = 12$. Because d_{opt} is independent of X_{vp}, it is constant for a particular frequency.

7.3.5.2 Minimum profile DRAs

Designs that have the lowest profile, for a particular resonant frequency, are also interesting. For low profile applications, the ratio a/d is much larger than unity. As observed from (7.13), the term $\pi a / 2d(2m+1)$ will dominate X_{vp} for small values of v and p. In this situation, the resonant frequency will approach the limit

$$f_m = \frac{c(2m+1)}{4d\sqrt{\varepsilon_r}} \qquad (7.38)$$

so that
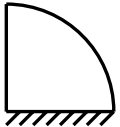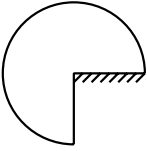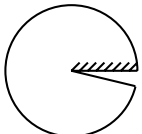
$$d = \frac{c(2m+1)}{4f_m\sqrt{\varepsilon_r}} \qquad (7.39)$$

which does not depend on the radius a [3]. Therefore this is a lower bound to the height of the DRA for a given resonant frequency and material. For 1.8GHz, $\varepsilon_r = 12$, m=0 the lower bound on is 12mm. However, even with a a/d ratio of say 3, the volume is very large at 49cm^3.

7.3.6   Proposed PCS Antenna Design

Using the analysis and results presented in previous sections, a compact circular sector DRA is proposed for mobile handsets for DCS1800 systems. From the

specifications [29], the uplink and downlink include two bands, 1710-1785MHz and 1805-1880MHz. A single-band antenna designed for this system should work at a centre frequency of 1795MHz and a bandwidth of 170MHz or 9.5%. To find the most compact DRA in terms of volume and profile, results from section 7.3.5 and Table 7.4 are used. If we select the smallest volume, we arrive at the geometry displayed in the final entry of Table 7.4. This, however, has a high profile of d=20.8mm. When we select the lowest profile d=12mm, the overall volume is roughly 14 times the minimum volume geometry and is also unsuitable.

Mode	X_{vp}	a (mm)	d (mm)	a/d	Volume (cm^3)	
$TM_{21\delta}$	3.054	28.6	20.8	1.375	6.711	
$TM_{11\delta}$	1.841	17.3	20.8	0.829	4.878	
$TM_{\frac{1}{2}1\delta}$	1.166	10.9	20.8	0.525	3.913	
$TM_{\frac{1}{3}1\delta}$	0.910	8.5	20.8	0.410	3.575	
$TM_{\frac{1}{4}1\delta}$	0.769	7.2	20.8	0.346	3.404	

Table 7.4: Theoretical optimal values of a and d for different modes with a metallic face and an open face, as sector faces at 1.80GHz, with α =0 and ε_r =12 (from [5], © 1999 IEEE)

To arrive at a compromise, we select the third entry in Table 7.4 and re-orient it, so the metallic plate for face (II) becomes the ground plane, as shown in Figure 7.9. The profile is only 10.9mm while the volume is only 15% larger than

the most compact form. In addition, this form is dimensionally suitable for handset design since the ground plane forms part of the circuit board of the telephone and therefore the antenna can be integrated into the handset, as shown in Figure 7.10.

Since the approximate theory generally predicts smaller resonant frequencies compared to the experiments, the actual dimensions of the antenna design is adjusted to a=12mm and d=22mm. The VSWR measurement of this antenna is shown in Figure 7.11 in which the dashed line is the measurement taken with a hand around the ground plane. With VSWR<2, the impedance bandwidth is from 1.68-2.30GHz, while VSWR<1.5 it is from 1.71-2.12GHz. This bandwidth easily satisfies the DCS1800 system specifications mentioned earlier. In fact, the bandwidth could be reduced and this could be performed by increasing ε_r. This would reduce the overall size further. The horizontal *x-y* plane far field measurement at 1.80GHz is presented in Figure 7.12, in which E_ϕ is in solid line and E_θ in broken line. E_ϕ radiation is directed towards the back of the handset and E_θ is mainly at two sides. This indicates that radiation towards the head of the user should be reduced.
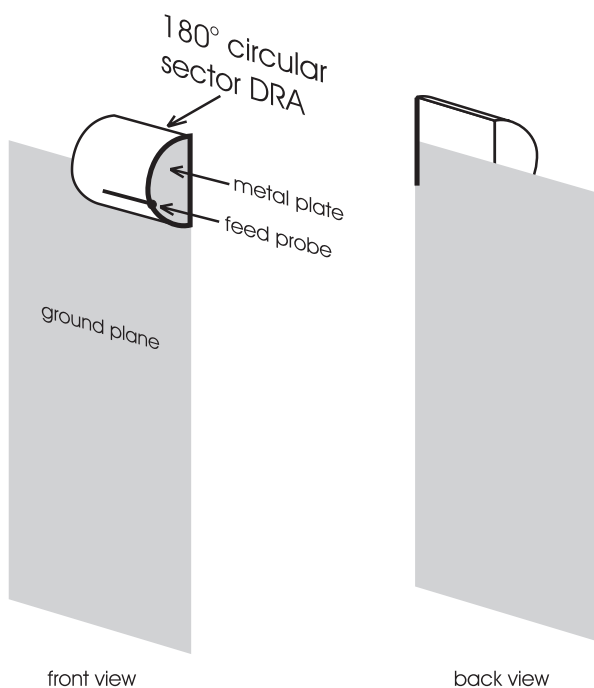
Figure 7.9: Proposed 180 degrees circular sector DRA design a=12mm, d=22mm mounted on a $100 \times 40\text{m}^2$ ground plane (from [5], © 1999 IEEE)
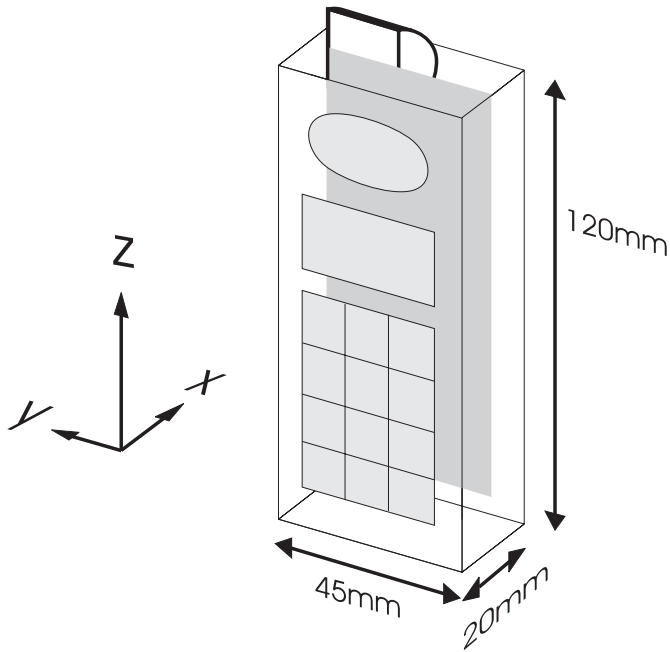
Figure 7.10: Illustration of the proposed circular sector DRA integrated into a mobile telephone handset (from [5], © 1999 IEEE)
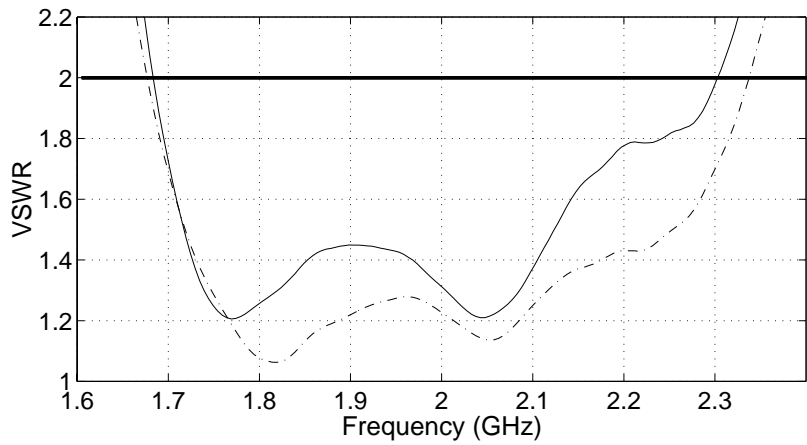
Figure 7.11: Experimental VSWR results of the circular sector DRA. As in Figure 7.9. Dashed line is the measurement taken with a hand around the ground plane. Solid line is without hand (from [5], © 1999 IEEE)

7.3.7 Summary

Using theory, simulations and experiments, various circular sector and annular sector DRAs have been investigated. A circular sector DRA design with sector angle 90 degrees, one metallic and one open sector face, provides the largest volume reduction for a given resonant frequency. It occupies 75% less volume than a conventional cylindrical DRA. Volume minimisation for compact sector DRA design at different operating modes is also discussed. Using this result, a compact (in both volume and profile) 180 degrees circular sector DRA with a=12mm, d=22mm is designed and proposed for future use in a mobile telephone handset. Experiments reveal the impedance bandwidth is 1.68-2.30GHz (VSWR < 2) which easily meets the DCS1800 system specifications and radiation towards the head of the user is reduced.
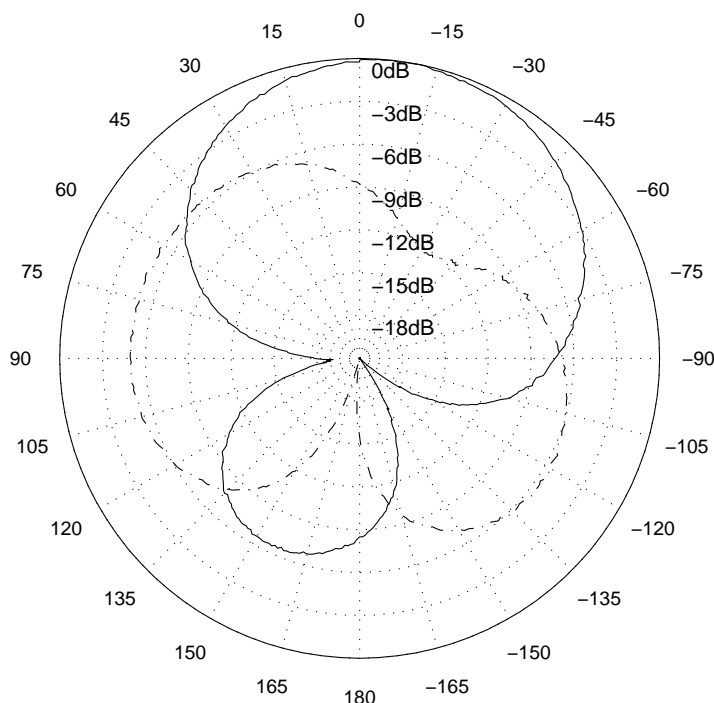
Figure 7.12: Experimental far field results of the circular sector DRA
As in Figure 7.9 at 1.80GHz in the x-y plane. Solid line represents horizontal polarisation and broken line, vertical polarisation (from [5], © 1999 IEEE)

7.4   DRA DESIGNS FOR CIRCULAR POLARISATION

In this section, we discuss the design of circularly polarised DRAs which are useful for satellite communication systems such as the Global Positioning Systems (GPS) and satellite-mobile communications. One reason circular polarisation is important for satellite communications is that the radio path is predominately line of sight with few reflected paths. To make the received power independent of the angular orientation of the receiver, circular polarisation is therefore used.

7.4.1   Polarisation of Waves

In general the electric field vector for arbitrary polarisation can be written as

$$E(t) = \hat{x}E_x \sin(\omega t + \delta) + \hat{y}E_y \sin(\omega t) \tag{7.40}$$

where δ is the phase difference with respect to the y-component, i.e. $\phi_x - \phi_y$. E_x and E_y are the horizontal and vertical magnitude components, respectively. $\hat{x}$ and $\hat{y}$ are the two-dimensional space unit vectors. ω is the angular frequency.

Phasor diagrams can be used to visualise the polarisations by plotting $|E_y(t)|$ against $|E_x(t)|$ over one period of time. The geometries formed in these diagrams are used to identify the polarisation types. In general, they are divided into three categories: linear, circular and elliptical shapes. The direction of rotation of the phasor determines whether the polarisation is left-handed or right-handed.

The definition for the sense of rotation adopted in this section is stated below.

For an observer viewing the wave approaching, the rotation of electric field vector in a stationary transverse plane is *clockwise* for *left-hand* circular polarisation (LHCP) as standardised by the *IEEE* [30].

E_x / E_y	δ (degrees)	Polarisation	Rotation
0, ∞	n.a.	Linear	n.a.
Any	0, 180	Linear	n.a.
1	90	Circular	RHCP
1	-90	Circular	LHCP
1	$0 < \delta < 180$, $\neq 90$	Ellipse	RHCP
1	$180 < \delta < 0$, $\neq 90$	Ellipse	LHCP
$\neq 0, 1, \infty$	$0 < \delta < 180$	Ellipse	RHCP
$\neq 0, 1, \infty$	$-180 < \delta < 0$	Ellipse	LHCP

Table 7.5: Classifications of wave polarisations.

Polarisation classifications are listed in Table 7.5. Circular polarisation occurs whenever $E_x = E_y$ and $\delta = \pm 90$. This condition is very difficult to achieve in antenna designs and in practice slightly elliptical polarisations are generally accepted provided the axial ratio, the magnitude ratio between the major and minor axes of the phasor ellipse, is within 3dB. An example of an elliptical polarisation, also known as a polarisation ellipse, with $E_x = 0.7$, $E_y = 1.0$, $\delta = 60$, is shown in Figure 7.13, where the major and minor axes are represented by a broken line. The axial ratio for this RHCP ellipse is 5.77dB.
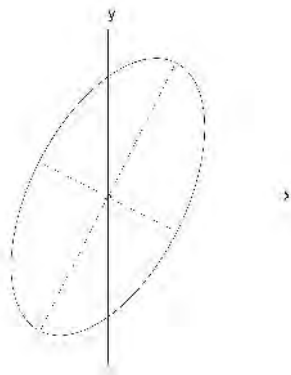
Figure 7.13: Phasor diagram of an elliptical polarisation $E_x = 0.7$, $E_y = 1.0$ $\delta = 60$ degrees (RHCP). Major and minor axes are in broken lines and the axial ratio is 5.77dB

7.4.2   Existing DRA Approaches

DRAs that exhibit circular polarisation applications are not new. An annular, or a ring, DRA using additional hardware comprising a 3dB quadrature phase coupler, and incorporated with double coaxial feeds was reported [10]. Another double-feed approach utilising a cylindrical DRA together with a 90 degree transmission line phase shifter was also reported [11]. Unfortunately these two approaches increase the construction complexity. On the other hand, rectangular DRAs fed by a single coaxial line or a slot, but without the use of any external quadrature phase devices, have been investigated [12],[31]. The technique involves two degenerate modes, which are excited within the same resonator, but are orthogonal in space and exhibit a 90 degree phase difference, thus producing a circular polarisation. Theories regarding this approach are also widely adopted in microstrip antennas [32].

7.4.2.1 Theory

Here the approach adopted in [32] to produce circularly polarised DRAs by circular sector geometries is used. The theory for obtaining orthogonal polarisation is described first, followed then by that of achieving a quadrature phase.

Orthogonal Polarisation Modes

Conventional circular DRAs radiate in the fundamental mode, $TM_{11\delta}$ like a linear magnetic dipole that forms a maximum at the boresight direction ($\theta = 0$, $\phi = 0$ in cylindrical coordinates) and the radiation decreases as θ increases. The next lowest order mode, $TM_{21\delta}$, on the other hand, radiates like a magnetic quadrupole that forms a null at the boresight and as θ increases, the radiation increases at first but decreases after a certain point. The presence of a null is owing to the cancellation by the symmetry at the rotational axis of the cylinder (as in Figure 7.5). The mismatch of the two radiation patterns makes conventional DRAs very difficult to use the single feed technique [12],[31] described in Section 7.4.2.

Sector DRAs with $\beta \leq 180$ and both open sector faces, however, not only avoid the total radiation cancellation in $TM_{21\delta}$ at the boresight, but also give a linear dipole-like radiation pattern. Figure 7.14 shows the theoretical calculation of the electric field distributions in a 180 degree sector DRA with horizontally polarised $TM_{11\delta}$ mode (fed at right) and vertically polarised $TM_{21\delta}$ mode (fed at center) in plane view. This figure suggests that orthogonal polarisations are both supported in this geometry. Sector DRAs with $90 \leq \beta \leq 180$ show similar behavior.

For a sector DRA with sector angle β, radius a, height d with open sector faces, the fundamental resonant mode is $TM_{v1\delta}$ and the next lowest resonant mode is $TM_{2v1\delta}$, where v is defined by

$$v = \frac{\pi}{\beta} \tag{7.41}$$

and the roots $X_{v,1}$ and $X_{2v,1}$ are determined by the characteristic equations of

$$J'_v (X_{v,1}) = 0 \quad \text{and} \quad J'_{2v} (X_{2v,1}) = 0$$

With reference to (7.13), the resonant frequencies of these modes are approximately given by

$$f = \frac{c}{2\pi a \sqrt{\varepsilon_r}} \sqrt{\begin{Bmatrix} X_{v,1}^2 \\ X_{2v,1}^2 \end{Bmatrix} + \left[\frac{\pi a}{2d} \right]^2} \tag{7.42}$$

The resonant frequencies and the separation between them are tuned by changing ε_r, a, d and β. In general, a larger ε_r scales the frequencies and bandwidths

down. A larger *a/d* ratio results in a closer separation between the two frequencies, but also changes the bandwidths. A larger β shifts both frequencies down with little effect on bandwidths.

Quadrature Phase Difference
A phase shift in the radiating field can be obtained by driving the mode above or below its resonant frequency. A +45 degree phase shift can be obtained by driving the mode below its resonant frequency until the magnitude of the reflection coefficient, $|S_{11}|$, is at -3dB [12]. Similarly for a -45 degree phase shift, the mode is driven by a frequency higher than its resonant such that $|S_{11}|$=-3dB, as shown in Figure 7.15. Therefore at a particular frequency, when the lower resonant mode is driven at –45 degrees, and the upper resonant mode is driven at +45 degrees, a total of 90 degree phase between these two modes can be obtained.
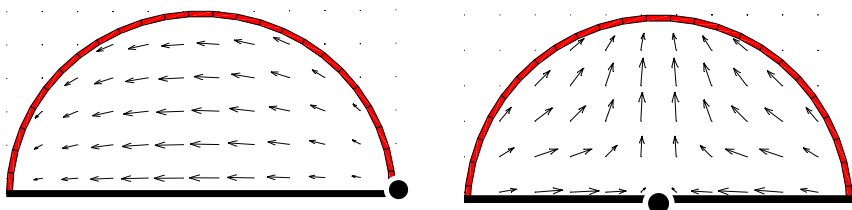
Figure 7.14: Theoretical calculations of the electric field distributions in a 180 degrees sector DRA Left: horizontally polarised $TM_{11\delta}$ mode. Right: vertically polarised $TM_{21\delta}$ (from [6], © 2000 IEEE)

Let the two resonant frequencies from the orthogonal modes be f_1 and f_2 with $f_1 < f_2$, the quadrature phase condition is fulfilled when

$$f_1 + \frac{\Delta f_1}{2} = f_2 - \frac{\Delta f_2}{2} \qquad (7.43)$$

where Δf is the 3dB bandwidth of $|S_{11}|$ and is related to the Q-factor by

$$Q = \frac{2f}{\Delta f} \qquad (7.44)$$

By choosing suitable values of a, d, ε_r and β such that (7.43) is satisfied, a circular polarised DRA is achieved.

7.4.3   Design Considerations
Good circularly polarised antennas generally have the following characteristics:

1. Single feed.
2. Small axial ratio over a wide beam width.
3. Same radiation shapes and almost equal magnitudes from two orthogonal polarisations.
4. Close to ±90 degree phase difference over a wide beam width.
5. Small axial ratio over a wide bandwidth
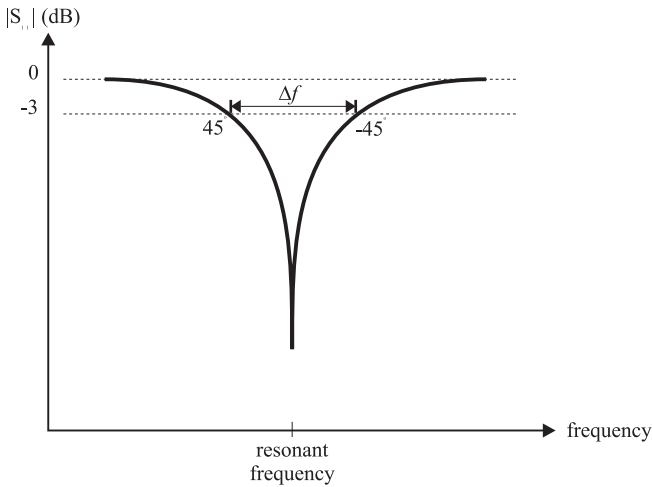
Figure 7.15: Theoretical |S₁₁| return loss showing an antenna under resonance and the ± 45 degrees phase points

To achieve a single feed, the theory described in Section 7.4.2 can be used. However, small AR is not guaranteed with wide bandwidth or beam width under this theory.

To compromise wide bandwidth, the individual bandwidths of the two orthogonal polarisations must be wide, so that the deviation from approx 90 degrees phase difference is small over a wide frequency range. Small values of ε_r and sector DRAs with open sector faces (as stated in Table 7.3) are therefore chosen.

To achieve a wide beam width, the same limitations are required to be compromised. When the sector DRAs (90 degrees $\leq \beta \leq 180$ degrees, a/d=1) are placed as in Figure 7.16, measurements show that the antennas radiate like y-polarisation dominated dipoles when fed at A, or as x-polarisation dominated dipoles, when fed at C. Tuning the feed point about B can achieve almost equal magnitudes and same radiation patterns from x- and y-polarisations. However,

when a/d>1, the radiation pattern of the y-polarisation begins to deviate from a dipole-like radiation shape, resulting in greater radiations at about $\theta = \pm 30$ degrees than at boresight direction, so the same orthogonal polarisation magnitudes over a wide beam width are not guaranteed for these values of a/d ratio.

It is also found that when the sector angle β decreases, the phase difference δ changes more rapidly in the x-z plane. In the y-z plane, δ changes more greatly than that in the x-z plane.

From the above observations, good circular polarisation would rely on the use of open face sector DRAs with low ε_r, β close to 180 degrees, a/d $\cong$ 1 and fed on the sector face at a radius around a/2.

7.4.4 Simulation Results

The far field radiation is analyzed by using FDTD simulations with $2 \times 2 \times 2mm^3$ cubic cells to model the circular sector DRA. The DRA, shown in Figure 7.17, is built with β =180 degrees, a=18mm, d=12mm, ε_r =12 and the area of the ground plane is $150 \times 150mm^2$. In Figure 7.18, the radiation patterns of the x- and y-polarisations in each plane are found in similar shapes and magnitudes over a wide beam angle. Moreover, at the left of Figure 7.19, the phase difference, δ in the horizontal x-z plane, stays between 80-100 degrees over a 100 degrees beam angle. However, δ in the vertical y-z plane, shown at the right side of the same figure, decreases rapidly away from 90 degrees phase difference as the beam angle deflects from the boresight direction. As a result, the beam width (AR 3dB) is about 80 degrees in the horizontal plane and about 30 degrees in the vertical plane.

7.4.5 Experimental Results

The configuration of the circularly polarised DRA under experimental investigation is the same as that described in the simulation and shown in Figure 7.17, except the height d is increased from 12mm to 15mm. In the measurement, when d=12mm, the phase difference δ is found too large. Both simulations and measurements reveal that the increase of the height d would decrease δ. Therefore d is experimentally tuned until the phase difference is about 90 degrees. This discrepancy would be due to the inaccuracy of bandwidth estimation, as observed in Table 7.3 in section 7.3, or inaccurate modeling of the probe feed.

The sector DRA is fabricated by machining 'ECCOSTOCK HiK' dielectric rod with ε_r =12 manufactured by Emerson and Cuming Inc. The measurement is made using an HP8753D network analyzer.

Figure 7.21 plots the return loss $|S_{11}|$ and clearly shows the two resonances. Far field radiation measurements of both magnitude and phase are taken twice, one set in x-polarisation and the other in y-polarisation, at 2.71GHz for one given plane. The magnitudes, E_y and E_x, in solid lines and broken lines respectively, are shown in Figure 7.22, measured in the horizontal x-z (left) and vertical y-z (right) planes.
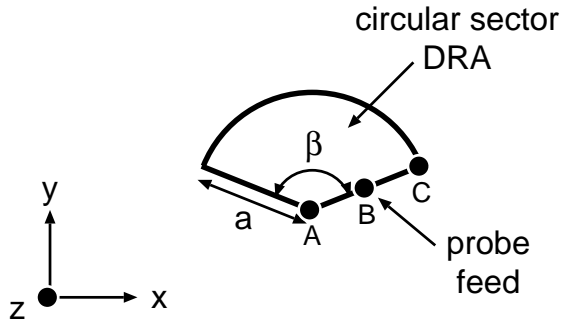
**Figure 7.16**: General geometry of a circularly polarised DRA in top view

plane view
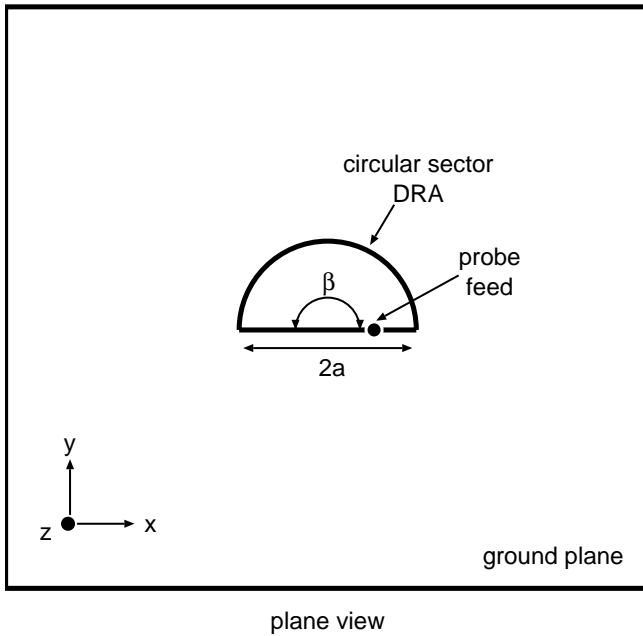
Figure 7.17: Simulation geometry of the circularly polarised DRA. ε_r =12, a=18mm, d=12mm, β =180 degrees, $2\times2\times2$mm^3 FDTD cell
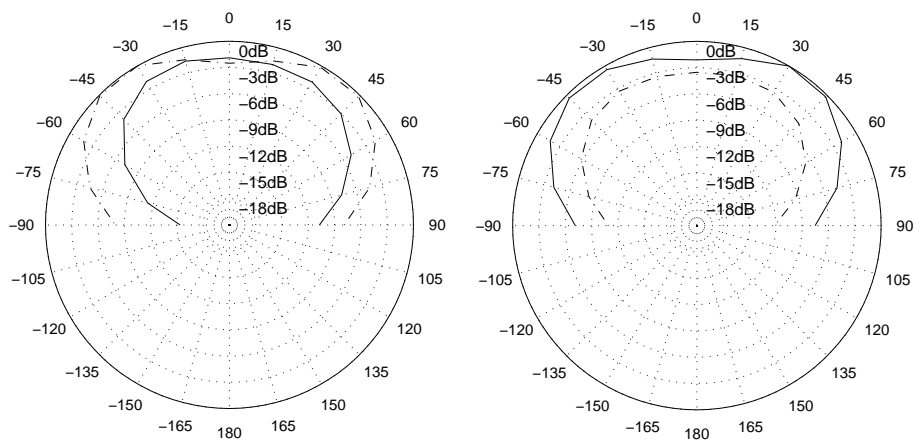
Figure 7.18: Simulations of the radiation patterns of the circularly polarised DRA. At 2.74GHz, y-polarisation shown as a solid line and x-polarisation as a broken line. Horizontal x-z plane on the left and vertical y-z plane on the right
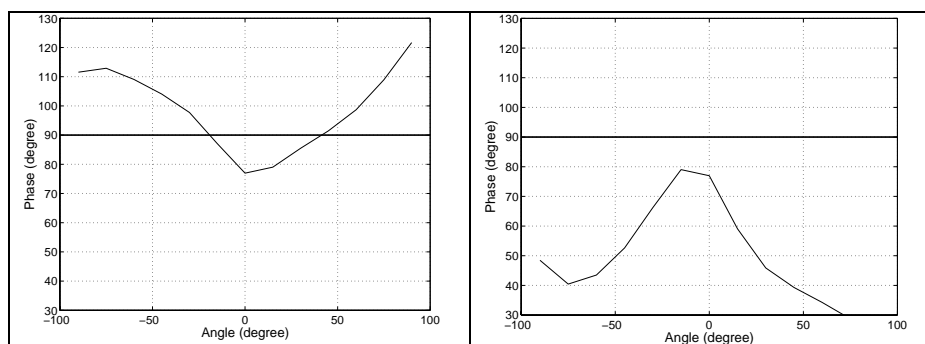
Figure 7.19: Simulations of the radiation phase difference δ of the circularly polarised DRA. At 2.74GHz, the horizontal x-z plane on the left and vertical y-z plane on the right
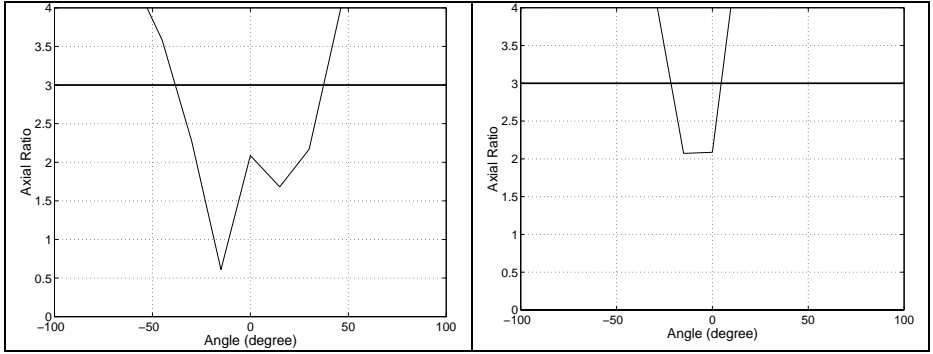
Figure 7.20: Simulations of the AR of the circularly polarised DRA. At 2.74GHz, the horizontal x-z plane is on the left and vertical y-z plane on the right

The phase difference δ, between E_x and E_y, are shown on Figure 7.23 in the horizontal x-z (left) and vertical y-z (right) planes. As seen in Table 7.5, the positive phase difference indicates that it is a right-hand circularly polarised (RHCP) antenna (LHCP is possible when the feed is placed at the opposite sector face).

With E_x, E_y and δ, the axial ratio (AR) is plotted in Figure 7.24. At 2.71GHz, the beam width covering the AR below 3dB is 117 degrees in the horizontal x-z plane and 34 degrees in the vertical y-z plane. Figure 7.25, synthesising a spinning linear source measurement [33], is generated from Figures 7.22 and 7.24. The importance of this figure is to indicate the axial ratio and the antenna gain simultaneously against the beam angle in a single figure. The amplitudes of the fluctuations on the radiation patterns are simply the axial ratio at that particular beam angle.

The AR bandwidth measurement is shown in Figure 7.26, in which AR <3dB at the boresight direction ($\theta = 0, \phi = 0$ in cylindrical coordinates) is found to be 2.54-2.81GHz or 10% relative to the center frequency 2.675GHz. Such wide bandwidth is contributed by the wide band features of sector DRA with open faces, as discussed in section 3.
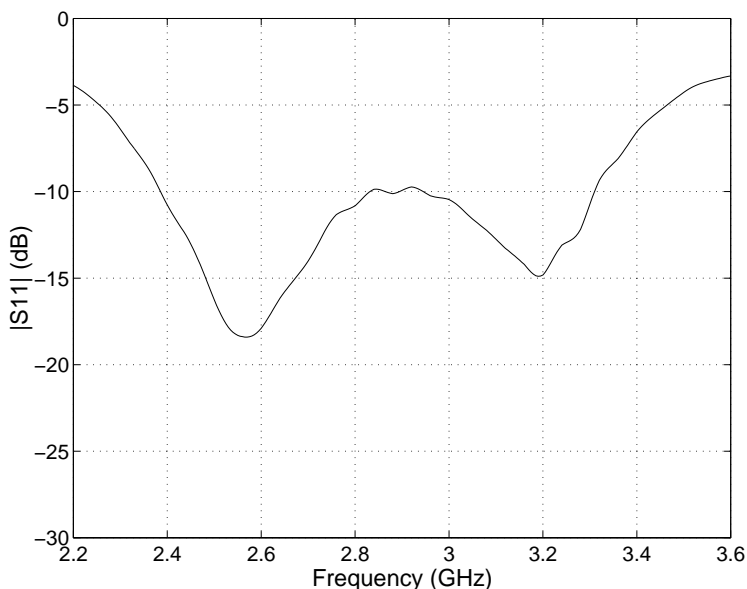
Figure 7.21: Measurement of the reflection coefficient, $|S_{11}|$, of the circularly polarised DRA. The DRA geometry is of ε_r =12, β =180 degrees, a=18mm and d=15mm (from [6], © 2000 IEEE)

7.4.6 Summary

Circular polarisation utilising a single-feed circular sector DRA was demonstrated. The design of a circular sector DRA with β =180 degrees, a=18mm, d=15mm and ε_r =12 was tested at 2.71GHz. The volume is 7.63cm^3. With the axial ratio (AR) below 3dB the beam width is about 117 degrees in the horizontal x-z plane and is 34 degrees in the vertical y-z plane, measured at 2.71GHz. The 3dB AR bandwidth is found to be 10% centered at 2.675GHz. It is a right-hand CP antenna, but LHCP is possible when the feed is placed at the opposite sector face.

For the sake of performance comparison, another compact design of circularly polarised rectangular DRA [12] was evaluated. After linear dimension scaling to the same dielectric material and resonant frequency, as in the design described above, the dimensions of the rectangular DRA become 23.27$\times$21.08$\times$23.27mm^3 and the volume is 11.41cm^3. The 3dB AR beam width was claimed to be 110 degrees in the vertical and horizontal planes. The 3dB AR bandwidth is 6.6% with ε_r =10.8.

As a result, in this section, a novel design of circularly polarised sector DRA with features of single feed, compact, simple geometry, high efficiency, wide band and moderate beam width, is demonstrated. The simple configuration may make this design easily scalable to other frequency bands. If a narrow bandwidth is allowed, the use of higher ε_r material might result in a more compact design. Therefore, it may be useful in GPSs and satellite-mobile communications.

7.5   DUAL FREQUENCY DRA

Different wireless applications are employed in different frequency bands, for example, GSM at 900MHz, PCS at 1.8GHz and wireless LAN at 2.4GHz. Integrating dual or multiple services is therefore an important issue to design a single antenna suitable for dual or multiple frequency bands. In this section, dual frequency sector DRA designs with different approaches are investigated and compared.

7.5.1   Theory

Dual frequency resonance can be obtained by simultaneous excitation of two resonant modes and is similar to the two nearly separated orthogonal modes used in the circular polarisation design discussed in section 7.4. Let the two required resonant frequencies be f_1 and f_2 ($f_1 < f_2$) such that
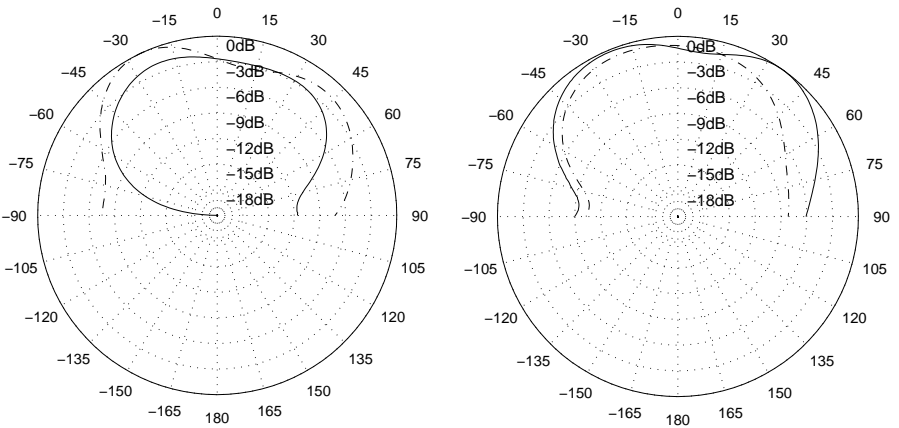

Figure 7.22: Measurements of the radiation patterns of the circularly polarised DRA. At 2.71GHz, the y-polarisation is shown as a solid line and x-polarisation as a broken line. Horizontal x-z plane in the left and vertical y-z plane in the right
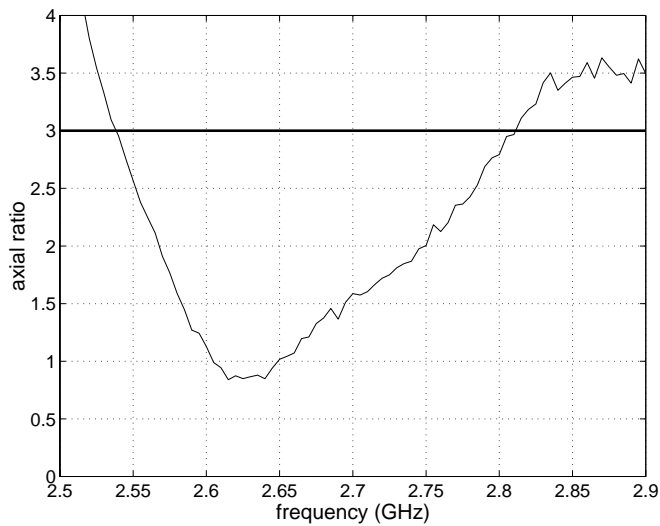(from [6], © 2000 IEEE)
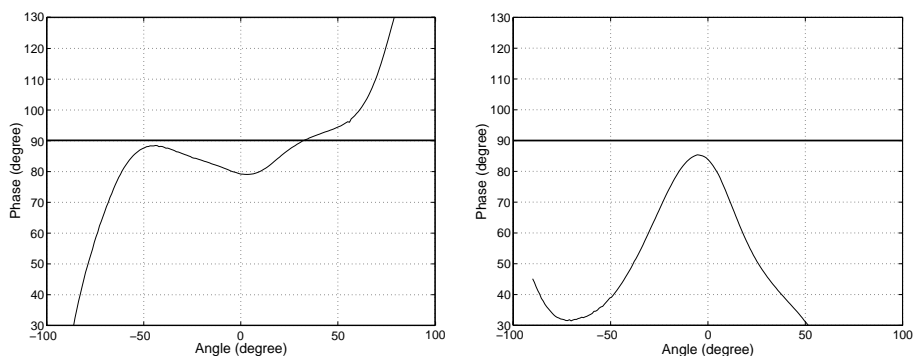
Figure 7.23: Measurements of the radiation phase difference δ of the circularly polarised DRA. At 2.71GHz, the horizontal x-z plane is on the left and vertical y-z plane on the right.
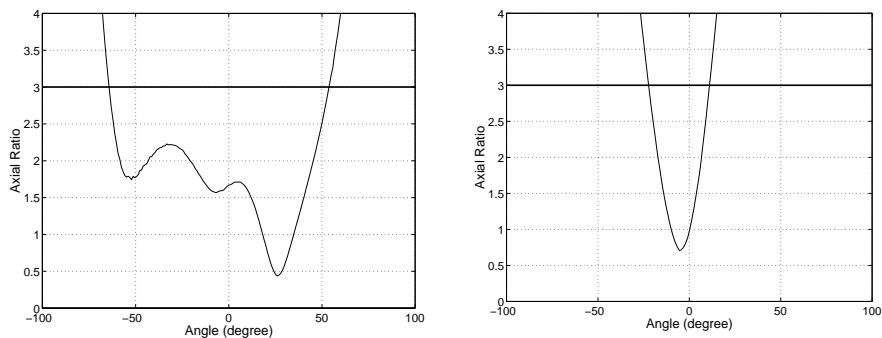
Figure 7.24: Measurements of the AR of the circularly polarised DRA. At 2.71GHz, the horizontal x-z plane is on the left and the vertical y-z plane on the right (from [6], © 2000 IEEE)
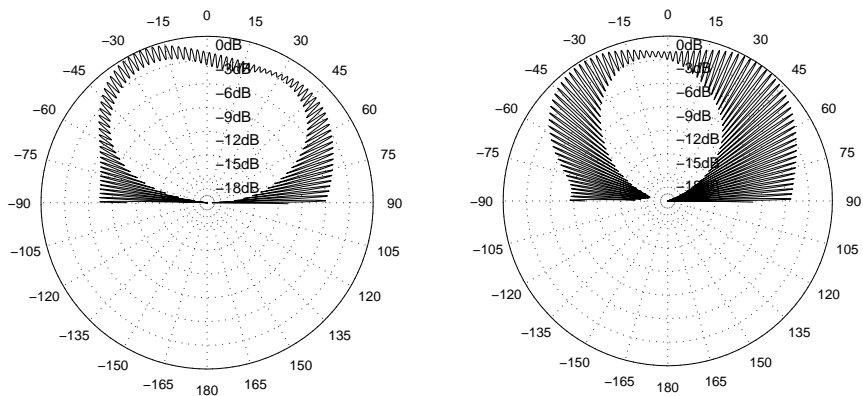
Figure 7.25: Measurements of the antenna gain imposed by AR. At 2.71GHz, the horizontal x-z plane is on the left and the vertical y-z plane on the right

Figure 7.26: Measurement of the AR at the boresight direction against frequency (from [6], © 2000 IEEE)

$$f_1 = \frac{c}{2\pi a \sqrt{\varepsilon_r}} \sqrt{X_{\nu 1}^2 + \left(\frac{\pi a}{2d}\right)^2} \tag{7.45}$$

$$f_2 = \frac{c}{2\pi a \sqrt{\varepsilon_r}} \sqrt{X_{\nu 2}^2 + \left(\frac{\pi a}{2d}\right)^2} \tag{7.46}$$

Dividing (7.45) by (7.46) gives

$$\frac{a}{d} = \frac{2}{\pi} \sqrt{\frac{f_1^2 X_{\nu 2}^2 - f_2^2 X_{\nu 1}^2}{f_2^2 - f_1^2}} \tag{7.47}$$

which gives us the ratio of dimensions required for the dual frequency operation at f_1 and f_2. With a given sector geometry and sector face types, ν_1 and ν_2 are fixed, as discussed in section 7.3. They are the two lowest resonant modes and the roots X_{ν_1} and X_{ν_2} can be determined by the first roots of the characteristic equations given by

$$J'_{\nu 1}(X_{\nu 1}) = 0 \quad \text{and} \quad J'_{\nu 2}(X_{\nu 2}) = 0 \tag{7.48}$$

With ν_1, ν_2, X_{ν_1}, X_{ν_2}, the required f_1 and f_2, there may exist a solution for a/d by (7.47). Substituting this a/d into (7.45) or (7.46) the values of a and d are determined.

In Table 7.6 some theoretically possible combinations of sector geometries and face types are listed for 900/1800MHz or 1800/2400MHz dual mode operations. In these modes, although the solutions of a and d exist, good matching resonances of the two required bands are not guaranteed.

Though the approximate theory provides multiple choices for dual frequency DRA designs for 900/1800MHz or 1800/2400MHz operations, bandwidth requirements from different wireless systems are important too. GSM and PCS require about 10% of bandwidth while wireless LAN needs only a few percent.

With reference to Table 7.3, it can be seen that while the use of one or both metallic sector face(s) will limit the bandwidth to a few percent, a smaller sector angle will give a larger bandwidth. However, DRAs with no metallic faces could increase the bandwidth close to 10%, but the resonant frequencies predicted by the approximate theory are generally far smaller than in reality.

7.5.2 Simulations and Experiments
In particular, since entry 5 in Table 7.6 is low in profile, this is chosen for simulation to test the feasibility of the dual frequency DRA design. The

approximate theory estimates that the resonances are at 1.8GHz and 2.4GHz. However, the FDTD simulation reveals that the dimensions of this DRA should be enlarged to a=22mm and d=14mm. The simulation uses $1\times1\times1$mm^3 cubic cells to model the antenna and the ground plane is 150×150mm^2.

|	f_1 MHz	f_2 MHz	β	face (I)	face (II)	ν_1	ν_2	$X_{\nu11}$	$X_{\nu21}$	a (mm)	d (mm)
1	900	1800	270	M	O	1/3	1	0.910	1.841	14.2	138.8
2	900	1800	180	M	O	½	3/2	1.166	2.461	19.2	66.3
3	900	1800	90	M	O	1	3	1.841	4.201	33.4	44.9
4	1800	2400	270	M	O	1/3	1	0.910	1.841	13.9	13.9
5	1800	2400	180	M	O	½	3/2	1.166	2.461	18.8	13.7
6	1800	2400	90	M	O	1	3	1.841	4.201	32.8	13.3
7	1800	2400	360	M	M*	½	1	1.166	1.841	12.4	17.4
8	1800	2400	270	M	M*	2/3	4/3	1.401	2.258	15.4	16.8
9	1800	2400	180	M	M*	1	2	1.841	3.054	21.2	16.1
10	1800	2400	90	M	M*	2	4	3.054	5.318	37.8	15.3

Table 7.6: Some theoretically possible combinations of sector geometries and face types for dual-frequency operations. * 'M' for Metallic face and 'O' for Open face. In ideal magnetic wall assumption M,M face combination is the same as O,O.

The probe feed is carefully chosen such that both resonances could be excited simultaneously. Simulations indicate that the probe could be fed on the circumference at $\phi \cong 80$ degrees, as shown in Figure 7.27. The simulated VSWR curves, shown in Figure 7.28 as solid lines, indicate that good matching is achieved at both 1.8GHz and 2.4GHz bands. Experimental VSWR curves are the broken lines, superimposed on the same figure. Close agreements with resonant frequencies and bandwidths between simulations and experiments are found.

7.5.3 Summary

In this section, using theory, simulations and experiments, the dual frequency operation capabilities of various sector DRAs are investigated and tested. The technique used involves the two lowest resonant modes excited from a single resonator with a single feed. Although conventional monopoles and helix are capable of resonating at the multiples of their fundamental frequencies (e.g. f_1=900MHz, f_2=1800MHz), the impedances of these are different and are hard to be tuned or optimised using a single feed. Sector DRAs, however, have more degrees of freedom to optimise for wider independent selections of the two lowest resonance modes. Good matching at both bands though is not guaranteed; probe feed locations and length may increase certain degrees of freedom. Dual frequency DRA designs might make compact integrations of multiple wireless services with a single antenna realisable and feasible.
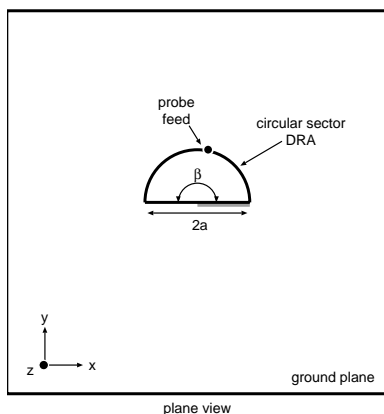
Figure 7.27: Geometry of the dual frequency DRA design β =180 degrees, a=22mm, d=14mm, ε_r =12 and ground plane is 150×150mm^2
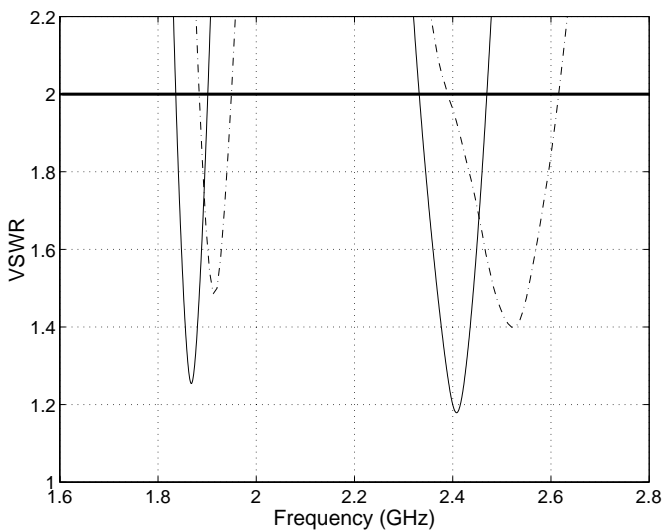
Figure 7.28: VSWR measurements of the dual frequency DRA design, β =180 degrees, a=22mm, d=14mm and ε_r =12. Simulation shown as solid lines and measurement shown as broken line

7.6   OVERALL CONCLUSIONS

The aim of this chapter is to provide DRA designs that are compact enough to be employed in wireless communication applications. The three novel designs investigated include: a circular sector DRA for PCS, a circularly polarised sector DRA for satellite communications and a dual-frequency sector DRA for integrated wireless services. This section summarises the findings presented in section 7.2-section 7.5.

7.6.1   Circular Sector DRAs

Various inner to outer radius ratios, sector angles and boundary conditions (metallic, open or mixed) are modeled using approximate theories and are verified with simulations and experiments. Of particular importance is a 90 degrees sector with one metallic and one open sector face which exhibits the same resonant frequency and bandwidth as the conventional 360 degree circular DRA. A volume reduction as large as 75% is demonstrated.

   In addition, a volume minimisation technique in which the values of radius and height are optimally matched with the resonant modes is proposed. A compact ($4.98cm^3$) and low profile (1.2cm) 180 degrees sector DRA is designed at 1.80GHz, This is verified by experiments and shown to satisfy the DCS1800 system specifications. The far field measurements also reveal that radiation towards the head of the user is reduced. To our knowledge, no DRA design until now is sufficiently compact, and of such a low profile, to be integrated into a handset while satisfying the DCS1800 requirements.

7.6.2   Circularly Polarised Sector DRA

An integrated circularly polarised sector DRA, with no external quadrature phase shifting device, is designed and tested. The single feed mechanism alleviates the construction complexity and helps reduce the antenna size. From the far field measurement made at 2.71GHz, the 3dB axial ratio (AR) beam width is 117 degrees in one plane and 34 degrees in the perpendicular plane. A wide 3dB AR bandwidth of 10% is achieved. This design gives a right hand circular polarisation which may be useful for GPS and satellite-mobile communications. The performance of this sector DRA is compact and has wide bandwidth and moderate beam width relative to the rectangular DRA design reported by other researchers.

7.6.3   Dual Frequency Sector DRA

The two lowest resonant frequencies of the same resonator is an approach to dual frequency operations for 900/1800MHz or 1800/2400MHz bands. Approximate theory predicts that various combinations of sector angle and sector face boundary conditions are possible. The various combinations differ only in bandwidths and volumes. The 180 degree sector DRA with 22mm radius, 14mm height and $\mathcal{E}_r = 12$ is simulated and experimented to resonate at 1.8GHz and 2.4GHz with a single probe feed. Therefore a compact integration of multiple wireless services with a single feed antenna becomes realisable and feasible.

7.6.4 Further Developments

The DRAs investigated in this chapter are for low permitivities (ε_r of the order of 10). More compact DRA designs could be created by using moderate ε_r materials. Moderate values may be considered in the range between 30-50. For example, the linear dimensions of DRAs with ε_r =50 are half of that with ε_r =12. However, to acquire sufficient bandwidths (approx 10%) for the requirements of existing wireless communication systems, bandwidth enhancement techniques would become a key problem to be solved. This is the important promising avenue that should be investigated in the future. Diversity DRA antennas where several antennas are located on one handset would also be of interest [34],[35].

REFERENCES

[1] R.K. MONGIA and P. BHARTIA, "Dielectric Resonator Antennas - A Review and General Design Relations for Resonant Frequency and Bandwidth", *Int. Journal of Microwave & Millimeter-Wave Computer-Aided Engineering*, 1994, vol. 4, no. 3, pp. 230-247.

[2] S.A. LONG, M.W. McALLISTER and L.C. SHEN, "The Resonant Cylindrical Dielectric Cavity Antenna", *IEEE Trans. Antennas Propagat*, 1983, vol. AP-31, no. 3, pp. 406-412.

[3] K.W. LEUNG and K.M. LUK, "Circular Dielectric Antenna of High Dielectric Constant for Low Profile Applications", *Ninth Int. Conference on Antennas and Propagat.,* 1995, vol. 1, pp. 517-519.

[4] A.A. KISHK, A. ITTIPIBOON, Y.M.M. ANTAR and M. CUHACI, "Slot Excitation of the dielectric disk radiator", *IEEE Trans. Antennas Propagat,* Feb 1995, vol 43, pp. 198-201.

[5] M.T.K. TAM and R.D. MURCH, "Compact Sector and Annular Sector Dielectric Resonator Antennas", *IEEE Transactions on Antennas and Propagation*, May 1999, vol 47. no. 5, pp. 837-842.

[6] M.T.K. TAM and R.D. MURCH, "Circularly Polarised Circular Sector Dielectric Resonator Antenna", *IEEE Transactions on Antennas and Propagation*, January 2000, vol. 48, No. 1, pp. 126-128.

[7] M.T.K. TAM, "Compact Dielectric Resonator Antenna Design for Wireless Communications", *Masters Thesis,* Department of Electrical and Electronic Engineering, Hong Kong University of Science and Technology, August 1998.

[8] M.T.K. TAM and R.D. MURCH, "Half Volume Dielectric Resonator Antenna Designs", *Electronics Lett.,* 1997, vol. 33, no. 23, pp. 1914-1916.

[9] M.T.K. TAM and R.D. MURCH, "Compact Cylindrical Sector Dielectric Resonator Antennas", 1998, *IEEE Antennas and Propagat. Society Int. Symposium,* 1998, pp. 1958-1961.

[10] R.K. MONGIA, A. ITTIPIBOON, M. CUHACI and D. ROSCOE, "Circular polarisat dielectric resonator antenna", *Electronics Lett.,* 1994, vol. 30, no. 17, pp. 1361-1362.

[11] G. DROSSOS, Z. WU and L.E. DAVIS, "Circular polarised cylindrical dielectric resonator antenna", *Electronics Lett.,* 1996, vol. 32, no. 4, pp. 281-283.

[12] M.B. OLIVER, Y.M.M. ANTAR, R.K. MONGIA and A. ITTIPIBOON, "Circularly Polarised Rectangular Dielectric Resonator Antenna", *Electronics Lett.*, 1995, vol. 31, no. 6, pp. 418-419.

[13] R.K. MONGIA and A. ITTIPIBOON, "Theoretical and Experimental Investigations on Rectangular Dielectric Resonator Antennas", *IEEE Trans. Antennas Propagat.,* 1997, vol. AP-45, no. 9, pp. 1348-1356.

[14] G. DROSSOS, Z. WU and L.E. DAVIS, "A Comparative Study of Circular Microstrip and Cylindrical Dielectric Resonator Antennas", *10th Int. Conference on Antennas and Propagat.,* 1997, no. 436, pp. 38-42.

[15] M.W. McALLISTER and S.A. LONG, "Resonant Hemispherical Dielectric Antenna", *Electron. Lett.,* 1984, vol. 20, no. 16, pp. 657-659.

[16] M.W. McALLISTER, S.A. LONG and G.L. CONWAY, "Rectangular Dielectric Resonator Antenna", *Electron. Lett,.* 1983, vol. 19, no. 6, pp. 219-220.

[17] Y. KOBAYASHI and S. TANAKA, "Resonant Modes of a Dielectric Rod Resonator Short Circuited at Both Ends by Parallel Conducting Plates", *IEEE Trans. Microwave Theory & Tech.,* 1980, vol. MTT-28, no. 10, pp. 1077-1085.

[18] D. KAJFEZ and P. GUILLON, Eds., "Dielectric Resonators", Artech House, 1986.

[19] D. KAJFEZ, A.W. GLISSON and J. JAMES, "Computed Modal Field Distributions for Isolated Dielectric Resonators", *IEEE Trans. Microwave Theory & Techniques,* 1984, vol. MTT-32, no. 12, pp. 1609-1616.

[20] G.P. JUNKER, A.A. KISHK, A.W. GLISSON and D. KAJFEZ, "Effect of an Air Gap around the Coaxial Probe Exciting a Cylindrical Dielectric Resonator Antenna", *Electron. Lett.,* 1994, vol. 30, no. 3, pp. 177-178.

[21] K.S YEE, "Numerical Solution of Initial Boundary Value Problems Involving Maxwell's Equations in Isotropic Media", *IEEE Trans. Antennas Propagat.,* 1966, vol. AP-14, pp. 302-307.

[22] R. LUEBBERS, L. CHEN, T. UNO and S. ADACHI, "FDTD Calculation of Radiation Patterns, Impedance, and Gain for a Monopole Antenna on a Conducting Box", *IEEE Trans. Antennas Propagat.,* 1992, vol. AP-40, pp. 1577-1583.

[23] R.J. LUEBBERS, K.S. KUNZ, M. SCHNEIDER and F. HUNSBERGER, "A Finite-difference Time-domain Near Zone to Far Zone Transformation", *IEEE Trans. Antennas Propagat.,* 1991, vol. AP-39, pp. 429-433.

[24] W.F. RICHARDS, J.D. OU and S.A. LONG, "A Theoretical and Experimental Investigation of Annular, Annular Sector, and Circular Sector Microstrip Antennas", *IEEE Trans. Antennas Propagat.,* 1984, vol. AP-32, no. 8, pp. 864-867.

[25] R.K. MONGIA, "Small Electric Monopole Mode Dielectric Resonator Antenna", *Electronics Lett.,* 1996, vol. 32, no. 11, pp. 947-949.

[26] S.-W. CHEN and K.A. ZAKI, "Dielectric Ring Resonators Loaded in Waveguide and on Substrate", *IEEE Trans. Microwave Theory & Tech*., 1991, vol. MTT-39, no. 12, pp. 2069-2076.

[27] C.R. ROWELL and R.D. MURCH, "A Capacitively Loaded PIFA for compact mobile telephone handsets", *IEEE Trans. Antennas Propagat.,* 1997, vol. 45, no. 5, pp. 837-842.

[28] C.R. ROWELL and R.D. MURCH, "A Compact PIFA Suitable for Dual-Frequency 900/1800-MHz Operation", *IEEE Trans. Antennas Propagat.,* 1998, vol. 46, no. 4, pp. 596-598.

[29] M. MOULY and M.B. PAUTET, "The GSM System for Mobile Communications", Palaiseau, France, 1992, pp. 217.

[30] R.C. JOHNSON, "Antenna Engineering Handbook", 3rd ed., McGraw-Hill, 1993.

[31] K.P. ESSELLE, "Circularly Polarised Low-Profile Rectangular Dielectric-Resonator Antenna: FD-TD and Experimental Results", *IEEE Antennas and Propagat. Society Int. Symposium*, 1996, vol. 1, pp. 577-580.

[32] D.M. POZAR and D.H. SCHAUBERT, Eds., "Microstrip Antennas: the Analysis and Design of Microstrip Antennas and Arrays", IEEE Press, New York, 1995.

[33] H. SCHRANK, D.S. DUNN and E.P. AUGUSTIN, "Measuring the Gain of Circularly or Elliptically Polarised Antennas", *IEEE Antennas and Propagat. Magazine*, 1994, vol. 36, no. 1, pp. 49-51.

[34] S.C.K. KO and R.D. MURCH, "Compact Integrated Diversity Antenna for Wireless Communications", *IEEE Transactions on Antennas and Propagation,* June 2001, vol. 49, no. 6, pp. 954-960.

[35] S.C.K. KO and R.D MURCH, "A Diversity Antenna for external mounting on Wireless handsets", *IEEE Transactions on Antennas and Propagation,* May 2001, vol. 49, no. 5, pp. 840-842.

CHAPTER 8

Feeding Methods for the Dielectric Resonator Antenna: Conformal Strip and Aperture Coupling with a Perpendicular Feed

Kwok Wa Leung

Department of Electronic Engineering
City University of Hong Kong,
Kowloon,
Hong Kong SAR

8.1   INTRODUCTION

The dielectric resonator antenna (DRA) can easily be coupled by nearly all kinds of transmission lines. A number of excitation schemes are summarised in Section 1.2 of Chapter 1. Among various excitation methods, the coaxial-probe feed was the first one which was used to demonstrate the radiation capability of the DRA [1]. In this method, a hole is drilled inside the DRA to accommodate the probe penetration. But two practical problems arise in using this method. First, drilling a hole in a super-hard DR is difficult. Secondly, it is impractical to have a probe that perfectly fits the size of the hole, and usually an air gap exists between the probe and the hole, causing the measured results to deviate from the predicted value. To avoid these problems, the probes in [2, 3] were placed outside the DRA. This approach, however, is only applicable to a DRA with a vertical side wall, such as the cylindrical and rectangular DRAs. For DRAs with a curved side wall (e.g., hemispherical and half-split cylindrical [4]), the coupling between the probe and DRA is rather inefficient. To solve this problem, a new excitation scheme that employs a conformal conducting strip was proposed [5]. In this method, a conducting strip is mounted on the DRA surface, as shown in Fig. 8.1. Since the electric current can flow on the DRA surface, the energy coupling is more efficient than those of [2, 3]. The new method possesses the same advantages of the coaxial-probe feed, and, in addition, it can easily be implemented by simply cutting a strip from an adhesive conducting tape. Furthermore, it admits very convenient post manufacturing trimmings, since the length of the conformal strip

can be adjusted very easily. Because of these promising features, the conformal strip excitation method has been used in the DRA development [6, 7].

Sometimes, excitation methods associated with a microstrip substrate are preferred for direct integration with active circuitry. In the direct microstripline and co-planar waveguide feed methods, the DRA is on the same side as the feed network. This may produce unwanted spurious radiation and coupling. Although the aperture-coupling and solder-through-probe excitation schemes solve these problems through the ground-plane isolation, they provide much smaller usable substrate areas for active-circuitry integration because the DRA occupies one side (ground plane) of the feed substrate. It is desirable to have an excitation scheme which first, isolates the DRA from active circuitry and, second, fully utilises the whole feed substrate for integration with active circuitry. Increasing the substrate area is especially important for large phased array antennas, where a large substrate area is required to accommodate phase shifters, amplifiers, feed line, bias lines, etc. to meet these requirements; for this purpose the aperture-coupled DRA with a perpendicular feed [8-9] was proposed. This excitation scheme was originally considered for the microstrip antenna [10]. It was found that the new configuration can be matched to a 50-Ω line as easy as in the microstrip antenna case.

In this chapter, the hemispherical DRA is used to demonstrate the conformal strip feed as well as the aperture coupling using a perpendicular feed, with the DRA excited in the fundamental broadside TE_{111} mode. Nevertheless, the excitation methods can be applied to other DRAs as well. The Green's function approach is used to formulate the problems, and the mode-matching method [11-12] is employed to obtain the exact Green's functions of the DRA. It is worth mentioning that the conformal strip and aperture coupling are examples for the electric and magnetic sources, respectively.
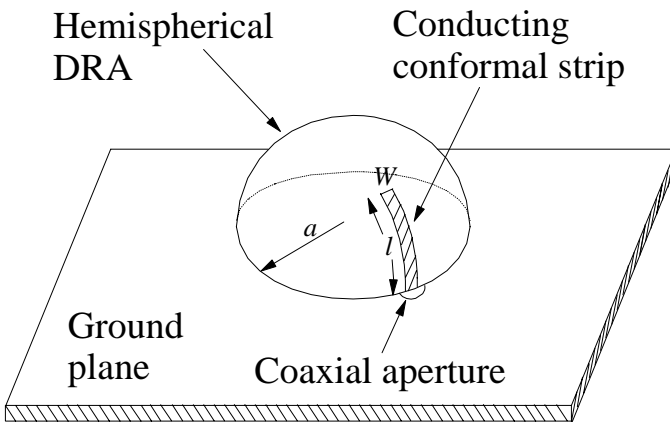
Fig. 8.1   The perspective view of the conformal strip-fed hemispherical DRA.

8.2   CONFORMAL STRIP EXCITATION

8.2.1   DRA Green's Function

Fig. 8.1 shows a perspective view of the configuration, where a hemispherical DRA of radius a and dielectric constant ε_r is fed by a conformal strip of length l and width W. To begin with, image theory is used to obtain an equivalent problem as shown in Fig. 8.2, where the coordinate system is chosen for ease of analysis. The equivalent conformal strip has length $2l$, and subtends the azimuthual and elevation angles from $-\phi_1$ to ϕ_1 (Fig.8.3(a)) and θ_1 to $\pi - \theta_1$ (Fig.8.3(b)), respectively. The input impedance of the original problem is then one-half of the new one.
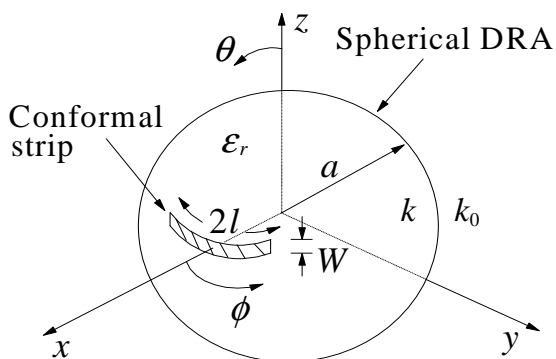
Fig. 8.2   The coordinate system adopted in the analysis.

(a)   (b)
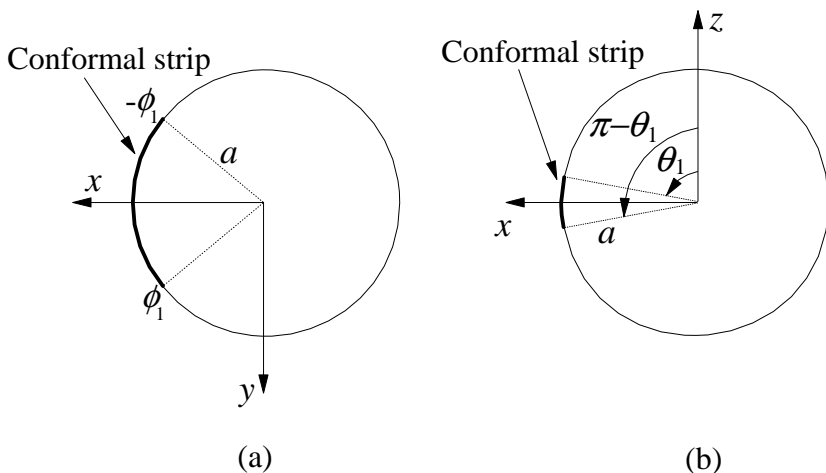
Fig. 8.3   The angles subtended by the strip of the equivalent configuration. (a) *x-y* plane. (b) *x-z* plane. (From [5], © 2000 IEEE)

In the following formulation, the time dependence $e^{j\omega t}$ is suppressed throughout the Chapter. The field and source points are denoted by $\vec{r}\ (r,\ \theta,\ \phi)$ and $\vec{r}'\ (r',\ \theta',\ \phi')$, and the numbers 1 and 2 are used to denote the interior ($r < a$) and exterior ($r > a$) regions, respectively. We start with the electric and magnetic potential Green's functions, F_r and A_r, in regions 1 and 2. The functions are found using the mode matching method:

Inside the DRA ($r < a$)

$$F_{r1} = \sum_{n=0}^{\infty} \sum_{m=-n}^{n} A_{nm}\, \hat{J}_n(kr)\, P_n^m(\cos\theta)\, e^{jm\phi} \tag{8.1}$$

$$A_{r1} = \sum_{n=0}^{\infty} \sum_{m=-n}^{n} B_{nm}\, \hat{J}_n(kr)\, P_n^m(\cos\theta)\, e^{jm\phi} \tag{8.2}$$

Outside the DRA ($r > a$)

$$F_{r2} = \sum_{n=0}^{\infty} \sum_{m=-n}^{n} C_{nm}\, \hat{H}_n^{(2)}(k_0 r)\, P_n^m(\cos\theta)\, e^{jm\phi} \tag{8.3}$$

$$A_{r2} = \sum_{n=0}^{\infty} \sum_{m=-n}^{n} D_{nm}\, \hat{H}_n^{(2)}(k_0 r)\, P_n^m(\cos\theta)\, e^{jm\phi} \tag{8.4}$$

where $k = \sqrt{\varepsilon_r}\, k_0$ is the dielectric wavenumber. In (8.1)-(8.4), $P_n^m(x)$ is the associated Legendre function of the first kind of order m and degree n, and $\hat{J}_n(x)$ and $\hat{H}_n^{(2)}(x)$ are the nth order Schelkunoff-type spherical Bessel function of the first kind and spherical Hankel function of the second kind [13, p. 268], respectively. All the other symbols have the usual meanings. The unknown modal coefficients A_{nm}, B_{nm}, C_{nm}, and D_{nm} are found by matching the following boundary conditions at the DRA-air interface:

$$\hat{r} \times (\vec{E}_2 - \vec{E}_1) = 0 \tag{8.5}$$

and

$$\hat{r} \times \left(\vec{H}_2 - \vec{H}_1\right) = J_{\phi s}\, \hat{\phi} \tag{8.6}$$

where $J_{\phi s}$ is the surface current density on the conformal strip. In (8.6) it has been assumed that the strip current is longitudinal and transversely independent, which is a valid approximation for a narrow strip ($W \ll 2l$ and $\sqrt{(\varepsilon_r + 1)/2}\, k_0 W \ll 1$). After the electric and magnetic potential Green's functions are obtained, the interior and exterior Green's functions of E_ϕ, namely G_1 and G_2, can be found easily [13]. On the DRA surface we have $r = r' = a$ and $G_1 = G_2 = G$, where the Green's function G is given by

$$G(\theta,\phi;\theta',\phi') = \frac{j\eta_0}{4\pi a^2} \sum_{n=1}^{\infty} \sum_{m=0}^{n} \frac{2n+1}{n(n+1)\Delta_n^{\mathrm{TE}}} \hat{J}_n(ka)\hat{H}_n^{(2)}(k_0 a) \cdot \frac{2}{\Delta_m} \cdot \frac{(n-m)!}{(n+m)!} \cdot$$

$$\frac{dP_n^m(\cos\theta)}{d\theta} \cdot \frac{dP_n^m(\cos\theta')}{d\theta'} \cos m(\phi-\phi') - \frac{j\eta_0}{4\pi a^2} \sum_{n=1}^{\infty} \sum_{m=1}^{n} \frac{2n+1}{n(n+1)\Delta_n^{\mathrm{TM}}} \cdot$$

$$\hat{J}_n'(ka)\hat{H}_n^{(2)}{}'(k_0 a) \cdot 2m^2 \cdot \frac{(n-m)!}{(n+m)!} \cdot \frac{P_n^m(\cos\theta)}{\sin\theta} \cdot \frac{P_n^m(\cos\theta')}{\sin\theta'} \cos m(\phi-\phi')$$

$$(8.7)$$

where

$$\Delta_n^{\mathrm{TE}} = \hat{J}_n(ka)\hat{H}_n^{(2)}{}'(k_0 a) - \sqrt{\varepsilon_r}\, \hat{J}_n'(ka)\hat{H}_n^{(2)}(k_0 a) \tag{8.8}$$

$$\Delta_n^{\mathrm{TM}} = \hat{J}_n'(ka)\hat{H}_n^{(2)}(k_0 a) - \sqrt{\varepsilon_r}\, \hat{J}_n(ka)\hat{H}_n^{(2)}{}'(k_0 a) \tag{8.9}$$

$$\Delta_m = \begin{cases} 1, & m > 0 \\ 2, & m = 0 \end{cases} \tag{8.10}$$

and η_0 is the wave impedance in vacuum. A prime denotes a derivative with respect to the whole argument. Although the double-summations in (8.7) can be reduced to single-summations by using the addition theorem for Legendre polynomials [14], they are retained here to allow analytical treatments for the solution.

8.2.2   Moment Method Solution for the Strip Current

Let E_ϕ^s and E_ϕ^i be the scattered and impressed fields due to the current density $J_{\phi s}$ and the excitation source, respectively. Then by enforcing the boundary condition so that the total tangential electric field vanishes on the (conducting) strip, we have

$$E_\phi^s + E_\phi^i = 0 \tag{8.11}$$

or

$$-\iint_{S_0} G(\theta,\phi;\theta',\phi') J_{\phi s}(\phi')\, dS' = E_\phi^i \tag{8.12}$$

where $G(\theta,\phi;\theta',\phi')$ is given in (8.7) and S_0 is the surface of the imaged conformal strip. Using the delta gap source model, the impressed field E_ϕ^i is given by $(V_0/a)\delta(\phi)$, where V_0 is the voltage amplitude at the feed point. Let $I(\phi) = J_{\phi s}W$ be the strip current, (8.12) then becomes

$$\frac{-1}{W} \iint_{S_0} G(\theta,\phi;\theta',\phi')\, I(\phi')dS' = \frac{V_0}{a}\delta(\phi) \tag{8.13}$$

Use is made of the moment method (MoM) to expand $I(\phi)$ in terms of unknown current coefficients I_q's as follows:

$$I(\phi) = \sum_{q=1}^{N} I_q f_q(\phi) \tag{8.14}$$

where $f_n(\phi)$ are piecewise sinusoidal (PWS) basis functions given by

$$f_q(\phi) = \begin{cases} \dfrac{\sin k_e(h - a|\phi - \phi_q|)}{\sin k_e h}, & a|\phi - \phi_q| < h \\ 0, & a|\phi - \phi_q| \ge h \end{cases} \tag{8.15}$$

in which

$$h = \frac{L}{N+1} \tag{8.16}$$

$$\phi_q = \frac{1}{a}\left(\frac{-L}{2} + qh\right) \tag{8.17}$$

and $k_e = \sqrt{(\varepsilon_r + 1)/2}\, k_0$ is the effective wavenumber at the DRA-air interface. Substitute (8.14) into (8.13) and set V_0 to unity for convenience, we get:

$$\frac{-1}{W}\sum_{q=1}^{N} I_q \iint_{S_0} G(\theta,\phi;\theta',\phi')\, f_q(\phi')dS' = \frac{1}{a}\delta(\phi) \tag{8.18}$$

The Galerkin's procedure is used to obtain the following matrix equation:

$$[Z_{pq}][I_q] = [f_p(0)] \tag{8.19}$$

where

$$Z_{pq} = \frac{-1}{W^2}\iint_{S_0}\iint_{S_0} f_p(\phi)\, G(\theta,\phi;\theta',\phi')\, f_q(\phi')\, dS'dS \tag{8.20}$$

Once I_q's are obtained, the input impedance is found easily from

$$Z_{in} = \frac{1}{\sum_{q=1}^{N} I_q f_q(0)} \cdot \tag{8.21}$$

Finally, the input impedance of the original problem is given by $Z_{in}' = Z_{in}/2$. In the next section, analytical treatments for Z_{pq} are carried out so that the solution can be implemented very easily and efficiently.

8.2.3 Evaluation of Z_{pq}

The Green's function $G(\theta,\phi;\theta',\phi')$ is singular as $\vec{r} \to \vec{r}'$. Thus, the impedance matrix elements Z_{pq} (8.20) cannot be integrated numerically, since excessive modal terms are required to accurately calculate $G(\theta,\phi;\theta',\phi')$ around $\vec{r} = \vec{r}'$, leading to numerical problems in calculating high-order Hankel functions. Furthermore, considerable computation time is required if many terms are included in the solution. To solve these problems, the quadruple integration is performed analytically using the recurrence approach [15-17]. It can be proved that (8.20) can be written as:

$$Z_{pq} = \frac{-ja^2\eta_0}{4\pi W^2} \sum_{n=1}^{\infty} \frac{2n+1}{n(n+1)} \left\{ \frac{\hat{J}_n(ka)\hat{H}_n^{(2)}(k_0 a)}{\Delta_n^{TE}} \sum_{m=0}^{n} \frac{2}{\Delta_m} \cdot \frac{(n-m)!}{(n+m)!} \right.$$

$$\left[\Theta_1(n,m)\right]^2 \Phi_1(p,q,m) - \frac{\hat{J}_n'(ka)\hat{H}_n^{(2)'}(k_0 a)}{\Delta_n^{TM}}$$

$$\left. \sum_{m=1}^{n} 2m^2 \cdot \frac{(n-m)!}{(n+m)!} \left[\Theta_2(n,m)\right]^2 \Phi_1(p,q,m) \left[\Theta_2(n,m)\right]^2 \Phi_1(p,q,m) \right\} \tag{8.22}$$

where

$$\Theta_1(n,m) = \int_{\theta_1}^{\theta_2} \frac{dP_n^m(\cos\theta)}{d\theta} \sin\theta \, d\theta \tag{8.23}$$

$$\Theta_2(n,m) = \int_{\theta_1}^{\theta_2} P_n^m(\cos\theta) \, d\theta \tag{8.24}$$

$$\Phi_1(p,q,m) = \int_{\phi=\phi_p-\phi_h}^{\phi_p+\phi_h} \int_{\phi'=\phi_q-\phi_h}^{\phi_q+\phi_h} f_p(\phi) \cos m(\phi-\phi') f_q(\phi') \, d\phi' \, d\phi \tag{8.25}$$

in which $\phi_h = h/a$. To calculate $\Theta_2(n,m)$ efficiently, two recurrence formulas were derived. The first one is recursive in n as given by :

$$\Theta_2(n+1,m) = \frac{1}{(n+1)(n-m+1)} \cdot$$

$$\left\{ -(2n+1)\left[1-(-1)^{n+m}\right]\sqrt{1-x_1^2} \, P_n^m(x_1) + n(n+m)\Theta_2(n-1,m) \right\} \tag{8.26}$$

where $x_1 = \cos\theta_1$. The initial values for $m = 0$ are given by $\Theta_2(0,0) = 2\sin^{-1}x_1$ and $\Theta_2(1,0) = 0$. From the initial values all $\Theta_2(n,0)$ can be found easily. After $\Theta_2(n,0)$ are obtained, $\Theta_2(n,m)$ can be calculated using the following formula which is recursive in m:

$$\Theta_2(n,m+2) = -2\left[1+(-1)^{n+m}\right]P_n^{m+1}(x_1) + (n+m+1)(n-m)\Theta_2(n,m) \quad (8.27)$$

and the initial values are $\Theta_2(n, 0)$ and $\Theta_2(n, 1) = [(-1)^n - 1]\,P_n(x_1)$.

Next the integral $\Theta_1(n,m)$ is found in terms of $\Theta_2(n, m)$ as follows:

$$\Theta_1(n,m) = \left[(-1)^{n+m} - 1\right]\sqrt{1-x_1^2}\,P_n^m(x_1) - \\ \frac{1}{2n+1}\left[(n+m)\Theta_2(n-1,m) - (m-n-1)\Theta_2(n+1,m)\right] \quad (8.28)$$

The last integral, $\Phi_1(p,q,m)$, can be integrated analytically and given by

$$\Phi_1(p,q,m) = \left[\frac{2k_e a(\cos k_e h - \cos m\phi_h)}{(m-k_e a)(m+k_e a)\sin k_e h}\right]^2 \cos m(\phi_p - \phi_q) \quad (8.29)$$

It should be mentioned that (8.29) was obtained by simplifying the previous result [5] that consists of 64 terms. Note that since x_1 is a simple constant, the values of $P_n^m(x_1)$ for all n and m are needed to be determined only once in one batch, with the results stored in an array. Similarly, the spherical Bessel and Hankel functions are needed to be calculated only once. Therefore, the result can be computed very quickly.

8.2.4 Radiation Fields

After the strip current is solved, the radiation fields E_θ and E_ϕ can be easily obtained. To begin with, the Green's functions for E_θ and E_ϕ are found as follows:

$$G_{J_\phi}^{E_\theta} = \frac{j\eta_0}{4\pi a r}\sum_{n=1}^{\infty}\sum_{m=0}^{n}\frac{2n+1}{n(n+1)\Delta_n^{\text{TE}}}\hat{J}_n(ka)\hat{H}_n^{(2)}(k_0 a)\cdot\frac{2m}{\Delta_m}\cdot\frac{(n-m)!}{(n+m)!}\cdot\frac{P_n^m(\cos\theta)}{\sin\theta}\cdot$$
$$\frac{dP_n^m(\cos\theta')}{d\theta'}\sin m(\phi-\phi') - \frac{j\eta_0}{4\pi a r}\sum_{n=1}^{\infty}\sum_{m=1}^{n}\frac{2n+1}{n(n+1)\Delta_n^{\text{TM}}}\hat{J}_n{}'(ka)\hat{H}_n^{(2)}{}'(k_0 a)\cdot$$
$$\frac{2m}{\Delta_m}\cdot\frac{(n-m)!}{(n+m)!}\cdot\frac{dP_n^m(\cos\theta)}{d\theta}\cdot\frac{P_n^m(\cos\theta')}{\sin\theta'}\sin m(\phi-\phi')$$

$$(8.30)$$

$$G_{J_\phi}^{E_\phi} = \frac{j\eta_0}{4\pi ar} \sum_{n=1}^{\infty} \sum_{m=0}^{n} \frac{2n+1}{n(n+1)\Delta_n^{\text{TE}}} \hat{J}_n(ka)\hat{H}_n^{(2)}(k_0 a) \cdot \frac{2}{\Delta_m} \cdot \frac{(n-m)!}{(n+m)!} \cdot \frac{dP_n^m(\cos\theta)}{d\theta} \cdot$$

$$\frac{dP_n^m(\cos\theta')}{d\theta'} \cos m(\phi-\phi') - \frac{j\eta_0}{4\pi a\, r} \sum_{n=1}^{\infty} \sum_{m=1}^{n} \frac{2n+1}{n(n+1)\Delta_n^{\text{TM}}} \hat{J}_n{}'(ka)\hat{H}_n^{(2)}{}'(k_0 a) \cdot$$

$$\frac{2m^2}{\Delta_m} \cdot \frac{(n-m)!}{(n+m)!} \cdot \frac{P_n^m(\cos\theta)}{\sin\theta} \cdot \frac{P_n^m(\cos\theta')}{\sin\theta'} \cos m(\phi-\phi')$$

$$(8.31)$$

From the Green's functions, the fields E_θ and E_ϕ are obtained:

$$E_\theta = \iint_{S_0} G_{J_\phi}^{E_\theta} J_\phi(\phi') dS' \tag{8.32}$$

$$E_\phi = \iint_{S_0} G_{J_\phi}^{E_\phi} J_\phi(\phi') dS' \tag{8.33}$$

The fields E_θ and E_ϕ are then given by

$$E_\theta(r,\theta,\phi) = \frac{-\eta_0 a}{4\pi W} \cdot \frac{e^{-jk_0 r}}{r} \sum_{q=1}^{N} I_q E_{\theta q}(\theta,\phi) \tag{8.34}$$

$$E_\phi(r,\theta,\phi) = \frac{-\eta_0 a}{4\pi W} \cdot \frac{e^{-jk_0 r}}{r} \sum_{q=1}^{N} I_q E_{\phi q}(\theta,\phi) \tag{8.35}$$

where

$$E_{\theta q}(\theta,\phi) = \sum_{n=1}^{\infty} j^n \frac{2n+1}{n(n+1)} \cdot$$

$$\left\{ j\frac{\hat{J}_n{}'(ka)}{\Delta_n^{\text{TM}}} \sum_{m=1}^{n} 2m \cdot \frac{(n-m)!}{(n+m)!} \cdot \frac{dP_n^m(\cos\theta)}{d\theta} \Theta_2(n,m)\Phi_2(\phi,q,m) \right.$$

$$\left. + \frac{\hat{J}_n(ka)}{\Delta_n^{\text{TE}}} \sum_{m=1}^{n} 2m \cdot \frac{(n-m)!}{(n+m)!} \cdot \frac{P_n^m(\cos\theta)}{\sin\theta} \Theta_1(n,m)\Phi_2(\phi,q,m) \right.$$

$$(8.36)$$

$$E_{\phi q}(\theta,\phi) = \sum_{n=1}^{\infty} j^n \frac{2n+1}{n(n+1)} \cdot$$

$$\left\{ j\frac{\hat{J}_n{'}(ka)}{\Delta_n^{\mathrm{TM}}} \sum_{m=1}^{n} 2m^2 \cdot \frac{(n-m)!}{(n+m)!} \cdot \frac{P_n^m(\cos\theta)}{\sin\theta} \Theta_2(n,m)\Phi_3(\phi,q,m) \right.$$

$$\left. + \frac{\hat{J}_n(ka)}{\Delta_n^{\mathrm{TE}}} \sum_{m=0}^{n} \frac{2}{\Delta_m} \cdot \frac{(n-m)!}{(n+m)!} \cdot \frac{dP_n^m(\cos\theta)}{d\theta} \Theta_1(n,m)\Phi_3(\phi,q,m) \right\}$$

$$(8.37)$$

in which

$$\Phi_2(\phi,q,m) = \int_{\phi_q-\phi_h}^{\phi_q+\phi_h} \sin m(\phi-\phi')f_q(\phi')d\phi'$$

$$= \frac{1}{\sin k_e h} \cdot \frac{2k_0 a \sin m(\phi-\phi_q)(\cos k_0 h - \cos m\phi_h)}{(m-k_0 a)(m+k_0 a)}$$

$$(8.38)$$

$$\Phi_3(\phi,q,m) = \int_{\phi_q-\phi_h}^{\phi_q+\phi_h} \cos m(\phi-\phi')f_q(\phi')d\phi'$$

$$= \frac{1}{\sin k_e h} \cdot \frac{2k_0 a \cos m(\phi-\phi_q)(\cos k_0 h - \cos m\phi_h)}{(m-k_0 a)(m+k_0 a)}$$

$$(8.39)$$

Again, the results of (8.38) and (8.39) are simplified forms of the previous ones [5]. In deriving the radiation fields (8.34) and (8.35), we have used the asymptotic expressions $\hat{H}_n^{(2)}(k_0 r) \sim j^{n+1} e^{-jk_0 r}$ and $\hat{H}_n^{(2)}{'}(k_0 r) \sim j^n e^{-jk_0 r}$ for $r \to \infty$. The magnetic far fields H_θ and H_ϕ can be found using $\vec{H} = (1/\eta_0)\,\hat{r} \times \vec{E}$.

8.2.5 Results

The convergence of the modal solution (8.22) is checked. We only focus on the summation of index n, since the summation of index m has a finite number of terms ($0 \le m \le n$). It is well known that the convergence rate of spherical modal solutions depends on the arguments of the Bessel and Hankel functions. As we are now only concerned with the fundamental TE_{111} mode, it is informative to know the value of $\mathrm{Re}(ka)$, where ka is the first complex root of $\Delta_1^{\mathrm{TE}} = 0$ (Δ_1^{TE} is given in (8.8)). The result as a function of ε_r is shown in Fig. 8.4 for $3 \le \varepsilon_r \le 200$.

It is observed that $\mathrm{Re}(ka) \sim 3$ for all values of ε_r. Therefore, the number of required terms should change only slightly for different hemispherical DRAs

operating at the mode. Fig. 8.4 also shows the number of required modal terms for the solution to converge for $a = 12.5$ mm, $\varepsilon_r = 9.5$, $l = 12.0$ mm, and $W = 1.2$ mm. The results were calculated with $N = 3$ in the MoM solution and at frequencies $f = c \cdot \text{Re}(ka)/(2\pi a \sqrt{\varepsilon_r})$, where c is the speed of light in vacuum. The convergence rule is given by $\left| [Z_{in}(\text{new}) - Z_{in}(\text{old})]/Z_{in}(\text{new}) \right| \leq 10^{-4}$. It is seen in the figure that the solution converges with 64-68 terms over the range of ε_r. It is worth mentioning that the number of required terms does not vary monotonically with $\text{Re}(ka)$, since the solution involves $k_0 a$ as well. However, if the dielectric constant ε_r is fixed, the number of required terms will increase monotonically with a and, thus, ka.
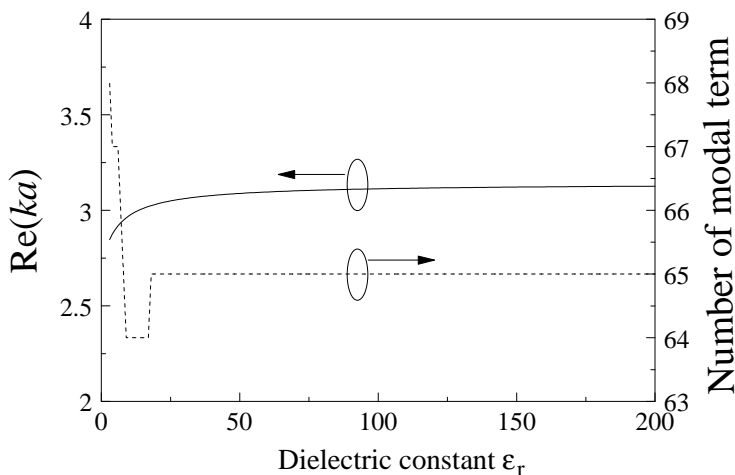
Fig. 8.4 The left axis shows the real part of the first root of the equation $\Delta_1^{TE} = 0$. The right axis shows the number of terms required for the solution to converge. The parameters are $a = 12.5$ mm, $\varepsilon_r = 9.5$, $l = 12.0$ mm, and $W = 1.2$ mm. (From [5], © 2000 IEEE)

Fig. 8.5 displays the convergence check using different numbers of modal terms. It shows that about 60 terms are enough for the solution to converge, which is very consistent with the result of Fig. 8.4. It was found that calculations of the solution are extremely fast, at an average value of 0.15 sec for each frequency point using a SunSPARC 20 Model 612 workstation. For reference, the calculation time for the previous probe feed solution [11] that requires numerical integration was also found; it was on average 2.07 sec for each frequency point.

The measured and calculated input impedances of the DRA are displayed in Fig. 8.6. The experiment was carried out using a hemispherical DRA of a = 12.5 mm and ε_r = 9.5. A conducting strip of length l = 12 mm and W = 1.2 mm was cut from an adhesive conductive tape. Initially, the DRA was put on an aluminium ground plane of size 30×30 cm, but an error of more than 4 % was found for the measured resonant frequency because of the air gap between the DRA and ground plane. To alleviate the air-gap problem, the DRA was first put on the adhesive side of the conducting tape. Since the conducting tape can be conformally adhered to the base of the DRA, the air gap was removed (to avoid the strip from shorting to the ground plane, there was no adhesive tape around the feed point where a very small air gap still existed). Additional adhesive tapes were used to mount the edges of the DRA-attached tape on the ground plane. With reference to the figure, reasonable agreement between theory and experiment is observed. The measured and calculated resonant frequencies (zero reactance) are 3.60 and 3.56 GHz, respectively. The error is now only 1.1 %, which is much smaller than without the use of the conductive adhesive tapes. The discrepancy is caused by the small air gap round the feed point and measurement tolerances in the experiment.
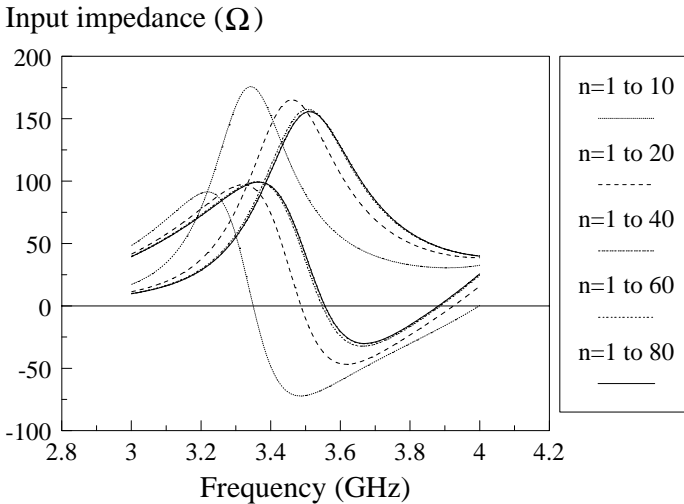
Fig. 8.5   The convergence check of the solution: a = 12.5 mm, ε_r = 9.5, l = 12.0 mm, and W = 1.2 mm. (From [5], © 2000 IEEE)

Fig. 8.7 shows the calculated input impedance for different strip lengths. It is seen that the strip length can be used to change the input impedance. The results are similar to those in the probe-feed case [11].
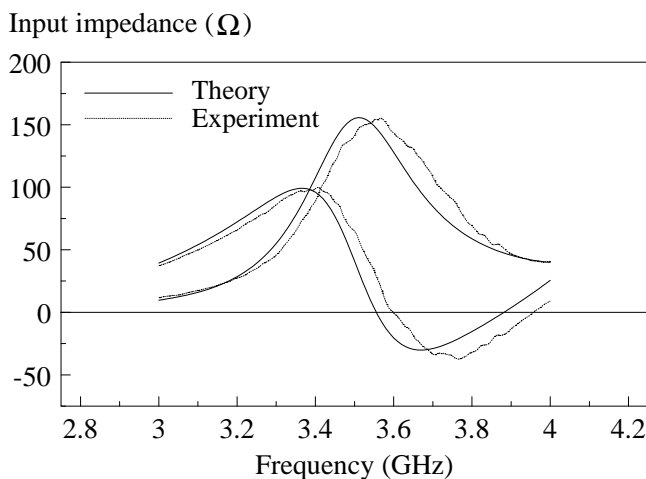
Fig. 8.6 Measured and calculated input impedances of the conformal strip-fed hemispherical DRA: $a = 12.5$ mm, $\varepsilon_r = 9.5$, $l = 12.0$ mm, and $W = 1.2$ mm. (From [5], © 2000 IEEE)
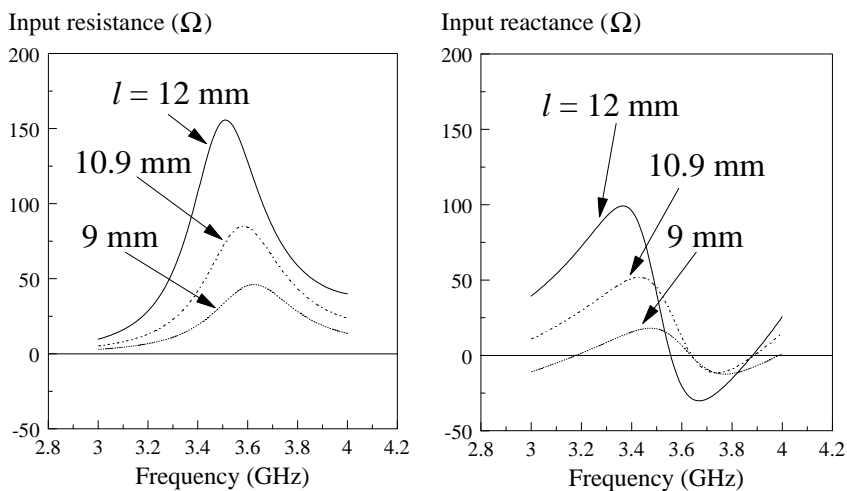
Fig. 8.7 Calculated input impedance of the DRA for different strip lengths: $a = 12.5$ mm, $\varepsilon_r = 9.5$, and $W = 1.2$ mm. (From [5], © 2000 IEEE)

Fig. 8.8 shows the calculated input impedance for different dielectric constants. Both the resonant frequency and the bandwidth decrease with increasing dielectric constant. The results are, again, similar to the probe-feed case. Note that the reactance is shifted upward for the case of $\varepsilon_r = 5$. This is because the modal fields of the DRA are weak when the dielectric constant is small, and the DRA fields are strongly influenced by the strip (monopole) mode.

Fig. 8.9 shows the calculated E-plane ($\theta = 90°$, $-90° \leq \phi \leq 90°$ in Fig. 8.2) and H-plane ($\phi = 0°$, $-0° \leq \theta \leq 180°$ in Fig.8.2) radiation field patterns. The maximum H-plane crosspolarised field is 24 dB lower than the maximum co-polarised fields, whereas it was only 6 dB in the probe-feed version [18]. It is because the latter has the J_r component, which contributes entirely to the crosspolarised field. The E-plane crosspolarised field is theoretically zero.

8.3 APERTURE-COUPLED DRA WITH A PERPENDICULAR FEED

8.3.1 Theory

The antenna configuration is shown in Fig. 8.10, where a hemispherical DRA of radius a and dielectric constant ε_{ra} is excited by a slot of length L and width W. In general the DRA has offsets from the slot center. A 50-Ω microstripline of width W_f is printed on the perpendicular feed substrate of dielectric constant ε_{rs} and thickness d. The cross section of the substrate was used to feed the slot. At the aperture position, the microstripline and its ground plane are electrically connected to that of the DRA.
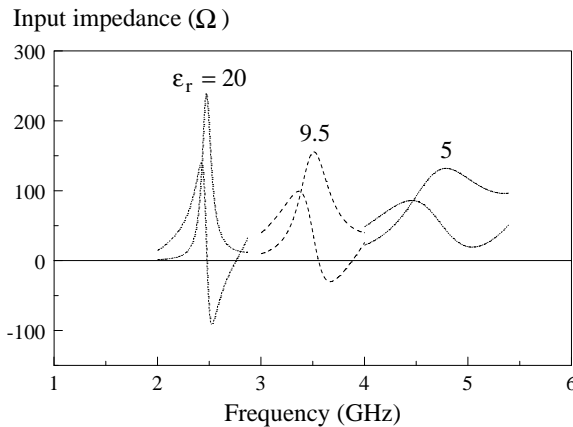
Fig. 8.8 Calculated input impedance of the DRA for different dielectric constants: a = 12.5 mm, l = 12.0 mm, and W = 1.2 mm. (From [5], © 2000 IEEE)
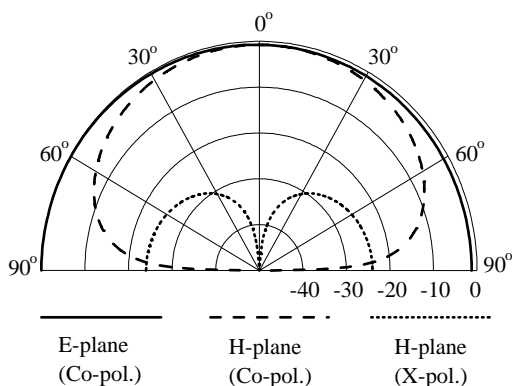
Fig. 8.9 Calculated co- and cross-polarised field patterns: $a = 12.5$ mm, $\varepsilon_r = 9.5$, $l = 12.5$ mm, and $W = 1.2$ mm. (From [5], © 2000 IEEE)

In the following formulation, the unprimed and primed coordinates refer to the field and source points, respectively. To begin, the equivalence principle is invoked and the slot becomes short-circuited. The fields are then generated by two equivalent magnetic currents flowing on adjacent sides of the DRA ground plane, as shown in Fig. 8.11. The feedline part is considered first. It is assumed that the microstripline is propagating a quasi-TEM mode of fields

$$\vec{E}^{\pm} = \vec{e}\,e^{\mp j\beta_f x} \tag{8.40}$$

$$\vec{H}^{\pm} = \pm\vec{h}\,e^{\mp j\beta_f x} \tag{8.41}$$
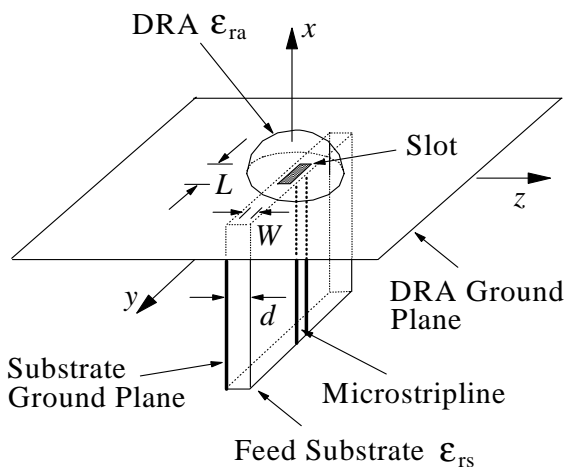
Fig. 8.10 The aperture-coupled hemispherical DRA with a perpendicular feed. (From [9], © 2000 IEEE)

where

$$\vec{e}(y,z) = e_y \hat{y} + e_z \hat{z} \tag{8.42a}$$

$$\vec{h}(y,z) = h_y \hat{y} + h_z \hat{z} \tag{8.42b}$$

are normalised traverse modal fields [19] as follows:

$$\int_{y=-\infty}^{\infty} \int_{z=0}^{\infty} \vec{e} \times \vec{h} \cdot \hat{x} \, dy \, dz = 1 \tag{8.43}$$

with β_f being the propagation constant of the microstripline fields.

Suppose there is an incident signal of fields $\vec{E}^+$, $\vec{H}^+$ propagating from the input microstripline port. Then, the reflected signal from the DRA ground plane consists of two parts; part A is a total reflection caused by the short-circuited slot and part B is the field excited by the equivalent magnetic current M_y on the substrate side. The total fields in part A are given by

$$\vec{E}_A = \vec{E}^+ + R_A \vec{E}^- \tag{8.44a}$$

$$\vec{H}_A = \vec{H}^+ + R_A \vec{H}^- . \tag{8.44b}$$
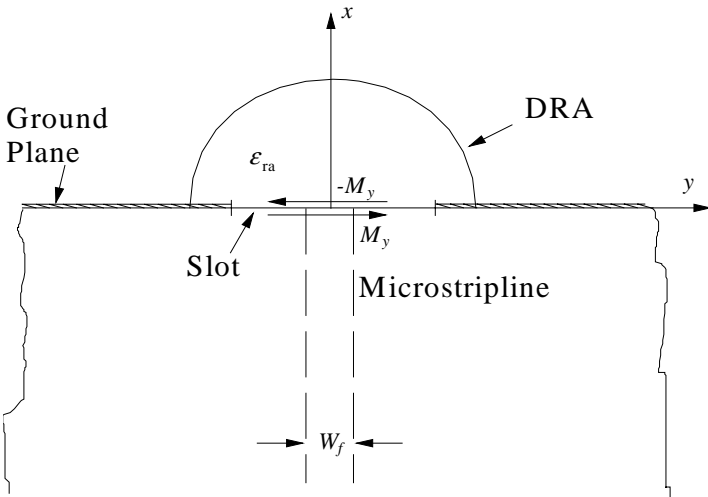
Fig. 8.11   The equivalent magnetic currents $-M_y$ and M_y on adjacent sides of the slot.

and in part B by

$$\vec{E}_B = R_B \vec{E}^- \tag{8.45a}$$

$$\vec{H}_B = R_B \vec{H}^- \tag{8.45b}$$

where $R_A = -1$ and R_B are the reflection coefficients of the short-circuited slot and the excitation coefficient of the magnetic current, respectively. By superposition, the total refection coefficient of the incident signal is given by $R = R_A + R_B$ or

$$R = R_B - 1. \tag{8.46}$$

To determine R_B, the reciprocity theorem is applied to $\vec{E}_A$, $\vec{H}_A$ and $\vec{E}_B$, $\vec{H}_B$ as follows:

$$\iint\limits_S \vec{E}_A \times \vec{H}_B \cdot d\vec{S} = \iint\limits_S \vec{E}_B \times \vec{H}_A \cdot d\vec{S} \tag{8.47}$$

where S is a closed surface consisting of three pieces, namely S_1, S_2, and S_W, as shown in Fig. 8.12. The surface S_1 is part of the DRA ground plane, S_2 is parallel to and displaced from S_1, and S_W is a side wall that connects S_1 and S_2. In Fig. 8.12, the distance D between S_1 and S_2 is arbitrary, since the terms associated with it will be eliminated in the algebraic simplification. It was found that the contribution of S_W to the integrals was zero. On S_1, we have $\vec{E}_A = 0$ but $\hat{n} \times \vec{E}_B = M_y \hat{y}$ on the original slot surface S_0.
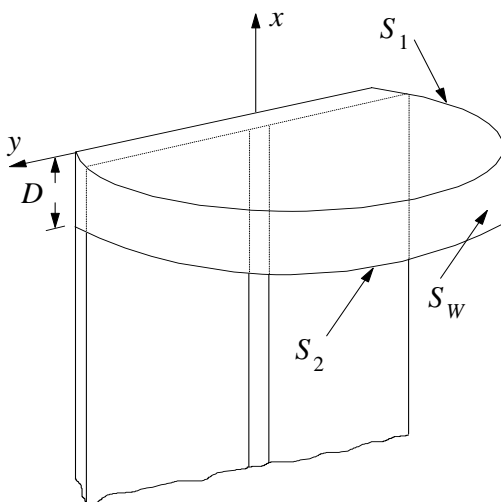
Fig. 8.12   Illustration of the surfaces S_1, S_2, and S_W used in the reciprocity analysis. (From [9], © 2000 IEEE)

Using these facts (8.47) can be simplified to:

$$R_B = \iint_{S_0} M_y(y,z) h_y(y,z) dS \tag{8.48}$$

which is the result of [20].

The next step is to enforce the continuity of the tangential H-field across the slot :

$$H_y^a(x=0^+) = H_y^s(x=0^-) + H_y^f(x=0^-) \tag{8.49}$$

where H_y^a, H_y^s, H_y^f are the DRA H-field due to $-M_y$, substrate H-field due to M_y, and substrate H-field due to the microstrip feedline, respectively. At $x=0^-$, we have $H_y^f = (1-R)h_y$ and (8.49) can be written as

$$H_y^a - H_y^s = (1-R)h_y \tag{8.50}$$

Defining two Green functions, $G_{M_y}^{H_y}$ and G_{yy}^{HM}, for the y-directed DRA and substrate H-fields due to M_y, respectively, then (8.50) becomes

$$\iint_{S_0} G_{M_y}^{H_y}(x=0,y,z;x'=0,y',z')[-2M_y(y',z')]dS'$$
$$-\iint_{S_0} G_{yy}^{HM}(x=0,y,z;x'=0,y',z')[2M_y(y',z')]dS' \tag{8.51}$$
$$= (1-R) \cdot \frac{1}{\sqrt{Z_c}} H_y(y,z)$$

where $H_y = \sqrt{Z_c}\, h_y$ [19]. In (8.51), M_y is multiplied by two to account for the effect of the DRA ground plane, whereas the minus sign of M_y in the first integral is to ensure that the tangential electric field is equal on each side of the slot region. Now we have two equations, (8.48) and (8.51), for the two unknowns, R_B and M_y. Using the MoM the magnetic current M_y is expanded in terms of unknown voltage coefficients V_n's as follows:

$$M_y(y,z) = \sum_{n=1}^{N} V_n f_n(y,z) \tag{8.52}$$

where

$$f_n(y,z) = f_u(z) f_p(y - y_n) \tag{8.53}$$

$$f_u(z) = \begin{cases} \dfrac{1}{W} & (d-W)/2 < z < (d+W)/2 \\ 0 & \text{elsewhere} \end{cases} \tag{8.54}$$

$$f_p(y) = \begin{cases} \dfrac{\sin k_e(h-|y|)}{W} & |y| < h \\ 0 & |y| > h \end{cases} \tag{8.55}$$

$$y_n = \frac{-L}{2} + nh \tag{8.56}$$

in which $k_e = \sqrt{(\varepsilon_{ra}+\varepsilon_{rs})/2}\, k_0$ and $h = L/(N+1)$ are the effective wavenumber of the slot and the piecewise sinusoidal (PWS) mode half-length, respectively. Insertion of (8.48) and (8.52) into (8.46) gives:

$$R = [\Delta v_n]^t [V_n] - 1 \tag{8.57}$$

where

$$\Delta v_n = \frac{1}{\sqrt{Z_c}} \iint\limits_{S_0} f_n(y,z) H_y(y,z) dS \tag{8.58}$$

and the superscript t denotes the transpose of a matrix. Evaluation of (8.58) is performed in the spectral domain:

$$\Delta v_m = \frac{1}{2\pi\sqrt{Z_c}\, W} \int_{k_y=-\infty}^{\infty} \left[\int_{z=(d-W)/2}^{(d+W)/2} \tilde{G}_{yx}^{HJ}(k_x=-\beta_f, k_y, z)\, dz \right] \cdot$$

$$F_u(k_y) F_p(k_y) \cos(k_y y_m)\, dk_y \tag{8.59}$$

where $\tilde{G}_{yx}^{HJ}(k_x, k_y, z)$, $F_u(k_y)$, and $F_p(k_y)$ are given in Appendix A. Note that the integration of z can be performed analytically, with the result given in the appendix. Using Galerkin's procedure, the following matrix equation for the unknown voltage coefficients V_n is obtained:

$$[Y_{mn}^a - Y_{mn}^s][V_n] = (1-R)[\Delta v_m] \tag{8.60}$$

where

$$Y_{mn}^a = -2 \iint\limits_{S_0} \iint\limits_{S_0} f_m(y,z) G_{M_y}^{H_y}(x=0,y,z;x'=0,y',z') f_n(y',z') dS' dS \tag{8.61}$$

and

$$Y_{mn}^s = 2 \iint\limits_{S_0} \iint\limits_{S_0} f_m(y,z) G_{yy}^{HM}(x=0,y,z;x'=0,y',z') f_n(y',z') dS' dS \tag{8.62}$$

are the antenna and substrate admittances, respectively. The substrate admittances, Y_{mn}^s, are evaluated in the spectral domain:

$$Y_{mn}^s = \frac{2}{4\pi^2 W^2} \int\limits_{-\infty}^{\infty}\int\limits_{-\infty}^{\infty} \left[\int_{z=(d-W)/2}^{(d+W)/2} \int_{z'=(d-W)/2}^{(d+W)/2} \tilde{G}_{yy}^{HM}(k_x,k_y,z,z')\,dzdz' \right] \cdot$$
$$F_p^2(k_y)\cos k_y(y_m - y_n)\,dk_x dk_y \tag{8.63}$$

where $\tilde{G}_{yy}^{HM}(k_x,k_y,z,z')$ and $F_p(k_y)$ are given in Appendix A. Again, the integration of z and z' is performed analytically. From (8.57) and (8.60), the voltage matrix is found:

$$\left[V_n\right] = \left\{ \left[Y_{mn}^a - Y_{mn}^s\right] + \left[\Delta v_m\right]\left[\Delta v_n\right]^t \right\}^{-1} \left[2\Delta v_m\right] \tag{8.64}$$

Substitution of (8.64) into (8.57) yields the reflection coefficient R, from which the input impedance at the slot position can easily be found:

$$Z_{in} = \frac{1+R}{1-R} \tag{8.65}$$

Evaluation of the antenna admittances Y_{mn}^a will be discussed in the next section.

8.3.2 The DRA Admittances Y_{mn}^a

For convenience, a new coordinate system is redefined in Fig. 8.13, so that the antenna admittances obtained in [12] can be reused here:

$$Y_{mn}^a = Y_{mn}^P + Y_{mn}^H \tag{8.66}$$

where

$$Y_{mn}^P = \frac{-2}{\eta^2} \cdot \left\{ \frac{-j\eta}{4\pi k} \int_{-\frac{L}{2}}^{\frac{L}{2}} \int_{-\frac{L}{2}}^{\frac{L}{2}} f_P(y - y_m) \frac{e^{-jk\zeta_e}}{\zeta_e^5} [(1+jk\zeta_e)(2\zeta_e^2 - 3a_e^2) \right.$$
$$+ a_e^2 k^2 \zeta_e^2] f_P(y' - y_n)dy'dy \} \tag{8.67}$$

$$Y_{mn}^H = \frac{-2}{W^2} \int\int_{S_0}\int\int_{S_0} f_p(y - y_m) G_H f_n(y' - y_n)dS'dS \tag{8.68}$$

in which

$$\zeta_e = \sqrt{(y-y')^2 + a_e^2} \tag{8.69}$$

and $a_e = W/4$ and η are the equivalent radius of the slot and the dielectric wave impedance, respectively. The expression inside the brackets $\{\cdot\}$ of (8.67) represents the self- and mutual-impedances of an electric strip dipole radiating in a

dielectric medium of wavenumber k, whereas the factor of $(1/\eta^2)$ is used to transform the electric quantities to magnetic ones. In (8.68) G_H is the homogeneous Green function (Appendix B), which accounts for the dielectric discontinuity at the DRA surface. It vanishes when $\varepsilon_r \rightarrow 1$, and in this case, the antenna side simply becomes a slot antenna. It should be mentioned that Y_{mn}^H can efficiently be evaluated by using a simple expression for frequencies around the DRA TE$_{111}$ mode [21], or a recurrence formula for an arbitrary frequency [22].

8.3.3   Results

Fig. 8.14 shows the measured and calculated input impedances for different slot lengths, with the slot located at the center of the DRA. In measurements, conducting adhesive tapes were mounted on a foam board to form the DRA ground plane. The DRA was then placed on the adhesive side of the conducting tapes to remove any possible air gaps between itself and the ground plane. This measurement technique has previously been used in Section 8.2.5 and in other DRA measurements as well [23-25], and the measured frequencies were improved significantly. With reference to the figure, reasonable agreement between theory and experiment is obtained. It is observed that the coupling (radius of impedance circle) increases with L, as found in the previous aperture-coupled DRA [12]. When $L = 14$ mm, an excellent impedance match is obtained. At this match point, the measured and calculated resonant frequencies (min. $\left|S_{11}\right|$) are 3.55 and 3.50 GHz (error 1.4 %), respectively, which are very close to the predicted value of 3.68 GHz [12].
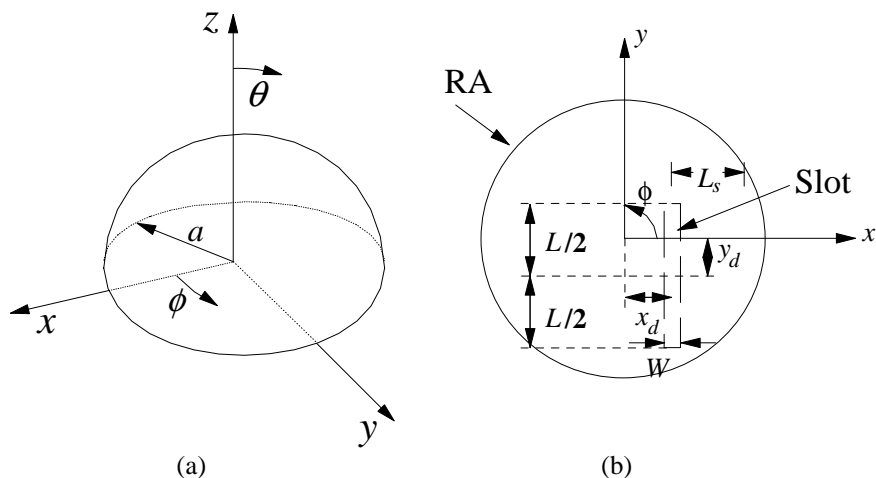
Fig. 8.13   (a) The new coordinate system for analysis of the DRA part.
(b) The slot offsets x_d and y_d with respect to the DRA center.

The effects of the offsets x_d and y_d on the input impedance are given in Figs. 8.15 and 8.16, respectively. It is seen that, as was found in the previous aperture-coupled case [12], the impedance match can be achieved by changing x_d and/or y_d.

The calculated input impedances for different substrate permittivities are shown in Fig. 8.17. In each case the width of the microstripline was adjusted to maintain a 50-Ω feedline. It is observed that using a higher ε_{rs} leads to a stronger coupling, since increasing ε_{rs} will decrease the effective wavelength in the slot and thus, electrically lengthen the slot.
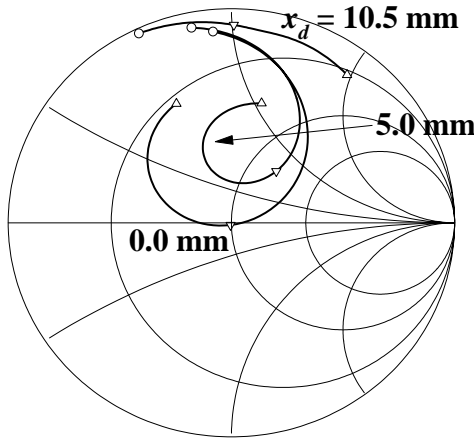
Fig. 8.14 Measured and calculated input impedance of the DRA for $L = 11.0$, 14.0, and 17.0 mm: $a = 12.5$ mm, $\varepsilon_{ra} = 9.5$, $W = 0.9$ mm, $\varepsilon_{rs} = 2.33$, $d = 1.57$ mm, and $W_f = 4.6$ mm. Solid line: theory, dashed line: experiment. O 3.2 GHz, ∇ 3.5 GHz (theory), $\square$ 3.55 GHz (experiment), Δ 3.8 GHz. (From [9], © 2000 IEEE)

8.4   CONCLUSION

The conformal strip feeding method and the aperture-coupling method with a perpendicular feed have been reviewed. A hemispherical DRA excited in the TE_{111} mode has been used to demonstrate the two feeding methods. The conformal strip feeding method shares the same advantages of the coaxial feed method, but desirably avoids errors that an oversized hole introduces. In the analysis, the mode-matching method has been used to obtain the exact Green's function, with the singularity problem eliminated through the application of newly developed recurrence formulas. The solution does not require any numerical integration;

therefore it is computationally very efficient. It has been found that it is easy to obtain an impedance match by simply varying the strip length. Reasonable agreement between theory and experiment has been obtained.
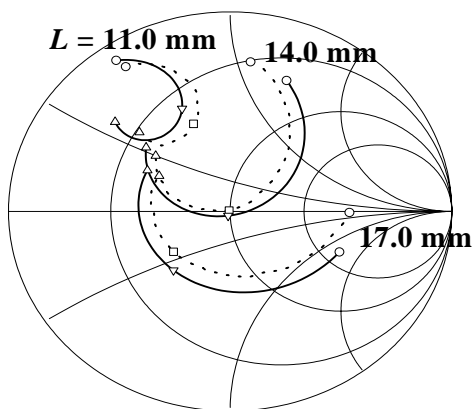
Fig. 8.15   Calculated input impedance of the DRA for different slot offsets x_d: $L =$ 11.0 mm. Other parameters are the same as in Fig. 8.14.
O 3.0 GHz, ∇ 3.5 GHz, Δ 4.0 GHz.
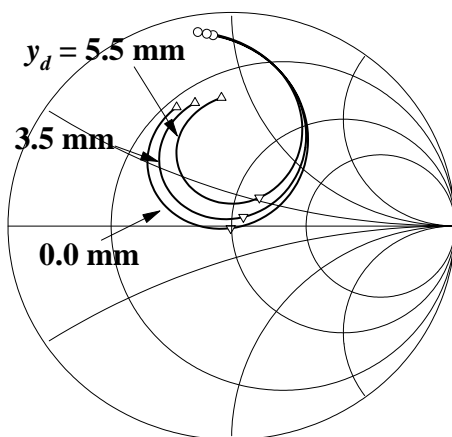
Fig. 8.16   Calculated input impedance of the DRA for different slot offsets y_d: $L =$ 11.0 mm. Other parameters are the same as in Fig. 8.14.
O 3.0 GHz, ∇ 3.5 GHz, Δ 4.0 GHz.
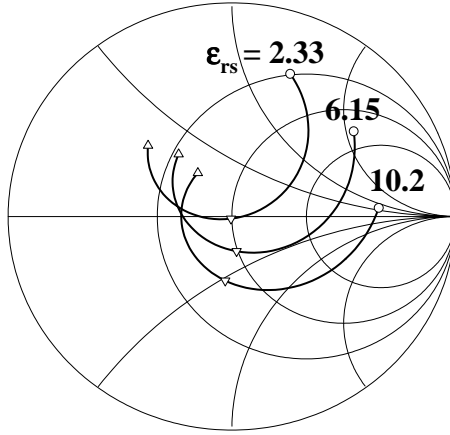
Fig. 8.17   Calculated input impedance of the DRA for different substrate permittivity:
$L = 14.0$ mm. Other parameters are the same as in Fig. 8.14.
O 3.2 GHz, ∇ 3.5 GHz, Δ 3.8 GHz. (From [9], © 2000 IEEE)

For the aperture-coupling method with a perpendicular feed, it first completely utilises the microwave substrate and, second, separates the DRA from the feeding network. The Green's function approach, together with the reciprocity method, have been used to formulate the integral equation for the slot current, which has been solved by using the MoM. To enhance the numerical efficiency, the calculations have been performed in spatial and spectral domains for the DRA and feedline parts, respectively. The theory has been verified by measurements. Again, it is easy to obtain an impedance match by varying the slot length and/or slot offset(s), showing its feasibility in practical designs.

8.5   APPENDIX A
This appendix lists the Green functions for the microstrip feedline part.

$$\tilde{G}_{yx}^{HJ}(k_x, k_y, z) = \frac{\varepsilon_{rs} k_1 k_2 \cos k_1 d + j[k_1^2 - k_x^2(\varepsilon_{rs} - 1)]\sin k_1 d}{T_e T_m} \cos k_1 z \quad (8.70)$$

$$\tilde{G}_{yy}^{HM}(k_x, k_y, z, z') = \frac{-1}{k_0 \eta_0} \Big[(\varepsilon_{rs} k_0^2 - k_y^2) \cdot$$

$$\frac{k_1 \cos k_1(d - z_>) + jk_2 \varepsilon_{rs} \sin k_1(d - z_>)}{k_1 T_m} - \frac{k_y^2 k_1 (\varepsilon_{rs} - 1)}{T_e T_m} \cos k_1 z_> \Big] \cos k_1 z_<$$

$$(8.71)$$

$$F_p(k_y) = \int_{-\infty}^{\infty} f_p(y) e^{-jk_y y} dy = \frac{2k_e (\cos k_y h - \cos k_e h)}{(k_e^2 - k_y^2) \sin k_e h} \tag{8.72}$$

$$F_u(k_y) = \frac{\sin(k_y W_f / 2)}{k_y W_f / 2} \tag{8.73}$$

$$F_u(k_x) = \frac{\sin(k_x W / 2)}{k_x W / 2} \tag{8.74}$$

where

$$z_> = \begin{cases} z, & z > z' \\ z', & z < z' \end{cases}, \qquad z_< = \begin{cases} z', & z > z' \\ z, & z < z' \end{cases} \tag{8.75}$$

$$T_e = k_1 \cos k_1 d + jk_2 \sin k_1 d \tag{8.76}$$

$$T_m = \varepsilon_{rs} k_2 \cos k_1 d + jk_1 \sin k_1 d \tag{8.77}$$

$$k_1^2 = \varepsilon_{rs} k_0^2 - \beta^2 \qquad \text{Im}(k_1) < 0 \tag{8.78}$$

$$k_2^2 = k_0^2 - \beta^2 \qquad \text{Im}(k_2) < 0 \tag{8.79}$$

$$\beta^2 = k_x^2 + k_y^2 \tag{8.80}$$

$$k_0^2 = \omega^2 \mu_0 \varepsilon_0 \tag{8.81}$$

$$\eta_0 = \sqrt{\mu_0 / \varepsilon_0} \tag{8.82}$$

The integrations of z, z' are performed analytically and the results are given here:

$$\int_{z=(d-W)/2}^{(d+W)/2}\int_{z'=(d-W)/2}^{(d+W)/2} \cos k_1(d-z_>)\cos k_1 z_< \, dz\, dz'$$
$$= \frac{1}{k_1^2}\left[k_1 W \sin k_1 d - 4\sin k_1(\frac{d-W}{2})\cos\frac{k_1 d}{2}\,\cos\frac{k_1 W}{2}\right] \tag{8.83}$$

$$\int_{z=(d-W)/2}^{(d+W)/2}\int_{z'=(d-W)/2}^{(d+W)/2} \sin k_1(d-z_>)\cos k_1 z_< \, dz\, dz'$$
$$= \frac{1}{k_1^2}\left[-k_1 W \cos k_1 d - \sin k_1(d-W) + \sin k_1 d\right] \tag{8.84}$$

$$\int_{z=(d-W)/2}^{(d+W)/2}\int_{z'=(d-W)/2}^{(d+W)/2} \cos k_1 z_> \cos k_1 z_< \, dz\, dz' = \left(\frac{2}{k_1}\cos\frac{k_1 d}{2}\,\sin\frac{k_1 W}{2}\right)^2 \tag{8.85}$$

8.6   APPENDIX B

Using the coordinate system of Fig. 8.4, the homogeneous Green function G_H ($z = z' = 0$) is given by [9]:

$$
\begin{aligned}
G_H &= \frac{-\sin\phi'\sin\phi}{4\pi\omega\mu_o kr^2 r'^2}\sum_{n=1}^{\infty} b_n n(n+1)(2n+1)P_n(\cos(\phi-\phi'))\hat{J}_n(kr')\hat{J}_n(kr)\\
&\quad - \frac{-\cos\phi'\sin\phi}{4\pi\omega\mu_o r^2 r'}\sum_{n=1}^{\infty} b_n(2n+1)\frac{\partial}{\partial\phi'}P_n(\cos(\phi-\phi'))\hat{J}'_n(kr')\hat{J}_n(kr)\\
&\quad - \frac{\sin\phi'\cos\phi}{4\pi\omega\mu_o rr'^2}\sum_{n=1}^{\infty} b_n(2n+1)\frac{\partial}{\partial\phi}P_n(\cos(\phi-\phi'))\hat{J}_n(kr')\hat{J}'_n(kr)\\
&\quad - \frac{\omega\varepsilon\cos\phi'\cos\phi}{4\pi krr'}\sum_{n=1}^{\infty} e_n\frac{(2n+1)}{n(n+1)}P'_n(\cos(\phi-\phi'))\hat{J}_n(kr')\hat{J}_n(kr)\\
&\quad - \frac{k\cos\phi'\cos\phi}{4\pi\omega\mu_o rr'}\sum_{n=1}^{\infty} b_n\frac{(2n+1)}{n(n+1)}\frac{\partial^2}{\partial\phi\partial\phi'}P_n(\cos(\phi-\phi'))\hat{J}'_n(kr')\hat{J}'_n(kr)
\end{aligned}
\tag{8.86}
$$

where

$$b_n = -\frac{\hat{H}_n^{(2)}(ka)\hat{H}_n^{(2)'}(k_0 a)-\sqrt{\varepsilon_{ra}}\hat{H}_n^{(2)'}(ka)\hat{H}_n^{(2)}(k_0 a)}{\hat{J}_n(ka)\hat{H}_n^{(2)'}(k_0 a)-\sqrt{\varepsilon_{ra}}\hat{J}_n'(ka)\hat{H}_n^{(2)}(k_0 a)} \tag{8.87}$$

$$e_n = -\frac{\hat{H}_n^{(2)'}(ka)\hat{H}_n^{(2)}(k_0 a)-\sqrt{\varepsilon_{ra}}\hat{H}_n^{(2)}(ka)\hat{H}_n^{(2)'}(k_0 a)}{\hat{J}_n'(ka)\hat{H}_n^{(2)}(k_0 a)-\sqrt{\varepsilon_{ra}}\hat{J}_n(ka)\hat{H}_n^{(2)'}(k_0 a)} \tag{8.88}$$

and $\hat{J}_n(x)$ and $\hat{H}_n^{(2)}(x)$ are the nth-order Schelkunoff-type spherical Bessel function of the first kind and spherical Hankel function of the second kind, respectively. $P_n(x)$ is the Legendre polynomial. A prime denotes a derivative with respect to the whole argument.

REFERENCES

[1]   S. A. Long, M. W. McAllister and L. C. Shen, "The resonant cylindrical dielectric cavity antenna", *IEEE Trans. Antennas Propagat.*, vol. 31, pp. 406-412, May 1983

[2]   R. K. Mongia, A. Ittipiboon, M. Cuhaci and D. Roscoe, "Circularly polarized dielectric resonator antenna," *Electron. Lett.*, vol. 30, pp. 1361-1362, Aug. 1994

[3]   G. Drossos, Z. Wu and L. E. Davis, "Circular polarized cylindrical dielectric resonator antenna," *Electron. Lett.*, vol. 32, pp. 281-283, Feb. 1996

[4]   R. K. Mongia, A. Ittipiboon, Y. M. M. Antar, P. Bhartia and M. Cuhaci, "A half-split cylindrical dielectric resonator antenna using slot-coupling," *IEEE Microwave and Guided Wave Lett.*, vol. 3, pp. 38-339, Feb. 1993

[5]   K. W. Leung, "Conformal strip excitation of dielectric resonator antenna," *IEEE Trans. Antennas Propagat.*, vol. 48, No. 6, pp. 961-967, June 2000

[6]   K. M. Luk, M. T. Lee, K. W. Leung and E. K. N. Yung, "Technique for improving coupling between microstripline and dielectric resonator antenna," *Electron. Lett.*, vol. 35, no. 5, pp. 357-358, Mar. 1999

[7]   R. T. Long, R. J. Dorris, S. A. Long, M. A. Khayat and J. T. Williams, "Use of parasitic strip to produce circular polarisation and increased bandwidth for cylindrical dielectric resonator antenna," *Electron. Lett.*, vol. 37, pp. 406-408, Mar. 2001

[8]   K. W. Leung and M. W. To, "Aperture-coupled dielectric resonator antenna with a perpendicular feed," *Electron. Lett.*, vol. 33, no. 12, pp. 1000-1001, June 1997

[9]   K. W. Leung, "Analysis of aperture-coupled hemispherical dielectric resonator antenna with a perpendicular feed," *IEEE Trans. Antennas Propagat.*, vol. 48, no. 6, pp. 1005-1007, June 2000

[10]   A. C. Buck and D. M. Pozar, "Aperture-coupled microstrip antenna with a perpendicular feed," *Electron. Lett.*, vol. 22, pp. 125-126, 1986

[11]   K. W. Leung, K. M. Luk, K. Y. A. Lai and D. Lin, "Theory and experiment of a coaxial probe fed dielectric resonator antenna," *IEEE Trans. Antennas Propagat.*, vol. 41, pp. 1390-1398, Oct. 1993

[12]   K. W. Leung, K. M. Luk, K. Y. A. Lai and D. Lin, "Theory and experiment of an aperture-coupled hemispherical dielectric resonator antenna," *IEEE Trans. Antennas Propagat.*, vol. 43, pp. 1192-1198, Nov. 1995

[13]   R. F. Harrington, *Time Harmonic Electromagnetic Fields*. New York : McGraw-Hill, 1961

[14]   K. W. Leung, "Theory and experiment of a rectangular slot on a sphere," *IEEE Trans. Microwave Theory and Techn.*, vol. 46, pp. 2117-2123, Dec. 1998

[15]   K. W. Leung, "Rectangular and zonal slots on a sphere with a backing shell: Theory and Experiment," *IEEE Trans. Antennas Propagat.*, vol. 51, June 2003 (in press)

[16]   K. W. Leung, "Analysis of zonal and rectangular slots on a conducting spherical cavity," *IEEE Trans. Antennas Propagat.*, vol. 49, pp. 1739-1745, Dec. 2001

[17]   K. W. Leung, "Efficient and accurate computation of an annular slot on a dielectric half-space," *IEEE Trans. Antennas Propagat.*, vol. 48, pp. 467-468, Mar. 2000

[18]   A.A. Kishk, G. Zhou, and A.W. Glisson, "Analysis of dielectric-resonator antennas with emphasis on hemispherical structures," *IEEE Antennas and Propagation Magazine*, vol. 36, pp. 20-31, Apr. 1994

[19]   D. M. Pozar, "A reciprocity method of analysis for printed slot and slot-coupled microstrip antennas," *IEEE Trans. Antennas and Propagat.*, vol. 34, pp. 1439-1446, Dec. 1986

[20]   N. K. Das, "Rigorous analysis of an aperture-coupled microstrip antenna fed by a microstrip line on a perpendicular substrate," *IEEE Microwave and Guided Wave Lett.*, vol. 4, pp. 202-204, June 1994

[21]   K. W. Leung and K. W. Ng, "Efficient computation for structures consisting of a slot and a metallic/dielectric hemisphere cavity," *IEEE Trans. Antennas Propagat.* vol. 46, pp. 457-458, Mar. 1998

[22]   K. W. Leung, "Efficient computation for the general solution of a slot loaded by a hemispherical dielectric and/or backing cavity," *IEEE Trans. Antennas Propagat.*, vol. 50, Dec. 2002 (in press)

[23]   K. Y. Chow, K. W. Leung, K. M. Luk and E. K. N. Yung, "Input impedance of the slot-fed dielectric resonator antenna with/without a backing cavity," *IEEE Trans. Antennas Propagat.*, vol. 49, pp. 307-309, Feb. 2001

[24]   K. Y. Chow and K. W. Leung, "Theory and experiment of the cavity-backed slot-excited dielectric resonator antenna," *IEEE Trans. Electromagnetic Compatibility*, vol. 42, 3, pp. 290-287, Aug. 2000

[25]   K. Y. Chow and K. W. Leung, "Cavity-backed slot-coupled dielectric resonator antenna excited by a narrow strip," *IEEE Trans. Antennas Propagat.*, vol. 50, no. 3, pp. 404-405, Mar. 2002

CHAPTER 9

Dielectric Resonator Antenna Arrays

Z. Wu

Department of Electrical Engineering and Electronics
UMIST
Manchester
United Kingdom

9.1 INTRODUCTION

The properties of dielectric resonator antennas (DRAs) of various geometries have been described in the previous chapters. With appropriate feed arrangements, the DRA elements can be used to form DRA arrays with directional radiation patterns providing enhanced antenna gain for terrestrial communication and radar applications. The DRA elements can also be phased to form adaptive arrays or functional arrays with beam-steering capability. Linearly or circularly polarised DRAs can also be used to construct circularly polarised arrays for applications in telecommunications via satellites.

Since the experimental study of a dielectric waveguide-fed series DRA array for millimetre wave applications by Birand and Gelsthorpe [1] at ERA Technology Ltd, UK in early 1980s, the studies of DRA arrays have been reasonably well reported in the literature [2-27]. In this chapter, linearly and circularly polarised arrays constructed using DRA elements will be reviewed, and the characteristics of DRA arrays will be described. The factors that may affect the performance of DRA arrays will also be discussed.

9.2 PARAMETERS OF DRA ARRAYS

9.2.1 DRA Elements and Feed Arrangement

The performance of a DRA array depends on the geometry and dimensions of the DRA elements, the spacing between elements, the number of elements, the mode of operation, and the feed arrangement. Various DRA geometries discussed in the previous chapters offer a range of choices of DRA elements, and a number of structures can be used to feed DRA arrays [2]. The DRAs and feed arrangements, which have been used for generating linearly and circularly polarised DRA arrays,

are summarised in Table 9.1, and three commonly used feed arrangements, i.e. slot coupling, probe coupling and microstrip coupling, are illustrated in Fig. 9.1(a)-(c).

Table 9.1: Choice of DRA Elements and Feed Arrangement

DRA Elements (Polarisation of Array)	Feed Arrangement
• Cylindrical DRAs, (Linear or Circular) • Rectangular DRAs, (Linear) • Hemispherical DRAs, (Linear) • Multi-segment Rectangular DRAs, (Linear) • Geometrically Modified Rectangular DRAs, (Circular) • Cross-shaped DRAs, (Circular)	• Probe excitation with microstrip corporate feed • Microstrip corporate feed • Rectangular or annular slot coupling with microstrip corporate feed • X-slot coupling with microstrip corporate feed for circular polarisation • Microstrip feed for series array • Microstrip branch line feed with slot coupling • Dielectric waveguide • Dielectric image guide • Co-planar waveguide feed
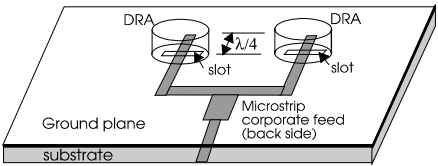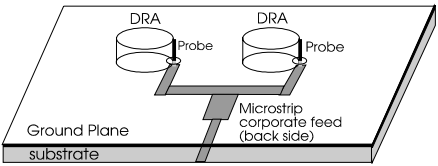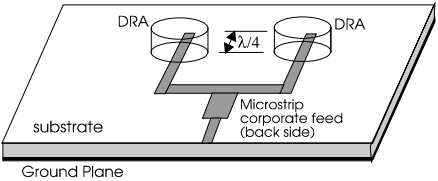
Fig. 9.1 Illustration of (a) slot, (b) probe and (c) microstrip coupling arrangements of DRA arrays (2 elements are shown)

9.2.2 Array Factors of Linear and Planar Arrays

As for other antenna arrays, the radiation pattern of a DRA array is determined by the radiation pattern of the single element and the array factor. In general, the radiated electric field in the far-field region of a DRA array can be written in the form,

$$E = n \times E_0 \times AF \tag{9.1}$$

where n is the number of elements of the array, E_0 is the electric field at the same field point produced by a single DRA positioned at the centre of the array, and AF is the array factor. The array factor depends on the geometrical structure of the array, the phase difference of currents between elements, and the operating frequency.

The array factor for a linear E-plane array with in-phase feed currents and an array axis in the x-direction, as shown in Fig. 9.2(a), can be expressed as

$$AF = \frac{1}{n} \frac{\sin[n(k_0 s \sin\theta \cos\phi)/2]}{\sin[(k_0 s \sin\theta \cos\phi)/2]} \tag{9.2}$$

and that for a linear H-plane array with an array axis in the y-direction, as shown in Fig. 9.2(b), as

$$AF = \frac{1}{n} \frac{\sin[n(k_0 s \sin\theta \sin\phi)/2]}{\sin[(k_0 s \sin\theta \sin\phi)/2]} \tag{9.3}$$

where $k_0 = 2\pi/\lambda_0$ is the wave number in free space, λ_0 is the free space wavelength, and s is the spacing between elements.
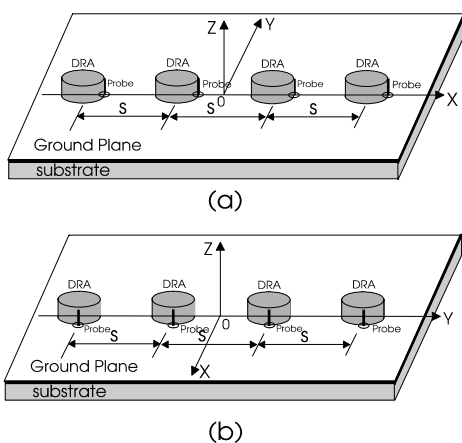
Fig. 9.2 (a) E-plane and (b) H-pane arrays

For different element numbers n=2, 4 and 8 and spacing s=0.25λ_0, 0.5λ_0 and λ_0, the array factor on the ϕ=0 plane for the E-plane array shown in Fig. 9.2(a) with an infinite ground plane is shown in Fig. 9.3. The pattern of the array factor on the ϕ=0 plane is directional in θ=0 direction for s<λ_0. The degree of the directivity increases with the number of elements. However, when s>0.5λ_0, the side lobes along the θ=π/2 direction start to develop, and the level of side lobes increases significantly when s>0.6λ_0. Hence, the spacing of 0.5λ_0 is commonly used in the design and study of DRA arrays.

For DRAs operating at the fundamental mode of the geometry with broadside radiation, the E-plane array with a typical spacing of 0.5λ_0 has higher directivity than the H-plane array.
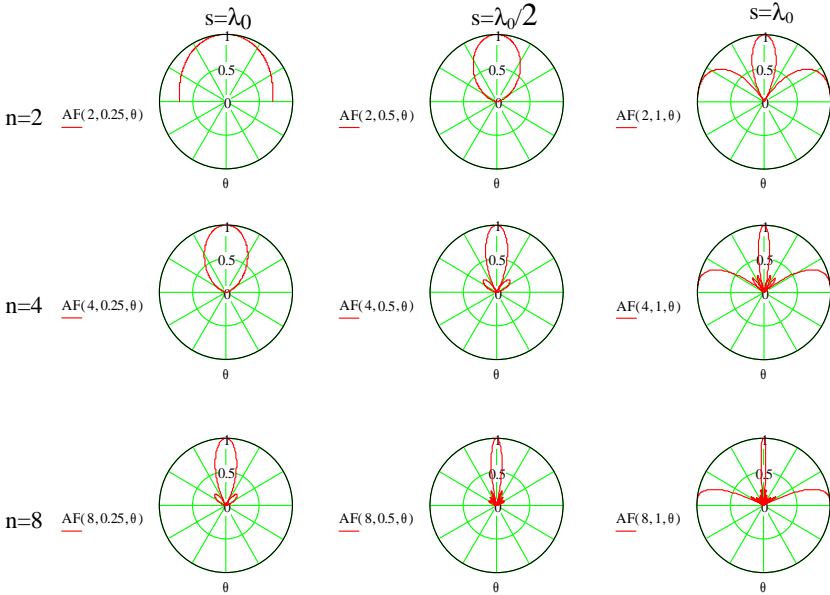
Fig. 9.3 Array factor, AF(n,s/λ_0,θ) on ϕ=0 plane, of E-plane arrays with n=2,4 and 8, and s=0.25λ_0, 0.5λ_0 and λ_0.

For a planar array of (m × n) elements with in-phase feed currents, as shown in Fig. 9.4, the array factor can be written as

$$AF = \frac{1}{mn} \frac{\sin[m(k_0 s_x \sin\theta \cos\phi)/2]}{\sin[(k_0 s_x \sin\theta \cos\phi)/2]} \frac{\sin[n(k_0 s_y \sin\theta \sin\phi)/2]}{\sin[(k_0 s_y \sin\theta \sin\phi)/2]} \qquad (9.4)$$

where s_x and s_y are the spacings between elements in the x- and y- directions respectively.
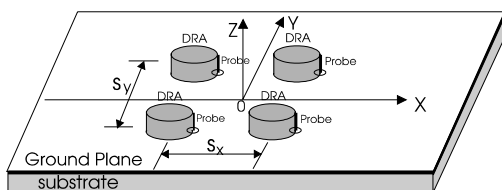
Fig. 9.4 Planar array

Since the radiation of DRAs operating at the fundamental modes, namely the $HE_{11\delta}$ mode for the cylindrical DRAs and the $TE^y_{11\delta}$ mode for the rectangular DRAs, can be equivalently modelled as a magnetic dipole [28], with a 3D radiation pattern shown in Fig. 9.5 [29], DRA arrays can equally be modelled as arrays of magnetic dipoles With this approximation, the radiation power patterns in linear scale for the E-plane arrays with $\lambda_0/2$-spacing and n=2, 4 and 8 are shown in Figs. 9.6 (a)-(c), H-plane arrays with n=2,4 and 8 in Fig. 9.7(a)-(c), and planar arrays with m=n=2, 4 and 8 in Fig. 9.8(a)-(c). For the same number of n or m and n, the E-plane and planar arrays are more directional in the broadside direction.
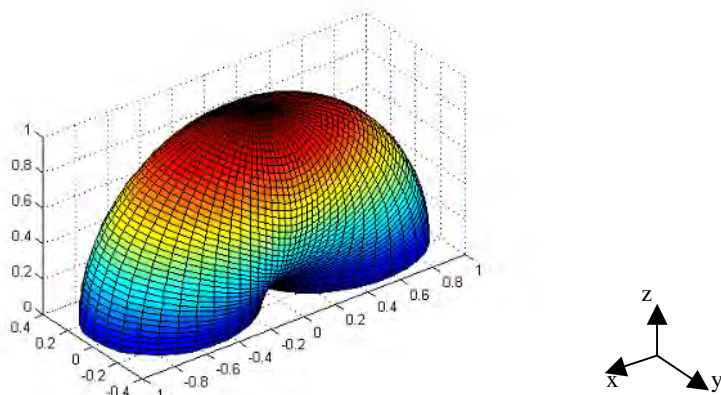
Fig. 9.5 3D radiation pattern of a horizontal magnetic dipole
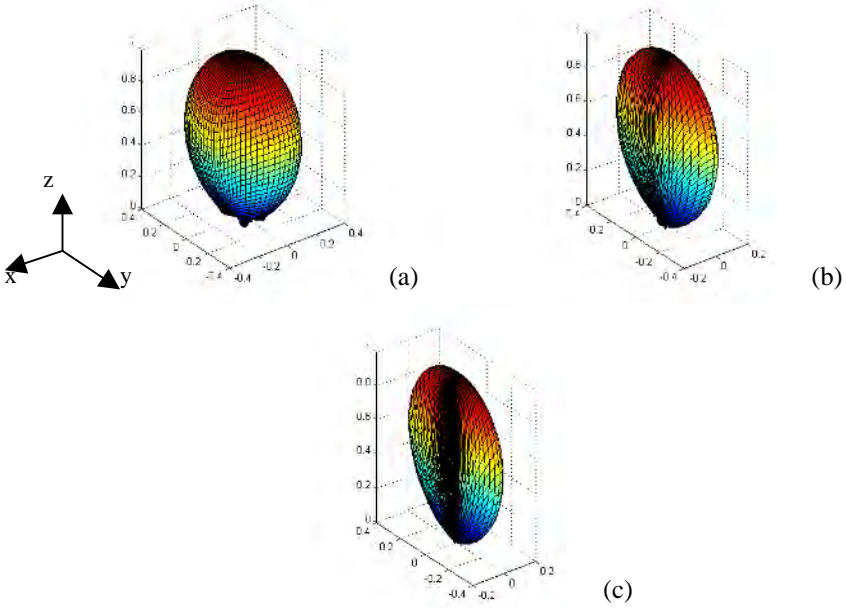
Fig. 9.6 3D radiation patterns of E-plane arrays with s=0.5λ_0 and (a) n=2, (b) n=4, and (c) n=8
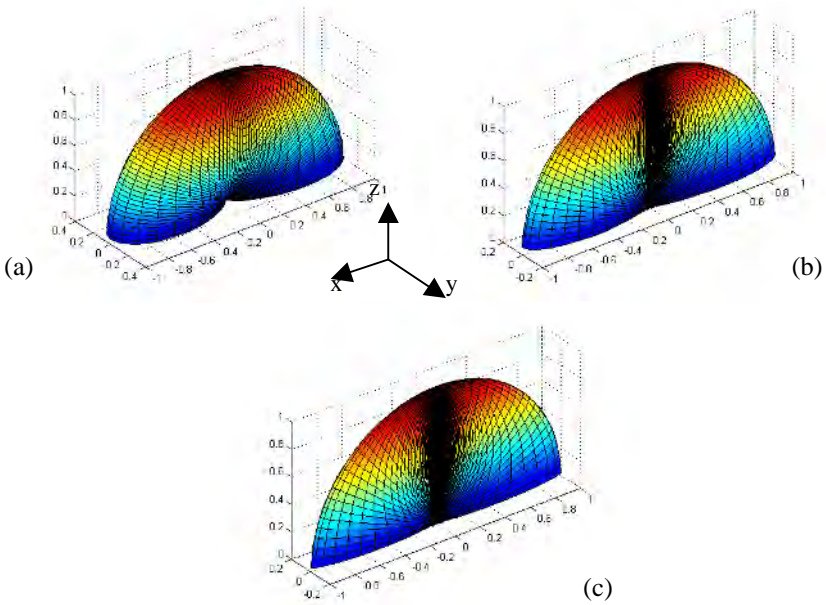
Fig. 9.7 3D radiation patterns of H-plane arrays with s=0.5λ_0 and (a) n=2, (b) n=4, and (c) n=8
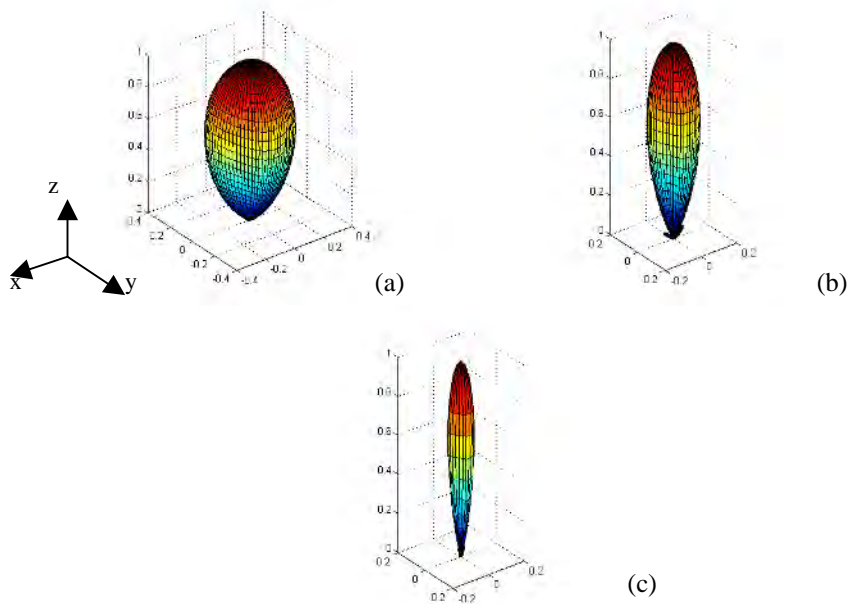
Fig. 9.8 3D radiation patterns of planar arrays with s=0.5λ_0 and (a) m=n=2, (b) m=n=4, and (c) m=n=8

The directivity in the broadside direction of the E-plane and H-plane arrays with $\lambda_0/2$ spacing is shown in Fig. 9.9, in dBi, for different element numbers. The directivity of the single element is 4.77dBi, and it increases to 8.5dBi, 11.75dBi and 15.9dBi for the two-element, four-element and ten-element E-plane arrays respectively. The directivity in the broadside direction of planar arrays with $\lambda_0/2$ spacing is tabulated in Table 9.2, in dBi, for different m and n. Directivity of 20dBi can be achieved using 8x4 elements. The 8x8 square array with the radiation pattern shown in Fig. 9.8(c) has the directivity of 23dBi.

n	DdBi_Eplane$_n$	n	DdBi_Hplane$_n$
1	4.77	1	4.77
2	8.5	2	6.63
3	10.39	3	8.23
4	11.75	4	9.34
5	12.77	5	10.26
6	13.61	6	11
7	14.3	7	11.64
8	14.9	8	12.2
9	15.43	9	12.69
10	15.9	10	13.14
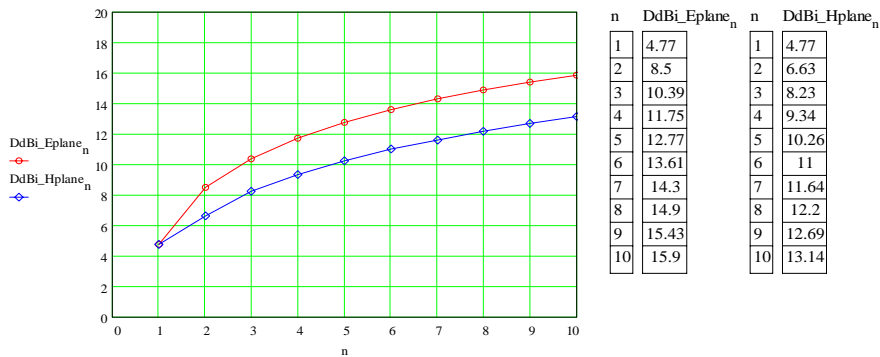
Fig. 9.9 The directivity (dBi) of linear arrays with $\lambda_0/2$ spacing against n

Table 9.2: The directivity (dBi) of planar arrays with $\lambda_0/2$ spacing against m and n

	n=1	2	3	4	5	6	7	8	9	10
m=1	4.773	6.63	8.226	9.342	10.26	11	11.64	12.2	12.69	13.14
2	8.499	10.83	12.6	13.75	14.72	15.48	16.14	16.7	17.21	17.66
3	10.39	12.58	14.21	15.35	16.28	17.03	17.69	18.24	18.75	19.19
4	11.76	14.03	15.76	16.93	17.89	18.66	19.31	19.87	20.38	20.83
5	12.77	15.02	16.69	17.83	18.76	19.52	20.17	20.73	21.48	21.68
6	13.61	15.88	17.59	18.77	19.72	20.48	21.14	21.7	22.21	22.65
7	14.3	16.56	18.25	19.39	20.33	21.08	21.74	22.3	22.81	23.25
8	14.9	17.18	18.88	20.05	21.01	21.77	22.43	22.98	23.49	23.94
9	15.43	17.7	19.39	20.54	21.48	22.24	22.89	23.45	23.95	24.4
10	15.9	18.18	19.88	21.04	22	22.76	23.42	23.98	24.5	24.93

These radiation patterns and directivity values will serve as a reference for the practical DRA arrays described in the following sections.

9.2.3 Mutual Coupling between DRAs

The formation of a directional DRA array requires that the DRA elements be positioned with a close spacing between elements. However, the proximity of the elements results in mutual coupling between elements due to the electromagnetic interaction between elements. The mutual coupling may be significant so that it substantially affects the performance of the array including radiation pattern, directivity, operating frequency and bandwidth. It also complicates the design of the matching network.

The level of mutual coupling depends not only on the spacing between elements, but also on the structure, dimensions and dielectric constant of the DRA elements and the mode of operation. The simulation and experimental studies of slot-coupled cylindrical DRAs operating at the fundamental $HE_{11\delta}$ mode with diameter 5.12mm, height 3.02mm and relative dielectric constant $\varepsilon_r =10$ by Guo *et al.* [3] show that for spacing s > $0.35\lambda_0$, the level of mutual coupling, i.e. $|S_{21}|$, between DRA elements for both E-plane and H-plane arrays is less than –10dB at 16GHz. The simulated and measured results are shown in Fig. 9.10. However, the mutual coupling in the H-plane array is stronger than that in the E-plane array when s ≤ $0.5\lambda_0$. For large spacing, e.g. s>$0.6\lambda_0$, the mutual coupling in the E-plane array becomes stronger than that in the H-plane array. At s= $0.5\lambda_0$, the level of mutual coupling for both E-plane and H-pane arrays is less than –15dB. A different experimental study of slot-coupled cylindrical DRAs with radius a=7mm, height h=10.8mm and $\varepsilon_r =9.5$ by Chow *et al.* [4] shows that the level of mutual coupling for both E-plane and H-plane arrays operating at 5GHz is less than –12dB when s≥$0.5\lambda_0$, but with a stronger coupling in the E-plane array, as shown in Fig. 9.11.
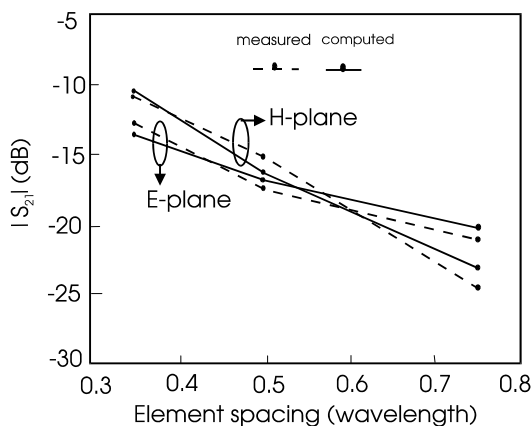
Fig. 9.10 The simulated and measured results of mutual coupling between two slot-coupled cylindrical DRAs with diameter 5.12mm, height 3.02mm and ε_r =10, in E-plane and H-plane array configurations (from [3], © 1999 IEEE)
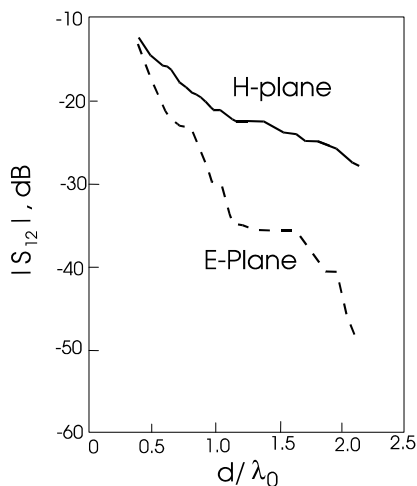
Fig. 9.11 Mutual coupling between DRA elements in E-plane (——) and H-plane (·············) arrays (from [4], reprinted with permission from IEE)

The experimental study of slot-coupled E-plane and H-plane rectangular DRA arrays operating at the $TE^y_{11\delta}$ mode with length L=15mm, width w=3.1mm, height

h=7.5mm and ε_r=10.8 by Loos *et al.* [5] also shows the level of mutual coupling for both E-plane and H-plane arrays operating at 7GHz is approximately –15dB at s=0.5λ_0, and the E-plane array has a stronger coupling when s>0.5λ_0. The mutual coupling could, however, reach –9dB for s≈0.3λ_0.

The experimental study of mutual coupling between two probe-coupled rectangular DRAs operating at the $TE^y_{11\delta}$ mode was also made by Neshati [6] using DRAs with length L=18 mm, width w=18 mm, height h=9 mm and ε_r=37. The E-plane and H-plane arrays constructed for the study with a circular ground plane of diameter 150mm are shown in Figs. 9.12(a) and (b).
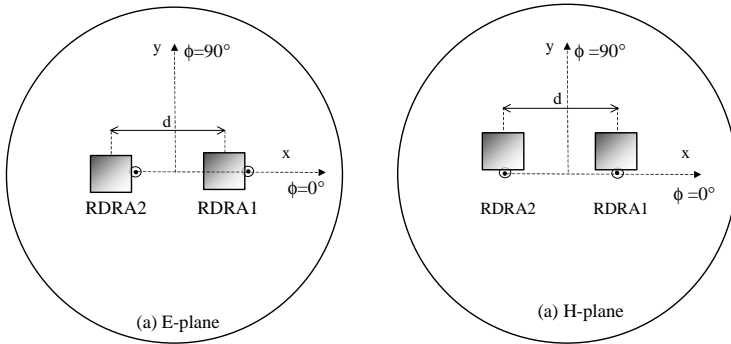
Fig. 9.12 (a) E-plane and (b) H-plane rectangular DRA arrays

The arrays operate around 2.35GHz with good impedance matching. For s=λ_0/2, the measured frequency responses of $|S_{11}|$ and $|S_{21}|$ of the E-plane and H-plane arrays are shown in Figs. 9.13(a) and (b) respectively. The level of the maximum coupling is –13.5dB for the E-pane array and –15dB for the H-plane array. Similarly the measured frequency responses of $|S_{11}|$ and $|S_{21}|$ of the E-plane and H-plane arrays with s= λ_0/4 are shown in Figs. 9.13(c) and (d). The level of the maximum coupling increases to –9.2dB for the E-pane array and to –4.1dB for the H-plane array. The coupling in the H-plane array is very strong at s= λ_0/4.

These studies indicate that the λ_0/2-spacing is preferably used for the construction of DRA arrays so that the mutual coupling between elements are less significant. In combination with E-plane array configuration, higher directivity can be obtained by using the λ_0/2-spacing.

Compared with microstrip antennas [30], the mutual coupling between DRAs is generally greater. But both types of antennas share similar coupling behaviours. The level of coupling between antenna elements increases with the thickness of the substrate or the height of the DRA, particularly in H-plane arrays. However, with λ_0/2-spacing, the coupling between DRAs or microstrip patches is usually negligibly small (<–15dB).
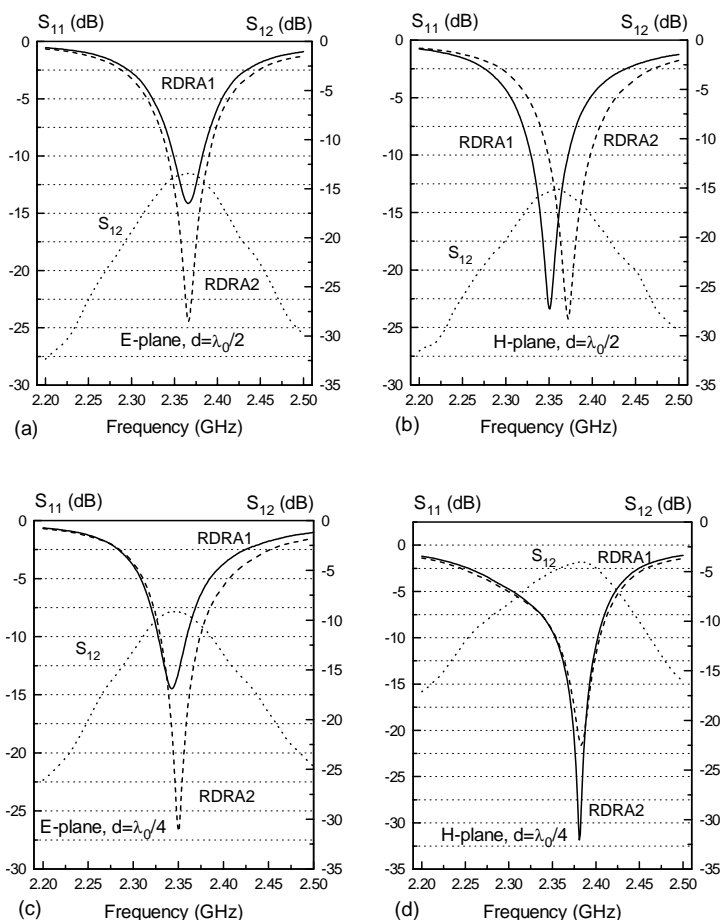
Fig. 9.13 The measured full 2–port S-parameters for the two-element (a) E- and (b) H-plane rectangular DRA arrays with $\lambda_0/2$ spacing, and those of the two-element (c) E- and (d) H-plane rectangular DRA arrays with $\lambda_0/4$ spacing (from [6])

9.3   LINEARLY POLARISED LINEAR DRA ARRAYS

9.3.1   Slot-Coupled Linear DRA Arrays with Microstrip Corporate Feed

Slot coupling with microstrip feed is one of the commonly used and simple methods for the excitation of DRAs and DRA arrays. It makes use of the electromagnetic coupling from a microstrip line to the DRA through a non-

radiating slot on the ground plane, as illustrated in Fig. 9.1(a) for a cylindrical DRA array. Both E-plane and H-plane linear arrays can be fed using slot coupling and microstrip corporate feed. Using slot coupling, the slot is usually positioned at a distance of $\lambda_g/4$ away from the open end of the microstrip line, where λ_g is the guided wavelength of the microstrip guiding structure. The width and length of the slot need to be appropriately chosen so that good matching to a 50Ω microstrip line is obtained for each DRA element.

With the following DRA element and array parameters:

DRA: radius a=7mm, height h=10.8mm and ε_r =9.5

Array: spacing $d_a=\lambda_0/2$ =29.8mm, slot position L_s=12.7mm

Slot: width w=0.9mm, length L=13.8mm

Microstrip Line: strip width =1.9mm, substrate ε_{rs} =2.94, thickness=0.762mm, Chow *et al.* [4] demonstrated that the two-element broadside E-plane and H-plane arrays, as shown in Fig. 9.14(a) and (b), operating at the fundamental broadside $TM_{11\delta}$ ($HE_{11\delta}$) mode of 5GHz, have a gain of 8.9dBi approximately, or 2.3dBi higher than that of a single element. The crosspolarised fields of the array are approximately 23dB less than the co-polarised fields in the broadside direction (θ=0), against 15dB less for the single element. However, due to the mutual coupling between DRA elements, as discussed in Section 9.1.3, and the effect of feed network (mutual coupling of microstrip lines, structure asymmetry, etc.), the frequency at which the best matching is obtained may change by $\pm2\%$ from that of the single element.
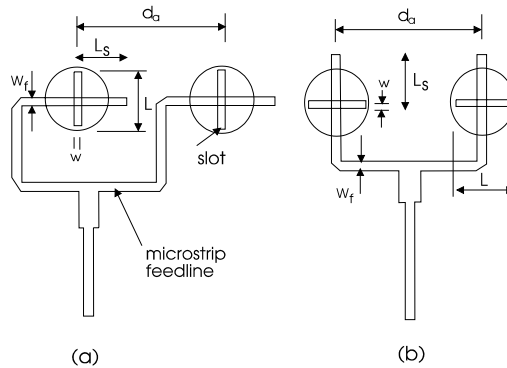
Fig. 9.14 Two-element slot-coupled cylindrical DRA array in (a) E-plane and (b) H-plane configurations (from [4], reprinted with permission from IEE)

Four-element linear E-plane and H-plane cylindrical DRA arrays using the slot coupling were demonstrated by Drossos *et al.* [7]. The fundamental $HE_{11\delta}$ mode of the DRAs was used to produce broadside radiation. Microstrip corporate feeds were also used for both E-plane and H-plane configurations, as shown in Fig.

9.15(a) and (b) respectively. The DRA elements and array structure have the following parameters:

DRA: radius a=6.35mm, height h=5.08mm and ε_r =37

Array: spacing $=\lambda_0/2$ =37.5mm, slot position L_s=13.5mm

                     ground plane =155mm x 100mm

Slot: width =1mm, length =4mm

Microstrip Line: strip width =4.91mm, substrate ε_{rs} =2.2, thickness=1.57mm.

(a)

(b)
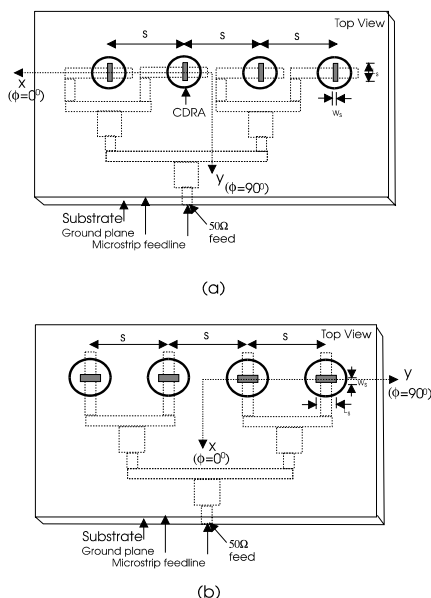
Fig. 9.15 Four-element slot-coupled cylindrical DRA array in (a) E-plane (Conf. A) and (b) H-plane (Conf. B) configurations (from [7], © 1999 John Wiley & Sons, Inc.)

The E-plane and H-plane arrays were well matched at 3.9GHz and 3.935GHz respectively. The measured radiation pattern at 3.9GHz on the E-plane (E_θ at ϕ=0) for the E-plane array is shown in Fig. 9.16 and that at 3.935GHz on the H-plane (E_ϕ at ϕ=90^0) for the H-plane array in Fig. 9.17. Compared with the single element, the E-plane array has a shaped directional pattern on the E-plane, and the H-plane array has a shaped directional pattern on the H-plane. The four-element E-plane array has a gain of 10.3dBi at 3.9GHz, and the H-plane array has a gain of 8.6dBi. Compared with the single element with a gain of 4.9dBi, the E-plane array has a gain enhancement of 5.4dB, and the H-plane array an enhancement of 3.7dB. These are very significant when using four elements and a small ground plane. The

arrays have a usual impedance bandwidth of 4.5% at VSWR=2. Compared with the theoretical values obtained using the Perfect Magnetic Wall Model (PMWM) for the same arrays but of infinite ground plane, the E-plane and H-plane arrays have an efficiency of 73% and 88% respectively which includes losses in the microstrip feed and backward radiation. The radiation patterns using the PMWM on both E- and H-planes for the single element and the arrays on an infinite ground plane are also shown in Figs. 9.16 and 9.17 for comparison.
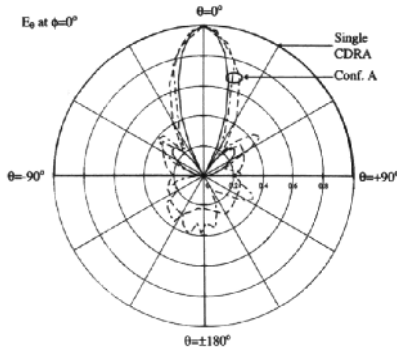
Fig. 9.16 E-plane radiation pattern of the E-plane array (Conf. A) in Fig. 9.15(a) and single element:(———) PMWM, (-·--·-·) HFSS, (·············) Experiment (from [7], © 1999 John Wiley & Sons, Inc.)
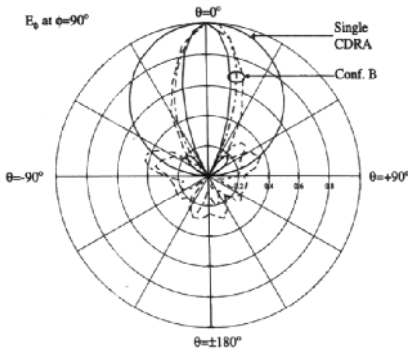
Fig. 9.17 H-plane radiation pattern of the H-plane array (Conf. B) in Fig. 9.15(b) and single element:(———) PMWM, (-·--·-·) HFSS, (·············) Experiment (from [7], © 1999 John Wiley & Sons, Inc.)

Drossos *et al.* [7] also demonstrated that the array structures with a finite ground plane could be simulated using the Finite Element Method (FEM) based

High Frequency Structure Simulator (HFSS), a product of Hewlett-Packard or Ansoft. The simulated results of radiation patterns are also shown in Figs. 9.16 and 9.17. The results agree well with the measured results, but with wider beamwidths than that of the PMWM due to the finite ground plane and backward radiation.

The slot coupling was also used by Keller *et al.* [8] in the study of a four-element linear H-plane rectangular DRA array, as shown in Fig. 9.18. The array operates at 40GHz using the lowest order TE^y_{111} mode of the resonator. The DRA elements and array have the following parameters:

DRA: length =1.91mm, width = 0.635mm, height =1.91mm
                    and ε_r =9.8

Array: spacing =$\lambda_0/2$ =3.75mm, slot position L_s=0.41mm

Slot: width =0.1mm, length =1.16mm

Microstrip Line: strip width =0.25mm, substrate ε_{rs} =9.8, thickness=0.254mm
                    R_1=1.32mm, R_2=3.05mm, W_{Q1}=0.67mm, W_{Q2}=0.932mm,
                    L_{Q1}=0.647mm, L_{Q2}=0.67mm.
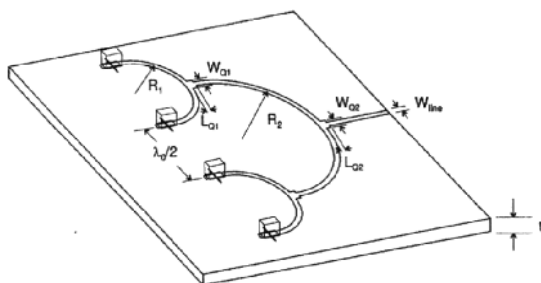
Fig. 9.18 Millimetre wave slot-coupled H-plane rectangular DRA array (from [8], © 1998 John Wiley & Sons, Inc.)

It was found that the precise positioning of the DRA over the slot is not required. This feature thus obviates the requirement for a precision technique for aligning the DRA element over the slot. The elements in the array are separated by $\lambda_0/2$ at 40GHz. Due to the high losses in the microstrip corporate feed at the EHF range, the overall performance of the array is not efficient. The four-element H-plane array has a gain of 6.2dBi measured at the optimal matching frequency of 40.3GHz, against the theoretical value of 10.8dBi. The efficiency is thus estimated to be 35%. The low efficiency was also believed to be partly due to poor matching and poor fabrication tolerances of the individual DRA elements. The crosspolarisation level of the array was found to be at least 15dB below the co-polarised peak value over the entire 3dB beamwidth of 30^0 on the H-plane and 100^0 on the E-plane, as shown in Fig. 9.19. The 10dB return loss bandwidth of the array was reported to be 0.5% as a result of poor matching with a minimum

reflection coefficient of -10.6dB. Nevertheless, the use of slot coupling for the formation of a millimetre wave array was demonstrated. The performance of the millimetre wave array could be improved significantly by using a low loss dielectric guide feed structure. When this is made, the benefit of using DRAs for millimetre wave arrays can be fully revealed.

Fig. 9.19 Measured gain/radiation pattern at 40.3GHz of the array shown in Fig.

DRA H-Plane Array
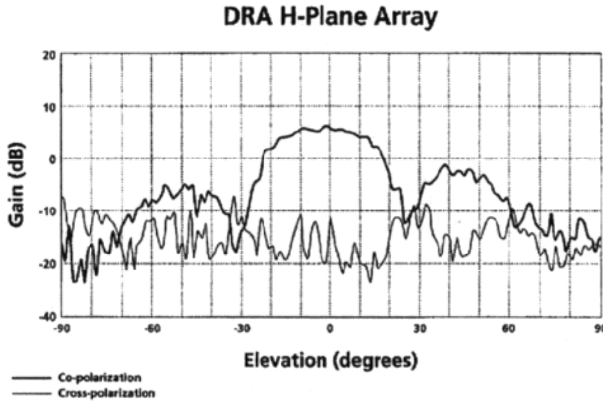
9.18 (from [8], © 1998 John Wiley & Sons, Inc.)

9.3.2   Probe-Coupled Linear DRA Arrays with Microstrip Corporate Feed

The probe coupling with microstrip corporate marching network illustrated in Fig. 9.1(b) is also a simple method for the feed of DRA arrays. This feed mechanism was used by Junker *et al.* [9] for the formation of a Dolph-Chebyshev hemispherical DRA array, and by Drossos *et al.* [10,11] and Wu [12] for the construction of linearly polarised linear cylindrical DRA arrays.

Using probe coupling, the probe is connected to the end of the microstrip line printed on the reverse side of the ground plane; the ground plane of the microstrip line also acts as the ground plane for the DRA elements. The probe may be placed inside the dielectric resonator, or on the edge of the resonator. The length of probe needs to be appropriately chosen so that each DRA element is matched to a 50Ω microstrip line.

Figs. 9.20 (a) – (c) show respectively the four-element linear E-plane and H-plane cylindrical DRA arrays using probe coupling and microstrip corporate feed studied by Drossos *et al.* [10]. The DRA elements and array structure have the following parameters:

DRA: radius a=6.35mm, height h=5.08mm and ε_r =37
Array: spacing =$\lambda_0/2$ =37.5mm, ground plane =135mm x 60mm
Probe: length =5.08mm
Microstrip Line: strip width =4.91mm, substrate ε_{rs} =2.2, thickness=1.57mm.

The fundamental $HE_{11\delta}$ mode was used to produce broadside radiation. Both E-plane and H-pane arrays were well matched at 4GHz. The measured radiation patterns at 4GHz on both E-plane (E_θ at $\phi=0$) and H-plane (E_ϕ at $\phi=90^0$) for E-plane and H-plane arrays are shown in Figs. 9.21 (a) and (b) and Figs. 9.22 (a) and (b) respectively. The E-plane array has a shaped directional pattern on the E-plane, and the H-plane array has a shaped directional pattern on the H-plane, compared with those of the single element. The four-element E-plane array has a gain of 11dBi measured at 4GHz, and the H-plane array has a gain of 9dBi. Compared with the single element of a gain 4dBi, the E-plane array has a gain enhancement of 7dB, and the H-plane array an enhancement of 5dB, which are very significant using four elements and a small ground plane. The arrays have an impedance bandwidth of greater than 3.6% at VSWR=2. The E-plane and H-plane arrays have an efficiency of 86% and 93% respectively, which includes losses on the microstrip feed and in the backward radiation.

The results of radiation patterns, using the PMWM for the single element and array with an infinite ground plane and the results using the HFSS, are shown in Figs. 9.21 and 9.22 for comparison. The results from the array agree well with the measured results.

(a)   (b)

(c)
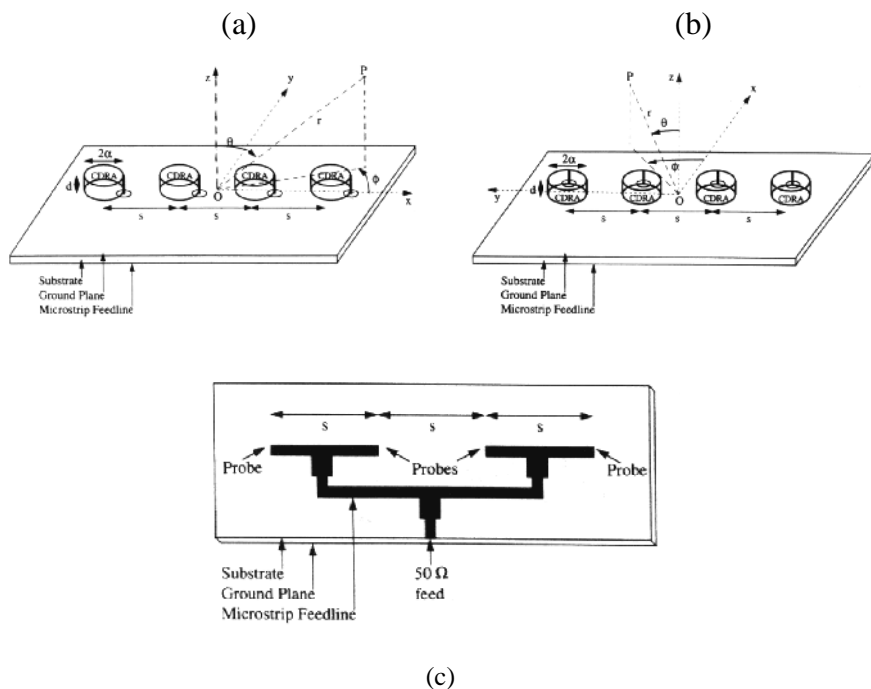
Fig. 9.20 Four-element linear (a) E-plane (Conf. A) and (b) H-plane (Conf. B) cylindrical DRA arrays using (c) probe coupling and microstrip corporate feed (from [10], © 1998 John Wiley & Sons, Inc.)
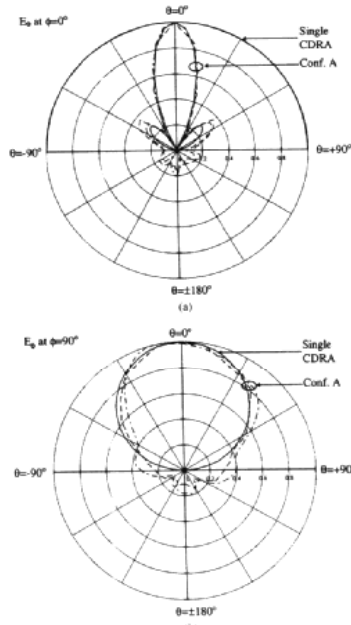
Fig. 9.21 (a)E-plane and (b) H-plane radiation patterns of the E-plane array (Conf. A) in Fig. 9.20(a) and single element: (———) PMWM, (·—··—··) HFSS, (··············) Experiment (from [10], © 1998 John Wiley & Sons, Inc.)
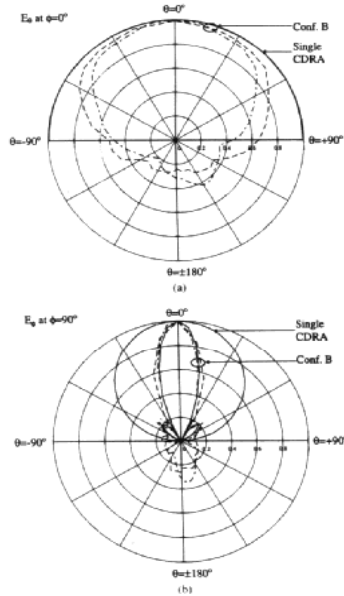
Fig.9.22 (a)E-plane and (b) H-plane radiation patterns of the H-plane array (Conf. B) in Fig. 9.20(b) and single element: (———) PMWM, (·—··—··) HFSS, (··············) Experiment (from [10], © 1998 John Wiley & Sons, Inc.)

A similar study by Drossos *et al.* [11] shows that a gain of 9.5dBi can be achieved using a two-element E-plane cylindrical DRA array which operates at 6.863GHz, compared with a theoretical value of 9.7dBi and a gain of 5.3dBi for the single element. The arrays have an efficiency of 86% (measured) as a result of the use of microstrip corporate feed.

9.3.3 Microstrip-Coupled Linear DRA Arrays

Direct coupling from microstrip lines to DRA elements, as illustrated in Fig. 9.1(c) is an alternative to slot- or probe- coupling described in Sections 9.3.1 and 9.3.2 for feeding DRA arrays, providing easy integration with printed microwave circuits. The microstrip-coupled four-element linear E-plane and H-plane cylindrical DRA arrays studied by Drossos *et al.* [13] are shown in Figs. 9.23 (a) and (b). Both arrays have broadside radiation. The DRA elements are positioned at a distance d_x away from the end of the microstrip line, so that critical coupling between the 50Ω microstrip line and the dielectric resonator at the frequency of the fundamental resonant mode ($HE_{11\delta}$) is obtained. The distance d_x generally depends on the dimensions and dielectric constant of the DRA elements, the width of the microstrip line, and the dielectric constant and thickness of the substrate. This distance is usually determined experimentally.
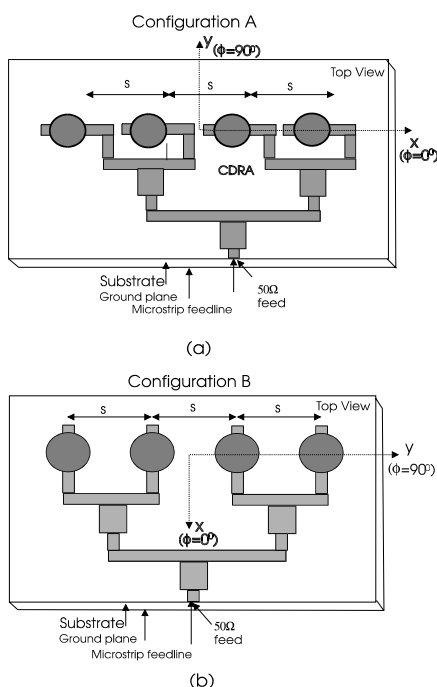
Fig. 9.23 Four-element microstrip coupled (a) E-plane (Conf. A) and (b) H-plane (Conf. B) cylindrical DRA arrays (from [13], © 1998 John Wiley & Sons, Inc.)

Unlike slot or probe coupling, the bottom surface of the dielectric resonator using the microstrip feed is not in direct contact with the ground plane, but with the surface of the substrate. The resonance frequency of the microstrip-coupled DRA element may be different from that coupled by a slot or probe, particularly when the thickness of the substrate is relatively large. With the microstrip feed in an open environment, the radiation of the DRA elements may be affected by the radiation from microstrip line and discontinuities, so that the radiation pattern of the array may be distorted.

With the following DRA and array parameters:

DRA: radius a=6.35mm, height h=5.08mm and ε_r =37
Array: spacing $=\lambda_0/2$ =37.5mm,
                ground plane (E-plane array) =155mm x 100mm
                ground plane (H-plane array) =155mm x 90mm
                d_x=18.9mm

Microstrip Line: strip width =4.91mm, substrate ε_{rs} =2.2, thickness=1.57mm, Drossos *et al.* [13] showed that the E-plane and H-plane arrays are well matched at 3.91GHz and 4.055GHz respectively, with d_x=18.9mm. The E-plane array has a gain of 10.8dBi measured at 3.91GHz, and the H-plane array has a gain of 9.2dBi measured at 4.055GHz. Compared with the gain of 5.2dBi measured for the single element, the four-element E-plane array has a gain enhancement of 5.6dB and the four-element H-plane array has an enhancement of 4dB. The gain enhancement using the microstrip coupling is approximately 1dB less than the similar probe-coupled array, as a result of the additional loss on the microstrip feed lines. The arrays have a usual impedance bandwidth of 4.5% measured at VSWR=2.

DRA elements can also be fed in series using an open-ended microstrip line as shown in Fig.9.24, which was first demonstrated by Petosa *et al.* [14, 15]. The elements are separated by approximately one guided wavelength, and they are placed along the microstrip line on one side with different coupling coefficients. With the use of 10 rectangular elements of dimensions: a=9mm, b=7.5mm and d=3.1mm and ε_r =10.8 on a ground plane of 30cm by 30cm, a gain of 13.2dBi was obtained at 8GHz with a crosspolarisation level of 20dB below the co-polarised peak value and side lobe levels more than 17.5dB below the peak value.
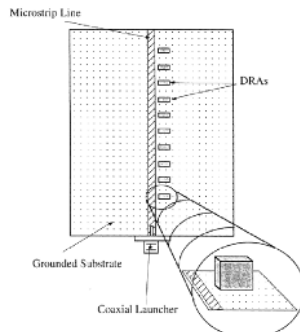
Fig. 9.24 Microstrip-fed series rectangular DRA array (from [14], © 1998 IEEE)

The array has narrow impedance bandwidth (~ 2%), as a result of the strong frequency dependence of the loaded microstrip line structure. However, Petosa *et al.* [16] showed that bandwidth could be improved significantly using paired DRA arrangement. In this structure, DRAs in each pair are separated slightly, with each element in the pair located on alternate sides of the microstrip line so as to reduce the mutual coupling between elements. A 10dB return loss bandwidth of 18% was obtained for an array of 16 rectangular DRA elements. The gain bandwidth is also improved using the paired structure.

At millimetre wave frequencies, the losses on the microstrip line in the series array become very significant. The microstrip line may then be replaced by a dielectric waveguide or an image guide, as illustrated by Birand and Gelsthorpe [1]. The dielectric waveguide coupled travelling wave DRA array studied in [1] operates in the vicinity of 32.5GHz. The array has a beamwidth of 8.5^0, which could scan approximately 20^0 from the broadside direction at 35.5GHz.

Compared with linear DRA arrays of the same number of elements with microstrip corporate feed and slot or probe coupling, the gain of the microstrip-fed series array is generally significantly lower. The main beam of the series array also has a strong frequency dependence, which precludes its use for wideband fixed-beam applications [14].

A more sophisticated, but compact microstrip feed is the use of the multi-layered slot-coupled microstrip branch line structure proposed by Petosa *et al.* [17], as shown in Fig. 9.25. The elements on opposite sides of the slot are fed in opposite directions as a result of the 180^0 phase reversal between two branches introduced by the slot, which is in turn coupled by a microstrip line. In their study, Petosa *et al.* used the structure to feed 10 multisegment rectangular DRAs forming a directional array with broadside radiation. The elements are separated by one guided wavelength, and the elements are placed at the ends of the branches. The measured co-polarisation and crosspolarisation radiation patterns of the array at a central frequency in C-band obtained by Petosa *et al.* are shown in Fig. 9.26 together with the simulated co-polarisation pattern using the short magnetic dipole representation of the MSDRA element. The gain of the 10-element multisegment DRA (MSDRA) was measured to be 15.4dBi against a theoretical value of 17.2dBi. The efficiency of the antennas was hence determined to be 66%. The crosspolarisation level of the array is 22dB below the co-polarised peak value, and the array has a 3dB gain bandwidth of 17% and a 10dB return loss bandwidth of approximately the same value as a result of using the MSDRA elements.

9.4   LINEARLY POLARISED PLANAR DRA ARRAYS

9.4.1   Slot-Coupled Planar DRA Arrays with Microstrip Corporate Feed

Using the linear E-plane or H-plane arrays described in Section 9.3, the E-plane or H-plane radiation patterns are mainly shaped with the corresponding one-dimensional array factor given in Eqn. (9.2) or Eqn. (9.3), and the radiation patterns on the orthogonal plane, i.e. H-plane or E-plane respectively, are unchanged.
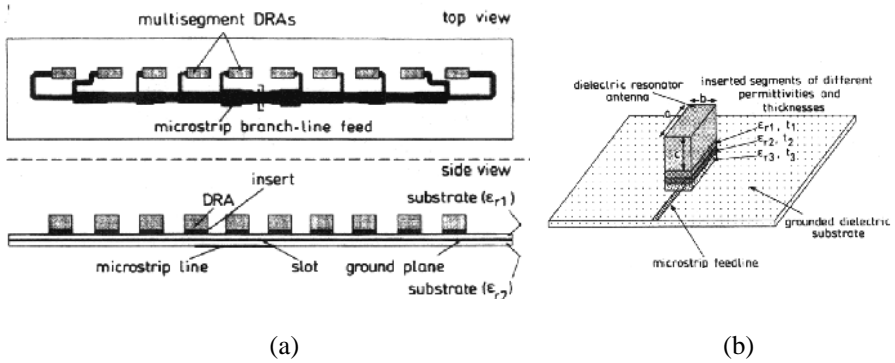
Fig. 9.25 (a) Multi-layered slot-coupled microstrip branch line feed structure and the MSDRA element (from [17], reprinted with permission from IEE)
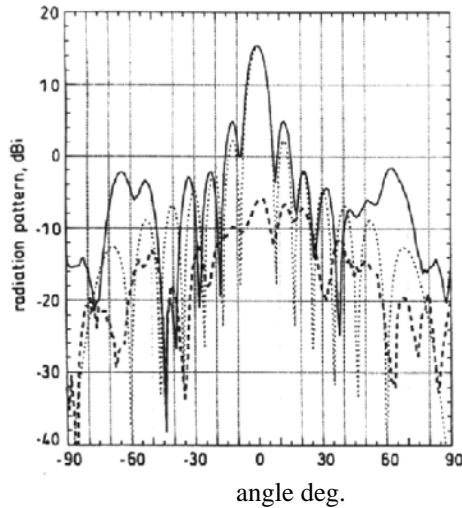
Fig. 9.26 Radiation patterns of the linear array in Fig. 9.25(a) (from [17], reprinted with permission from IEE):
(————) Measured Co-polarisation,
(--------) Measured Cross-polarisation,
(··············) Simulated Co-polarisation,

The planar array is a combination of both E-plane and H-plane arrays, in which the radiation patterns on both E- and H- planes are shaped with a two-dimensional array factor given in Eqn. (9.4). Hence, the complete 3D pattern of the single element is shaped by the array factor.

With the use of slot coupling for a 2 x 2 planar rectangular DRA array operating at the $TE^{y}_{11\delta}$ mode of 7GHz with the following DRA element and array parameters:

DRA: length =15mm, width =3.1mm, height =7.5mm and ε_r =10.8

Array: spacing =λ_0/2 by λ_0/2 at 7GHz, slot position L_s=2.2mm, ground plane radius =$7\lambda_0$

Slot: width w=1.2mm, length L=6.1mm

Microstrip Line: substrate ε_{rs} =10.2, thickness=0.64mm,

Loos and Antar [5] demonstrated that a gain of 11.3dBi could be achieved using the four-element array with broadside radiation at 7.35GHz. This represents approximately 6dB gain enhancement over the single element. The array has a low crosspolarisation level, and it has a 10dB return loss bandwidth of 18% against 10% for the single element. The increase in bandwidth may be helped by the mutual coupling between elements and the tolerance of the feed structure, DRA elements and their positions.

Leung *et al.* [18] also used the slot coupling together with a microstrip corporate feed to study a four-element planar cylindrical DRA subarray, as shown in Fig. 9.27. The DRA elements operate at the lowest $TM_{11\delta}$ ($HE_{11\delta}$) mode of 4.5GHz. The DRA elements and array have the following parameters:

DRA: radius =5.96mm, height =9.82mm and ε_r =16

Array: spacing =33.5mm(λ_0/2) by 33.5mm, slot position L_s=12mm,

Slot: width w=0.8mm, length L=8mm

Microstrip Line: strip width=4.7mm, substrate ε_{rs} =2.33, thickness=1.57mm.

(a)   (b)
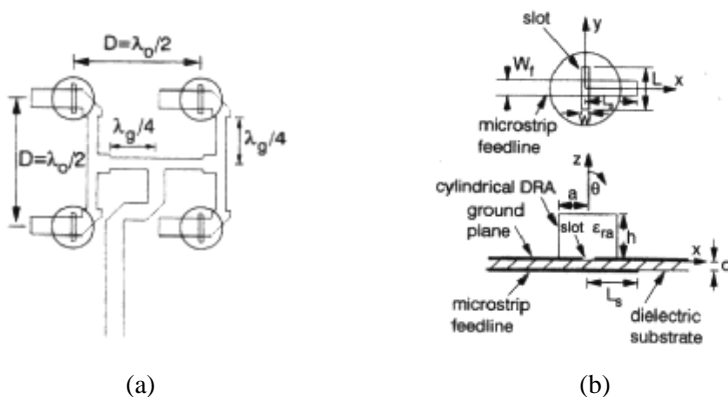
Fig. 9.27 (a) A 2x2 planar cylindrical DRA array and (b) element structure (from [18], reprinted with permission from IEE)

The gain of the array at 4.5GHz was measured to be 10.8dBi, which represents 6dB enhancement over the single element. The array has a low crosspolarisation level. The 3dB beamwidths in the H-plane and E-plane are 54^0 and 49^0 respectively, compared with 75^0 and 148^0 for the single element. The array also has a 10dB return loss bandwidth of 4.4%, which is slightly less than that of the single element, i.e. 4.9%, as a result of the mutual coupling between elements and the tolerance of the feed structure and DRA elements. The effects of mutual coupling and fabrication tolerance are opposite to that observed by Loos and Antar [5], indicating the importance and sensitivity of the design of feed networks for DRA arrays. Leung *et al.* [18] also showed that an infinite phased array making use of the subarray might have a scan angle of 35^0 at 4.5GHz with respect to $\theta=0$ direction.

9.4.2   Probe-coupled Planar DRA Arrays with Microstrip Corporate Feed

Extending from the study of the probe-coupled linear DRA array described in Section 9.3.2, Drossos *et al.* [19, 20] made use of the same cylindrical DRA elements to form both broadside and end-fire planar arrays. The geometry of the broadside array (Configuration A) and the microstrip corporate feed for probe coupling are shown in Figs. 9.28 (a) and (b). The DRA element and array parameters are as follows:

DRA: radius a=6.35mm, height h=5.08mm and ε_r =37
Array: spacing $s_x=s_y=\lambda_0/2$ =37.5mm at 4GHz,
                 ground plane =80mm x 80mm
Probe: length =5.08mm
Microstrip Line: strip width =4.91mm, substrate ε_{rs} =2.2, thickness=1.57mm.

(a)   (b)
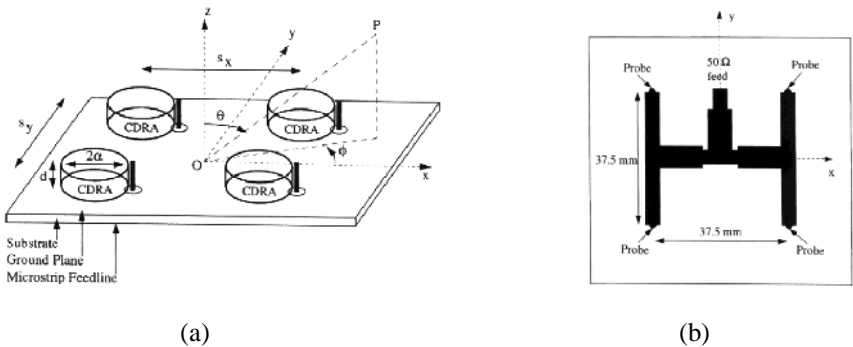
Fig. 9.28 (a) Four-element probe-fed cylindrical DRA array, and (b) its feed network (from [19], © 1998 John Wiley & Sons, Inc.)

The DRA elements operate at the fundamental $HE_{11\delta}$ mode producing broadside radiation. The array was well matched at 3.925GHz. The measured radiation patterns at 3.925GHz on both E-plane (E_θ at $\phi=0$) and H-plane (E_ϕ at $\phi=90^0$) are shown in Figs. 9.29 (a) and (b) respectively. Compared with that of the single element, both E-plane and H-plane patterns are shaped and become directional. The four-element planar array has a gain of 10dBi at 3.925GHz against a theoretical value of 10.7dBi obtained using the PMWM for a similar array with an infinite ground plane. The measured gain of the planar array represents 6dB enhancement over the single element, and it indicates that the efficiency of the array is over 87% including the effect of backward radiation due to finite ground plane. The array has a 10dB return loss bandwidth of 3%, against 2.1% for the single element. This increase may be due to the mutual coupling between DRA elements and the effect of the microstrip corporate feed network.

It was again demonstrated by Drossos *et al.* [19] that the planar array could be simulated using the HFSS. The numerical results of radiation patterns are also shown in Fig. 9.29 for comparison, which agree well with the measured results.
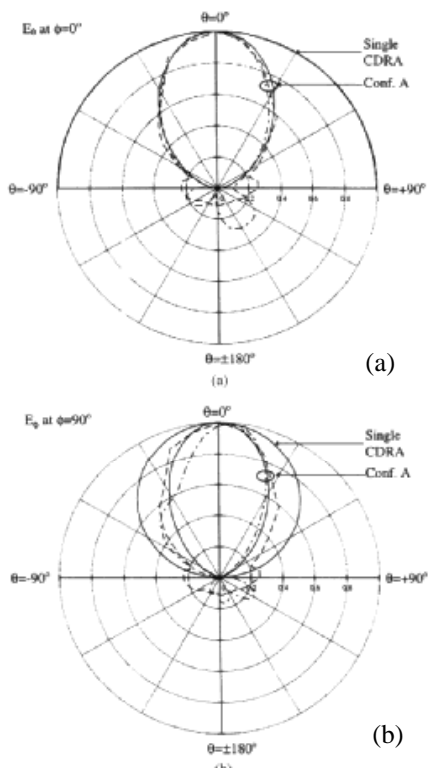
Fig. 9.29 (a)E-plane and (b) H-plane radiation patterns of the planar in Fig. 9.28(a) and single element: (————) PMWM, (–·–·–·) HFSS, (··············) Experiment (from [19], © 1998 John Wiley & Sons, Inc.)

9.4.3   Microstrip-Coupled Planar DRA Arrays

Also developing from the linear branch line-coupled rectangular DRA array described in Section 9.3.3, Petosa *et al.* constructed 8x8 and 32x10 low-profile planar MSDRA arrays, with integrated amplifiers, digital phase shifters and filters providing electronic beam steering capability [14, 21, 22]. The 320-element array is shown in Fig. 9.30. The radiation patterns of the 320-element array are shown in Figs. 9.31 (a) and (b). The crosspolarisation level is over 15dB below the co-polarised peak. Excluding the 15dB-gain of the LNAs in the array system, the 320-element planar array has a gain 24dBi. It also has a 3dB-gain bandwidth of 15%. This array represents the largest DRA antenna engineering reported in the literature to-date.
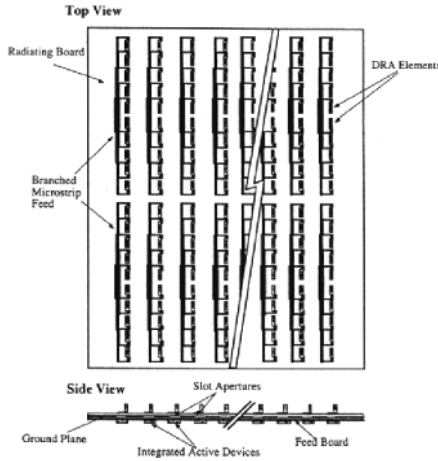
Fig. 9.30 A 32x10 low-profile MSDRA array (from [14], © 1998 IEEE)
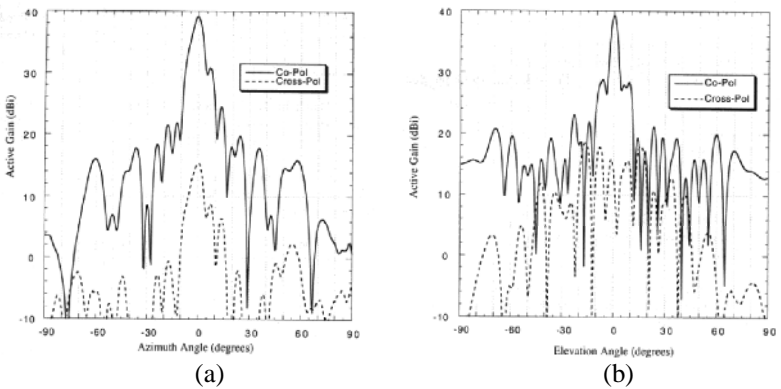
Fig. 9.31 Radiation patterns of the 320-element arrays as a function of the (a) azimuthal and (b) elevation angle (from [14], © 1998 IEEE)

9.5 CIRCULARLY POLARISED DRA ARRAYS

Circularly polarised (CP) DRA arrays can be constructed using linearly polarised (LP) DRA elements or CP DRA elements [23-26]. The CP arrays formed using CP DRA elements give better performance in terms of 3dB axial ratio bandwidth, gain and 3dB-gain bandwidth [23].

Using four CP cylindrical DRAs with cross-slot coupling of unequal slot lengths and a sequentially rotated microstrip feed, as shown in Figs. 9.32(a) and (b), Pang *et al.* [23] demonstrated that left-hand CP (LHCP) could be realised. The DRA elements and array structure have the following parameters:

DRA: radius =5.96mm, height =9.82mm and ε_r =16
Array: spacing D=33.5mm(or $\lambda_0/2$), slot position L_s=11mm,
Slot: width w=0.8mm, lengths L_{ap1}=11mm, L_{ap2}=9mm
Microstrip Line: strip width=4.7mm, substrate ε_{rs} =2.33, thickness=1.57mm.
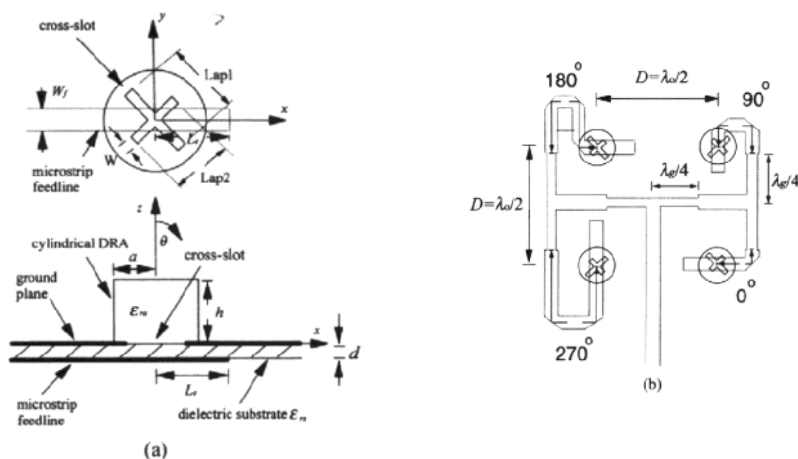
Fig. 9.32 (a) Cross-slot coupling of unequal slot lengths and (b) four-element sequentially rotated microstrip feed circularly polarised array (from [23], © 2000 John Wiley & Sons, Inc.)

The measured LHCP and right-hand CP (RHCP) radiation patterns for the single CP DRA element and the four-element CP DRA array operating at 4.46GHz and 4.4GHz respectively are shown in Figs. 9.33(a) and (b). There is a good isolation between RHCP and LHCP, which is over 14dB in the broadside direction. The array has a gain of 12dBi, or 6dB improvement over the single element. The 3dB axial ratio bandwidth of the array is also improved to 16%, compared with 5.6% for the single element. The 10dB return loss bandwidth is also increased to 19% from 9% for the single element. Hence, the CP radiation and impedance parameters are much improved using the CP DRA array.

(a)   (b)
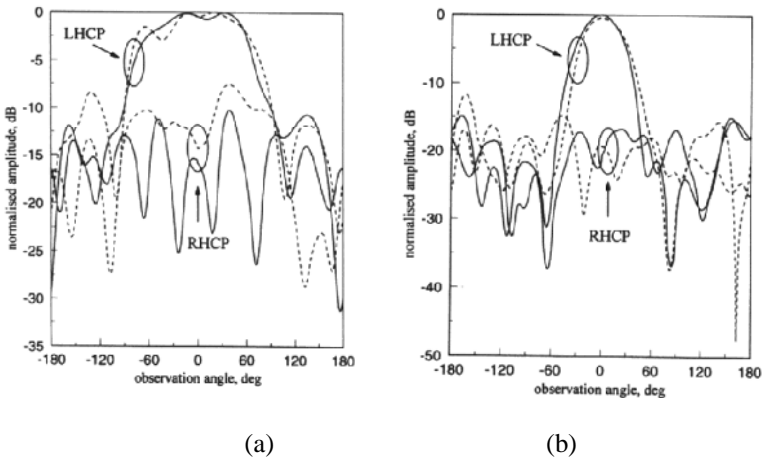
Fig. 9.33   The measured LHCP and RHCP radiation patterns for (a) the single CP
DRA element and (b) the four-element CP DRA array operating at
4.46GHz and 4.4GHz (from [23], © 2000 John Wiley & Sons, Inc.)

An array based on geometrically modified rectangular DRAs, as shown in Fig.
9.34(a), was also demonstrated by Haneishi and Takazawa [25]. The 16-element
array with paired units illustrated in Fig. 9.34(b) was designed to operate at X-band
frequencies. The DRA elements have a/h=1.26, ε_r =9.4 and D=0.68λ_0, and they
were fed using 16-way microstrip power dividers mounted on the rear panel of the
array. The 3dB axial ratio bandwidth of the array was measured to be
approximately 18%, or 4.5 times larger than that of the ordinary array without the
use of paired units. A broadside axial ratio less than 1dB over the frequency range
between 9.5GHz and 10GHz was also obtained.

(a)   (b)
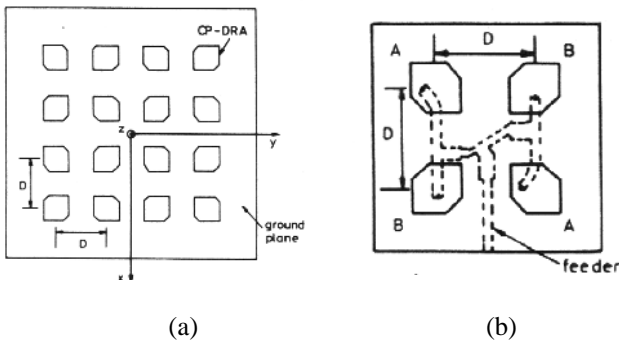
Fig. 9.34   (a) Circularly polarised geometrically modified rectangular DRA array,
and (b) the paired unit in the array (from [25], reprinted with permission
from IEE)

A four-element CP cross-DRA (XDRA) array, as shown in Fig. 9.35, was reported by Petosa *et al.* [26]. The XDRAs are coupled by single slots together with a microstrip feed, with the arms of the XDRAs rotated by 45^0 with respect to the length of the slot, so that each arm is excited with equal amplitude. The XDRA elements are sequentially rotated so as to increase the CP bandwidth. The array operates at 11.5GHz with a 3dB axial ratio bandwidth of 16% over a beamwidth of 40^0, and a 10dB return loss bandwidth of 25%. The advantage of using the XDRAs and single slot feed was demonstrated.
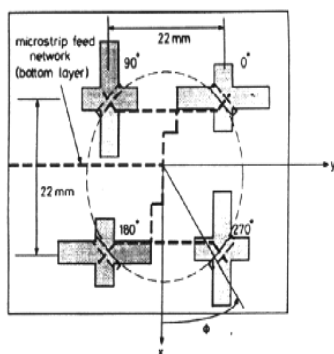
Fig. 9.35 Four-element circularly polarised XDRA array (from [26], reprinted with permission from IEE)

9.6   APPLICATIONS OF DRA ARRAYS

The studies described in Sections 9.3-9.5 show that DRA arrays have various advantages over single DRA elements including directional radiation patterns, increased gain, and often wider bandwidths. DRA arrays generally have low crosspolarisation levels. These arrays are competitive with other types of antenna arrays, in terms their performance and fabrication process. They will *predominately* find applications in point-to-point, point-to-multipoints, and satellite communication systems, and also in dynamic radar systems.

DRA arrays may also be used for the determination of the Direction of Arrival (DOA) of the signal. This application example, which has been demonstrated in a laboratory scale by Neshati [6], is described below.

The block diagram of the DOA finding receiver is shown in Fig. 9.36. Two rectangular DRA elements of length=18mm, width=18mm, height=9mm and $\varepsilon_r=37$ are used to form an E-plane array in the receiver. The DRA elements are separated by $d=\lambda_0/4$ at the operating frequency of 2.35GHz. The mutual coupling between two elements was measured to be –9.15dB. The receiver has two channels, one for each of the rectangular DRA element used. Each channel contains a LNA, a mixer, a BPF and a 2-way splitter for phase difference and amplitude measurements. A local oscillator together with a 2-way splitter is used to provide the same mixing

frequency for both channels. The phase shift between two outputs of the splitter is used to control the output characteristics of the phase detector (PD).
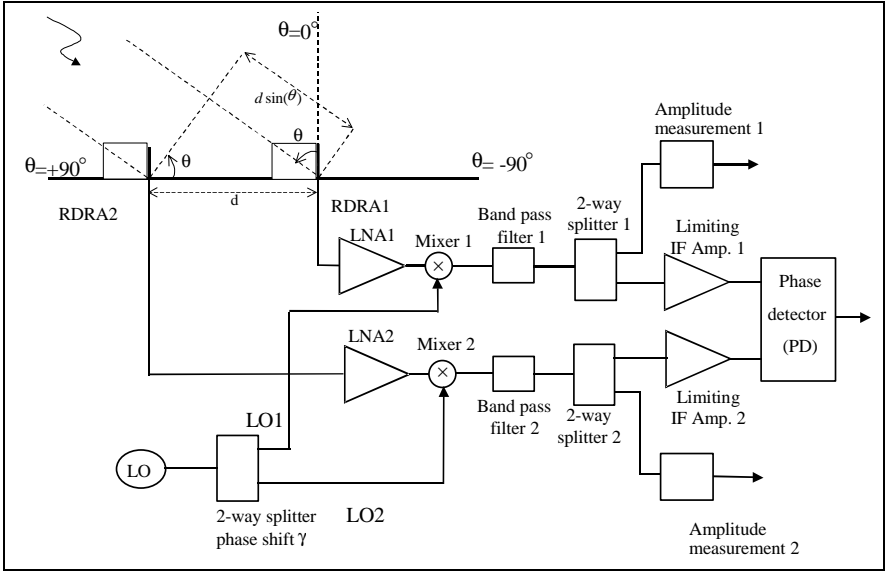
Fig. 9.36 Block diagram of the direction finding receiver

For $\gamma=0$, the PD output is related to the phase difference, ϕ, of the signals received by two DRA elements by

$$\text{PD output} = A\cos(\phi) = A\cos\left[2\pi(d/\lambda_0)\sin\theta\right], \quad (9.5)$$

and for $\gamma=\pi/2$, the PD output is related to the phase difference ϕ by

$$\text{PD output} = A\sin(\phi) = A\sin\left[2\pi(d/\lambda_0)\sin\theta\right]. \quad (9.6)$$

Hence, the PD output is related to the DOA, or the angle θ. With the use of the test arrangement shown in Fig. 9.37, the phase difference is related to the horizontal displacement x by

$$\phi = \frac{2\pi}{\lambda_0}\left(\sqrt{h^2 + (x+d/2)^2} - \sqrt{h^2 + (x-d/2)^2}\right) \quad (9.7)$$

where h=1.8m. The measured DC outputs of the PD for different values of x, and their corresponding phase difference values when γ was set to zero are shown in

Figs. 9.38(a) and (b). The theoretical values obtained using Eqns. (9.5) and (9.7) are also shown in Figs. 9.38(a) and (b) for comparison. Fig. 9.38(a) indicates that the displacement x can be well determined from the PD output, hence the DOA. However, since $\gamma=0$ was used, the PD output has a cosine distribution with respect to ϕ so that +x or –x could not be differed. This could be overcome by using $\gamma=\pi/2$ in the local oscillator splitter. In such a case, the PD output would be zero when the signal comes from $\theta=0$, and be positive or negative when θ is greater or less than zero.
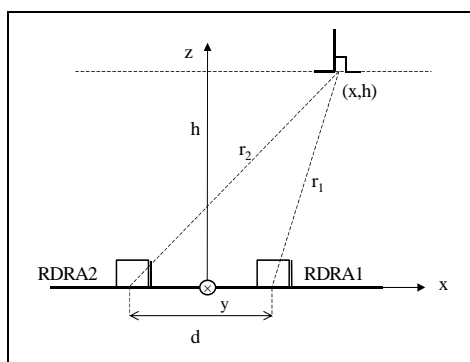
Fig. 9.37 Test set-up for DOA determination

(a)

(b)
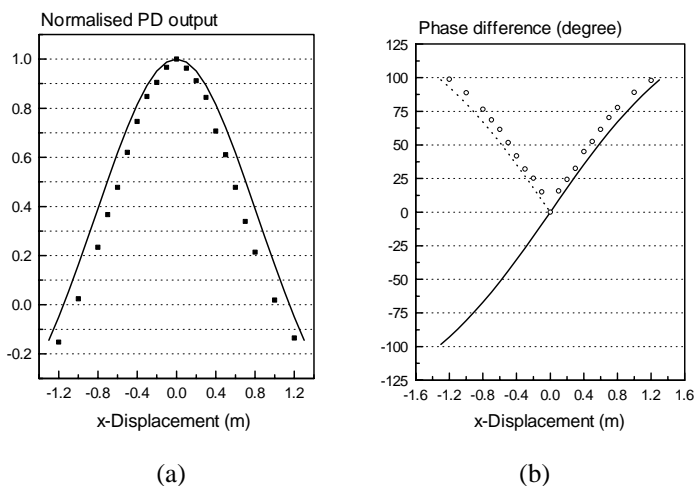
Fig. 9.38 The measured results for the rectangular DRA array with $d=\lambda_0/4$ and $\gamma=0°$: (a) normalised DC voltage at PD output, (b) detected phase difference between DRA elements. (Data points = measured values, graphs = theoretical predictions (from [6])

9.7   DISCUSSION AND CONCLUSIONS

This chapter has featured the advances in DRA arrays in recent years. The DRA arrays have the inherited advantages of single DRAs, most noticeably the high radiation efficiency from DRA elements. They also have directional radiation patterns with low crosspolarisation levels, sufficient gain and bandwidth for practical applications. Adaptive arrays and phased arrays with beam steering capability can also be designed using DRAs. Compared with microstrip antenna arrays, DRA arrays have the flexibility in the feed design and they are made using a different manufacturing process which allows easy post-fabrication adjustments.

For simplicity and convenience, microstrip lines are usually used in the feed network of DRA arrays in the lower gigahertz range of microwave frequencies. High operation efficiency can be obtained for small arrays. At millimetre wave frequencies, the efficiency becomes significantly lower due to the losses on the microstrip lines. Therefore, it would be beneficial to use low loss dielectric guides to construct the feed network for DRA arrays. The superior performance of DRA arrays over microstrip antenna arrays at millimetre wave frequencies may be fully revealed.

The ultimate performance of DRA arrays may be affected by a number of factors including:

- Non-uniformity of dielectric materials between elements,
- Fabrication tolerance of DRA elements and the feed structure,
- Mutual coupling between elements and within the feed structure,
- Loss in the feed structure,
- Finite size ground plane,
- DRA mounting technology,
- Air gaps, and
- The presence of protection enclosure.

These effects need to be considered in the design of DRA arrays. Non-uniformity, fabrication tolerance and air gaps should be minimised in the manufacturing process, so that DRA arrays with desirable performance or least post-fabrication adjustments may be manufactured.

The experimental studies reviewed in this chapter demonstrate that DRA arrays are competitive with other types of antenna arrays at microwave frequencies, and they can outperform microstrip antenna arrays at millimetre wave frequencies. As DRA manufacturing technology becomes mature, DRA arrays will find their applications at microwave and millimetre wave communication and radar systems in the years to come.

REFERENCES

1. M. T. Birand and R. V. Gelsthorpe, "Experimental millimetric array using dielectric radiators fed by means of dielectric waveguides", *Electronics Letters*, Vol. 17, No. 18, pp. 633-635, 1981.
2. A. Petosa, R. K. Mongia, A. Ittipiboon and J. S. Wight, "Experimental investigation on feed structures for linear arrays of dielectric resonator antennas", *Proceedings of IEEE AP-S* Conference, California, USA, pp. 1982-1985, 1995.

3. Y. X. Guo, K. M. Luk and K. W. Leung, "Mutual coupling between millimeter-wave dielectric resonator antennas", *IEEE Trans. on Microwave Theory and Techniques*, Vol. 47, No. 11, pp. 2164-2166, 1999.
4. K. Y. Chow, K. W. Leung, K. M. Luk and E. K. N. Yung, "Cylindrical dielectric resonator antenna array", *Electronics Letters*, Vol. 34, No. 13, pp. 1283-1285, 1998.
5. G. D. Loos and Y. M. M. Antar, "A new aperture-coupled rectangular dielectric resonator antenna array", *Microwave and Optical Technology Letters*, Vol. 7, No. 14, pp. 642-644, 1994.
6. H. M. Neshati, "Numerical modelling and application studies of rectangular dielectric resonator antennas", PhD thesis, UMIST, Manchester, UK, 2001.
7. G. Drossos, Z. Wu and L. E. Davis, "Aperture-coupled cylindrical dielectric resonator antennas forming four-element linear array", *Microwave and Optical Technology Letters*, Vol. 20, No. 2, pp. 151-153, 1999.
8. M. G. Keller, M. B. Oliver, D. J. Roscoe, R. K. Mongia, Y. M. M. Antar and A. Ittipiboon, "EHF dielectric resonator antenna array", *Microwave and Optical Technology Letters*, Vol. 17, No. 6, pp. 345-349, 1998.
9. G. P. Junker, A. W. Glisson and A. A. Kishk, "Mutual coupling effects and radiation characteristics of a linear array of dielectric resonator elements fed by coaxial probes", *IEEE AP-S International Symposium Digest*, pp.1998-2001, 1995.
10. G. Drossos, Z. Wu and L. E. Davis, "Linear arrays consisting of four probe-fed cylindrical dielectric resonator antennas", *Microwave and Optical Technology Letters*, Vol. 18, No. 6, pp. 367-370, 1998.
11. G. Drossos, Z. Wu and L. E. Davis, "Two-element broadside arrays using cylindrical dielectric resonator antennas", *Microwave and Optical Technology Letters*, Vol. 11, No. 6, pp. 342-345, 1996.
12. Z. Wu, "Cylindrical dielectric resonator antenna arrays", *IEE International Conference on Antennas and Propagation*, Manchester, UK, pp. 668-671, April 2001.
13. G. Drossos, Z. Wu and L. E. Davis, "Implementation of four-element linear arrays using microstrip-coupled cylindrical dielectric resonator antennas," *Microwave and Optical Technology Letters*, Vol. 19, No. 5, pp. 375-379, 1998.
14. A. Petosa A., A. Ittipiboon A., Y.M.M. Antar, D. Roscoe and M. Cuhaci, "Recent advances in dielectric resonator antenna technology", *IEEE Antennas and Propagation Magazine*, Vol. 40, No. 3, pp. 35-48, June 1998.
15. A. Petosa, R. K. Mongia, A. Ittipiboon and J. S. Wight, "Design of microstrip-fed series array of dielectric resonator antennas", *Electronics Letters*, Vol. 31, No. 16, pp. 1306-1307, 1995.
16. A. Petosa, A. Ittipiboon, M. Cuhaci and R. Larose, "Bandwidth improvement for a microstrip-fed series array of dielectric resonator antennas", *Electronics Letters*, Vol. 32, No. 7, pp. 608-609, 1996.
17. A. Petosa, R. Larose, A. Ittipiboon and M. Cuhaci, "Microstrip-fed array of multisegment dielectric resonator antennas", *IEE Proc.–on Microwave, Antennas Propagation*, Vol. 144, No. 6, pp. 472-476, 1997.

18. K. W. Leung, H. Y. Lo, K. M. Luk and E. K. N. Yung, "Two-dimensional cylindrical dielectric resonator antenna array", *Electronics Letters*, Vol. 31, No. 18, pp. 1536-1537, 1998.

19. G. Drossos, Z. Wu and L. E. Davis, "Four-element planar arrays employing probe-fed cylindrical dielectric resonator antennas", *Microwave and Optical Technology Letters*, Vol. 18, No. 5, pp. 315-319, 1998.

20. G. Drossos, Z. Wu and L. E. Davis, "Two planar arrays using four probe-fed cylindrical dielectric resonator antennas", *IEE Conference on Antennas and Propagation*, York, UK, pp. 283-286, 1999.

21. A. Petosa, A. Ittipiboon, M. Cuhaci and R. Larose, "Low profile phased array of dielectric resonator antennas", *Proceedings of IEEE International Symposium on Phased Array Systems and Technology*, Boston, USA, pp. 182-185, 1996.

22. A. Petosa, A. Ittipiboon, M. Cuhaci and R. Larose, "Active phased array of dielectric resonator antennas", *International Symposium on Antennas and Propagation*, Montreal, Canada, pp. 690-693, 1997.

23. K. K. Pang, H. Y. Lo, K. W. Leung, K. M. Luk and E. K. N. Yung, "Circularly polarised dielectric resonator antenna subarrays", *Microwave and Optical Technology Letters*, Vol. 27, No. 6, pp. 377-379, 2000.

24. C. Y. Huang, K. L. Wong, C. F. Yang and J. Y. Wu, "Planar array composed of two linearly polarised dielectric resonator antennas for circular polarisation", *Microwave and Optical Technology Letters*, Vol. 21, No. 5, pp. 323-324, 1999.

25. M. Haneishi and H. Takazawa, "Broadband circularly polarised planar array composed of a pair of dielectric resonator antennas", *Electronics Letters*, Vol. 21, No. 10, pp. 437-438, 1985.

26. A. Petosa, A. Ittipiboon and M. Cuhaci, "Array of circular-polarised cross dielectric resonator antennas", *Electronics Letters*, Vol. 32, No. 19, pp. 1742-1743, 1996.

27. G. Drossos, Z. Wu and L. E. Davis, "Two-element endfire dielectric resonator antenna array", *Electronics Letters*, Vol. 32, No. 7, pp. 618-619, 1996.

28. R. K. Mongia and P. Bhartia, "Dielectric resonator antennas-a review and general design relations for resonant frequency and bandwidth", *Int. J. Microwave Millimetre Wave Computer-Aided Eng.*, Vol. 4, pp. 230-247, 1994.

29. T. S. M. Maclean and Z. Wu, "Radiowave Propagation Over Ground", Chapman & Hall, London, pp. 40-42, 1993.

30. R. P. Jedlicka, M. T. Poe and K. R. Carver, "Measured mutual coupling between microstrip antennas", *IEEE Trans. on Antennas and Propagation*, Vol. AP-29, No. 1, pp. 147-149, 1981.

CHAPTER 10

Leaky-Wave Dielectric Resonator Antennas Based on NRD Guides

Kwai Man Luk and Ming Tat Lee

Department of Electronic Engineering
City University of Hong Kong
Kowloon, Hong Kong SAR

10.1   INTRODUCTION

Modern communication systems require wide bandwidth to support the demand on high data rate transfer for various multi-media applications. To fulfill this requirement, most wireless mobile systems have to be operated at microwave frequencies [1-2]. Also, for ease of installation and space allocation, it is highly desirable to have small-size, low-profile equipment. Hence, antennas for modern wireless systems should be low in profile and efficient at high frequencies.

Microstrip antennas have been investigated extensively in the literature [3-5]. They have the advantages of light weight, low cost and low profile. However, due to high conductor loss and strong excitation of surface waves, this class of antennas is poor in radiation efficiency when operated at millimeter waves. Recently, dielectric antennas are becoming popular choices in RF designs [6-8], since they are easily to be incorporated with dielectric integrated circuits at the front end of a transceiver. Apart from the dielectric resonator antenna (DRA), leaky-wave antennas based on the non-radiative dielectric (NRD) may be a desirable choice because of their properties of compact size, low loss, and ease of fabrication [13-14]. These features are attractive for wideband wireless applications at millimeter wave frequencies.

10.1.1   Antennas Based on NRD Guides

The NRD guide was proposed by Yoneyama and Nishida [13] in 1981. Although it is classified as an open dielectric waveguide, as shown in Fig. 10.1, it has the attractive feature of no leakage. Structurally, it is identical to the H-guide except that the plate separation of the NRD guide is less than a half of the free-space wavelength. Under this condition, both TM^y and TE^y modes are cutoff in nature, and the NRD guide can suppress radiation at curved sections and discontinuities. Referring to the notation used by Yoneyama [14], the TM^y and TE^y modes are referred, respectively, as longitudinal section magnetic (LSM) and longitudinal

section electric (LSE) modes. Because of its attractive features and its high potential in realisation of millimeter wave circuits, the NRD guide has been studied extensively [4-5,16-24].
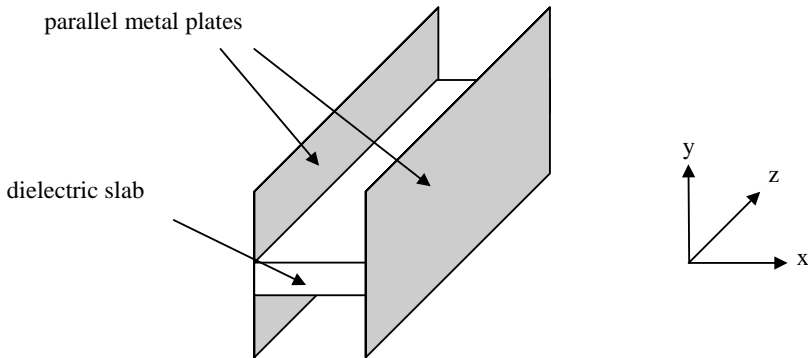
Fig. 10.1   Structure of a NRD guide.

Although the NRD guide does not radiate, it can be leaky if suitable perturbation is introduced into the structure of the guide. In the literature, several methods have been investigated. In general, the antenna can radiate strongly in the end-fire or off-broadside direction, which depends on the mode of excitation. Leaky waves are produced by perturbing the geometry of the NRD guide in such a way that the original bound mode be converted into a leaky mode. Most leaky-wave antennas operated at millimeter wave frequencies are based on NRD guides with selected open structures to generate the leakage, including those with a foreshortened side [15-16], an asymmetric air-gap [17], and a trapezoidal dielectric slab [18]. Leaky waves radiate in the form of a narrow beam, which can be scanned with frequency. Several theoretical studies and numerical techniques [15-17,19] for characterising NRD guide antenna have been proposed in the literature. However, only a few experimental studies were presented [18, 20-21].

Previous studies have provided a clear understanding on both waveguide transition and leaky-wave generation. Here, we will first consider feeding methods for NRD guides, then methods for exciting leaky waves.

10.1.1.1   Feeding methods
(i) Horn feed
Feeding the NRD guide with a horn requires special techniques [22]. With a suitable tapered dielectric slab down to the horn in the H-plane, good performance in impedance matching is achieved. However, the relatively large horn size makes it not popular in real applications demanding compact antennas. Moreover,

horn-fed antennas generally have two ports. One is for the input and the other is for the matching termination. This design cannot produce broadside radiation.

(ii) Probe feed

By inserting a coaxial probe normal to the y-z plane into the dielectric slab inside the NRD guide, the LSM_{11} waveguide mode can be excited. But this mode is not the desirable mode for our design (LSE_{11}). If the coaxial probe is located in line with the dielectric slab, the LSE_{11} waveguide mode will be excited. However, like the horn feeding technique, its two-port configuration cannot produce broadside radiation. Moreover, its impedance matching performance is not as good as the horn feeding technique mentioned above.

(iii) Aperture coupling method

A NRD guide can be fed by an aperture that is etched on the ground plane which transforms the NRD guide becomes a NRD image guide, as shown in Fig. 10.2. That kind method can excite the image guide with the LSE_{11} mode. If the aperture is located at the middle of the NRD image guide, with suitable modification in structure, the NRD image can work as a leaky-wave antenna [20]. The antenna is also resonant in nature since energy is reflected back at the two ends of the slab. Hence, in this chapter, it is designated as a leaky-wave dielectric resonator antenna, which has a broadside radiation pattern.
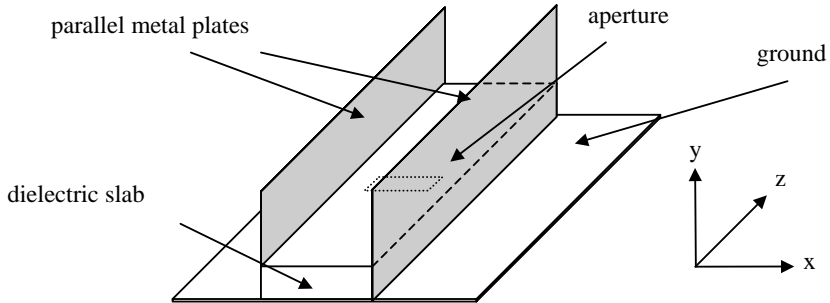
Fig. 10.2   NRD image guide with a coupling aperture.

10.1.1.2   Generation of leaky waves

In the literature, several methods have been proposed to generate leaky waves from a NRD guide.

(i) Foreshortened sides of parallel metal plates

As shown in Fig. 10.3 for a NRD guide with foreshortened sides, the distance between one open end and the dielectric slab is made smaller. The fields would not

decay completely and so some power will leak out of the open end. The leakage increases with decreasing displacement *d* [16].
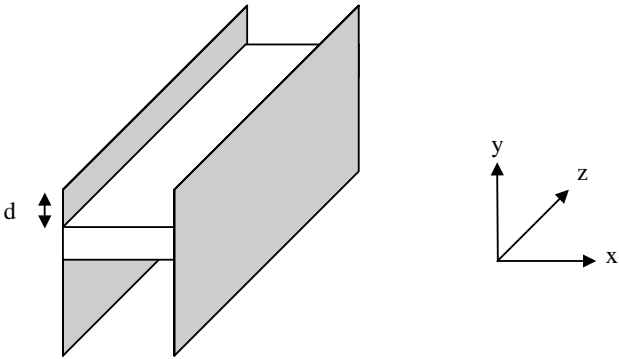
Fig. 10.3 NRD guide with foreshortened sides.

(ii) Asymmetric air gap
The geometry of a NRD guide with an asymmetric air gap is shown in Fig. 10.4. The asymmetry produces a net horizontal field, which creates a TEM field in the air-filled region. As a result, power leaks out of the two open ends [15]. However, the requirement of very accurate air-gap size is difficult to be implemented.
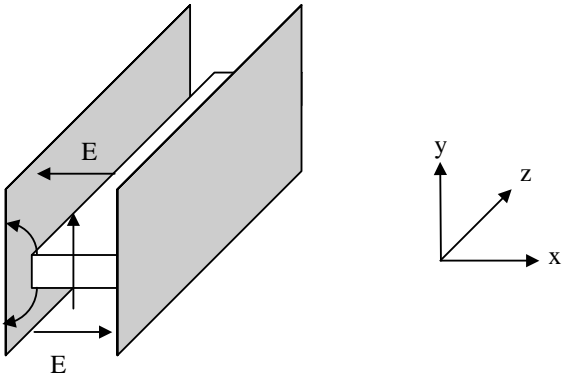
Fig. 10.4 NRD guide with an asymmetric air gap.

(iii) Trapezoidal dielectric slab

Fig. 10.5 shows the configuration of a NRD guide with a trapezoidal dielectric slab [18]. Similarly, this asymmetric structure introduces a small amount of horizontal electric field, which excites a TEM mode.
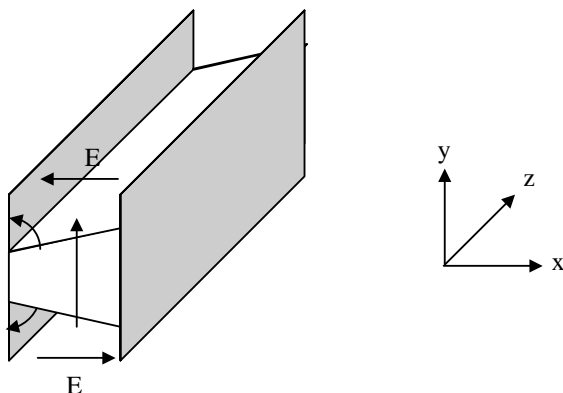
Fig. 10.5   NRD guide with a trapezoidal dielectric slab.

10.1.2   Leaky-wave Antennas using Asymmetric NRD Guide

A NRD guide itself is a transmission line and so it is non-radiative. However, introducing suitable perturbation to the NRD guide structure can produce leaky waves that propagate away from the dielectric slab to the two open ends. This mechanism makes the NRD guide working as a leaky-wave antenna. Although this kind of antenna has a frequency-scanning characteristic, the radiation beam is usually pointed to the end-fire or off-broadside direction. Therefore, it may not be applicable in modern communication systems.

A leaky-wave dielectric resonator antenna based on a NRD guide is presented in this chapter. The effects of using different kinds of dielectric slabs on the SWR, gain and radiation pattern are studied. The aperture-coupling technique is chosen to feed the leaky-wave DRA so that a radiation beam pointed to the broadside of the E-plane is obtained. With a metal cavity covering the aperture, the back lobe radiation can be substantially reduced. Also, a flared horn is attached to the open end of the antenna. It effectively controls the H-plane beam width. The asymmetric-type leaky-wave DRAs are of particular interest since the antenna usually offers better antenna performance. The principle of operation of the antenna is discussed in the following section.

10.1.2.1 Principle of operation

The configuration of the antenna is basically an asymmetric image NRD guide fed by the aperture-coupling method. It is excited in the LSE_{11} mode and is operated at the frequency that is lower than the cutoff frequency of the air-filled region. With reference to Fig. 10.2, the attenuation factor along the y-direction will become small so that the field will decay slowly towards the open end [16]. Hence, the degree of leakage is mainly controlled by the height of parallel plates. By adjusting the height of parallel plates, suitable amount of leaky waves can be obtained to produce a practical radiation pattern.

A broadside radiation pattern can be achieved by fulfilling two factors. One is to choose the operating frequency of the antenna close to the cutoff frequency of the LSE_{11} mode of the image NRD guide. By so doing, the guide wavelength can be adjusted to be twice of the length of the dielectric slab. Second, with the feeding slot located at the middle of the NRD guide, a half-sinusoidal field distribution is excited [20]. As a result, a broadside radiation with narrow beam width from the open end of the NRD guide is obtained.

10.1.2.2 Applications

The NRD guide has been identified to be useful as a transmission line for microwave and millimeter-wave frequencies due to its low loss characteristic at very high frequencies. Therefore, NRD guide based leaky-wave antennas would be inherently low in metallic loss. Moreover, when the antenna is designed with a microstrip line as its feed, no transition between the antenna and a practical microwave device, such as a microwave filter, power divider or directional coupler, is required. The antenna offers high antenna gain with narrow beamwidth. This is definitely an advantage for point-to-point communications. The design of antenna arrays, using microstrip line feed, is a practical choice since the feed network is low in profile and simple in structure compared with structures using coaxial lines or waveguides as feeds.

10.2 LEAKY-WAVE DIELECTRIC RESONATOR ANTENNAS BASED ON SYMMETRIC IMAGE NRD GUIDES

Recently, several techniques have been proposed to design-leaky wave antennas using NRD guides. These designs usually radiate with the main beam off the broadside direction. However, by using an aperture-coupled feed [20], a NRD antenna can be operated in a broadside mode. This antenna is designated as a leaky-wave DRA in this chapter. The antenna however has an aperture that leads to high backlobe radiation. On the other hand, changing the operating frequency of the antenna is not an easy task for antenna designers. In general, the solution is to alter the antenna size in proportion to operating wavelength. However, if the antenna has already been integrated with an electronic device, it may be required to re-design the device's layout due to the change in antenna size. In this section, a leaky wave antenna based on an inverted T-shaped image NRD guide operated in LSE_{11} mode is presented. It is demonstrated that symmetric perturbations applying to the NRD guide is a possible way to increase the operating frequency without affecting other antenna characteristics. With a metallic cover introduced for the slot,

the backlobe level can be kept over 18dB below the broadside radiation. For comparison, experiments were also done on the antenna using ordinary rectangular NRD guide without perturbation.

10.2.1   Rectangular Leaky-wave DRA

Several feeding techniques have been proposed for the excitation of NRD guides [20, 22-23], including horn feed, coaxial probe feed, and aperture coupling. Among these methods, the aperture coupling technique has an attractive feature. It has been reported that if the coupling aperture is placed in the middle of the NRD guide, a broadside radiation can be obtained [20]. This feeding method has a drawback that the aperture causes a relatively high undesirable backlobe radiation. In this section, the measured SWR, gain, and radiation pattern of the antenna are presented. To reduce the backlobe radiation, a metal cavity is installed to cover the backside of the antenna. An improvement of 8dB in backlobe can be achieved.

10.2.1.1   Antenna characteristics

Figs. 10.6 and 10.7 show the geometry of an ordinary rectangular leaky-wave DRA. The NRD guide is fed by a slot-coupled microstripline. The $(7x1)mm^2$ slot is coupled by a 50Ω microstripline with a stub length of $L_S=5mm$. The microstripline is printed on a 0.785mm thick substrate of $\varepsilon_r=2.53$. With the appropriate height of parallel plates, leaky waves can be produced and the antenna is radiated with broadside radiation pattern. If the two parallel plates are different in height, the radiation pattern will alter. In the following sections, experimental results with detailed discussion are given.
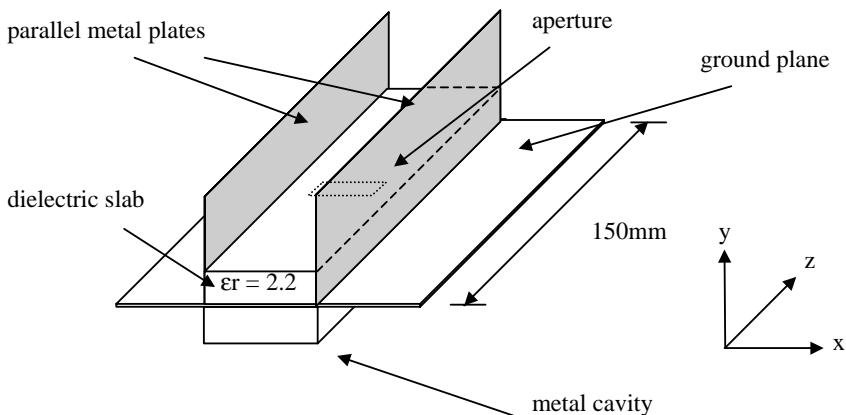
Fig. 10.6   Configuration of an ordinary rectangular leaky-wave DRA.

metal parallel plates

dielectric slab

10mm

H

$\varepsilon r = 2.2$

6mm

ground plane

T
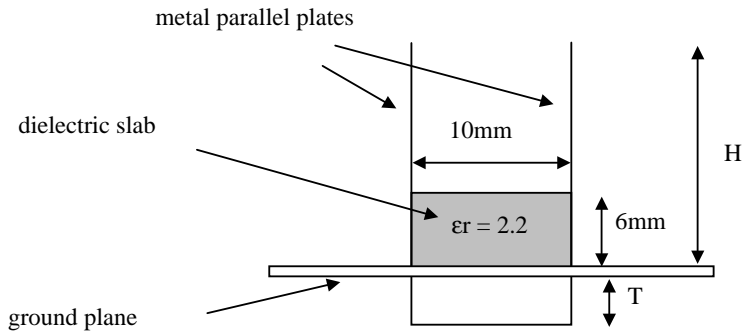
Fig. 10.7 Side view of the rectangular leaky-wave DRA.

H = 15mm   H = 20mm   H=22mm
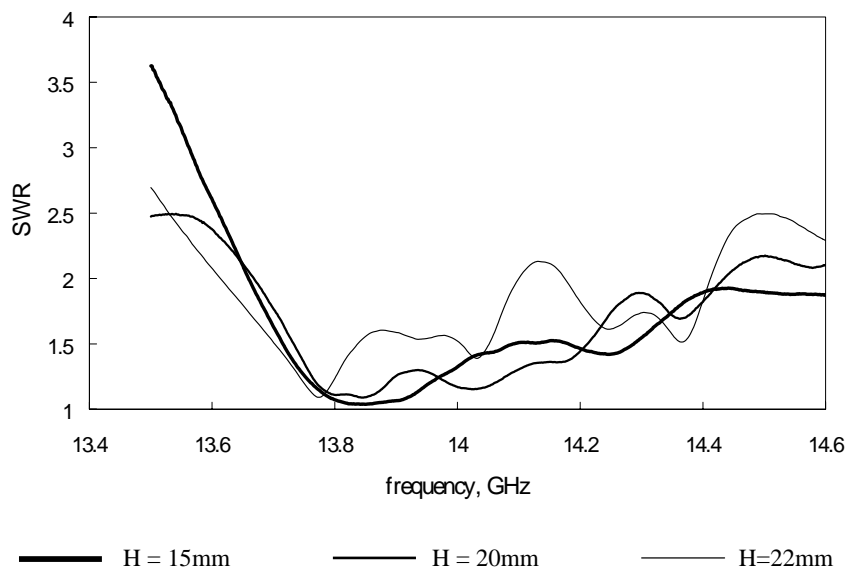
Fig. 10.8 Measured SWR of the rectangular leaky-wave DRA.

10.2.1.2   Effect of height of parallel plates

The input SWR (Standing Wave Ratio) of the antenna was measured by a HP8510C network analyzer and the result is shown in Fig. 10.9. It can be observed that when $H = 15mm$, the best impedance matching with 4.3% bandwidth (SWR < 2) is obtained. If H increases, the SWR increases which reduces the impedance bandwidth. When $H = 20mm$ is chosen, the impedance bandwidth is 3.9%. For the worst case of $H = 22mm$, the impedance obtained is only 3.8%.
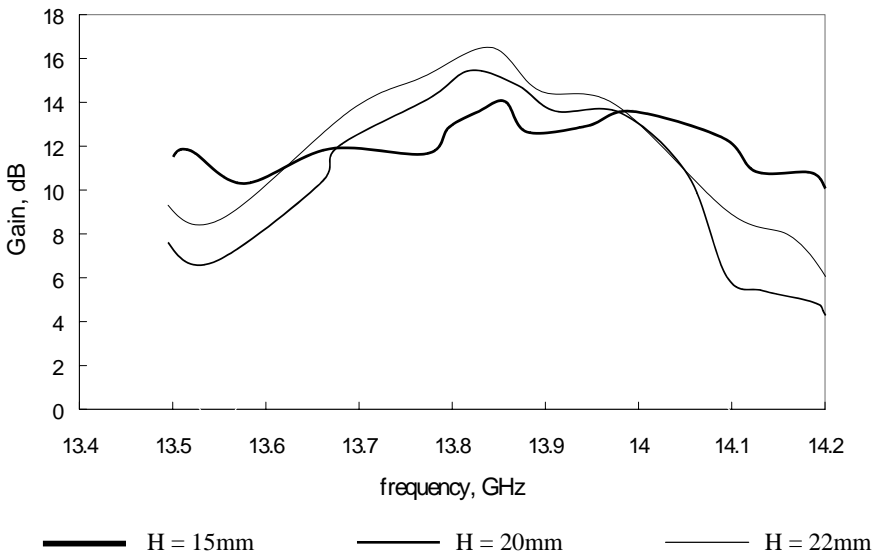
Fig. 10.9   Measured antenna gain of the rectangular leaky-wave DRA.

As shown in Fig. 10.8, the antenna gain decreases with decreasing height H. It is found that the case with H = 22mm ($\sim 1.01\lambda_o$) attains the maximum gain of 16.2dBi. The measured radiation patterns of the three antennas with different H are shown in Fig. 10.10 (a-f).

(a)

(b)

(c)

(d)

co-polarisation ——— cross-polarisation 10dB/div.

(e)   (f)
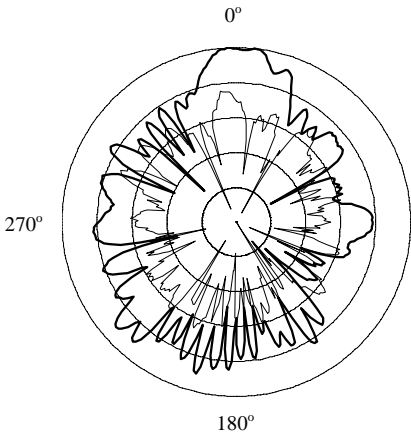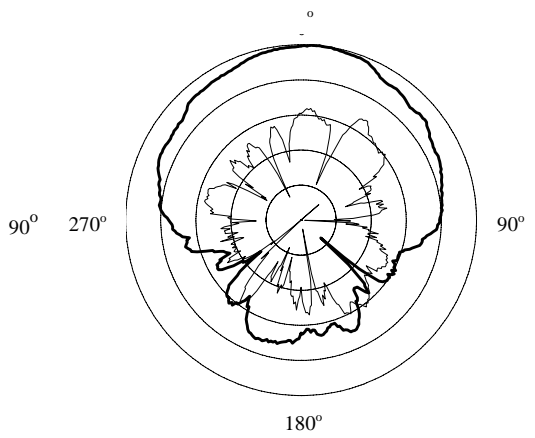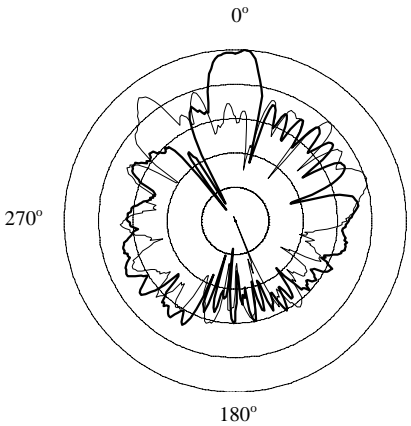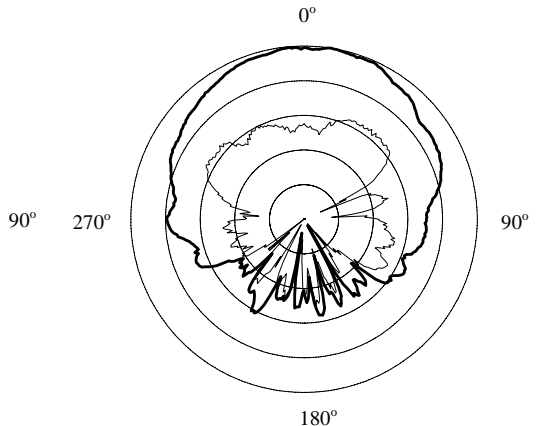
━━━━ co-polarisation   ────── cross-polarisation   10dB/div.
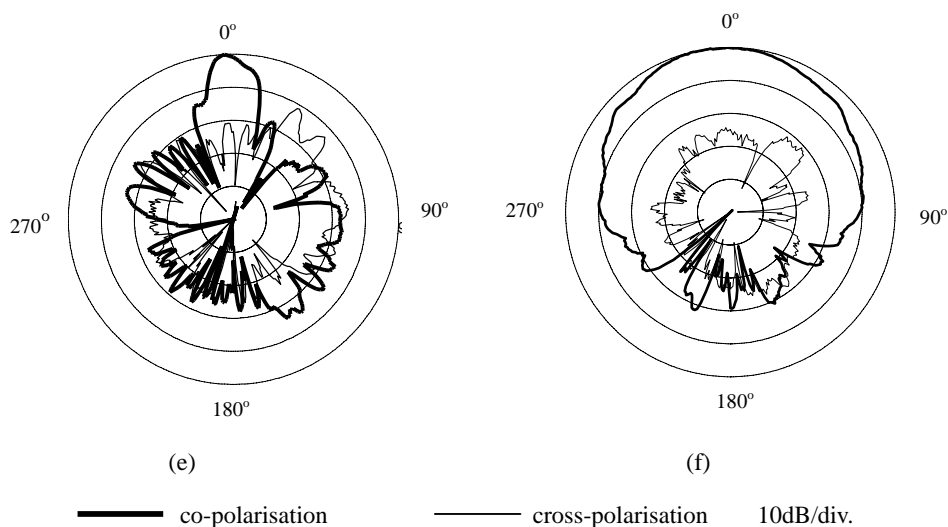
Fig. 10.10 Measured radiation patterns of the rectangular leaky-wave DRA. (a) H = 15mm (E-plane). (b) H = 15mm (H-plane). (c) H = 20mm (E-plane). (d) H = 20mm (H-plane). (e) H = 22mm (E-plane). (f) H = 22mm (H-plane).

It can be observed from Fig. 10.10 (a-b) that the backlobe is quite high (only -8dB below the main lobe) which is not desirable for practical applications. Therefore, metal covers were applied to the cases of H = 20mm and 22mm. Thus, as shown in Fig. 10.10(c-f), the backlobes are decreased substantially. Moreover, we found that the 3dB-beamwidth in the E-plane decreases with increasing height H of the two parallel plates.

10.2.1.3   Effect of using unequal parallel plates

Consider the leaky-wave antenna shown in Fig. 10.11. It has a configuration similar to that shown in Fig. 10.7 except that the two parallel plates are unequal in height with a difference of D = 5mm ($\sim \lambda_o/4$). It is found that the boresight in the H-plane steers off the broadside direction. However, it does not produce significant change on other antenna characteristics such as the SWR and the antenna gain.
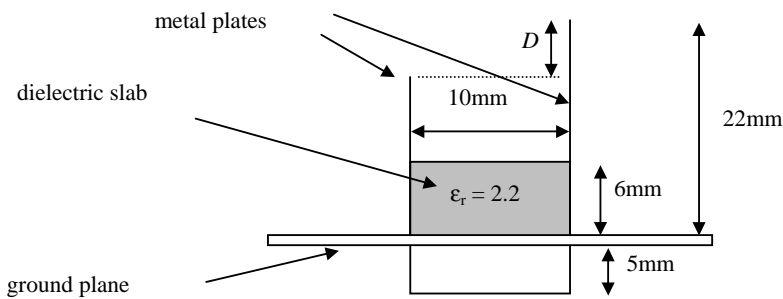
Fig. 10.11 Side view of the leaky-wave antenna with unequal heights of parallel plates.

Fig. 10.12 Measured SWR of the antenna.

Fig. 10.12 shows the measured SWR of the antenna, which offers 3.0% impedance bandwidth with centre frequency of 14.1GHz. The bandwidth is smaller than that of the original antenna configuration shown in Fig. 10.7, about 4.3% and 3.5% for $H = 15$mm and 22mm respectively. This result does not imply a reduction of the usable bandwidth. For this kind of antennas, the 3-dB gain bandwidth is usually narrower than the impedance bandwidth. Hence, the usable bandwidth depends

mainly on the gain bandwidth. Observing the measured antenna gain shown in Fig. 10.13, it is found that the 3-dB gain bandwidth is only 0.7% and the maximum gain is 14.08dBi. The gain is very close to that of the antennas shown in Fig. 10.7, which have 0.8% gain bandwidth.

The radiation pattern is shown in Fig. 10.14. In the E-plane, it is symmetrical about the broadside direction with a beamwidth of 9°. This shows that the radiation pattern in the E-plane is not affected when using unequal heights of parallel plates. However, in the H-plane, it is shifted to the direction of -27° away from the broadside. The 3-dB beamwidth in this plane is 36°.
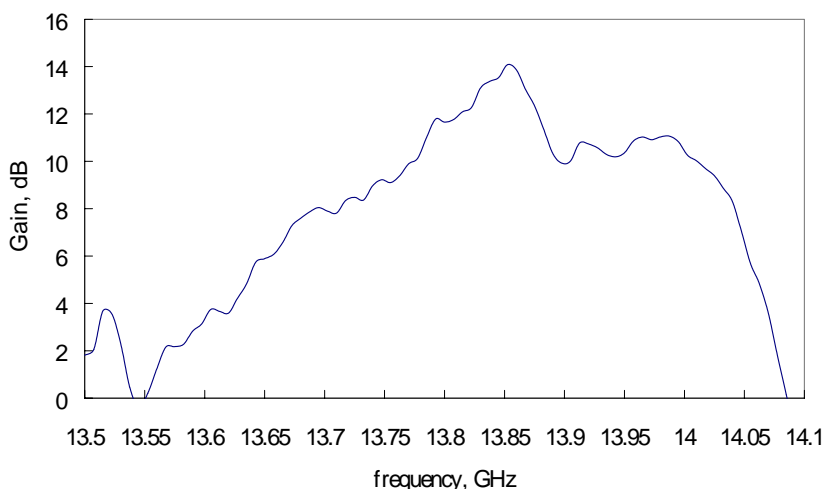
Fig. 10.13   Measured antenna gain against frequency.

10.2.1.4   Discussion

After extensive measurements on the rectangular leaky-wave DRA, it is found that the vertical heights of the parallel plates are important for controlling the impedance bandwidth, antenna gain, and radiation pattern. The use of a smaller value of H will give better input impedance matching performance across the bandwidth. However, if H=15mm is chosen, it will give a lower value of antenna gain. Therefore, a larger height of H=20mm or 22mm is selected to achieve higher antenna gain. It is also observed that when H=20mm or 22mm, cleaner radiation patterns are obtained. From the experimental study, it is found that the case with H=22mm is the optimum to achieve good radiation pattern with desirable bandwidth and antenna gain.
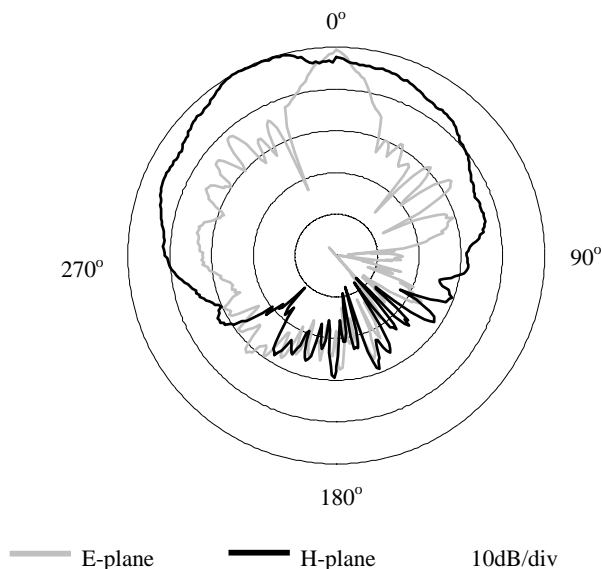
Fig. 10.14   Measured radiation pattern of the antenna.

A measurement was also carried out for the antenna using unequal height of parallel plates. The result shows that the radiation in the H-plane is oriented off the broadside direction. When a 22mm higher plate and a 17mm lower plate are selected for the antenna, the boresight of the antenna will point to the side of the lower plate with –27° elevation. This finding gives a very useful guideline to antenna engineers who want to design such a leaky-wave antenna with different boresight angles in the H-plane.

10.2.2   Inverted T-shaped Leaky-wave DRA

Fig. 10.15 shows the configuration of a leaky-wave DRA with an inverted T-shaped dielectric slab. The image NRD guide of this antenna is fed by a microstripline through a slot of width 1mm and length 5mm. The dielectric slab inside the image NRD guide has a thickness of 6mm, a width of 10mm, a length of 150mm and a dielectric constant $\varepsilon_r = 2.2$. Two identical perturbations are in the dielectric slab. Two metal plates of length 210mm and height H are attached to the dielectric slab. The microstripline is printed on a substrate of thickness $l = 0.785$mm and relative permittivity of 2.53. The stub length is 7.5mm.
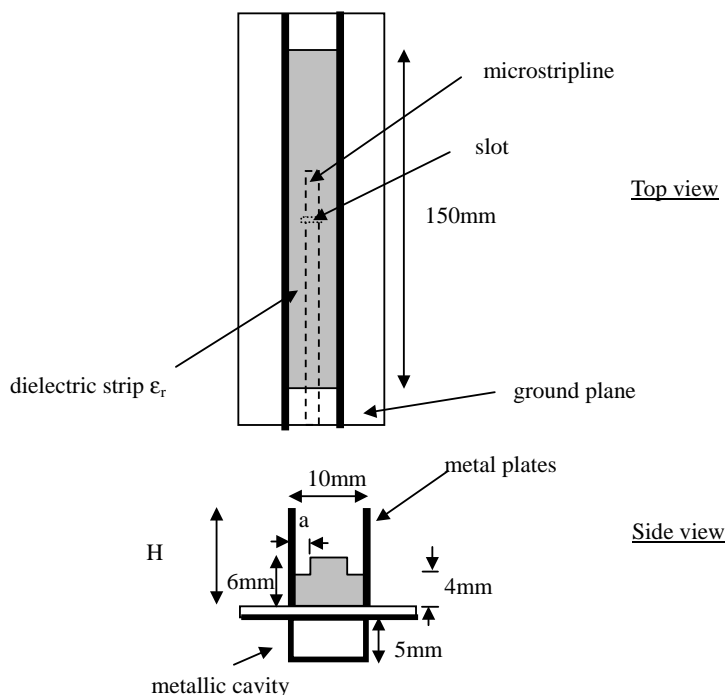
Fig. 10.15 Configuration of a leaky-wave DRA with an inverted-T shaped dielectric slab.

10.2.2.1   Experimental results

The measured SWRs against frequencies are plotted in Fig. 10.16. For the case with a=2mm and H=25mm, the antenna with an inverted T-shaped NRD guide attains the maximum impedance bandwidth (SWR < 2) of 3.8% with the centre frequency of 14.6GHz. For the case with a=2mm and H=22mm, the impedance bandwidth is 1.6%. It is only a half of the previous case. On the other hand, when a=3mm and H=25mm are used, the impedance bandwidth is 3.2%. The results show that the impedance bandwidth is very sensitive to the height of the parallel plates. Fig. 10.17 shows the measured gain of the antenna with a=2mm and H=25mm. For this case, the maximum gain is 16.5dBi and the 3-dB gain bandwidth is 0.7%.

      a = 2mm, *H* = 25mm.   *a* = 2mm, *H* = 22mm   *a* = 3mm, *H* = 25mm
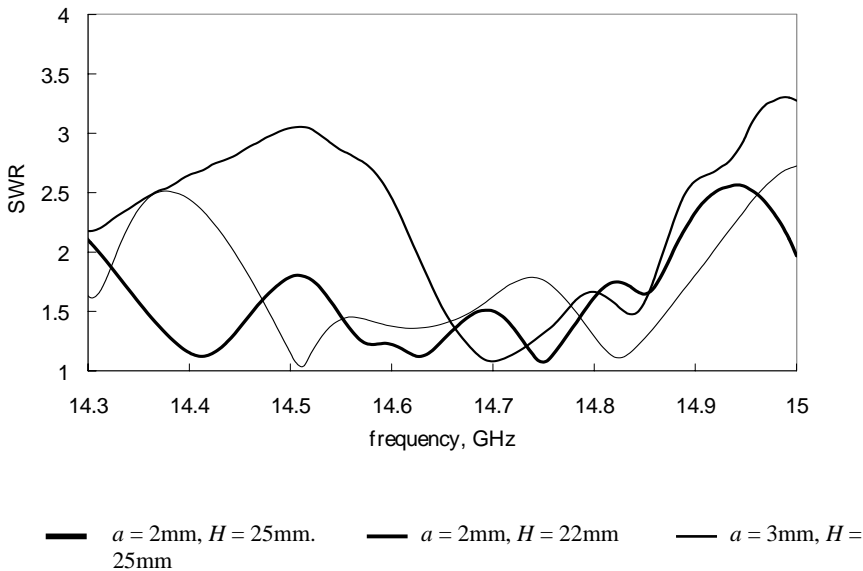
Fig. 10.16   Measured SWR against frequency.
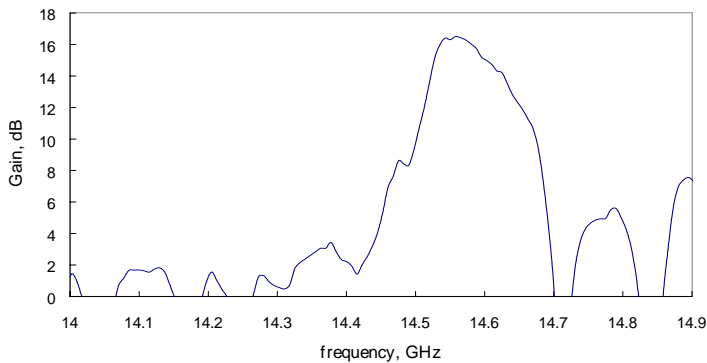
Fig.10.17   Measured antenna gain against frequency.

The measured radiation patterns in both E- and H-planes of the antenna are shown in Fig. 10.18. It can be observed that the main beam directs towards the broadside direction with 3dB beamwidth of about 10° in the E-plane and 71° in the H-plane. Fig. 10.19 shows that the measurement is in good agreement with the simulated result.

E-plane   H-plane

——— co-polarisation   ——— cross-polarisation   10dB/div.
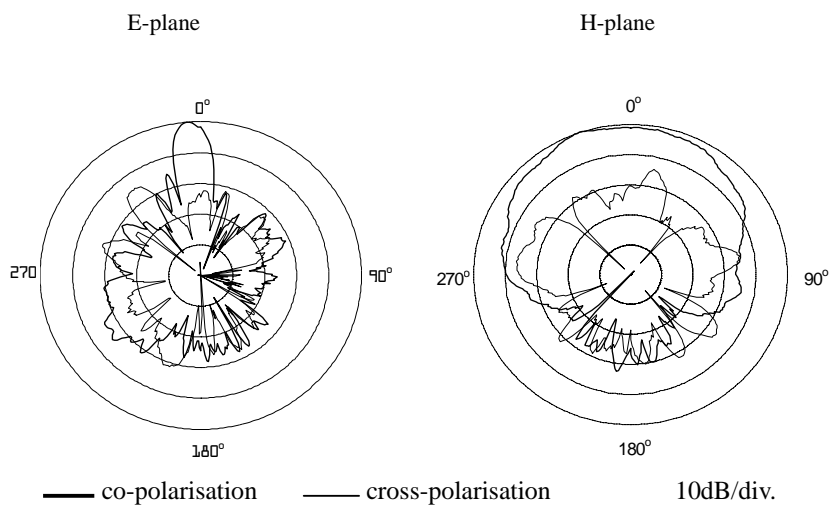
Fig. 10.18   Measured radiation pattern at centre frequency.

———   Simulated (E-plane)   ·······   Simulated (H-plane)

·············   Measured (E-plane)   ———   Measured (H-plane)
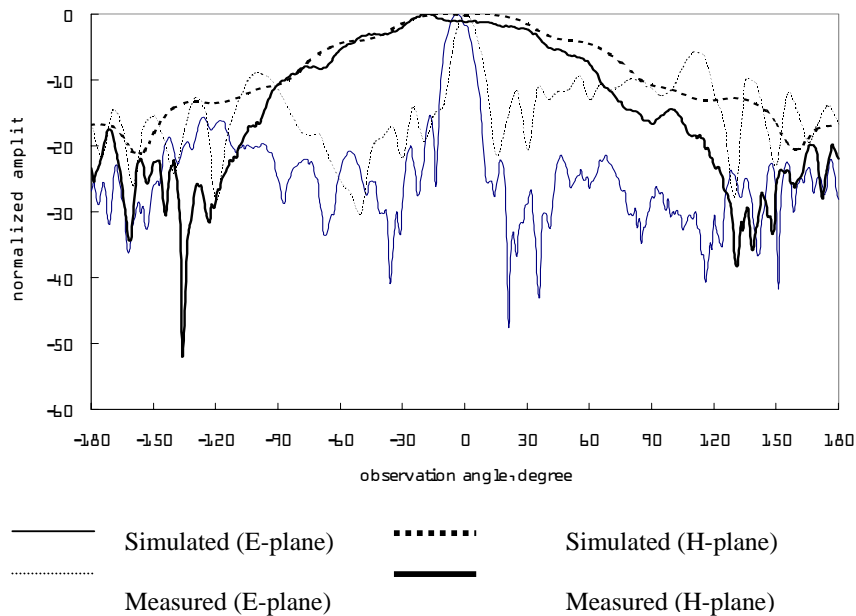
Fig. 10.19   Simulated and measured co-polarised radiation pattern of the antenna.

Table 10.1   Characteristics of leaky-wave antennas with inverted T slab

Configuration	Impedance Bandwidth	Gain Bandwidth	Max. Gain	Beamwidth		Centre frequency, f_o
				E-plane	H-plane	
no perturbation						
H=15mm	4.3%	0.9%	13.6dBi	22°	54°	14.0GHz
H=20mm	3.9%	0.7%	14.3dBi	11°	66°	13.9GHz
H=22mm	3.5%	0.8%	16.2dBi	12°	72°	13.8GHz
H=25mm	0.8%	1.0%	15.3dBi	10°	78°	13.7GHz
H=32mm	0.7%	0.9%	14.3dBi	12°	87°	13.7GHz
H=44mm	0.6%	0.7%	14.1dBi	11°	88°	13.8GHz
H=22mm, D=5mm	3.0%	0.7%	14.1dBi	9°	36°	14.0GHz
with perturbation						
a=2mm, H=25mm	3.8%	0.8%	16.5dBi	10°	71°	14.6GHz
a=2mm, H=22mm	1.6%	0.7%	14.2dBi	16°	70°	14.72GHz
a=3mm, H=25mm	3.2%	0.6%	13.6dBi	15°	71°	14.67GHz

10.2.2.2   Discussion

A leaky-wave DRA using an inverted T-shaped NRD guide is investigated. Comparing with the basic one, which uses an ordinary rectangular NRD guide with no perturbation, this new antenna has nearly no change in characteristics. Table 10.1 summarises the characteristics of both the conventional antenna and the proposed antenna. It shows that only the operating frequency range is shifted upward from 13.8-14.0GHz to 14.6-14.7GHz. The frequency shift is expected because the introduction of a symmetric perturbation makes the effective height of the dielectric slab smaller, and effectively makes the cuttoff frequency of the LSE_{11} image guide mode higher. Furthermore, one important finding is that even though the NRD structure is perturbed, the major characteristics of the antenna do not changed if the antenna structure is kept symmetrical about the yz-plane.

10.2.3   Summary

Leaky-wave antennas based on two symmetric NRD guides are studied. For the structure with a rectangular NRD guide, it has been shown that the heights of the two parallel plates could be used to control the impedance bandwidth, antenna gain and radiation pattern. Good matching performance across the bandwidth can be achieved if the heights of the two parallel plates are around $0.75\lambda_o$. However, it is found that a clean radiation pattern with the maximum antenna gain of about 16dBi can be obtained if the heights are set to be around one free-space wavelength. Moreover, if the heights of the two parallel plates are unequal, the beam in the H-plane will steer to the side of the shorter plate. In addition, it has been shown by experiment that a metal cavity with $\lambda_o/4$ thick plate placed behind the antenna can

reduce the backlobe radiation substantially. In the literature, it was reported that the thickness of the dielectric slab inside the NRD guide will affect the operating frequency of the NRD guide [14]. An inverted T-shaped NRD guide is proposed in this section. It provides a way for changing the centre frequency of the leaky-wave antenna.

10.3   LEAKY-WAVE DIELECTRIC RESONATOR ANTENNAS BASED ON ASYMMETRIC NRD GUIDES

In the last section, we have introduced a leaky-wave antenna based on an inverted-T shaped NRD guide. It has been showed that symmetric perturbations on the NRD guide can control the antenna's operating frequency. However, the antenna still has the problem of narrow bandwidth. Wider bandwidth is required for modern wireless applications. In order to solve this problem, two newly designed leaky-wave DRAs using asymmetric NRD guide are introduced in this section. They include the one with an asymmetric inverted T-shaped NRD guide, and the other one with a staircase-shaped NRD guide. It will be shown that the use of an asymmetric dielectric slab, which is located inside the NRD guide, can provide a wider gain bandwidth.

10.3.1   Using Asymmetric Inverted-T-shaped Dielectric Slab

The antenna shown in Fig. 10.20 is a modification of the leaky-wave DRA with an inverted T-shaped NRD guide depicted in Section 10.2.3. The major difference is that two unequal perturbations are applied on the dielectric slab, so that the antenna structure becomes asymmetric about the z-axis.

10.3.1.1   Experimental results

In this experiment, two different sets of geometric parameters for the dielectric slab were selected. The measured SWRs are shown in Fig. 10.21. With a perturbation of $a = 2$mm and $b = 4$mm, the antenna was found to have a resonant frequency of 14.3GHz and a bandwidth of 2.5%. Alternatively, if $a = 3$mm and $b = 5$mm are selected, the bandwidth is reduced slightly to 2.1%. Also, the operating frequency is increased to 14.8GHz.

Antenna gains of the two leaky-wave DRAs were measured and shown in Fig. 10.22. A gain of 15.2dBi and a gain bandwidth of 1.1% are achieved for the first antenna (with a = 2mm, b = 4mm). For the second antenna (with a = 3mm, b = 5mm), it offers a gain of 13dBi only but with a wider gain bandwidth of 1.8%. Both antennas offer wider gain bandwidths than the antenna with a rectangular NRD guide (0.8% only).

The measured radiation pattern of the first antenna, which has a higher gain, is shown in Fig. 10.23. It radiates symmetrically about the broadside direction with a 3dB beamwidth of 11° in the E-plane and 75° in the H-plane. It can also be observed that the cross-polarisation is at least 16dB below the co-polarisation.
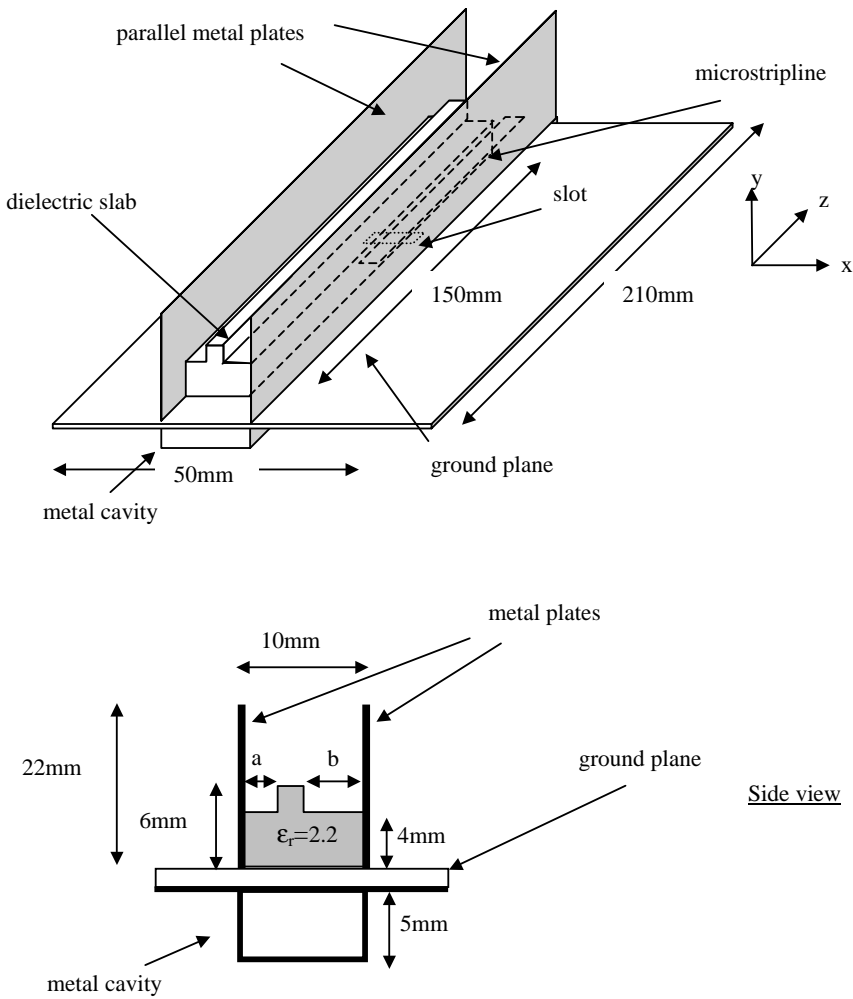
Fig. 10.20   Configuration of the leaky-wave DRA with an asymmetric inverted-T shaped NRD guide.
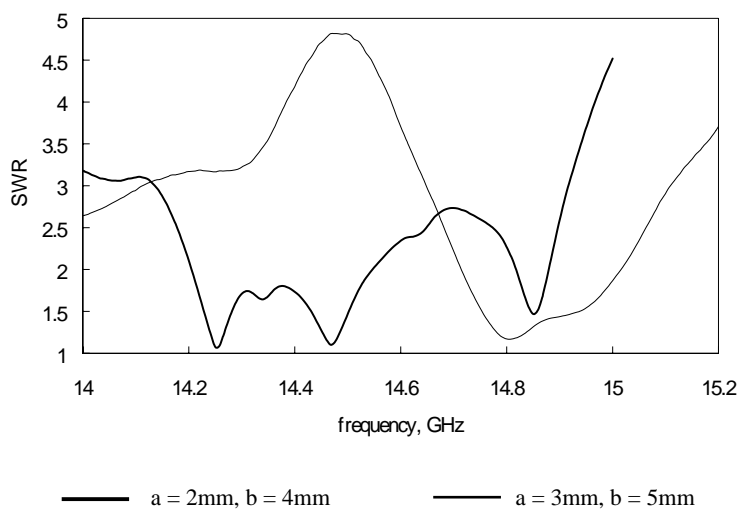
Fig. 10.21   Measured SWR against frequency.
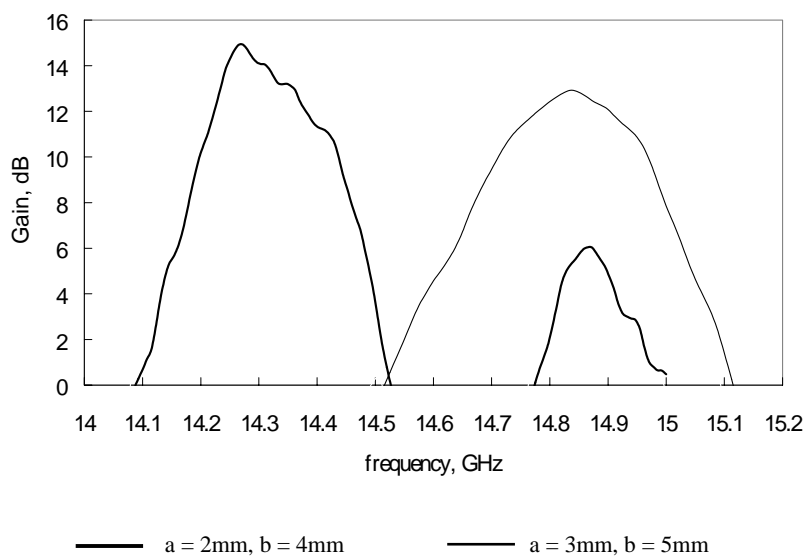
Fig.10.22   Measured gain against frequency.

E-plane   H-plane

——— co-polarisation   ——— cross-polarisation   10dB/div.
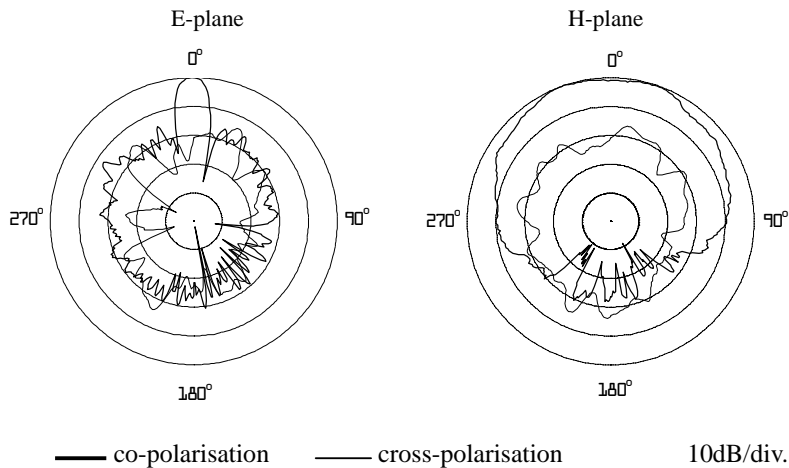
Fig. 10.23   Measured radiation pattern at centre frequency.

Table 10.2   Characteristics of a leaky-wave DRA with an asymmetric inverted T-shaped dielectric slab

Configuration		Impedance Bandwidth	Gain Bandwidth	Max. Gain	Beamwidth		Centre frequency, f_o
A	b				E-plane	H-plane	
0mm	0mm	3.5%	0.8%	16.2dBi	12°	72°	13.8GHz
2mm	4mm	2.5%	1.1%	15.2dBi	11°	75°	14.3GHz
3mm	5mm	2.1%	1.8%	13.0dBi	12°	80°	14.8GHz

10.3.1.2   Summary and discussion

A leaky-wave DRA based on an asymmetric inverted-T-shape NRD guide was studied. By applying two unequal perturbations on the NRD guide, the gain bandwidth can be increased substantially. Table 10.2 shows the characteristics of the antenna. Although the impedance bandwidth is slightly decreased, the overall usable bandwidth is enhanced as the gain bandwidth is increased significantly by about 100%. As mentioned before, the perturbation will make the operating frequency shifting upward.

10.3.2   Using Staircase-shaped Dielectric Slab

In this section, an antenna based on a staircase-shaped NRD guide is studied [38]. It will be demonstrated that this antenna can achieve a gain bandwidth of 2.2%, which is 2.75 times of the bandwidth of a leaky-wave DRA with a rectangular dielectric slab. Moreover, this leaky-wave antenna gives an impedance bandwidth of 12%

and a gain of about 16dBi. With a flared horn attached to the open end of the antenna, the H-plane beamwidth can be adjusted.

The configuration of the staircase-shaped NRD antenna is shown in Fig. 10.24. For comparison, an experiment for another antenna without a flared horn was carried out, as shown in Fig. 10.25.

Top view   Side view
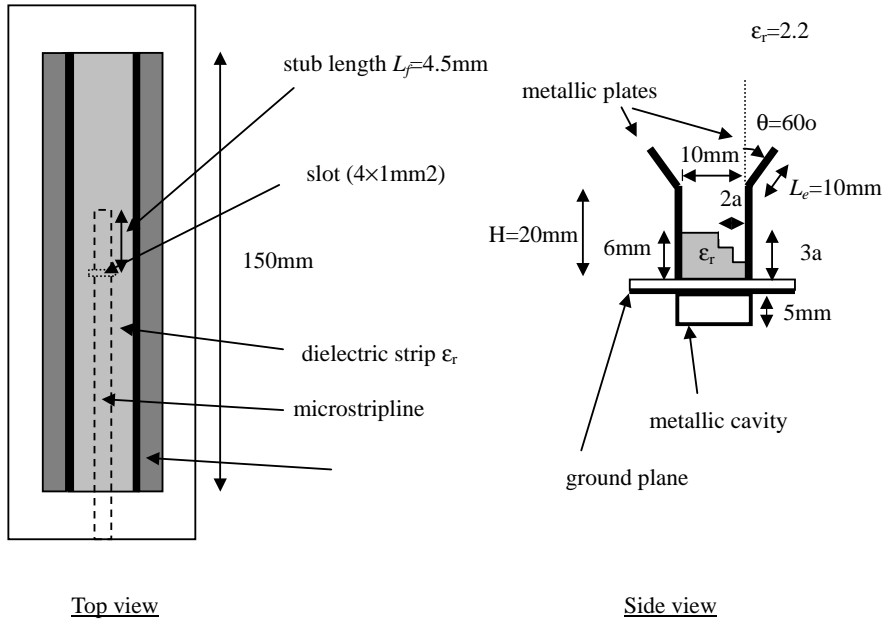
Fig. 10.24   Configuration of leaky wave antenna based on staircase-shaped image NRD guide with flared horn (from [38], reprinted with permission from IEE).
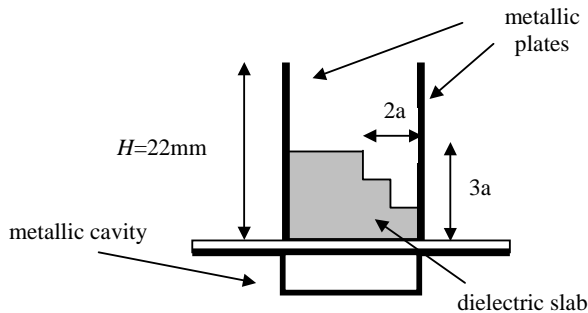
Fig. 10.25   Side view of staircase shaped image NRD antenna with no flared horn (from [38], reprinted with permission from IEE).

10.3.2.1   Experimental results

The measured SWRs are shown in Fig. 10.26. It is found that the antenna with staircase-shaped NRD guide achieves the maximum impedance bandwidth of 9.6% with centre frequency at 14.3GHz. For the antenna with a flared horn, its impedance bandwidth is slightly increased to be 12%. Fig. 10.27 shows the measured antenna gain of each antenna in the broadside direction. Both antennas achieve the maximum gain of 15.8dBi. It should be noted that, the measured values of 3-dB gain bandwidth of the antennas shown in Fig. 10.24 and Fig. 10.25 are 2.7% and 2.2%, respectively. The ordinary one with a rectangular NRD guide has only 0.8% gain bandwidth.
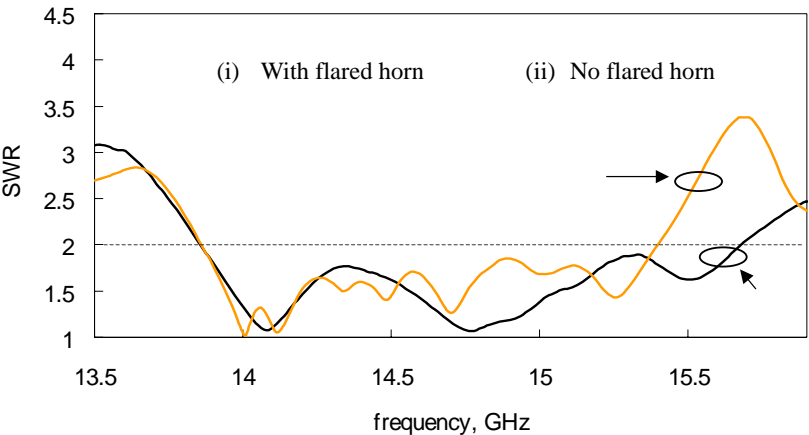
Fig. 10.26   Measured SWR of staircase shaped leaky-wave DRAs (from [38], reprinted with permission from IEE).

Measured radiation patterns of the two proposed antennas are shown in Fig. 10.28. They all radiate strongly in the broadside direction. In the E-plane, both antennas exhibit a 3dB bandwidth of about 10° and sidelobes at least 15dB below the main beam. In the H-plane, the beamwidths are about 71° and 94° for the antennas shown in Fig. 10.24 and Fig. 10.25 respectively. It shows that the flared horn can reduce the H-plane beamwidth. Moreover, both antennas offer a symmetric radiation pattern about the broadside direction. In addition to the measured result discussed above, more results were obtained by adjusting the dimensions of the two antennas. They are summarised in Table 10.3.
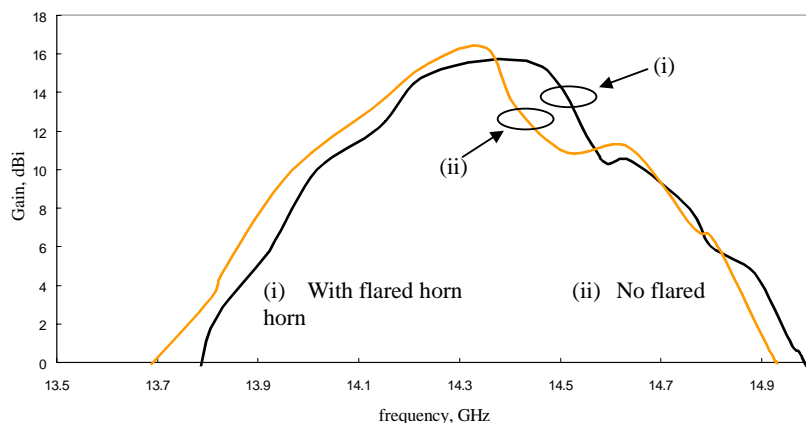
Fig. 10.27 Measured antenna gain of staircase shaped leaky-wave DRAs (from [38], reprinted with permission from IEE).

Table 10.3 Parametric study of the staircase-shaped leaky-wave DRA

Configuration			Impedance Bandwidth	Gain Bandwidth	Max. Gain	Beamwidth		Centre frequency
	H	L_e	θ				E-plane	H-plane	
I	20mm	0mm	0°	10.2%	1.9%	15.2dBi	11°	90°	14.3GHz
II	22mm	0mm	0°	9.6%	2.2%	15.8dBi	10°	94°	14.3GHz
III	20mm	10mm	60°	12.0%	2.7%	15.8dBi	10°	71°	14.4GHz
IV	22mm	10mm	60°	10.5%	2.4%	15.6dBi	10°	73°	14.4GHz
V	15mm	32mm	30°	12.0%	1.0%	10.2dBi	21°	73°	14.7GHz

10.3.2.2   Discussion

As shown in Table 10.3, the configurations of cases I and II are only different in height H. This result is similar to that described in Section 10.2.1.2. The optimum antenna gain (15.8dBi) can be obtained by using parallel plates of height 22mm ($\sim 1.05\lambda_o$).

Moreover, case III shows that the flared horn benefit to a wider antenna gain bandwidth than that of the one has no flared horn (case I). Also, it offers 1.42 times more gain bandwidth than that of the case I. Besides, it is found that the highest antenna gain of 15.8dBi is obtained in case II and III. It may be explained by the same vertical height of the parallel plate producing the same antenna gain. Since the height H of the parallel plate is one of the parameters to control the antenna gain,

the same effective height should produce the same antenna gain.

Considering the case III, IV, and V that have flared horns, it is found that the vertical portion of the parallel plate is also a factor affecting the maximum obtainable gain and gain bandwidth. If $H = 22$mm (case IV) is selected instead of $H = 20$mm (case III), the maximum gain decreases from 15.8dBi to 15.6dBi. Furthermore, its 3-dB gain bandwidth is 0.4% less than that of case III. More significantly, the measured results given from case V are much worse than case IV. Its maximum gain is only 10.2dBi and gain bandwidth is 1.0% only. It shows that the vertical portion $H = 20$mm is an optimum value for the highest gain and the widest gain bandwidth. It is also shown that the flared horn can reduce the H-plane 3-dB beamwidth by about 20°.

10.4   CONCLUSION

The development of leaky-wave DRAs has been presented in this chapter. This class of antennas is simple in structure, easy in production and efficient in performance. It has high and extensive potential in to many wideband wireless applications.

E-plane   H-plane

(a)

(b)

——— co-polarisation   ——— cross-polarisation   10dB/div.
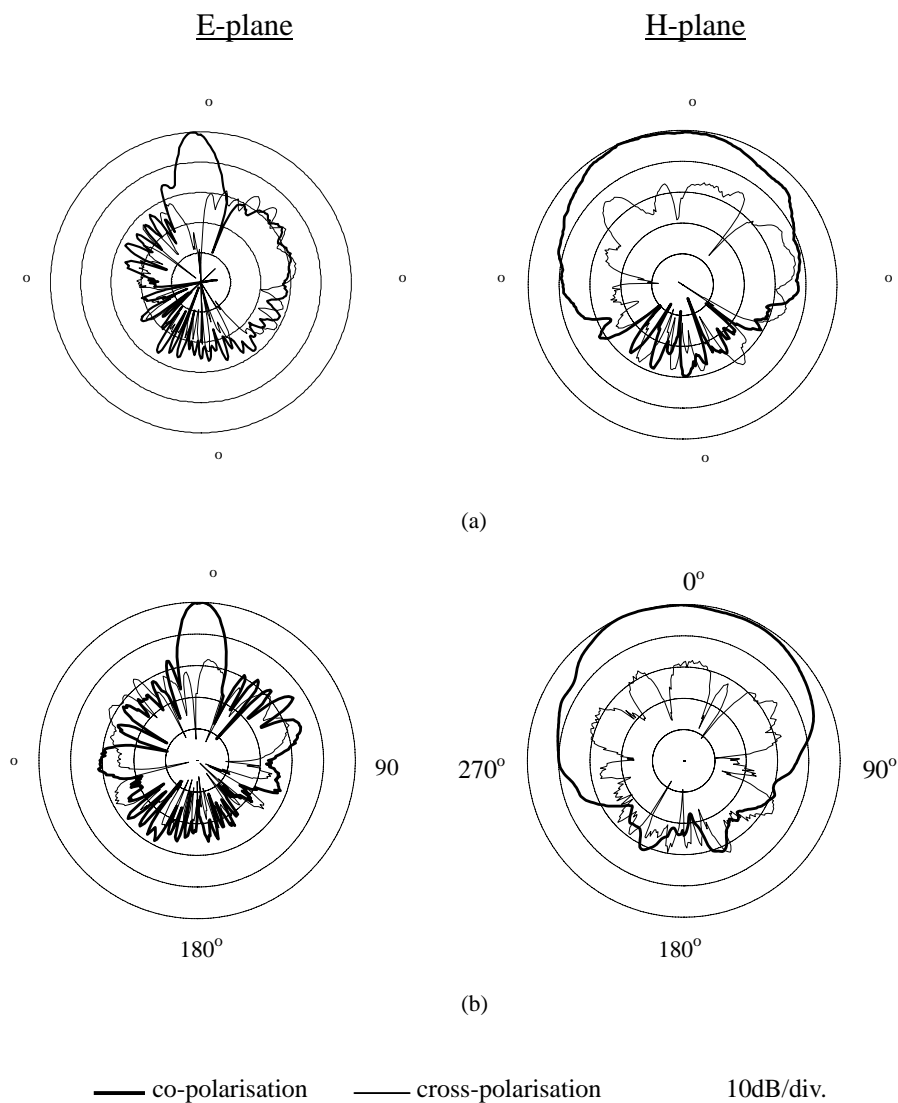
Fig. 10.28   (a) Measured radiation pattern of the antenna with flared horn:
(b) Measured radiation pattern of the antenna without flared horn.
(from [38], reprinted with permission from IEE).

ACKNOWLEDGEMENT

REFERENCES

[1]　R. BEKKERS and J. SMITS: 'Mobile telecommunication: Standards, Regulations, and Application' Artech House Publishers, chapt. 2, 1999

[2]　P. BEDELL: 'Cellular/PCS Management', McGraw-Hill, chapt. 27, 1999

[3]　R. WATERHOUSE: 'Small microstrip patch antenna', *Electron. Lett.*, **31**, pp. 604-605, 1995

[4]　R. CHAIR, K.M. LUK and K.F. LEE: 'Small dual patch antenna', *Electron. Lett.*, **35**, pp. 762-764, 1999

[5]　K.T. LO: 'Miniature aperture-coupled microstrip antenna of very high permittivity', *Electron. Lett.*, **33**, pp. 9-10, 1997

[6]　R. CHATTERJEE: 'Dielectric and dielectric-loaded antennas' *Research Studies Press, Lechworth, UK*, 1985

[7]　Y. SHIAU: 'Dielectric rod antennas for millimetre-wave integrated circuits' *IEEE Trans. Microwave Theory Tech.*, **24**, pp. 869-872, 1976

[8]　R.E COLLIN and F.J. Zucker, 'Antenna Theory', **1** and **2**, McGraw-Hill, New York, 1969

[9]　R.A. KRANENBRUG and S.A. LONG: 'Microstrip transmission line excitation of dielectric resonator antennas', *Electron. Lett.*, **24**, pp. 1156-1157, 1988

[10]　K.W. LEUNG, K.Y. CHOW, K.M. LUK and E.K.N. YUNG: 'Excitation of dielectric resonator antenna using a soldered-through probe', *Electron. Lett.*, **33**, pp. 349-350, 1997

[11]　J.T.H. ST. MARTIN, Y.M.M. ANTAR, A.A. KISHK and A. ITTIPIBOON: 'Dielectric resonator antenna using aperture coupling', *Electron. Lett.*, **26**, pp. 2015-2016, 1990

[12]　S.M. SHUM and K.M. LUK: 'Characteristics of dielectric ring resonator antenna with an air gap' *Electron. Lett.,* **30**, pp. 277-278, 1994

[13]　T. YONEYAMA and S. NISHIDA: 'Nonradiative dielectric waveguide for millimeter-wave integrated circuits', *IEEE Trans. Microwave Theory Tech.*, **29**, pp. 1188-1192, 1981

[14]　T. YONEYAMA: 'Nonradiative dielectric waveguide', *Infrared and Millimeter Waves*, vol. 11, K.J. Button (Ed.), chapt. 2, Academic Press, Orlando, FL, 1984

[15]　A.A. OLINER: 'New leaky wave antennas for millimeter waves', *International Symposium on Antenna and Propagation*, ISAP Digest, pp. 89-92, 1985

[16]　A. SANCHEZ and A.A. OLINER: 'Accurate theory for a new leaky-wave antenna for millimeter waves using non-radiative dielectric waveguide' *Radio Sci.*, **19(5)**, pp. 1225-1228, 1984

[17] A.A. OLINER, S.T. PENG and K.M. SHENG: 'Leakage from a gap in NRD guide', *Dig. IEEE Int. Microwave Symp.*, pp. 619-622, 1985

[18] T. YONEYAMA, T. KUWAHARA and S. NISHIDA: 'Experimental study of nonradiative dielectric waveguide leaky wave antenna', *Proc. Int. Symp. Antennas Propag.*, 1985

[19] S.J. XU, X.Y. ZENG, K.WU and K.M. LUK: 'Characteristics and design consideration of leaky-wave NRD-guides for use as millimeter antenna', *IEEE Trans. Microwave Theory Tech.*, **46**, pp. 2450-2456, 1998

[20] M. YAMAMOTO and K. ITOH: 'Resonant type leaky-wave antenna using image NRD guide', *Electron. Lett.*, **35**, pp. 857-858, 1999

[21] W.X. ZHANG and L. ZHU: 'New leaky-wave antenna for millimetre waves constructed from groove NRD guide', *Electron. Lett.*, **23**, pp. 1191-1192, 1987

[22] J.A.F. MALHERBE, J.H. CLOETE and L.E. LOSCH: 'A transition from rectangular to non-rectangular dielectric waveguide', *IEEE Trans. Microwave Theory Tech.*, **33**, pp. 539-543, 1985

[23] T. YONEYAMA: 'Properties of guided waves and leaky waves in NRD-guide' *Asia Pacific Microwave Conference*, **1**, pp. 255-263, 1998

[24] S. K. KOUL, *Millimeter wave and optical dielectric integrated guides and circuits*. John Wiley & Sons, chapt. 2, 1997

[25] S. K. KOUL, *Millimeter wave and optical dielectric integrated guides and circuits*. John Wiley & Sons, chapt. 6, 1997

[26] S.D. TARGONSKI and R.B. WATERHOUSE: 'Reflector elements for aperture and aperture coupled microstrip antennas', *IEEE Antennas Propag. Symp*. Dig., **3**, pp. 1840-1843, 1997

[27] S.D. TARGONSKI, R.B. WATERHOUSE, and D.M. POZAR: 'Wideband aperture coupled microstrip patch array with backlobe reduction', *Electron. Lett.*, **33**, pp. 2005-2006, 1997

[28] K.M. LUK, X.Y. ZENG, S.J. XU, and L. YANG: 'Theoretical investigation on the leakage characteristics of modified two-layer NRD guide leaky wave antenna' (To be published in IEEE Trans. Microwave Theory Tech.)

[29] T. YONEYAMA, H. TAMAKI, and S. NISHIDA: 'Analysis and measurement of non-radiative dielectric waveguide', *IEEE Trans. Microwave Theory Tech.*, **34**, pp. 876-882, 1986

[30] T. YONEYAMA, N. TOZAWA, and S. NISHIDA: 'Coupling characteristics of non-radiative dielectric waveguide', *IEEE Trans. Microwave Theory Tech.*, **31**, pp. 648-654, 1983

[31] T. YONEYAMA: 'Millimetre wave integrated circuits using non-radiative dielectric waveguide', *Proceedings of the Yagi Symposium on Advanced Technology Bridging the Gap Between Light and Microwaves*, pp. 57-66, 1990

[32] T. YONEYAMA, S. FUJITA and S. NISHIDA: 'Insulated non-radiative dielectric waveguide for millimetre-wave integrated circuits', *IEEE Trans. Microwave Theory Tech.*, **31**, pp. 1002-1008, 1983

[33] T. YONEYAMA, M. YAMAGUCHI and S. NISHIDA: 'Bends in non-radiative dielectric waveguides', *IEEE Trans. Microwave Theory Tech.*, **30**, pp. 2146-2150, 1982

[34] T. YONEYAMA and S. NISHIDA: 'Non-radiative dielectric waveguide circuit components ', *Int. J. Infrared Millimetre waves*, **4(3)**, pp. 439-449, 1983

[35] T. YONEYAMA, F. KUROKI and S. NISHIDA: 'Design of non-radiative dielectric waveguide filters', *IEEE Trans. Microwave Theory Tech.*, **32**, pp. 1659-1662, 1984

[36] F. KUROKI and T. YONEYAMA: 'Non-radiative dielectric waveguide circuit components using beam lead diodes', *Trans. IEICE (C-I).*, **J-73-C-I(2)**, pp. 71-76, 1990

[37] T. YONEYAMA, N. TOZAWA and S. NISHIDA: 'Loss measurement of non-radiative dielectric waveguide', *IEEE Trans. Microwave Theory Tech.*, **32**, pp. 943-946, 1984

[38] M. T. LEE, K. M. LUK, S. J. XU and E. K. N. YUNG: 'Leaky wave antenna based on image NRD guide with staircase-shaped dielectric slab', *Electronics Letters,* **36**, pp. 1102-1103, 2000

Index